Transactions of the ASME®

Transactions of the ASME, Journal of Turbomachinery (ISSN 0889-504X) is published quarterly (Jan., Apr., July, Oct.) for $100 per year by The American Society of Mechanical Engineers, 345 East 47th Street, New York, NY 10017. Second-class postage paid at New York, NY and additional mailing offices. POSTMASTER: Send address change to Transactions of the ASME, Journal of Turbomachinery, c/o The AMERICAN SOCIETY OF MECHANICAL ENGINEERS, 22 Law Drive, Box 2300, Fairfield, NJ 07007-2300.

CHANGES OF ADDRESS must be received at Society headquarters seven weeks before they are to be effective. Please send old label and new address.

PRICES: To members, $29.00, annually; to nonmembers, $100.00. Add $15.00 for postage to countries outside the United States and Canada.

INDEXED by Applied Mechanics Reviews and Engineering Information, Inc.

Journal of Turbomachinery

Published Quarterly by The American Society of Mechanical Engineers

VOLUME 112 • NUMBER 1 • JANUARY 1990

TECHNICAL PAPERS

ANNOUNCEMENTS

Automotive Research Compressor Experience

R. C. Pampreen
Manager, Advanced Technology,
Williams International,
Walled Lake, MI

The design features and development experience of an advanced automotive gas turbine centrifugal compressor are presented. The compressor was designed with moderately low specific speed, high blade aerodynamic loading, and design point on the choke characteristic. A cascade diffuser was used; a new design approach brought about an unusual performance characteristic. The influence of impeller blade loading on performance is presented. Lessons learned are summarized.

Introduction

Some unusual compressor development results were discovered on a company sponsored automotive gas turbine program at the Chrysler Corporation in the 1970s. The compressor design departed in three significant ways from usual aerospace design practice to meet the requirements of an advanced automotive engine design. The compressor was designed for a static-total pressure ratio of 5.5:1. The design features and the test experience of the compressor are the subjects of this paper.

Compressor Design Requirements

The three design features that differed from usual practice were:

1 moderately low specific speed
2 design point on compressor choke line
3 high aerodynamic blade loading

The specific speed of the compressor was determined from the results of a design study early in the program. Shaft rotational speed at the design point was varied to optimize the engine cycle thermodyanmic efficiency. As design speed was varied, centrifugal compressor specific speed was varied. Included in the review were the turbine work coefficient and AN-squared. The properties of equiaxed MAR-M 246 were used for a duty cycle requirement of 1000 h at maximum power. A major concern was engine acceleration. The majority of the shaft polar moment of inertia was set by the turbine rotor. To minimize inertia, high work coefficient values were considered. Compressor and turbine loss models were employed to account for changes in component efficiency. The study showed that the product of compressor and turbine efficiencies was maximized over a broad range of speeds. From 50,000 to 60,000 rpm, the product varied less than one-half percent. The decision was made to select a design speed of 50,000 rpm. The design specific speed was 79 based on English units and the conventional definition of specific speed as shown in the nomenclature list. This was one percent higher than that of the compressor of the previous engine generation.

This is lower than specific speed values of typical aerospace compressors and even some other automotive compressors. A clearer view on this point can be obtained from the specific speed based on the square root of the product of inlet and exit volume flow rates. This approach takes into account the change in exit conditions as stage pressure ratio increases (Pampreen et al., 1970). This is illustrated in Fig. 1 in a plot that uses polytropic efficiency to level out the effects of stage pressure ratio. The figure was taken from the work of Pampreen (1979), which contains an update of the original plot. The solid points are data taken from compressor tests of this and other Chrysler compressors. The plot clearly shows the low specific speed of the Chrysler compressors relative to other designs.

Putting the design point on the choke line was considered to be a necessary design feature. The automotive engine duty cycle requires a wide range of surge-free, stall-free operation from 50 to 100 percent speed. Acceleration power is provided at 100 percent speed, idle power occurs at 50 percent speed, and city driving power ranges from 50 to 65 percent speed. The regenerative engine operating line crosses the compressor map from near-choke at 100 percent speed to near-surge at 50 percent speed city driving power. To accomplish a wide range of stable operation for this new engine, the design point was placed on the choke characteristic, as shown in Fig. 2. This is

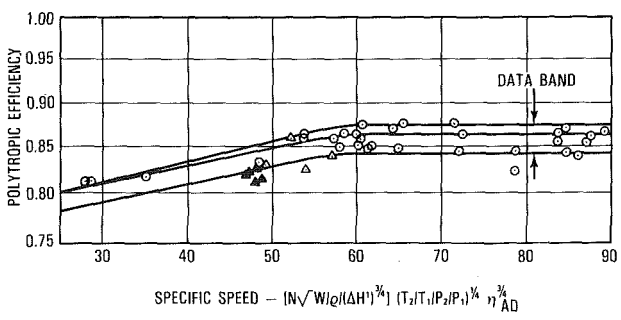

Fig. 1 Single-stage centrifugal compressor specific speed plot

Contributed by the International Gas Turbine Institute and presented at the 34th International Gas Turbine and Aeroengine Congress and Exhibition, Toronto, Ontario, Canada, June 4-8, 1989. Manuscript received at ASME Headquarters January 13, 1989. Paper No. 89-GT-61.

Table 1 Impeller width/exit-tip-radius ratio values from various sources

SOURCE	RATIO
CHRYSLER 4:1 PR COMPRESSOR	0.732
CHRYSLER 5.5:1 PR COMPRESSOR, RADIAL	0.452
RODGERS, REFERENCE 5	0.695
PAMPREEN, REFERENCE 3	0.885

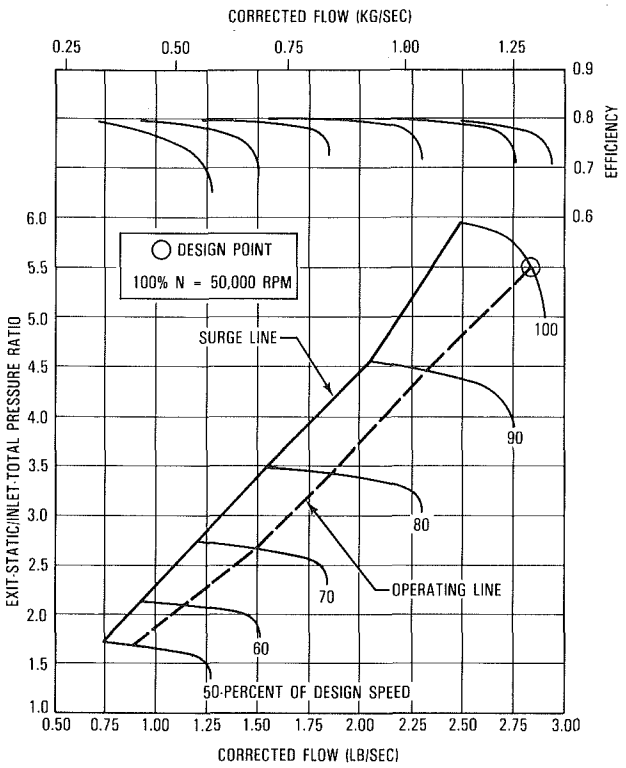

Fig. 2 Performance goal for advanced automotive compressor

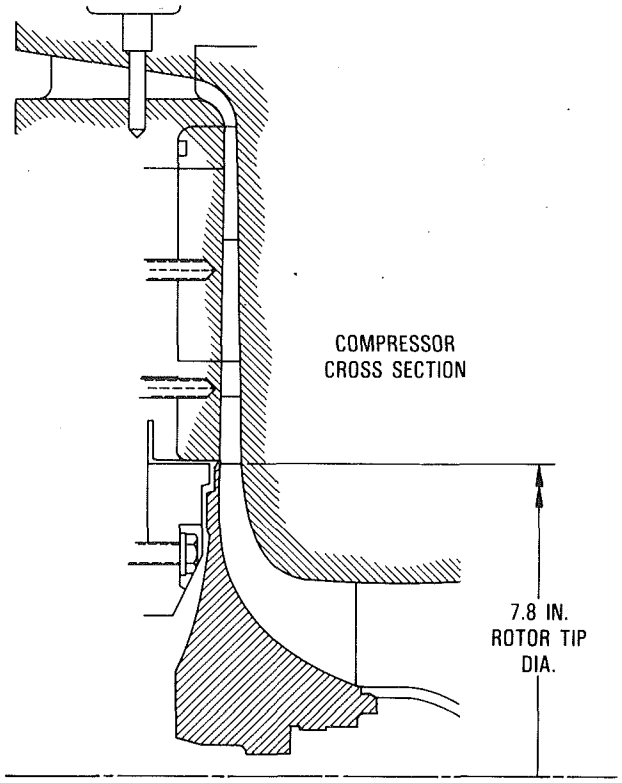

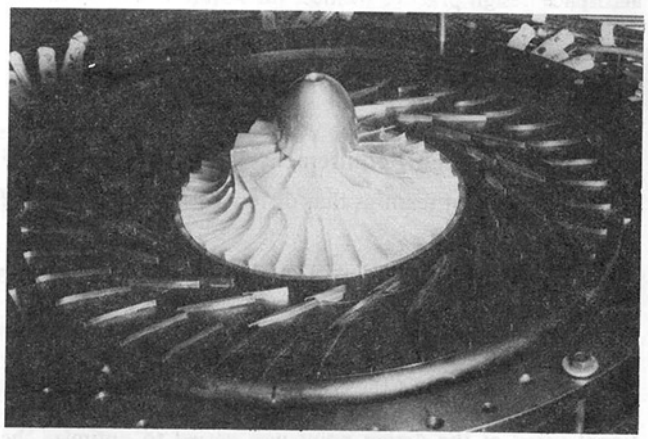

Fig. 3 Compressor flow path

not unusual for multistage axial compressors, but it is very unusual for centrifugal compressors.

Engine accleration drove the compressor rotor to be designed with a short axial width. Compressor work dictated rotor tip radius. To minimize rotor polar moment of inertia, axial width was reduced to half of the value normally expected in impeller design. Table 1 shows some values of impeller dimensionless widths based on tip radius from impeller geometries reported in the literature. Note the small ratio of axial width to impeller tip radius for this rotor. This had the effect of doubling blade aerodynamic loading with the use of typical blade count and had a major impact on compressor performance.

Compressor Design

The compressor was designed for a mass flow of 1.3 kg/s at an exit-static/inlet-total pressure ratio of 5.5:1. The estimated performance is shown in Fig. 2. The performance estimate was obtained from impeller and diffuser loss and stall models. The flow path is shown in Fig. 3. It consists of the rotor, a vaneless space, and a three-row cascade radial diffuser. The front view of the diffuser is shown in Fig. 4. The design point inlet Mach number to the first row was 0.91.

The diffuser vane arrangement is different from those reported by Pampreen (1972). In that reference, the original diffuser designs were configured with twice the number of

Nomenclature

H' = ideal total enthalpy, cal/kg, as used in Fig. 1
N = rotational speed, rpm
N_s = conventional specific speed $= N\sqrt{W/\rho}/(\Delta H')^{3/4}$
P = pressure, kPa
T = temperature, K
W = mass flow, lbsm/sec
Wm = midchannel relative velocity, m/s
ΔW = blade surface velocity difference
η = efficiency $= \Delta H$ (ideal)/ΔH (actual)
ρ = inlet stagnation density, lbsm/cu. ft.

Subscripts

1 = inlet
2 = exit

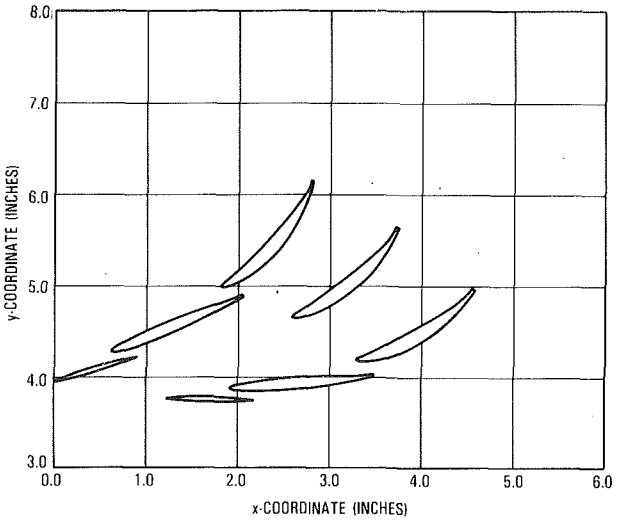

Fig. 4 Cascade diffuser configuration of automotive engine compressor

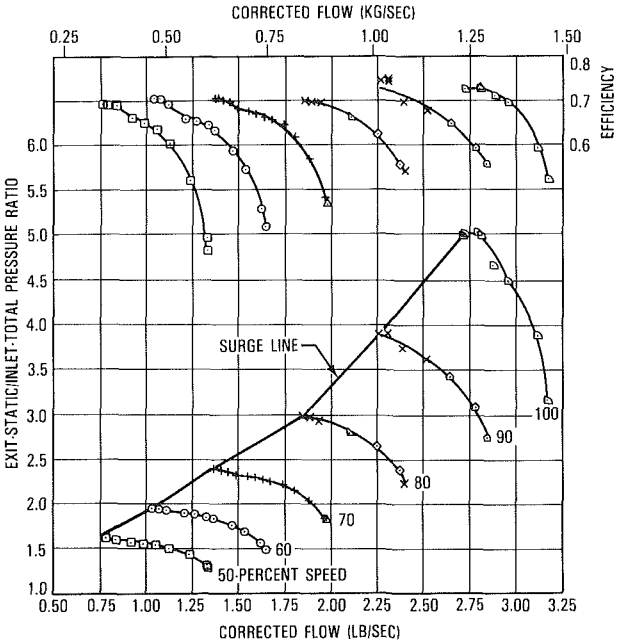

Fig. 5 First test results

vanes in the second row as in the first row. The vanes were arranged so that the wakes of the first row would pass through the vanes of the second row. Test results, however, showed that the second-row vane should be placed close to the trailing edge of the first-row vane. It was also felt that the intermediate vane should be eliminated so that there would be an unobstructed two-row channel as indicated in Fig. 4. To do this and maintain the required solidity based on cascade data, the chord of the second-row vane had to be doubled relative to the lengths of the original designs with twice as many vanes in the second row. Futhermore, since the first-row vanes were performing the function of the semi-guided region of a channel diffuser, it was felt that the chord length should be determined by having the throat be bounded by the leading edge of one vane and the trailing edge of the adjacent vane, again as shown in Fig. 4. This was a major departure from the original designs of Pampreen (1972), for the first-row vane chord length was now much smaller than that of the second-row vane. In this configuration the second row now plays a role closer to the throat and earlier in the diffusion process than it

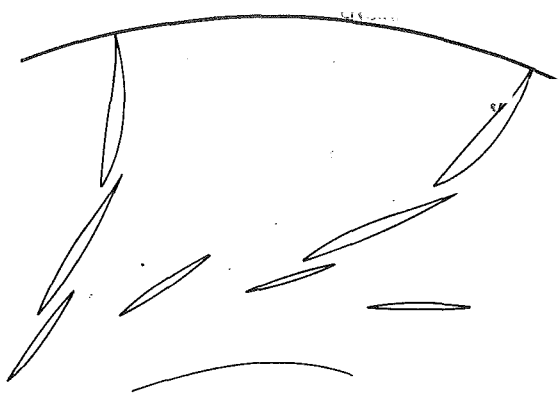

Fig. 6 Low-solidity cascade diffuser for automotive engine compressor

did in previous designs. In the earlier designs, the first row performed the role of throat and partial diffusing channel. In this configuration, it is principally preparing the flow for the second row, which takes on a more prominent role in the diffusion process.

Test Results

Testing was conducted on a compressor test rig. The uncertainty in static pressure measurement varied from 0.1 percent to 0.9 percent of the value measured. The temperature uncertainty was $\pm 0.5°C$. Mass-flow measurement uncertainty was within ± 0.5 percent, and rotational speed uncertainty was within 0.3 percent of the measured values. At 20:1 odds, all values measured are believed to be within the uncertainties stated. This is an estimate based on uncertainties of data recording and instrument errors.

The performance of the first test build was very disappointing. The performance is shown in Fig. 5. The flow is 12 percent high, pressure ratio was badly missed, and the speedline characteristics are very strange looking. In subsequent tests, the rotor leading edge was bent closed, and the first-row diffuser vanes were rotated closed by 2 deg. These modifications achieved more rational looking characteristics. In the course of the work a number of changes were made to vane-row solidity in the radial diffuser. The best performance was achieved with the vane configuration shown in Fig. 6. This extremely low solidity produced the performance shown in Fig. 7.

All the changes to the diffuser, however, did not achieve the pressure ratio goal of the program. It was assumed that rotor blade loading was adversely affecting performance. The basis for this is the relatively short width of the rotor as illustrated in Table 1. Blade loading calculations made with shroud static pressure data revealed a large loading on the full blades ahead of the splitter leading edge position. The leading edge position of the splitter was moved forward to lower the loading, and another rotor was fabricated. The test results are shown in Fig. 8. Compared to Fig. 7, the principal changes in performance are small increases in efficiency and choke flow at 90 and 100 percent speeds.

At this point, it was clear that only a major change in rotor design would bring about the design pressure ratio. Detailed analytical reviews were made of the loadings of four different rotors. From these reviews, a correlation was developed that related rotor exit deviation angle to blade suction surface diffusion. Large blade loading produces large ratios of maximum suction surface velocity to exit velocity. This implies the possible generation of large amounts of boundary layer blockage, which could promote excessive deviation angle at the rotor exit. This led to the correlation presented by Pampreen and Musgrave (1978), which related deviation angle coefficient to suction-surface diffusion ratio.

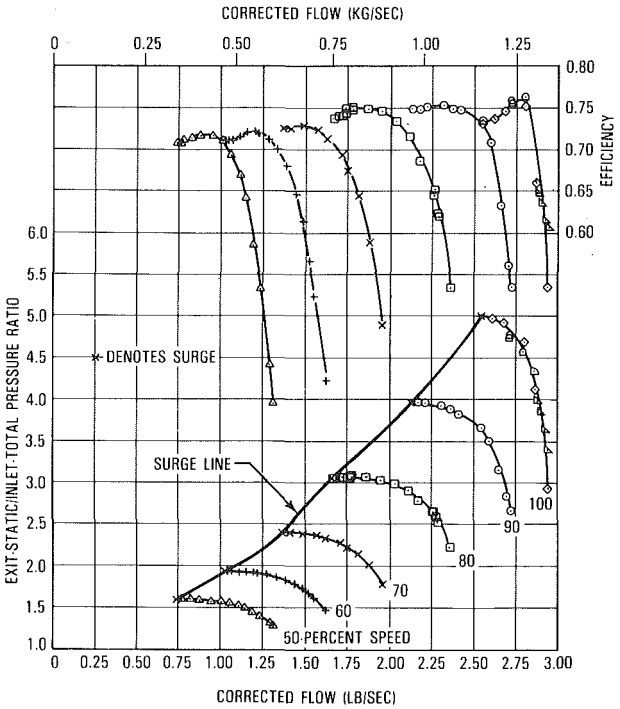

Fig. 7 Best performance with original impeller

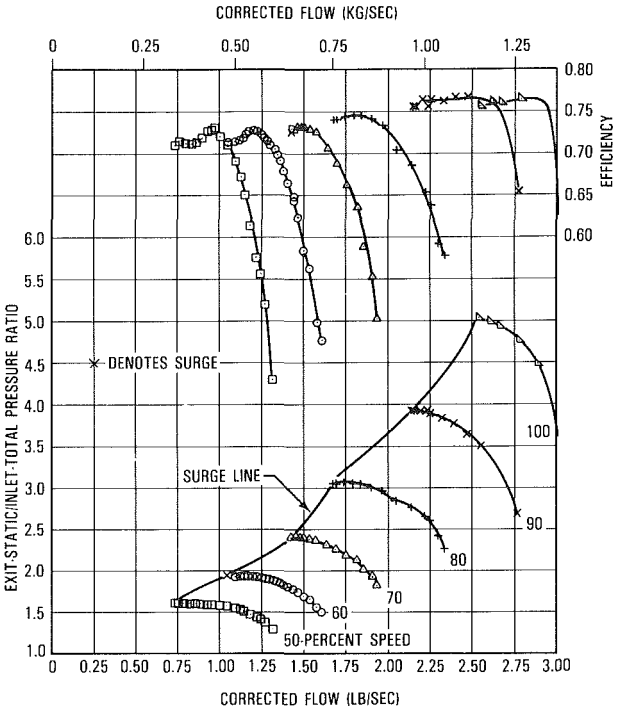

Fig. 8 Performance with rotor with extended splitter leading edge and same diffuser as used in configuration for Fig. 7

The loadings of the rotor with the two splitter leading edge positions are shown in Fig. 9. The solid line shows the loading of the original rotor; the dashed line shows the loading with the lengthening of the splitter. This change made a much needed reduction in blade inlet loading. The increase in rotor choke flow at 90 and 100 percent speeds as shown in Fig. 8 implies a reduction in rotor blockage. The large pressure difference across the blade clearance due to the loading possibly causes shroud blockage buildup as a result of leakage through the inducer clearance space. At the rotor exit, large loading may increase deviation angle through leakage in the rotor tip

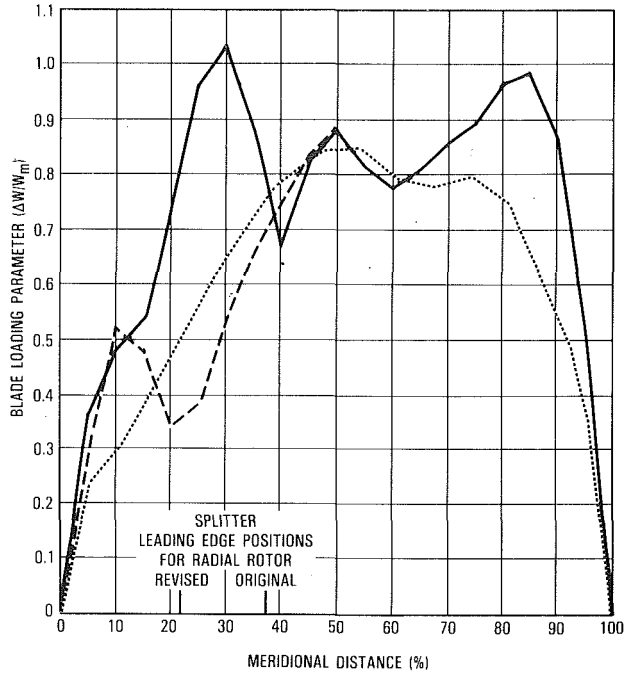

ORIGINAL ROTOR: RADIAL BLADED, 16 FULL BLADES, 16 SPLITTERS
SAME AS ORIGINAL EXCEPT CHANGE OF SPLITTER LEADING EDGE LOCATION
30-DEGREE BACKSWEPT ROTOR, 24 FULL BLADES
W_m MIDCHANNEL VELOCITY
Δ DIFFERENCE BETWEEN PRESSURE AND SUCTION SURFACE VELOCITIES

Fig. 9 Variation of shroudline blade loading among three rotor designs

clearance space. To reduce these effects, a third rotor was designed with the loading shown by the dotted line. The rotor had 30 deg of backsweep. This helped reduce the dimensionless loading parameter because of the increase in relative velocity at the rotor exit that naturally comes about in this type of rotor. Even though the inlet and exit loading peaks were eliminated by this redesign, the midblade loading is still very high.

As a check on the severity of the blade loading, comparison was made to loadings published in the open literature. Loadings from Rogers (1976) and Kenny and Morris (1968) are shown in Fig. 10. These are loadings from rotors with stage design pressure ratios of 5–6:1. The loadings of the automotive rotors are 2–3 times as large. This serves to illustrate the technology push of the impellers in this program.

The test results with the backswept rotor are shown in Fig. 11. The goal pressure ratio of 5.5:1 has been achieved. The 100 percent speedline characteristic is fuller than that of Fig. 8, but efficiency is down about 2 points. At all other speeds, there is a kink in the pressure ratio characteristic, and the kink is reflected in the efficiency plots.

The radial diffuser is responsible for the unusual pressure ratio characteristics. Static pressure data at the exit of each blade row showed that the pressure ratio characteristic was caused by the static pressure recovery characteristic of the first row. Like the compressor map, the data showed the presence of two choke lines. As the exit throttle was closed and the compressor was brought out of deep choke, there appeared another choke characteristic before maximum pressure ratio was achieved. The data did not reveal how two choke characteristics could be generated. However, the diffuser geometry provides a clue.

In a channel diffuser, a shock structure occurs in the vane channel downstream of the throat. As the test rig throttle is closed, the shock moves forward to the throat. The loss across the system decreases and compressor pressure ratio increases. Eventually the shock is disgorged as mass flow is reduced. The walls of a channel diffuser are continuous. The cascade flow

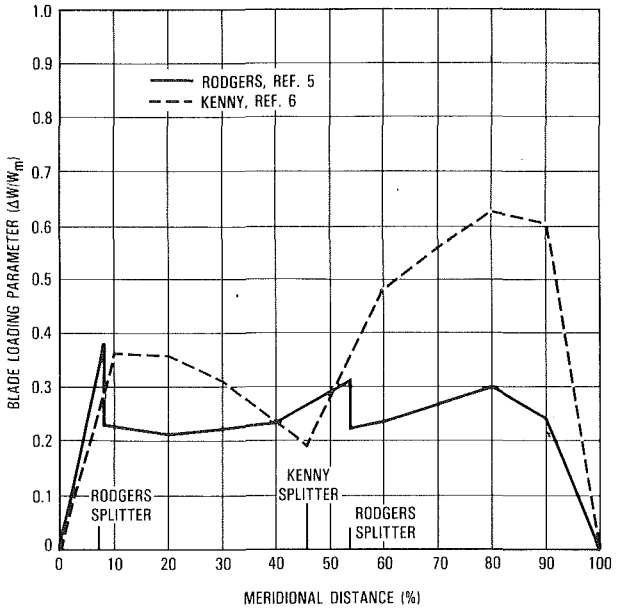

Fig. 10 Comparison of blade loadings reported in the literature

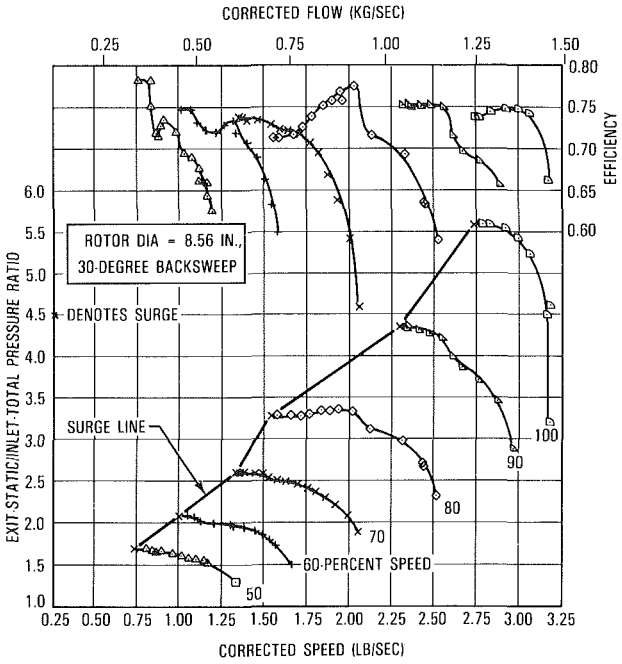

Fig. 11 Performance with backswept impeller

path is discontinuous. In previous designs (Pampreen, 1972) the first-row vanes were about twice as long as the second-row vanes, and the performance characteristics were typical of centrifugal compressors. In this design, the first-row vanes were only 0.6 times as long as the second-row vanes. Because of this, as Fig. 6 shows, the second-row vanes protrude into the flow field of the first-row vanes. It is possible that the discontinuous flow path influenced the passage of the shock such that a discrete change of shock position and structure occurred to produce the kink in the speedline characteristics. If the first-row vane were allowed to operate in the absence of the other rows, there would be no kink in the performance characteristics, based on the experience with the diffusers discussed by Pampreen (1972). Consequently, it is possible that the interference of the second rows in this design caused the kink in the pressure ratio characteristics. Therefore it could be concluded that the relationship between the lengths

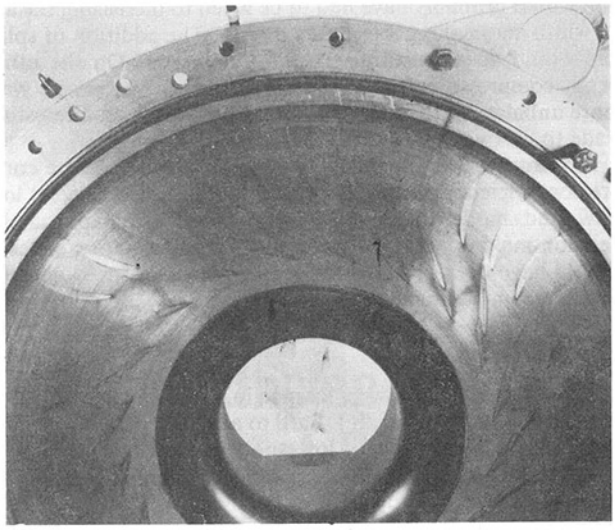

Fig. 12 Lampblack pattern of shock structure

of the first and second rows should be as indicated in the designs shown by Pampreen (1972).

Figure 12 shows a lampblack picture of the shock pattern in the diffuser. The shock begins on the pressure surface of the first-row vane and terminates on the suction surface of the second-row vane. Note that the shock is positioned well back of the throat. This is a pattern that was obtained frequently in the test program. On one test, lampblack was injected at the high-flow side of a pressure jump at the juncture of the double characteristic. The same type of pattern was observed. It is not shown here because of poor photographic reproduction.

As a last consideration, the influence of the rotor might be questioned. While not shown in the compressor maps for the sake of brevity, the work coefficient data (enthalpy rise/tip speed squared) showed a consistent linear variation with flow for all diffuser configurations and rotor configurations.

Commentary

The program ended at this point without completing the development of the compressor. The next step would have been to redesign the diffuser to conform to the configurations developed by Pampreen (1972). Figure 11 shows substantial range, but the diffuser redesign is needed to clean up the pressure ratio characteristics. Whether the efficiency would have increased very much is speculative. The data points show signs of speedline peaks that might vary from 74–76 percent efficiency. The goal was to achieve 79 percent at 5.5:1 pressure ratio. From the results shown in Fig. 11, the goal was missed by 4 points. The polytropic efficiency corresponding to the goal adiabatic efficiency is 84 percent, which occurs on the upper band of the data in Fig. 1 at the specific speed of 48 shown for the Chrysler compressors. On this basis, it appears that the goal would have been achievable.

To achieve the goal, however, it appears that more than diffuser redesign would be necessary. Significant changes in rotor blade loading were needed to attain the target pressure ratio. Splitters added to the rotor would reduce the loading. However, the blade spacing at the blade root would dictate the position of the splitter leading edge. The spacing at the blade root at 30 percent meridional distance was only 0.25 in. (6.35 mm). Considering machining constraints, the most likely position for inserting a splitter was the 50 percent meridional distance. Figure 9 shows that the most desirable position would be at least at the 30 percent position. At the 50 percent position, the forward loading would still be high. The implication here is that, if reduction in blade loading would have been absolutely necessary to meet the target efficiency, considera-

tion would probably have had to be given to increasing the axial width and making a trade on inertia. The addition of splitters would also constitute a trade on inertia. On the other hand, compressor efficiency provides the drive turbine with more unbalanced torque. This would have been an interesting trade to carry out experimentally.

In retrospect, it should have been observed that the compressor efficiency goal of 79 percent had to be achieved at low flow and moderately low specific speed. Perhaps at the decision-making stage early in the program, more concern should have been given to the level of specific speed and the possible compressor development risk.

Conclusion

A number of lessons were learned in the design and development of this compressor. It is hard to achieve nearly 80 percent efficiency at a moderately low specific speed. It is hard to achieve this goal with peak rotor blade loading parameters of 0.8–1.0. For the cascade diffuser, trying to make the first-row vane a kind of slat for the second row did not work. It is obvious that the first-row solidity should be sufficient to have the choke characteristic dictated by the first row alone and not shared by the second row.

Acknowledgments

The author expresses his thanks to the Chrysler Corporation and to Mr. Bud Mann, who was program manager for the company-sponsored program, for permission to present this material. At the time this work was going on, Mr. George Ball was Manager of the Research Department, and Mr. Chuck Wagner was program manager for the Chrysler/NASA Upgraded Engine Program. All of these men provided their insight and experience into the requirements for the automotive gas turbine engine.

Permission to write and present the paper was also given by Williams International.

References

Kenny, D. P., and Morris, R. E., 1968, "High Pressure Ratio Centrifugal Compressors for Small Gas Turbine Engines," presented at the 31st Meeting of the Propulsion and Energetics Panel of AGARD, "Helicopter Propulsion Systems," pp. 6-1–6-47.

Pampreen, R. C., Firman, P. A., Erwin, J. R., and Dawson, R. W., 1970, "A Small Axial-Centrifugal Compressor Matching Study Program," USAAVLABS Technical Report 70-34.

Pampreen, R. C., 1972, "The Use of Cascade Technology in Centrifugal Compressor Vaned Diffuser Design," ASME *Journal of Engineering for Power*, Vol. 94, No. 3, pp. 187–192.

Pampreen, R. C., and Musgrave, D. S., 1978, "A Method of Calculating the Slip Factor of Centrifugal Compressors From Deviation Angle," ASME *Journal of Engineering for Power*, Vol. 100, No. 1, pp. 121–128.

Rodgers, C., 1976, "Impeller Stalling as Influenced by Diffusion Limitations," in: *Centrifugal Compressor and Pump Stability, Stall and Surge*, proceedings of the 1976 Gas Turbine Conference, ASME, New York.

Wagner, C. E., and Pampreen, R. C., 1979, "Conceptual Design Study of an Improved Automotive Gas Turbine Powertrain—Final Report," C. E. Wagner and R. C. Pampreen, eds., Chrysler Corporation, NASA CR-159672.

Secondary Flows and Vortex Motion in a High-Efficiency Backswept Impeller at Design and Off-Design Conditions

C. Hah
GE Research and Development Center,
Schenectady, NY

H. Krain
DFVLR-Institut für Antriebstechnik,
Köln, Federal Republic of Germany

The three-dimensional viscous flowfield of a 4.7:1 pressure ratio backswept impeller was studied experimentally and numerically by using laser velocimetry and an advanced three-dimensional viscous code. The impeller was designed by a CAD method, and a maximum rotor efficiency of 94 percent was achieved. Both the experimental and the theoretical approach revealed comparatively smooth impeller discharge velocity profiles at all three operating conditions (design, choke, and near surge) differing widely from the well-known jet/wake-type flow pattern. The three-dimensional viscous code was used for detailed flowfield studies, i.e., secondary flows; vortex motion and tip-clearance effects were analyzed at design and off-design conditions. The comparison of experimental and numerical results indicates that the tip-clearance effect should be properly modeled to predict the impeller flow pattern properly and that optimum shape of rotor exit flow pattern can be obtained by controlling the swirling vortex motion.

Introduction

The requirements in small aircraft engine design for increasingly higher pressure-ratio centrifugal compressors with sustained aerodynamic efficiency necessitate a better understanding of the basic centrifugal compressor aerodynamics. Both the well-developed optical measurement techniques and today's advanced three-dimensional viscous calculation methods are useful tools for reaching additional progress in this field.

Flow range and efficiency of centrifugal compressors are believed to be strongly determined by the impeller/diffuser interactions. It is well known that the jet/wake type flow profiles at the impeller exit cause highly unsteady flows in the absolute frame with significant flow angle fluctuations (Eckardt, 1976; Lapworth et al., 1988). These fluctuations are generally accompanied by a strong incidence distribution across the diffuser height (Krain, 1981). Therefore, a rather smooth impeller discharge flow pattern should contribute to a reduction of the overall aerodynamic losses of centrifugal compressor stages. Recent experimental studies showed impeller discharge flow profiles quite different from the traditional jet/wake pattern (Hamkins and Flack, 1987; Krain, 1988) indicating that a distinct shaping of the impeller discharge velocity profile should be possible by using analytical tools capable of predicting correctly the complex three-dimensional rotor flowfield. In recent years various studies have been made to calculate the impeller flowfield with full three-dimensional flow codes (Moore, 1980; Rhie et al., 1985; Dawes, 1988; Hah et al., 1988). However, most calculations were carried out for modest pressure ratios and conventional impeller designs showing the traditional discharge flow pattern. In this paper a three-dimensional viscous flow code was applied to a modern backswept impeller having a fully three-dimensional blade geometry, a 4.7:1 rotor pressure ratio, a high aerodynamic efficiency, and smooth impeller discharge velocity profiles. The experimental and numerical procedures are described. Numerical results are compared with measured data at three operating conditions.

Test Rig and Instrumentation

The test rig was equipped with a 30 deg backswept impeller and a vaneless diffuser of constant area, which ensured a wide operating range. The rotor used had 24 full blades and its tip diameter was 400 mm (Fig. 1). The experimental investigations were primarily concerned with optical measurements in the rotor area. For these tests the Laser-Two-Focus velocimeter developed at DFVLR (Schodl, 1980) was used to analyze the three-dimensional flowfield inside the rotating passages. This measurement system gives information about the mean absolute velocity vector and its turbulent components. The components of the relative velocity vector are easily calculated from the local absolute velocity vector and the corresponding circumferential velocity. Measurement accuracy is satisfactory. Generally the uncertainty of flow angle measurements is less than ± 1 deg and the error in mean velocity measurements is below ± 1 percent.

Measurements were performed for 70, 90, and 100 percent shaft speed. For each speed, three mass flow rates—located

Contributed by the International Gas Turbine Institute and presented at the 34th International Gas Turbine and Aeroengine Congress and Exhibition, Toronto, Ontario, Canada, June 4-8, 1989. Manuscript received at ASME Headquarters January 27, 1989. Paper No. 89-GT-181.

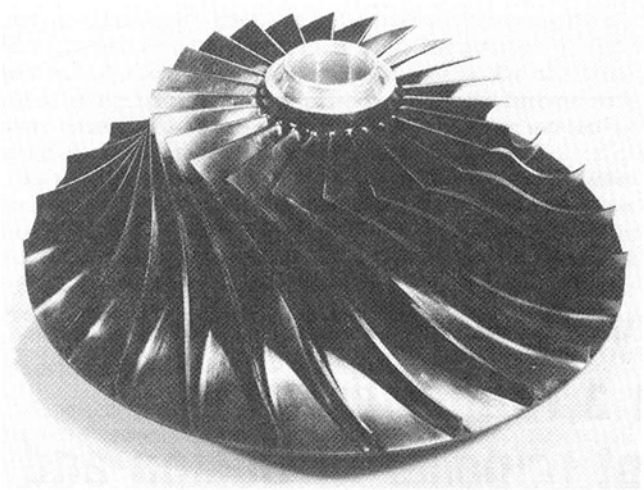

Fig. 1 30 deg backswept test impeller

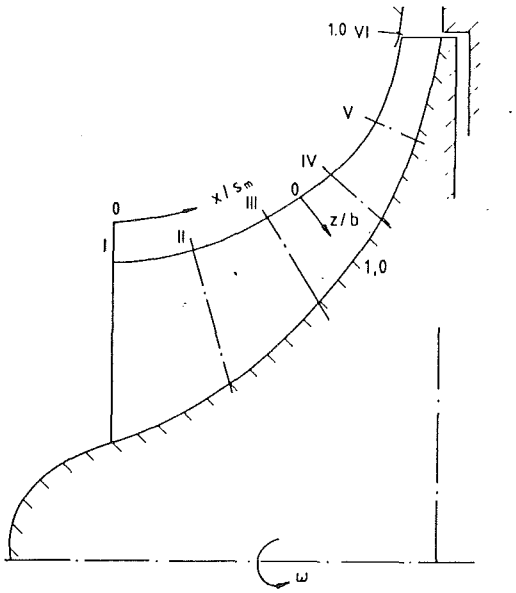

Fig. 2 Arrangement of L2F measurement planes

close to stall, at peak efficiency, and close to choke—were selected.

The internal flowfield was analyzed at six measurement planes located at 0, 20, 40, 60, 80, and 100.4 percent meridional shroud length (Fig. 2). All planes were perpendicular to the shroud contour. At each plane, measurements were carried out at five channel depths and, depending on the blade thickness, at 13 or 14 circumferential positions.

During the compressor operation total temperatures and total pressures were measured ahead of and aft of the rotor. The data measured at the inlet were taken for a continuous computer-controlled shaft speed and mass flow correction. Mass flow rate was measured with a venturi nozzle located in the inlet pipe. Honeycombs were used for flow-straightening ahead of the wheel.

Governing Equations and Numerical Scheme

The following Reynolds-averaged Navier–Stokes equations are solved for the current problem:

$$\frac{\partial}{\partial x_i}(\rho U_i) = 0 \tag{1}$$

$$\frac{\partial}{\partial X_j}(\rho U_i U_j) + 2\rho\epsilon_{ijk}\Omega_j U_k = -\frac{\partial p}{\partial x_i} + \frac{\partial}{\partial x_j}\left[\mu\left(\frac{\partial U_i}{\partial x_j} + \frac{\partial U_j}{\partial x_i} - \frac{2}{3}\frac{\partial U_k}{\partial x_k}\delta_{ij}\right) - \rho\overline{u_i u_j}\right] + F_i \tag{2}$$

$$\frac{\partial}{\partial x_j}(\rho U_j e) = \frac{\partial}{\partial x_j}\left[\left(\frac{\mu}{\mathrm{Pr}}\right)_{eff}\frac{\partial T}{\partial x_j}\right] - \frac{\partial}{\partial x_j}(pU_j) + U_i F_i + \frac{\partial}{\partial x_j}\left[U_i\mu\left(\frac{\partial U_i}{\partial x_j} + \frac{\partial U_j}{\partial x_i} - \frac{2}{3}\frac{\partial U_k}{\partial x_k}\delta_{ij}\right)\right] \tag{3}$$

$$P = \rho RT \tag{4}$$

where U_i = mean velocity, u_i = fluctuating velocity, e = total energy, Ω_i = angular velocity; F_i = additional body force,

Nomenclature

$C_1, C_2, C_3, C_4, C_\mu, \sigma_{dk}, \sigma_\epsilon$ = constants in turbulence closure models
C_m = total relative meridional velocity
C_V = specific heat
F_i = additional body force in equation (2)
k = turbulence kinetic energy
k_c = thermal conductivity
P = $-\overline{u_i u_j} U_{ij}$
p = static pressure
R = gas constant
U_2 = impeller tip speed
y/t = dimensionless blade pitch
z/b = dimensionless channel depth
β = coefficient of thermal expansion
Ω_i = angular velocity of impeller
δ_{ij} = Kronecker delta
ϵ_{ijk} = permutation tensor
ν = kinematic viscosity
ρ = density
$\dot{m}$ = mass flow rate
N_s = specific speed
n/n_o = shaft speed/design speed
PS = pressure side
SH = shroud
SS = suction side
HU = hub
x/s_m = dimensionless shroud length
η_{stt} = total/total isentropic efficiency
π_t = total pressure ratio

Subscripts

w = value at the wall
τ = total
0 = upstream condition
1 = impeller inlet
2 = impeller exit
3 = vaned diffuser inlet
4 = diffuser exit
red = corrected

Superscripts

$(\bar{\ })$ = average value

$$\left(\frac{\mu}{\mathrm{Pr}}\right)_{eff} = \left(\frac{\mu}{\mathrm{Pr}}\right)_{laminar} + \left(\frac{\mu}{\mathrm{Pr}}\right)_{turbulent}$$

and

$$e = C_v T + \frac{1}{2} U_i U_i$$

A modified k–ϵ, two-equation turbulence model is used to estimate Reynolds stresses. The turbulence model is an extension of the standard k–ϵ model toward the solid wall where molecular viscosity should be properly accounted for. The model is based on the studies of Chien (1982) and wall function treatment is not used. The following additional transport equations are solved for turbulence stress terms:

$$\frac{\partial(\rho U_i k)}{\partial x_i} = \frac{\partial}{\partial x_i}\left(\frac{\mu_{eff}}{\sigma_k}\frac{\partial k}{\partial x_i}\right) - \rho\,\overline{u_i u_j} U_{i,j} - \rho\epsilon - \frac{2\mu k}{\rho^2} \tag{5}$$

$$\frac{\partial(\rho U_i \epsilon)}{\partial x_i} = \frac{\partial}{\partial x_i}\left(\frac{\mu_{eff}}{\sigma_\epsilon}\frac{\partial \epsilon}{\partial x_i}\right) + C_1 \frac{\rho\epsilon}{k}\left(\overline{u_i u_j} U_{i,j}\right) - \frac{\rho\epsilon}{k}\left(C_2 f\epsilon + \frac{2\,\nu k e \exp(-c_4 u_* l/\nu)}{l^2}\right) \tag{6}$$

where l = distance from the wall,

$$\mu_{eff} = \mu + C_\mu \frac{k^2}{\epsilon}\left[1 - \exp(-C_3 u_* l/\nu)\right]$$

and

$$f = 1 - \frac{0.4}{1.8}\exp\left[-\left(\frac{k^2}{6\nu\epsilon}\right)^2\right]$$

The effects of turbulence modeling or modification of the currently applied model for the flow inside the centrifugal compressor are not the purpose of the present work. Therefore, standard values of various constants of the turbulence model are used; the values are

$C_\mu = 0.09$, $C_1 = 1.35$, $C_2 = 1.8$, $\sigma_k = 1.0$,
$\sigma_\epsilon = 1.3$, $C_3 = 0.0115$, $C_4 = 0.5$

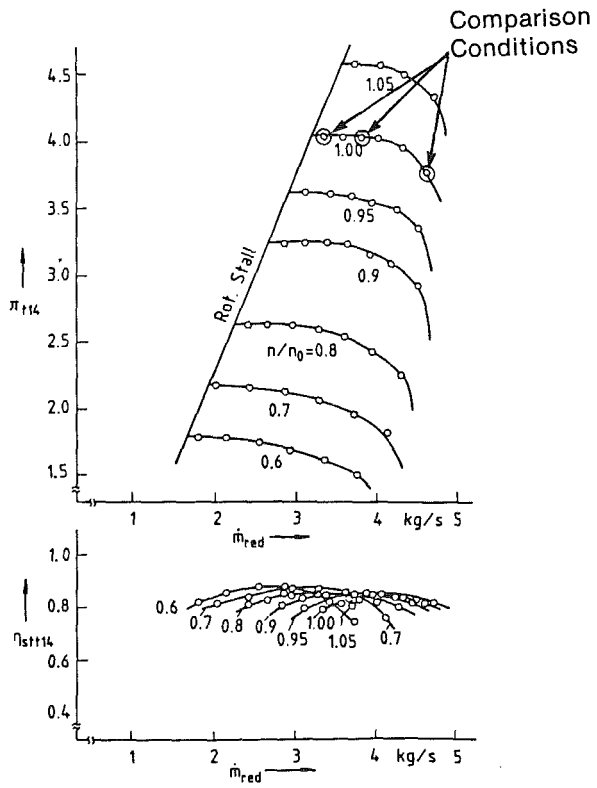

Fig. 3 Performance map and comparison conditions

Equations (1) through (6) are solved numerically with a fully conservative control volume approach. The finite difference equations are formulated in terms of Cartesian momentum (ρU_i), static pressure (p), total internal energy (e), turbulence kinetic energy (k), and turbulence energy dissipation rate (ϵ). The numerical fluxes through control volume surfaces are estimated with a quadratic upwinding scheme, and so the formal spatial accuracy is third order on smoothly varying meshes. The steady-state solution is obtained through the elliptic relaxation of the finite difference equations and each relaxation consists of one semi-implicit prediction and two implicit correction steps. During each iteration, pressure-based correction equations are used to ensure global conservation. The details of the numerical procedure and applications to other flows are given by Hah (1984, 1987).

The computations were carried out on an H-type grid. The computational mesh consisted of 26 blade-to-blade stations, 23 hub-to-tip stations, and 48 streamwise stations. In the spanwise direction, five nodes are located inside the clearance and exponential stretching is applied in all directions. The nondimensional distance of the first node from the wall (y^+) is about the order of 5 at the blade suction surface at the rotor exit. Previous studies (Krain, 1988; Moore, 1980; Rhie et al., 1985; Dawes, 1988; Hah et al., 1988) indicate that very thick shear layers are developed inside the centrifugal compressor and relatively coarse grids produce grid-independent solutions. The flow inside tip clearance is computed as a part of the entire flow domain with a stationary shroud (this corresponds to a moving shroud with constant speed when the flow is analyzed with a coordinate fixed on the impeller). Details of the numerical handling of tip leakage flow are described by Hah (1986). No-slip and no-flux conditions are applied on the solid wall. The physical periodicity condition upstream and downstream of the impeller and inside tip clearance is imposed implicitly. At the inflow boundary, the radial distribution of total pressure, total temperature, and relative flow angles are fixed. At the outflow boundary, the static pressure is fixed.

Analysis of Experimental and Numerical Results

The performance map of the centrifugal compressor stage composed of the test impeller and a vaneless constant area diffuser is shown in Fig. 3. Detailed experimental data at design condition with 100 percent speed were reported previously (Krain, 1988). For the present work, further experimental data at choke and near surge conditions are presented. The numerical predictions are made at three operating conditions (design, choke, and near surge) that are marked in Fig. 3. Two sets of computations are performed at each operating condition, one with and one without the tip clearance.

Shroud Static Pressure and Mean Velocity

Figure 4 compares the calculated circumferentially averaged shroud static pressure distribution with the time-mean measurements at three operating points. The overall agreement between calculation and measurement is very good. At choke and design conditions, the calculation predicts greater static pressure drop near the inlet and the leading edge region than the measurement. This might be due to calculated mass flow rates that are slightly higher than the measurements even though the exit static pressure is maintained the same as the measurements.

The development of meridional velocity inside the impeller is shown in Fig. 5 in the form of contour lines of C_m/U_2. The calculations with and without tip clearance are compared with the measured data at six measurement planes at optimum design condition. At plane I, both the numerical results show good agreement with measurement and only minor variations

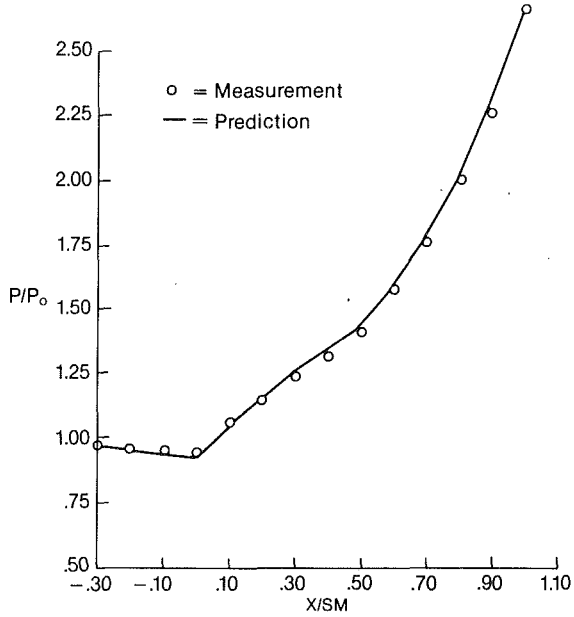

Fig. 4(a) Comparison of circumferentially averaged shroud static pressure at surge condition ($n/n_0 = 1$, $\dot{m} = 34$ kg/s)

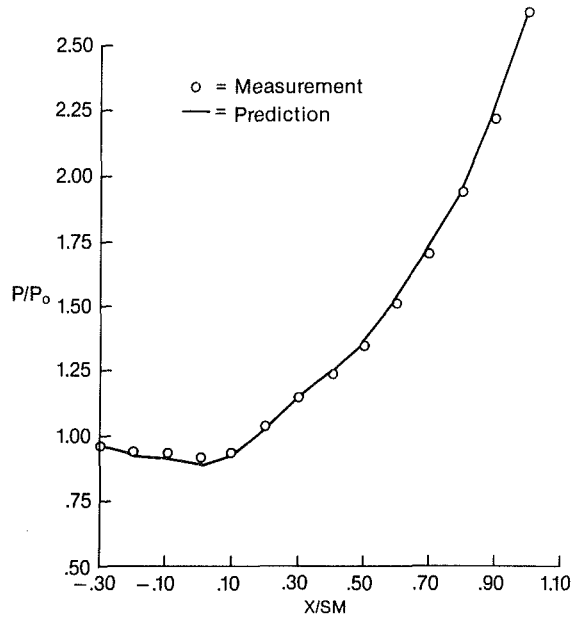

Fig. 4(b) Comparison of circumferentially averaged shroud static pressure at design condition ($n/n_0 = 1$, $\dot{m} = 4$ kg/s)

of contour values are observed. At plane II, the calculations with and without tip-clearance effect show almost identical results because the tip-clearance flow has not yet developed significantly. However, as shown for the shroud statics (Fig. 4), the calculated results again indicate more acceleration of the flow than the measurement.

At plane III ($x/s_m = 0.4$), the numerical results show significant influence of tip-clearance flow near the shroud and suction surface. Because of the tip-clearance flow, a low-velocity fluid area is formed near the shroud and blade suction surface. Again, the numerical results indicate more acceleration of core flow than the measurement, but the overall patterns of the contour lines are similar between experiment and calculation. At planes II and III, the numerical results show closely spaced contours near the hub. These contours indicate three-dimensional flow activity in this region (spanwise movement,

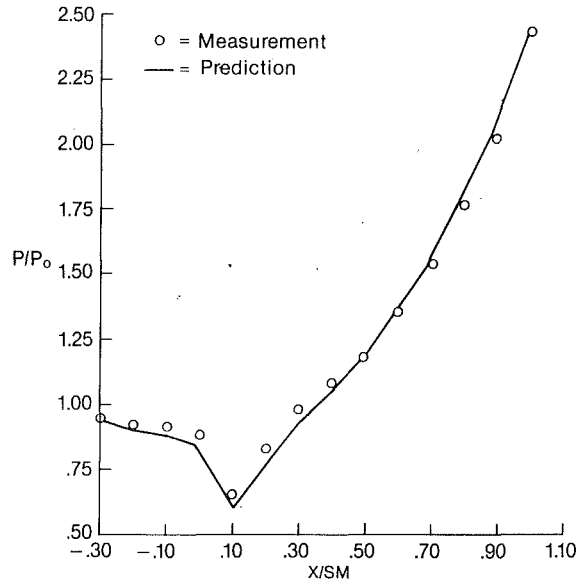

Fig. 4(c) Comparison of circumferentially averaged shroud static pressure at choke condition ($n/n_0 = 1$, $m = 4.6$ kg/s)

corner vortex, and so forth), which is located mostly outside of the current optical measurement domain.

From plane III to IV the low-velocity fluid area is propagating toward the middle of the channel and the center of the low-velocity fluid is moved away from the suction surface. Two calculations with and without tip clearance indicate clearly that this movement of low-momentum fluid is caused by tip-clearance flow. Good agreement between measurement and calculation with tip-clearance effect is shown in planes V and VI. The location of minimum velocity is measured near the center between the pressure and suction sides, and the distribution of meridional velocity is very smooth, which is quite different from the traditional jet/wake profile. Interestingly, calculation without the tip-clearance effect shows much steeper velocity profiles at the exit, and the location of low-momentum fluid is predicted about a half-pitch length away from the measurement. Comparisons in plane VI clearly indicate that tip-clearance effect must be properly modeled to predict the flow characteristics at the impeller discharge.

Flow-Angle Analysis

Information as to whether or not a vortex is present in the flowfield can be extracted from the shape of the lines of constant relative flow angles (isoclines). The basic equations for the isoclines of a real vortex moving with relative velocity W_b are derived in Fig. 6(a). The result of the analysis for a throughflow inclined against the drawing plane ($\beta = 35$ deg) is shown in Fig. 6(b). According to this analysis the isoclines are parallel to each other in the solid body vortex area and are of elliptical shape in the potential vortex area. The vortex center is always located in the middle of the parallel isoclines. A real vortex, which consists of a solid-body vortex and a potential vortex part, is assumed to be present when isoclines similar to those shown in Fig. 6(b) are identified.

A detailed flow-angle analysis at design condition is given in Fig. 7. The numerical calculations with and without tip-clearance effects are compared with measured data. At plane I, both numerical results show good agreement with measurement and no effect of tip-clearance flow causing a vortex structure is noticed at this plane. A good agreement between measurement and calculation was also obtained at plane II. Here, for the first time, shroud corner vortices appear that are identified by the calculation taking care of tip-clearance ef-

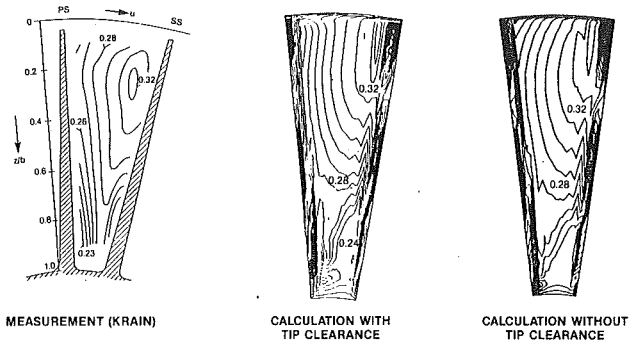

Fig. 5(*a*) Comparison of meridional velocity contours at plane I (design condition)

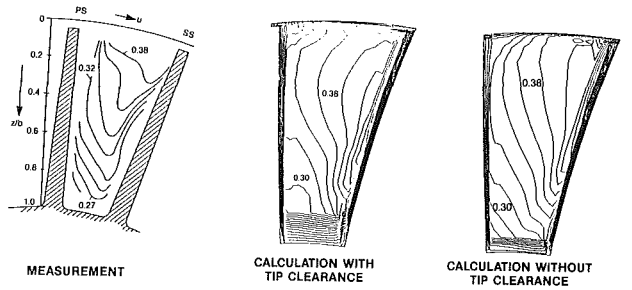

Fig. 5(*b*) Comparison of meridional velocity contours at plane II (design condition)

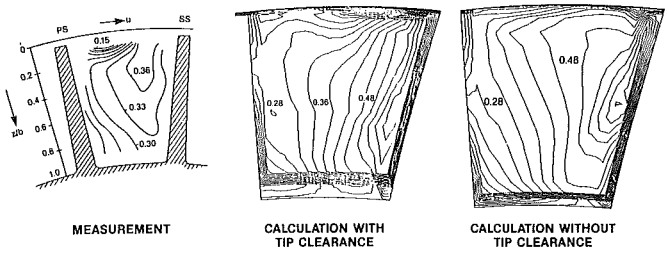

Fig. 5(*c*) Comparison of meridional velocity contours at plane III (design condition)

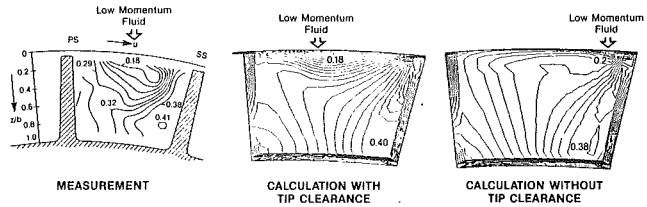

Fig. 5(*d*) Comparison of meridional velocity contours at plane IV (design condition)

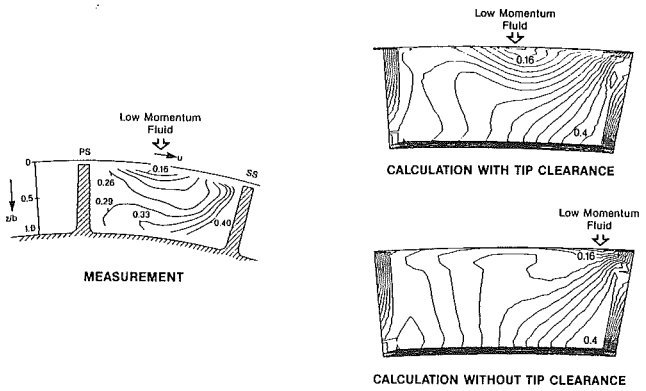

Fig. 5(*e*) Comparison of meridional velocity contours at plane V (design condition)

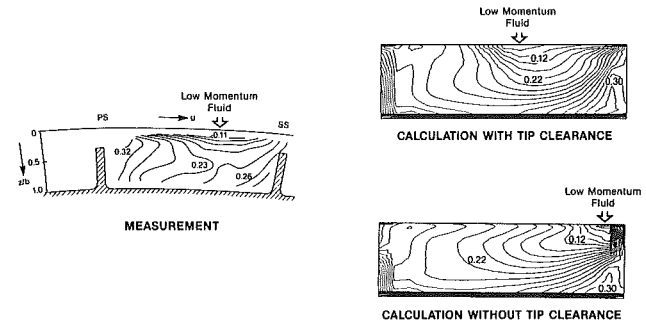

Fig. 5(*f*) Comparison of meridional velocity contours at plane VI (design condition)

fects rather than by the solution without tip-clearance effects.

At plane III, the isoclines indicate a clear vortex in the middle of the passage away from the blade surfaces. The calculation with tip-clearance effect shows an additional strong vortex inside the shroud boundary layer, which is located outside of the laser measurement domain. At plane IV, both the measurement and the calculation with tip-clearance effect point to two counterrotating channel vortices. This vortex system is not clearly predicted by the calculation neglecting tip-clearance effects, indicating that the complex vortex structure inside of the flow passage is also caused by the tip-clearance flow. Similar results were obtained for plane V. Here the vortex flow dominates most of the flowfield. Again the character of the swirling flow is not predicted when the effect of tip clearance is not properly modeled in the numerical solution. Good agreement beween measurement and calculation with tip-clearance effects was also obtained for plane VI. A quite different isocline pattern is predicted by the solution without tip-clearance effects that points to high flow angle variations in the shroud/suction side area. The comparisons in Fig. 7 strongly suggest that the overall vortex motion in the unshrouded impeller is initiated and dominated by the relative motion between the moving rotor and the stationary casing and the resulting tip-leakage flow.

Impeller Exit Velocity Profile

Figure 8 compares impeller exit velocity profiles for the three operating points indicated in Fig. 3. For these operating conditions very smooth impeller exit velocity profiles were measured that significantly differed from the jet/wake-type profiles. All profiles show relatively mild variations in the pitchwise direction, which was a goal during the impeller design process. The numerical results show very good agreement with the experimental data. At choke, the exit velocity profile has a higher gradient from hub to shroud than at design and surge conditions. This might be because the swirling vortex motion superimposed on the main throughflow becomes less influential with increasing mass flow rate. Additionally, the flow does not have time to mix out the low-velocity fluid that has its origin near the shroud.

From the results in Figs. 5, 7, and 8, we observe that the rotor exit flow pattern is determined mainly by the interaction at the swirling vortex motion and the main flow. The optimum rotor exit flow profile (like the current smooth profile compared to the classical jet/wake type) can be obtained by controlling this vortex motion and its interaction with the main flow.

Figure 9 shows the particle trajectory inside the gap. The lines show the path of particles that enter the channel near the

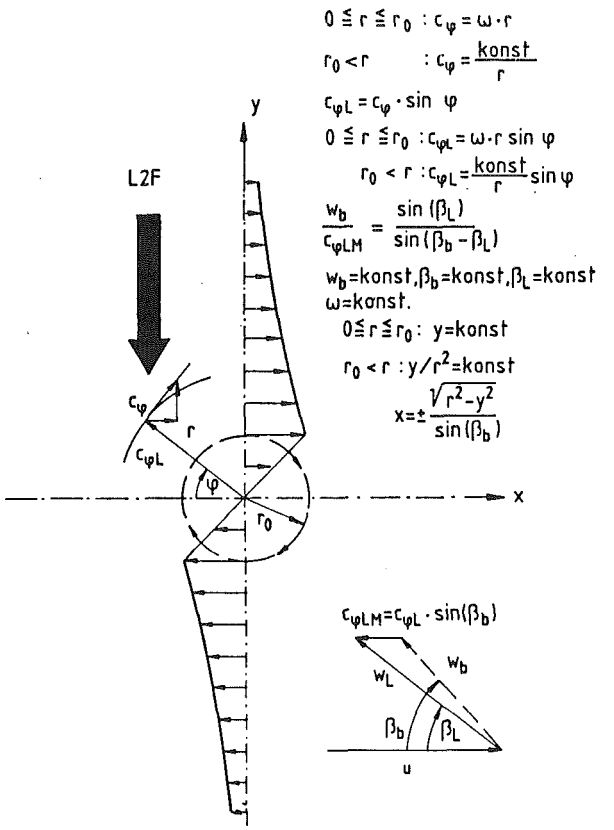

Fig. 6(*a*) Measurement of vortex flow with L2F measurement technique

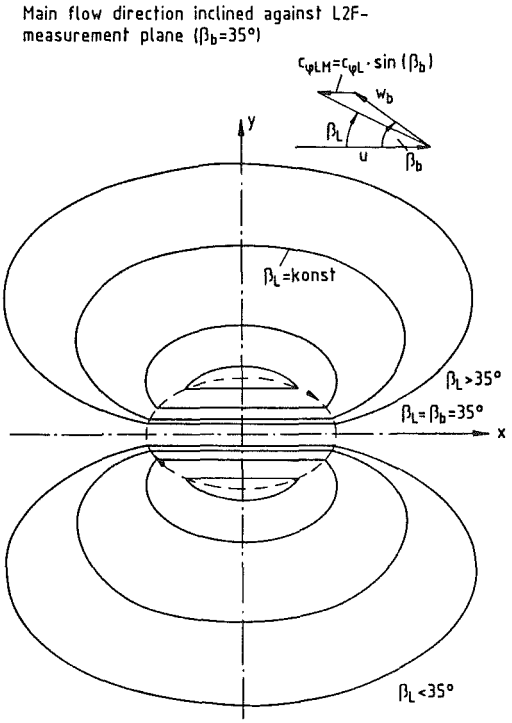

Fig. 6(*b*) Isocline structure for a real vortex, composed of a solid-body and a potential vortex

shroud and stay in the passage. As indicated in the figure, the stream sheet is rolled substantially by the vortex motion and the tip-clearance flow.

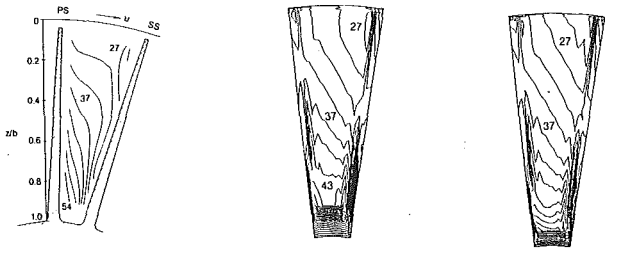

Fig. 7(*a*) Comparison of isocline pattern at plane I (design condition)

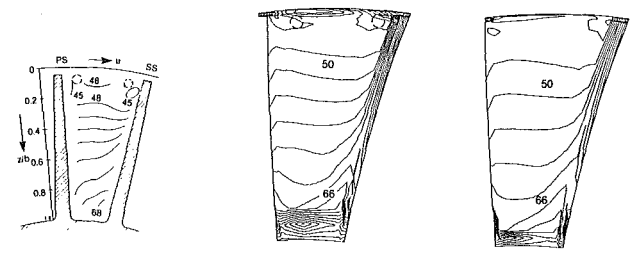

Fig. 7(*b*) Comparison of isocline pattern at plane II (design condition)

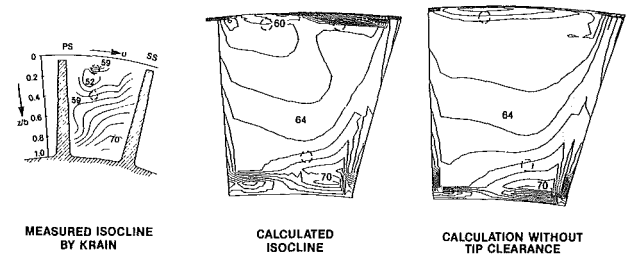

Fig. 7(*c*) Comparison of isocline pattern at plane III (design condition)

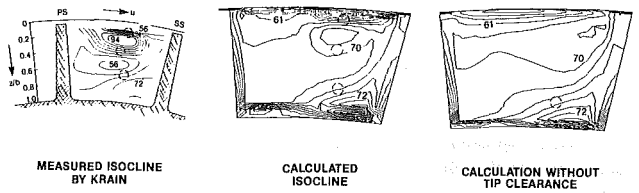

Fig. 7(*d*) Comparison of isocline pattern at plane IV (design condition)

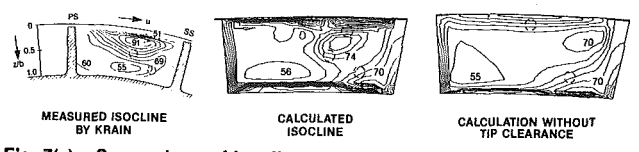

Fig. 7(*e*) Comparison of isocline pattern at plane V (design condition)

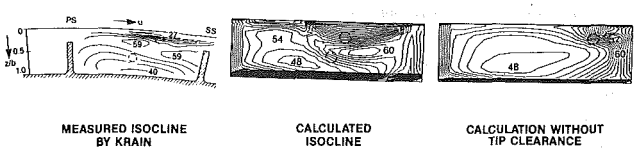

Fig. 7(*f*) Comparison of isocline pattern at plane VI (design condition)

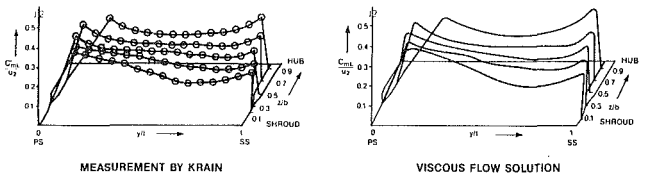

Fig. 8(a) Comparison of impeller exit velocity profile at surge condition ($n/n_0 = 1$, $\dot{m} = 3.34$ kg/s)

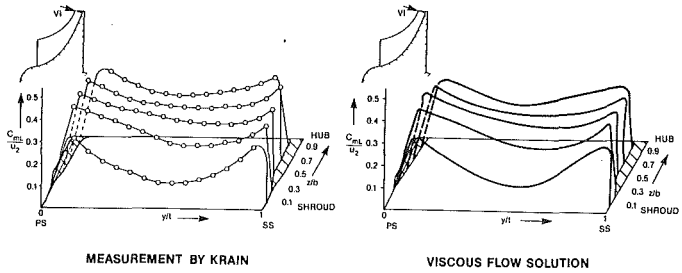

Fig. 8(b) Comparison of impeller exit velocity profile at design condition ($n/n_0 = 1$, $\dot{m} = 4$ kg/s)

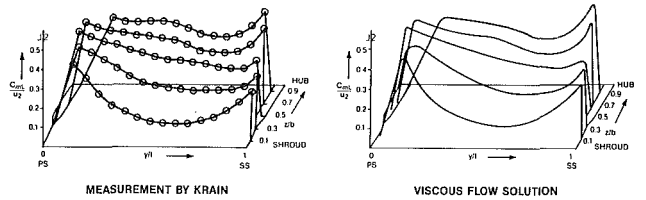

Fig. 8(c) Comparison of impeller exit velocity profile at choke condition ($n/n_0 = 1$, $\dot{m} = 4.6$ kg/s)

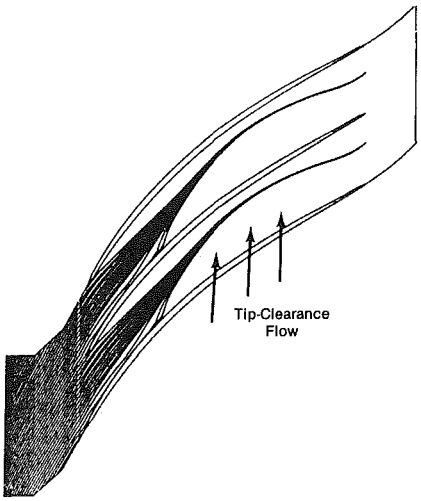

Fig. 9 Particle trajectories near the shroud (90 percent of tip clearance)

Concluding Remarks

Three-dimensional flowfields in a high-efficiency backswept impeller at design and off-design conditions have been studied experimentally and numerically. The measurement results reveal relatively smooth discharge flow patterns for all operating points investigated that differ strongly from the well-known jet/wake-type flow pattern. A three-dimensional viscous flow code was used to study the development of secondary flows, vortex motion, and tip-clearance flow effects on these flow structures. A comparison between measurement and calculation indicates that the swirling flow and vortex motion inside the unshrouded impeller are greatly influenced by the relative motion between the rotating impeller and the stationary shroud as well as by the resulting tip-leakage flow. Therefore, tip-clearance effects should be properly modeled when a realistic flowfield prediction is required for a complex flowfield similar to that occurring in high-pressure ratio centrifugal impellers. Probably, the control of the swirling vortex motion during the design process can result in an optimum shape of impeller discharge flow characteristics.

Acknowledgments

The authors would like to thank D. Miller and A. Bryans of the General Electric Company for constructing the initial computational grid and L. H. King for his guidance of the numerical part of the current work.

References

Chien, K. Y., 1982, "Predictions of Channel and Boundary-Layer Flows With a Low-Reynolds Number Turbulence Model," *AIAA Journal*, Vol. 20, No. 1, pp. 33–38.

Dawes, W. N., 1988, "Development of a 3D Navier–Stokes Solver for Application to All Types of Turbomachinery," ASME Paper No. 88-GT-70.

Eckardt, D., 1976, "Detailed Flow Investigations Within a High Speed Centrifugal Compressor Impeller," ASME *Journal of Fluids Engineering*, Vol. 98, pp. 390–402.

Hah, C., 1984, "A Navier–Stokes Analysis of Three-Dimensional Turbulent Flows Inside Turbine Blade Rows at Design and Off-design Conditions," ASME *Journal of Engineering for Gas Turbines and Power*, Vol. 106, pp. 421–429.

Hah, C., 1986, "A Numerical Modeling of Endwall and Tip-Clearance Flow of an Isolated Compressor Rotor," ASME *Journal of Engineering for Gas Turbines and Power*, Vol. 108, pp. 15–21.

Hah, C., 1987, "Calculation of Three-Dimensional Viscous Flows in Turbomachinery With an Implicit Relaxation Method," AIAA *Journal of Propulsion and Power*, Vol. 3, No. 5, pp. 415–422.

Hah, C., Bryans, A. G., Moussa, Z., and Tomsho, M. E., 1988, "Application of Viscous Flow Computations for the Aerodynamic Performance of a Backswept Impeller at Various Operating Conditions," ASME JOURNAL OF TURBOMACHINERY, Vol. 110, pp. 303–311.

Hamkins, C. P., and Flack, R. D., 1987, "Laser Velocimeter Measurements in Shrouded and Unshrouded Radial Flow Pump Impellers," ASME JOURNAL OF TURBOMACHINERY, Vol. 109, pp. 70–76.

Krain, H., 1981, "A Study on Centrifugal Impeller and Diffuser Flow," ASME *Journal of Engineering for Power*, Vol. 103, pp. 688–697.

Krain, H., 1988, "Swirling Impeller Flow," ASME JOURNAL OF TURBOMACHINERY, Vol. 110, pp. 122–128.

Lapworth, B. L., and Elder, R. L., 1988, "Computation of the Jet-Wake Flow Structure in a Low Speed Centrifugal Impeller," ASME Paper No. 88-GT-217.

Moore, J., and Moore, J. G., 1980, "Three-Dimensional Viscous Flow Calculation for Assessing the Thermodynamic Performance of Centrifugal Compressors, Study of the Eckardt Compressor," *Proc. AGARD Meeting on Centrifugal Compressors, Flow Phenomena and Performance*, Brussels.

Rhie, C. M., Delaney, R. A., and Mckain, T. F., 1985, "Three-Dimensional Viscous Flow Analysis for Centrifugal Impellers," *J. Propulsion*, Vol. 1, No. 4, pp. 257–258.

Schodl, R., 1980, "A Laser-Two-Focus (L2F) Velocimeter for Automatic Flow Vector Measurements in the Rotating Components of Turbomachines," in: *Measurement Methods in Rotating Components of Turbomachinery*, pp. 139–147.

Effect of Blade Tip Configuration on Tip Clearance Loss of a Centrifugal Impeller

M. Ishida
Professor,
Faculty of Engineering,
Nagasaki University,
Nagasaki 852, Japan

H. Ueki
Associate Professor,
Faculty of Engineering,
Nagasaki University,
Nagasaki 852, Japan

Y. Senoo
Director,
Miura Company,
Matsuyama, 799-26, Japan
Fellow ASME

According to the theory presented by the authors, the tip clearance loss of an unshrouded centrifugal impeller mainly consists of two kinds of loss; one is the drag due to the leakage flow through the blade tip clearance and the other is the pressure loss to support the fluid in the thin annular clearance space between the shroud and the blade tip against the pressure gradient in the meridional plane without blades. The former is proportional to the leakage flow or the contraction coefficient of leakage flow. The authors have conducted performance tests using an impeller with 16 backward-leaning blades in three configurations of the blade tip: round edge, sharp square edge, and edge with an end-plate. The experimental tip clearance effects can be predicted by the theory assuming reasonable contraction coefficients. They are 0.91, 0.73, and 0.53 for the respective tip configurations. The impeller efficiency is improved by about 1.5 point by reducing the contraction coefficient from 0.91 to 0.53, providing that the tip clearance ratio at the exit of impeller is 0.1. More improvement is expected for an impeller with highly loaded blades where the leakage loss shares the major part of the tip clearance loss.

Introduction

Recently, there has been much interest in problems regarding tip clearance effects, and many experimental and theoretical researches have been reported in the literature. The authors have also presented a theoretical model to predict quantitatively the tip clearance loss, the efficiency drop, and the variation of input power due to the tip clearance in unshrouded centrifugal and axial impellers (Senoo et al., 1986, 1987).

According to the theory, the tip clearance loss mainly consists of two kinds of loss: one is the drag due to the leakage flow through the blade tip clearance and the other is the pressure loss to support the fluid in the annular clearance space between the shroud and the blade tip against the pressure gradient in the meridional plane without blades. The former is proportional to the leakage flow, or the leakage velocity and the contraction coefficient of leakage flow. Furthermore, according to the model, the change of input power due to the tip clearance is also related to the contraction coefficient of the leakage flow.

The present work examines the effect of tip configuration on the impeller performance experimentally and compares the results with the prediction based on the theory where the only variable parameter is the contraction coefficient of the leakage flow. For this purpose, the authors have conducted performance tests using an impeller with 16 backward-leaning blades in three configurations of the blades tip: round edge, sharp square edge, and edge with an end-plate.

Contributed by the International Gas Turbine Institute and presented at the 34th International Gas Turbine and Aeroengine Congress and Exhibition, Toronto, Ontario, Canada, June 4-8, 1989. Manuscript received at ASME Headquarters January 17, 1989. Paper No. 89-GT-80.

Experimental Setup

The meridional profile of the test blower is shwon in Fig. 1. The impeller is identical to the B′-impeller of the literature (Senoo et al., 1986), which has 16 backward-leaning blades with inlet and exit angles of 28 and 45 deg, respectively, from the tangential direction; the outlet diameter is 510 mm, the exit blade height is 17 mm, the blade thickness is about 2 mm, and the specific speed is about 0.43. The impeller was initially fully shrouded as a conventional centrifugal blower, then the front shroud was machined off to be a semi-open impeller with sharp square edge at the blade tip as shown in the middle of Fig. 2. In the present experiment, in order to clarify the effect of blade tip configuration on the tip clearance loss, the tip

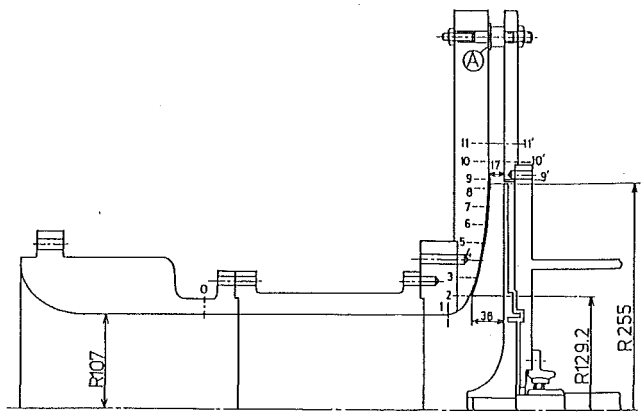

Fig. 1 Meridional section of test blower

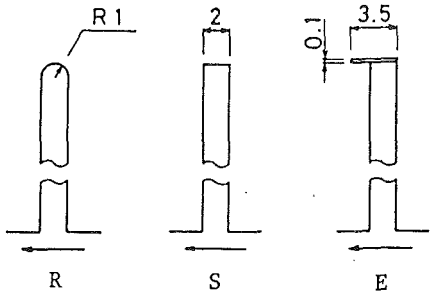

Fig. 2 Tested blade tip configurations: R = round edge; S = sharp square edge; E = edge with end-plate

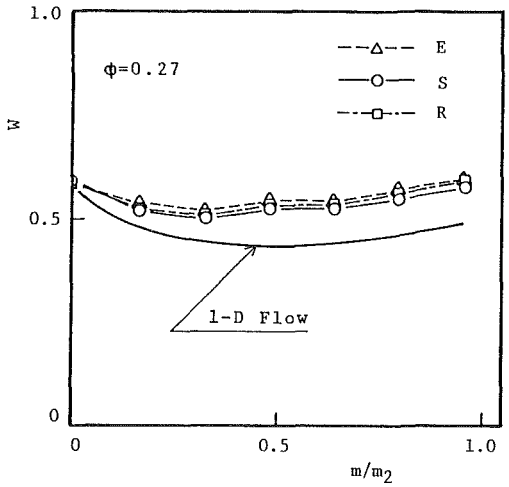

Fig. 3 Relative velocity distribution along the shroud (uncertainty of W is ±0.006)

configuration was changed in three cases shown in Fig. 2: round edge (R-type), sharp square edge (S-type), and edge with a very thin end-plate (E-type) 3.5 mm wide and 0.1 mm thick, which was stuck out toward the direction of rotation of the impeller as shown in the left of Fig. 2.

The clearance between the blade tip and the stationary shroud was changed by inserting a shim at the position marked, Ⓐ in Fig. 1 so that the shroud moved axially relative to the impeller. The axial clearance at the exit of impeller was varied from the minimum of 0.3 mm to the maximum of 3.5 mm. The air was axisymmetrically discharged from the blower to the atmosphere through a parallel wall vaneless diffuser. The flow rate was controlled with a conical damper at the entrance of a plenum chamber upstream of the suction pipe of the blower. Between the plenum and the suction pipe, there was an entrance nozzle with which the flow rate was measured. Static pressure was measured at 11 radial positions along the shroud. These positions are numbered from 1 to 11 in Fig. 1, and the static pressure at each radial position was indicated as the mean value measured at four pressure taps located circumferentially.

The impeller was run at a constant speed of 2000±2 rpm. The outputs of the various instruments for pressure, flow rate, and torque were converted to electrical signals and they were read by a data acquisition control unit that was commanded by a desktop computer. By using this system, a slight change in pressure distribution along the shroud due to a change in tip clearance was confirmed on-line and real-time with a high accuracy. Although the tip clearance was changed, the flow rate was kept constant with an accuracy of 0.2 percent by controlling with a conical damper, and the pressure and the input shaft torque were measured and compared with each other.

Results and Discussions

Relative Velocity Distribution Along the Shroud. The experimental relative velocity distributions shown in Fig. 3 are evaluated from the measured wall static pressure along the shroud at the design flow rate of $\phi = 0.27$ under the minimum tip clearance condition assuming the potential core in the impeller channel from the inlet to the exit. The difference among the experimental velocity distributions of the three kinds of blade tip configuration is insignificant and the slight difference seems to be attributed to the difference of minimum tip clearance in the three cases. The impeller was designed so that the deceleration of relative velocity in the impeller was small. The flow is decelerated a little in the inlet portion, but it is accelerated a little in the last half, and the overall deceleration ratio from the inlet to the exit of impeller is almost unity. The thick solid line in Fig. 3 is the value predicted by the one-dimensional flow analysis. The difference between experiment and theory becomes larger downstream because of growth of the boundary layer and accumulation of the leakage flow.

Change in Pressure Distribution Along the Shroud. The pressure along the shroud was measured for each tip configuration at three flow rates for seven different values of tip clearance. Figures 4(a), 4(b), and 4(c) show the pressure distributions along the shroud at the representative flow rate of $\phi = 0.27$. The pressure distributions at the minimum tip clearance indicated by open circles in Figs. 4(a), 4(b), and 4(c) are almost identical despite the difference of tip configuration, as mentioned in Fig. 3, because the leakage flow through the tip clearance is inherently small under a fairly narrow clearance condition.

In all three cases with different tip configurations, the effect of tip clearance on the pressure distribution appears only in the inlet zone between the inlet and the throat of impeller blades, where the rate of pressure rise is decreased significantly with the increase of tip clearance, while downstream of the throat, the rate of pressure rise is hardly changed by the tip clearance. The decrement of static pressure due to the tip clearance is relatively small in the case of E-type blade tip as shown in Fig. 4(c) compared with the cases of S-type and R-type shown in Figs. 4(a) and 4(b).

Figure 5 shows the change of blade-to-blade pressure distributions due to the tip clearance measured at seven measuring points A to G, which are identical to the measuring position numbers 3 to 9 in Fig. 1, where the position A cor-

Nomenclature

E = edge with end-plate
m = meridional distance along shroud
R = round edge
S = sharp square edge
U = tip speed at impeller exit
Vu = tangential component of absolute velocity normalized by U
W = relative velocity normalized by U
α = contraction coefficient of leakage flow
η = impeller efficiency
λ = tip clearance ratio
ϕ = flow coefficient at impeller exit
Ψ = pressure coefficient of impeller
Ψt = total pressure coefficient of impeller

Subscripts

2 = impeller exit

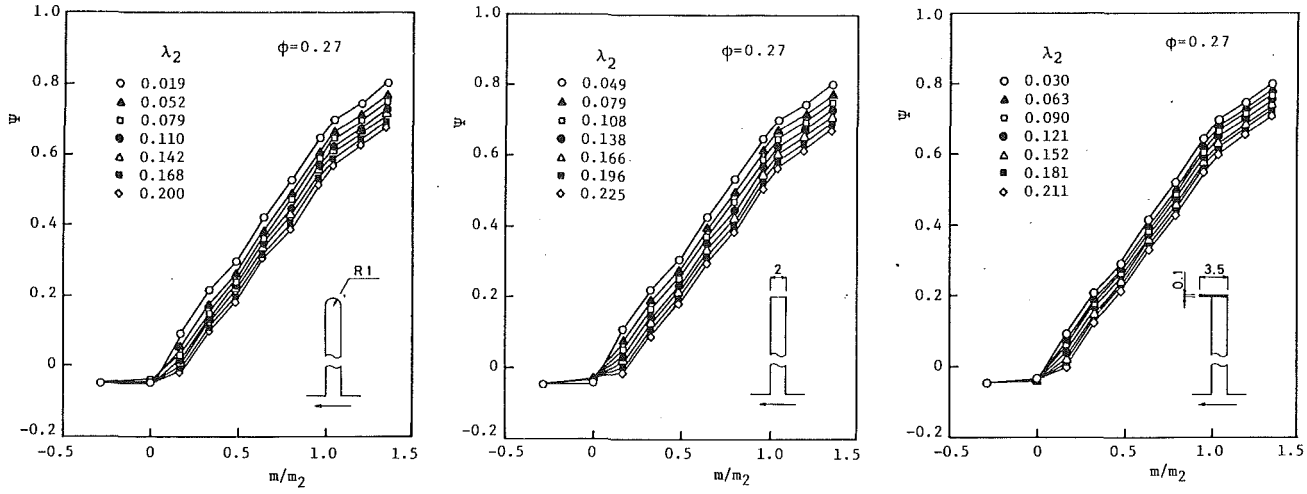

(a) Round edge (b) Sharp square edge (c) Edge with an end-plate

Fig. 4 Effect of tip clearance on pressure distribution along the shroud (uncertainty of Ψ is ±0.008): (*a*) round edge; (*b*) sharp square edge; (*c*) edge with an end-plate

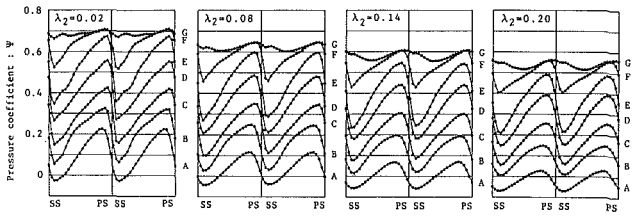

Fig. 5 Change of blade-to-blade pressure distribution due to tip clearance; round edge, $\phi = 0.27$ (uncertainty of Ψ is ±0.008)

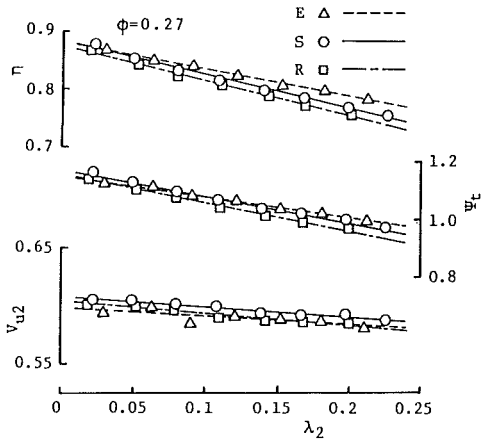

Fig. 6 Effect of tip clearance on impeller performance (uncertainties of η, Ψf, and Vu_2 are ±0.013, ±0.019, ±0.007, respectively)

responds to the throat of the impeller blades. The amplitude of pressure variation between blades is significantly decreased at position A with the increase of tip clearance. The significant decrease of pressure rise at the throat section shown in Fig. 4 seems to be mainly attributed to the reduction of blade loading at the tip and it is partly based on the pressure loss due to the tip clearance.

Change in Impeller Performance. Figure 6 shows the effect of blade tip configuration on the impeller performance at the design flow rate. The straight lines by the least-squares method are fitted to the data in each case. In the figure, η is the impeller efficiency, Ψ_T is the total pressure coefficient at the exit of impeller, where the averaged wall static pressure was measured at the hub and shroud walls immediately downstream of the impeller, and the dynamic pressure was estimated using the measured flow rate and the input shaft torque. Vu_2 is the tangential component of the absolute velocity at the exit of impeller normalized by the impeller tip speed, which was estimated from the measured input shaft torque and the flow rate excluding the disk friction torque and the bearing torque.

With the increase of tip clearance, the input power, the total pressure at the exit of impeller, and the impeller efficiency decrease, but the reduction rates are different depending upon the blade tip configurations. It is clearly shown in Fig. 6 that the rates of reduction in impeller efficiency and in the total pressure become smaller in the order: R-type, S-type, E-type. It is generally difficult to get a high accuracy in shaft torque measurement, but a delicate difference in the rate of reduction in input power due to the tip configuration is found, although there is some scattering in the data. Similar effects of tip configuration are observed at other flow rates.

Comparison Between Experiment and Theory

As shown in Fig. 6, the impeller efficiency is reduced almost linearly by the increase of tip clearance in the range of present experiment. Figs. 7(*a*), 7(*b*), and 7(*c*) show the decrement of impeller efficiency $-\Delta\eta$ due to the increment of tip clearance $\Delta\lambda_2$ relative to the minimum tip clearance condition at the flow rates of $\phi = 0.20$, 0.27, and 0.34, respectively. In the figures, the experimental data of the three tip configurations are indicated as different symbols while the predicted relationships are presented as straight lines. The rate of efficiency drop is lower in the E-type edge and higher in the R-type edge compared with the S-type edge at any flow rate. The efficiency drop due to the 10 percent increment of the tip clearance is less in the E-type edge by about 1 and 1.5 point compared with the other two cases.

The literature (Senoo et al., 1987) suggests estimating the contraction coefficient of the leakage flow from the rate of reduction in measured input power. Then the efficiency drop can be predicted, since they are theoretically interrelated. However, in the present analysis, the contraction coefficient was estimated from the measured efficiency drop because the efficiency drop is more sensitive to the leakage flow rate than

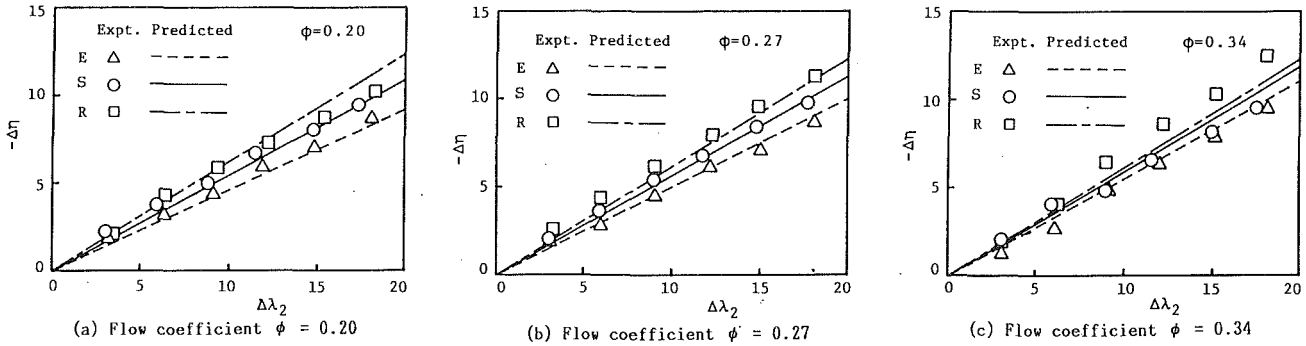

Fig. 7 Effect of tip configuration on efficiency drop (uncertainties of $-\Delta\eta$ and $\Delta\lambda_2$ are ± 0.013 and ± 0.007): (a) flow coefficient $\phi = 0.20$; (b) flow coefficient $\phi = 0.27$; (c) flow coefficient $\phi = 0.34$

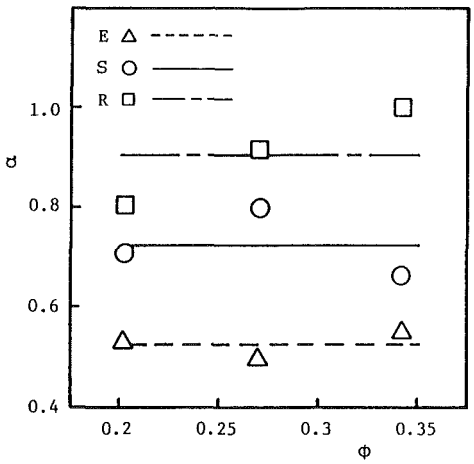

Fig. 8 Estimated contraction coefficient of leakage flow (uncertainties of α and ϕ are ± 0.1 and ± 0.001)

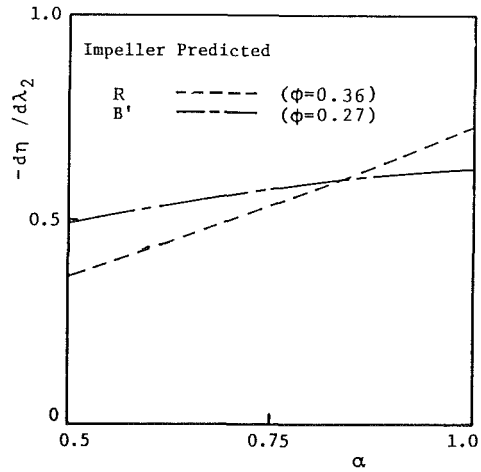

Fig. 9 Predicted effect of contraction coefficient on efficiency drop rate

is the input power. The estimated contraction coefficients are shown in Fig. 8 as the nine symbols for different tip configurations and flow rates.

In principle, the contraction coefficient can neither be less than 0.5 nor larger than 1.0. Two of the estimated coefficients are slightly outside of the range. Although the estimated values α show some scattering, the averaged value was adopted for the respective tip configuration disregarding the variation due to the flow rate, assuming that the contraction coefficient should be dependent only on the geometric configuration of the blade tip. The values of contraction coefficient α were 0.91, 0.73, and 0.53 for the R-type, S-type, and E-type edges, respectively, which are shown as straight lines in Fig. 8. These values are agreeable with our common sense. The predicted efficiency drop presented by straight lines in Figs. 7(*a*), 7(*b*), and 7(*c*) are calculated using these averaged contraction coefficients. Some of the experimental data of the R-type edge are not on the predicted straight lines. This is related to the systematic variation of α with respect to ϕ only in the R-type edge.

Judging from these results, it is clear that the leakage loss is significantly influenced by the blade tip configuration, and that the leakage loss can be reduced by means of a device to reduce the contraction coefficient such as the short end-plate at the blade tip adopted in this experiment.

The influence of the contraction coefficient on efficiency drop should be different depending on impeller design, because the ratio of the leakage loss to the tip clearance loss varies considerably from impeller to impeller. For example, in case of the R-impeller with 20 radial blades and inducers, presented in the literature (Senoo et al., 1986), the ratio of leakage loss to the tip clearance loss is about 68 percent at a flow coefficient of $\phi = 0.36$ while it is only 32 percent at a flow coefficient of $\phi = 0.27$ in this experiment. The larger the ratio is, the more significant the influence of contraction coefficient would be. Figure 9 shows an example of the predicted effect of contraction coefficient on the rate of efficiency drop in the above two cases.

In general the impellers with highly loaded blades suffer from a large leakage loss. They offer more promise for efficiency improvement by reducing the contraction coefficient than do impellers with lightly loaded blades.

Conclusions

The effect of blade tip configuration on the tip clearance loss was examined experimentally using an unshrouded centrifugal impeller with backward-leaning blades. The tested tip configurations were of three kinds: round edge, sharp square edge, and edge with an end-plate. The experimental tip clearance effects were compared with the theory presented previously by the authors. As a result, the following conclusions were obtained.

1 The experimentally observed tip clearance effects can be predicted by the theory assuming reasonable values of the contraction coefficient, which are $\alpha = 0.91$ for the round edge, $\alpha = 0.73$ for the sharp square edge, and $\alpha = 0.53$ for the edge with end-plate, respectively.

2 The impeller efficiency was improved by about 1.5 point by reducing the contraction coefficient from 0.91 to 0.53, in the case where the tip clearance ratio at the impeller exit was 0.1.

3 The effect of contraction coefficient on the impeller efficiency is dependent on the ratio of leakage loss to the tip clearance loss. By reducing the contraction coefficient, more improvement in efficiency is expected for impellers with highly loaded blades.

Acknowledgments

The authors wish to thank Messrs. K. Kurokawa, K. Matsuo, and I. Matsumoto for construction of the experimental apparatus and for securing the experimental data.

References

Senoo, Y., and Ishida, M., 1986, "Pressure Loss Due to the Tip Clearance of Impeller Blades in Centrifugal and Axial Blowers," ASME *Journal of Engineering for Gas Turbines and Power*, Vol. 108, pp. 32–37.

Senoo, Y., and Ishida, M., 1987, "Deterioration of Compressor Performance Due to Tip Clearance of Centrifugal Impeller," ASME JOURNAL OF TURBOMACHINERY, Vol. 109, No. 1, pp. 55–61.

Secondary Flow Due to the Tip Clearance at the Exit of Centrifugal Impellers

M. Ishida
Professor,
Faculty of Engineering,
Nagasaki University,
Nagasaki 852, Japan

Y. Senoo
Director,
Miura Company,
Matsuyama 799-26, Japan
Fellow ASME

H. Ueki
Associate Professor,
Faculty of Engineering,
Nagasaki University,
Nagasaki 852, Japan

The velocity distribution was measured at the exit of two different types of unshrouded centrifugal impeller under four different tip clearance conditions each; one with 20 radial blades and inducers and the other with 16 backward-leaning blades. The effect of tip clearance on input power was also measured. By increasing the tip clearance, the input power was hardly changed in the radial blade impeller and was reduced in the backward-leaning blade impeller. The velocity distribution normalized by the passage width between hub and shroud wall was hardly changed at the exit of the radial blade impeller by varying the tip clearance. On the other hand, the relative flow angle was reduced significantly and monotonously by an increase of tip clearance in the backward-leaning blade impeller. The change in input power due to the tip clearance was clearly related to the change of flow pattern at the exit of impeller due to the secondary flow. This is most likely caused by the component, normal to the blade, of the shear force to support the fluid in the clearance space against the pressure gradient in the meridional plane without blades.

Introduction

In recent high-pressure-ratio centrifugal compressors, blade height is short near the impeller exit due to the high pressure ratio and the high rotational speed. In such cases, the ratio of the tip clearance to the blade height is relatively large, and deterioration of the compressor performance due to the tip clearance is not negligible. Up to now many studies have been conducted experimentally and theoretically, and several models have been proposed to predict the tip clearance loss and the efficiency drop, e.g., Pfleiderer (1961), Eckert and Schnell (1961), Hesselgreaves, (1969), Lakshminarayana (1970), and Senoo and Ishida (1986, 1987). Engeda and Rautenberg (1987) studied also the effects of tip clearance on the efficiency drop and on the tangential component of the absolute velocity, on the basis of experimental investigations of five centrifugal pump impellers with backward-leaning blades, and they showed that the work factor at the optimal flow rate was hardly influenced by the tip clearance variations. Most researchers have disregarded the variation of input power due to a change of tip clearance, partly because it is difficult to get a high accuracy in the shaft torque measurement. In the literature (Senoo et al., 1986, 1987; Ishida et al., 1981), the authors have related the change of input power based on the tip clearance to the change of effective blockage in the impeller channel.

In order to predict impeller efficiency more accurately and to design a vaned diffuser behind an unshrouded impeller properly, it is necessary to be informed of the tip clearance effect on the flow behavior in the impeller. It has already been indicated in the literature (Eckardt, 1976) that the flow behavior in an unshrouded impeller is quite different from that in a shrouded impeller. In cases of shrouded impellers where the shroud rotates with the impeller, there is a secondary flow along the shroud from the pressure side of a blade to the suction side of the adjacent blade. On the other hand, in cases of unshrouded impellers, where the shroud is a stationary casing and there is a narrow clearance between the shroud and the blade tip, the secondary flow along the shroud, from the pressure side of a blade to the suction side of the adjacent blade, is intercepted by the leakage flow through the clearance and also by the motion of the stationary shroud relative to the impeller blade. Figure 1 is a representative result presented by Eckardt (1976) measured in the impeller passage.

In the present work, the change of velocity distribution due to a change of tip clearance was measured precisely at the exit of two different types of unshrouded centrifugal impellers, and the variation of secondary flow induced by increasing the tip clearance was studied together with the effect of tip clearance on the input power.

Test Impellers and Measurements

The two investigated unshrouded centrifugal impellers, one with radial blades and the other with backward-leaning blades, are identical to those shown in the literature (Senoo et al., 1986; Ishida et al., 1981). The R-impeller was designed for a turbocharger with 20 radial blades and inducers, and it had an exit diameter of 210.8 mm, exit blade height of 15 mm, specific speed of 0.58, and design flow coefficient of 0.36. The B′-impeller was originally a shrouded conventional centrifugal impeller and it had 16 backward-leaning blades with

Contributed by the International Gas Turbine Institute and presented at the 34th International Gas Turbine and Aeroengine Congress and Exhibition, Toronto, Ontario, Canada, June 4-8, 1989. Manuscript received at ASME Headquarters January 17, 1989. Paper No. 89-GT-81.

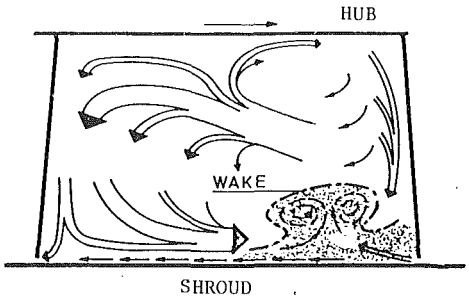

Fig. 1 Secondary flow pattern in the radial part of centrifugal impeller presented by Eckardt (1976)

exit angle of 45 deg; the exit diameter was 510 mm, the exit blade height was 17 mm, the specific speed was 0.43, and the design flow coefficient was 0.27. The front shroud was machined off to be an unshrouded impeller. The principal particulars of the two impellers are listed in Table 1.

The experimental setup consists of a suction plenum tank, a test impeller, and a vaneless diffuser. Air was axisymmetrically discharged from the blower to the atmosphere through a parallel wall vaneless diffuser with an exit radius ratio of about 1.8. The tip clearance on these impellers was changed by inserting shims at the exit position of the vaneless diffuser so that the axial clearance at the exit of the impeller was varied stepwise from 0.1 to 3.4 mm for each impeller. In the present experiment, the R-impeller was operated at a constant speed of 4000 ± 4 rpm, and the B′-impeller at 2000 ± 2 rpm. The flow rate was measured with an entrance flow nozzle, which was located between the plenum and the suction pipe. Although the tip clearance was changed, the flow rate was kept constant with an accuracy of 0.2 percent by controlling with a conical damper, which was located at the entrance of the plenum chamber, and the input shaft torque was measured with an accuracy of 1.0 percent.

The velocity distribution between the hub and the shroud was measured at the position immediately downstream of the impeller by means of a wedge-type two-hole yaw probe and a total pressure probe successively, which were made of 0.7-mm-dia. tube, to minimize the disturbance on the flow. The two-dimensional periodic flow was measured at the same position using a specially designed single hot-wire probe. The 5-μm-dia hot wire, supported by two prongs of 0.4 mm diameter, was placed parallel to the diffuser walls, and they were rotated together with the holder. The surface of the holder was flush with the diffuser wall and only the prongs and the hot wire were traversed lengthwise perpendicular to the diffuser walls.

Table 1 Principal particulars of test impellers

	R-impeller	B′-impeller
Exit diameter(mm)	210.8	510
Exit blade height(mm)	15	17
Exit blade angle(deg)	90	45
Inlet blade angle(deg)	34	28
Number of blades	20	16
Design flow coefficient	0.36	0.27
Specific speed	0.58	0.43

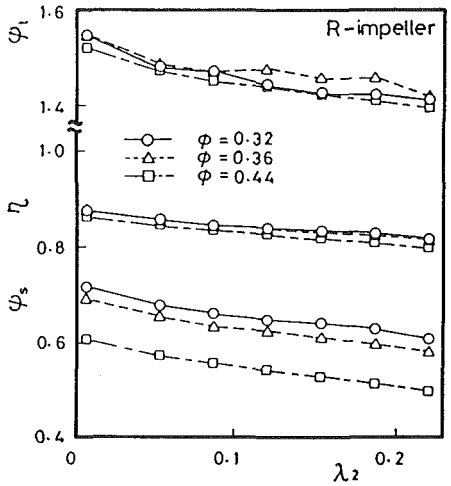

Fig. 2 Effect of tip clearance on the R-impeller performance (uncertainties of ψt, η, and ψs are ± 0.019, ± 0.013, and ± 0.008, respectively)

Experimental Results and Discussion

Changes in Efficiency and Input Power. Figure 2 shows an example of performance change due to increase of the tip clearance in the R-impeller; ψt and ψs are the total and static pressure coefficients at the exit of impeller, respectively, and η is the impeller efficiency. The abscissa is the tip clearance ratio at the exit of impeller, and the parameter is the flow coefficient ϕ. The tip clearance decreases the impeller efficiency,

Nomenclature

b = blade height
c = tip clearance
k = slip coefficient
m = meridional length along the shroud
p = pressure
r = radius
R = radius ratio referred to the impeller radius
U_2 = peripheral speed of impeller outer diameter
Vm = meridional component velocity normalized by U_2
Vu = tangential component velocity normalized by U_2
W = relative velocity normalized by U_2
Wb = component of W along the blade
Wn = component of W normal to the blade
y = axial distance from the hub surface along the blade height
y' = axial distance from the shroud wall surface
Z = number of blades
β = relative flow angle from circumference
βb = blade angle
η = impeller efficiency
λ_2 = tip clearance ratio at impeller exit
ρ = density of fluid
τ = shear force due to meridional pressure gradient; defined by equation (2)
ϕ = flow coefficient at impeller exit
ϕn = secondary flow coefficient
ψ = pressure coefficient of impeller

Subscripts

1 = impeller inlet
2 = impeller exit
3 = diffuser inlet
PS = pressure surface
s = static pressure
SS = suction surface
t = total pressure

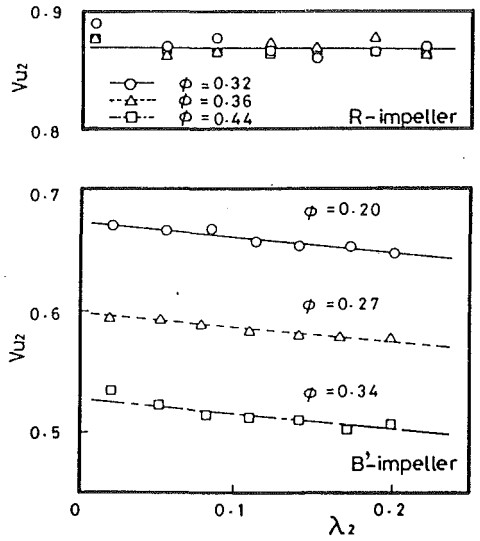

Fig. 3 Effect of tip clearance on input power (uncertainties of Vu_2 and λ_2 are ± 0.007)

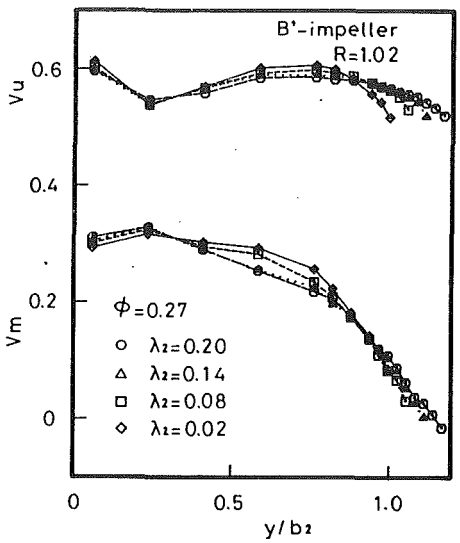

Fig. 5 Effect of tip clearance on the discharge velocity distribution; B′-impeller, $R = 1.02$, $\phi = 0.27$ (uncertainties of Vu and vm are ±0.006)

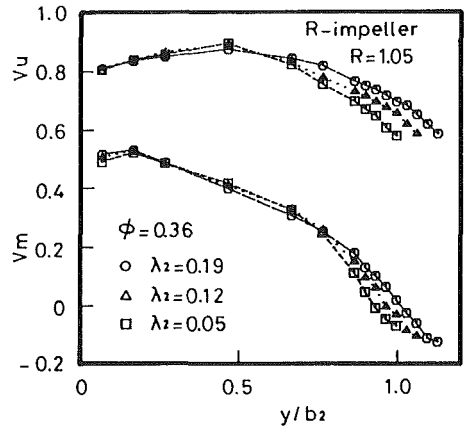

Fig. 4 Effect of tip clearance on the discharge velocity distribution; R-impeller, $R = 1.05$, $\phi = 0.36$ (uncertainties of Vu and Vm are ± 0.006)

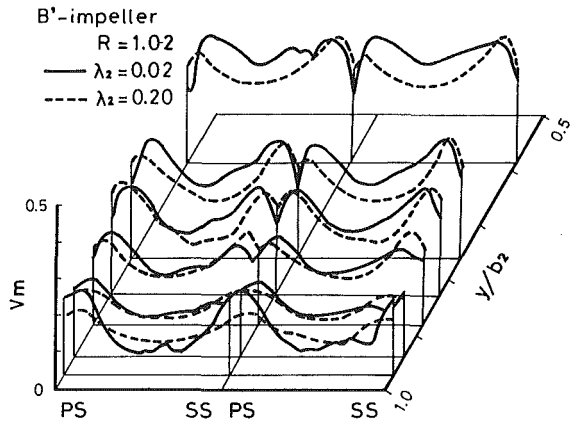

Fig. 6 Effect of tip clearance on the blade-to-blade distribution of the meridional component velocity; B′-impeller, $\phi = 0.27$ (uncertainty of Vm is ± 0.006)

showing a tendency similar to those reported in other studies; the decrement of efficiency is about 3 points for a change of 10 percent in the tip clearance ratio.

The tangential component of the absolute velocity at the impeller exit was estimated from the measured shaft torque and the flow rate subtracting the disk friction torque and the bearing torque. Figure 3 shows the effect of tip clearance on the work factor, or the tangential component of velocity referred to the impeller tip speed. In the case of the R-impeller, work factors were hardly influenced within the accuracy of the torque measurement by increasing the tip clearance and also by varying the flow rate. Only in the case of the minimum tip clearance ratio $\lambda_2 = 0.007$, the work factor was slightly different from other tip clearance conditions. This seems to be due to a relative misalignment between the impeller disk and the diffuser hub wall because the minimum tip clearance of 0.1 mm was attained by axially moving the impeller away from the hub.

On the other hand, in the case of the B′-impeller, work factors were decreased by increasing the tip clearance for all flow rates. It is noticed that the decreasing rates due to the tip clearance were almost equal in the present three flow rates, that was, $dVu_2 / d\lambda_2 \fallingdotseq 0.13$. A similar trend is reported in the literature (Ishida et al., 1981).

Comparison of Velocity Distributions With Respect to the Impeller Blade Height. Figures 4 and 5 show the hub-to-shroud distributions of the meridional and tangential components of the absolute velocity measured at the radial positions of $R = 1.05$ for the R-impeller and $R = 1.02$ for the B'-impeller, respectively. The abscissa is the axial distance y from the hub along the blade height, which is normalized by the exit blade height b_2. The change in velocity distributions is partly similar in both impellers, that is, the tangential and meridional components of the velocity are decreased near the middle of the blade height by increasing the tip clearance, and on the contrary, both Vu and Vm are increased in the blade tip region by an increase of the tip clearance. The increase of tip clearance affects not only the flow near the blade tip but also the flow in the whole region between hub and shroud.

The mass-averaged tangential component of the absolute velocity at the impeller exit was evaluated from the following equation:

$$Vu_2 = \frac{\int_0^{1+\lambda 2} R^2\ Vm\ Vu\ d(y/b_2)}{\int_0^{1+\lambda 2} R\ Vm\ d(y/b_2)} \tag{1}$$

The value of Vu_2 evaluated by equation (1) agreed well with the value evaluated from the measured shaft torque shown in Fig. 3.

Figure 6 shows the blade-to-blade distributions of the meridional component velocity Vm, which were measured at the radial position $R = 1.02$ for the B′-impeller by means of a hot-wire probe. The data in the diagram were the values

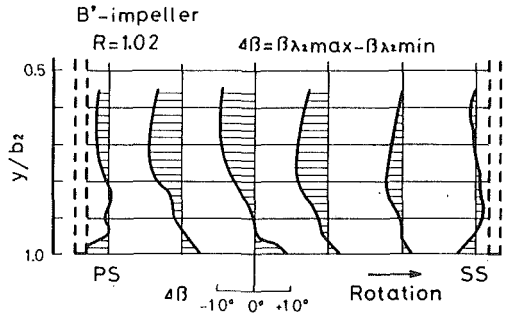

Fig. 7 Secondary flow pattern presented in the form of $\Delta\beta$ distribution; B′-impeller, $\phi = 0.27$ (uncertainty of $\Delta\beta$ is ± 1.0 deg)

averaged over 100 revolutions and, furthermore, averaged by superposing every two pitches of 16 blades; the scale of blade height is magnified about 12 times the scale of blade spacing. The measuring area is about half the blade height in the tip side. The solid lines designate the minimum tip clearance condition $\lambda_2 = 0.02$ and the broken lines the maximum tip clearance condition $\lambda_2 = 0.20$.

By increasing the tip clearance, the meridional velocity component is described significantly in the middle of the blade height, and what's more, the velocity decrement is larger near the pressure side than the suction side. It seems that the low-momentum fluid is carried from the suction side shroud corner toward the pressure side midblade height of the adjacent blade. It can be also seen that the blade wake has disappeared near the blade tip. The trailing vortex induced by the leakage through the tip clearance may be responsible for smoothing the circumferential variation of velocity near the tip.

Figure 7 shows the secondary flow pattern, which is represented in the form of $\Delta\beta$ distributions, in the same measuring areas as Fig. 6, where $\Delta\beta = \beta(\lambda_{2\max}) - \beta(\lambda_{2\min})$. The secondary flow, which moves from the pressure side of a blade toward the suction side of the adjacent blade along the shroud, and the other secondary flow, which crosses from the suction side shroud corner toward the middle of the adjacent pressure surface, are combined with the tip leakage flow. This secondary flow pattern is similar to those presented by Eckardt (1976) and Farge et al. (1989). The observed secondary flow in this experiment seems to be inherent in unshrouded centrifugal impellers, and it is strengthened by an increase of the tip leakage flow.

Comparison of Velocity Distributions With Respect to the Passage Height. In the preceding section, the secondary flow pattern induced by the tip clearance was shown and studied relative to the impeller blade, as is seen in most studies. From the flow pattern with respect to the impeller blade height, the changes in the flow pattern and the input power due to the tip clearance were different from each other for the two different types of impellers. In this section, the velocity distribution between the hub and the shroud was re-examined from the viewpoint of passage height between the hub and shroud wall.

Figures 8 and 9 show the hub-to-shroud distributions of the relative flow angle β and the relative velocity W, which were measured at the radial position $R = 1.05$ for the R-impeller and $R = 1.02$ for the B′-impeller, respectively. The abscissa is the axial distance y' from the shroud wall surface referred to the diffuser inlet width b_3, where $y' = b_3 - y$ and $b_3 = b_2 + c_2$; the hatched boundaries designate the locations of the blade tip at each tip clearance condition.

It is noticed in the figures that, in the case of the R-impeller, the relative flow angle is hardly changed by varying the tip clearance and the flow rate in the whole region between the hub and the shroud. On the other hand, in the case of the B′-impeller, the relative flow angle is significantly and monotonously reduced by increasing the tip clearance in

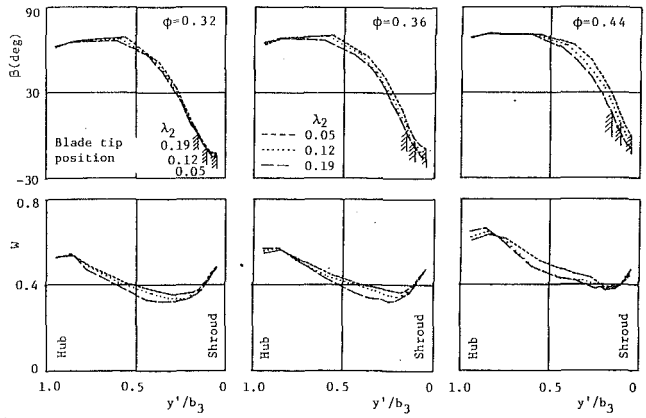

Fig. 8 Hub-to-shroud distributions of the relative flow angle and the relative velocity referred to the shroud wall surface; R-impeller, $R = 1.05$ (uncertainties of β and W are ± 1.0 deg and ± 0.006)

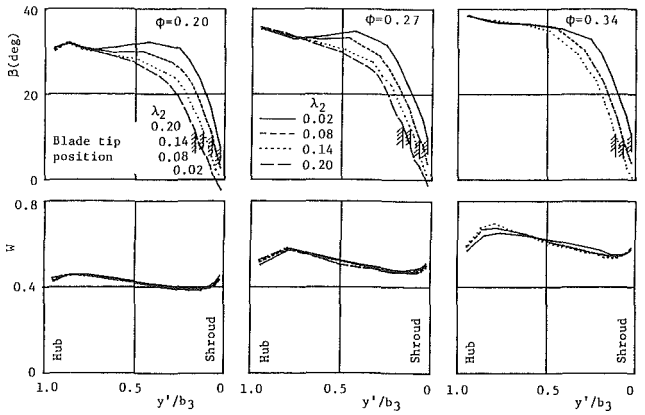

Fig. 9 Hub-to-shroud distributions of the relative flow angle and the relative velocity referred to the shroud wall surface; B′-impeller, $R = 1.02$ (uncertainties of β and W are ± 1.0 deg and ± 0.006)

almost all of the exit section except near the hub side. The change of relative flow angle in the two impellers seems to be directly related to the change of input power shown in Fig. 3. Regarding the relative velocity distribution, there is little change caused by varying the tip clearance in both impellers. A small change in relative flow angle in the R-impeller seems to be attributed to the inducer with backward-leaning blades.

In the case of the R-impeller, the fact that the relative flow angle was hardly change in spite of the large tip clearance means that the fluid in the tip clearance was supported by the fluid in the impeller passage. This was achieved by greater work of the blade especially near the tip, therefore, the relative flow angle was increased at the blade tip as shown in Fig. 8 by the hatched boundary. Judging from this fact, the significant reduction of relative flow angle in the case of the B′-impeller is not due to an increase of the leakage flow through the tip clearance, but to other causes.

Secondary Flow Normal to the Blade. According to the theory presented by the authors (Senoo et al., 1986, 1987), the tip clearance loss mainly consists of two kinds of loss: one is the drag due to the leakage flow through the tip clearance, and the other is the pressure loss to support the fluid in the thin annular clearance space between the shroud and the blade tip against the pressure gradient in the meridional plane without blades. Regarding the tip leakage loss, the situation is identical for the radial blade impeller and the backward-leaning blade impeller, but regarding the second loss, it is different between the two types of impeller. The shear force to support the meridional pressure gradient has a component normal to the

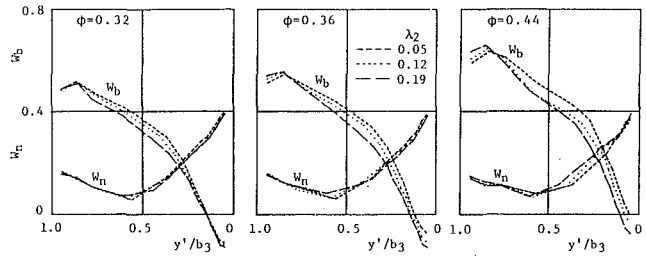

Fig. 10 Velocity distributions of the component along blade and the component normal to blade; R-impeller, $R = 1.0$ (uncertainties of *Wb* and *Wn* are ± 0.006)

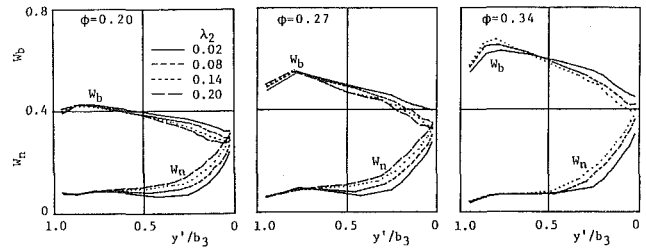

Fig. 11 Velocity distributions of the component along the blade and the component normal to bladed; B′-impeller, $R = 1.0$ (uncertainties of *Wb* and *Wn* are ± 0.006)

blade in the case of the backward-leaning blade impeller. On the other hand, there is no normal component of the shear force in the radial blade impeller. This is the only difference between the two impellers. That is, the secondary flow in the B′-impeller passage section normal to the blade must be increased by the normal component of the shear force.

The meridional component of the shear force along the surface of revolution was estimated by the following equation in the literature (Senoo et al., 1986):

$$\tau = c\,\{dp/dm - (dp/dm)_c\} \tag{2}$$

where dp/dm is the meridional pressure gradient along the shroud induced by an impeller; $(dp/dm)_c$ is the pressure gradient that can be supported by the centrifugal force in the annular space. $(dp/dm)_c$ is estimated by assuming that the circumferential velocity of fluid in the annular space is equal to that in the impeller. The component of the shear force normal to the blade is integrated using equation (3) from the inlet to the exit of the impeller in order to correlate with the secondary flow rate normal to the blade at the exit of the impeller, which is evaluated by equation (4).

$$Fn = \frac{\int_{m_1}^{m_2} 2\pi r\,\tau\cos\beta_b\,d_m}{2\pi r_2 b_2(\rho/2)U_2^2} \tag{3}$$

$$\phi n = (b_3/b_2)\int_0^1 Wn\,d(y'/b_3) \tag{4}$$

Figures 10 and 11 show the velocity distributions of the component along the blade *Wb* and the component normal to the blade *Wn* at the exit of impeller for the R-impeller and the B′-impeller, respectively. These components of the velocity at the impeller exit were reduced from the measured data by using the relations of continuity and conservation of angular momentum. As is seen in the figures, the normal component of the velocity is significantly increased in the case of B′-impeller but it is hardly changed in the case of the R-impeller. Furthermore, the normal component under the minimum tip clearance condition shown in the figures is based mainly on the slip near the exit of impeller and partly on the tip leakage flow.

Figure 12 shows the correlation between the secondary flow coefficient ϕn and the normal component of the shear force

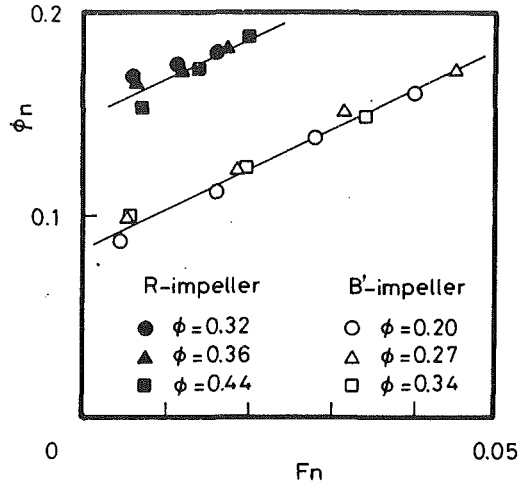

Fig. 12 Effect of tip clearance on the secondary flow rate (uncertainty of ϕn is ± 0.009)

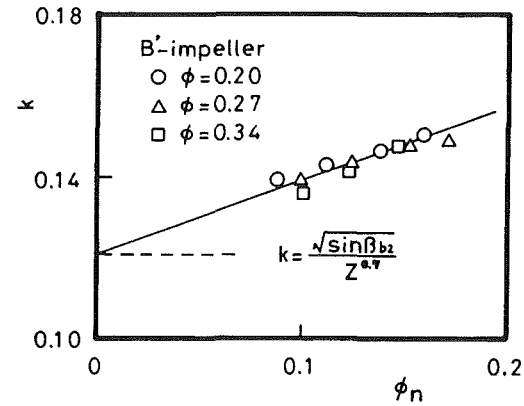

Fig. 13 Effect of secondary flow on slip coefficient (uncertainty of k is ± 0.007)

due to the meridional pressure gradient Fn for the two impellers. The figure shows a good correlation for the respective impellers. It is noticed that the secondary flow is linearly increased by the force Fn, and what's more, the increasing rate is almost identical in both impellers. The difference of ϕn at $Fn = 0$ between the two impellers is based on the difference of slip near the exit of impeller. The secondary flow is, therefore, significantly induced in the backward-leaning blade impeller because the driving force Fn varies largely by an increase of the tip clearance. It is insignificant in the radial blade impeller because of a small change in the driving force, which originates only in the inducer portion with backward-leaning blade.

Figure 13 shows the correlation between the slip coefficient and the secondary flow coefficient for the B′-impeller. The experimental slip coefficient was calculated by the following equation:

$$k = 1 - \phi\cot\beta b_2 - Vu_2 \tag{5}$$

where Vu_2 is the experimental value evaluated by equation (1). A good correlation is observed between them. The k value at $\phi n = 0$, which is obtained by extrapolation of the fitted straight line, is extremely close to the value evaluated by the Wiesner's empirical equation; $k = \sqrt{\sin\beta b_2}/Z^{0.7}$ (Wiesner, 1967).

As the effect of tip clearance on the secondary flow rate was nearly equal at the three flow rates of the B′-impeller, the rate of reduction in the input power was almost identical at the three flow rates shown in Fig. 3. Furthermore, in the case of

the R-impeller, the variation of slip coefficient due to the tip clearance was so small that the correlation was not clear.

Conclusions

The effects of tip clearance on the flow pattern at the exit of impeller and on the input power were examined experimentally using two entirely different types of impellers. The principal conclusions are as follows:

1 The input power was hardly changed in the radial blade impeller and was reduced in the backward-leaning blade impeller by the increase of tip clearance.

2 From the flow pattern referred to the impeller blades, a secondary flow different from that in shrouded impellers is induced at the impeller exit by the tip clearance and the stationary shroud. The observed pattern at the impeller exit was quite similar to those observed inside of centrifugal impeller passages. However, the difference of the flow patterns between the two impellers could not be made clear from this viewpoint.

3 The flow pattern referred to the shroud wall was hardly changed at the exit of the radial blade impeller by increasing the tip clearance. On the other hand, in the case of the backward-leaning blade impeller, the relative flow angle was reduced significantly and monotonously by an increase of the tip clearance. The change in input power due to the tip clearance was clearly related to the change of the secondary flow normal to the blade.

4 The secondary flow due to the tip clearance is most likely caused by the component, which is normal to the blade, of the shear force to support the fluid in the thin annular clearance space between the shroud and the blade tip against the pressure gradient in the meridional plane without blades.

Acknowledgments

The authors wish to thank Messrs. H. Egami, T. Mitsutake, and H. Shibahara for construction of the experimental apparatus and for securing the experimental data.

References

Eckardt, D., 1976, "Detailed Flow Investigations Within a High-Speed Centrifugal Compressor Impeller," ASME *Journal of Fluids Engineering*, Vol. 98, No. 3, pp. 390–402.

Eckert, B., and Schnell, E., 1961, *Axial- und Radial-Kompressoren*, 2nd ed., Springer-Verlag, Berlin, pp. 192, 357.

Engeda, A., and Rautenberg, M., 1987, "Comparisons of the Relative Effect of Tip Clearance on Centrifugal Impeller," ASME JOURNAL OF TURBOMACHINERY, Vol. 109, No. 3, pp. 545–549.

Farge, T. Z., Johnson, M. W., and Maksoud, T. M. A., 1989, "Tip Leakage in a Centrifugal Impeller," ASME JOURNAL OF TURBOMACHINERY, Vol. 111, pp. 244–249.

Hesselgreaves, J. E., 1969, "A Correlation of Tip-Clearance, Efficiency Measurements on Mixed-Flow and Axial-Flow Turbomachines," NEL Report, No. 423.

Ishida, M., and Senoo, Y., 1981, "On the Pressure Losses Due to the Tip Clearance of Centrifugal Blowers," ASME *Journal of Engineering for Power*, Vol. 103, No. 2, pp. 271–278.

Lakshminarayana, B., 1970, "Methods of Predicting the Tip Clearance Effects in Axial Flow Turbomachinery," ASME *Journal of Basic Engineering*, Vol. 92, No. 3, pp. 476–482.

Pfleiderer, C., 1961, *Die Kreisel Pumpen*, Vol. 5, Springer-Verlag, Berlin, p. 99.

Senoo, Y., and Ishida, M., 1986, "Pressure Loss Due to the Tip Clearance of Impeller Blades in Centrifugal and Axial Blowers," ASME *Journal of Engineering for Gas Turbines and Power*, Vol. 108, pp. 32–37.

Senoo, Y., and Ishida, M., 1987, "Deterioration of Compressor Performance Due to Tip Clearance of Centrifugal Impeller," ASME JOURNAL OF TURBOMACHINERY, Vol. 109, No. 1, pp. 55–61.

Wiesner, F. J., 1967, "A Review of Slip Factors for Centrifugal Impellers," ASME *Journal of Engineering for Power*, Vol. 89, No. 4, p. 558.

H. Hayami
Professor,
Institute of Advanced Material Study,
Kyushu University 86,
Kasuga 816, Japan
Mem. ASME

Y. Senoo
Director,
Miura Company, Ltd.,
Matsuyama 799-26, Japan
Fellow ASME

K. Utsunomiya
Engineer,
Mitsubishi Kasei Corp.,
Yokohama 227, Japan

Application of a Low-Solidity Cascade Diffuser to Transonic Centrifugal Compressor

Low-solidity circular cascades, conformally transformed from high-stagger linear cascades of double-circular-arc vanes with solidity 0.69, were used as a part of the diffuser system of a transonic centrifugal compressor. Performance test results were compared with data of the same compressor with a vaneless diffuser. Good compressor performance and a wider flow range as well as a higher pressure ratio and a higher efficiency, superior to those with a vaneless diffuser, where the flow range was limited by choke of the impeller, were demonstrated. The test circular cascade diffusers demonstrated a good pressure recovery over a wide range of flow angles, even when the inflow Mach number to the cascade was over unity.

Introduction

Two types of diffuser are commonly used for centrifugal compressors. One is a vaned diffuser, which achieves a high pressure recovery but has a narrow flow range of operation, and the other is a vaneless diffuser, which can operate over a wide flow range but has a low pressure recovery coefficient. If the pressure ratio of a compressor is larger than four, the velocity relative to the inducer and to the diffuser usually exceeds the velocity of sound. Since a conventional vaned diffuser is sensitive to the angle of incidence, especially at a supersonic condition, the flow range of high pressure ratio compressors with a vaned diffuser is very narrow. Many centrifugal compressors are used as a component of a large-capacity refrigeration system. As the sonic velocity of refrigerants is low due to their high molecular weight, the flow at the impeller inlet and at the diffuser inlet is often transonic or supersonic. Since compressors for refrigeration units are required to operate over a wide flow range corresponding to load conditions, a vaneless diffuser is commonly adopted at the expense of efficiency.

In the preceding paper using a low-speed centrifugal blower, Senoo et al. (1983) demonstrated that a diffuser with a low-solidity cascade had a wide range of stable operation comparable to that of a vaneless diffuser and that the diffuser achieved considerably better pressure recovery compared to that of a good vaneless diffuser. In the present paper, low solidity circular cascades, conformally transformed from high-stagger linear cascades of double-circular-arc vanes with solidity 0.69, were adopted as a part of the diffuser system of a transonic centrifugal compressor, which had an impeller with 30 backward swept blades. Good compressor performance, a wide flow range as well as a high pressure ratio, and a high efficiency were demonstrated up to a rotor speed where the inflow Mach number to the cascade was 1.1.

Experimental Apparatus

A high-pressure-ratio centrifugal compressor was tested in a closed loop with Freon R-12 gas at four speeds up to 19,000 rpm. The meridional profile of the test compressor is shown in Fig. 1. The test impeller is shown in Fig. 2(*b*). The diameter

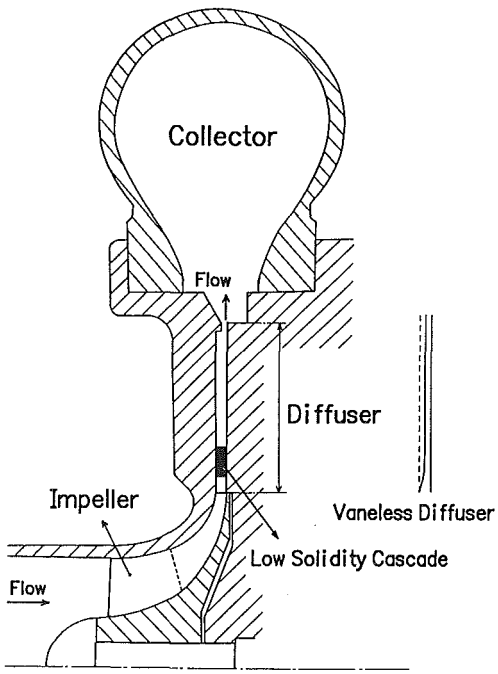

Fig. 1 Meridional profile of test compressor

Contributed by the International Gas Turbine Institute and presented at the 34th International Gas Turbine and Aeroengine Congress and Exhibition, Toronto, Ontario, Canada, June 4–8, 1989. Manuscript received at ASME Headquarters January 13, 1989. Paper No. 89-GT-66.

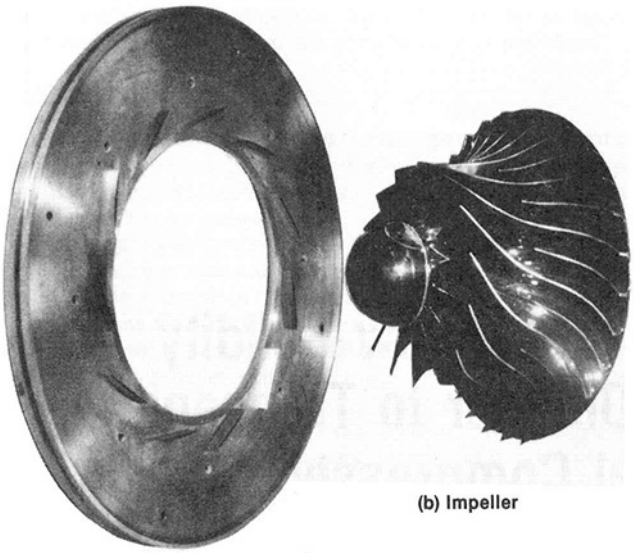

Fig. 2 Cascade diffuser and impeller

of the impeller was 280 mm, the exit blade width was 8.9 mm, and the inducer diameter was 172 mm. The open shroud impeller had 15 main blades and 15 splitter blades with a backward sweep angle of 40 deg at the exit.

Downstream of the impeller was a diffuser, which consisted of a cascade and two parallel walls 9.4 mm apart; The outer diameter was 560 mm. The diffuser was connected to an axisymmetric collector and finally to a delivery pipe. To increase stability a circular fence was installed so that the exit width of the diffuser was made one half of the diffuser width, as shown in Fig. 1.

The cascade of interest was installed between the two parallel walls, so that the leading edges of the blades were located at 308 mm in diameter or 1.1 in radius ratio to the impeller exit. A double-circular-arc vane, with 10 deg blade turning angle and 4 percent thickness, was adopted as the original airfoil section of the reference linear cascades. The solidity of the linear cascades was 0.69 and the stagger angles were 69 deg and 72 deg, respectively. The linear cascades were conformally transformed to circular cascades with eleven blades. They are identified as the SVD69 cascade and the SVD72 cascade, respectively. The thickness of the leading and trailing edges of each vane was 0.2 mm. The SVD69 cascade is shown in Fig. 2(*a*).

For comparison, the impeller was also tested with a vaneless diffuser. In the case of high-pressure-ratio compressors, the mean flow angle from the tangent reduces with radius in a vaneless diffuser with parallel walls due to the effect of compressibility. In order to avoid local reverse flow at a large radius, the passage width of the test vaneless diffuser (VLD) was linearly reduced from 9.4 mm at the inlet to 4.7 mm at the radius ratio 1.1, and then the diffuser width was kept constant all the way down to the exit, as shown in Fig. 1.

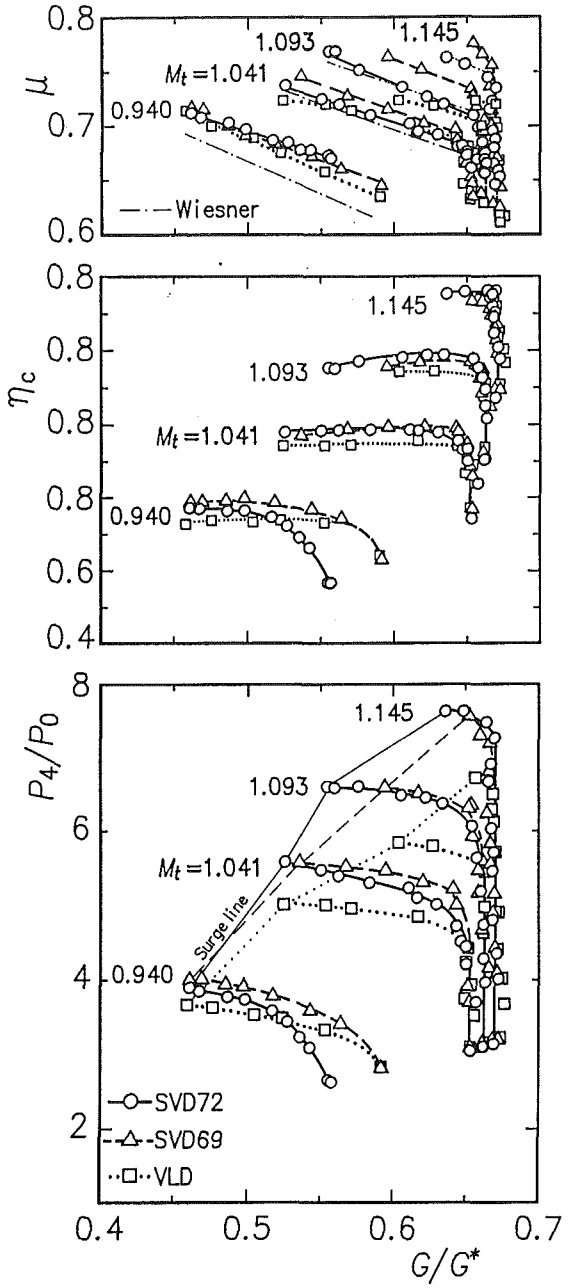

Fig. 3 Characteristics of compressor; G^* = choking mass flow rate in suction pipe

Experimental Results and Discussions

Characteristics of Compressor. The characteristic curves of the compressor with different diffusers are presented in the three graphs of Fig. 3. The ordinates of the graphs from the

Nomenclature

C_p = pressure coefficient = $(p-p_2)/(P_2-p_2)$
G = mass flow rate
M = Mach number
M_t = nominal Mach number of inducer tip speed
P = stagnation pressure
p = static pressure
R = radius ratio = r/r_2
α = absolute flow angle from the tangent
η_c = total-to-total efficiency for compressor stage
η_d = diffuser efficiency, see equation (1)
μ = work factor

Subscripts

0 = compressor inlet
1 = impeller inlet
2 = impeller exit
3 = cascade diffuser inlet
4 = compressor exit

bottom to the top are the total pressure ratio P_4/P_0, the compressor efficiency η_c, and the impeller work factor μ, respectively. The abscissa G/G^* is the ratio of the mass flow rate to the choking flow rate in the suction pipe. The parameter M_t is the nominal Mach number of the inducer tip speed, which corresponds to the corrected speed. The total pressure at the compressor exit is the sum of the static pressure and the dynamic pressure in the delivery pipe of the compressor. The dynamic pressure was less than 1 percent of the inlet total pressure. The input head or the impeller work factor was estimated from the stagnation temperature difference between the inlet and the exit of the compressor after subtracting the disk friction power, which was 0.02 to 0.05 of the input power.

In cases of $M_t \geq 1.041$, the characteristic curves are vertical at the right end, and the flow rate at a given corrected speed is constant regardless of the diffuser. This means that the inducer was choked. One of the special features of a low-solidity cascade is that the diffuser is hardly choked. At the left extremities of the characteristic curves the compressor fell into surge except for the case of $M_t = 0.940$, where the inducer fell into stall but the compressor was not in surge.

The minimum flow conditions at different shaft speeds are connected by thin lines in the pressure versus flow characteristic curves in the bottom graph. The lines, including inducer stall points, are called surge lines. In comparison with the surge line of the vaneless diffuser, the surge line has moved toward the left in the case of SVD69 and moved farther in the case of SVD72. That is, the available flow range of the cascade diffusers was wider than that of the VLD. For instance, at a pressure ratio $P_4/P_0 = 6.5$, the ratio of the available flow range to the maximum flow rate for VLD was only 3.6 percent, while it was improved to 11.1 percent for SVD69 and 17.0 percent for SVD72, and the difference of the flow ranges of these diffusers remained about constant at pressure ratios over 7.0.

In the case of $M_t \leq 1.041$, the critical flow rates for surge were almost identical regardless of the type of diffuser. Furthermore, the flow rate was equal to the critical flow rate for inducer stall in the test of the isolated impeller. That is, the surge was caused by stall of the impeller. On the other hand, in the cases of $M_t \geq 1.093$, the critical flow rates for surge with SVD69 and SVD72 diffusers were larger than that of inducer stall, and they depended on the type of diffusers. That is, the surge was induced by stall of the diffusers.

The experimental data for work factor μ lie on straight lines except at the choking condition. The chain dotted lines represent the prediction based on one-dimensional flow analysis using Wiesner's slip coefficient for SVD72. The experimental data agreed fairly well with the prediction except for the case of $M_t = 0.940$. By closer examination it is noticed that the input head was increased by installation of the cascades and the difference increased at a higher corrected speed. This may be related to the reverse flow to the impeller from the diffuser. One of the special features of a cascade with a high stagger angle is that the boundary layer along the side walls flows inward from the suction side of a vane to the pressure side of the adjacent vane due to the radial adverse pressure gradient. Therefore, the vane does not stall even at a large incidence angle. On the other hand, if the secondary flow re-enters the impeller, the input head increases. Referring to Fig. 7, the inlet Mach number relative to the cascade was above unity, and shock waves were unavoidable. It is suspected that the shock waves were stronger and the reverse flow rate increased as the Mach number increased, as a result extra input power was required.

The efficiency of the compressor with a cascade diffuser was better than that with a vaneless diffuser for a wide flow range, and the maximum value of the efficiency was improved from 0.75 for the vaneless diffuser to 0.80 for SVD69 and to 0.79 for SVD72 respectively. The shaft speed, where the maximum efficiency was achieved, differed depending on the diffuser type. SVD69 demonstrated superior characteristics at a lower speed, while SVD72 did at a higher speed. It is understandable that the optimum operating speed increases with the stagger angle. As a whole, the pressure ratio, the efficiency, and the flow range of the compressor with cascade diffusers were all superior to those with the vaneless diffuser.

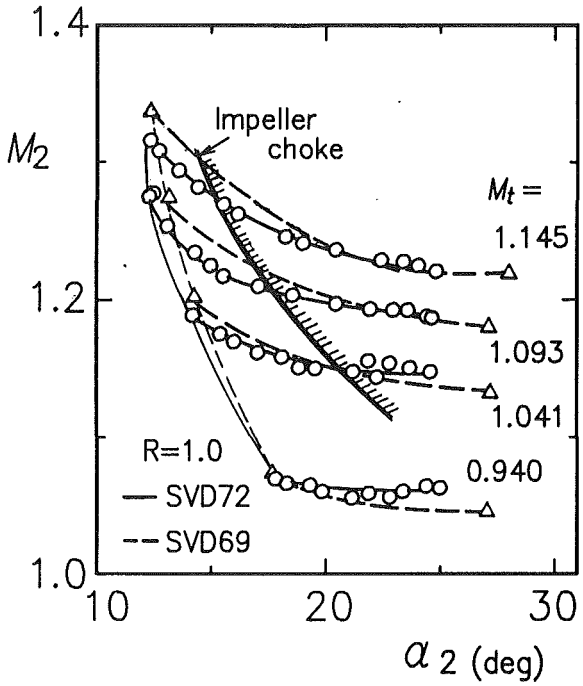

Fig. 4 Flow condition at impeller exit

Flow at Diffuser Inlet. The relationship between the inflow angle α_2 and the inflow Mach number M_2 at $R = 1.0$, the diffuser inlet, is presented in Fig. 4. Due to the supersonic velocity at the diffuser inlet, the flow velocity and the flow angle were not directly measured but were estimated using the tangential velocity evaluated from the work factor and the radial velocity calculated from the measured pressure and the flow rate assuming that there was no preswirl at the impeller inlet. The line of the critical conditions of impeller choke is also plotted in the figure.

Although the mass flow rate was constant at the condition of impeller choke, α_2 became larger as the back pressure was reduced. At a given corrected speed, the relationship between α_2 and M_2 varied smoothly passing through the line of critical condition of impeller choke. The minimum inflow angle corresponds to the critical condition for surge or inducer stall. The minimum value of α_2, 12.2 deg, was observed at the maximum value of $M_2 = 1.34$. Apparently the measured minimum values of inflow angle α_2 at the lower M_t line do not indicate the stall of the cascade.

Regarding the uncertainty of M_2 and α_2, if the measured input head is less than the true input head by 1 percent due to the cooling effect from the casing, the true value of M_2 would be larger by about 1 percent and α_2 would be less by 0.1 to 0.2 deg. On the other hand, if the increase in the input head is caused by recirculation at the impeller exit as mentioned before, the true value of the tangential velocity is less than the measured data. If it is assumed that the flow rate of recirculation is 5 percent of the delivery flow rate and it loses 20 percent of the original tangential velocity in the diffuser during recirculation, 1 percent of the input head is absorbed by the recirculation flow, and as a result, M_2 is less by about 1 percent and α_2 is larger by 0.1 to 0.2 deg.

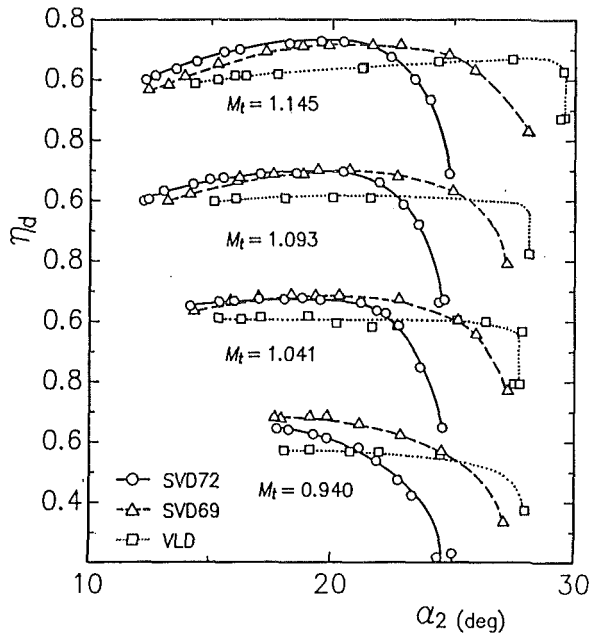

Fig. 5 Relationship between inflow angle and diffuser efficiency

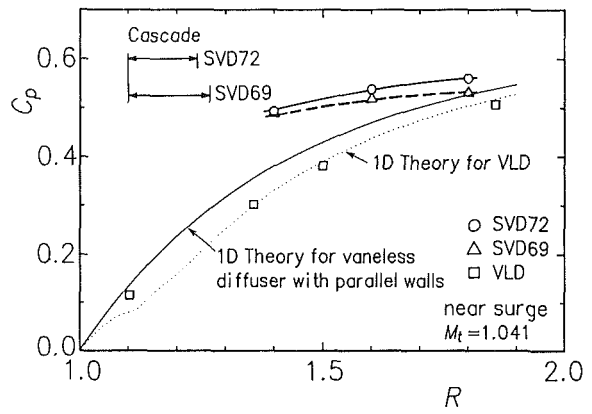

(a) Near the surge condition

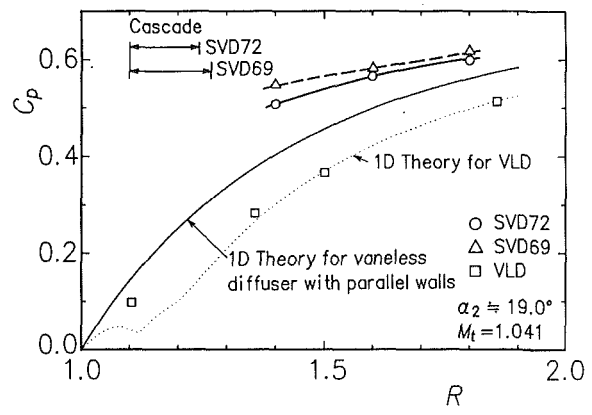

(b) $\alpha_2 \fallingdotseq 19$ deg (near the maximum flow rate)

Fig. 6 Radial distribution of pressure: *(a)* $\alpha \fallingdotseq 15$ deg; *(b)* $\alpha_2 \fallingdotseq 19$ deg

Efficiency of Diffuser. Figure 5 represents the relationship between the inflow angle to the diffuser α_2 and the diffuser efficiency η_d including the collector, where η_d is defined as follows:

$$\eta_d = c_p T_2 [(p_4/p_2)^{(\kappa-1)/\kappa} - 1]/[V_2^2/2] \quad (1)$$

κ and c_p are the specific heat ratio and the specific heat at constant pressure, respectively. T_2 is the static temperature at the impeller exit. $V_2^2/2$ in the denominator is the kinetic energy of flow at the impeller exit, which was estimated using the blockage factor of 0.15 at the impeller exit. The blockage factor includes the blockage due to the tip clearance considering reduction of the blade loading near the tip clearance of impeller blade (Senoo and Ishida, 1987) as well as that due to the boundary layer in addition to the geometric blockage 0.08 due to impeller blades. That is, it is assumed that at the diffuser inlet the width of flow passage is abruptly enlarged by a factor of 1/0.85. The static pressure rise and the pressure loss due to the sudden enlargement was included in the performance of the diffuser, where the expansion loss was 2–5 percent of the dynamic pressure of the absolute velocity.

The diffuser efficiency of the vaneless diffuser was nearly constant for the whole range, except at the right-hand extremities, where choking occurred in the diffuser. The diffuser efficiency of the present cascade diffusers demonstrated higher value over a wide range of flow angle. The optimum flow angle, where η_d was the maximum at a given corrected speed, increased slightly with the corrected speed. The dif-

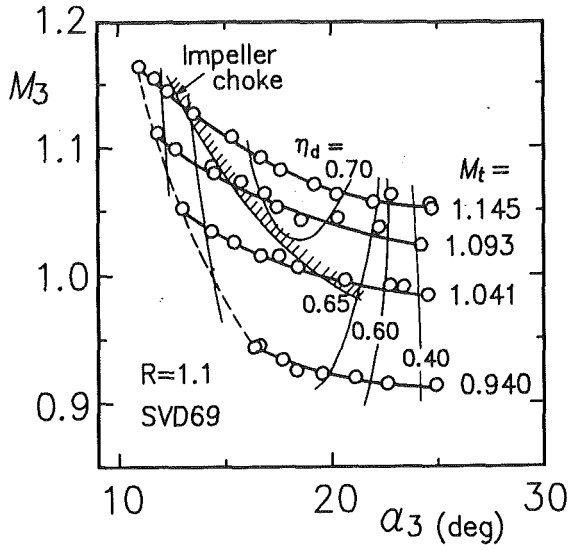

(a) SVD69

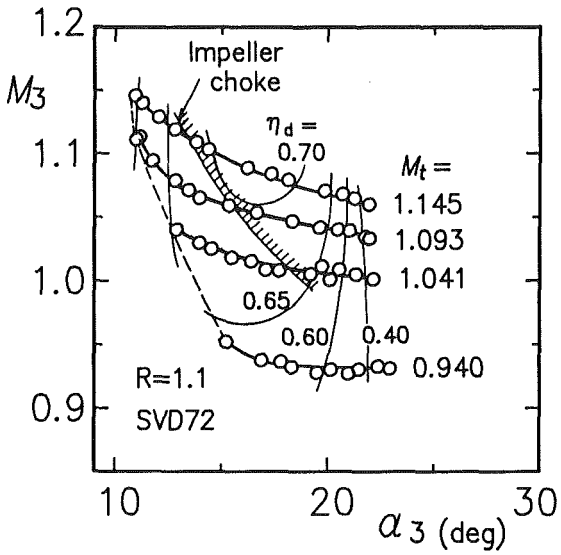

(b) SVD72

Fig. 7 Flow condition at cascade inlet

ference between the optimum flow angle for SVD72 and that for SVD69 was about 3 deg, which corresponded to the difference between the stagger angles, but the minimum flow angles for the two diffusers were almost identical regardless of the shaft speed. It is suspected that the minimum flow angle was controlled either by stall of the impeller or by reverse flow along the vaneless walls in the diffuser upstream of the cascade $1.0 < R \leq 1.1$. According to the three-dimensional boundary layer analysis for vaneless diffusers, developed by Senoo and Kinoshita (1977), reverse flow was predicted in the boundary layer at $R = 1.1$ just upstream of the cascade at this flow rate.

Radial Distribution of Wall Static Pressure in Diffuser. The radial distribution of wall static pressure between the impeller exit and the diffuser exit at $M_t = 1.041$ is shown in Fig. 6, where case (a) represents the critical condition of surge ($\alpha_2 \fallingdotseq 15$ deg) and case (b) represents the inflow angle $\alpha_2 \fallingdotseq 19$ deg, a large flow rate without impeller choke. The ordinate C_p is the pressure coefficient, that is, the ratio of the static pressure rise to the nominal dynamic pressure $(P_2 - p_2)$ including a blockage factor of 0.15 at the impeller exit. The pressure distribution in the test vaneless diffuser (VLD) was predicted based on a one-dimensional analysis assuming frictional, steady, and compressible flow and is plotted as a dotted line, where the skin friction coefficient was a function of Mach number M and was assumed to be 0.04 for $M = 0$. The agreement is satisfactory on the whole in both cases.

If the pressure coefficient at the cascade exit is evaluated by extrapolating the three sets of data to the exit of the cascade, the pressure rise from the diffuser inlet to the cascade exit is as high as 0.45 to 0.50. For comparison, the thin full line represents the predicted values for the vaneless diffuser with parallel walls. In reality such a vaneless diffuser with a wide flow passage does not work well because the flow angle is small and reverse flow occurs on the wall. However, if such a vaneless diffuser works well, the pressure rise of 0.3 is achieved at $R = 1.25$, and the net pressure rise due to the cascade is 0.15 to 0.2. That is, the turning angle of the mean flow is not large, therefore the low-solidity cascade can achieve this much turning. It is also important that the flow angle downstream of the cascade is made larger by the cascade and the flow in the diffuser is stable.

Flow at Cascade Inlet. The relationship between the flow angle α_3 and the Mach number M_3 at the cascade inlet, $R = 1.1$, is indicated in Fig. 7. The flow in the vaneless diffuser zone upstream of the cascade was analyzed by a one-dimensional method as mentioned before. The impeller choke conditions and contours of equal diffuser efficiency are also indicated in the figure. The Mach number is certainly smaller than that at the diffuser inlet in Fig. 4, but it is still supersonic except at a low speed. At the same time, the flow angle α_3 becomes a little smaller due to the increase in gas density.

The inlet vane angle of the diffuser was 16 deg for SVD69 and 13 deg for SVD72. The value of η_d reached its maximum when the incidence angle was negative by -2 to -3 deg. It was unfortunate that the best efficiency condition of the diffuser corresponded to the choke condition of the impeller, and the best combination of the two was not demonstrated in the performance map of the compressor.

At the supersonic inflow condition, generation of shock waves is expected. In cases of a channel-type diffuser, shock waves generated near the leading edge of a vane reach the suction side of the adjacent vane, and the flow in the boundary layer on the suction surface may be separated and the vane stalled. In the present low-solidity cascade, however, the diffuser efficiency rather increased a little with an increase in the inflow Mach number. This implies that the ill effects of shock waves were not significant. It is presumed that a shock wave generated near the leading edge of a vane did not intersect with the adjacent vane, which was far away; therefore, shock waves had little effect on diffuser performance.

Conclusions

Low-solidity circular cascades, conformally transformed from linear cascades of double-circular-arc vanes with solidity 0.69, were used as a part of diffuser system of a transonic centrifugal compressor. Good compressor performance, a wider flow range as well as a higher pressure ratio and a higher efficiency, superior to those with a vaneless diffuser, were demonstrated, although the maximum flow rate was limited by choke of the impeller. The test cascade diffusers demonstrated a good pressure recovery over a wide range of inflow angle, and furthermore the pressure recovery was improved a little by an increase in the inlet Mach number up to 1.1.

Acknowledgments

The authors are grateful to Messrs. H. Hasegawa and N. Kawaguchi who assisted in designing the diffuser and running the experiment.

References

Senoo, Y., and Kinoshita, Y., 1977, "Influence of Inlet Flow Conditions and Geometries of Centrifugal Vaneless Diffusers on Critical Flow Angle for Reverse Flow," ASME *Journal of Fluids Engineering*, Vol. 99, pp. 98–103.

Senoo, Y., Hayami, H., and Ueki, H., 1983, "Low Solidity Cascade Diffusers for Wide-Flow-Range Centrifugal Blowers," ASME Paper No. 83-GT-3.

Senoo, Y., and Ishida, M., 1987, "Deterioration of Compressor Performance Due to Tip Clearance of Centrifugal Impellers," ASME JOURNAL OF TURBOMACHINERY, Vol. 109, pp. 55–61.

Experiments With a Low-Specific-Speed Partial Emission Centrifugal Compressor

C. Rodgers
Sundstrand Turbomach,
San Diego, CA 92138-5757

This paper describes experiments that were conducted several years ago on a single-stage open-face centrifugal partial emission compressor with a nondimensional specific speed of 0.15 (19.3 dimensional). The purpose of the experiments was experimentally to evaluate the partial emission compressor as a possible candidate for a high-speed low-flow natural gas fuel pump, the alternative to which was a larger heavier reciprocating compressor. A review and re-analysis of the test data were conducted. They used updated compressor data reduction performance procedures and flow models to redefine the experimental compressor as a reference case in the low-specific-speed range of single-stage centrifugal compressors. Normalized performance characteristics are presented for the experimental compressor in terms of efficiencies, diffuser recovery, and head coefficients versus diffuser relative flow parameter, or choke margin. Peak efficiency, obtained at a De Laval number of 1.16, and nondimensional specific speed of 0.15, was 34.5 percent. Stage performance is found to be dominated by diffuser geometry and choke margin, plus windage losses.

Introduction

The wide diversity of applications for centrifugal compressors and pumps covers impeller designs ranging from nondimensional inlet specific speeds as low as 0.3 to as high as 1.5, where

$$N_s = \omega\left(\frac{W}{\rho_1}\right)^{0.5} (gH_{ad})^{-0.75}$$

Although low-specific-speed stages are inherently inefficient, they may be used as exit stages in multistage industrial compressors, gas turbine fuel pumps, and in special low-flow circumstances where optimal choice of rotational speed is not possible.

The classical specific speed charts of Balje (1999) indicate that choices for very low specific nonreciprocating compressors are of the following types:

- Partial emission
- Drag
- Pitot pump
- Multiple lobe (vane motor)

Additionally, Wedge type impellers are recommended by Rusak (1982) for low-specific-speed centrifugal compressor applications.

Extensive development of partial emission pumps for rocket motor applications was described by Barske (1959), who found that some aspects of common centrifugal pump design, such as optimum blade geometries, were apparently less important in very low flow regimes. The major advantage of dynamic (nonreciprocating) compressors is compactness inherent in high-speed operation, and in weight/volume constrained intermittent duty applications where compressor efficiency may be compromised in favor of compactness.

The design requirements for special propulsion systems faced by Barske suggested the employment of some kind of positive displacement pump or a multistage centrifugal pump. A preliminary design assessment, however, showed that such approaches were too heavy and complicated.

Following the innovative work of Barske, the author in 1962 became associated with the development of a partial emission natural gas compressor to be driven directly at 35,000 rpm by a gas turbine as its own fuel pump.

The partial emission centrifugal compressor, or pump, is categorized by a simple paddle rotor or impeller, enclosed in a tight-fitting scroll, usually with a single port diffuser capturing the impeller exit flow over a small arc of its periphery.

This paper describes experiments that were conducted on a 10.38-in. (263-mm) diameter partial emission gas compressor and identifies design performance parameters that basically influence the pressure, flow, and efficiency characteristics of such turbomachines.

Compressor Design Features

Adhering to the design recommendations of Barske, the partial emission gas compressor shown in Fig. 1 was designed and fabricated for an exploratory compressor test program.

The gas compressor was designed for the following conditions:

Contributed by the International Gas Turbine Institute and presented at the 34th International Gas Turbine and Aeroengine Congress and Exhibition, Toronto, Ontario, Canada, June 4–8, 1989. Manuscript received by the International Gas Turbine Institute September 1988. Paper No. 89-GT-1.

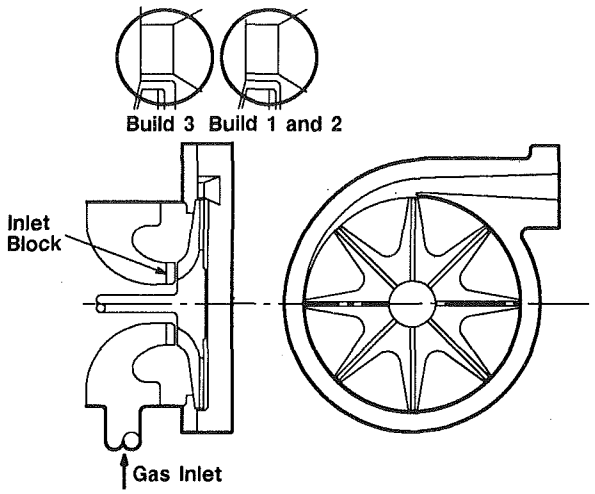

Fig. 1 Partial emission compressor

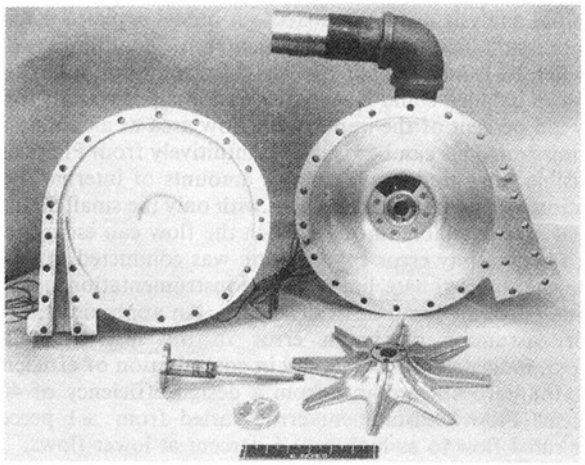

Fig. 2 Partial emission compressor components

Natural gas flow	320 pph (121 kg/h)
Pressure ratio	2.3
Rotational speed	35,000 rpm
Gas specific heat ratio, γ	1.27
Gas constant, R	86
Inlet pressure	15.0 psia (1.02 bar)
Inlet temperature	540 R (300 K)
De Laval number, $U\sqrt{(g\gamma RT_1)^{0.5}}$	1.25

The open-face eight radially bladed impeller and single channel discharge diffuser are shown in Fig. 2. Geometric

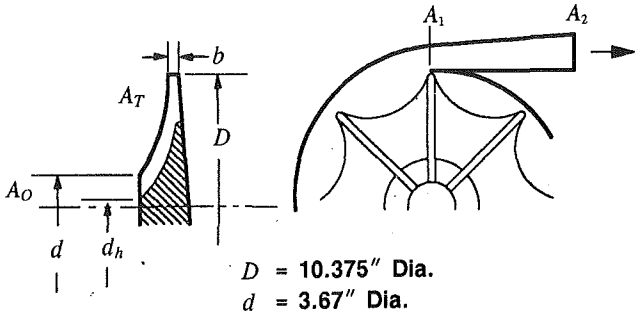

D = 10.375″ Dia.
d = 3.67″ Dia.
d_h = 2.05″ Dia.

	Build Number		
	1	2	3
D/DTH	19.5	19.5	20.3
D/d	2.74	2.74	2.74
b/D	0.0472	0.0472	0.289
A_o (sq. in.)	7.803	1.951	1.951
A_T (sq. in.)	15.971	16.971	9.778
A_T/A_o	2.05	8.19	6.01
A_1 (sq. in)	0.220	0.220	0.204
A_2 (sq. in)	1.375	1.375	1.360
A_2/A_1	6.25	6.25	6.67

Fig. 3 Compressor geometric features

features of the impeller and diffuser are listed in Fig. 3. The impeller inlet design was constrained by the requirement to adapt an existing compressor rig, shaft, and bearing capsule assembly. The design diffuser had an area ratio of 6.25 combined with a length-to-inlet width ratio of 15.0. The expected static pressure recovery coefficient was approximately 0.5 assuming an inlet blockage of 0.05.

Compressor Rig and Instrumentation

Figure 4 shows a photograph of the partial emission compressor installed in the test facility. The compressor was driven by a 200-hp electric dynamometer driving through a step-up gearbox with a speed increasing ratio of 23.8. The dynamometer was trunnion mounted, and provided input torque data to determine compressor power. This is of particular importance in low-specific-speed compressor perform-

Nomenclature

A = throat area
b = axial width
C = absolute velocity
Cf = friction coefficient
C_p = static pressure recovery
D = diameter
g = gravitational constant
H = head
M_u = De Laval number
N = rotational speed
N_s = specific speed (dimensionless)
P = total pressure
p = static pressure
q = work factor
R = radius; gas constant
RWD = relative flow parameter
Re = Reynolds number
S = tip gap
U = tangential velocity
W = flow
γ = specific heat ratio
Δ = difference
δ = standard pressure correction
η = adiabatic efficiency
Θ = standard temperature correction
ν = kinematic viscosity
ρ = density
ω = angular velocity

Subscripts

1 = impeller inlet
2 = impeller tip
3 = diffuser throat
4 = diffuser exit
ad = adiabatic
Crit = critical
m = meridional
ov = overall
RDF = recirculation and disc friction
th = theoretical

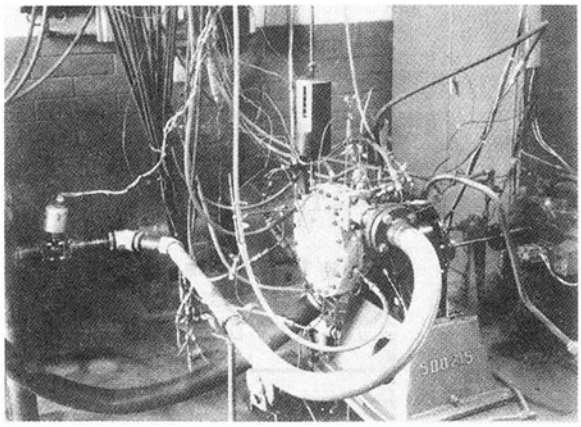

Fig. 4 Test facility

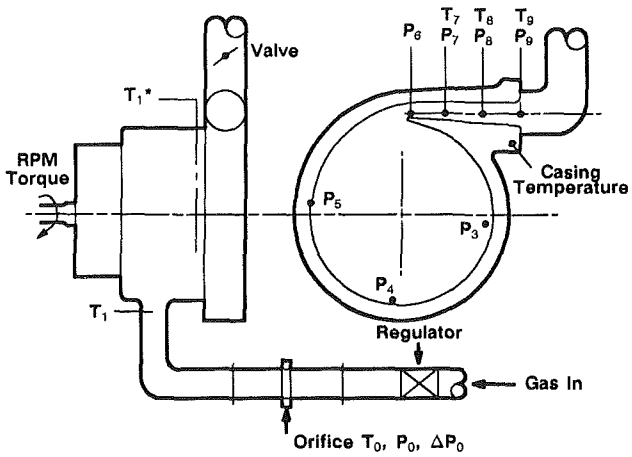

Static Pressures, Total Temperatures

Data	Description	No.
T_0	Orifice Temperature	1
P_0	Orifice Pressure	1
ΔP_0	Orifice Differential	1
T_1	Inlet Temperature	1
T_1*	Rotor Inlet Temperature	3
P_3, P_4, P_5	Rotor Tip Pressure	3
P_6, P_7, P_8, P_9	Diffuser Pressures	4
T_7, T_8, T_9	Diffuser Temperatures	3

Fig. 5 Test instrumentation

ance assessment where casing heat losses can represent a significant fraction of the enthalpy rise.

Natural gas was introduced from a regulator, controlled at the operating panel through a standard ASME orifice run to the compressor inlet casing. Compressor flow was controlled by a butterfly valve located in the discharge pipe. The natural gas used during testing was piped to a burner located on the test facility roof.

The compressor casing and volute were fabricated from aluminum and testing was therefore limited to a maximum casing temperature of 910°F (506 K). Casing insulation was installed for test calibrations.

Compressor test instrumentation is shown in Fig. 5. A 0.6-in.-dia (15.2-mm) orifice was used in a 2.375-in.-dia (60.5-mm) pipe for flow measurement.

Calculation Procedure

The stage static pressure rise, total temperature rise, and adiabatic efficiency were computed from the measured pressures and temperatures using a constant average specific heat ratio of 1.27.

Impeller and diffuser performances were calculated from the measured overall temperature rise and static pressures at the impeller tip, diffuser throat, and diffuser exit, using standard data reduction codes with Wiesner slip factor as input to assess average (mixed-out) vector triangles at the three stations. This technique, although not an absolute measurement, has provided a convenient yardstick for impeller efficiency assessment.

An intrinsic weakness of the technique, however, is the inability to rate the quality of the impeller exit flow distribution and wake mixing effects on the downstream diffusion system. It has been determined that impeller performance calculated in this manner does not always exhibit acceptable repeatability when the downstream diffusion process is changed.

Represenation of the impeller tip flow conditions by either blockage, jet and wake momentum deficiency, or profile corrections is a debatable subject in both radial and axial compressor design. It becomes a matter of the taste and experience of the individual designers.

Initial analysis using the mixed-out model revealed stagnation pressure inconsistencies between vector conditions at the impeller tip and diffuser throat. A meaningful stagnation pressure balance could be satisfied (with slip as input) using only 2.5 percent of the impeller tip flow area as an active arc of emission. This can be visualized intuitively from Fig. 1 as a plausible flow model, where large amounts of internal recirculation occur within the impeller, with only the small diffuser throat area available through which the flow can escape.

An uncertainty error computation was conducted to determine the approximate limits of the instrumentation used to evaluate overall compressor efficiency. An approximation of error, assuming maximum error in the instrumentation system, indicated an uncertainty in computation of efficiency of ± 0.8 percentage points from a design efficiency of 40.0 percent. Flow measurement error varied from ± 1 percent near rated flow to as high as ± 6 percent at lower flows.

The calculations did not take into account any errors caused by actual installation of sensors in the system. The system was calibrated prior to testing, and all calibration corrections were applied. The system was operated at a stable ambient temperature very near the design conditions when calibrated. At 100 percent design speed, the variations in upstream pipe inlet and exit discharge temperatures were 2.0 and 4.0°F, respectively.

Test data analysis was originally completed using desk-top calculators. For re-examination purposes all data were recompiled and computed with current compressor rig performance analysis codes.

Due to the dominance of partial emission compressor performance by the single exit diffuser, it was elected to present test data using the following compressor performance parameters:

Relative Flow Parameter (or Choke Margin)

$$\text{RWD} = \frac{\left(\frac{W\sqrt{T}}{AP}\right)_3}{\left(\frac{W\sqrt{T}}{AP}\right)_{3\text{critical}}}$$

Overall Efficiency

$$\text{Based on } \frac{p_4}{p_1}$$

Impeller Efficiency

$$\text{Based on } \frac{P_2}{p_1}$$

Table 1 Test configurations; impeller tip diameter = 10.375 in.

		BUILD NUMBER 1	2	3
Impeller Inlet Area	sq in	7.8	1.95	1.95
Impeller Exit Width	in	0.49	0.49	0.30
Diffuser Throat Area	sq in	0.22	0.22	0.204
Diffuser Exit Area	sq in	1.38	1.38	1.36

Diffuser Static Pressure Recovery

$$C_{p\,3-4} = \frac{p_4 - p_3}{P_2 - p_2}$$

Work Factor

$$q = \frac{gJC_p\Delta T}{U_2^2}$$

Windage and Recirculation

$$q_{\mathrm{RDF}} = \frac{q - gJC_p\Delta Tth}{U_2^2}$$

Test Results

Compressor testing encompassed three different compressor configurations, identified in Table 1. Test results for each of the three builds are discussed as follows.

Build 1. A complete performance characterization was acquired for the initial configuration covering 60, 80, 90, and 100 percent corrected speed from choke to the minimum flow constrained by either the maximum casing temperature limit, or one inch Hg differential pressure across the orifice plate. No surging characteristics were exhibited by the compressor. Inlet temperatures immediately adjacent to the impeller in the recirculation zone exhibited an increasing spread as flow was reduced. At minimum flow and rated speed the temperature rise above the upstream inlet temperature was of the order of 80°F (27°C).

The performance characteristics for Build 1 are normalized on Fig. 6 in terms of the selected performance parameters versus the relative flow parameter (choke margin), RWD. Although some scatter is apparent, a near unique stage characteristic results. A peak overall adiabatic efficiency of 31.8 percent was obtained at a rated speed with relative flow parameter RWD of 0.97. Corresponding overall pressure ratio was 2.38, close to the design goal of 2.3.

It was apparent from both examination of the windage and recirculation factor q_{RDF} and inlet temperature recirculating measurements, that the major loss was stemming from impeller windage effects. Diffuser static pressure recovery of 0.4 to 0.5 was close to expected limits for an area ratio of 6.25 and length-to-width ratio of 15.0 (covered passage/throat).

Examination of the compressor efficiency computed from work and temperature rise showed that at the near choke the two methods agreed within the limits of the test accuracy, but at the minimum flow, efficiency computed from work was subject to increased scatter as a consequence of flow measurement inaccuracies toward shutoff.

Impeller tip static pressure ratios at each of the test speeds and near peak overall efficiency are shown in Fig. 7. A large static pressure rise occurs toward the diffuser throat as a consequence of diffusion on the prethroat region. Some possible acceleration of the flow in the confined interspace toward the prethroat is indicated. Impeller efficiency was computed using the arithmetic average tip static pressures (p_3, p_4, p_5).

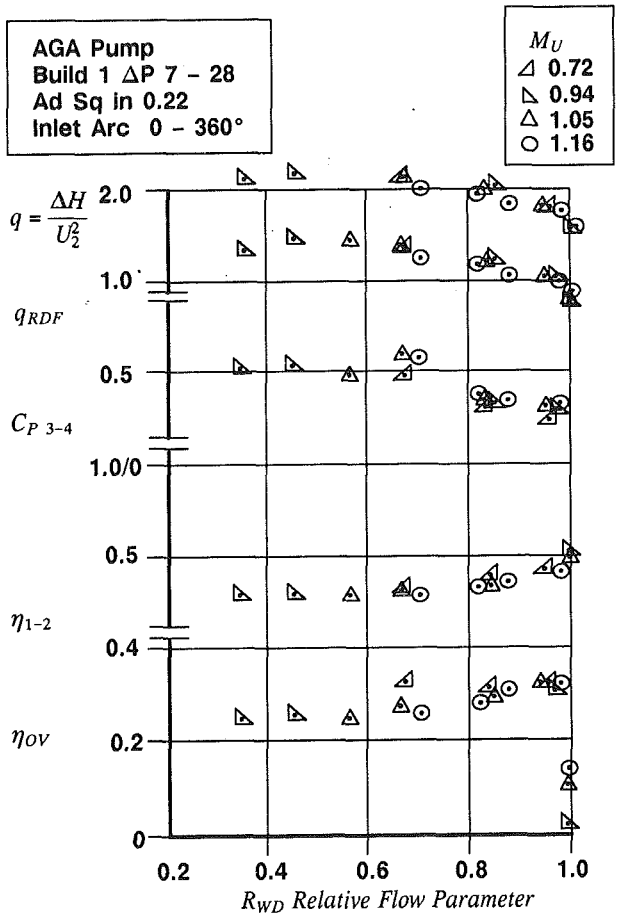

Fig. 6 Build 1 performance characteristics

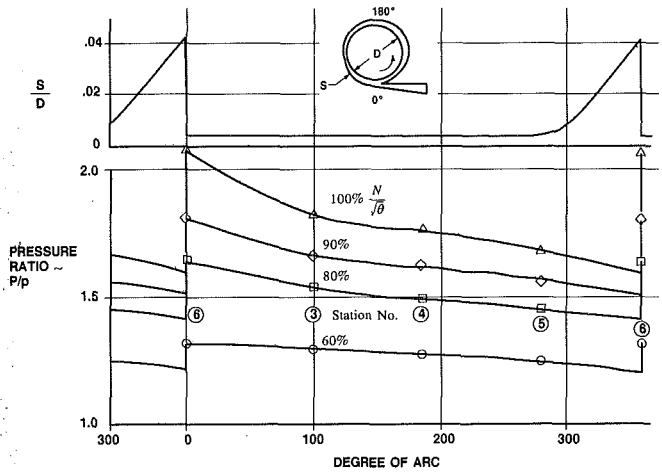

Fig. 7 Impeller tip static pressure distribution at peak efficiency

The large windage and recirculation effects encountered on the first build suggested that the use of an inlet block similar to that tried by Van Le (1961) could diminish recirculation losses. An inlet blockage plate was therefore fabricated as shown in Fig. 2 blocking off 75 percent of the impeller inlet eye annulus. Evidence of flow recirculation back to the impeller inlet is illustrated by the flow traces in Fig. 8.

Build 2. The inlet block was installed initially to block off

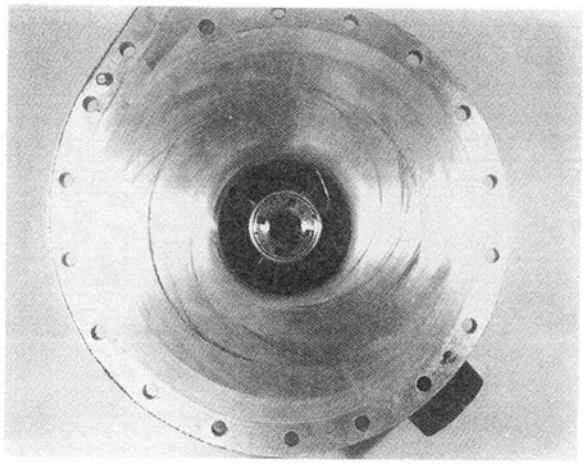

Fig. 8 Recirculation flow traces

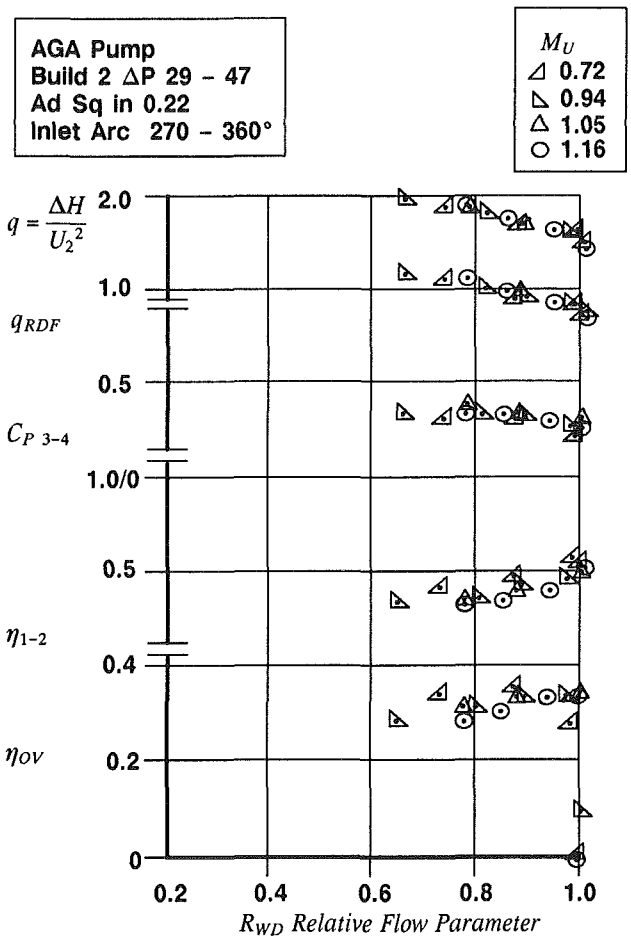

Fig. 9 Build 2 test results

Table 2 Test results 100 percent corrected speed

		BUILD NUMBER 1	2	3
Data Point Number		24	44	79
Overall Efficiency	%	31.4	34.5	32.2
Relative Flow Parameter	RWD	0.97	0.99	0.98
Dimensionless Specific Speed		0.145	0.156	0.161
Pressure Ratio		2.38	2.31	2.10
Inlet Corrected Flow	pps	0.123	0.135	0.118
Work Factor		1.75	1.54	1.43
Windage & Recirculation Factor	q_{RDF}	.974	0.76	0.66
Impeller Efficiency	1-2 %	39.0	45.3	45.9
Efficiency	1-3 %	42.0	50.7	47.0
Diffuser Static Pressure Recovery	$C_{P\ 3-4}$	0.34	0.29	0.21
Compressor Horsepower		34.5	33.7	28.7
Windage Recirculation Horsepower		19.2	16.6	13.1

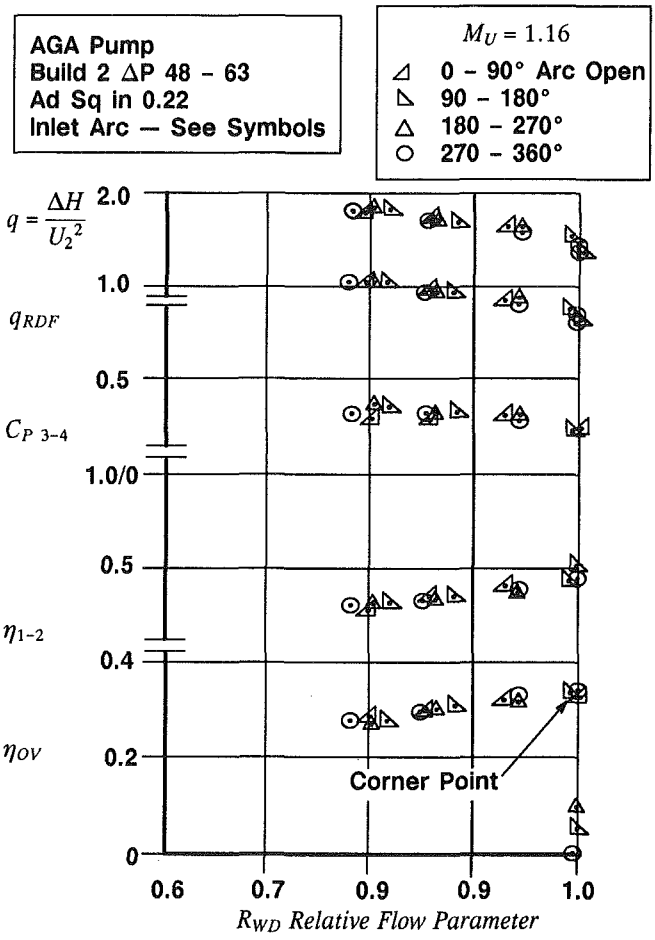

Fig. 10 Build 2 test results with various blockage orientations

the first 270 deg arc from top dead center (TDC). A complete performance map was rerun and the test results are shown in Fig. 9. Windage and recirculation losses were reduced 25 percent and maximum recorded overall efficiency increased to 34.5 percent. Commensurate with the reduction in windage and recirculation losses, the overall work factor also decreased with a corresponding reduction in pressure ratio from 2.38 to 2.31 as listed in Table 2. The performance improvement further suggested extending test calibrations to include the effect of blockage circumferential orientation in relation to the throat tongue or TDC. Accordingly additional testing was conducted on Build 2 at rated speed only with various blockage orientations, and the results are depicted in Fig. 10. These data indicate no distinct optimum orientation of the blockage plate. Some minor shifts in impeller tip static pressure distributions were noticed, dependent upon blockage plate orientation.

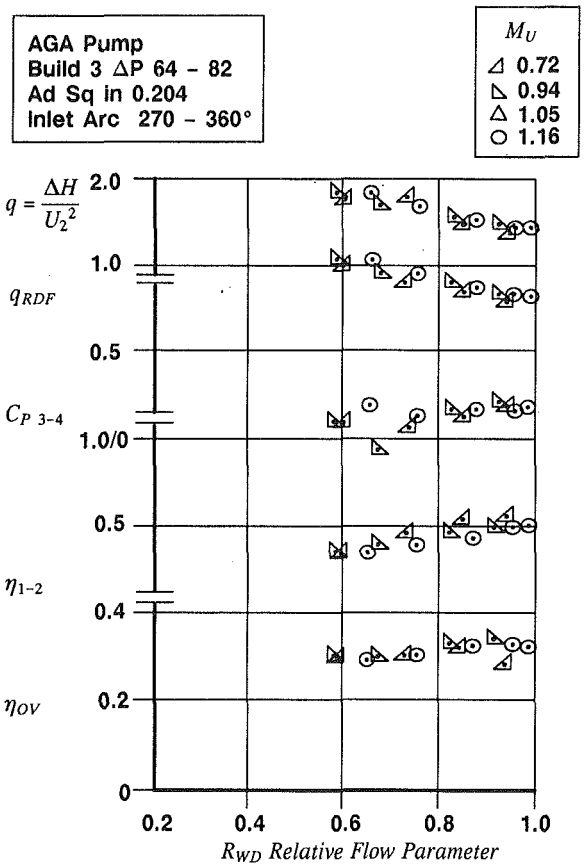

Fig. 11 Build 3 test results

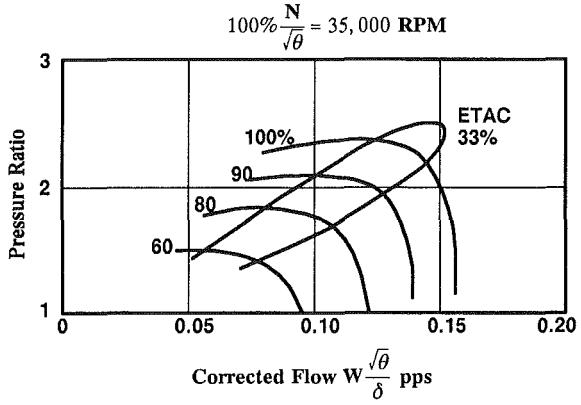

Fig. 12 Partial emission compressor map, Build 2

Build 3. In an attempt to achieve the design goal efficiency of 40 percent, it was postulated that windage recirculation losses could be reduced further by increasing the radial velocity component at the impeller tip. Accordingly the impeller tip width was reduced by approximately one-third and restricted to the diffuser as shown in Fig. 1. This restacking caused a reduction in diffuser throat area of 7 percent in addition to passage width expansion of 27 percent between the impeller tip and throat.

Test data for Build 3 are shown in Fig. 11 and indicate that although windage and recirculation losses were further slightly reduced, the diffuser static pressure recovery coefficient fell to 0.2.

Comparative performances for all three builds at rated speed and near-peak efficiency are listed in Table 2.

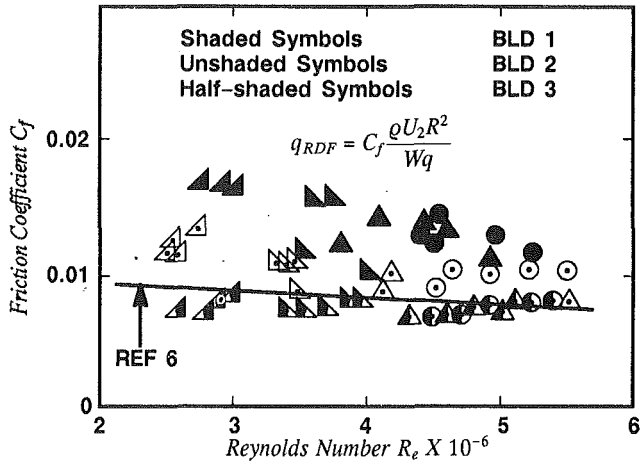

Fig. 13 Windage and recirculation losses

Discussion

The test data obtained from the three compressor builds can be summarized in the following findings:

- Windage and recirculation losses are large, but do contribute to the stage head rise capability.
- Diffuser performance corroborates with expected levels of static pressure recovery (Reneau et al., 1967) providing the interspace transition is smooth.
- No surge instabilities of the partial emission compressor were observed for the test range of pressure ratios.
- Peak efficiency occurred near diffuser choke and attained a test maximum level of 34.5 percent.
- Diffuser performance decreased insignificantly with a 27 percent increase in passage width between the impeller tip and throat.

A conventional compressor map representation of Build 2 test performance is shown in Fig. 12 in terms of inlet corrected airflow, pressure ratio, and efficiency, with corrected speed as a parameter. Note that the low-flow endpoints are not surge points but a low-flow limit constrained by casing temperature limitations.

Balje (1981, Fig. 6.81) indicates that slightly higher peak efficiency islands of 40 percent are attainable and corroborates that recirculation losses are dominant. An equivalent disk friction coefficient and Reynolds number were computed from the windage and recirculation losses defined by

$$Cf = \frac{g_{\text{Torque}}}{\rho\omega^2 R^5} \qquad \text{Re} = \frac{\omega R^2}{\upsilon_{1-2}}$$

Test friction coefficients are plotted on Fig. 13 and show decreasing values for successive builds 1, 2, and 3. Superimposed in Fig. 13 are the data from Furuya and Watabe (1964) for an eight-bladed rotor in an enclosed vessel with a hub/tip ratio less than 0.6 and b/D_2 ratio of 0.047. Comparison of the data indicates that the major loss source is indeed windage, as would be expected as the compressor specific speed approaches zero. Wider tip widths and full inlet admission appear to increase recirculation (or pumping) losses.

A quick evaluation of the corner-point peak efficiency (near choke) performance of a partial emission compressor can be assessed using the procedure of Appendix 1. Either the flow can be input to determine the required diffuser throat area or alternately the flow capability of a given geometry can be calculated using the throat area as input. The impeller efficiency model assumes efficiency increases with increasing speed according to the trends of Barske (1959) and Sundstrand (1986).

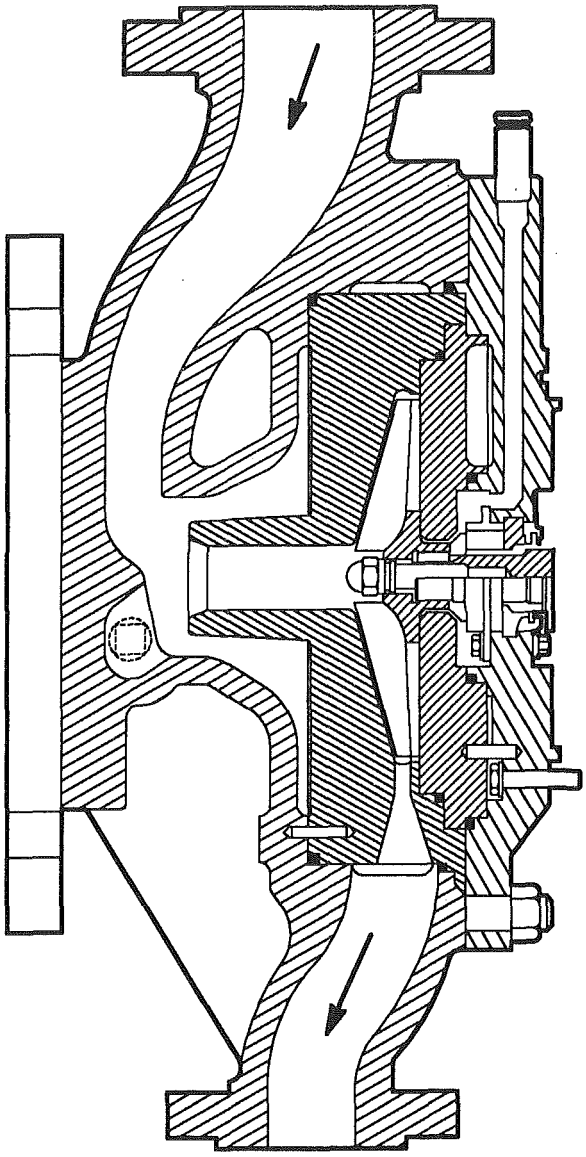

Fig. 14 Commercial partial emission compressor

Conclusion

A major intent of reviewing and re-analyzing the experimental single-stage partial emission compressor was to establish it as a reference case in low-specific-speed centrifugal compressor turbomachinery technology. It is fundamentally difficult to obtain good efficiencies in such applications intrinsically due to large windage and recirculation losses. Examination of the stage test data indeed confirms that these losses can equal the theoretical heat input. Although such losses detract from the efficiency potential of partial emission compressors, they do provide useful head.

Windage and recirculation losses were reduced 25 percent by blocking off three quarters of the impeller inlet annulus. This, combined with the same effective blockage at the impeller tip, left one quarter of the impeller flow path actively scavenging and exhausting. Tests with various angular orientations of the inlet blockage plate to the diffuser throat tongue revealed no distinct optimum location.

Windage and recirculation losses were further reduced 14 percent by decreasing the impeller tip width one third. This however resulted in a passage expansion between the impeller tip and diffuser throat, adversely influencing the diffuser performance and reducing overall stage efficiency by up to 3 percentage points.

The diffuser dominated the whole stage matching, performing close to expectations in terms of static pressure recovery. Stage performance was normalized on the basis of diffuser relative flow parameter (RWD) or choke margin, and as such revealed a near unique characteristic for all test speeds. Peak stage efficiency occurred adjacent (within 10 percent) to diffuser choke and attained a maximum value of 34.5 percent at a nondimensional specific speed of 0.15.

Balje (1981) shows that efficiencies as high as 57 percent can be obtained at higher specific speeds in the 0.3 range with pumps, and probably more pump performance data may be found in open literature. Commercial partial emission compressors are produced under the trade name of Sundyne (see Sundstrand, 1986, and Fig. 14), and are capable of peak adiabatic efficiencies in the 41 percent region at an optimum specific speed of 0.3 with Mach numbers M_u of 1.15.

A major disadvantage of partial emission compressors is the high heat generated by the windage and recirculation losses that can severely limit their application.

References

Balje, O. E., 1981, *Turbomachines*, Wiley Interscience, New York.

Barske, V. M., 1959, "Development of Some Unconventional Centrifugal Pumps," *Proc. IMechE*, Vol. 21.

Furuya, Y., and Watabe, K., 1964, "On the Racing Power of Impellers," *Bulletin of JSME*, Vol. 7, No. 36.

Reneau, L. R., Johnston, J. P., and Kline, S. J., 1967, "Performance and Design of Straight Two Dimensional Diffusers," ASME *Journal of Basic Engineering*, Vol. 89.

Rusak, V., 1982, "Development and Performance of the Wedge-Type Low Specific Speed Compressor Wheel," ASME Paper No. 82-GT-214.

Sundstrand Fluid Handling, 1986, "Sundyne Compressor Fuel Selection Procedure," P.O. Box FH, Avrada, CO 80004.

Van Le, N., 1961, "Partial Flow Centrifugal Compressors," ASME Paper No. 61-WA-135.

APPENDIX

Corner Point Model

Input Inlet pressure, temperature, flow P, T, W
Impeller Tip Speed U_2
Work Factor $(q_{slip} + q_{RDF})$
Diffuser Static Pressure Recovery $C_{p\,3-4}$

Impeller pressure ratio

$$\frac{P_2}{P_1} = \left(1 + \eta_{1-2}\,\frac{q}{gJC_p}\left(\frac{U_2}{\sqrt{T_1}}\right)^2\right)^{\frac{\gamma}{\gamma-1}} \tag{1}$$

Initially assume $\eta_{1-2} = 0.45$
Assume no core stagnation loss between stations 2 and 3

$$\frac{P_3}{P_1} = \frac{P_2}{P_1}\quad \frac{T_3}{T_1} = \frac{T_2}{T_1} = \left(\frac{P_2}{P_1}\right)^{\frac{\gamma-1}{\gamma}} \tag{2}$$

Assume peak corner point pressure ratio of RWD = 0.975 ($M_3 \simeq 0.85$), then diffuser throat area is given by

$$A_3 = \frac{1}{\text{RWD}}\,\frac{W\sqrt{T_1}}{P_1}\sqrt{\frac{T_3}{T_1}}\,\frac{P_1}{P_3}\,\frac{1}{\left(\dfrac{W\sqrt{T_3}}{(P_3A_3)}\right)_{\text{CRIT}}} \tag{3}$$

$$\left(\frac{P}{p}\right)_3 = \left(1 + \frac{\gamma-1}{2}M_3^2\right)^{\frac{\gamma}{\gamma-1}} \tag{4}$$

Diffuser Geometry

Select A_4, L_{3-4} and determine C_{p3-4} from Reneau et al. (1967).

$$P_4 = \left(\frac{p}{P}\right)_3 + C_{P3-4}\left(1 - \left(\frac{p}{P}\right)_3\right) \tag{5}$$

$$\frac{P_4}{P_1} = \frac{P_3}{P_1}\frac{P_4}{P_2}$$

$$\text{Overall Efficiency } \eta_{1-4} = \left[\frac{\left(\frac{P_4}{P_1}\right)^{\frac{\gamma-1}{\gamma}} - 1}{\left(\frac{P_3}{P_1}\right)^{\frac{\gamma-1}{\gamma}}}\right]\eta_{1-3} \tag{6}$$

$$\text{Specific Speed } N_s = \omega\frac{\sqrt{\frac{W}{\rho_1}}}{(gH_{ad})^{0.75}} \tag{7}$$

$$\text{Check Impeller Efficiency } \eta_{1-2} = 0.6\left|1 - \left(1 - \frac{N_s}{0.3}\right)^2\right|$$

Experimental and Theoretical Study of the Swirling Flow in Centrifugal Compressor Volutes

R. A. Van den Braembussche
Professor.

B. M. Hände
Research Assistant.

von Karman Institute for Fluid Dynamics,
B-1640 Rhode-Saint-Genèse, Belgium

Measurements of the three-dimensional flow in a simplified model of a centrifugal compressor volute at design and off-design operation are presented. A nearly constant swirl velocity is observed near the walls and a forced vortex type of flow is observed in the center. This velocity distribution is almost identical at all cross sections and all operating points. An explanation is given on how this swirl distribution results from the specific way a volute is filled with fluid. The throughflow velocity component shows a large crosswise variation. A minimum or maximum velocity is observed at the volute center depending on the operating point. A simple analytic model, based on the radial equilibrium of forces, is described. Calculations for isentropic flows reveal the relation between the swirl distribution and the large increase of throughflow velocity toward the center. This explains why volutes should be designed with negative blockage. Nonisentropic calculations, using the experimental loss distribution, correctly reproduce the measured throughflow velocity and static pressure distribution.

Introduction

The volute is probably the most neglected component in centrifugal compressor research. Only a limited number of studies have been published, compared to numerous reported investigations on diffuser and impeller flow.

The majority of the published research on volutes concerns the influence of global geometric parameters on overall performance, and so gives no detailed information about the velocity distribution inside the volute. Experiments to date have been restricted to measurements of the circumferential static pressure variation and total pressure losses (Stiefel, 1972; Mishima and Gyobu, 1978; Sideris and Van den Braembussche, 1986, 1987). Published theoretical predictions assume a uniform flow in each cross section, and are based on overall volute dimensions (Japikse, 1982; Lorett and Gopalakrishnan, 1986).

At higher than optimum mass flows, the fluid enters the volute with large radial and small tangential velocity components. The radial velocity component results in a large cross-sectional swirl. The incoming tangential velocity is too small to transport the fluid through the volute, and so increases in magnitude from volute tongue to volute outlet. This results in a pressure decrease along the volute circumference and a discontinuous rise at the volute tongue.

Small radial and large tangential velocity components occur at mass flows below optimum value. This results in less swirl and a circumferential static pressure rise due to the decrease of the tangential velocity between the volute tongue and outlet.

The variation of cross-sectional swirl and the acceleration or deceleration of the throughflow velocity have an important impact on the circumferential pressure distribution. Therefore, further improvements in volute performance require a detailed knowledge of the complex three-dimensional structure of the flow inside the volute, at design and off-design conditions.

Laser-Doppler-Anemometer (LDA) measurements by Escudier (1979), in a constant cross section, ring-type exit chamber with asymmetric inlet flow, show a free-vortex-type swirling flow with a forced vortex inner core. The studies of Kettner (1965) and Schweikert (1969) reveal two counterrotating forced vortices in a symmetric volute of rectangular cross section. Measurements by Peck (1951) in a symmetric pump volute of circular cross section show a similar flow pattern at design flow rate, but a single forced vortex at maximum and minimum mass flow conditions.

This large uncertainty, in terms of velocity profile in different volute cross sections, prevents an estimation of the local blockage, and an accurate prediction of the circumferential pressure distribution at the volute inlet cannot be made.

The aim of the present study is to contribute to a better understanding of the problem. In order to achieve this, detailed measurements are made of the three-dimensional flow in a volute, at design and off-design flow conditions. Also comparisons are made with the predictions of a simple analytical model.

Experimental Facility

The measurements have been made in the test facility shown in Fig. 1. This consists of a 5-to-1 simplified model of a typical turbocharger overhung volute. The conical channel and the parallel walled inlet at the outer diameter represent an asymmetric volute and diffuser. The main difference between the

Contributed by the International Gas Turbine Institute and presented at the 34th International Gas Turbine and Aeroengine Congress and Exhibition, Toronto, Ontario, Canada, June 4–8, 1989. Manuscript received at ASME Headquarters January 27, 1989. Paper No. 89-GT-183.

model and a real volute is the absence of circumferential curvature between the volute tongue and outlet. However, the curvature radius (defined by the diffuser outlet radius) is normally much larger than the volute cross-sectional radius, and its influence on the flow is considered to be of secondary importance.

A blower provides air to a settling chamber upstream of the rectangular inlet duct, from where it enters the inlet section and the volute. The variable blockage in the inlet duct enables the longitudinal pressure distribution at the volute inlet to be varied. Volute inlet flow angles can be adjusted by variable guide vanes in the inlet section. An empirical procedure is used to adjust the vane setting angle and variable blockage until the required volute inlet flow conditions, corresponding to maximum, optimum, or minimum mass flow, are obtained.

Four static pressure taps, equally distributed on the circumference, are installed in five axial positions, as shown on Fig. 2. They allow the evaluation of the circumferential and longitudinal static pressure variations. Only two static pressure taps can be located at the five intermediate positions (one at the top and one at the bottom) because of probe traverses in the z direction. Velocity components (V_R and V_T) and pressures (P and $P°$) are measured using a three-hole probe. The swirl component is indicated by V_R because it is created by the radial velocity component at the diffuser exit. The throughflow velocity component is related to the tangential velocity at the diffuser outlet, and so is indicated by V_T.

The volute has a discontinuity at the tongue region and flow is admitted only downstream of the tongue. This corresponds to a volute with zero clearance between the diffuser vanes and the volute tongue.

The velocity at the volute discharge is about 20 m/s, corresponding to a Reynolds number of 200,000, based on the outlet diameter. This value is of the same order as that for a typical turbocharger volute. The Mach number similarity is not conserved, but compressibility is negligible for Mach numbers below 0.5.

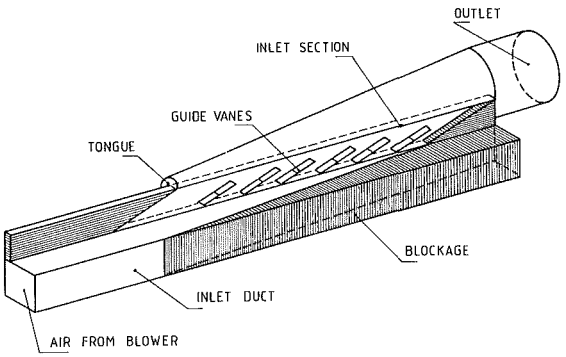

Fig. 1 Straight volute model

The static pressure distribution along the volute wall is shown on Figs. 3(a, b, c) for three operating conditions.

Figure 3(a) corresponds to an operating point at less than optimum mass flow, where the pressure is increasing from volute tongue to outlet. This is obtained with a linear increase of the blockage in the inlet duct. The vane setting angle α, defined in Fig. 2, is fixed at 69 deg, corresponding to a typical diffuser outlet flow angle at low mass flow.

The static pressure variation shown in Fig. 3(b) corresponds to an operating point close to optimum mass flow. The discontinuous change of pressure for $0.0 < x < 0.20$ is typical for the flow perturbation in the tongue region. Only a small pressure increase is observed downstream of $x = 0.20$. This pressure distribution was obtained with no blockage in the inlet duct and a more radial vane setting angle ($\alpha = 50$ deg).

The static pressure distribution shown in Fig. 3(c) corresponds to an operating point at high mass flow. This is obtained with no blockage in the inlet duct and no vanes in the inlet section. The flow enters the volute with large radial and small tangential-velocity components, typical for diffuser outlet conditions at high mass flow. The volute is too small to accumulate so much fluid and the throughflow velocity is increasing toward the outlet. This results in a static pressure decrease between volute tongue and outlet.

Results of Probe Traverses

The results of the probe traverses at different axial locations are shown in Figs. 4, 5, and 6 for the three operating points. Each figure shows the variation of the two velocity components V_R and V_T and the static and total pressure distribution.

Only one traverse is made at each cross section because one can assume that the flow is axisymmetric in a conical channel. Data are taken every 2 mm from the diffuser side wall ($Z/D = 0$) to the opposite volute wall ($Z/D = 1$). The symbols in Figs. 4–6 are merely to distinguish between the results at different longitudinal positions and do not indicate individual data points.

The swirl velocity V_R is constant in the region close to the walls and has a forced vortex distribution in the center. The velocity close to the walls is decreasing from volute tongue to outlet at minimum mass flow (Fig. 4a). This results from a larger V_R at the volute inlet close to the tongue, where the static pressure is low and more fluid is aspirated. The opposite

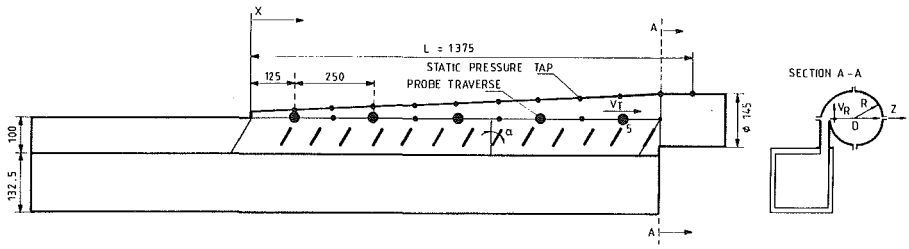

Fig. 2 Straight volute dimensions

Nomenclature

A = area
C_f = friction coefficient
C_d = total pressure loss coefficient
D = volute diameter
L = volute length
P = static pressure
$P°$ = total pressure
V = velocity
x = distance along the volute
z = distance across the volute
α = vane setting angle (measured from radial)
∇ = curl operator
ρ = density

Subscripts

R = radial or swirl component
T = tangential or throughflow component

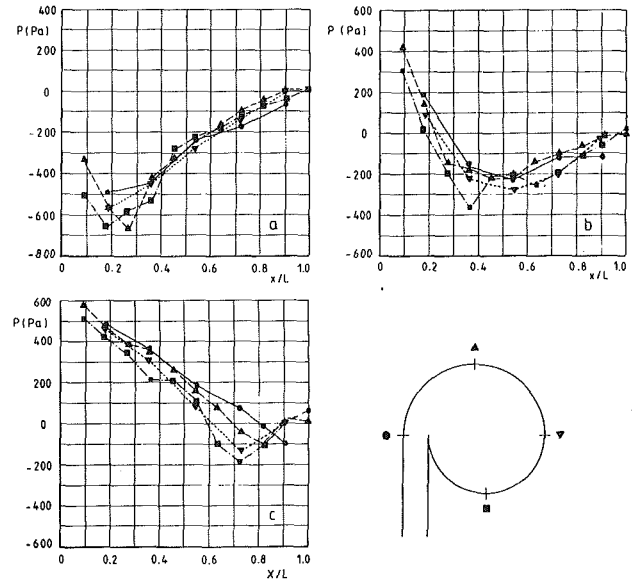

Fig. 3 Longitudinal and circumferential static pressure variation corresponding to small (*a*), optimum (*b*), and large (*c*) mass flow

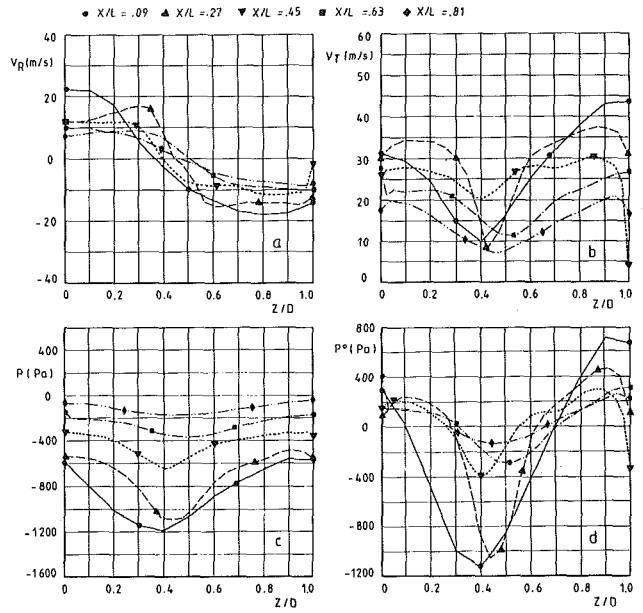

Fig. 4 Measured velocity and pressure distribution corresponding to small mass flow

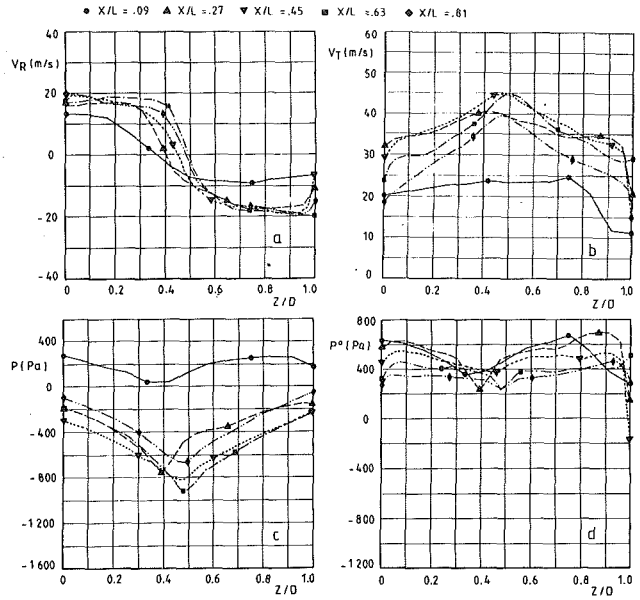

Fig. 5 Measured velocity and pressure distribution corresponding to optimum mass flow

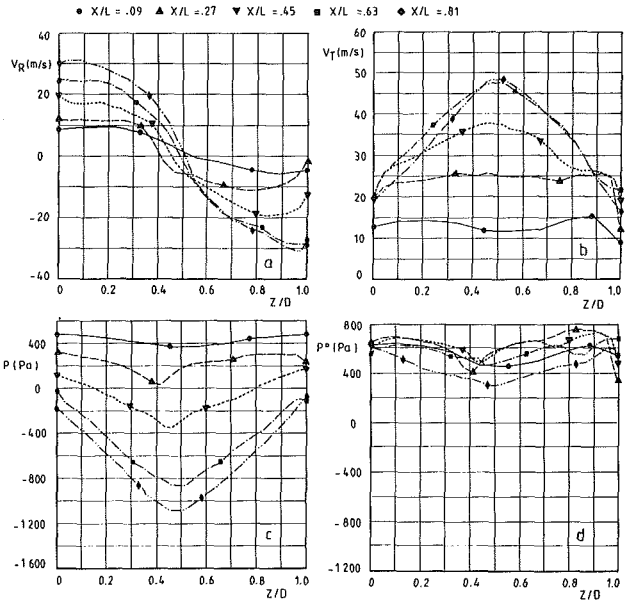

Fig. 6 Measured velocity and pressure distribution corresponding to large mass flow

situation is clearly observed at maximum mass flow (Fig. 6*a*), where the static pressure is decreasing from the tongue to the outlet.

The forced vortex region extends from $Z/D = 0.35$ to 0.65 at all axial locations and is almost independent of the operating point.

This type of flow is very different from the flow in a classical vortex tube, where the fluid enters at the constant outer radius (Escudier et al., 1980). Migration of the fluid from the outer radius to the center results in an increase of V_R due to the conservation of momentum

$$R \cdot V_R = C^{te}$$

Vortex tubes, therefore, have a free vortex circulation near the walls and a forced vortex circulation in the center.

A free vortex occurs also with swirling flow in conical diffusers (Senoo et al., 1978), where the fluid migrates from a small radius at the inlet to a large radius at the outlet.

However, a completely different situation occurs in a volute.

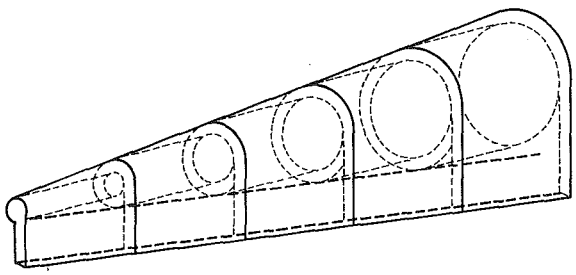

Fig. 7 Superposition of vortex tubes in a volute

The fluid entering close to the tongue at small radius fills the center of the volute. New fluid enters farther downstream at a larger radius and starts rotating around the upstream fluid. Vortex tubes of increasing radius are wrapped around each other (Fig. 7), and each part of the fluid remains at constant radius. This explains the nearly constant velocity V_R near the

walls. The swirl velocity V_R at a given radial position depends on the radial velocity of the fluid at the position where it has entered the volute.

The radial distribution of throughflow velocity V_T is very different for the three operating points. It shows a minimum in the volute center at low mass flow (Fig. 4*b*) and a maximum at the high mass flow operating points (Fig. 6*b*).

At low mass flow, the fluid enters the volute with a large tangential velocity component V_T. Continuity, however, requires a small V_T inside the volute. A deceleration of the tangential velocity takes place and the volute acts like a diffuser. This is observed in Fig. 4(*b*) where the average throughflow velocity V_T is decreasing from volute tongue to volute outlet. The swirl component keeps the fluid close to the walls and a zone of low throughflow velocity occurs in the center. This reduces the effective cross section, decreases the static pressure recovery, and avoids flow separation at the walls.

An opposite phenomenon takes place at high mass flow where V_T is small at the volute inlet and at the walls, and increases toward the volute center to satisfy continuity. The high throughflow velocity in the volute center results in a mass flow that is larger than the one predicted using the pressure measurements at the walls and at the volute inlet. This is similar to a negative blockage in the volute and explains the experimental observation of Stiefel (1972) that "the optimum scroll operation is achieved for a scroll-area 10 to 15 percent smaller than the frictionless computed one."

The static and total pressures show nearly symmetric distributions over each cross section with a minimum at the center. The minimum static pressure occurs close to the volute tongue at low mass flow (Fig. 4*c*), and close to the volute outlet at high mass flow (Fig. 6*c*). The largest total pressure variations are observed at low mass flow (Fig. 4*d*). These are much smaller at medium and maximum mass flow (Figs. 5*d*, 6*d*) where a variation between volute tongue and outlet is observed. The total pressure measurements at the volute inlet section can be used to distinguish between the losses in the inlet duct and inlet between the losses in the inlet duct and inlet section, and the losses inside the volute. The three-dimensional swirling motion of the fluid prevents a rapid mixing and some axial distance is required before the fluid that has entered the volute begins to influence the measurements in a cross section. The measurements indicate that the large variation in maximum total pressure between each cross section is mainly due to diffusion and friction in the inlet duct and inlet section. The crosswise total pressure variation, and only part of the decrease of maximum total pressure, are due to the swirling flow inside the volute.

The strong asymmetry observed at the first two positions at minimum mass flow are due to the fact that it takes some distance to fill the volute with fluid, if the flow is very tangential at the inlet. These high losses in the center gradually disappear because of mixing with new incoming fluid.

Thin boundary layers are observed near the walls. This is attributed to the replacement of the boundary layers with new fluid coming out of the diffuser and the effect of curvature on the boundary layer. Low-energy fluid, generated in the boundary layer, is pushed toward the center of the tube by the radial pressure gradient. This results in high turbulent mixing and explains the region of low total pressure in the center of the volute (Johnston, 1970).

Analytical Method

The equation of motion for steady, isentropic, and homoenthalpic flows is given by

$$\bar{V} \times (\nabla \times \bar{V}) = 0$$

It is convenient, for a straight volute, to write the equations in axisymmetric coordinates. Neglecting the velocity components normal to the volute axis, this results in

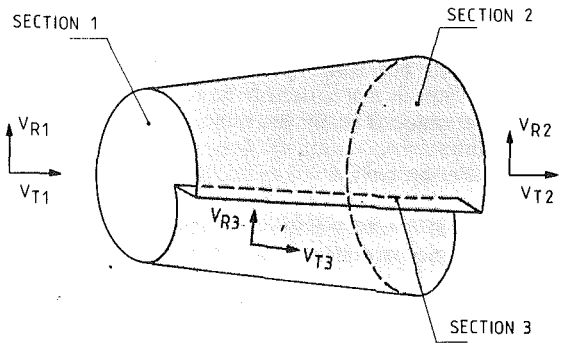

Fig. 8 Volute segment and notations

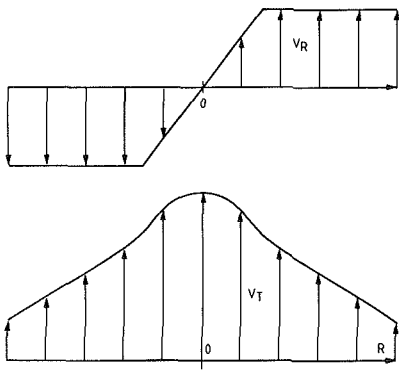

Fig. 9 Imposed V_R distribution and corresponding V_T distribution (inviscid calculations)

$$\frac{\partial RV_R}{\partial z} = 0 \tag{1}$$

$$V_T \frac{\partial V_T}{\partial R} = -\frac{V_R}{R} \frac{\partial (RV_R)}{\partial R} \tag{2}$$

Equation (1) expresses the conservation of swirl. Equation (2) is valid for isentropic flows only and is derived from the following radial equilibrium of forces:

$$\frac{\partial P}{\partial R} = \rho \frac{V_R^2}{R} \tag{3}$$

Conservation of mass and energy complete the above system of equations.

The control volume is used to calculate the flow. The volumes are defined by dividing the volute into n segments of equal length (Fig. 8). The flow across section 1 is defined by the outlet (section 2) of previous volume. Section 3 is the diffuser outlet where the measured velocity distribution is imposed. Section 2 is the outlet of the volume where the flow is calculated. The calculation starts at the first volume close to the tongue, where the flow enters from the diffuser only.

The following integral equations are solved for each control volume:

$$\int_{A_1} \rho_1 V_{T1} dA_1 + \int_{A_3} \rho_3 V_{R3} dA_3 = \int_{A_2} \rho_2 V_{T2} dA_2 \quad \text{(continuity)} \tag{4}$$

$$\int_{A_1} \rho_1 R_1 V_{R1} V_{T1} dA_1 + \int_{A_3} \rho_3 R_3 V_{R3}^2 dA_3 - \text{swirl loss} = \int_{A_2} \rho_2 R_2 V_{R2} V_{T2} dA_2 \text{ (conservation of swirl)} \tag{5}$$

One will first examine isentropic flows in which the swirl losses are zero. The equations (4) and (5) can then be solved if the V_T and V_R distributions are known.

The experimental data show a remarkable similarity between

the V_R distributions at all cross sections and operating conditions (Figs. 4*a*, 5*a*, 6*a*). A general nondimensional velocity contribution, with constant V_R near the walls and a forced vortex distribution in the center of the volute, can be derived from this observation (Fig. 9). Introducing this into equations (2) and (3) allows the definition of the nondimensional pressure and V_T distribution over a volute cross section. An iterative procedure is used to define the absolute values of V_R and V_T, by satisfying the integral equations (4) and (5). A reference value of the static pressure can be defined at the reference point, by subtracting the kinetic energy from the total pressure, which is constant everywhere for isentropic flows.

Results obtained using the above procedure do not agree with the experimental data. A unique V_R distribution always results in a unique V_T distribution, because of equation (2). This V_T distribution (Fig. 9) has a maximum velocity at the volute centers, whereas the experiments sometimes show a minimum value (Fig. 4*b*).

The main reason for this discrepancy is the assumption of isentropic flow, which is not supported by the large pressure losses observed in Figs. 4(*d*), 5(*d*), 6(*d*). The calculation procedure can be modified, as follows, in order to account for these losses.

The radial equilibrium of forces, equation (3), is valid also for nonisentropic flows, and can be used to define the static pressure variation. The results, however, are influenced by friction, through a reduction of swirl. The swirl losses in equation (5) are defined by

$$\text{swirl loss} = C_f\, 0.5\rho V_R^2 \cdot \text{volute surface} \cdot \text{wall radius}$$

where the friction coefficient C_f is taken from the explicit expression of the equation of Colebrook and White (Colebrook, 1950)

$$C_f = 0.0625 \Big/ \left(\log\left(\frac{K}{2.7D} - \frac{5}{\mathrm{Re}} \log\left(\frac{K}{2.7D} - \frac{5}{\mathrm{Re}} \log \frac{K}{2.7D} \right) \right) \right)^2$$

K is the relative roughness of the walls and Re is the Reynolds number based on the local hydraulic diameter D of the volute cross section.

Equation (2) is valid only for isentropic flows and can no longer be used to calculate the V_T distribution. The absolute value of V_T is therefore calculated as a function of the local difference between total and static pressure

$$P^\circ - P = \rho/2(V_T^2 + V_R^2)$$

The total pressure distribution, required to solve this equation, will also be defined by a typical nondimensional distribution, and an integral value obtained from a friction loss model. The use of a standard total pressure distribution does not allow an exact modeling of the measured distribution, and leads to nonnegligible errors in the V_T distribution.

Total pressure losses are generated in the boundary layers and the resulting total pressure variation should be similar to a boundary layer profile. Curvature effects, however, are responsible for a migration of low-energy fluid toward the center of rotation and a decrease of the boundary layer thickness. This means that a typical total pressure distribution in a volute has a nearly constant value in the wall region and a minimum value at the center. Defining a standard nondimensional total pressure distribution is basically not different from defining a boundary layer velocity profile.

The following integral equation allows the definition of absolute value of total pressure

$$\int_{A_1} \rho_1 V_{T1} P_1^0 dA_1 + \int_{A_3} \rho_3 V_{R3} P_3^0 dA_3 - \text{dissipation loss} = \int_{A_2} \rho_2 V_{T2} P_2^0 dA_2 \qquad (6)$$

Dissipation loss = $C_d\, 0.5\, \rho V^2 (\rho V) \cdot$ volute surface where $C_d = C_f + 0.0015$, which is equal to the value proposed by Schmalfuss (1972) for radial vaneless diffusers.

Comparisons

Calculations have been performed for the present three experimental test cases and the results are shown in Figs. 10, 11, and 12 (to be compared with Figs. 4, 5, and 6).

The swirl conservation equation allows correct reproduction of the absolute values of the radial velocity components V_R (Figs. 10*a*, 11*a*, 12*a*). The very good agreement between the experimental and predicted results confirms the generality of the nondimensional distribution of swirl velocity.

The throughflow velocity (Figs. 10*b*, 11*b*, 12*b*) shows a more qualitative agreement for the three operating conditions. A

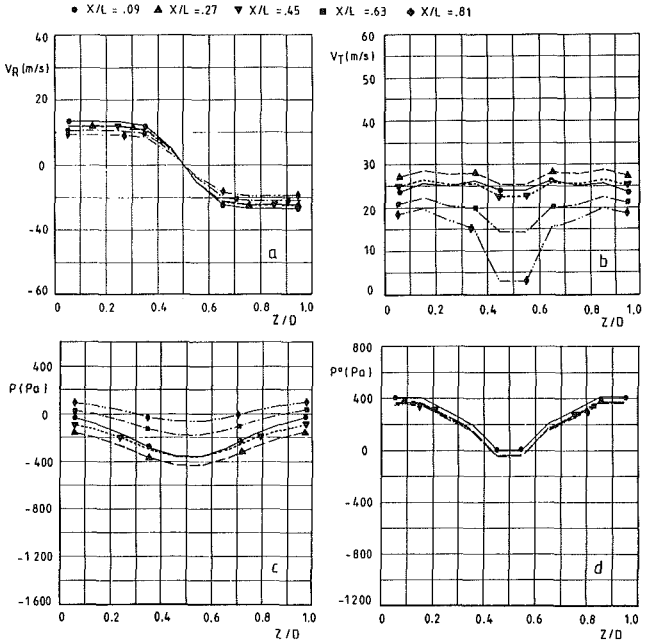

Fig. 10 Calculated velocity and pressure distribution corresponding to small mass flow

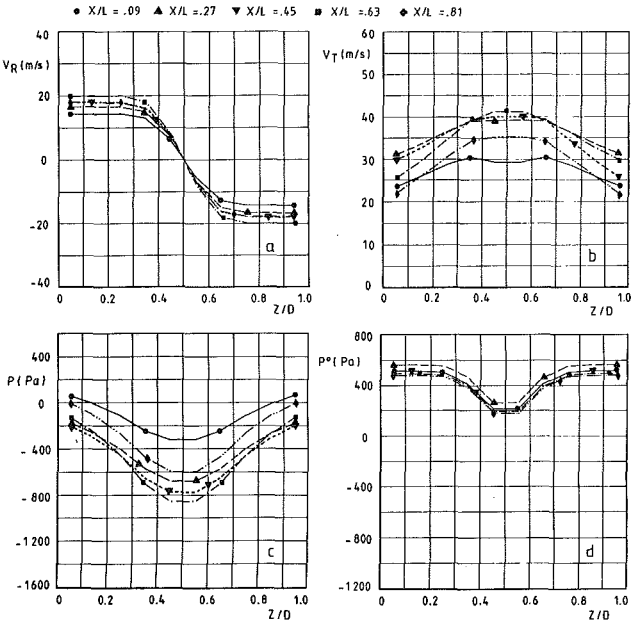

Fig. 11 Calculated velocity and pressure distribution corresponding to optimum mass flow

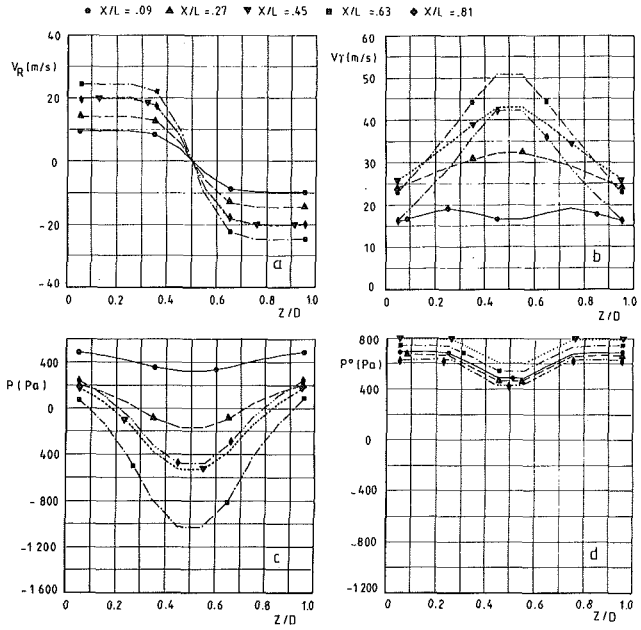

Fig. 12 Calculated velocity and pressure distribution corresponding to large mass flow

decrease of V_T toward the volute center at low mass flow changes into an increase at optimum and larger mass flow, similar to the behavior observed in the experiments. The very large velocity variation near the volute outlet is correctly predicted. The V_T component in the center changes from 5 m/s at low mass flow to 50 m/s at high mass flow. The velocity near the walls remains almost unchanged at 20 m/s.

The general shape of the static pressure distribution at the different cross sections (Figs. 10*c*, 11*c*, 12*c*) agrees fairly well with the experimental values. However, the amplitude of the static pressure variation in the cross sections near the tongue is underestimated at minimum flow. This is due to an underestimation of the local total pressure losses.

The distribution of the total pressure losses (Figs. 10*d*, 11*d*, 12*d*) is an input of the calculation, and is defined as an average of the measured distributions. The variation of the maximum total pressure between sections 1 and 5 is calculated.

The use of the same standard total pressure loss distribution for all operation points does not result in a good prediction of the experimental results. The influence of a total pressure variation at the volute inlet and the asymmetric flow in the tongue region at low mass flow are not included in the model. Nevertheless, the calculation allows the evaluation of the effect of total pressure losses on the velocity distribution inside the volute. Indeed the calculated influence on V_T is similar to the influence that can be derived from the measurements. Comparisons with experimental data show that the losses in the inlet duct and inlet section are responsible for the large decrease of maximum total pressure observed at minimum mass flow. Friction in the volute is the main source of total pressure losses at maximum mass flow.

Conclusions

The following conclusions are drawn from the experiments and calculations on a simplified model. It is expected that they are sufficiently general to be valid also for real volutes.

The main conclusions from the experimental results are:

- the invariance of the radial distribution of swirl velocity V_R and the large variations between the throughflow velocity distributions at the different volute cross sections for the different operating conditions;
- flow and pressure measurements near the walls are not representative of the average values. The velocity deficit in the volute center at minimum mass flow changes into a higher than average velocity at maximum mass flow. This has the same effect as a positive and negative blockage and influences the optimum volute dimensions;
- total pressure losses do not appear where they are generated. The radial pressure gradient pushes the low-energy fluid toward the center.

The isentropic flow calculations explain the high throughflow velocity observed in the volute center and the negative blockage factor generally used in design procedures.

The nonisentropic flow calculations:

- explain how the total pressure losses influence the throughflow velocity and result in a blockage at the volute center;
- allow the evaluation of total pressure losses as a function of flow parameters and a friction coefficient. Some uncertainty exists concerning the total pressure distribution over a volute cross section;
- allow for a more accurate design of an optimum volute geometry, and enable the flow at the volute outlet to be predicted.

It is expected that the gap at the volute tongue will perturb in some way the observed flow pattern. Also the circumferential curvature of a real volute will result in a smaller V_T velocity at the outer radius of the volute and a larger velocity at the inner radius.

More research is required to evaluate the influence of the gap and circumferential curvature on losses and optimum dimensions and to complete the analytical model of the flow.

References

Colebrook, C. F., 1939, "Turbulent Flow in Pipes With Particular Reference to the Transition Region Between the Smooth and Rough Pipe Laws," *J. Institution Civil Engineers*; see also: *Engineering Hydraulics*, H. Rouse, ed., Chap. VI, Steady Flow in Pipes and Conduits, by V. L. Streeter, New York, 1950.

Escudier, M., 1979, "Estimation of Pressure Loss in Ring-Type Exit Chambers," ASME *Journal of Fluids Engineering*, Vol. 101, No.4, pp. 511–516.

Escudier, M., Bornstein, J., and Zehnder, N., 1980, "Observations and LDA Measurements of Confined Turbulent Vortex Flow," *J. Fluid Mechanics*, Vol. 98, Part 1, pp. 49–63.

Japikse, D., 1982, "Advanced Diffusion Levels in Turbocharger Compressors and Component Matching," *Proc. Ist Int. Conf. on Turbocharging and Turbochargers*, London, IMechE, pp. 143–155.

Johnston, J. P., 1970, "The Effects of Rotation on Boundary Layers in Turbomachine Rotors," *Fluid Mechanics, Acoustics and Design of Turbomachinery*, Part 1, NASA SP 304, pp. 207–242.

Kettner, P., 1965, "Strömung in der spirale radialer Strömungarbeitsmaschinen," TH Karlsruhe Ström. Masch, Vol. 3.

Lorett, J. A., and Gopalakrishnan, S., 1986, "Interaction Between Impeller and Volute of Pumps at Off-Design Conditions," ASME *Journal of Fluids Engineering*, Vol. 108, No. 1, pp. 12–18.

Mishima, H., and Gyobu, I., 1978, "Performance Investigations of Large Capacity Centrifugal Compressors," ASME Paper No. 78-GT-3.

Peck, J. F., 1951, "Investigations Concerning Flow Conditions in a Centrifugal Pump, and the Effect of Blade Loading on Head Slip," *Proc. Inst. Mech. Engin.*, Vol. 164, pp. 1–30.

Schweickert, H., 1969, "Strömung und Druckverlust in Spiralgehäuse einer Kreiselpumpe," TH Karlsruhe Ström. Masch., Vol. 7.

Senoo, Y., Kawaguchi, N., and Nagata, T., 1978, "Swirl Flow in Conical Diffusers," *Bull. JSME*, Vol. 21, No. 151, pp. 112–119.

Sideris, M., and Van den Braembussche, R., 1986, "Evaluation of the Flow in a Vaneless Diffuser Followed by a Volute," *Proc. of 3rd Int. Conf. on Turbocharging and Turbochargers*, London. I.M.E. Conf. Public. 1986–4, pp. 15–20.

Sideris, M., and Van den Braembussche, R., 1987, "Influence of a Circumferential Exit Pressure Distortion on the Flow in an Impeller and Diffuser," ASME JOURNAL OF TURBOMACHINERY, Vol. 109, No. 1, pp. 48–54.

Schmalfuss, H. G., 1972, "Strömungen in Parallel-wändigen radial Diffusoren," *Zeitsch. Flugwiss*, Vol. 20, pp. 22–26.

Stiefel, W., 1972, "Experiences in the Development of Radial Compressors," in: *Advanced Radial Compressors*, von Karman Institute Lecture Series 50.

An Approximate Three-Dimensional Aerodynamic Design Method for Centrifugal Impeller Blades

Zhao Xiaolu

Qin Lisen

Institute of Engineering Thermophysics,
Chinese Academy of Sciences,
Beijing, People's Republic of China

An aerodynamic design method, which is based on the Mean Stream Surface Method (MSSM), has been developed for designing centrifugal compressor impeller blades. As a component of a CAD system for centrifugal compressor, it is convenient to use the presented method for generating impeller blade geometry, taking care of manufacturing as well as aerodynamic aspects. The design procedure starts with an S_{2m} indirect solution. Afterward from the specified S_{2m} surface, by the use of Taylor series expansion, the blade geometry is generated by straight-line elements to meet the manufacturing requirements. Simultaneously, the fluid dynamic quantities across the blade passage can be determined directly. In terms of these results, the designer can revise the distribution of angular momentum along the shroud and hub, which are associated with blade loading, to get satisfactory velocities along the blade surfaces in order to avoid or delay flow separation.

Introduction

It is well known that the efficiency and operating range of centrifugal compressors are significantly influenced by the impeller performance, the impeller efficiency, and its discharge flow pattern. A major problem of impeller design is the avoidance of separation, especially for the high-pressure-ratio compressors. The separation results in a jet/wake pattern flow within the impeller exit and diffuser inlet area (Hamrick et al., 1954; Eckardt, 1976; Krain, 1981), which has a major effect on the diffuser performance.

Most modern impellers are designed by potential flow methods, which have obviously been successful in delaying separation and avoiding high suction velocity peaks. Most of these methods are based on a geometric method in forming blade geometry. Traditionally, as proposed by Krain (1984), a design algorithm includes two parts. Initially, the impeller geometry is generated based on a geometric conception. Afterward, the fluid dynamic quantities within the impeller passage are calculated by a direct full three-dimensional solution, or a quasi-three-dimensional iterative solution based on Wu's stream surface approach (Wu, 1952). After knowing the distributions of velocity and pressure along the casing walls and blade surfaces, the designer can adjust the input data handling the meridional contours and the blade geometry to correct rapid decelerations and accelerations. By repeating the regeneration of geometry and analysis of the flow field, the desired velocity distributions can be obtained. For such a design optimization, the iterative process is time consuming even in view of high-speed digital computers. In addition, the shortcomings of the geometric method are that the selected range of blade geometry is not wide, and there is no obvious connection between geometric concept and aerodynamic performance, so the success in optimization is much more dependent on the experience and art of the designers.

It is well known that the meridional channel geometry and the blade geometry are interdependent and influence each other. However, the meridional velocity is predominantly governed by the meridional impeller geometry, and the blade geometry mainly reacts on the circumferential velocity component. In practice, in order to make the optimization of impeller design much easier, the meridional contour and blade profiles are optimized separately. The design procedure presented in this paper is used to optimize the blade profiles when the meridional channel geometry is always kept unchanged.

Based on the Mean Stream Surface Method, which was proposed initially by Wu in the early 1950s (Wu, 1952), and expanded recently by Zhao et al. (1985), an impeller blade design method has been developed. This method satisfies three main important requirements in designing centrifugal impeller. First, besides the desired blade thickness distribution, the designer can specify the blade loading to get satisfactory velocity distribution along the blade surfaces. In addition, a description of the flow field in the impeller can be obtained in the design course at the same time. Finally, the method takes care of the manufacturing, so the camber surface and outer surfaces of blades can be generated by straight-line elements connecting the hub and shroud. In order to get the information about the actual boundary-layer behavior on the blade surfaces, a simple boundary-layer method proposed by Nash and MacDonald (1966) has been applied to inspect the boundary layer stability.

This design procedure is similar to a prescribed-loading method described by Jansen and Kirschner (1974); however,

Contributed by the International Gas Turbine Institute and presented at the 34th International Gas Turbine and Aeroengine Congress and Exhibition, Toronto, Ontario, Canada, June 4-8, 1989. Manuscript received at ASME Headquarters January 13, 1989. Paper No. 89-GT-73.

the latter is based on a one-dimensional solution, and the present method on a full three-dimensional solution.

Mean Stream Surface Method

Prof. Wu suggested (Wu, 1952) that a complete three-dimensional solution within a turbomachine passage can be obtained by an iterative procedure between a blade-to-blade S_1 solution and a hub-to-shroud S_2 solution. At the same time he also proposed an alternative simple full three-dimensional solution, i.e., the blade-to-blade variations of fluid properties can be determined by extending the solution obtained on the mean S_2 streamsurface by the use of power series in the circumferential direction (without the assumption that the S_1 flow surfaces are revolving)

$$q(\varphi) = q(\varphi_m) + (\varphi - \varphi_m) q'(\varphi_m) + \frac{(\varphi - \varphi_m)^2}{2} q''(\varphi_m) + \ldots \quad (1)$$

The various derivatives involved in the series, such as W^1, W^2, W_φ, are updated from the flow condition on the mean S_2 streamsurface as follows:

$$\begin{bmatrix} \sqrt{a_{22}} \cos\theta_{12} & \sqrt{a_{22}} & r\dfrac{\partial\varphi}{\partial x^2} \\ \sqrt{a_{11}} & \sqrt{a_{11}} \cos\theta_{12} & r\dfrac{\partial\varphi}{\partial x^1} \\ \dfrac{1}{\sqrt{a_{11}}}\dfrac{\partial\varphi}{\partial x^1} & \dfrac{1}{\sqrt{a_{22}}}\dfrac{\partial\varphi}{\partial x^2} & \dfrac{1}{r} \end{bmatrix} \cdot \begin{bmatrix} \dfrac{\partial W^1}{\partial\varphi} \\ \dfrac{\partial W^2}{\partial\varphi} \\ \dfrac{\partial W_\varphi}{\partial\varphi} \end{bmatrix} = \begin{bmatrix} \dfrac{\partial(V_\theta r)}{\partial x^2} \\ \dfrac{\partial(V_\theta r)}{\partial x^1} \\ C \end{bmatrix} \quad (2)$$

where

$$C = \left[\frac{\partial}{\partial x^1}(r\rho W^1\sqrt{a_{22}}\sin\theta_{12}) + \frac{\partial}{\partial x^2}(r\rho W^2\sqrt{a_{11}}\sin\theta_{12})\right] \cdot \frac{1}{r\rho\sqrt{a_{11}}}$$

After solving the inverse problem of flow along the S_{2m} streamsurface, the shape of S_{2m} and the fluid varieties along it are obtained; then a series of S_2 streamsurfaces within the passage can be extended successively in the circumferential direction to the suction or pressure surfaces of blade, so the blade coordinates can be determined in this manner (see Fig. 1).

By the use of a coordinate system transformation, an alternative direct expansion method has been developed in determining the blade coordinates from a known S_{2m} streamsurface. The Φ coordinate of any S_2 streamsurface, especially the two S_2 surfaces that coincide with the suction or pressure surface of the two neighboring blades, can be determined by the formulation

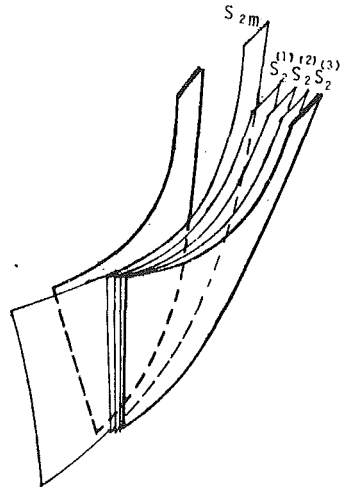

Fig. 1 Family of S_2 surfaces formed progressively from S_{2m}

$$\varphi_s = \varphi_m + B\Delta\psi_2 + \frac{1}{2}\frac{\partial B}{\partial\psi_2}(\Delta\psi_2)^2 + \frac{1}{6}\frac{\partial^2 B}{\partial\psi_2^2}(\Delta\psi_2)^3 + \ldots \quad (3)$$

$$\varphi_p = \varphi_m - B\Delta\psi_2 + \frac{1}{2}\frac{\partial B}{\partial\psi_2}(\Delta\psi_2)^2 - \frac{1}{6}\frac{\partial^2 B}{\partial\psi_2^2}(\Delta\psi_2)^3 + \ldots \quad (4)$$

The involved derivatives can be calculated from the flow variables along the S_{2m} streamsurface.

For inverse problems, the MSSM process is usually shorter, especially for high-solidity axial turbomachinery passages. In this case, employing the close relation between the blade thick-

Nomenclature

a_{ij} = basic metric tensor for S_{2m} computation
B = integrating factor in the continuity equation for S_2 surface and the circumferential thickness of S_2 surface
g_{ij} = basic metric tensor for MSSM computation
M/M_i = (meridional length)/(meridional length at impeller exit)
P = blade placing
q = any fluid quantity
r, Φ, z = relative cylindrical coordinates
t = circumferential thickness of blade
t_n = normal thickness of blade
$V_\vartheta r$ = angular momentum of fluid about axis of rotation
W^i = physical component of W tangent to x^i
x^1, x^2, Φ = general nonorthogonal coordinates
β = relative angle from meridional plane
Θ_{ij} = angle included by coordinate lines x^i and x^j
Φ_c = circumferential coordinate of blade camber or middle surface of blade passage
Φ_m = circumferential coordinate of S_{2m} surface
Φ_p = circumferential coordinate of blade pressure surface
Φ_s = circumferential coordinate of blade suction surface
Ψ = stream function value
ω = angular velocity of impeller

Subscripts

1 = impeller inlet
2 = impeller exit
h = hub
i = inlet
m = mean (midchannel)
s = shroud

ness distribution and the local angular thickness of the S_{2m} stream sheet, the estimated value of B for a desirable blade thickness distribution can be given by the designer. Besides the distribution of the S_{2m} stream sheet, the designer has the freedom to specify the distribution of swirl (angular momentum $V_\vartheta r$) by which the blade loading and velocity distribution are controlled directly. Based on the experience of the designer, the first solution may give satisfactory results.

However, for some axial and radial compressor passages with low solidity, the blade thicknesses obtained in the previous calculation are not satisfactory, since it is difficult for the designer in specifying the distribution of the S_{2m} stream sheet thickness B to insure blade thickness distribution equal to the desired values. In this case, the distribution of B along the S_{2m} streamsurface should be modified successively in an iterative procedure. In terms of formulations (3) and (4), an important relation between the distribution of stream sheet thickness on the S_{2m} surface and the desired blade thickness t can be set up as follows:

$$B=\frac{p-t}{p}-\frac{1}{6}\frac{\partial^2 B}{\partial\psi_2^2}(\Delta\psi_2)^2-\frac{1}{120}\frac{\partial^4 B}{\partial\psi_2^4}(\Delta\psi_2)^4+\ldots \quad (5)$$

Simultaneously, another important formulation, which sets up the connection between the shapes of the S_{2m} streamsurface and blade camber, can be obtained:

$$\varphi_m=\varphi_C-\frac{1}{2}\frac{\partial B}{\partial\psi_2}(\Delta\psi_2)^2-\frac{1}{24}\frac{\partial^3 B}{\partial\psi_2^3}(\Delta\psi_2)^4+\ldots \quad (6)$$

Design Procedure

Theoretically, the impeller blade profiles could be designed only on the basis of aerodynamic considerations to give good velocity distributions throughout. This can be accomplished by loading a number of streamlines on the S_{2m} streamsurface in an optimum manner. The major difficulty with this ideal approach is that in almost all cases the blade shape obtained would be practically impossible to manufacture in a reasonable manner. Therefore, some compromises are necessary in order to insure reasonable blade configurations can be obtained. Generally, in order to make the manufacture easy and economical, the centrifugal impeller blade is always designed in a fairly straightforward manner. The camber surface and outer surfaces of blades are generated by straight-line elements passing from shroud to hub.

In this case, geometric constraints are imposed on the design process, and the designer's freedoms for specifying the optimal blade loading are reduced. However, in addition to ease and economy of manufacture, the straight-line element blade can be designed with variable work distributions in critical regions, such as along the shroud streamline. Generally, there are three categories of impeller blade that can be defined by straight-line elements, in axial, radial, and arbitrary directions. For the former two blade types, only the blade loading along the shroud streamline where the flow conditions are critical can be optimized. In general, shroud separation appears critical to the design of the optimum centrifugal impeller. The last type of blade seems more favorable, since it provides the designer with much flexibility to specify the optimal loading distribution along the S_{2m} streamsurface.

The general procedure used for determining the blade shape and the inside flow field involves an iterative calculation to make sure the blade geometry constraint on straight-line elements and the distribution of blade thickness equal the values given in advance. Figure 2 shows the iterative loop of the computing process. The input data include rotating speed, average efficiency, impeller meridional contour, distributions of blade thickness along hub and shroud, desired distributions of swirl at both inlet and outlet of the impeller, and number of blades.

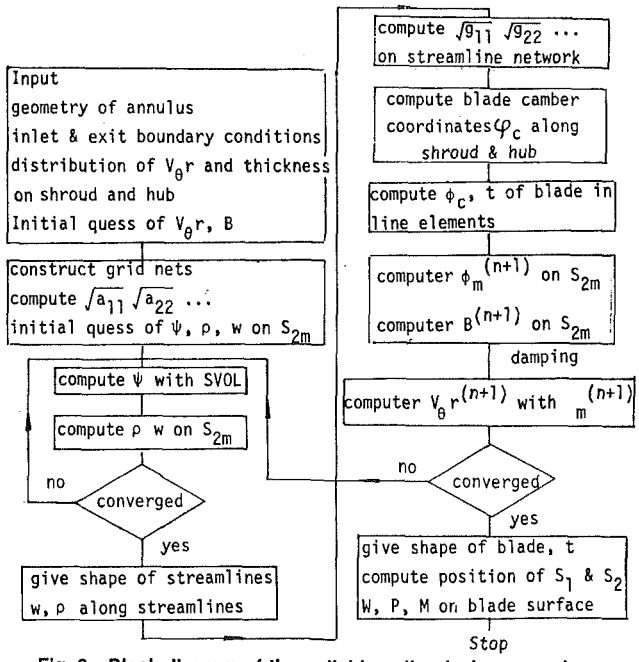

Fig. 2 Block diagram of the radial impeller design procedure

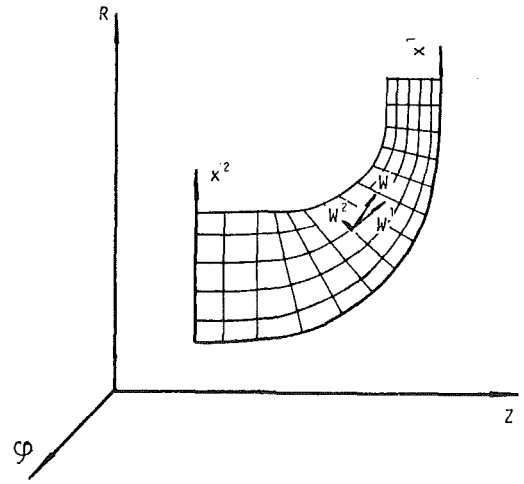

Fig. 3 Meridional coordinate system

At the start of the loop, a tentative S_{2m} calculation of flow field on the S_{2m} streamsurface is carried out. The specified swirl distributions are applied to the shroud and hub streamlines, and the distribution along the others is assumed to be a linear variation from hub to tip. For the computation of S_{2m}, based on a method proposed by Zhu (1980), the flow field matrix line relaxation has been used to solve the stream function equation governing the flow along the S_{2m} streamsurface. Figure 3 illustrates the nonorthogonal curvilinear coordinates set up on the meridional plane and the corresponding velocity components in the S_{2m} and Mean Stream Surface Method calculations. After obtaining the shape of S_{2m} and the distribution of the velocity and density on the S_{2m} streamsurface, the derivatives of W^1, W_φ, and ρ as well as the derivatives of B with respect to the ψ_2 streamfunction value can be determined. In terms of formulation (6) the blade camber coordinates along the shroud and hub can be dated up from the coordinates of S_{2m} streamsurface

$$\varphi_C\Big|_{s,h}=\varphi_m\Big|_{s,h}+\frac{1}{2}\frac{\partial B}{\partial\psi_2}(\Delta\psi_2)^2+\frac{1}{24}\frac{\partial^3 B}{\partial\psi_2^3}(\Delta\psi_2)^4+\ldots \quad (7)$$

Then the tentative blade camber surface can be described

by a number of straight-line elements, which are lines joining the points distributed along the shroud and hub camberlines.

In order to meet the described straight-line constraint condition, the distributions of B and $V_\vartheta r$ along the S_{2m} surface should be adjusted. The circumferential thickness of the blade is updated from the normal thickness, which is given in a linear manner from hub to shroud after obtaining the shape of blade camber surface. By the use of equation (5), the new distribution of the S_{2m} sheet thickness can be calculated from the circumferential thickness of the blade.

Once the blade camber is updated, equation (6) gives the new location of the S_{2m} streamsurface $\Phi_m^{(1)}$ (x^1, x^2). After updating the new location of the S_{2m} streamsurface, recalculation of $V_\vartheta r$ by the equations

$$W_\varphi = (r/\sqrt{g_{11}})\,(\partial\varphi/\partial x^1)\,W^1 \tag{8}$$

$$V_\vartheta r = (\omega r + W_\varphi) r \tag{9}$$

leads to a new distribution of $V_\vartheta r$ on the S_{2m} surface. (The distributions of $V_\vartheta r$ along shroud and hub streamlines given in the input data are not changed in the iterative procedure.)

Then a new cycle of iteration can be started with the recalculation of S_{2m} flow. The convergence criteria require the maximum change in the location Φ_m and thickness B at any grid point on the S_{2m} surface to be less than prescribed tolerances.

When the iterative process is completed, in addition to the blade geometry, the three-dimensional flow field within the impeller passage can be described by the Taylor series expansion from the S_{2m} streamsurface. It provides the characters of three-dimensional flow field and the distribution of aerodynamic variables on the blade surface or at any points inside the passage, such as velocity and density, Mach number, and pressure. The blade geometry as well as the velocity, Mach number, and pressure distributions are plotted. In order to get further information about the actual boundary-layer behavior on the impeller, these profiles can be taken as input data for succeeding boundary layer calculations. The reactions of boundary-layer calculation on the inviscid three-dimensional flow calculation are neglected; only the skin friction coefficient C_f is sketched to show the stability of boundary layer.

In any event, examination of the flow field for the initial design will indicate whether any alterations in the distribution of blade loading are required. If so, a repeating design can be performed after making the necessary changes about the distribution of blade loading along the shroud and hub until the desired velocity distributions are obtained, especially in the critical shroud region.

In the calculation for the flow field within the axial turbomachine cascades, Taylor series methods failed to deal with the deviation angle problem, inasmuch as these methods are not accurate near the leading and trailing edges and in such a manner that it makes no sense to impose the Kutta condition. Similarly, for a radial impeller design procedure, the slip problem cannot be solved by means of the Mean Stream Surface Method, so after obtaining the optimized design, a necessary modification of this design is to be carried out for the fact that slip occurs; that is the flow direction will deviate from the blade surface in the trailing region. From the leading edge to the point where slip starts, the flow follows the blade surface, but in the slip region, the blade camber angle is obtained by fitting a parabola distribution from the point where slip starts and passing through the point defined by β_2. The exit blade angle β_2 can be specified by the designer, or determined by the slip factor η as follows:

$$\beta_2 = \tan^{-1}\left[\frac{1}{W_{m\,\text{exit}}}\left(\frac{(V_\theta r)_{\text{exit}}}{r_2} - \eta\,\omega\,r_2\right)\right] \tag{10}$$

The location of point where slip starts may be specified by the designer based on the information obtained in the design procedure. Generally, slip was assumed to begin at the point where tangential blade turning was completed.

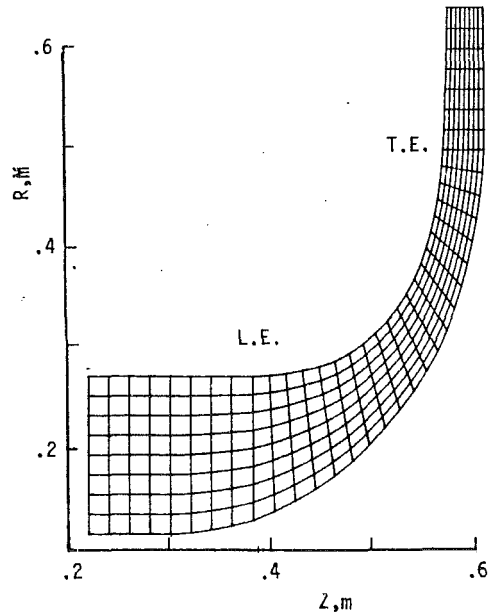

Fig. 4 Flowpath of sample radial impeller

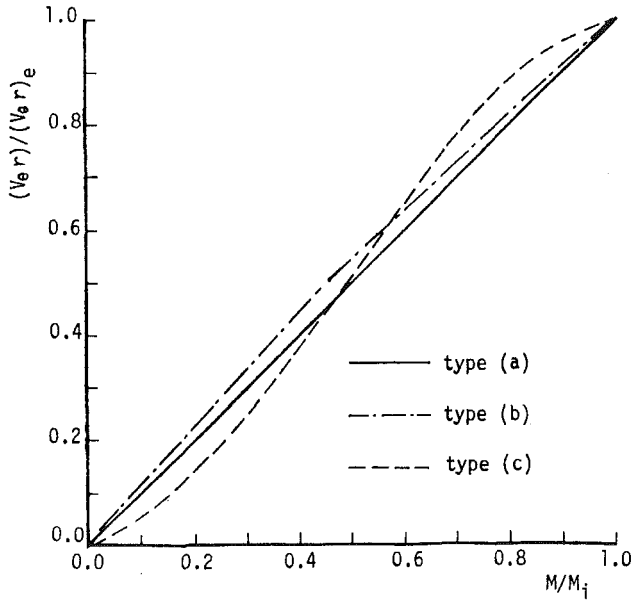

Fig. 5 The different $V_\vartheta r$ distributions along the shroud

After adjusting the distribution of blade camber angle along hub and shroud streamlines, the angular coordinates of the blade camber surface along hub and shroud are obtained by integrating the β distribution. Then the coordinates of blade camber surface can be obtained in terms of straight-line elements from hub to shroud.

Sample Design

In order to illustrate this impeller blade design method, a sample for designing a radial impeller is presented herein. The meridional projection of flow field on S_{2m} is defined by 9 quasi-streamlines and 38 quasi-normal stations. Among the latter, eight are upstream and eight are downstream of the impeller (see Fig. 4). The major impeller design specifications are: mass flow 21.84 kg/s; shaft speed 8000 rpm; outlet swirl 158.58 m^2/s on shroud, 155.42 m^2/s on hub, and the swirl varies from

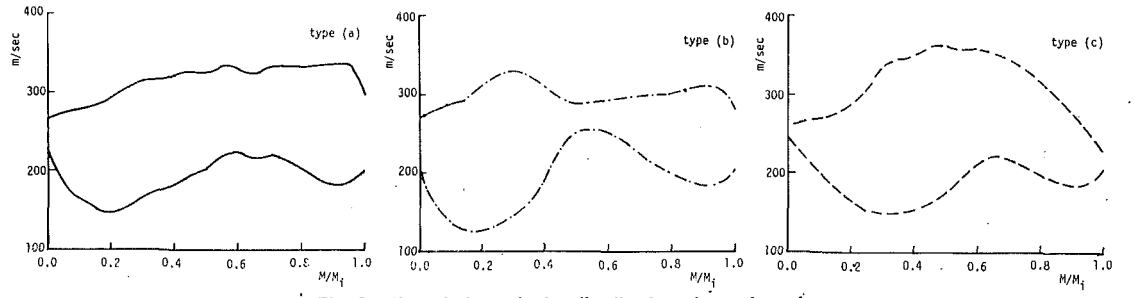

Fig. 6 The relative velocity distribution along shroud

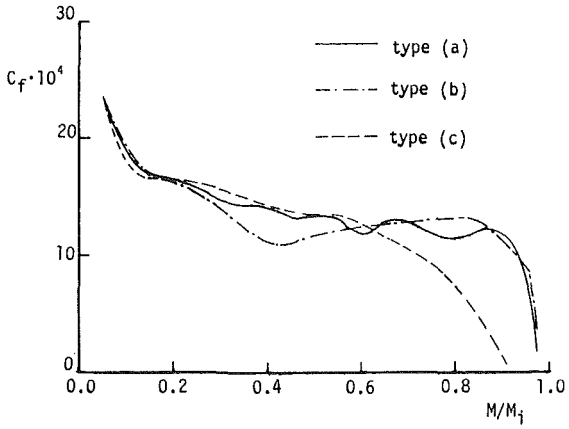

Fig. 7 Local skin friction coefficients at shroud/suction

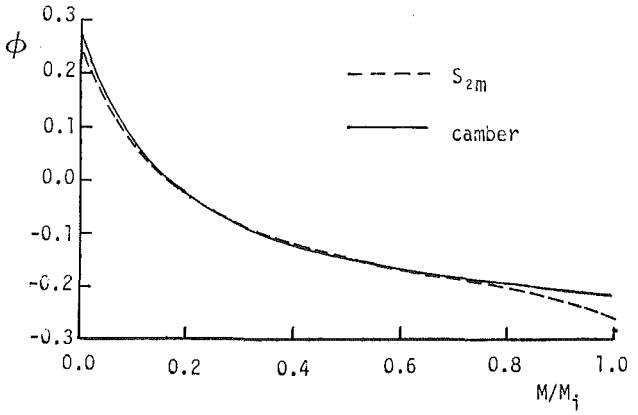

Fig. 9 The difference between the blade camber surface and the S_{2m} surface on the shroud of impeller (*a*)

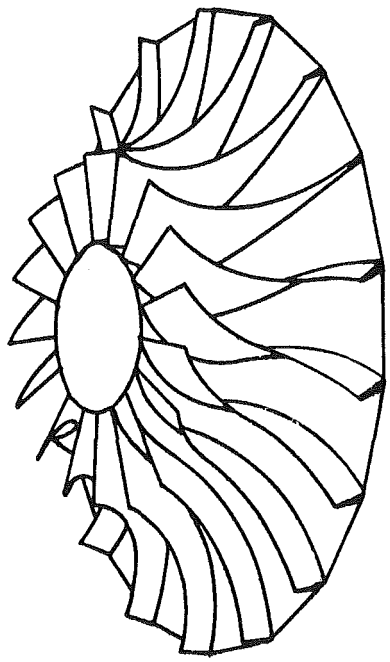

Fig. 8 Blade geometry of impeller (*a*)

hub to shroud linearly; inlet swirl 0; blade number 17; the blade lean at leading edge 0 deg.

Because there is a lack of systematic experiments to determine the relative merits of possible loading, it is difficult to choose preferable loading distributions along the shroud and hub streamlines. Four possible types of loading distribution have been suggested by Jansen and Kirschner (1974). The linear loading and double linear loading seem to be more favorable, which may have the merit of minimizing the secondary flows or the streamwise velocity reduction rates. In our numerical experiments, three types of blade loading have been selected to design different impeller blade geometry with the same meridional contours. The angular momentum $V_\vartheta r$ distributions along the shroud streamline were specified in linear, double linear, and general third-order cases, respectively, which are sketched in Fig. 5 versus the meridional length. The corresponding distributions of $V_\vartheta r$ along the hub have been adjusted to make the lean of design impeller camber reasonable. The calculated relative velocity distributions on the shroud obtained in the design procedure have been shown in Fig. 6 with respect to the three types of loading distribution. Additionally, the corresponding C_f coefficient, which shows the stability of boundary layer developed along the shroud/suction, is also sketched in Fig. 7. From the above results, the linear loading distribution seems to be better than the others. The maximum difference between the relative velocities along the suction and pressure surface, which can be used to show the blade loading, for case (*a*) is less than cases (*b*) and (*c*). The C_f variation also shows that the rapid deceleration of velocity along shroud/suction streamline in case (*a*) has been avoided. Naturally, this kind of loading distribution can be optimized further by a number of numerical experiments, since the present design procedure can run on a moderate or even a personal computer with a moderate amount of CPU time. For this model design, only five or six iterations are necessary to meet the convergence tolerance, and the corresponding total computer time is approximately two minutes on a UNIVAC 1100 computer system.

Figure 8 shows the final design impeller blade for case (*a*). The differences between the blade camber surface and the S_{2m} surface on the shroud are shown in Fig. 9. It is shown on the sketch that although the streamline and camber line on the shroud are in the same direction, some clear differences exist in the inlet and exit region. Figure 10 shows the distribution of blade lean angle α_ϑ and blade slope angle α_Z along the meridional distance. The α_ϑ varies from 0 deg at the leading edge to a negative or forward 21 deg at the trailing edge. Some numerical experiments show that by means of adjusting the

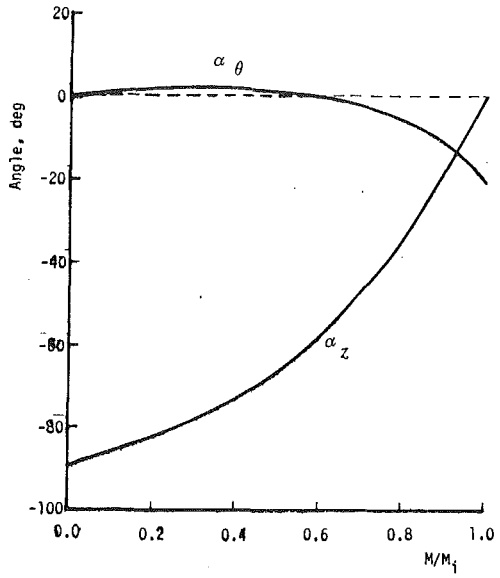

Fig. 10 Variation of blade-element orientation along shroud for impeller (*a*)

loading distribution along the hub streamline, the distribution of lean angle can be changed to meet the consideration of bending stress limitation in the inducer region.

Concluding Remarks

An aerodynamic impeller blade design method for centrifugal compressors has been developed with regard to the manufacturing process. Based on the simple full three-dimensional flow field approach MSSM, the impeller blade surfaces can be generated by straight lines connecting the hub and shroud, which can be machined today on a five-axis milling machine.

In the present design procedure, the designer can specify the blade loading according to his experience to obtain desired velocity distributions on the blade surfaces in order to avoid or delay the occurrence of separation.

Unlike most current procedures, detailed flow field analysis after obtaining the blade geometry is unnecessary in the present method, since it can be carried out while the blade is being generated by a Taylor series expansion. Detailed information about the distribution of velocity and pressure along the blade surfaces and casing walls, as well as the boundary-layer stability, which is obtained by coupling a boundary layer calculation, can be offered to the designer. In terms of all this information, he can adjust the input blade loading to make his design more favorable. Furthermore, our calculation procedure is fast enough to allow a number of iterative operations in searching for an optimum blade design.

References

Eckardt, D., 1976, "Detailed Flow Investigations Within a High Speed Centrifugal Compressor Impeller," ASME *Journal of Fluids Engineering*, Vol. 98, pp. 390-402.

Hamrick, J. T., Mizisin, J., and Michel, D. J., 1954, "Study of Three Dimensional Flow Distribution Based on Measurements in a 48-Inch Radial-Inlet Centrifugal Impeller," NACA TN 3101.

Jansen, W., and Kirschner, A. M., 1974, "Impeller Blade Design Method for Centrifugal Compressors," NASA SP-304, pp. 537-556.

Krain, H., 1981, "A Study on Centrifugal Impeller and Diffuser Flow," ASME *Journal of Engineering for Power*, Vol. 103, pp. 688-697.

Krain, H., 1984, "A CAD Method for Centrifugal Compressor Impellers," ASME *Journal of Engineering for Gas Turbines and Power*, Vol. 106, pp. 482-488.

Nash, J. F., and MacDonald, A. G. J., 1966, "The Calculation of Momentum Thickness in a Turbulent Boundary Layer at Mach Numbers up to Unity," A.R.C. CP, No. 963.

Wu Chung-Hua, 1952, "A General Theory of Three-Dimensional Flow in Subsonic or Supersonic Turbomachines of Axial Radial and Mixed Flow Types," ASME Paper No. 50-A-79, *Trans. ASME*, Vol. 74, Nov.; NACA TN 2604.

Zhao Xiaolu, Sun Chunlin, and Wu Chung-Hua, 1985, "A Simple Method for Solving Three-Dimensional Inverse Problems of Turbomachine Flow and the Annular Constraint Conditions," ASME *Journal of Engineering for Gas Turbines and Power*, Vol. 107, pp. 293-300.

Zhu, R. G., 1980, "Flow-Field Line-Relaxation Solution for Inverse Problem of Flow Along S_2 Relative Stream Surface Employing Non-orthogonal Curvilinear Coordinates and Corresponding Non-orthogonal Velocity Components," *Journal of Engineering Thermophysics*, Vol. 1, pp. 28-35.

The Preliminary Design of Radial Inflow Turbines

A. Whitfield
Senior Lecturer,
University of Bath,
Bath, United Kingdom

A procedure is described that develops the nondimensional design of a radial inflow turbine rotor. The design is developed, for any specified nondimensional power ratio, with the objective of minimizing the inlet and discharge Mach numbers so that the passage losses are minimized. Initially state-of-the-art efficiencies are assumed, but these are later modified through the specification of empirical losses. The resultant nondimensional design can be transformed to absolute dimensions through the specification of the inlet stagnation conditions and the mass flow rate of the working fluid.

1 Introduction

The design of radial inflow turbines is described by Rohlik (1968, 1975), Glassman (1976), Rodgers and Geiser (1987), Rodgers (1987), and Whitfield and Baines (1989). These procedures are developed through the application of the fundamental turbomachinery and gas dynamic equations, similarity techniques (particularly specific speed), and empirical loss models. The procedure developed by Rohlik (1968) led to a series of correlations with specific speed, which could be used as design charts. These results are, however, restricted by the limitations built into the original analysis procedure.

At the initial stage of a turbine design proposal the designer will have available a range of specified parameters. These may include the power output, mass flow rate, inlet stagnation conditions, rotational speed, and possible restraints on the overall size. Alternatively only the required power output may be specified, and it will be necessary for the designer to specify parameters so that the design can proceed. The objectives for each design may differ; however, a common aim will generally be to maximize the efficiency and/or develop a compact power unit. It may be necessary to compromise the efficiency in order to achieve a compact design; in such cases the cost in terms of reduced efficiency needs to be known so that a well-judged compromise can be made.

Precise prediction of efficiencies at the initial design stage, or at any other stage, is difficult, and the designer usually relies upon empirical loss models and correlations; see Rohlik (1968, 1975), Glassman (1976), and Rodgers (1987). The predicted efficiencies are then as good as the underlying empirical loss models. Efficiency is maximized when the irreversibilities associated with the flow process are minimized. The energy loss is generally a function of the square of the velocity relative to the component under consideration, and if the losses are to be minimized it is essential that the flow velocities be no larger than necessary. The procedure developed here assesses the rotor inlet and discharge conditions with a view to minimizing the velocities in terms of the absolute and relative Mach numbers. The resultant design should then give minimum losses irrespective of the loss model, and associated uncertainties, used.

2 Initial Design Specification

In order to develop a general procedure, it will be assumed initially that only the desired power output is specified. The power developed by the turbine is given by

$$\dot{W}/\dot{m} = h_{01} - h_{03} = \frac{\gamma R}{\gamma - 1}(T_{01} - T_{03})$$

and can be developed to the nondimensional power ratio

$$S_w = \frac{\dot{W}}{\dot{m} h_{01}} = 1 - \frac{T_{03}}{T_{01}} \tag{1}$$

If the required power output, mass flow rate, and inlet stagnation temperature are known, then S_w can be calculated directly. If, however, only the power output is known, then S_w must be specified and the design analysis used to select an appropriate magnitude; this may be an iterative procedure. Once a magnitude of power ratio has been determined, the required mass flow rate follows for any specified inlet stagnation temperature, which is usually limited by rotor material and stress capabilities.

The design procedure will therefore be developed from a specification of the power ratio S_w. As the mass flow rate is not necessarily known initially it will not be possible to calculate the absolute dimensions of the rotor, and the objective of the analysis is to develop a nondimensional design, that is the dimensions will be nondimensionalized by the rotor inlet radius, and the fluid and rotor velocities by the inlet stagnation speed of sound. As the design proceeds and it becomes possibe to quantify the mass flow rate, it will then be possible to convert the nondimensional design to give the required size.

The power ratio is related to the stage expansion ratio through the efficiency definition, which is given, on a total-to-static basis, by

$$\eta_{ts} = \frac{1 - T_{03}/T_{01}}{1 - (P_{01}/P_3)^{(\gamma-1)/\gamma}}$$

The derived pressure ratio is shown in Fig. 1. The pressure ratio can be interpreted as a total-to-total pressure ratio pro-

Contributed by the International Gas Turbine Institute and presented at the 34th International Gas Turbine and Aeroengine Congress and Exhibition, Toronto, Ontario, Canada, June 4–8, 1989. Manuscript received at ASME Headquarters January 17, 1989. Paper No. 89-GT-83.

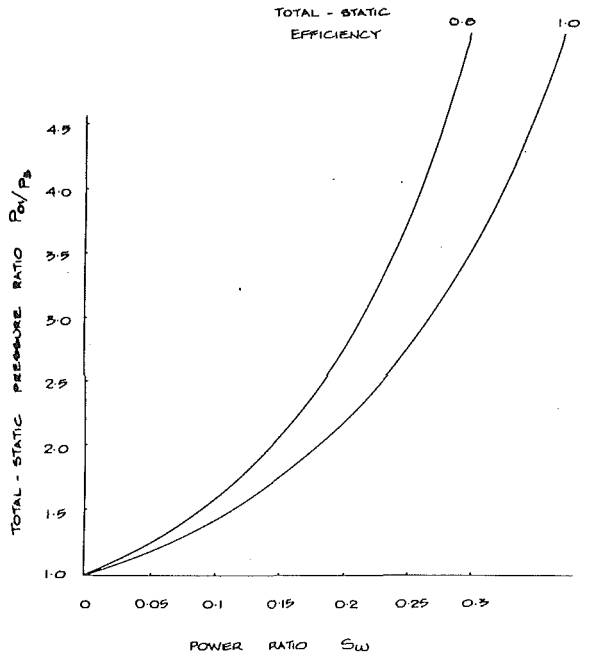

Fig. 1 Turbine expansion ratio as a function of power ratio S_W

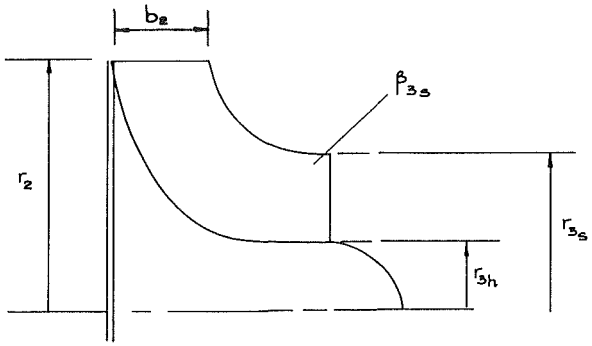

Fig. 2 Turbine rotor geometry

vided the efficiency is defined in a like manner. A good order of magnitude for the power ratio can be obtained from Fig. 1 if the turbine expansion ratio is known.

3 Rotor Inlet Design

A typical turbine rotor is illustrated in Fig. 2. The rotor blades are usually radial at inlet as this provides the best condition with respect to stressing; this will be assumed to be the case here. At the best efficiency point early design procedures assumed that the inlet relative velocity vector was aligned with the radial blade, thereby giving a right-angled velocity triangle. It has, however, been shown both experimentally and by incidence loss models that at the best efficiency point a

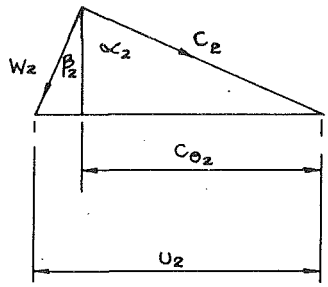

(c) INLET VELOCITIES

Fig. 3 Rotor velocity components

significant angle of incidence occurs and the velocity triangle of Fig. 3 is more appropriate. It is necessary, therefore, to specify the incidence angle at which the best efficiency point will occur. Rodgers (1987) quotes incidence angles of the order of -20 deg, and Rohlik gives magnitudes as high as -40 deg. Assessment of an appropriate magnitude for the optimum inlet flow angle is given in the next section after the inlet velocity triangle has been established.

At the best efficiency point it is usually assumed that the fluid discharges from the rotor in an axial direction, that is, there is no discharge swirl. The Euler turbomachinery equation then becomes

$$\dot{W}/\dot{m} = U_2 C_{\theta 2} - U_3 C_{\theta 3} = U_2 C_{\theta 2} \tag{2}$$

and it follows that

$$\frac{U_2 C_{\theta 2}}{a_{01} a_{01}} = \frac{S_w}{\gamma - 1} \tag{3}$$

The objective now is to calculate all parameters associated with the inlet velocity triangle, as this information is necessary not only for the following rotor design, but also for the preceding stator.

From the velocity triangle (Fig. 3)

$$C_{\theta 2} = U_2 + C_{m2} \tan \beta_2 = U_2 + \frac{C_{\theta 2}}{\tan \alpha_2} \tan \beta_2 \tag{4}$$

which can be developed to

$$\tan^2 \alpha_2 \left\{ 1 - \frac{U_2 C_{\theta 2}}{a_{01}^2} \frac{a_{01}^2}{C_2^2} \right\} - \tan \alpha_2 \tan \beta_2 - \frac{U_2 C_{\theta 2}}{a_{01}^2} \frac{a_{01}^2}{C_2^2} = 0 \tag{5}$$

Equation (5) is a quadratic equation in $\tan \alpha_2$, which can be solved if the stagnation Mach number C_2/a_{01} is known or specified. This is equivalent to specifying the inlet Mach number as it can be derived through

$$M_2^2 = M_{02}^2 / \left(1 - \frac{\gamma - 1}{2} M_{02}^2 \right)$$

Nomenclature

A = flow area
a = speed of sound
C = absolute velocity
h = enthalpy
M = Mach number
M′ = relative Mach number
$\dot{m}$ = mass flow rate
P = pressure
R = gas constant
r = radius
S_w = power ratio
T = temperature
U = blade velocity
W = relative velocity
$\dot{W}$ = power
Z_B = number of blades
α = absolute flow angle
β = relative flow angle
γ = ratio of specific heats
η = efficiency
θ = nondimensional mass flow
ρ = density

Subscripts

0 = stagnation condition
1 = turbine stage entry
2 = rotor inlet
3 = rotor discharge
s = shroud position

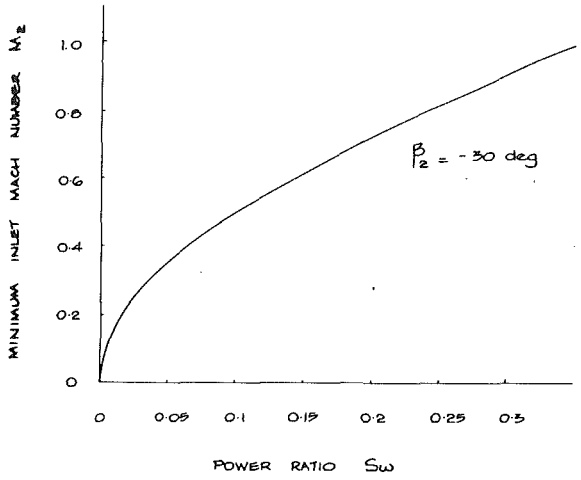

Fig. 4 Rotor minimum inlet Mach number

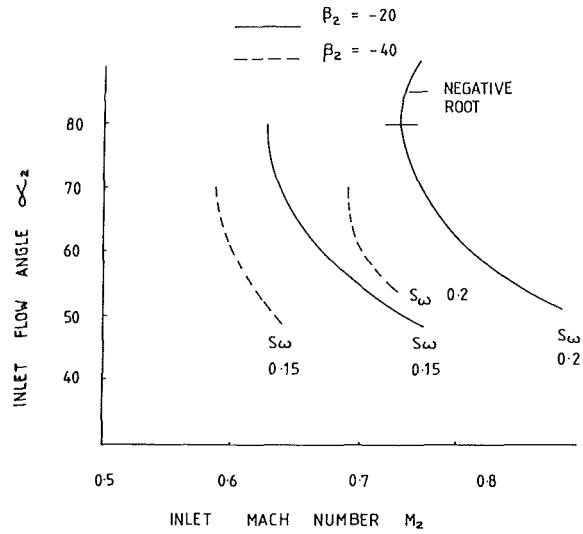

Fig. 5 Variation of inlet flow angle with Mach number

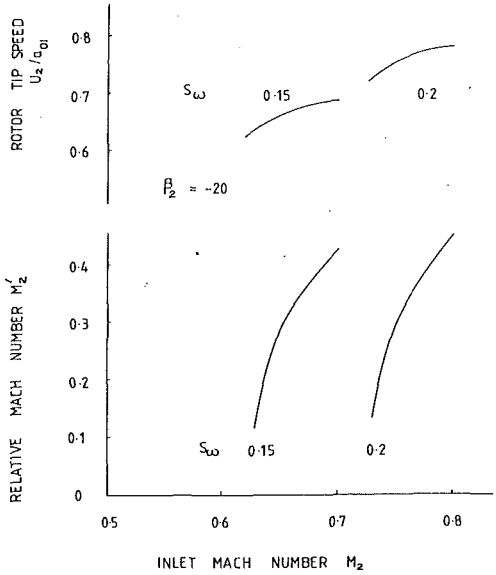

Fig. 6 Effect of inlet Mach number on relative Mach number and rotor tip speed

with the assumption of adiabatic flow through the stator, that is $T_{02} = T_{01}$. However, equation (5) can only be solved if the stagnation Mach number is sufficiently large to yield a positive root. The limiting value of C_2/a_{01} is such that

$$\tan^2 \beta_2 + 4\left(1 - \frac{U_2 C_{\theta 2}}{a_{01}^2}\frac{a_{01}^2}{C_2^2}\right)\frac{U_2 C_{\theta 2}}{a_{01}^2}\frac{a_{01}^2}{C_2^2} = 0$$

Substituting from equation (3) it follows that

$$4\left(\frac{S_w}{\gamma - 1}\frac{a_{01}^2}{C_2^2}\right)^2 - 4\frac{S_w}{\gamma - 1}\frac{a_{01}^2}{C_2^2} - \tan^2 \beta_2 = 0 \tag{6}$$

the solution of which yields

$$\frac{C_2^2}{a_{01}^2} = \left(\frac{S_w}{\gamma - 1}\right)\frac{2 \cos \beta_2}{1 + \cos \beta_2} \tag{7}$$

The application of equation (7) enables the minimum absolute Mach number of the incidence gas to be derived through the specification of the power ratio S_w and the optimum inlet angle relative to the rotor β_2. The minimum inlet Mach number is shown in Fig. 4 as a function of power ratio S_w for an incidence angle of -30 deg. The effect of the assumed incidence angle on the minimum Mach number is small relative to that of the power ratio. The associated turbine expansion ratio can be observed through Fig. 1. Mach numbers in excess of that given through equation (7) can, of course, be specified by the designer. However, high Mach numbers will lead to increased stator losses, increased relative Mach numbers, and consequently increased incidence and rotor losses, and increased rotational speeds of the rotor.

With the inlet Mach number specified or derived through equation (7) the rotor inlet velocity triangle is fully defined. The absolute flow angle is given by equation (5), and for the specific case where the minimum Mach number is used it can be shown that

$$\tan \alpha_2 = \frac{\sin \beta_2}{\cos \beta_2 - 1} \tag{8}$$

Also for the minimum Mach number condition the nondimensional speed of the rotor is given by

$$\left(\frac{U_2}{a_{01}}\right)^2 = \left(\frac{1}{\gamma - 1}\right)\frac{S_w}{\cos \beta_2} \tag{9}$$

Equation (5) is illustrated in Fig. 5, where the absolute flow angle is presented as a function of the inlet Mach number for different magnitudes of power ratio and inlet relative flow angle. From this it can be seen that as the inlet Mach number is increased beyond the minimum permissible, the absolute flow angle decreases. However, as shown in Fig. 6 the nondimensional speed of the rotor and the relative Mach number both increase as the absolute Mach number is increased.

The solution to equation (5) does, of course, contain two roots. The negative root yields a flow angle that increases rapidly to 90 deg; see Fig. 5. As a consequence the relative Mach number approaches zero, and if the design is continued using these flow angles an unacceptably large rotor diameter is needed in order to provide sufficient flow area to carry the required mass flow.

Clearly the minimum Mach number condition provides a satisfactory base from which the turbine design can be developed. If it is eventually found advantageous to increase the Mach number, this can be readily done and the proposed design modified.

3.1 Calculation of the Optimum Inlet Relative Flow Angle. The high optimum incidence angles of radial inflow rotors are attributed to the fact that the incoming flow has to board a rotor passage, which is sustaining a relative eddy. This is analogous to the phenomenon that gives rise to slip in centrifugal compressor impellers. The radial inflow turbine

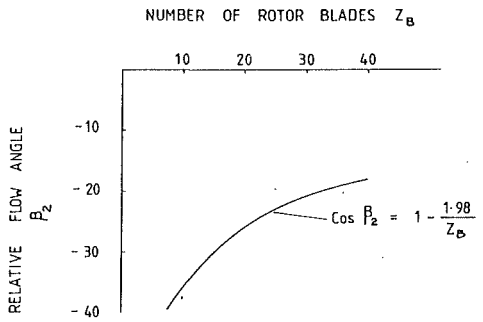

Fig. 7 Effect of blade number on optimum relative flow angle

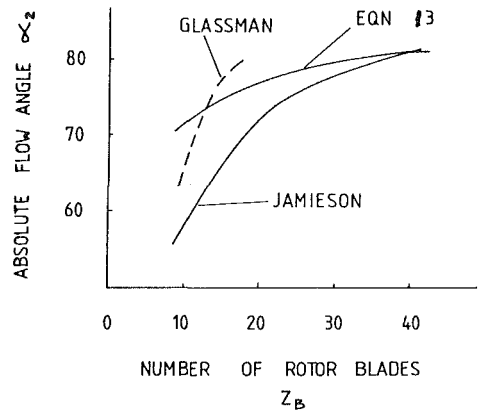

Fig. 8 Absolute flow angle as a function of the number of blades

studies by Woolley and Hatton (1973) and Sugimoto et al. (1975) confirm this pattern. An incidence factor is usually defined in a similar manner to the specification of the slip factor for centrifugal compressors. The analysis by Stanitz (1952) for the two-dimensional inviscid blade-to-blade flow in a centrifugal compressor impeller (which is equally valid for the turbine rotor if all velocity vectors are reversed) gave the tangential component of velocity as (see also Rohlik, 1968)

$$C_{\theta 2} = U_2\left(1 - \frac{0.63\pi}{Z_B}\right) \tag{10}$$

From equation (4) it follows that

$$C_{\theta 2} = U_2 \frac{\tan \alpha_2}{\tan \alpha_2 - \tan \beta_2} \tag{11}$$

At the minimum Mach number condition equation (8) can be combined with equations (10) and (11) to give

$$\cos \beta_2 = \left(1 - \frac{0.63\pi}{Z_B}\right) \tag{12}$$

This expression is shown in Fig. 7. For radial turbine rotors with 12 to 20 blades, optimum relative flow angles between -33 and -26 deg are predicted.

The optimum relative flow angle of equation (12) can be combined with equation (8) to give the corresponding absolute flow angle as

$$\cos^2 \alpha_2 = \frac{0.63\pi}{2Z_B} \tag{13}$$

This expression is shown in Fig. 8. For comparison the expressions given by Jamieson (1955) and Glassman (1976) are also included. Jamieson gave the relationship

$$Z_B = 2\pi \tan \alpha_2$$

This relationship is strictly applicable only if induced incidence effects are neglected. Glassman (1976) considered that the Jamieson expression gave too many blades and modified it to

$$Z_B = \frac{\pi}{30}(110 - \alpha_2)\tan \alpha_2$$

Equation (13), based on the minimum inlet Mach number condition and equation (10), compares well, over the range of number of blades most commonly adopted, with the expression given by Glassman (1976). For any specified number of rotor blades equation (12) enables the optimum relative flow angle to be calculated. This is dependent on the empirical incidence factor relationship chosen, and following centrifugal compressor practice for slip factors a number of alternative expressions could be quoted. Care should, however, be exercised in the use of compressor slip factor relationships as they have often been developed empirically to provide good order of magnitude values for the separated flows at compressor impeller discharge. Such conditions do not apply at the turbine rotor inlet, and in general compressor slip factor correlations may not be applicable. The correlation used above was developed from a two-dimensional inviscid analysis and did not attempt to include separated flows. Equation (12) can only be used as a guide to the optimum incidence angle. Judging from the limited data given by Rodgers (1987) the values given by equation (12) are a little high. Inclusion of blade and boundary layer blockage will reduce the effective passage size and hence the magnitude of the optimum incidence angle.

4 Rotor Discharge Design

For the design of a compressor impeller inducer a procedure was described by Stanitz (1953) and Coppage et al. (1956), which led to the derivation of the inlet relative flow angle, which ensured that the nondimensional mass flow rate was achieved with the minimum inlet relative Mach number. A similar analysis can be applied to the rotor exducer in order to ensure that the desired mass flow rate is achieved with the minimum discharge relative Mach number. For the case of zero discharge swirl, the relative Mach number can be shown to be given by

$$M_3'^2 = M_3^2 + \frac{\theta M_u^2}{1-\nu^2}\frac{1}{M_3}\left\{1 + \frac{\gamma - 1}{2}M_3^2\right\}^{0.5}\sqrt{\frac{T_{01}}{T_{03}}}\frac{P_{01}}{P_3} \tag{14}$$

where θ is the nondimensional mass flow rate $\dot{m}/\rho_{01} a_{01} \pi r_2^2$.

In order to use equation (14) the pressure ratio P_{01}/P_3 must be derived through the specification of a total-to-static efficiency for the turbine. Then

$$\left(\frac{P_3}{P_{01}}\right)^{\frac{\gamma-1}{\gamma}} = 1 - \frac{1 - T_{03}/T_{01}}{\eta_{ts}} = 1 - \frac{S_w}{\eta_{ts}} \tag{15}$$

Equation (14) is presented in Fig. 9. It can be seen that the relative Mach number is a minimum when the relative flow angle is of the order of -55 deg. The use of larger flow angles (e.g., -70 deg) cannot, however, be dismissed as this leads to a reduction in the absolute Mach number. There is, therefore, a compromise to be made between low relative Mach number to minimize the rotor losses, and a reduced absolute Mach number to reduce the exit loss, which is directly proportional to the square of the discharge Mach number. This choice cannot be made at this stage, and the above analysis can only be used to provide a good order of magnitude for the relative flow angle; magnitudes in the range 0 to -50 deg can be ruled out as unsatisfactory. The analysis is, therefore, continued with the relative flow angle simply specified.

To proceed further and derive the discharge velocity triangle

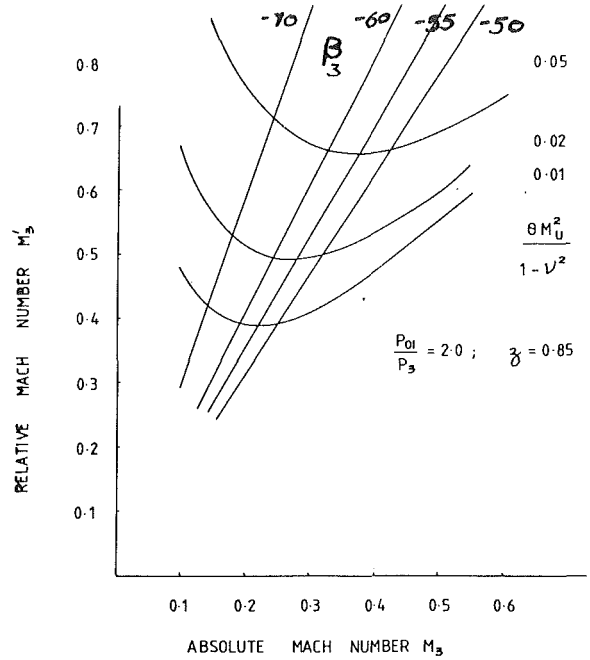

Fig. 9 Relative flow angle for minimum relative Mach number

it is necessary to specify a further parameter. Rohlik (1968) assumed a relative velocity ratio, W_3/W_2, and maintained this constant at 2.0. In axial turbine design the degree of reaction is often specified. Rodgers and Geiser (1987) correlated the efficiency against the discharge velocity ratio C_{m3}/U_2 and showed that optimum values lay between 0.2 and 0.3. Any of these parameters can be selected and the others derived. For convenience the relative velocity ratio, $W_R = W_{3s}/W_2$, is adopted here, and will be systematically increased from unity to any desired upper limit.

The discharge relative Mach number can be derived through

$$M_3'^2 = W_R^2 M_2'^2 \frac{T_2}{T_{02}} \frac{T_{02}}{T_{03}} \frac{T_{03}}{T_3} \tag{16}$$

where T_{03}/T_3 is given by

$$\frac{T_3}{T_{03}} = 1 - \frac{\gamma - 1}{2} \frac{W_3^2 \cos \beta_3^2}{a_{03}^2}$$

and

$$\frac{W_3}{a_{03}} = W_R \frac{W_2}{a_{01}} \sqrt{\frac{T_{01}}{T_{03}}}$$

The absolute Mach number is then

$$M_3 = M_3' \cos \beta_3 \tag{17}$$

and the discharge velocity triangle is established. The other parameters, degree of reaction and discharge velocity ratio C_{m3}/U_2, can be readily found.

5 Calculation of the Rotor Nondimensional Geometry

Through the specification of the relative velocity ratio, the discharge velocity triangle is fully defined with all velocity vectors nondimensionalized by the stagnation speed of sound a_{03}, or the speed of sound a_3. As the stagnation temperature ratio across the rotor is known through the initial specification of the power ratio, equation (1), the velocity vectors of the discharge velocity triangle can be modified so that they are nondimensionalized by the inlet stagnation speed of sound. The radius ratio of the rotor can then be found through

$$\frac{r_{3s}}{r_2} = \frac{U_3}{a_{01}} \frac{a_{01}}{U_2} \tag{18}$$

For the specific case where the minimum inlet Mach number is used, it can be shown that the rotor radius ratio is given by

$$\left(\frac{r_{3s}}{r_2}\right)^2 = W_R^2 \frac{1 - \cos \beta_2}{1 + \cos \beta_2} \sin^2 \beta_3 \tag{19}$$

The radius ratio is a linear function of the relative velocity ratio for any specified inlet and discharge relative flow angle, provided the minimum inlet Mach number condition is applied (it is not a function of any assumed stage or rotor efficiency). In terms of the discharge velocity ratio, C_{m3}/U_2, the discharge velocity triangle with zero swirl gives

$$\frac{r_{3s}}{r_2} = \frac{C_{m3}}{U_2} \tan \beta_3 \tag{20}$$

The geometric parameter remaining to be calculated relates to the rotor inlet blade height b_2, which can be determined in the nondimensional form b_2/r_2. The area ratio across the rotor can be determined through the application of the continuity condition between rotor inlet and discharge. As the inlet and discharge Mach numbers are known, the nondimensional mass flow at each station, defined as

$$\theta = \frac{\dot{m}}{\rho_0 a_0 A}$$

can be derived through

$$\theta_2 = \cos \alpha_2 M_2 \left[1 + \frac{\gamma - 1}{2} M_2^2\right]^{-\frac{\gamma+1}{2(\gamma-1)}}$$

at the inlet, and at the discharge

$$\theta_3 = M_3 \left[1 + \frac{\gamma - 1}{2} M_3^2\right]^{-\frac{\gamma+1}{2(\gamma-1)}} \tag{21}$$

The rotor area ratio is, therefore, given by

$$\frac{A_3}{A_2} = \frac{\theta_2 \rho_{02} a_{02}}{\theta_3 \rho_{03} a_{03}} = \frac{\theta_2 \rho_{02}}{\theta_3 \rho_{03}} \sqrt{\frac{T_{01}}{T_{03}}} \tag{22}$$

Before equation (22) can be solved for the area ratio, it is necessary to determine the stagnation density ratio across the rotor. This can only be done if the irreversibilities associated with the complete stage and the stator are quantified. This is most easily done by specifying appropriate efficiencies. Through the state equation the density ratio can be rewritten in terms of pressure and temperature ratios to give

$$\frac{\rho_{02}}{\rho_{03}} = \frac{P_{02}}{P_{03}} \frac{T_{03}}{T_{02}} = \frac{P_{02}}{P_{01}} \frac{P_{01}}{P_{03}} \frac{T_{03}}{T_{01}} \tag{23}$$

The pressure ratio P_{01}/P_{03} can be derived through the combination of P_{01}/P_3, given by equation (15), and P_{03}/P_3, which can be derived from the known discharge Mach number. The stagnation pressure ratio across the stator, P_{02}/P_{01}, must be derived through a specification of the stator efficiency. With the efficiency defined as

$$\eta_N = \frac{1 - T_2/T_{01}}{1 - (P_2/P_{01})^{\frac{\gamma-1}{\gamma}}} \tag{24}$$

the pressure ratio P_2/P_{01} can be determined and combined with the pressure ratio P_{02}/P_2, which can be derived from the known inlet Mach number, to yield the desired pressure ratio P_{02}/P_{01}.

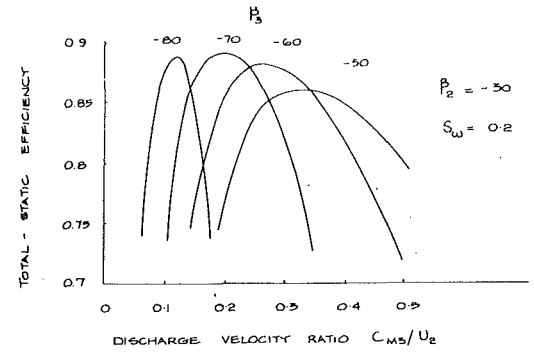

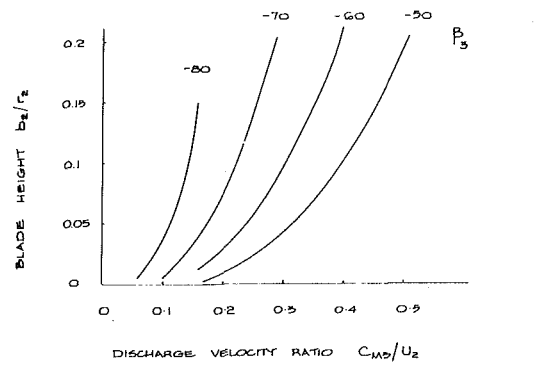

Fig. 10 Efficiency and blade heights

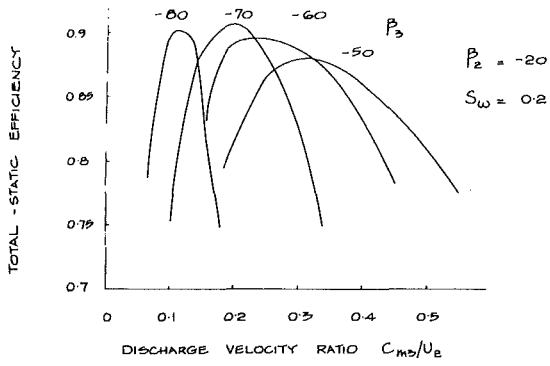

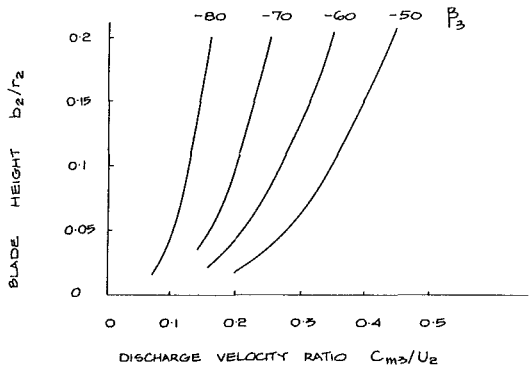

Fig. 11 Efficiency and blade heights

Equation (22) can now be solved for the rotor area ratio, A_3/A_2, and with the additional specification of the exducer hub to shroud radius ratio the nondimensional blade height at inlet can be determined through

$$\frac{b_2}{r_2}=\frac{1}{2}\left(\frac{r_{3s}}{r_2}\right)^2(1-\nu^2)/\frac{A_3}{A_2} \tag{25}$$

The exducer hub-to-shroud radius ratio is specified through consideration of the number of blades that must be accommodated around the hub, and through stress considerations to ensure an adequate diameter, and may have to be refined as the design progresses. The results shown in Figs. 10 and 11 were obtained with a hub shroud radius ratio of 0.4.

6 Design Optimization

An optimum incidence angle of -30 deg was generally adopted to develop alternative designs. For comparative purposes results with an optimum incidence angle of -20 deg are also included. Design selection reduces to the specification of the relative velocity ratio, which will maximize the rotor efficiency. Rohlik (1968) used a relative velocity ratio of 2, based on the mean radius of the exducer. Rodgers and Geiser (1987) showed that peak efficiencies occurred at exit velocity ratios, C_{m3}/U_2, between 0.2 and 0.3. These criteria can be used to select the desired design. If this is not considered suitable the losses associated with the flow process must be calculated in order to identify the peak efficiency point.

The internal loss processes usually identified for the rotor are those due to passage friction and curvature, blade-shroud clearance, blade loading, and exit kinetic energy. Empirical equations for the evaluation of these losses are given by Rohlik (1968), Glassman (1976), and Rodgers (1987). The empirical loss equations adopted followed those given by Rodgers (1987) with the exception that the loss due to passage curvature was arbitrarily modified from

$$\Delta q_k=\left(\frac{\frac{b_2}{r_2}+\frac{b_3}{r_2}}{1-\frac{r_3}{r_2}}\right)\left(\frac{W_2^2+W_3^2}{2a_{01}^2}\right)\left(\frac{a_{01}^2}{U_2^2}\right)$$

to

$$\Delta q_k=0.5\left(\frac{\frac{b_2}{r_2}+\frac{b_3}{r_2}}{1-\left(\frac{r_3}{r_2}\right)^2}\right)\left(\frac{W_2^2+W_3^2}{2a_{01}^2}\right)\left(\frac{a_{01}^2}{U_2^2}\right)$$

This was done as it was found that the original formulation led to low efficiencies at high radius ratios (in excess of 0.8), while turbocharger turbines operate with acceptable efficiencies with radius ratios in excess of 0.8.

The friction loss was given by

$$\Delta q_F=\frac{0.03((W_2/a_{01})^2+(W_3/a_{01})^2)}{4(D_h/L_h)(U_2/a_{01})^2}$$

The blade loading loss by

$$\Delta q_{BL}=\frac{2(C_{\theta 2}/U_2)^2}{Z_B Z/r_2}$$

As this blade loading loss is a function of the inlet velocity triangle only, it does not change as the relative velocity ratio is varied. For the clearance loss

$$\Delta q_{CL}=0.4(\epsilon/b_2)(C_{\theta 2}/U_2)^2$$

and the exit loss was given by

$$\Delta q_{EX}=0.5(C_3/U_2)^2$$

To apply the clearance loss equation the clearance-to-radius ratio was assumed to be 0.008. For the computation of the hydraulic length-to-diameter ratio, required in the friction loss equation, an axial length-to-radius ratio of 0.7 and 15 blades were assumed. The objective here is not to assess or develop suitable empirical loss equations, but to illustrate the design procedure.

As the nondimensional radius and blade height increase with increasing relative velocity ratio both the passage friction

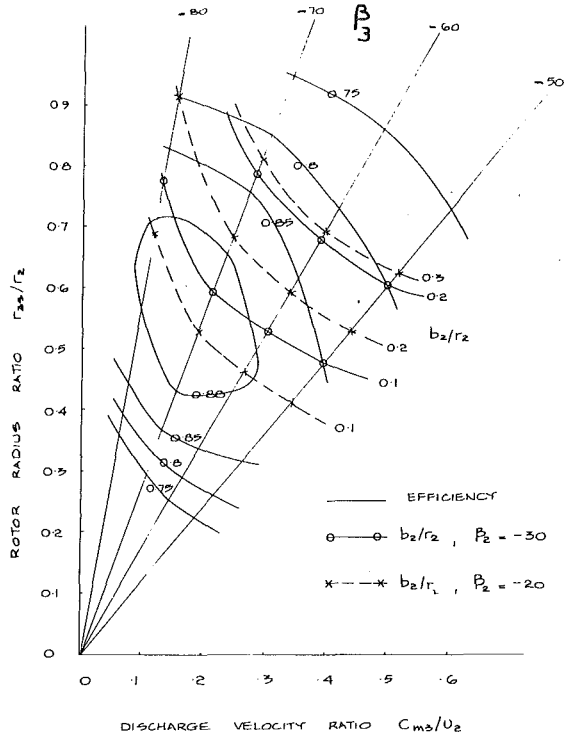

Fig. 12 Rotor efficiency contours

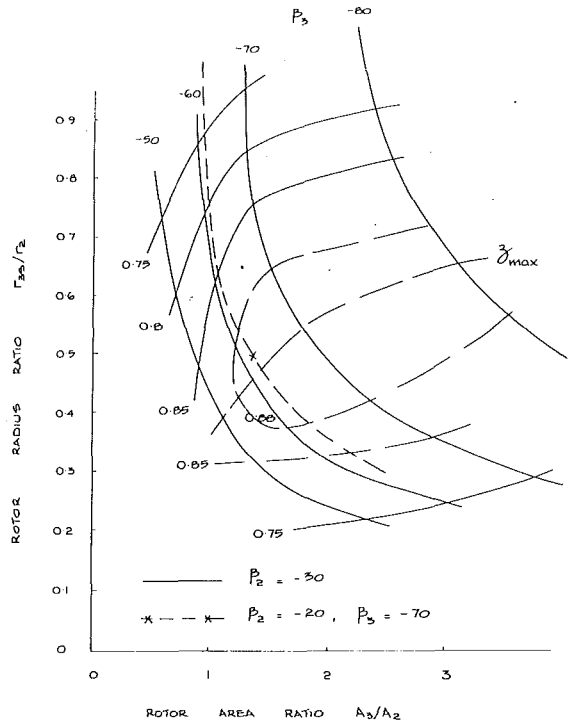

Fig. 13 Efficiency contours as a function of rotor geometry

loss and the clearance loss will decrease. With the assumption that the exhaust kinetic energy is not recovered, or used, the losses that increase with increasing relative velocity ratio are the exit and passage curvature losses. The best efficiency point occurs where the falling friction and clearance losses combine with the exit and curvature losses to yield the minimum loss condition. Application of the empirical loss equations showed that the clearance loss, which falls more rapidly than the passage friction loss, plays the dominant role in locating the best efficiency point.

7 Presentation of Results

All results presented were obtained at the minimum inlet Mach number condition, and while the analysis procedure used the specification of the relative velocity ratio, it was found that the results correlated better with the discharge velocity ratio. Predicted efficiencies are shown in Fig. 10 along with the calculated inlet blade height for an inlet flow angle of -30 deg and a series of discharge flow angles. Comparative results are shown in Fig. 11 for an assumed inlet flow angle of -20 deg. The location of the peak efficiency point was not changed by the assumed inlet flow angle (compare Figs. 10 and 11), but it is clearly a function of the assumed discharge flow angle. The rapid increase in efficiency as C_{m3}/U_2 increases is due to a reduction in the clearance loss as the nondimensional blade height increases; the rate at which the efficiency then falls again is a function of the increasing passage curvature and exit kinetic energy losses relative to the friction and clearance losses, which continue to decrease. The results shown are all for a power ratio S_w of 0.2. The use of magnitudes of 0.1 and 0.3 did not significantly modify the location of the peak efficiency point, while the absolute magnitudes were decreased as S_w increased due to the increasing inlet Mach number. If the turbine installation is such that the exhaust kinetic energy can be recovered in an exhaust diffuser, the exducer blade angle could be of the order of -55 to -50 deg; see Fig. 8. The high exducer blade angles (e.g., -80 deg) could lead to excessive blade blockage at the hub. This would have to be assessed further as the design progressed.

The rotor radius ratio is a linear function of the discharge velocity ratio for any specified discharge flow angle (see equation (20)), and is shown in Fig. 12. The efficiency contours were added from Fig. 10. Also included are contours of nondimensional blade height from Figs. 10 and 11. The main effect of modifying the assumed optimum incidence angle, either by design or due to uncertainties as to the correct magnitude, is to change the calculated nondimensional blade height. The blade heights shown are based on the calculated flow areas required and the geometric area and blade height will be largely due to boundary layer blockage. Clearly Fig. 12 could be replotted with any of the contours as the x axis and C_{m2}/U_2 as a contour. As the inlet blade height is a function of the specified exducer hub-to-shroud radius ratio (here a value of 0.4 has been assumed), the rotor area ratio is used for the x axis in Fig. 13. Contours of discharge flow angle and efficiency are superimposed. The rotor inlet blade height can be calculated from the rotor area ratio through equation (25) with the inclusion of a suitable boundary layer blockage factor. The rotor geometry can be obtained from the nondimensional design with the specification of the gas mass flow rate and inlet stagnation conditions.

8 Conclusions

Through the specification of the power ratio S_w and the optimum angle of incidence on to a radial blade, the minimum absolute Mach number at rotor inlet can be determined. This leads to the rotor inlet velocity triangle and the minimum nondimensional speed for the rotor. Consequently the inlet velocity triangle is no longer a variable during the design optimization process. This not only simplifies the initial design procedure but also enables the results to be concisely presented in the form of contour plots.

The design optimization can be carried out nondimensionally without the need to specify the gas mass flow rate.

The empirical loss equations used showed that the magnitude of the discharge velocity ratio at which the peak efficiency occurred was a strong function of the discharge flow angle, but only a weak function of the assumed optimum angle of incidence.

When inlet Mach numbers in excess of the minimum were specified reduced efficiencies and nondimensional inlet blade heights followed, and no justification for modifying the inlet Mach number could be found.

With the computation of the nondimensional design of the turbine rotor all nondimensional performance parameters can be determined and used in the design assessment. For example, the specific speed, specific diameter, nondimensional mass flow, nondimensional power coefficient, nondimensional torque coefficient, and isentropic expansion ratio can be determined.

References

Coppage, J. E., Dallenbach, F., et al., 1956, "Study of Supersonic Radial Compressors for Refrigeration and Pressurization Systems," WADC Tech Rept 55-257.

Glassman, A. J., 1976, "Computer Program for Design Analysis of Radial Inflow Turbines," NASA TN D-8164.

Jamieson, A. W., 1955, "The Radial Turbine," in: *Gas Turbine Principles and Practice*, Newnes, United Kingdom.

Rodgers, C., 1987, "Small High Pressure Ratio Radial Turbine Technology," VKI Lecture series 1987-07.

Rodgers, C., and Geiser, R., 1987, "Performance of a High-Efficiency Radial/Axial Turbine," ASME JOURNAL OF TURBOMACHINERY, Vol. 109, p. 151.

Rohlik, H. E., 1967, "Analytical Determination of Radial Inflow Turbine Design Geometry for Maximum Efficiency," NASA TN D-4384.

Rohlik, H. E., 1975, "Radial Inflow Turbines," NASA SP 290, Vol. 3.

Stanitz, J. D., 1952, "Some Theoretical Aerodynamic Investigations of Impellers in Radial and Mixed Flow Centrifugal Compressors," *Trans. ASME*, Vol. 74, p. 473.

Stanitz, J. D., 1953, "Design Considerations for Mixed Flow Compressors With High Flow Rates per Unit Frontal Area," NACA RM E53A15.

Sugimoto, A., Nakamura, K., and Matsumoto, K., 1975, "An Experimental Investigation of Flow in Blade Passages of Radial Inflow Turbine," *Bull. JSME*, Vol. 18(126), p. 1432.

Whitfield, A., and Baines, N. C. B., 1989, *The Design of Radial Turbomachines*, in press.

Woolley, N. H., and Hatton, A. P., 1973, "Viscous Flow in Radial Turbomachine Blade Passages," *IMechE Conference publication* 1973-3, p. 175.

H. Hayami
Professor,
Institute of Advanced Material Study,
Kyushu University 86,
Kasuga 816, Japan
Mem. ASME

Y. Senoo
Director,
Miura Company, Ltd.,
Matsuyama 799-26, Japan
Fellow ASME

Y. I. Hyun
Graduate Student,
Interdisciplinary Graduate School of
Engineering Sciences,
Kyushu University 39,
Kasuga 816, Japan

M. Yamaguchi
Research Associate,
Institute of Advanced Material Study,
Kyushu University 86,
Kasuga 816, Japan

Effects of Tip Clearance of Nozzle Vanes on Performance of Radial Turbine Rotor

In radial turbines with variable nozzles, the flow downstream of the nozzles could be distorted by the leakage flow through the tip clearance of the upstream nozzle vanes. To investigate the effects of flow distortion on the performance of turbine rotors, two rotors with different numbers of blades were tested for three types of distorted velocity distribution at the rotor inlet. In the case of the 20-blade rotor with moderate blade loading, the flow distortion at the rotor inlet had a negligible effect on the rotor characteristics, and the measured data on the turbine performances agreed well with prediction. Predictions were made with a conventional one-dimensional flow model applied to the rotor flow, while a two-layer flow model was applied to the flow in the nozzle with clearance. In the case of the 10-blade rotor with heavy blade loading, however, the rotor performance was found to be sensitive to the inlet flow distortion and was considerably lower than the prediction.

Introduction

If a variable nozzle system is adopted for the turbine of a turbocharger (Satoh et al., 1983; Hirabayashi et al., 1986) or the turbine of a gas turbine engine, the part-load performance can be improved over a wide range of flow rates (Watson, 1980). In cases where the nozzle vanes are pivoted, however, there are clearances between the casing and both edges of the nozzle vanes, and the performance of the turbine may be considerably deteriorated by the leakage flow through nozzle clearances (Berenyi and Raffa, 1979; Penny, 1963; Benstein and Wood, 1963).

In the preceding reports (Hayami et al., 1987; Senoo et al., 1987; Hyun et al., 1988), the present authors carried out a series of experiments on nozzles with various values of tip clearance at various nozzle angles. They observed a reduction in the blade loading near the vane tip due to the leakage flow through clearance. The reduction rate was correlated with a conventional contraction coefficient of the leakage flow. Furthermore, they have proposed a method to predict the nozzle performance using a simple theory based on a two-layer flow model, where the span of the nozzle passage including the clearance was divided into two layers. The experimental data were compared with the prediction. Good agreement was demonstrated for the mean exit-flow angle and the pressure loss of the nozzle.

Contributed by the International Gas Turbine Institute and presented at the 34th International Gas Turbine and Aeroengine Congress and Exhibition, Toronto, Ontario, Canada, June 4-8, 1989. Manuscript received at ASME Headquarters January 17, 1989. Paper No. 89-GT-82.

In automobile turbocharger applications, the number of turbine rotor blades is often less than that proposed by a conventional design method to reduce the moment of inertia of the rotor. In the present experiment, two rotors with different number of blades were tested, to investigate the effects of the leakage flow through the nozzle tip clearance on the performance of the rotors. The test results were compared with prediction, and it became clear that the distorted velocity distribution at the rotor inlet, due to the clearance of nozzle vanes, deteriorated the performance of the rotor in the case of heavily loaded blades.

Apparatus and Experimental Methods

The experimental apparatus is shown in Fig. 1. To secure axisymmetry a scroll was avoided, and air was sucked from the atmosphere through 18 fixed preswirl guide vanes so that the nozzle-inlet swirl (38.2 deg from the tangent) was typical of that at the exit of a scroll in a conventional radial turbine. Air flowed through the adjustable nozzle into the rotor and was sucked out into a straight pipe with a standard orifice flow meter, and subsequently discharged to the atmosphere through a blower.

The diameter of the test rotor was 210 mm, the exducer diameter was 148 mm, the inlet width was 18.6 mm, and the height of exducer was 44 mm. The direction of blades was radial at the inlet of the rotor. The original number of blades of the rotor was 20. After a series of experiments it was re-

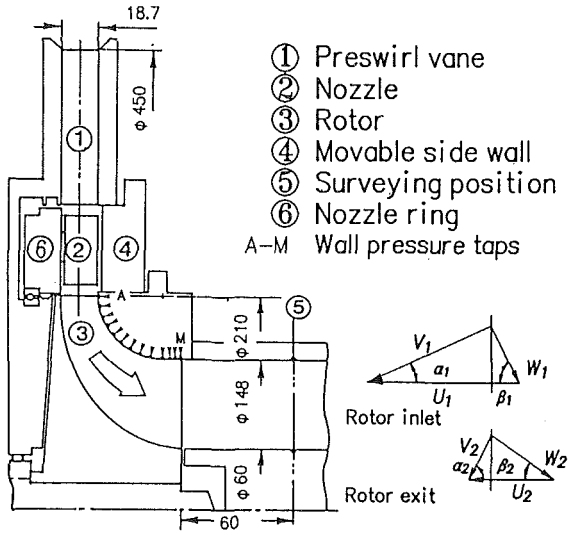

Fig. 1 Experimental apparatus and velocity triangles

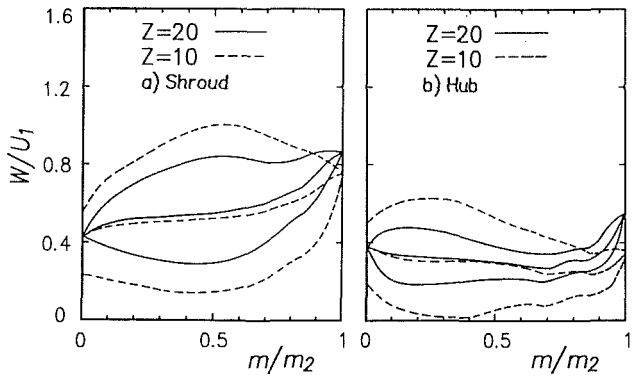

Fig. 2 Rotor blade loadings at design condition

duced to 10, and a similar series of experiments was repeated. The specific speed was 31 [m, m^3/min, rpm] or 0.587, which was in the range of preferred design condition suggested by Rohlik (1968). The predicted blade loadings at design condition are presented in Fig. 2 for the two rotors. The blade loadings were estimated using a quasi-three-dimensional method based on the potential theory, originally developed by Senoo and Nakase (1971, 1972) for impellers of centrifugal compressors and modified for turbine rotors.

Nozzle vanes with a pivot mechanism usually have clearances on both edges of vanes. In the present experiment, however, the turbine nozzle had clearance on only one end of the nozzle vanes. Three types of nozzle settings were tested, without clearance N, with clearance on the hub side H, and clearance on the shroud side S. In cases of H and S, the annular plate ④ was moved axially to make clearance so there was a recess along the shroud at the nozzles.

The total pressure loss and flow angle distributions at the

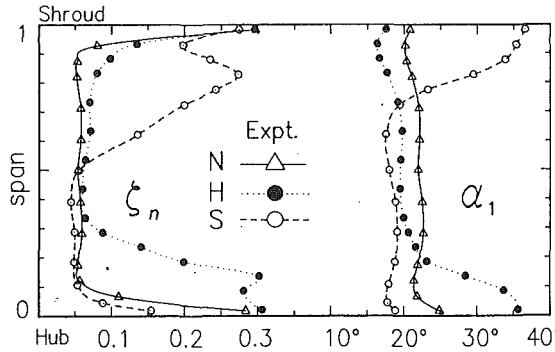

Fig. 3 Flow distortion at rotor inlet induced by three types of nozzle tip clearance

Table 1 Three types of test nozzle and their characteristics

	Nozzle geometry				Flow condition	
Nozzle Type	Nozzle Clearance	Stem	c/b	Nozzle Angle	Flow Angle	Loss Coefficient
N	No		0	23.3 deg	21.9 deg	0.064
H	Hub-side	Yes	0.081	20.6 deg	21.5 deg	0.125
S	Shroud-side	No	0.046	20.6 deg	21.8 deg	0.169

nozzle exit are presented in Fig. 3. They were measured using a cobra probe after removing the rotor. The presented results represent the mass-weighted average values over one pitch of the nozzle vanes. The nozzle angle, the clearance ratio, the mean rotor inlet flow angle, and the nozzle loss coefficient are listed in Table 1. The nozzle angle is defined by the throat opening o and the nozzle pitch t as $\sin^{-1}(o/t)$. The nozzle angle was adjusted depending on the clearance ratio of nozzle so that the mass-averaged mean flow angle at the rotor inlet was about 22 deg in all cases. There was a nozzle stem in the hub-side clearance, and hence a larger clearance ratio was needed for the H-type nozzle compared to the S-type nozzle in order to materialize the identical mass-averaged flow angle at the rotor inlet while keeping the nozzle angle identical. In those cases, the pressure loss coefficient was much larger for the S-type nozzle than for the H-type nozzle as indicated in Table 1.

For a given flow rate, the swirl at the rotor inlet was evaluated using the measured moment acting on the turbine rotor and the rotor exit swirl, and was found to be identical in the two rotors. The variation in the mean flow angle was within ± 0.5 deg. Therefore, it was assumed in the analysis that the flow characteristics of the nozzle were not influenced by the rotors. In the present experiments, the rotor speed was varied between 4000 and 7000 rpm in each of the three clearance types, N, H, and S, keeping the mass flow rate constant at 0.335 ± 0.005 kg/s. In addition to measuring conventional turbine performance characteristics, the wall static pressure was measured at 13 points along the shroud, and the velocity distributions were measured with a cobra probe at a section 60 mm downstream of the exducer trailing edges.

Nomenclature

b = span of nozzle vane
c = clearance
C_o = spouting velocity
m = meridional length along shroud or hub
U = peripheral rotor speed
V = absolute velocity
W = relative velocity
Z = number of rotor blades
α = absolute flow angle from the tangent
β = relative flow angle from the tangent
δ = deviation angle
ζ_n = total-pressure-loss coefficient of nozzle
η_r = total-to-static rotor efficiency
η_s = total-to-static stage efficiency
τ = torque coefficient
ϕ = flow coefficient

Subscripts

1 = rotor inlet
2 = rotor exit
b = rotor blade
m = meridional
u = tangential

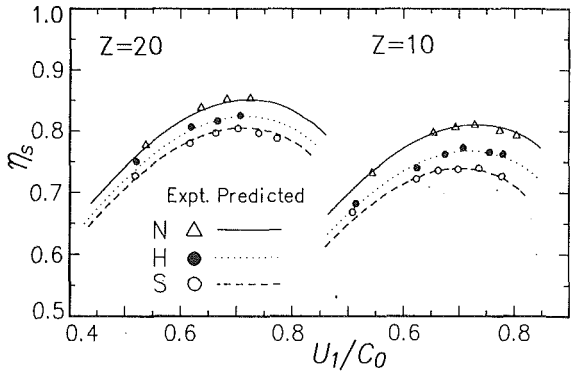

Fig. 4 Change of stage efficiency due to nozzle clearance type

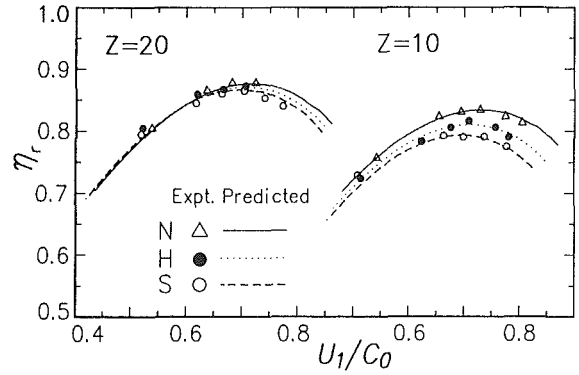

Fig. 5 Change of rotor efficiency due to nozzle clearance type

Results and Discussions

Stage Efficiency and Rotor Efficiency. The measured stage efficiencies $\eta_s = \Gamma\omega/(GH_s)$ are plotted against the turbine velocity ratio U_1/C_o in Fig. 4 for the three clearance types. C_o denotes the spouting velocity defined as $\sqrt{2H_s}$, ω is the shaft angular speed, G is the mass flow, and H_s is the isentropic total-to-static enthalpy drop across the turbine stage. The measured shaft torque Γ includes the bearing friction torque, which is approximately 3.5 percent of the shaft torque at peak efficiency. The relative uncertainty of stage efficiency was estimated at about 1.3 percent.

In all three clearance types, the efficiency was maximum at $U_1/C_o \fallingdotseq 0.7$, where the inflow condition to the rotor blades was nearly shockless. The efficiency decreased with the nozzle clearance at all turbine velocity ratios. The efficiency drop was larger in the case of the shroud clearance compared to that of the hub clearance. The efficiency drop due to the tip clearance was magnified considerably when the number of rotor blades was 10. A similar effect regarding the number of rotor blades has been reported by Rodgers and Geiser (1987).

The nozzle loss, which was not identical for the three types of nozzle clearance (Table 1), is included in the stage efficiency η_s. To discuss the effect of the distorted velocity distribution due to different clearance types on the rotor performance, the total-to-static rotor efficiencies $\eta_r = \Gamma\omega/(GH_r)$ were evaluated excluding the nozzle loss and are presented in Fig. 5. H_r is the isentropic total-to-static enthalpy drop across the rotor.

The rotor performance was predicted using a conventional one-dimensional method (Wasserbauer and Glassman, 1975). The predictions included four kinds of energy loss in the rotor, namely, the shock loss (Rodgers, 1966), the internal loss, the disk friction loss, and the discharge loss. Concerning the discharge loss, it was assumed that flow angle at the rotor exit was determined by the throat opening and the blade pitch at the root-mean-square diameter. The rotor internal loss was assumed to be proportional to the mean value of the kinetic energies based on the relative velocities at the inlet and the exit of the rotor. The proportionality constant was adjusted for the respective rotors and clearance types and was assumed not to change over the whole range of rotational speeds. The values of the rotor internal loss coefficient so determined are given in Table 2. There was little variation in the rotor loss coefficients with clearance type for the rotor with 20 blades, but there were large changes for the rotor with 10 blades. The internal loss of the 10-blade rotor behind the *H*-type nozzle and that behind the *S*-type nozzle were 1.3 and 1.6 times that behind the *N*-type nozzle, which was much larger than the internal loss of the 20-blade rotor. The predicted stage and rotor efficiencies are also presented in Figs. 4 and 5. The agreement of the prediction with the experimental data is fair over the whole operating range. Although the rotor performance deterioration was largest for the *S*-type clearance, the loss coefficient of the nozzle and the distortion were also largest for the *S*-type clearance in the present series of experiments, as shown in Table 1. Therefore, it should not be concluded that the shroud clearance has larger effects on the rotor performance than the hub clearance.

Table 2 Comparison of rotor internal loss coefficients

	Z= 10	Z= 20
N	0.870	0.535
H	1.150	0.585
S	1.360	0.625

Takamura and Itoh (1987) correlated the maximum efficiency of turbine rotors with the diffusion ratio. The latter is defined as the ratio of the maximum value of local velocity to the exit velocity along the shroud suction surface of the rotor blade. They recommended a maximum allowable limit of 1.44 based on a quasi-three-dimensional flow analysis. In the present rotors, the diffusion ratio was about 1 for $Z = 20$ and 1.4 for $Z = 10$ according to Fig. 2. Both values are within the proposed allowable range, but present results suggest that the limit should be reduced in the case of distorted velocity distribution at the rotor inlet. Rohlik (1968) proposed 15 as the minimum number of rotor blades. As a whole, the blade loading for the 10-blade rotor is believed to be too high to achieve a good performance when the nozzle vanes have clearances.

Velocity Distribution at Rotor Exit. The hub-to-tip distributions of the meridional velocity component V_{m2} and of the tangential component of the absolute velocity V_{u2} at the rotor exit are presented in Figs. 6 and 7 for two rotational speeds. U_1 denotes the peripheral rotor speed. The flow rate, estimated by integrating the V_{m2} distribution, differed less than 5 percent from the orifice flow rate.

The value of V_{m2} was much larger near the hub than it was near the tip and the profiles of the V_{m2} distribution were almost similar to each other regardless of the number of rotor blades and nozzle clearance type. In the case of the 10-blade rotor only small changes in the velocity distributions at the rotor exit were measured, although the internal loss of the 10-blade rotor was increased by the nozzle clearance considerably.

The swirl at the rotor exit was somewhat stronger near the tip than near the hub. This trend was also observed in the literature (Kofskey and Wasserbauer, 1969; Matsuo et al., 1987), where the flow near the tip seemed to be much underturned. The intensity of the swirl near the tip was magnified for the 10-blade rotor. This may be attributed to accumulation of boundary layer near the tip and to the secondary flow in the

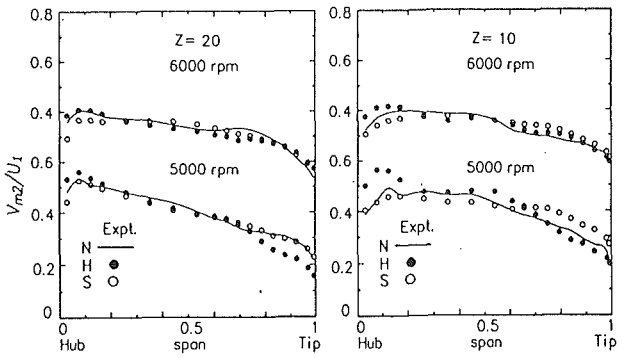

Fig. 6 Meridional component of velocity at rotor exit

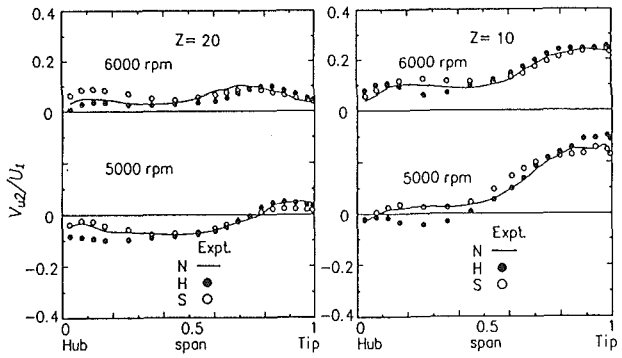

Fig. 7 Tangential component of absolute velocity at rotor exit

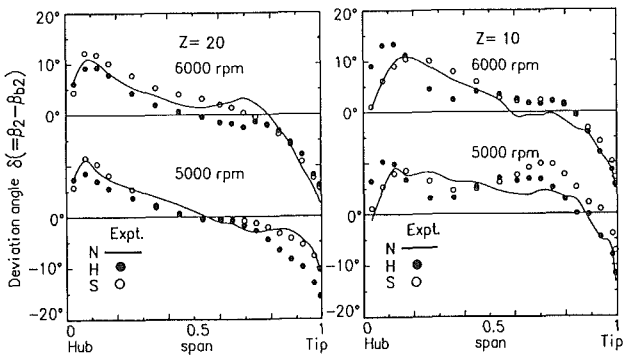

Fig. 8 Hub-to-tip distribution of deviation angle

flow passage of the rotor, which were larger for $Z=10$ than those for $Z=20$. However, the discharge loss due to the swirl was relatively small.

The deviation angle δ represents the difference between the relative flow angle β_2 at the rotor exit and the exit blade angle β_{b2}. The exit blade angle β_{b2} is defined as $\sin^{-1}(o/t)$, where o and t are the throat opening and the blade pitch. The hub-to-tip distribution of the deviation angle δ is plotted in Fig. 8, where the uncertainty of δ was increased by the variation in the absolute velocity. It is evident that the effect of the inlet flow distortion on the distribution of the deviation angle was negligible. Furthermore, the effect of the number of rotor blades on the distribution of the deviation angle was also negligible, although it was somewhat more scattered for $Z=10$ than it was for $Z=20$. The value of δ decreased from hub to tip almost monotonously and it was negative near the tip, i.e., the flow seemed to be overturned near the tip. This trend is not contradictory to the previous discussion for V_{u2} distribution but it is contrary to the literature (Mizumachi et al., 1975). Two reasons are conceivable. One is that the exducer of the test rotor is relatively lightly loaded and long. The other is that

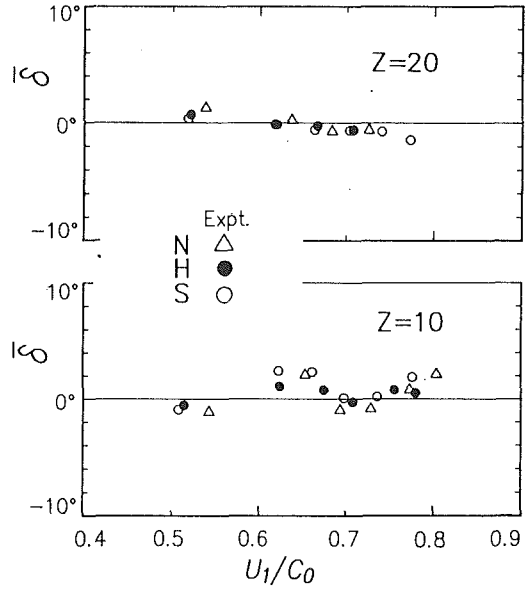

Fig. 9 Relationship between mean deviation angle and turbine velocity ratio

the swirl at the rotor exit was stronger and the axial velocity in the rotor was larger than what were measured at the downstream station, due to the wall friction, the mixing and the blockage effects of blades. Both the stronger swirl and the larger axial velocity at the rotor exit mean a larger relative flow angle β_2 and a larger deviation angle δ than were measured at the downstream station.

The mean deviation angle $\bar{\delta}$ is plotted against the turbine velocity ratio in Fig. 9, where $\bar{\delta}$ was evaluated using the mass flow rate, the mass-averaged value of the moment of momentum of the exit flow, and the exit blade angle at the root-mean-square (rms) diameter of the exducer. The values of β_{b2} at the rms diameter were 33.5 deg for the 20-blade rotor and 38.7 deg for the 10-blade rotor, respectively. The blade exit angle along the camber-line was 28 deg in both rotors. $\bar{\delta}$ was nearly zero and the data points were almost on a straight line with a slight negative gradient in the case of the 20-blade rotor. The data for $Z=10$, on the other hand, were somewhat scattered although $\bar{\delta}$ was still nearly zero. Generally, the rotor inlet flow distortion was not found to affect the flow at the rotor exit significantly, although it strongly influenced the rotor internal loss.

Acceleration Along the Shroud. The performance of a turbine rotor is deteriorated by deceleration of the relative velocity in the rotor. The pressure distribution along the shroud is obviously important in this respect, but it includes the pressure drop due to the centrifugal effect. The relative velocity was calculated using the measured wall pressure assuming isentropic flow. The relative velocity W calculated in this manner for the conditions $N=6000$ rpm is plotted in Fig. 10.

In the case of $Z=20$, the flow along the shroud was hardly changed by the flow distortion at the rotor inlet, and was smoothly accelerated, except just near the inlet portion at $m/m_2<0.2$. On the other hand, in the case of $Z=10$, the inlet flow distortion affected the flow at the inlet portion in particular, and the exit/inlet velocity ratio was increased with the inlet distortion. The difference may be attributed to either the development of boundary layer or the pressure loss in the rotor. However, the flow at $m/m_2>0.3$ was smoothly accelerated in all cases.

Prediction of Turbine Performance and Comparison With Experimental Data. For the stage performance prediction, the turbine stage was divided into two parts: one was the noz-

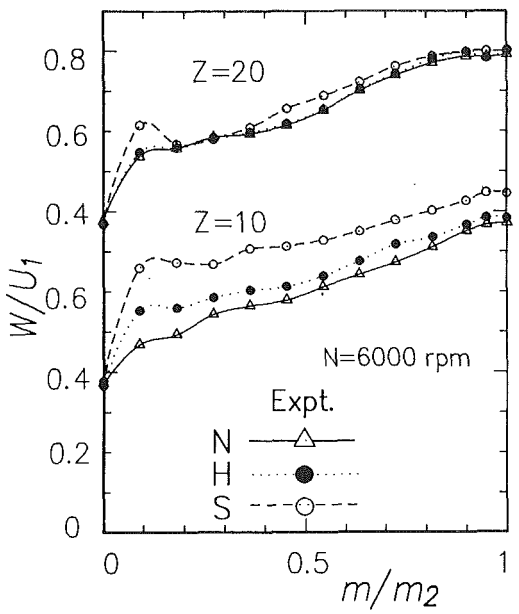

Fig. 10 Distribution of relative velocity along shroud

The nozzle performance was analyzed using the method proposed by the authors (Senoo et al., 1987; Hyun et al., 1988), in which two layers of flow, one through the nozzle and the other through the effective clearance, mixed together at the nozzle exit to uniform conditions at the rotor inlet. The rotor performance, on the other hand, was analyzed by the conventional one-dimensional method described previously.

Another series of experiments using the 20-blade rotor was conducted, in which the shroud clearance of the nozzle was varied up to $c/b=0.1$, keeping the nozzle angle at 19.2 deg and a constant flow rate of 0.346 kg/s. The stage efficiency η_s, the torque coefficient τ, and the flow coefficient ϕ are presented in Fig. 11 corresponding to the five values of clearance ratio. In all the predictions, the internal loss coefficient of the rotor was kept constant, which was decided at the best efficiency condition without clearance. It is evident that the prediction agreed fairly well even at off-design operating points for any nozzle clearance ratios except the case $c/b=0.099$. The efficiency was significantly decreased by increasing c/b, but its maximum was always observed at about $U_1/C_o \fallingdotseq 0.7$ regardless of the clearance ratio.

The torque coefficient in Fig. 11(b) was defined as $\tau=(U_1V_{u1}-U_2V_{u2})/2U_1C_o$. The agreement of the prediction with the experimental data was fair. The tip clearance decreased the torque coefficient considerably and uniformly regardless of the rotor speed. As a result, the relative decrement of torque coefficient was more significant at a larger rotational speed.

Regarding Fig. 11(c), the tip clearance of nozzle vanes increased the flow coefficient ϕ $(=G/\rho\pi D_t^2 C_o)$. Therefore, a large tip clearance changes the design flow rate of a turbine considerably. The predicted values are somewhat smaller than the experimental data at all conditions. A little modification of the assumed throat area in the prediction may be in order.

Conclusions

Two turbine rotors with 10 blades and 20 blades were tested for three kinds of inlet velocity distribution distorted by the nozzle clearance. The effects of flow distortion on the rotor performance were investigated experimentally and theoretically. A conventional one-dimensional prediction method was applied for the rotor performance, and an analysis based on a two-layer flow model was applied for the nozzle with tip clearance. In the case of a 20-blade rotor with a moderate

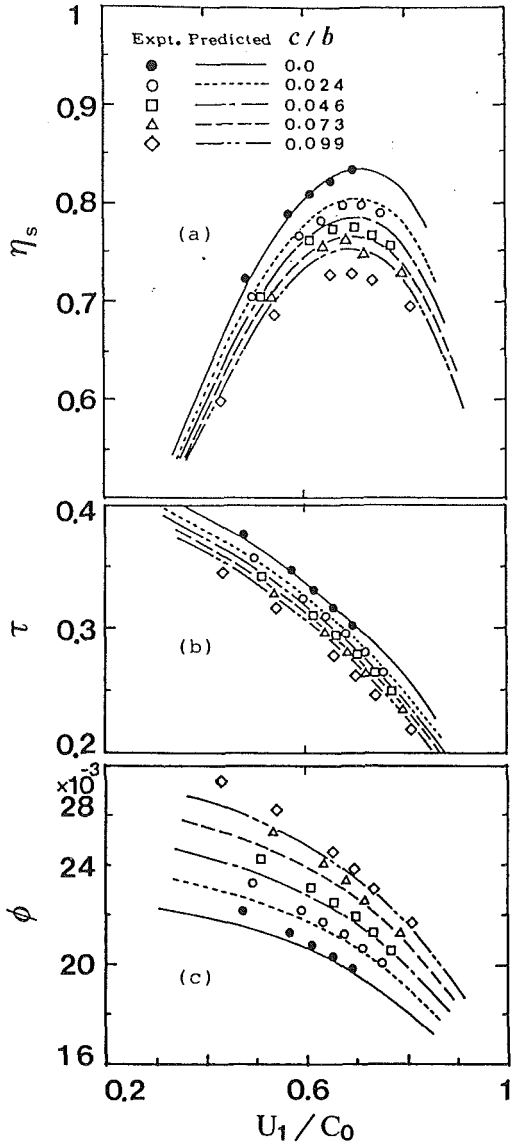

Fig. 11 Comparison of predicted turbine characteristics with different clearance ratios with experimental data, $Z=20$, $G=0.346$ kg/s, nozzle angle 19.2 deg

blade loading, the predicted stage performance, such as the efficiency, the torque coefficient, and the flow coefficient, agreed well with the experimental data, indicating the distortion of inlet flow hardly affected the rotor performance. In the case of the 10-blade rotor with a heavy blade loading, however, the nozzle clearance caused the rotor performance to deteriorate much more than the predictions. It appeared therefore that distortion of the velocity distribution at the rotor inlet had a significant influence on the performance of the 10 blade rotor. As a whole, the turbine performances can be predicted well even when tip clearance of nozzle vanes exists, provided that the blade loading of the rotor is moderate.

References

Benstein, E. H., and Wood, H. J., 1963, "Applications and Performance Levels of Radial Inflow Turbines," SAE Paper No. 653D.

Berenyi, S. G., and Raffa, C. J., 1979, "Variable Area Turbocharger for High Output Diesel Engines," SAE Paper No. 790064.

Hayami, H., Hyun, Y. I., Senoo, Y., and Yamaguchi, M., 1987, "Flow Fields Behind a Variable-Area Nozzle for Radial Turbines," *The Reports of the Research Institute of Industrial Science* (in Japanese), Kyushu University, No. 82, pp. 149-158.

Hirabayashi, Y., Sumi, Y., Nishiguchi, F., 1986, "Development of Nissan Variable Geometry JET Turbo-charger," SAE Paper No. 860105.

Hyun, Y. I., Senoo, Y., Yamaguchi, M., and Hayami, H., 1988, "The Influences of Tip-Clearance on the Performance of Nozzle Blades of Radial Turbines (2nd Report, Experiment and Performance-Prediction at Three Nozzle Angles)," *JSME International Journal*, Vol. 31, No. 2, pp. 258–262.

Kofskey, M. G., and Wasserbauer, C. A., 1969, "Experimental Evaluation of a 3.50-inch Radial Turbine Designed for a 10-kilowatt Space Power System," NASA TN D-5550.

Matsuo, E., Imakiire, K., and Matsudaira, N., 1987, "Development of High Performance Radial Turbine Blades," GTSJ Paper No. 87-TOKYO-IGTC-106.

Mizumachi, N., Endo, T., and Kitano, M., 1975, "Study on Outlet Flow Angle and Velocity Coefficient of Radial Inflow Turbine Rotor," *Trans Jpn. Soc. Mech. Eng.* (in Japanese), Vol. 41, No. 345, pp. 1471–1478.

Penny, N., 1963, "Rover Case History of Small Gas Turbines," SAE Paper No. 634A.

Rodgers, C., 1966, "Efficiency and Performance Characteristics of Radial Turbines," SAE Paper No. 660754.

Rodgers, C., and Geiser, R., 1987, "Performance of a High-Efficiency Radial/Axial Turbine," ASME JOURNAL OF TURBOMACHINERY, Vol. 109, pp. 151–154.

Rohlik, H. E., 1968, "Analytical Determination of Radial Inflow Turbine Design Geometry for Maximum Efficiency," NASA TN D-4384.

Satoh, T., Miyauchi, J., Nakasawa, N., and Matsuo, E., 1983, "Development of a Variable Geometry Turbocharger for Trucks and Buses," GTSJ Paper No. 83-TOKYO-IGTC-77.

Senoo, Y., and Nakase, Y., 1971, "A Blade Theory of an Impeller With an Arbitrary Surface of Revolution," ASME *Journal of Engineering for Power*, Vol. 93, No. 4, pp. 454–460.

Senoo, Y., and Nakase, Y., 1972, "An Analysis of Flow Through a Mixed Flow Impeller," ASME *Journal of Engineering for Power*, Vol. 94, No. 1, pp. 43–50.

Senoo, Y., Yamaguchi, M., Hyun, Y. I., and Hayami, H., 1987, "The Influences of Tip-Clearance on the Performance of Nozzle Blades of Radial Turbines," *JSME International Journal*, Vol. 30, No. 263, pp. 929–935.

Takamura, T., and Itoh, T., 1987, "A Consideration of Blade Loading Criteria for Radial Inflow Turbine Blades," GTSJ Paper No. 87-TOKYO-IGTC-5.

Wasserbauer, C. A., and Glassman, A. T., 1975, "Fortran Programming for Predicting Off-Design Performance of Radial Inflow Turbine," NASA TN D-8063.

Watson, N., 1980, "Turbochargers for the 1980's—Current Trends and Future Prospects," SAE Paper No. 790063.

Effect of Inlet Flow Angle on the Erosion of Radial Turbine Guide Vanes

H. Eroglu

W. Tabakoff

Department od Aerospace Engineering and Engineering Mechanics, University of Cincinnati, Cincinnati, OH 45221

The results of an investigation of the particle dynamics and the blade erosion at the impact locations in radial turbine guide vanes are presented. Attention is focused in particular on the effect of inlet flow angle on the erosion of the blades, since the flow entering the guide vanes usually has an incidence angle due to the upstream scroll geometry. The total erosion per blade is calculated as a function of inlet flow angle for three different particle diameters, which are 5, 15, and 60 μm, respectively. According to the results of this investigation, for each particle size there is an inlet flow angle for minimum erosion of the guide vanes. This fact has to be accounted for in the design of radial turbines operating in particulate flow environments.

Introduction

In many applications, radial inflow turbines have to operate in a particulated environment, where they may be exposed to atmospheric particles or byproducts due to the combustion of advanced fuels. They may also be exposed to coal ash particles when pulverized coal is used as fuel in industrial applications and power generation. It is usually difficult to separate the particles with diameters less than 15 μm from air using cyclones or other particle separation techniques. These suspended solid particles in the air enter the turbine and cause serious erosion damage in various components. Much higher erosion rates are observed in radial inflow turbines than in axial machines due to higher particle concentrations impacting smaller metal areas. Montgomery and Clark (1962) report that even particles smaller than 5 μm can cause serious loss over the radial turbine engine operating lifetime.

There is a growing interest in the accurate determination of erosive effects in radial turbines because of their stronger effect on the engine operating lifetime. Particle dynamics and their erosive effects in radial inflow turbines were studied by Clevenger and Tabakoff (1974), Tabakoff et al. (1987), and Tabakoff and Hamed (1988). Clevenger and Tabakoff (1974) report the results of particle trajectory calculations in the scroll, guide vanes, free vortex region, and the rotor of the radial inflow turbine. They present similarity parameters to relate the particle trajectories in equivalent gas flow fields for different particle material density and size combinations. These parameters are used to investigate the particle trajectories for several particle characteristics from one set of computed trajectories. Experimental results are also presented and illustrate the particle motion phenomena in the nozzle and the free vortex region. Tabakoff et al. (1987) present the results of an analytical study of particle dynamics in a radial turbine rotor and of the experimental measurements of metal erosion in a high-temperature erosion wind tunnel. The analytical investigation reveals the internal surfaces subjected to erosion while the experimental measurements provide data for erosion prediction. Tabakoff and Hamed (1988) report the results of an analytical investigation of blade erosion in addition to the study of particle dynamics in a radial turbine rotor. The results are presented at cold and hot inlet flow conditions in order to determine the effect of temperature.

This paper presents the results of an investigation of particle dynamics and resulting blade erosion in the guide vanes of a radial inflow turbine. In particular, the effect of inlet flow angle on the erosion of guide vanes is studied, since the flow enters the guide vanes usually with an incidence angle due to the upstream scroll geometry or because of the off-design operation. The computations are performed at the particle sizes 5, 15, and 60 μm. The results of these computations show that the effect of flow incidence on the particle dynamics and blade erosion displays a different character at each particle size. The details of the results for the 5-μm particle size are reported in this paper, because such small particles are the most difficult to separate from the air entering the turbine.

Particle Dynamics

In the particle trajectory computations, only the aerodynamic forces are considered, while the electrostatic forces are neglected. The general forms of the equations of motion for the particles suspended in air are written in cylindrical coordinates. These equations are

$$\frac{\partial^2 r}{\partial t^2} - r\left(\frac{\partial \phi}{\partial t}\right)^2 = \frac{1}{2}\frac{\rho W^2 A C_D}{m}\frac{W_r}{|\bar{W}|} - g\cos(\phi+\sigma) \quad (1)$$

$$r\frac{\partial^2 \phi}{\partial t^2} + 2\frac{\partial t}{\partial t}\frac{\partial \phi}{\partial t} = \frac{1}{2}\frac{\rho W^2 A C_D}{m}\frac{W_\phi}{|\bar{W}|} + g\sin(\phi+\sigma) \quad (2)$$

$$\frac{\partial^2 z}{\partial t^2} = \frac{1}{2}\frac{\rho W^2 A C_D}{m}\frac{W_z}{|\bar{W}|} \quad (3)$$

Contributed by the International Gas Turbine Institute and presented at the 34th International Gas Turbine and Aeroengine Congress and Exhibition, Toronto, Ontario, Canada, June 4–8, 1989. Manuscript received at ASME Headquarters February 1, 1989. Paper No. 89-GT-208.

where r, ϕ, and z are the radial, circumferential, and axial coordinates, respectively while m, A, and ρ are the particle mass, cross-sectional area, and density. t is time, g is gravity, and σ is the angular position of the reference axis where $\phi = 0$ in the vertical direction.

The first term on the right-hand side of equations (1), (2), and (3) represent the drag force on the particles and is a function of the relative velocity W between the gas and the particles. The components of this relative velocity are

$$W_r = U_r - \frac{\partial r}{\partial t}$$

$$W_\phi = U_\phi - r\frac{\partial \phi}{\partial t}$$

$$W_z = U_z - \frac{\partial z}{\partial t} \tag{4}$$

where U_r, U_ϕ, and U_z are the radial, circumferential, and axial components of the gas velocity, and $\partial r/\partial t$, $r\partial\phi/\partial t$, and $\partial z/\partial t$ are the radial, circumferential, and axial components of the particle velocity. The value of the drag coefficient C_D in equations (1)–(3) can be written in algebraic form as follows:

$$C_D = 5.4 + \frac{24}{\mathrm{Re}} \qquad \mathrm{Re} < 1.0 \tag{5}$$

$$C_D = 28.5 - 24.0(\log \mathrm{Re}) + 9.0682(\log \mathrm{Re})^2 - 1.7713(\log \mathrm{Re})^3 + 0.1718(\log \mathrm{Re})^4 - 0.0065(\log \mathrm{Re})^5 \quad 1.0 < \mathrm{Re} < 3000.0 \tag{6}$$

$$C_D = 0.4 \qquad 00.0 < \mathrm{Re} < 2.5 \times 10^5 \tag{7}$$

The Reynolds number (Re) is defined as

$$\mathrm{Re} = \frac{\rho_g |W| D_p}{\mu_g} \tag{8}$$

The formulae of equations (5)–(7) are based on experimental data and are contained in various textbooks.

The particle trajectories are determined from the numerical integration of equations (1)–(3) for the particles in the flow field (Grant and Tabakoff, 1975; Tabakoff and Hussein, 1971).

Particle–Blade Impacts and Blade Erosion. Empirical correlations of the restitution parameters are used to calculate the particle rebound conditions after impacts with blade surfaces in the computation of particle trajectories. These correlations (Tabakoff et al., 1984) are based on the experimental data obtained using Laser-Doppler Velocimetry (LDV) for the particle impacts with the material samples and the consequent rebounds in a special wind tunnel. In the present study, the magnitude and direction of the rebounding particle velocities after impact were obtained using the following empirical equations for AM355 steel alloy:

$$e_V = V_2/V_1 = 0.99727 + 0.3062\beta_1 - 4.25271\beta_1^2 + 5.3818\beta_1^3 - 1.9896\beta_1^4 \tag{9}$$

$$e_\beta = \beta_2/\beta_1 = 0.99866 - 2.82902\beta_1 + 4.65083\beta_1^2 - 2.319\beta_1^3 + 0.27404\beta_1^4 \tag{10}$$

The empirical expressions for the tangential and normal velocity restitution ratios were similarly obtained and are given as

$$e_T = V_{T2}/V_{T1} = 1.01645 - 0.17002\beta_1 - 1.95975\beta_1^2 + 2.48495\beta_1^3 - 0.82729\beta_1^4 \tag{11}$$

$$e_N = V_{N2}/V_{N1} = 0.98268 - 3.49691\beta_1 + 6.15641\beta_1^2 - 4.39336\beta_1^3 + 1.10941\beta_1^4 \tag{12}$$

In equations (9)–(12), β_1 is in radians, and the subscripts 1 and 2 refer to the conditions before and after impact.

The experimental data from the erosion tests was used to derive a semi-empirical erosion rate equation for AM355 steel alloy (Tabakoff et al., 1984). This equation is written as a function of tangential and normal velocity restitution ratios obtained by equations (11) and (12) as follows:

$$\epsilon = 0.004995 \times 10^{-4} \left[\left(\frac{V_{T1}}{100}\right)^{2.8} (1 - e_T^2) + 0.894\left(\frac{V_{N1}}{100}\right)^{1.792} (1 - e_N^2)\right] \tag{13}$$

where ϵ is expressed in $\mathrm{cm}^3/\mathrm{ft}^2$-g of total ingested particles. Equation (13) is used to calculate the erosion rates at the impact locations using the particle impact conditions as inputs.

Computation Procedure. The particle trajectory and blade erosion computations require the flow field as an input, in order to provide the aerodynamic drag forces acting on the particles. The flow computations were performed for the guide vanes of the radial inflow turbine as shown in Fig. 1. The encircled flow passage was selected for the particle trajectory and blade erosion calculations. Figure 2 shows this passage at a larger scale with the velocity and angle definitions as well as some of the geometric parameters and dimensions.

MERIDL (Katsanis, 1977) and TSONIC (Katsanis, 1968) flow codes were used for the flow field computations. Since the incidence angle was considered to be the parameter of importance, the flow fields were computed for eight different in-

Nomenclature

A = particle cross-sectional area
C_D = particle drag coefficient
D_p = particle diameter
g = gravitational acceleration
m = particle mass
r = radial coordinate
t = time
$\bar{U}$ = gas velocity
$\bar{V}$ = particle velocity
$\bar{W}$ = relative velocity between the gas and the particles
z = axial coordinate
β_1 = inlet flow angle
γ = impact frequency
ϵ = erosion rate
μ_g = gas viscosity
ρ = gas density
σ = circumferential position of the reference axis where $\phi = 0$ from the vertical direction
ϕ = circumferential coordinate

Subscripts

N = refers to normal component
p = particle
r = component in radial direction
T = refers to tangential component
z = component in axial direction
ϕ = component in circumferential direction
1 = refers to particle impact conditions
2 = refers to particle rebound conditions after surface impacts

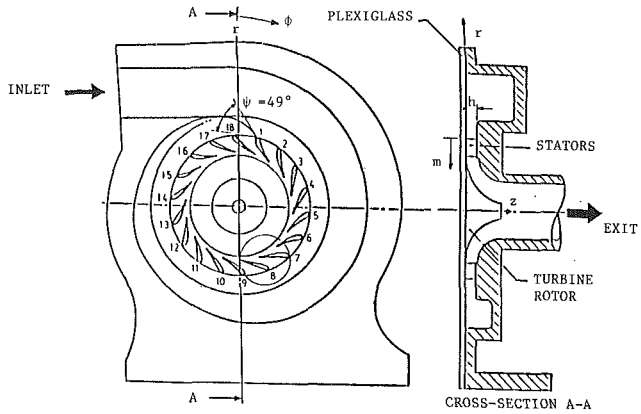

Fig. 1 Schematic showing the radial turbine configuration

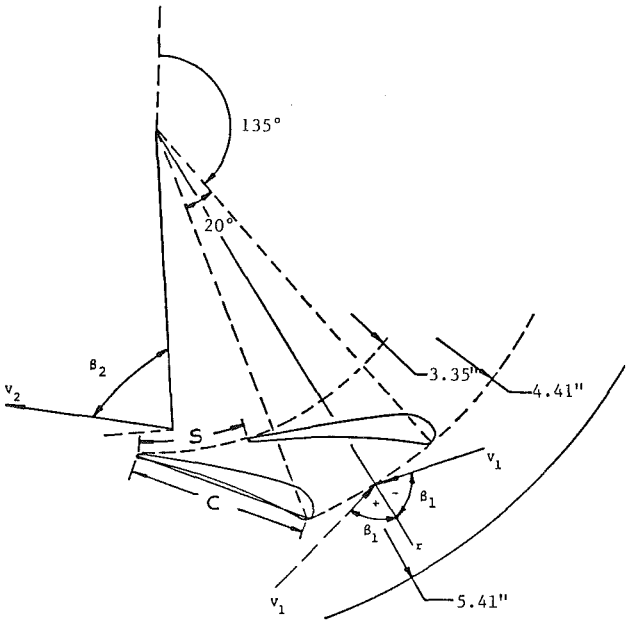

Fig. 2 Schematic showing the flow passage geometry

let flow angles, which are −66, −45, −30, −10, 0, 20, 40, and 60 deg, respectively, with the radial direction according to the angle definition of Fig. 2. The exit flow velocity was kept the same for each flow field computation with a different inlet flow angle, in order to provide the same mass flow rate, which is 0.2 lb/s through the radial turbine.

During the trajectory calculations, the initial particle velocities were assumed to be equal to the gas velocities. This is not a realistic assumption, because the actual particle velocities at the nozzle inlet are generally different from the gas velocities depending on the scroll geometry and particle size. However, for the small particle sizes these differences are not significant and a more realistic investigation would be very tedious, involving computations through different scroll geometries to provide various incidence conditions for the guide vanes.

A simple erosion rate calculation program was developed. This program used the output of the trajectory program and computed the erosion rates at the impact locations on the blade surfaces.

Results and Discussions

The particle trajectory and blade erosion computations were performed for 18,000 particles of diameters 5, 15, and 60 μm ingested through the guide vanes of the radial turbine shown in Fig. 1. However, the details of the results are reported only for the 5-μm-dia particles in Figs. 3–9, because they are encountered most frequently in practical radial turbine applications. These results are presented in terms of the particle trajectory, impact location, impact velocity, impact frequency, and erosion rate distributions for the inlet flow angles of −30, −10, and 20 deg. These correspond to a negative, an optimum, and a positive incidence angle, respectively, for the guide vanes.

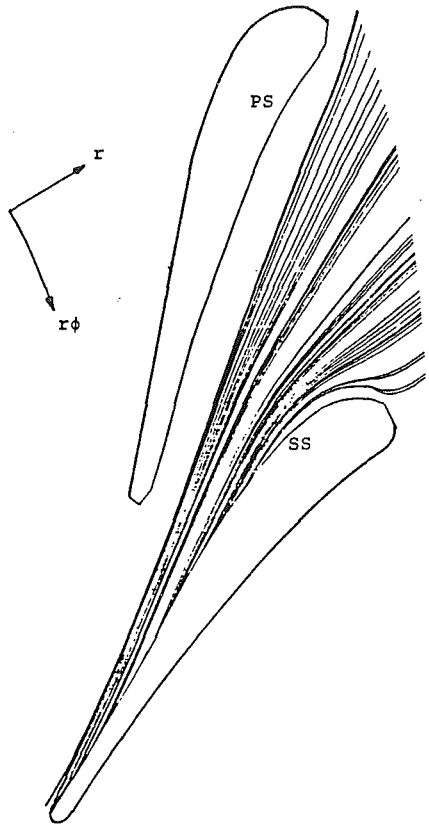

Fig. 3 Projection of the particle trajectories on the blade-to-blade plane for $D_p = 5$ μm and $\beta_1 = -30$ deg

The projected particle trajectories are plotted on the blade-to-blade plane parallel to the end walls as shown in Figs. 3–5. Figure 3 shows the projected particle trajectories for the inlet flow angle β_1 of −30 deg, which correspond to the negative incidence angle. The particles entering the passage are transported toward the vane suction surface in the figure. Almost all the particles impact the suction surface. The particles entering the passage near the pressure surface impact the rear suction side of the next blade. The rest of the particles that enter the passage closer to the suction surface impact this surface farther upstream. However, the region of the suction surface just downstream of the leading edge is not exposed to particle impacts. Figure 4 shows the projected particle trajectories for $\beta_1 = -10$ deg, which corresponds to the optimum flow incidence angle. This figure displays the same general features as the previous figure (Fig. 3). These features are that no pressure surface impacts are observed, and all the particles are transported toward the suction surface. However, a considerable number of the particles entering the passage close to the pressure surface approach this surface near the leading edge, and leave the passage without impacting the vane surfaces. The impact locations on the suction surface start further downstream as compared with the previous figure. Figure 5 shows the particle trajectories for the positive incidence angle ($\beta_1 = 20$ deg). Similar to Figs, 3 and 4, the par-

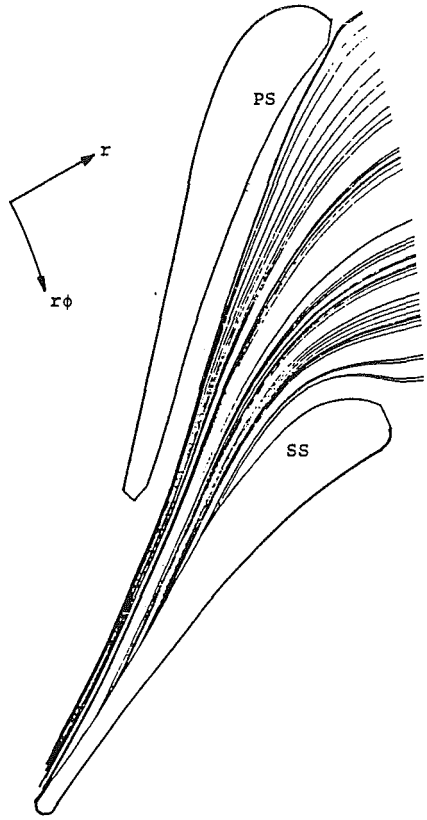

Fig. 4 Projection of the particle trajectories on the blade-to-blade plane for $D_p = 5$ μm and $\beta_1 = -10$ deg

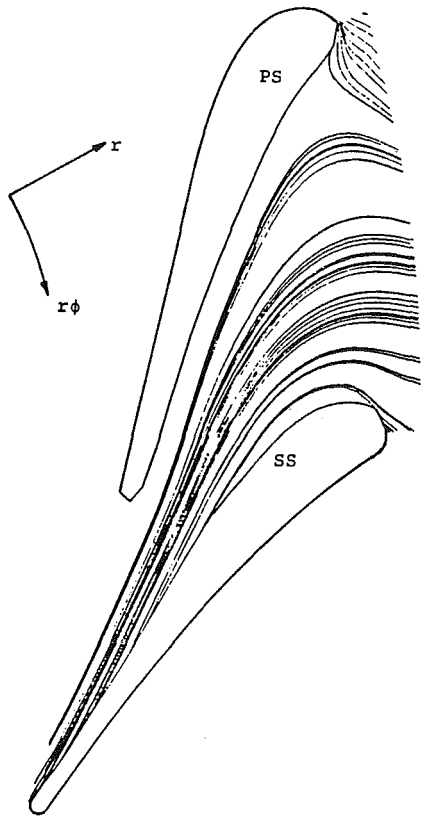

Fig. 5 Projection of the particle trajectories on the blade-to-blade plane for $D_p = 5$ μm and $\beta_1 = 20$ deg

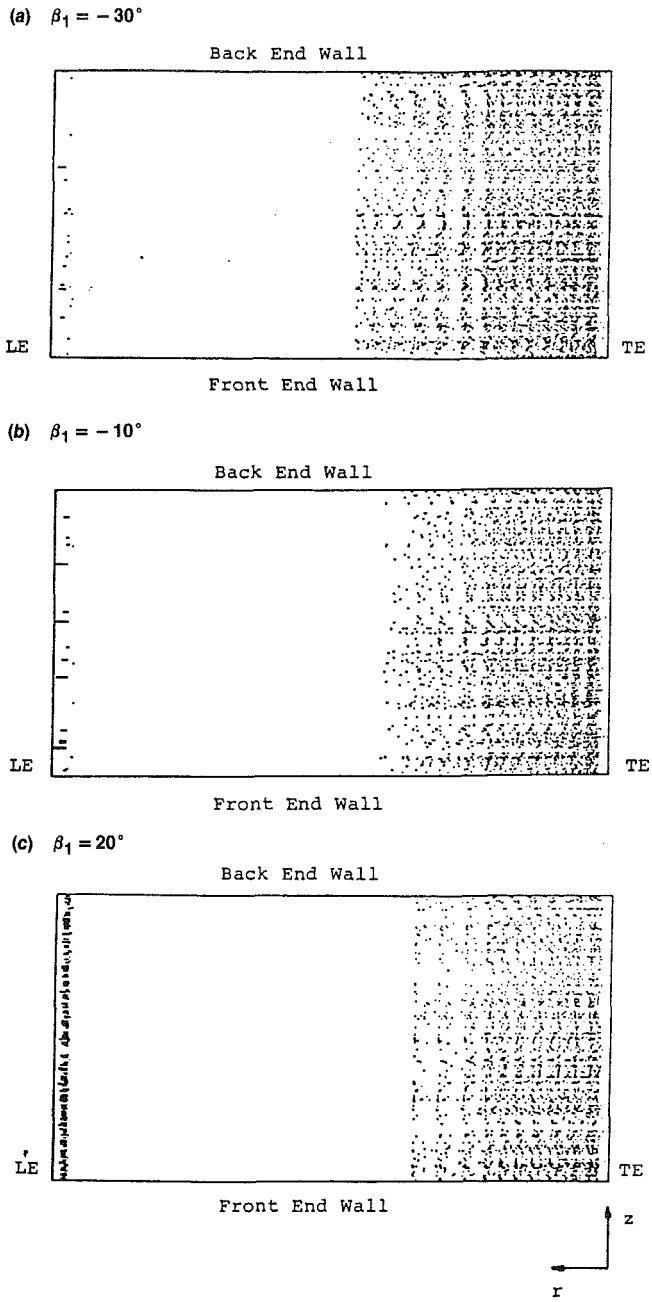

Fig. 6 Particle impact locations on the blade suction surface for $D_p = 5$ μm

ticles are carried toward the suction surface, and impact most of the downstream portion of the vane. The region of the suction surface unaffected by the impacts is larger. As in Fig. 4, a considerable number of particles leave the passage without impacting the vane surfaces. However, some of the particles impacted the suction side and some others impacted the pressure side of the leading edge. A number of these particles reentered the flow passage, while the rest rebounded back or lost their energy at the stagnation region.

Except for a few impacts on the pressure side of the leading edge, there are not any impacts on the vane pressure surface. Therefore, the impact locations are presented only for the suction surface. Figures 6(*a*), 6(*b*), and 6(*c*) show the projected blade suction surface impact locations on the *r*–*z* plane for inlet flow angles of -30, -10, and 20 deg, respectively. A vast majority of the particle impacts occurred in an area from a radial location upstream of the rear suction surface to trailing

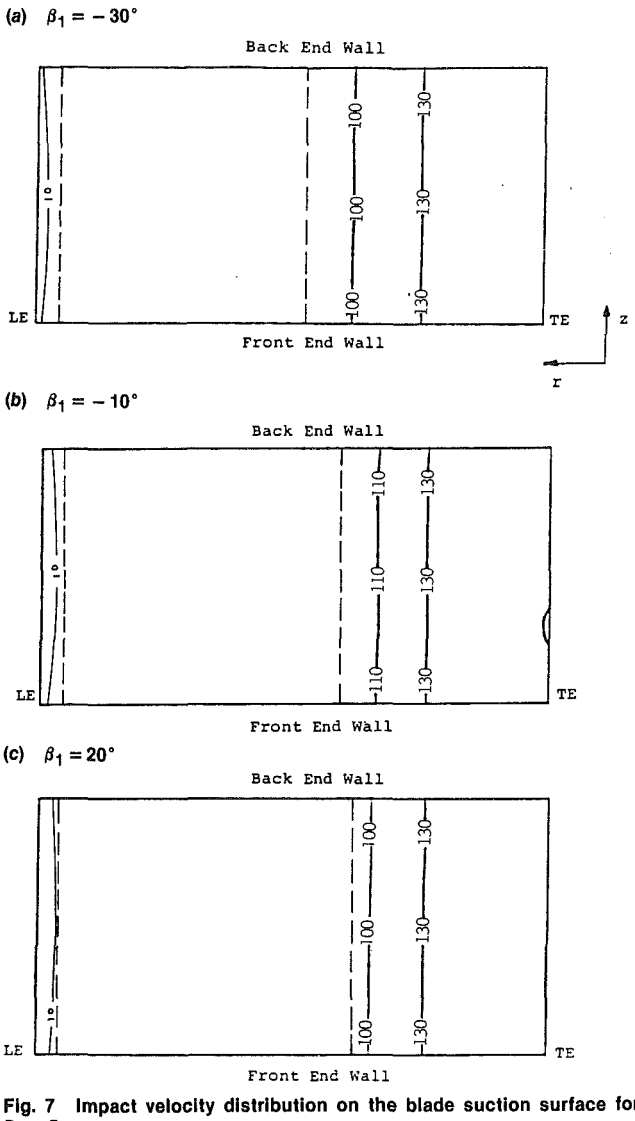

Fig. 7 Impact velocity distribution on the blade suction surface for $D_p = 5$ μm

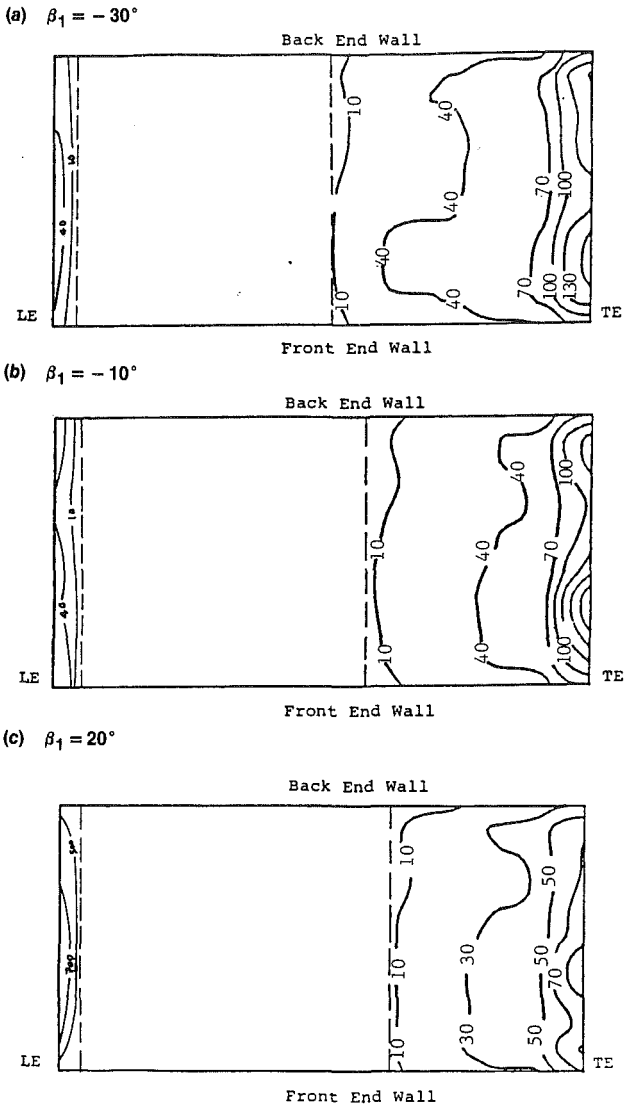

Fig. 8 Impact frequency distribution on the blade suction surface for $D_p = 5$ μm

edge in these figures, as a result of the particle trajectories in Figs. 3–5. Significantly fewer impacts were encountered at the leading edge region, and they did not have any significant effect on the blade erosion, as will be explained later. The particle impact locations on the rear suction surface start at a closer radial location to the leading edge for the negative incidence angle ($\beta_1 = -30$ deg) as shown in Fig. 6(a). The impacted area decreases consistently as the inlet flow angle β_1 corresponds first to the optimum incidence (Fig. 6b) and then to the positive incidence (Fig. 6c) angles. The radially inward shift of the particle impact locations is consistent with the trajectory plots of Figs. 3–5, where the particles impact the suction surface at closer radial locations to the trailing edge, and an increasing number of particles pass through the flow passage without any impacts as the flow incidence changes from negative to positive.

Figures 7(a), 7(b), and 7(c) present the projected impact velocity distributions on the r–z plane for the blade suction surface, at inlet flow angles of -30, -10, and 20 deg, respectively. The impact velocities are in ft/s in these plots. The impact velocities at the leading edge region are only about 10 ft/s, while their magnitude reaches to 130 ft/s on the rear suction surface. The regions where there are no impacts are in the upstream half, and are separated by dashed lines from the impacted areas, as shown in Figs. 7(a)–7(c). Although no figures are presented, the impact angles were about 1–7 deg at all impact locations. This is reasonable, because for the 5-μm particle diameter, the particles follow the flow very closely. Since the impact angles encountered for this particle size are much smaller than the impact angles corresponding to maximum erosion rate (30 deg), this parameter is relatively insignificant for the blade erosion.

Figures 8(a) through 8(c) show the projected suction surface impact frequency γ distributions on the r–z plane for the inlet flow angles -30, -10, and 20 deg, respectively. The impact frequency is expressed as (the number of impacts)/(ft^2 blade surface area × number of total ingested particles). Referring to Figs. 8(a)–8(c), the leading edge impact frequencies reach to 40 for the negative and optimum incidence angles, while they are much higher (700) for the positive incidence. However, since the particle impact velocities are very small in this region (Figs. 7a–7c), the resulting erosion rates are not significant. The impact frequencies increase toward the trailing edge for all the impact angles, as shown in Figs. 8(a)–8(c). However, they are lower for the positive incidence angle, as compared with the negative and optimum incidence angles. This result is expected, because higher numbers of particles pass through the passage without any impacts as shown in the trajectory plots of Figs. 3–5.

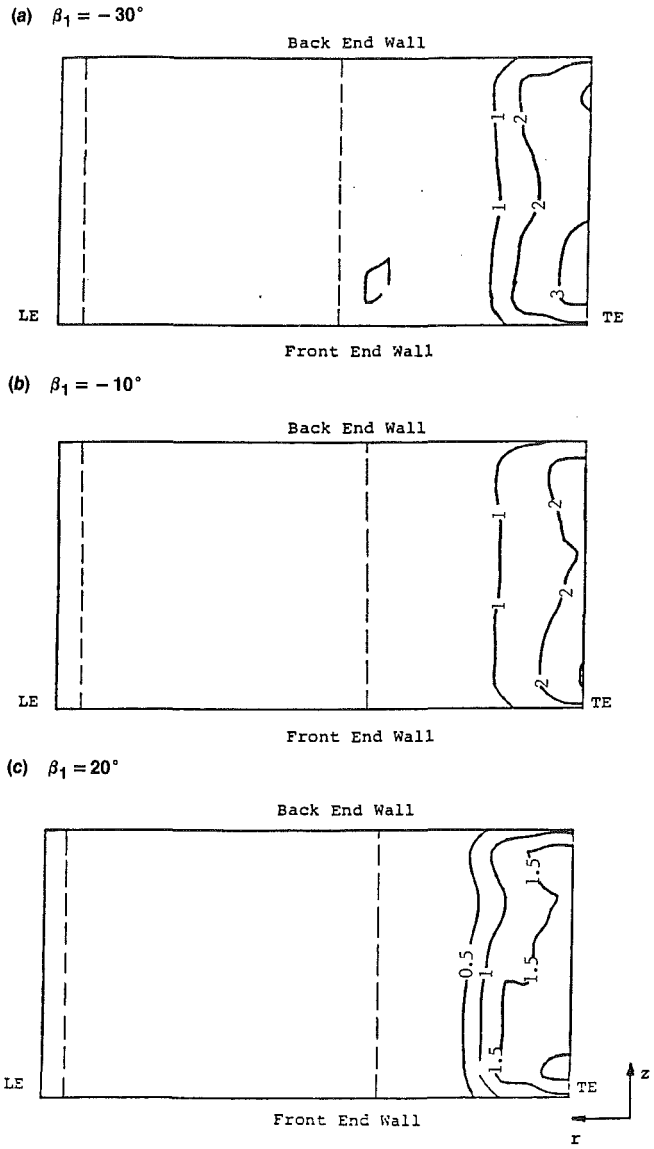

Fig. 9 Erosion parameter distribution on the blade suction surface for $D_p = 5$ μm

Figures 9(*a*)-9(*c*) show the erosion parameter ϵ distributions for the inlet flow angles of -30, -10, and 20 deg on the vane suction surface. The erosion parameter is expressed as (cm^3 erosion)/(ft^2 blade surface area × gram of total ingested particles). Although there are considerable numbers of impacts at the leading edge, because of the very small particle velocities, the erosion is not significant. The dashed lines represent the boundaries with the regions where there are no impacts. The projected areas exposed to erosion are in the downstream half on the *r*–*z* plane. The erosion is maximum close to the trailing edge for all the impact angles (Figs. 9*a*–9*c*). This is a result of the higher impact velocities (Figs. 7*a*–7*c*) and frequencies (Figs. 8*a*–8*c*). A comparison of Figs. 9(*a*)-9(*c*) shows that the erosion parameter decreases as the inlet flow angle changes from negative to positive incidence angles.

Although the results of particle dynamics and blade erosion computations were presented at only three different inlet flow angles and for 5-μm-dia particles in Figs. 3–9, these computations were performed for eight different incidence angles and were repeated for 15 and 60-μm-dia particles. Figures 10–12 show the results of these computations. They present the total erosion/blade against inlet flow angle for 5, 15, and 60-μm-dia particles. The total erosion/blade is calculated by summing

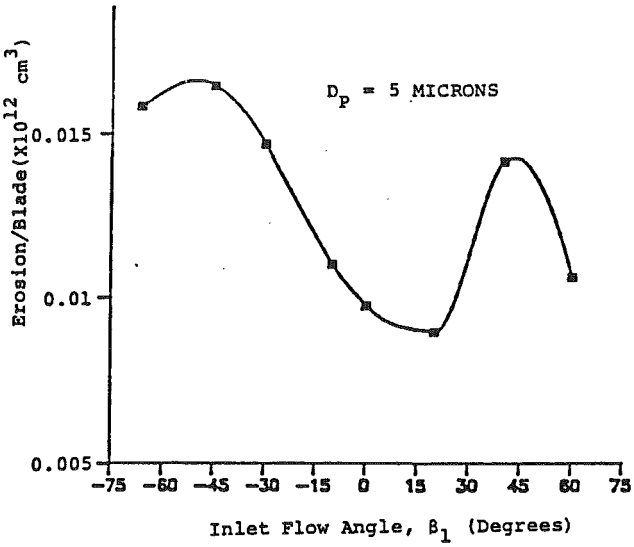

Fig. 10 Variation of blade erosion with inlet flow angle β_1

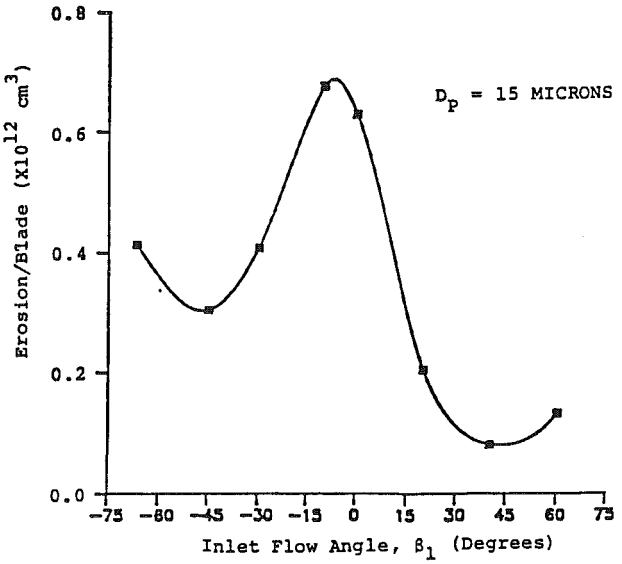

Fig. 11 Variation of blade erosion with inlet flow angle β_1

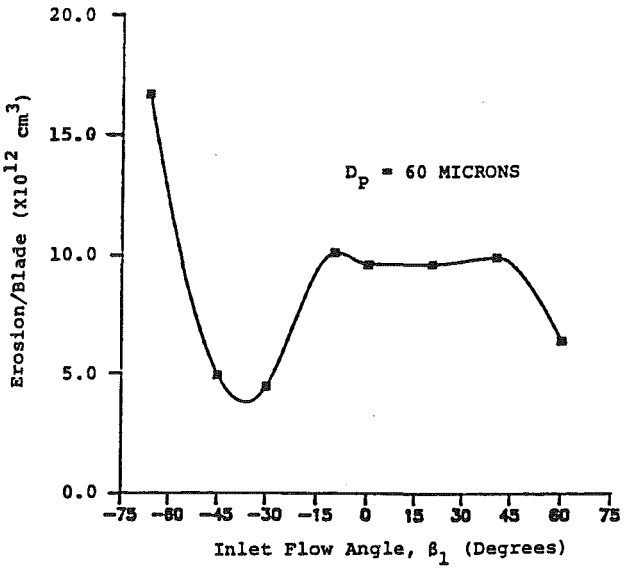

Fig. 12 Variation of blade erosion with inlet flow angle, β_1

the erosion per unit blade area due to each particle and integrating over the blade surface, and is expressed in cm^3. A comparison of Figs. 10–12 illustrates that the magnitude of total blade erosion increases with the particle size. The effect of inlet flow angle on the blade erosion strongly depends on the particle size. For the inlet angles that cause fewer impacts and result in impacts at locations where particles do not gain high velocities or angles corresponding to maximum erosion rate, the total blade erosion is generally low. Since the particle trajectories depend strongly on particle size, the minimum blade erosion is obtained at a different range of inlet angles for the different particle sizes. For example, this range is from -45.0 to -30.0 deg for the 60-μm particles. For 15-μm-dia particles, a 30.0 to 60.0 deg range gives less erosion. However, for 5-μm particles, which are practically important since larger particles can usually be separated before entering the engine, -10.0 to 20.0 deg gives better results. It appears that smaller particles cause less erosion at a positive inlet flow angle for the present radial turbine guide vanes. As the particle size decreases, the inlet flow angle for minimum erosion approaches the optimum aerodynamic incidence angle, since the particles follow the flow better. Using a positive incidence angle may improve erosion behavior for small particles, but it may also cause a significant increase in blade loading. Since the particle dynamics and erosion of scroll and the rotor were not considered in this paper, the overall erosion of the radial turbine is yet to be investigated, including these components in the computations together with the guide vanes.

Conclusions

For all three different inlet flow angles, the 5-μm-dia particles were transported toward the vane suction surface. Most of these particles impacted the suction surface covering a large surface area from a radial location in the upstream half to trailing edge. The radial location where the impacts started shifted more downstream, reducing the impacted area, as the flow incidence angle changed from negative to positive. This is a result of the particle trajectories, which resulted in a higher number of particles passing through the flow passage without any impacts at the positive incidence angle as compared with the negative incidence. A small area at the leading edge was also exposed to particle impacts. However, because of the very small impact velocities, there was not any significant erosion at this region, although for the positive incidence angle the impact frequency was very high. Maximum erosion was observed close to the trailing edge for all the inlet angles, because of the high impact frequency and velocities. Highest erosion occurred at the inlet flow angle corresponding to negative flow incidence. The erosion decreased for the optimum incidence angle, and it was minimum at the positive incidence angle.

The total blade erosion was found to increase with the particle diameter. The computation results also showed that erosion behavior depends strongly on the particle size and the minimum blade erosion occurs at a different range of inlet flow angles for the different particle diameters. This range corresponds to positive incidence angles for the 5-μm-dia particles.

Acknowledgments

This research work was sponsored by the U.S. Department of Energy, Contract No. 19X-89628C, Oak Ridge National Laboratory, Oak Ridge, TN.

References

Clevenger, W. B., and Tabakoff, W., 1974, "Similarity Parameters for Comparing Erosive Particle Trajectories in Hot Air and Cold Air Radial Inflow Turbines," ASME *Journal of Engineering for Power*, Vol. 96, pp. 358–364.

Grant, G. and Tabakoff, W., 1975, "Erosion Prediction in Turbomachinery Due to Environmental Solid Particles," *Journal of Aircraft*, Vol. 12, No. 5, pp. 441–478.

Katsanis, T., 1968, "Computer Program for Calculating Velocities and Streamlines on a Blade-to-Blade Stream Surface of a Turbomachine," NASA TN D-4525.

Katsanis, T., 1977, "Revised Fortran Program for Calculating Velocities and Streamlines on the Hub–Shroud Mid-channel Stream Surface of an Axial-Radial- or Mixed-Flow Turbomachine or Annular Duct. I: User's Manual," NASA TN D-8430.

Montgomery, J. E., and Clark, J. M., Jr., 1962, "Dust Erosion Parameters for a Gas Turbine," SAE Paper No. 538.

Tabakoff, W., and Hussein, M. F., 1971, "Trajectories of Particles Suspended in Fluid Flow Through Cascades," *AIAA Journal of Aircraft*, Vol. 9, pp. 1514–1519.

Tabakoff, W., Hamed, A., and Eroglu, H., 1984, "Study of Particle Rebound Characteristics and Material Erosion at High Temperature," Final Technical Report, Fossil Energy Materials Program, U.S. Department of Energy, ORNL/Sub/84-89628/01.

Tabakoff, W., Hamed, A., and Mansour, M. L., 1987, "Dynamics of Two-Phase Flow Through a Radial Turbine," *Proceedings of the 1987 ASME-JSME Thermal Engineering Joint Conference*, Honolulu, HI, pp. 135–141.

Tabakoff, W., and Hamed, A., 1988, "Temperature Effect on Particle Dynamics and Erosion in Radial Inflow Turbine," ASME JOURNAL OF TURBOMACHINERY, Vol. 110, pp. 258–264.

Optimum Design of a Low-Pressure, Double Inflow, Radial Steam Turbine for Open-Cycle Ocean Thermal Energy Conversion

T. Schobeiri
Associate Professor,
Turbomachinery Laboratory,
Department of Mechanical Engineering,
Texas A&M University,
College Station, TX 77843-3123
Mem. ASME

This paper describes the thermo-fluid design concept of a low-pressure, radial inflow steam turbine for the Open-Cycle Ocean Thermal Energy Conversion (OTEC). For the optimum design consideration, the necessary theoretical tools are developed. The design concept permits the utilization of single-stage and multistage configurations for small and medium power ranges, respectively.

Introduction

Ocean Thermal Energy Conversion (OTEC) converts the thermal energy difference due to the temperature difference between the ocean surface and some depths into mechanical energy. The energy conversion can be established by open and closed-cycle systems, as reviewed by Apte (1981), Cohen (1982, 1980), and Lavi (1980). A comprehensive literature list is found in Penney et al. (1984). This paper focuses on the open-cycle OTEC concept that originated with Claude (1930) and Claude et al. (1935). According to this concept, the steam generated from warm seawater is expanded into the turbine, where its total energy is converted into mechanical energy.

Since the available specific turbine enthalpy difference is extremely low, the turbine efficiency is of fundamental importance for producing the net power required. On the other hand, the required high efficiency should not cause additional research and investment costs. These facts make the turbine a crucial component in the entire OC-OTEC system.

Because of the low amount of available thermal energy and the large mass flow, Westinghouse (1979) and Creare (1985) proposed an axial flow turbine configuration, which is based on the existing design technology applied to the last stage of conventional or nuclear large LP-steam turbines. Since the pressure ratio, the pressure level, and thus the thermodynamic properties across the OC-OTEC turbine are different from those in the conventional application, the last LP stage cannot be applied to the OC-OTEC turbine without a major modification. For a steam turbine producer, this modification exhibits a new turbine blade design that requires extensive research and development costs. To find a practical and inexpensive solution to this problem, the Solar Energy Research Institute in cooperation with the Department of Energy invited the Turbomachinery Laboratory of the Texas A&M University to design an alternative turbine component. The major criteria determining the design concept are simplicity in design, feasibility in economical and technical aspects, and reliability.

Problem Definition, Solution Concept

A brief thermodynamic system analysis and description of open-cycle ocean thermal energy conversion is reported by Parsons et al. (1985). In the open-cycle system, warm tropical sea water (~25°C) is pumped into an evacuated evaporator chamber where the pressure is below the vapor pressure at the water inlet temperature. Therefore, flash evaporation takes place, producing steam. After the expansion in the turbine, the steam enters the condenser section of the chamber where cold water (~5°C) is pumped from depths of nearly 1000 m. The thermodynamic operation conditions for the turbine are therefore dictated by the evaporator and condenser temperatures. Based on these boundary conditions, the Solar Energy Research Institute formulated in the research contract SERI-TEXAS A&M (1988) the following operation conditions for the turbine component:

Inlet temperature	T_{in} = 22.5°C
Inlet pressure	p_{in} = 2.757 kPa
Outlet pressure	p_{out} = 1.17–1.3 kPa

These thermodynamic boundary conditions show that the turbine component does not undergo any significant thermal and structural stresses or fluid mechanical loading. Since the isentropic enthalpy difference for the above conditions is constant, the turbine power is determined entirely by the turbine mass flow and the efficiency. Assuming the highest available turbine efficiency, a reasonable turbine power for commercial operation requires high mass flows. For low-pressure and high-mass-flow operation, the application of axial design concept is common, where LP stages with high efficiency blades are used (BBC, KWU, Westinghouse). The design report from Westinghouse (1979) shows that for turbine power of 10 MW, the axial turbine has an outer diameter of 14.4 m with a blade length of 4.3 m. This solution, which leads to extremely large

Contributed by the International Gas Turbine Institute and presented at the 34th International Gas Turbine and Aeroengine Congress and Exhibition, Toronto, Ontario, Canada, June 4–8, 1989. Manuscript received at ASME Headquarters January 13, 1989. Paper No. 89-GT-60.

geometry and machine building, and consequently to high investment costs, cannot be considered appropriate and cost effective. An alternative solution to this problem that can be realized easily is the radial turbine design concept. There are two important reasons for application of the radial inflow concept. First, the specific mechanical energy of the stage is higher than that of the axial stage, which means smaller turbine size. Second, because of the double inlet configuration and the facts explained above, the radial rotor is inherently stiff. These special circumstances permit manufacture of the blading from either thin rolled sheet metal or cast plastic, which reduces the investment cost considerably.

Radial Inflow Steam Turbine Design Concept

The existing radial turbine technology, unlike the radial turbine for OC-OTEC application, deals with relatively high enthalpy differences and low mass flows (Rohlik, 1968; Kofsky, 1972; Futral et al., 1970). There is no information available for the application of radial turbine design to conditions encountered in OC-OTEC. This situation suggests a need for investigating the problem systematically. In the following, first the parameters defining the radial stage are derived. Then the flow cascade theory is developed, where the lift-solidity coefficients are derived. These relations with the significant loss correlations are then implemented into the design procedure for a systematic optimum design consideration of radial inflow turbines and application to the OC-OTEC conditions.

Description of Radial Stage

As shown by Schobeiri (1988), a turbomachinery stage can be described simply by the following stage parameters:

$$\mu_S = \frac{V_{m1}}{V_{m2}}, \quad \mu = \frac{V_{m2}}{V_{m3}}, \quad \nu = \frac{U_2}{U_3}, \quad \phi = \frac{V_{m3}}{U_3}$$

$$\lambda = \frac{l_m}{U_3^2} = \frac{U_2 V_{u2} + U_3 V_{u3}}{U_3^2}, \quad r = \frac{\Delta h_R}{\Delta h_R + \Delta h_S}$$

with V_m, U from the velocity diagram (Fig. 1), l_m the specific mechanical energy of the stage, and Δh_R and Δh_S the specific static enthalpy difference in rotor and stator. The dimensionless parameters μ_S and μ represent the meridional velocity ratio for the stator and rotor, respectively, ν the circumferential

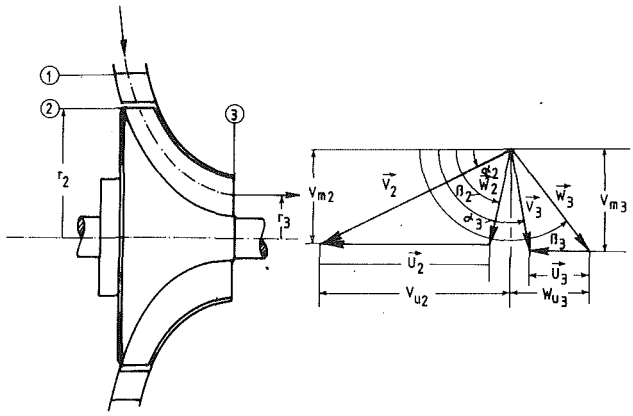

Fig. 1 Radial inflow turbine stage, velocity diagram, angle definition

velocity ratio, ϕ the stage flow coefficient, λ the stage load coefficient, and r the degree of reaction. Introducing these parameters into the equations of continuity, energy, moment of momentum, and the relation for degree of reaction, the radial turbine stage is defined completely by a set of four equations:

$$\cot \alpha_2 - \cot \beta_2 = \frac{\nu}{\mu\phi} \tag{1}$$

$$\cot \alpha_3 - \cot \beta_3 = \frac{1}{\phi} \tag{2}$$

$$\lambda = \phi(\mu\nu \cot \alpha_2 - \cot \beta_3) - 1 \tag{3}$$

$$r = 1 + \frac{\phi^2}{2\lambda}\{1 + \cot^2\alpha_3 - \mu^2(1 + \cot^2\alpha_2)\} \tag{4}$$

These equations can be expressed in terms of the flow angles α_2, α_3, β_2, and β_3, which lead to a set of four nonlinear equations:

$$\mu^2\phi^2(1-\nu^2)\cot^2_{\alpha_2} + 2\mu\nu\phi\lambda \cot \alpha_2 - \lambda^2 - 2(1-r)\lambda + (\mu^2 - 1)\phi^2 = 0 \tag{5}$$

Nomenclature

c = blade chord
c = closed curve
C_L = lift coefficient
$C_L c/s$ = lift-solidity coefficient
D = diameter
F = lift force
h = specific static enthalpy
H = $h + V^2/2$ = specific total enthalpy
k_i = $\rho V_i^2/2$ = specific kinetic energy at station i
l_m = $U_2 V_{u2} + U_3 V_{u3}$ = specific mechanical energy of stage
$\dot{m}$ = mass flow
n = turbine frequency
p = static pressure
P_i = $p_i + \rho V_i^2/2$ = total pressure at station i
r = degree of reaction
Re = Reynolds number
U = circumferential rotor velocity
V = absolute flow velocity
V_m, V_u = components of absolute flow velocity
W = relative flow velocity
W_m, W_u = components of relative flow velocity
Z = $\Delta h_{\text{loss}}/l_m$ = stage loss coefficient
α = absolute flow angle
β = relative flow angle
Γ = circulation
δ = tip clearance
ΔH = $H_1 - H_3$ = actual total enthalpy difference
ΔH_s = $H_1 - H_{3s}$ = isentropic total enthalpy difference
ζ = $(P_i - P_{i+1})/k_{i+1}$ = (total pressure) loss coefficient
η_s = $\Delta H/\Delta H_s$ = stage isentropic efficiency (total to total)
λ = stage load coefficient
Λ = lift function
μ = ratio of meridional velocities
ν = ratio of circumferential velocities
ρ = density
ϕ = stage flow coefficient

Subscripts

e, p, s = exit, profile, secondary
i = ideal
L = lift
m = meridional direction
opt = optimum
u = circumferential direction
s = isentropic
S = stator
R = rotor
ref = reference
1, 2, 3 = stations

$$\phi^2(1-\nu^2)\cot^2_{\alpha_3}+2\phi\lambda\cot\alpha_3+\lambda^2 - 2(1-r)\lambda\nu^2+(\mu^2-1)\phi^2\nu^2=0 \quad (6)$$

$$(1-\nu^2)(\mu\phi\cot\beta_2+\nu)^2+2\nu\lambda(\phi\mu\cot\beta_2+\nu) - \lambda^2-2(1-r)\lambda+(\mu^2-1)\phi^2=0 \quad (7)$$

$$(1-\nu^2)(\phi\cot\beta_3+1)^2+2\lambda(\phi\cot\beta_3+1) + \lambda^2-2(1-r)\lambda\nu^2+(\mu^2-1)\phi^2\nu^2=0 \quad (8)$$

The four pairs of equations (1)–(4) and (5)–(8), which reflect the conservation laws of thermo-fluid mechanics, include nine unknowns. The other five parameters required to solve these equation sets can be defined from the boundary conditions pertaining to the individual problem under consideration. For a preliminary design for example, the circumferential velocity or diameter ratio ν can be assumed as given. Furthermore, for a single-stage machine the absolute exit flow angle can be set at $\alpha_3 \simeq 90$ deg, for which the exit loss is a minimum. Additional information is provided if the enthalpy difference is known. This in connection with the known turbine frequency and the outer diameter determines the stage load coefficient λ. The stage flow coefficient ϕ can be estimated from the turbine mass flow $\dot{m}$, which dictates the turbine power. As will be shown, the meridional velocity ratio μ affects the type of the blade. With equations (1)–(4) or (5)–(8) the turbomachinery stage is described completely.

Radial Cascade Aerodynamics, Optimum Lift-Solidity Coefficient

The optimum design of the turbine component requires information about the optimum lift-solidity coefficient. The corresponding relationship derived by Zweifel (1945) for the axial turbine is restricted to the stage flows where the stream lines are parallel to the cascade axis. Similar situations are encountered in high-pressure stages of an axial turbine or compressor, where the stream surfaces are approximated by cylindrical sections with constant diameters. In general, the flow through the intermediate and low-pressure stages of axial machines, and also through the stages of radial machines, has stream-surfaces with different radii that result in different blade spacing at the inlet and exit. Furthermore, the meridional velocity at the inlet might differ from that at the exit. The Zweifel criterion does not account for these differences. In order to calculate the blade lift-solidity coefficient correctly, the radius and the axial velocity changes must be taken into account. In the following, the corresponding relations for a turbine stator and rotor are derived. Extending the derivation to compressor stator and rotor leads to the same results.

Calculation of the lift-solidity coefficient for a viscous flow requires the equations of continuity, momentum in circumferential and meridional directions, and the energy equation. As a result, a relation is obtained that contains the profile loss coefficient (Schobeiri, 1988). Since, for the calculation of the optimum lift-solidity coefficient, the contribution of the profile loss coefficient is negligible, the flow can be considered as inviscid. For an inviscid incompressible flow through the turbine stator shown in Fig. (2), the lift force is given by the Kutta–Joukowski relation

$$\mathbf{F}_i = \rho_\infty \mathbf{V}_\infty x \boldsymbol{\Gamma} \quad (9)$$

where the subscript i refers to the inviscid flow. The circulation is

$$\Gamma = \oint_c \mathbf{V}\cdot d\mathbf{c} = V_{u1}s_1 + V_{u2}s_2 + \int_2^3 \mathbf{V}\cdot d\mathbf{c} + \int_4^1 \mathbf{V}\cdot d\mathbf{c} \quad (10)$$

Since the last two integrals cancel each other, equation (10) reduces to

$$\Gamma = V_{u1}s_1 + V_{u2}s_2 = s_2\,(V_{u2}+\nu V_{u1}) \quad (11)$$

The magnitude of the mean velocity vector is

$$V_\infty = \frac{1}{2}\frac{V_{m2}(1+\mu_s)}{\sin\alpha_\infty} \quad (12)$$

where $\sin\alpha_\infty$ can be obtained from

$$\cot\alpha_\infty = \frac{\mu_S\cot\alpha_1 + \cot\alpha_2}{1+\mu_S} \quad (13)$$

Introducing equations (11) and (12) into (9), the stator lift-solidity coefficient for an inviscid flow is

$$C_L\frac{c}{s_2} = \frac{\sin^2\alpha_2}{\sin\alpha_\infty}(1+\mu_S)[\cot\alpha_2 - \nu\mu_S\cot\alpha_1] \quad (14)$$

Similarly, the lift-solidity coefficient for rotor in a relative frame of reference is obtained from

$$C_L\frac{c}{s_3} = \frac{\sin^2\beta_3}{\sin\beta_\infty}(1+\mu)[\nu\mu\cot\beta_2-\cot\beta_3] \quad (15)$$

For the calculation of rotor lift-solidity coefficient in an absolute frame of reference, the absolute circulation must be calculated. This with the dimensionless parameters defined above and the relations for the circumferential velocities yields

$$C_L\frac{c}{s_3} = \frac{\sin^2\alpha_3}{\sin\alpha_{\infty R}}\frac{(1+\mu)}{\phi} [\mu\nu\phi\cot\beta_2 - \phi\cot\beta_3 + \nu^2-1] \quad (16)$$

Equations (14)–(16) determine the lift-solidity coefficient for radial stator and rotor cascades. The optimum solidity and therewith the optimum number of blades can be found if the optimum lift coefficient is known. Systematic experimental investigations on a great number of stationary turbine cascades by Pfeil (1964, 1969) show that

$$(C_L)_{\text{opt}} \simeq 1.1$$

The optimum solidities and blade numbers for stator and rotor are found easily by applying this criterion to equations (14) and (16) to find the optimum blade number.

Calculation of Stage Efficiency

To calculate the stage efficiency, first the individual stage losses must be identified. The significant losses determining the efficiency of a double inflow, single-stage, radial steam turbine are exit, primary (profile), and secondary losses. In the calculation procedure, however, the less significant losses such as trailing edge mixing losses and wetness losses are incorporated using methods by Schobeiri (1985) and Traupel (1977). Unlike the axial machine, there is a lack of published data from systematic investigations concerning the radial tur-

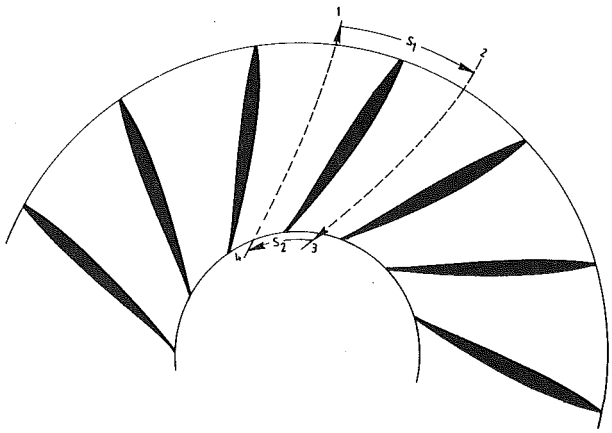

Fig. 2 Circulation around a radial cascade, $s_1 \neq s_2$

bine. Despite this fact, a reasonable solution is found by extending the correlations for axial flow turbine to the radial machines.

Profile Losses

The available turbine profile loss correlations, including those of Ainley (1955), Traupel (1977), Balje et al. (1968), Deic et al. (1973), and Craig et al. (1971), consider generally the influence of the flow deflection, solidity, and Mach and Reynolds numbers. Triebnig et al. (1966) discuss the possibility of optimum design. Pfeil (1969) is the most recent author of comprehensive information on optimum loss correlations for turbine cascades. From experimental investigations for turbine and compressor cascade profiles with the thickness-chord ratio $(d/c) = 0.15$–0.1, hydraulically smooth surfaces, and the Reynolds number

$$\mathrm{Re}_{\mathrm{ref}} = 3.5 \times 10^5$$

Pfeil (1969) proposes for the optimum profile losses the correlation

$$\zeta = K_1 \left\{ 1 + K_2 \left(\frac{c}{s} \right)^3_{\mathrm{opt}} \right\} C_L \frac{c}{s} \frac{1}{\sin \alpha_\infty} \tag{17}$$

where ζ is defined as the ratio of the total pressure difference divided by exit kinetic energy with $K_1 = 0.0107$ and $K_2 = 0.25$ for axial machines. For radial turbine applications, the incorporation of equation (17) into the efficiency calculation procedure with the constant $K_1 = 0.0215$ and the Reynolds number correction

$$\frac{\zeta}{\zeta_{\mathrm{ref}}} = \left(\frac{\mathrm{Re}_{\mathrm{ref}}}{\mathrm{Re}} \right)^{0.2}$$

yields reasonable results. The stage profile loss consists of the stator and rotor total pressure losses, which lead to the stage profile loss coefficient Z_p:

$$Z_p = \zeta_{pS} \frac{V_2^2/2}{l_m} + \zeta_{pR} \frac{W_3^2/2}{l_m}$$

Secondary Losses

The principal concept of secondary flow loss calculations is based on the analogy between the drag forces induced by the secondary flow within the cascade and the wing tip vortices generated by a wing with finite length. For an elliptical lift distribution, Prandtl (1934) found an analytical relation between the induced drag and the lift. Since then, that relation is encountered in many publications dealing with the calculation of secondary flow losses within the turbomachinery stages. Based on the results of Wolf (1961), Utz (1972), and Roeder (1969), Traupel (1977) developed a secondary flow loss correlation. Berg (1973) investigated the influence of stage load parameter λ, particularly on the secondary flow losses. The results of his investigations on five different axial turbine rotors without shrouds lead to the following correlation used in this paper:

$$\zeta_s = K\Lambda \left(\frac{\delta - \delta_o}{c} \right)^m \tag{18}$$

with Λ as the lift function:

$$\Lambda = 4(\cot \beta_2 - \cot \beta_3)^2 \frac{\sin^2 \beta_3}{\sin \beta_\infty} \tag{19}$$

In equation (18) δ represents the actual tip clearance and δ_o the smallest tip clearance that does not cause a tip clearance flow. The constants $K = 0.169$, $m = 0.6$, and $\delta_o/c = 0.005$ were found from experiments. Applying this relation to the radial turbine stage yields

$$\zeta_s = K(1+\mu)^2(\nu\mu \cot \beta_2 - \cot \beta_3)^2 \frac{\sin^2 \beta_3}{\sin \beta_\infty} \left[\frac{\delta - \delta_o}{c} \right]^{0.6} \tag{20}$$

This correlation considers all significant parameters governing the radial stage secondary flow and is incorporated into the loss calculation procedure. The stage secondary flow loss coefficient is calculated from

$$Z_x = \zeta_{sS} \frac{V_2^2/2}{l_m} + \zeta_{sR} \frac{W_3^2/2}{l_m}$$

Exit Losses

For a single-stage machine, the exit loss has a significant influence on the overall stage efficiency. The exit loss coefficient is defined as the ratio of the exit kinetic energy with respect to specific mechanical energy of the stage l_m:

$$Z_e = \frac{V_3^2/2}{l_m} = \frac{V_3^2}{2\lambda U_3^2} \tag{21}$$

Expressing the exit velocity vector V_3 in terms of axial velocity component and using the stage dimensionless parameter, equation (21) is written as

$$Z_e = \frac{\phi^2}{2\lambda(\sin \alpha_3)^2} \tag{22}$$

Stage Loss Coefficient, Stage Efficiency

After calculating the individual stage loss coefficients Z_i, the stage loss coefficient is calculated as

$$Z = \sum_{i=1}^{n} Z_i = Z_p + Z_s + Z_e + \ldots \tag{23}$$

where the index i represents individual stage losses, for example, profile losses or secondary losses. The isentropic stage loss coefficient Z_s is

$$Z_s = \frac{\Delta h_{\mathrm{loss}}}{\Delta H_s} \tag{24}$$

where Δh_{loss} represents all the enthalpy losses from the different loss mechanisms, and ΔH_s the available stage isentropic enthalpy difference. For the turbine stage equation (24) is written as

$$Z_s = \frac{\Delta h_{\mathrm{loss}}}{l_m + \Delta h_{\mathrm{loss}}} = \frac{Z}{Z+1}$$

with the stage loss coefficient Z from equation (23).

The stage isentropic efficiency for the turbine stage is defined as the ratio of actual total enthalpy difference, which is identical with stage mechanical energy, divided by the isentropic stage total enthalpy difference. The isentropic stage efficiency in terms of Z_s and Z is

$$\eta_s = \frac{\Delta H}{\Delta H_s} = \frac{H_1 - H_3}{H_1 - H_{3s}} = \frac{l_m}{\Delta H_s} = \frac{\Delta H_s - \Delta h_{\mathrm{loss}}}{\Delta H_s} = 1 - Z_s \tag{25}$$

$$\eta_s = \frac{\Delta H}{\Delta H_s} = \frac{l_m}{\Delta H_s} = \frac{l_m}{l_m + \Delta h_{\mathrm{loss}}} = \frac{1}{1+Z} \tag{26}$$

Optimum Design of a 30 Hz Radial Steam Turbine With a Power Output of 2.8 MW

For OC-OTEC conditions, an optimum double inflow radial steam turbine should be found. A calculation procedure is established that contains the relations derived above. For accurate calculation of the turbine expansion line, the standard steam program is implemented in the calculation procedure. To find the optimum solution, the significant parameters must

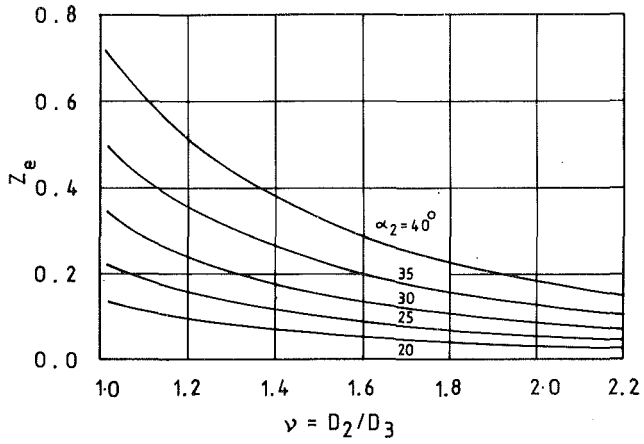

Fig. 3 Exit loss coefficient Z_e as a function of diameter ratio $\nu = D_2/D_3$ with the absolute inlet flow angle α_2 as parameter

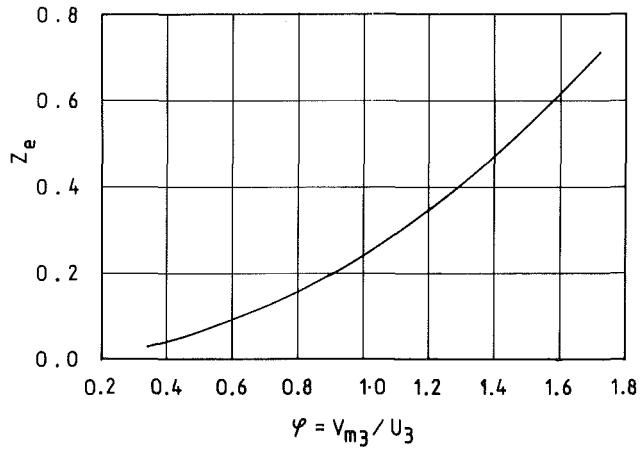

Fig. 4 Exit loss coefficient Z_e as a function of stage flow coefficient $\phi = V_{m3}/U_3$ with the absolute inlet flow angle α_2 as parameter

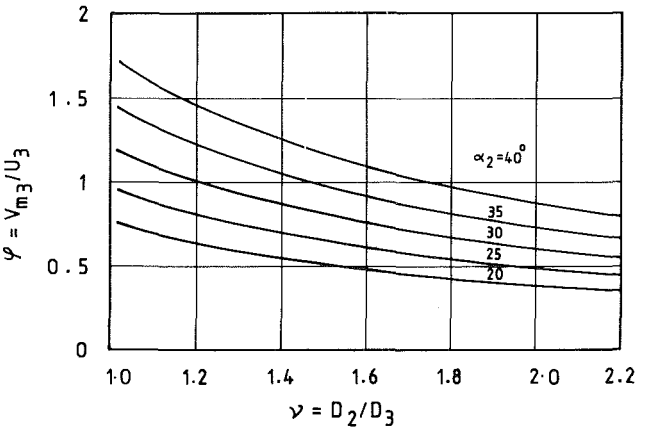

Fig. 5 Stage flow coefficient $\phi = V_{m3}/U_3$ as a function of diameter ratio $\nu = D_2/D_3$ with the absolute inlet flow angle α_2 as parameter

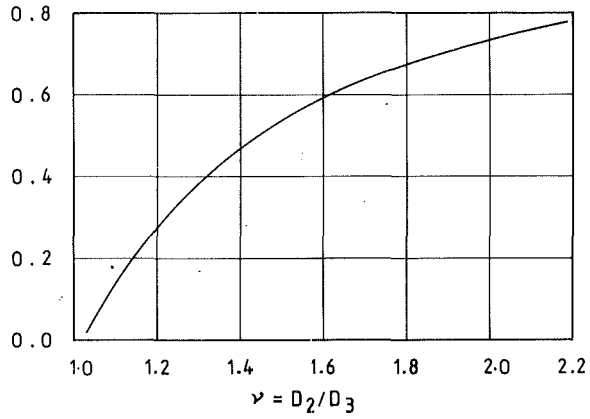

Fig. 6 Degree or reaction r as a function of diameter ratio $\nu = D_2/D_3$ with the absolute inlet flow angle α_2 as parameter

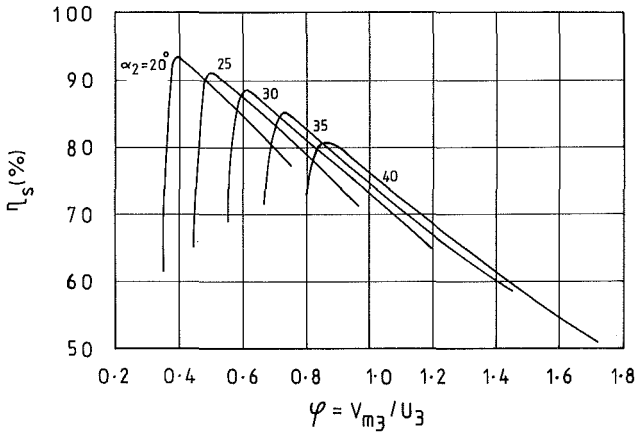

Fig. 7 Stage isentropic efficiency η_s as a function of stage flow coefficient $\phi = V_{m3}/U_3$ with the absolute inlet flow angle α_2 as parameter

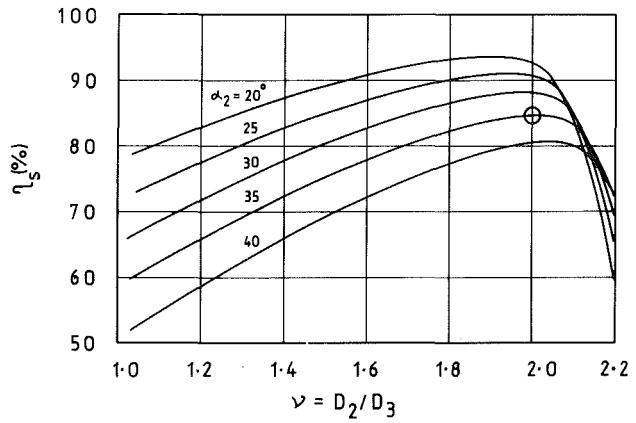

Fig. 8 Stage isentropic efficiency η_s as a function of diameter ratio $\nu = D_2/D_3$ with the absolute inlet flow angle α_2 as parameter: (○) design point

be identified. This requires a systematic parameter study, from which the best combination of the stage parameters with respect to the optimum efficiency is selected. In the following, a single-stage and a two-stage turbine are investigated.

Single-Stage, Double Inflow Radial Steam Turbine

Starting from a turbine frequency $n = 30$ Hz and an exit radius $r_3 = 1.2$ m dictated by the turbine mass flow and the exit blade height, the influence of the stage parameters is investigated. Figure 3 show the exit loss coefficient Z_e versus diameter ratio ν with α_2 as parameter. Increasing ν decreases the exit loss. A large exit radius, however, results in a very large machine size, which is not desirable. In Fig. 4, Z_e is plotted against stage flow coefficient ϕ with α_2 as parameter. As expected, a higher stage flow coefficient ϕ, which decreases with the radius ratio ν (Fig. 5), results in higher exit losses Z_e. Figure 6 shows the course of the degree of reaction r versus radius ratio ν. For the axial velocity ratio $\mu = 1$, the inlet flow

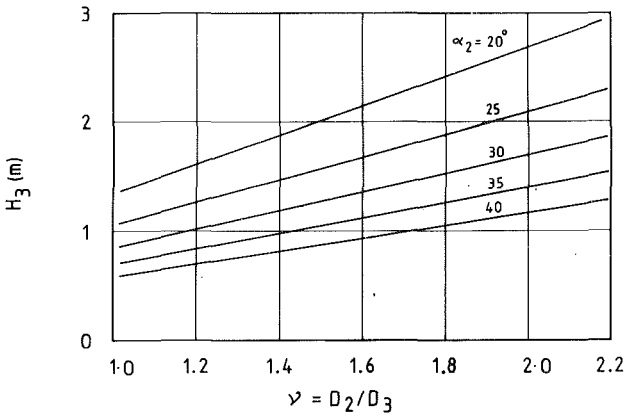

Fig. 9 Exit blade height as a function of diameter ratio $\nu = D_2/D_3$ with the absolute inlet flow angle α_2 as parameter

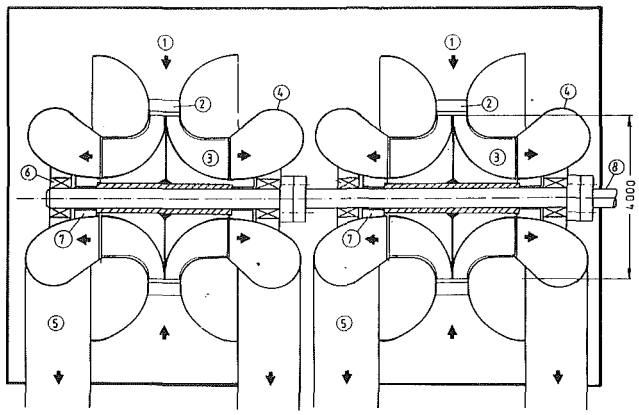

Fig. 11 Two-stage double inflow radial steam turbine, dimensions in mm: 1 = inlet from evaporator, 2 = stator, 3 = rotor, 4 = exit diffuser, 5 = exit pipe, 6 = bearing, 7 = sealing, 8 = coupling; number of blades = 31

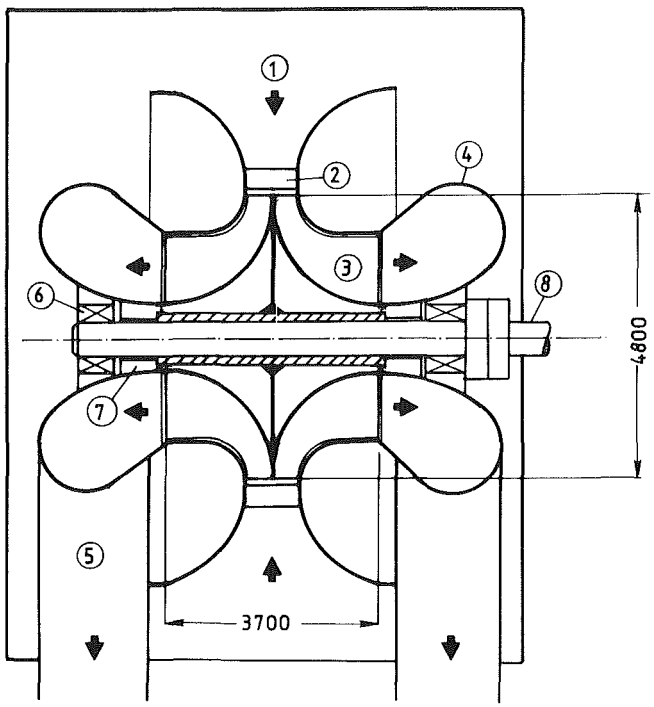

Fig. 10 Single-stage double inflow radial steam turbine, dimensions in mm: 1 = inlet from evaporator, 2 = stator, 3 = rotor, 4 = exit diffuser, 5 = exit pipe, 6 = bearing, 7 = sealing, 8 = coupling; number of blades $n = 23$

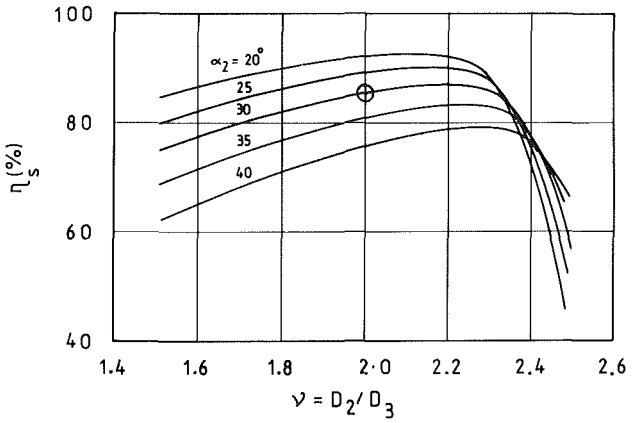

Fig. 12 Stage isentropic efficiency η_s as a function of diameter ratio $\nu = D_2/D_3$ with absolute inlet flow angle α_2 as parameter: (○) design point

angle α_2 has no influence on the degree of reaction r. The stage isentropic efficiency η_s versus the flow coefficient ϕ with α_2 as parameter is shown in Fig. 7. The optimum efficiency decreases with increasing inlet flow angle α_2. Detailed information about the efficiency and the geometry is given in Figs. 8 and 9. The most significant parameters determining the efficiency and the geometry of the turbine stage are radius ratio ν and inlet flow angle α_2. As shown in Fig. 8, the maximum efficiency occurs at relatively high radius ratio ($\nu \simeq 2.0$) and low inlet flow angle ($\alpha_2 = 20$). A high radius ratio causes an increase in overall size of the machine, whereas a small inlet flow angle results in a very high exit blade height. The optimum solution with an acceptably high efficiency and size is a compromise between these two opposite tendencies. As shown in Fig. 8, such a solution is found for a diameter ratio $\nu = 2$ and inlet flow angle $\alpha_2 = 35$ deg with maximum efficiency $\eta_s = 84.8$ percent. The corresponding turbine configuration with a total mass flow $\dot{m} = 26.27$ kg/s is shown in Fig. 10. By keeping the inlet flow angle $\alpha_2 = 35$ deg = const, a reduction of the diameter ratio ν causes a decrease in blade height, which is associated with a reduction in efficiency. A smaller blade height with a reasonably good efficiency $\eta_s = 82.18$ percent can be obtained by $\nu = 1.8$ and $\alpha_2 = 35$ deg.

Two-Stage, Double Inflow Radial Steam Turbine

A simple and economic solution to reduce the size and increase the output of the turbine is the multistage configuration. In this case, identical stages can be utilized that are designed for the same inlet and exit conditions. Figure 11 shows a two-stage configuration with two separate inlet and exits. As shown in Fig. 12, for an exit radius $r_3 = 1$ m, $\nu = 2$, and $\alpha_3 = 30$ deg, a reasonably high efficiency $\eta_s = 84.7$ percent could be achieved.

Conclusion

In this paper the thermo-fluid design concept of a low-pressure radial inflow steam turbine for the Open-Cycle Ocean Thermal Energy Conversion (OTEC) is described. For the optimum design consideration, the necessary theoretical tools are developed and applied to a single and a two-stage, double inflow, radial steam turbine. For a single-stage turbine with output $P = 2.8$ MW, total mass flow $\dot{m} = 26.27$ kg/s, $n = 30$ Hz, $\mu = 1$, $\nu = 2$, $r_3 = 1.2$ m, and $\alpha_2 = 35$ deg, an isentropic stage efficiency $\eta_s = 84.8$ percent was calculated. With respect to blade height reduction, an alternative solution was presented. The design concept enables the turbine power

augmentation by using the multistage configuration. For a two-stage turbine with the same output and frequency as the single-stage turbine with $\mu = 1$, $\nu = 2.0$, $r_3 = 1.0$ m, $\alpha_2 = 30$ deg, and total mass flow $\dot{m} = 26.38$ kg/s, a reasonably high isentropic efficiency $\eta_s = 84.7$ percent was achieved.

Acknowledgments

The author expresses his gratitude to Mr. Shelpuk, manager of the SERI Ocean Program, for financial support for this project.

References

Ainley, D. G., and Mattieson, G. C. R., 1955, "An Examination of Flow and Pressure Losses in Blade Rows of Axial Flow Turbines," ARC-R&M.

Apte, A., 1981, "Ocean Thermal Energy Conversion Reference Manual," PRC R-4017, PRC System Services, McLean, VA.

Balje, O. E., and Binsley, R. L., 1968, "Axial Turbine Performance Evaluation Part A: Loss-Geometry Relationship," ASME *Journal of Engineering for Power*, Vol. 90.

Berg, H., 1973, "Untersuchungen über den Einfluss der Leistungszahl auf Verluste in Axialturbinen," Dissertation der Technischen Hochschule Darmstadt, D17, Federal Republic of Germany.

Cloude, G., 1930, *Mech. Engng.*, Vol. 52, pp. 1039–1044.

Cloude, G., and Boucherot, P., 1935, "Methods and Apparatus for Obtaining Power From Sea Water," U.S. Patent No. 3,006,985.

Cohen, R., 1980, "Electric Power Generation, Ocean Thermal Energy Conversion," Solar Energy Technology Handbook, Part B, W. C. Dickinson and P. N. Chereminsinof, eds., Marcel Dekker, Inc., New York–Basel, pp. 379–438.

Cohen, R., 1982, "Energy From the Ocean," *Phil. Trans. R. Soc. London, A*, Vol. 307, pp. 405–437.

Craig, H. R. M., and Cox, H. J. A., 1971, "Performance Estimation of Axial Flow Turbines," *Proc. Inst. Mech. Engrs. 1970–71*, Vol. 185, pp. 32–71.

CREARE, 1985, "Design and Cost Study of Critical OC-OTEC Plant Components," Final Report (unpublished), SERI Contract No. XX-5-05001-1.

Deic, M. E., and Trojanovsky, B. M., 1973, *Untersuchung und Berechnung axialer Turbinenstufen*, VEB Verlag Technik, Berlin, German Democratic Republic.

Futral, S. M., and Holski, D. E., 1970, "Experimental Results of Varying the Blade-Shroud Clearance in a 6.02-inch Radial-Inflow Turbine," NASA TN D-5513.

Kofskey, M. G., and Nusbaum, W. J., 1972, "Effects of Specific Speed on Experimental Performances of a Radial-Inflow Turbine," NASA TN D-6605.

Lavi, A., 1980, "Energy," *The International Journal*, Vol. 5, No. 6, Pergamon Press, New York.

Parsons, K., Bharathan, D., and Althof, J., 1985, "Thermodynamic System Analysis of Open-Cycle Ocean Thermal Energy Conversion (OTEC)," SERI/TR-252-2234, Dec85-016867.

Penny, T., Bharathan, D., Althof, J., and Parsons, B., 1984, "Open-Cycle Ocean Thermal Energy Conversion (OTEC) Research: Progress Summary and Design Study," ASME Paper No. 84-WA/SOL-26.

Pfeil, H., 1964, "Beitrag zur optimalen Auslegung von Axialschaufelgittern," Dissertation Darmstadt, D17, Federal Republic of Germany.

Pfeil, H., 1969, "Optimale Primärverluste in Axialgittern und Axialstufen von Strömungsmaschinen," *VDI-Forschungsheft*, Vol. 535.

Prandtl, L., and Tietjens, O. G., 1934, *Applied Hydro- and Aeromechanics*, Dover Publications, Inc., New York.

Roeder, A., 1969, "Experimentelle Bestimmung der Einzelverluste in einer einstufigen Versuchsturbine," *Mitteilung des Institutes für Thermische Turbomaschinen der Eidgenissischen Technischen Hochschule Zürich*, No. 15, Switzerland.

Rohlik, H. E., 1968, "Analytical Determination of Radial Inflow Turbine Design Geometry for Maximum Efficiency," NASA TN D-4384.

Schobeiri, T., 1988, "Lecture Notes on Turbomachinery," Graduate Course Texas A&M University, Turbomachinery Laboratory, Spring 1988.

Schobeiri, T., 1985, "Einfluß der Hinterkantenaus-blasung auf die hinter den gekühlten Schaufeln entstehenden Mischungsverluste," *VDI-Zeitschrift Forschung im Ingenieurwesen*, Vol. 51, No. 1.

SERI-TEXAS A&M Research Contract No. HX-7-07262-2, 1988.

Traupel, W., 1977, *Thermische Turbomaschinen*, Vol. I, No. 3, Auflage, Springer-Verlag, New York–Heidelberg–Berlin.

Triebnig, H., and Mukherjee, D. K., 1966, "Über Verluste in Axialturbinenstufen und die Möglichkeiten einer optimalen Auslegung," *VDI-Zeitschrift*, Vol. 6, No. 7.

Utz, C., 1972, "Experimentelle Untersuchungen der Strömungsverluste in einer Mehrstufigen Axialturbine," *Mitteilung des Institutes für Thermische Turbomaschinen der Eidgenissischen Technischen Hochschule Zürich*, No. 19, Switzerland.

Westinghouse Electric Corporation, 1979, "100 MW OTEC Alternate Power Systems," Final Report, Contract No. EG-77-C-05-1473.

Wolf, H., 1961, "Die Randverluste in geraden Schaufelgittern," *Wissenschaftliche Zeitschrift der Technischen Hochschule Dresden*, Vol. 10, No. 2.

Zweifel, O., 1945, "Die Frage der optimalen Schaufelteilung bei Beschaufelungen von Turbomaschinen insbesondere bei grosser Umlenkung in den Schaufelreihen," *BBC-Mitteilung*, Dec.

W. Tabakoff
Fellow ASME

A. N. Lakshminarasimha
Assoc. Mem. ASME

M. Pasin
Graduate Student.

Department of Aerospace Engineering and Engineering Mechanics,
University of Cincinnati,
Cincinnati, OH 45221

Simulation of Compressor Performance Deterioration Due to Erosion

Experimental results obtained from cascades and single-stage compressor performance tests before and after erosion were used to test a fault model to represent erosion. This model was implemented on a stage stacking program developed to demonstrate the effect of erosion in a multistage compressor. The effect of individual stage erosion on the overall compressor performance is also demonstrated.

Introduction

The vulnerability of high-performance aircraft, ship, and power plant gas turbines to particle-laden flows is of serious concern to both manufacturers and users of these turbomachines. In the case of aircraft operating in a particulated environment, these particulates are usually sand or volcanic ash. In addition, during the winter airport runways are sprayed with salt particles. These particles enter the engine during landing and take-off. Gas turbines in marine applications are subjected to salt spray and those in power plants to fly ash and other industrial pollutants. Under certain flow conditions, these particles can severely erode the compressor blades. This is of serious concern to gas turbine users due to a reduction in power output, costly fuel expenses, frequent overhaul periods, and in some instances the safety of the operation itself.

According to Upton (1974), the following particulate air loadings are listed for different areas:

Country, coastal, and industrial 0.01–0.1 ppm by weight
Desert 0.1–700 ppm by weight

A gas turbine uses, roughly, half a ton of air for each one horsepower (hp) output for every 24 h of operation. If only one ppm of solid enters the compressor, a 10,000 hp unit will ingest 10 lb of foreign material every 24 h (Upton, 1974). With such a high rate of foreign particle ingestion, even a highly efficient filtering system can mitigate but not eliminate the problem of erosion, which represents a permanent loss of performance. Usually, the erosion of the engine components is associated with changes in the airfoil profiles and an increase in the overall surface roughness. Tabakoff (1984) has reviewed experimental and analytical aspects of various effects of erosion in turbomachines. Balan (1984) has reported detailed investigations of erosion pattern, change in the blade shape, surface roughness, and their consequences on the compressor cascade aerodynamic performance. These studies are mainly concerning the effect of performance deterioration due to erosion in cascades and single-stage compressors. However, it is the effect of erosion in multistage compressors that is of interest to gas turbine users and for Engine Health Monitoring (EHM) applications. Primary concern for such an application is that the developed prediction method should be simple, and results have to be explicitly presented. Also it should be noted that users will be more interested in the trend of performance deterioration, rather than accuracy of the predicted results. Thus a clear need exists to use a simple method to simulate erosion in compressors.

The overall performance of a gas turbine engine is governed by the performance of its individual components. Thus, if a fault in its individual components (e.g., compressors, turbines) can be simulated, then its effect on the overall performance can be evaluated by matching calculations. Earlier works used scaling of the individual component characteristics to represent performance degradation, and for the development of fault matrices. The current trend (Saravanamuttoo and Lakshminarasimha, 1985; Lakshminarasimha and Saravanamuttoo, 1986; Muir et al., 1989; Aker and Saravanamuttoo, 1989) however is to develop procedures to scale the subcomponent (individual stages in a multistage compressor) for a particular cause of degradation and to combine them together to develop a deteriorated component (compressor) performance map. This procedure has been successfully applied to fouling and Foreign Object Damage (FOD). In a recent work (Batcho et al., 1987), this method was also extended to the simulation of erosion. Fouling and FOD deterioration models are based on the field observations and an heuristic understanding of the behavior of the compressor stages. However detailed experimental data both for cascade and single-stage compressors are available for compressor erosion simulation (Bammert and Woelk, 1980; Tabakoff and Balan, 1981; Tabakoff, 1986). In the present work, the effectiveness of a simple fault model, which can be used to alter the stage characteristics to simulate the performance degradation due to erosion, is illustrated. The experimental and simulation results describing the effects of erosion are presented for both cascade and single-stage compressor. The effect of single-stage erosion on a multistage compressor is illustrated using the stage stacking method. Interpretations of the results are summarized.

Contributed by the International Gas Turbine Institute and presented at the 34th International Gas Turbine and Aeroengine Congress and Exhibition, Toronto, Ontario, Canada, June 4–8, 1989. Manuscript received at ASME Headquarters January 27, 1989. Paper No. 89-GT-182.

Effect of Erosion on Performance

The basic aerodynamic performance degradation of a gas turbine engine, due to particulate flow, can be divided into two categories: temporary loss of performance during the period of particle ingestion (Tabakoff and Balan, 1981), and a permanent loss of performance due to blade erosion. Wulf (1980) points out that within 6000–8000 h of engine operation, some compressor blades had blunt leading edges and increased surface roughness. Due to bluntness of the leading edge alone, specific fuel consumption (sfc) had increased by almost 0.38 percent. The average surface roughness on the concave surface of the blades had increased from 55 μin. to 120 μin., and caused sfc to increase by another 0.13 percent. Similar observations are also reported by Olsso and Sallee (1979) and Jay and Todd (1979). While low-pressure compressor erosion losses are due to surface roughness and tip clearance, erosion losses in high-pressure compressor are created by blade length reduction and loss of air seal materials (Schwind and McMillan, 1979) in addition to increase in roughness. The physical blade damages due to the erosion for the compressor reported by Schwind and McMillan (1979) are summarized below.

Stage	Region	Comment
1	tip	leading- and trailing-edge blunting
1	midspan	leading- and trailing-edge blunting
1	hub	leading- and trailing-edge blunting
3	tip	chord reduction
6	tip	chord reduction, airfoil thinning
8	tip	chord reduction
8	midspan	leading-edge blunting
11	tip	great chord reduction, leading- and trailing-edge thinning
11	midspan	chord reduction, trailing edge thinning and loss of camber
13	tip	great chord reduction, trailing-edge loss of camber
13	midspan	great chord reduction, trailing-edge loss of camber

From the above description and from the many detailed cascade and single-stage compressor tests at the University of Cincinnati, typical regions of the blade erosion can be depicted as shown in Fig. 1. In general, the blade erosion can be described as blunting of leading edge, thinning of the trailing edge, and as a general increase in the surface roughness. These profile and surface quality changes alter the blade boundary layer development, causing an increase in the total pressure loss across the blade row and a decrease in the overall efficiency of the power plant.

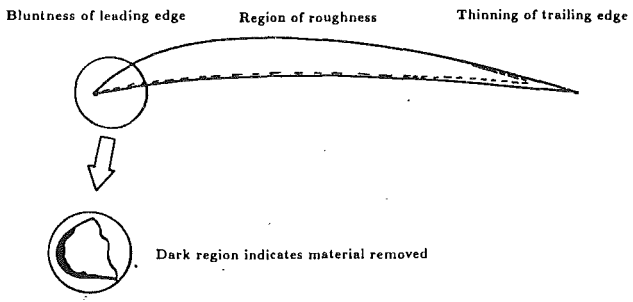

Fig. 1 Typical erosion pattern of a compressor blade

Erosion Simulation

Blade erosion is a complex function of the physical properties of the particles and blade material such as particle mass flow, particle size, velocity and direction of impinging particles, geometry, and the material of the blade row. In view of this complexity, the prediction of erosion and the change in compressor performance present a difficult problem. The usual method of calculation has two parts (Balan, 1984). First the development of roughness and its distribution is calculated by using particle trajectory and erosion calculations. The additional total pressure loss coefficient due to roughness is then calculated using an inviscid–viscous interaction technique. This procedure can be applied to a two-dimensional cascade. Application of this procedure even to a single-stage compressor is difficult and tedious. For health monitoring applications, the fault model used for performance deterioration calculation should be simple and therefore simplifying assumptions are essential.

It is evident that the stage stacking method has been increasingly used for multistage compressor analysis. It has the advantages of introducing faults in the individual stages, so that its cumulative effect on the whole compressor can be seen by stage stacking. Thus the compressor is viewed as a component and each of its individual stages as subcomponents. The performance of individual stages can be simulated by using rotor blade inlet and exit velocity diagrams, normalized with respect to tip blade speed. They are often presented in terms of:

(*a*) Flow coefficient (ϕ):

$$\phi = C_a/U \tag{1}$$

(*b*) Pressure coefficient (ψ):

$$\psi = \frac{C_p T_{0s}(Pr_s^{\gamma-1/\gamma}-1)}{U^2} \tag{2}$$

Nomenclature

ϕ = flow coefficient
C_a = axial velocity
P = total pressure
U = blade speed
T_{os} = stage inlet total air temperature
ΔT_o = increase in stage total temperature
τ = stage temperature ratio
Pr = stage pressure ratio
ψ = total pressure coefficient
η = efficiency
C_l = lift coefficient
ΔC_l = change in lift coefficient
C = chord
ξ = loss coefficient
β = relative fluid angle
α_m = particle loading ratio
λ = tip clearance/blade height
σ = $1-0.3\lambda$
M_{ts} = sand mass flow parameter
t = time of exposure of cascade to sand
ρ = density
$\frac{\Delta W}{W_{des}}$ = reduction in compressor mass flow rate
W_{des} = compressor design mass flow rate
θ = normalized temperature ratio with respect to sea level conditions
δ = normalized pressure ratio with respect to sea level conditions
τ = temperature ratio across a compressor stage

Subscripts

t = tip
h = hub
m = mean
i = inlet
is = isentropic
I = stage number
N = nth stage

(*c*) Efficiency (η):

$$\eta = \frac{T_{0s}(Pr_s^{\gamma-1/\gamma}-1)}{\Delta T_0} \tag{3}$$

Faults of different types in a compressor stage can be introduced by developing appropriate expressions for them in terms of the above factors. Recently Lakshminarasimha et al. (1985) introduced a model to simulate fouling. Batcho et al. (1987) similarly developed a model for predicting the change in lift coefficient (ΔC_l) due to erosion. It is a simple model based on classical thin airfoil theory. Since erosion is usually accompanied by blunting of leading edge and trailing edge thinning, an expression is developed to relate the change in lift coefficient (ΔC_l) to a reduction in chord (ΔC) as:

$$\Delta C_l = 1.5\pi E(\Delta C) \tag{4}$$

where

$$E(\Delta C) = \frac{Z_0/C}{1-\Delta C/C}$$

This reduction in lift coefficient can be used to calculate the reduction in pressure coefficient and an increase in the loss coefficient.

Equally important loss due to erosion occurs because of increased tip clearance and can be calculated using (Batcho, 1987)

$$\xi_{\text{TIP}} = \left[\frac{0.759}{\bar{r}/r_t}\sqrt{\frac{\phi^2\sigma C_L}{\sin^3\beta_m\cos\beta_m}} + \frac{1.17\phi}{\sigma^2\bar{r}/r_t\tan\beta_m}\right]\psi_{is}\lambda \tag{5}$$

The increase in this loss can be again obtained in terms of a reduction in pressure coefficient. Finally, for each stage altered, stage performance can be obtained by subtracting the reduction in the pressure coefficient due to erosion (or any other fault) from that of the uneroded pressure coefficient.

$$\psi_{\text{eroded}} = \psi_{\text{uneroded}} - (\Delta\psi)_{\text{erosion}} \tag{6}$$

Knowing the chord reduction and the increase in the tip clearance for each stage, the cumulative effect of erosion on overall compressor performance could be illustrated by using the stage stacking technique.

The uneroded stage characteristics can be obtained from experimental data or can be calculated if stage design pressure ratio and efficiency are known (Koch and Smith, 1976). If individual stage characteristics are available, then cumulative compressor performance can be obtained by a stage stacking procedure, using the following steps:

(*i*) Calculate the flow coefficient from the compressor mass flow and speed.

(*ii*) From stage characteristics obtain the overall adiabatic efficiency (η_{ad}) and pressure coefficient (ψ) for stage flow coefficient (ϕ).

(*iii*) Calculate the representative mean line velocity diagram at the rotor outlet and then the overall total pressure (P) and temperature (T) at the stage outlet, and use these values for the next stage.

Since the stages in a multistage compressor are coupled together, the compatibility of mass and speed are applicable. Thus

$$\left(\frac{W\sqrt{\theta}}{\delta}\right)_{N+1} = \left(\frac{W\sqrt{\theta}}{\delta}\right)_N \frac{\sqrt{\tau}}{Pr_N} \tag{7}$$

where Pr is the pressure ratio, τ is the temperature ratio, θ and δ are normalized temperature and pressure with respect to standard sea level conditions, respectively. The overall compressor performance consists of a map of adiabatic efficiency and pressure ratio versus flow for various speeds

$$\left(\frac{U_t}{\sqrt{\theta}}\right)_{N+1} = \left(\frac{U_t}{\sqrt{\theta}}\right)_N \frac{r_{t_{N+1}}}{r_{t_n}} \frac{1}{\sqrt{\tau_N}} \tag{8}$$

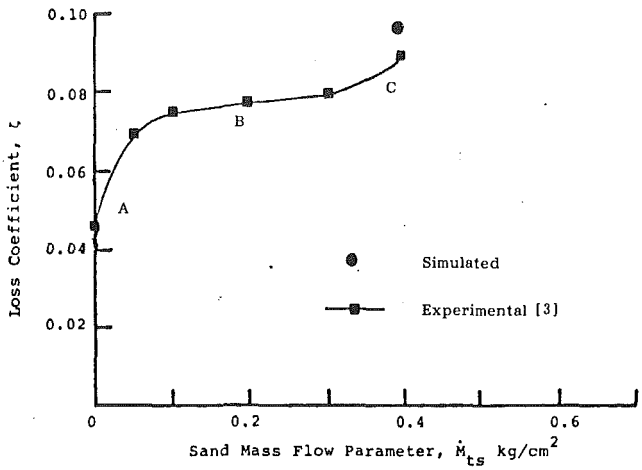

Fig. 2 Effect of erosion on cascade losses

and the cumulative performances are obtained using

$$Pr_{\text{tot}} = Pr_{\text{I}} + Pr_{\text{II}} \ldots Pr_N \tag{9}$$

$$\tau_{\text{tot}} = \tau_{\text{I}} + \tau_{\text{II}} \ldots \tau_N \tag{10}$$

$$\eta_{\text{tot}} = \frac{(Pr_{\text{tot}})^{\gamma-1/\gamma}-1}{\tau_{\text{tot}}-1} \tag{11}$$

In this work, the above model is checked first with cascade erosion tests and then with single-stage compressor performance tests. Finally the results are also presented to illustrate the effect of erosion on a multistage compressor performance (Milner et al., 1975).

(a) Effect of Erosion on Cascade Performance. The cascade performance is estimated by the loss in the total pressure across the cascade. Erosion experiments were carried out using 50.8 mm chord NACA 65-(10)-10 cascade blades and using 165-μm-dia sand. The result of measured increase in loss coefficient as a function of cumulative sand mass flow through the cascade for an inlet air angle of 45 deg and a stagger angle of 25 deg is illustrated in Fig. 2. In the figure, the sand mass flow parameter (M_{ts}) is defined as

$$M_{ts} = \alpha_m t \rho_i C_{a_i}$$

where ρ_i, C_{a_i} are the density and axial velocity of the fluid at the cascade inlet, α_m is the particle mass concentration, and t is the cascade exposure time to particles. From inspection of the experimental loss coefficient curve in Fig. 2 it can be seen that there are three distinctive regions (A, B, and C) of loss due to the effect of erosion. In region A, the loss coefficient increases steeply and reaches a plateau, while in region B, the loss coefficient remain essentially constant. In region C, the loss coefficient increases steeply once again. The last point of the curve shows that the loss coefficient is more than twice that of an uneroded blade.

Measurements after cascade erosion tests when the sand mass flow parameter was 0.4 kg/cm^2 indicated an increase in surface roughness from 10 to 20 μin. and a reduction in chord of 1.6 percent (Balan, 1984). The loss due to increased surface roughness was calculated using the procedure given by Koch and Smith (1976). This loss was calculated as 0.022. The increase in the loss due to a reduction in chord was evaluated using the procedure of Batcho et al. (1987) as 0.04. The cumulative loss due to roughness and that due to reduction in chord in addition to the loss of uneroded cascade was found to be 0.096. This is plotted against experimentally evaluated loss in Fig. 2. It can be seen that there is a good agreement between

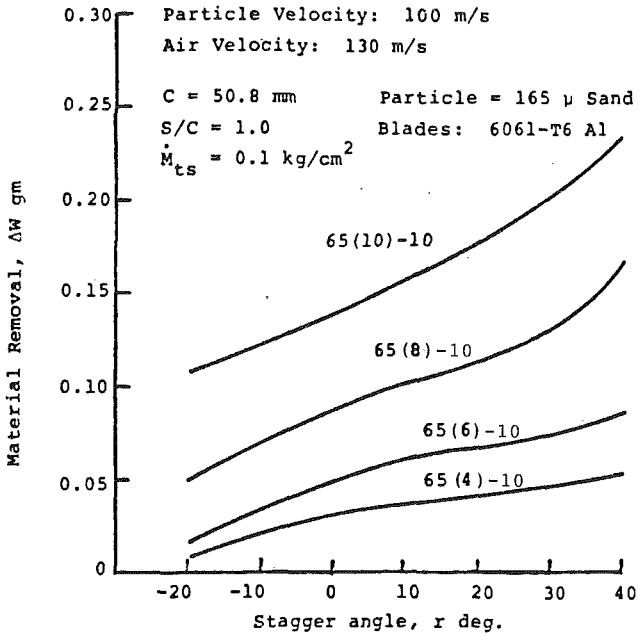

Fig. 3 Effect of cascade parameters on erosion of 65 series of blades (Balan, 1984)

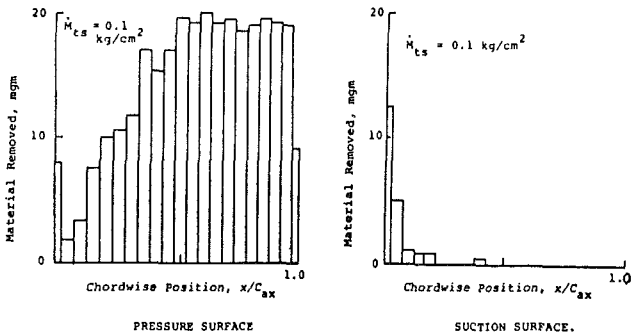

Fig. 4 Computed material removal on the blade surface of 65(10)10 cascade. $\gamma = 50$ (Balan, 1984)

measured and simulated results, considering the simplicity of the procedure.

The only disadvantage of the above procedure is that the experimental details of the surface roughness development and reduction of the chord due to erosion are necessary. At the University of Cincinnati research has been conducted on the effect of erosion on the performance as well as on the *material erosion through erosion tests and particle rebound characteristics* (Tabakoff and Hussein, 1971a, 1971b; Grant and Tabakoff, 1975; Tabakoff, 1984; Hamed, 1986; Hamed et al., 1986). This procedure, based on the particle trajectory calculations and the empirical parameters obtained using the particle rebound characteristics, could be adopted to calculate the parameters necessary to simulate erosion using the stage stacking technique described above. Figure 3 gives a summary of the effect of stagger on the erosion of the NACA 65 series airfoils (Balan, 1984). The 65-(4)-10 airfoil has the least camber, while the 65-(10)-10 airfoil has the highest camber. The particle velocities of 100 m/s and 130 m/s were assumed in the analysis. The inlet and exit angles were chosen for optimum performance at the given stagger setting. It can be observed from the figure that the higher erosion occurs for the positive stagger angles while the lowest erosion occurs at high negative stagger angles. Under identical conditions, the blades with higher cambers are subjected to higher erosion than the blades with lower camber.

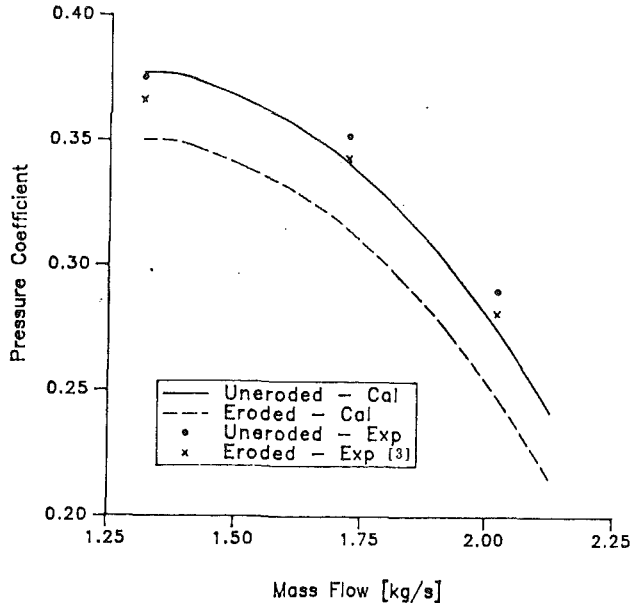

Fig. 5 Simulation of effect of erosion on 1-stage compressor performance

In addition, the theoretical analyses yield information on the amount of material removed along the blade surfaces. Figure 4 shows the computed material removal along the blade surface of the 65-(10)-10 cascade (a typical high-efficiency blade profile used in compressors). There is a considerable amount of material removal near the leading edge on the blade pressure surface. The amount of material removed decreases to a minimum in the region immediately following the leading edge and then increases to a nearly constant value on the rear half of the blade pressure surface. The blade suction surface is not subjected to any significant erosion except for the region near the leading edge. These predictions were in conformation with the detailed experimental results.

(b) Effect of Erosion on Single-Stage Compressor Performance. Before the effect of erosion on multistage compressor performance can be demonstrated, the predictive capability of the erosion fault model was tested with the experimental results from a single-stage compressor. The test compressor has the following design specifications:

Mass flow: 3.67 kg/s
Tip diameter: 300 mm
Speed: 9000 rpm
Hub-to-tip ratio: 0.75
Blade profile: NACA 65-(10)-10
Blade chord: 50.8 mm
Rotor stagger angle: 41 deg

The results of erosion experiments on the above compressor are shown in Fig. 5. It can be observed from this figure that there is a decrease in the pressure coefficient of 2.4 percent at a mass flow of 1.36 kg/s, 3.32 percent at a mass flow of 1.732 kg/s, and 4.27 percent at a mass flow of 2 kg/s after an injection of 25 kg of sand through the machine. Physical damage of erosion on the blades was measured as an average increase in tip clearance from 0.3 in. to 0.5 in. and a reduction in the blade chord of 1.6 percent. The increase in losses due to chord reduction and tip clearance were calculated using the procedure given by Batcho et al. (1987). The stage characteristics themselves were developed using the procedure given by Lakshminarasimha and Saravanamuttoo (1985). The results from simulation are shown in addition to the experimental results in Fig. 5. Both the experimental and simulation indicate a general shift in the pressure coefficient line to a lower value, while the results from the simulation predict higher losses. This can be expected since the loss model is based on

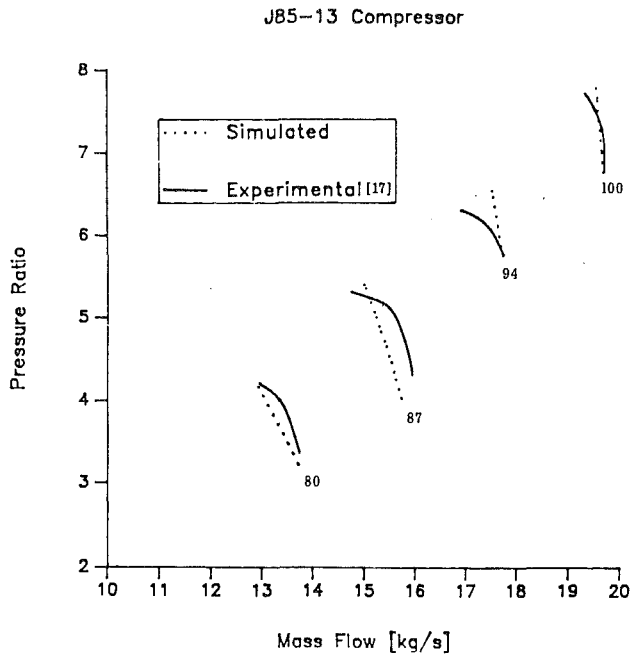

Fig. 6 Simulation of J85-13 eight-stage compressor performance

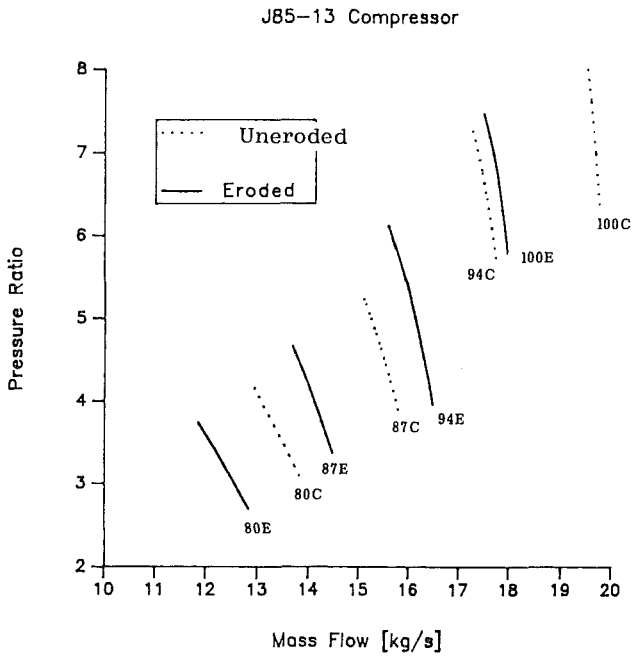

Fig. 7 Effect of erosion on J85-13 compressor performance

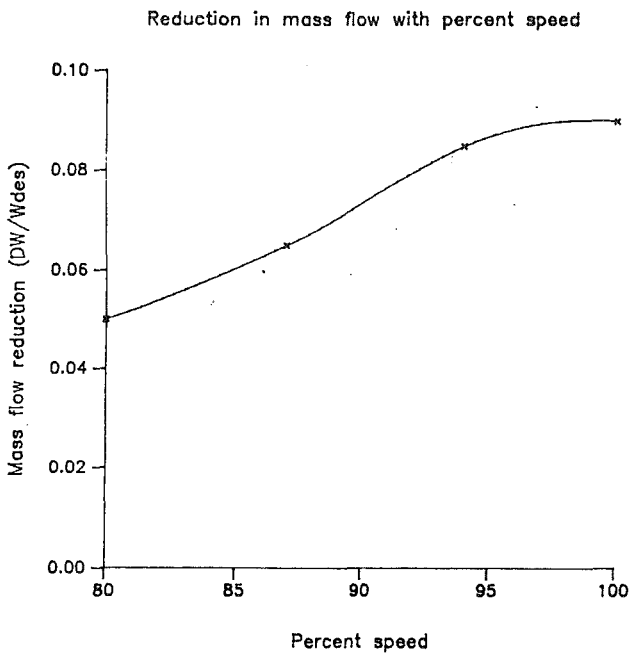

Fig. 8 Reduction in mass flow rate due to erosion

the cascade performance. This conservative overprediction of the loss estimated from simulation is safer for Engine Health Monitoring (EHM) applications, where the trend in the performance change is more important than the accuracy of the predicted result.

(c) Erosion Simulation in Multistage Stage Compressors. The real use of the stage stacking method in EHM is to study the cumulative effect of faults of the individual stages in a multistage machine. Having successfully demonstrated the predictive capability of the erosion fault model using cascade and single-stage tests, the next step would be to predict the effect of erosion on the performance of multistage compressors. Schwind and McMillan (1979) have given the details necessary for simulation of the effects of erosion on a multistage compressor by providing both new and eroded blade profile measurements after an extensive wear in airline service. Due to the restrictive nature of the publishable results involved, a different compressor was chosen to illustrate the effects of erosion. In this work, using the compressor data available from Milner et al. (1977), both stage characteristics and compressor map were simulated. The comparison of the present simulation and that of the experimental measurements (Milner, 1977) is shown in Fig. 6. The results indicate a good agreement between simulated and measured results for the case when the compressor blades were not eroded. For the case of eroded compressor performance only a reduction in chord was assumed to be adequate for simulation purposes. Increase in tip clearance was not assumed, due to unavailability of data. Decrease in the blade chord was taken to be in the same proportion as in the compressor of Schwind and McMillan (1982) and is summarized below:

Stage No.	$\Delta C/C$, percent
1	8.2
2	4.2
3	1.6
4	1.6
5	1.9
6	1.9
7	3.9
8	5.7

The results of the simulation are shown in Fig. 7. It can be clearly seen that when the stage characteristics are altered to simulate erosion, the stages match, for the same speed at a lower mass flow rate. Reduction in the pressure rise can also be clearly seen. From Fig. 8 it can be observed that the reduction in the mass flow rate is a function of compressor speed, being higher at higher speeds. These observations are similar to those of Batcho et al. (1987).

The advantage of the stage stacking method is in isolating the effect of individual stages on the overall compressor performance. This can be illustrated as follows. In order to bring out the effect of stage location on the compressor map, the effects of erosion on first and last stage were analyzed separately, while assuming the other stages were not eroded. The results from this calculation are shown in Figs. 9 and 10.

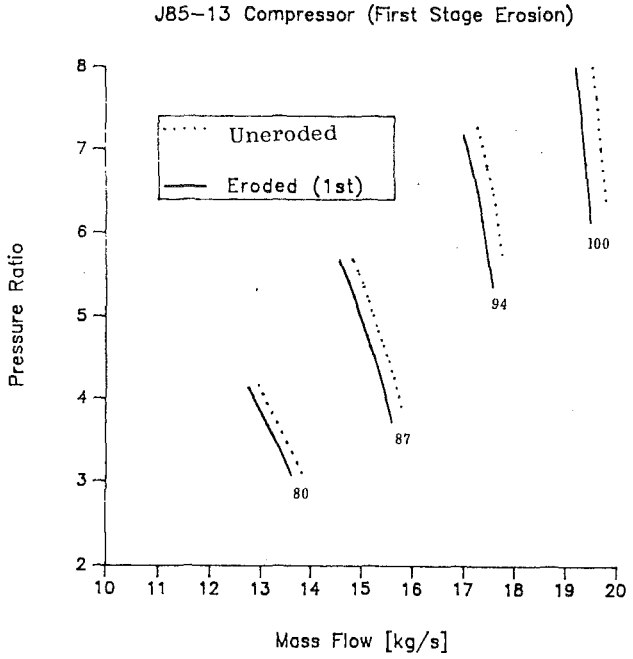

Fig. 9 Effect of first-stage erosion on J85-13 compressor performance

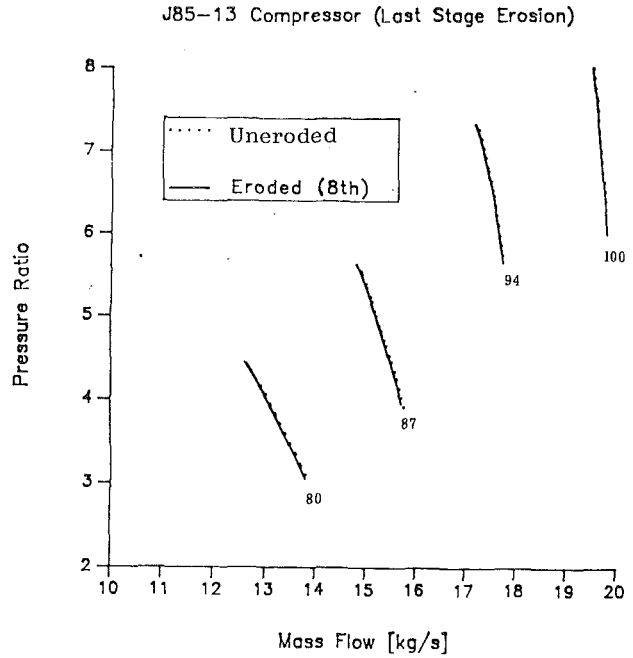

Fig. 10 Effect of last (eighth) stage erosion on J85-13 compressor performance

Reduction of the chord in these two cases was taken to be the same as in the previous case. It can be clearly seen that the first stage erosion has a pronounced effect on the compressor performance deterioration, while the last stage has almost no effect at all. This study suggests that the downtime of a compressor for refurbishment could be reduced substantially if the front stage could be made out of highly erosion resistant material, for these stages have the largest effect on performance.

Conclusions

The effects of erosion in cascades, single-stage, and multistage compressors are described. The potential of the stage stacking technique to study systematically the effect of individual stage erosion in multistage compressor performance is demonstrated. Theoretical prediction of performance deterioration, using an erosion fault model based on chord length reduction, compared well with both cascade and single-stage compressor experimental results. The simulation of erosion indicated that erosion causes both the pressure and the mass flow rate to decrease. In multistage compressors, this reduction was found to be a function of compressor speed and the location of the stage where erosion occurs. The reduction in mass flow rate was found to increase with speed. The front stage was found to affect the overall compressor performance more than the rear stages. The application of particle trajectory and rebound characteristics used to predict the blade material loss pattern indicates that it can also be successfully utilized to obtain parameters necessary in performance simulation to describe the effect of erosion.

References

Aker, G. F., and Saravanamuttoo, H. I. H., 1989, "Predicting Gas Turbine Performance Degradation Due to Compressor Fouling Using Computer Simulation Techniques," ASME *Journal of Engineering for Gas Turbines and Power*, Vol. 111, pp. 343–350.

Balan, C., 1984, "Performance Deterioration of Cascades Exposed to Solid Particles," Ph.D. Dissertation, University of Cincinnati, Cincinnati, OH.

Bammert, K., and Woelk, G. V., 1980, "The Influence of the Blading Surface Roughness on the Aerodynamic Behavior and Characteristics of an Axial Compressor," ASME *Journal of Engineering for Power*, Vol. 102, Apr.

Batcho, P. F., Moller, J. C., Padova, C., and Dunn, M. G., 1987, "Interpretation of Gas Turbine Response Due to Dust Ingestion," ASME *Journal of Engineering for Gas Turbines and Power*, Vol. 109, pp. 344–352.

Grant, G., and Tabakoff, W., 1975, "Erosion Prediction of Turbomachinery Resulting From Environmental Solid Particles," *Journal of Aircraft*, pp. 471–478.

Hamed, A., 1986, "Effect of Particle Characteristics on Trajectories and Blade Impact Patterns," AIAA/ASME 4th Joint Fluid Mechanics, Plasma Dynamics, and Laser Conference, Atlanta, GA, May 12–14.

Hamed, A., Tabakoff, W., and Mansour, M. L., 1986, "Turbine Erosion Exposed to Particulate Flow," ASME Paper No. 86-GT-258.

Jay, A., and Todd, E. S., 1978, "Effect of Steady Flight Loads on JT9D-7 Performance Deterioration," NASA CR-135407.

Koch, C. C., and Smith, J. H., Jr., 1976, "Loss Sources and Magnitudes in Axial Flow Compressors," ASME *Journal of Engineering for Power*, Vol. 98, July.

Lakshminarasimha, A. N., and Saravanamuttoo, H. I. H., 1986, "Simulation of Fouling Using Stage Stacking Techniques," AIAA/ASME 4th Joint Fluid Mechanics, Plasma Dynamics and Laser Conference, Atlanta, GA, May 12–14.

Milner, E. J., et al., 1975, "Performance of a J85-13 Compressor With Clean and Distorted Inlet FLow," NASA-TM-X-3304, Dec.

Muir, D. E., Saravanamuttoo, H. I. H., and Marshall, D. J., 1989, "Health Monitoring of Variable Geometry Gas Turbines for the Canadian Navy," ASME *Journal of Engineering for Gas Turbines and Power*, Vol. 111, pp. 244–250.

Olsson, W. J., and Sallee, G. P., 1979, "Performance Deterioration Based on In-Service Engine Data," NASA CR-159525, Apr.

Saravanamuttoo, H. I. H., and Lakshminarasimha, A. N., 1985, "A Preliminary Assessment of Compressor Fouling," ASME Paper No. 85-GT-153; *Turbomachinery International*, Vol. 26, No. 7.

Schwind, R. G., and McMillan, O. J., 1982, "Blade Erosion Effects on Aircraft Engine Compressor," Nelson Engineering and Research, Inc., Mountain View, CA, Report No. N83-16347.

Tabakoff, W., and Hussein, M., 1971a, "Effect of Suspended Solid Particles on the Properties on Cascade Flow," *AIAA Journal*, Vol. 9, Aug.

Tabakoff, W., and Hussein, M. 1971b," Pressure Distribution on Plates in Cascade Nozzle for Particulated Flow," *AIAA Journal of Aircraft*, Vol. 8, No. 9.

Tabakoff, W., and Balan, C. 1981, "Effects of Solid Particles Suspended in Fluid Flow Through an Axial Flow Compressor Stage," presented at the 5th International Symposium on Air Breathing Engines, Bangalore, India, Feb. 16–21.

Tabakoff, W., 1984, "Review – Turbomachinery Performance Deterioration Exposed to Solid Particulate Environment," ASME *Journal of Fluids Engineering*, Vol. 106, June.

Tabakoff, W., 1986, "Compressor Erosion and Performance Deterioration," AIAA/ASME 4th Joint Fluid Mechanics, Plasma Dynamics, and Laser Conference, Atlanta, GA, May 12–14.

Upton, A. W. J., 1974, "Axial Flow Compressor and Turbine Blade Fouling: Some Causes, Effects and Cleaning Methods," First Symposium in Gas Turbine Operations and Maintenance, National Research Council of Canada, Oct.

Wuff, R. H., 1980, "CF6-6D Engine Performance Deterioration," NASA CR-159786, Jan.

Flow in a Centrifugal Fan of the Squirrel-Cage Type

R. J. Kind

M. G. Tobin[1]
Undergraduate Student.

Department of Mechanical and Aeronautical Engineering,
Carleton University,
Ottawa, Ontario, Canada K1S 5B6

This paper presents the results of performance measurements and detailed measurements of the mean flow field at rotor inlet and rotor exit in three squirrel-cage fan configurations. The flow-field measurements were taken with a five-hole probe and yield total pressure, static pressure, and the three components of velocity. Measurements were taken for two casing throat areas and for two different rotors. For each configuration the flow field was measured for flow rates below, near, and above the best-efficiency point. Flow patterns are complex and there is reverse flow through the rotor blading even at the best-efficiency operating condition. Although complex, the main features of flow behavior can be understood. They were common to all three fan configurations.

1 Introduction

Squirrel-cage fans have two main features that distinguish them from other types of centrifugal fan. First, the rotor exit-to-inlet area ratio is unusually large, at about 3:1. Second, the rotor blades are of short chord, typically about 0.1 D_2, and a large number (about 35 or more) are generally used. The latter feature gives rise to the name of this type of fan. In Europe they are sometimes referred to as "drum-rotor fans," again because of the appearance of the rotor. Eck (1973) uses the term "Sirocco fan." Figure 1 illustrates a squirrel-cage fan. Fans of this type are widely used in applications requiring low noise, small size, relatively high capacity, and low cost. Applications include circulating fans for forced air residential heating systems, hair-dryer blowers, and blowers for automobile heater units. Rotor diameters range from about 4 to 40 cm. The rotor blades are generally made of a single thickness of sheet metal with forward curvature to assist in obtaining high capacity at low rotational speeds, and thus with low noise. There are no diffuser vanes.

The large rotor exit-to-inlet area ratio has important aerodynamic consequences. Uniform throughflow, or uniform radial velocity, across the width of the rotor is impossible if the area ratio greatly exceeds unity, which corresponds to $4b/D_1 = 1$. Uniformity would require the flow entering the rotor blades to simultaneously turn to the radial direction and undergo a large deceleration. The static pressure distribution that would be required to turn the flow is incompatible with that associated with a large deceleration, since total pressure must be approximately uniform in the entry region of the rotor. In reality the flow tends to separate at the front of the rotor, as sketched in Fig. 2. The flow is thus highly nonuniform across the rotor. This is a primary cause of the flow complexity in squirrel-cage fans.

An assessment of squirrel-cage fans in relation to other

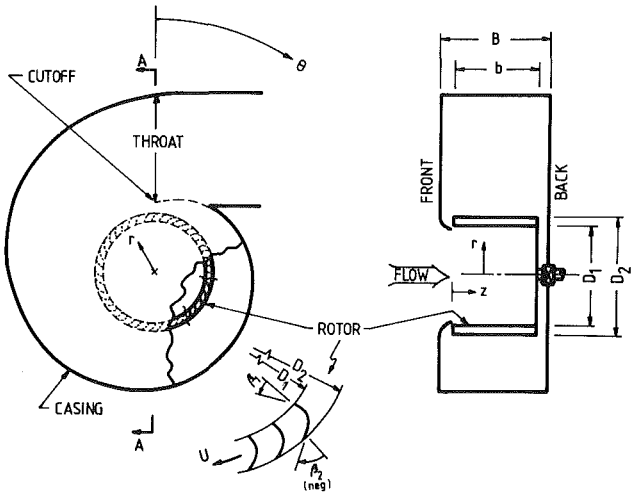

Fig. 1 Diagram of a squirrel-cage fan

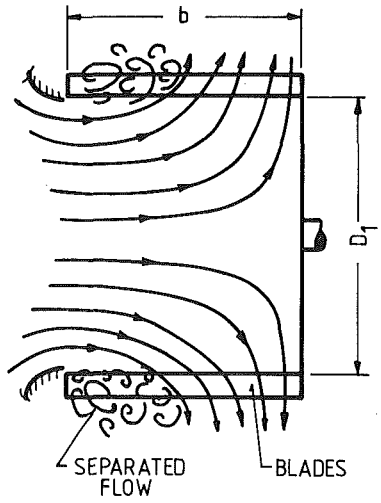

Fig. 2 Sketch of flow into rotor

[1]Present address: GasTOPS Ltd., Gloucester, Ontario, Canada.

Contributed by the International Gas Turbine Institute and presented at the 34th International Gas Turbine and Aeroengine Congress and Exhibition, Toronto, Ontario, Canada, June 4–8, 1989. Manuscript received at ASME Headquarters January 13, 1989. Paper No. 89-GT-52.

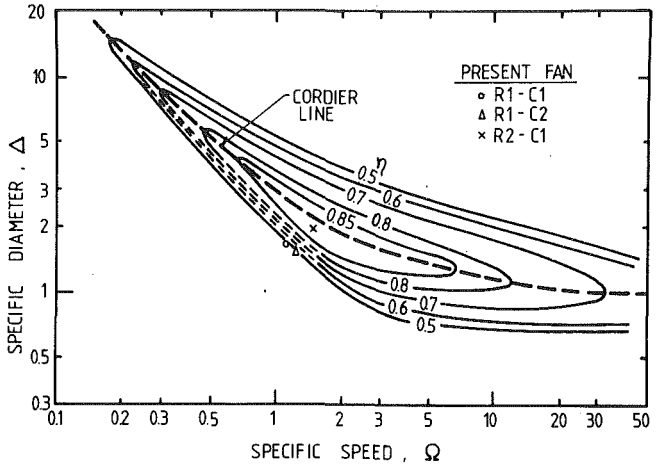

Fig. 3 Specific speed, specific diameter diagram for single-disk pumps and low-pressure-ratio compressors (after Baljé, 1962)

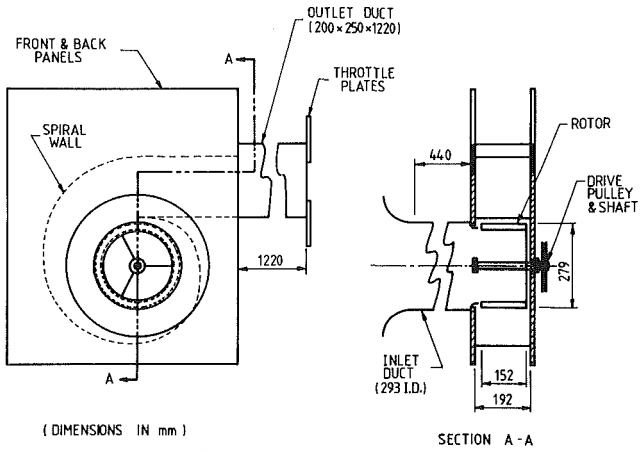

Fig. 4 Diagram of apparatus

types of turbomachinery can be made by evaluating the nondimensional specific speed Ω, and specific diameter Δ (Csanady, 1964). The present Rotor 1-Casing 1 (R1-C1) fan configuration is typical of the type and has $\Omega = 1.1$ and $\Delta = 1.7$.

The specific speed of 1.1 is quite high for a radial flow machine. On a Cordier diagram (Fig. 3), the typical squirrel-cage fan falls significantly below the Cordier line, which defines the correlations between specific speed and specific diameter for maximum efficiency of turbomachines. This reflects the fact that squirrel-cage fans are of relatively small diameter for a given capacity. The small size comes at the price of low efficiency, however, as suggested by Fig. 3.

Table 1 Parameters of the tested fan configurations

Designation	R1-C1	R1-C2	R2-C1
Rotor	rotor 1	rotor 1	rotor 2
D1 (mm)	225	225	229
D2 (mm)	279	279	279
b (mm)	152	152	152
4b/D1	2.7	2.7	2.67
no. of blades	50	50	70
β_1, β_2 (deg.)	0, -65	0, -65	60, 0
blade chord (mm)	32	32	28
blade radius (mm)	30	30	28
blade thickness (mm)	1.0	1.0	0.84
Casing	casing 1	casing 2	casing 1
B (mm)	192	192	192
radius to cutoff (mm)	168	168	168
throat area (m^2)	0.0317	0.0476	0.0317
spiral angle at $\theta = 180^\circ$ (deg.) (area increase linear with θ)	6.0	7.7	6.0
dia. of inlet opening (mm)	240	240	240
inlet lip radius (mm)	25	25	25

This paper outlines an experimental investigation of the flow field in three variants of a squirrel-cage fan. One rotor was tested with two different casings and a second rotor was tested with one of the casings. Table 1 lists the main parameters of the three fan configurations; Fig. 4 gives additional information. A five-hole probe was used to measure mean velocity, flow direction, and total pressure at 64 points inside the rotor ($r/D_2 = 0.30$) and at 48 or more points outside the rotor ($r/D_2 = 0.64$). These measurements were taken at three flow rates, designated HIGH, MED, and LOW for each fan configuration. The MED rate was close to the best efficiency point (BEP) for the R1-C1 and R2-C1 configurations. Approximate flow patterns and distributions of local work input and losses are deduced from these measurements. Overall fan performance was also measured. The measurements were supplemented by flow visualization using smoke.

2 Related Previous Work

Relatively little work on squirrel-cage fans has been reported in the literature.

Eck (1973) presents a design method for rotors; it neglects the separation that tends to occur near the front of the rotor (Fig. 2) and is thus somewhat unrealistic. He presents some performance data that exhibit the relatively high pressure-rise

Nomenclature

b = rotor width
B = casing width
D = rotor diameter
p = nondimensional static pressure
$\bar{p}$ = $(p_1 + p_2 + p_3 + p_4)/4$
p_t = nondimensional total pressure
P = total pressure rise across fan
q = nondimensional dynamic pressure
Q = volume flow rate through fan
r, θ, z = cylindrical coordinates (see Fig. 1)
FP, PL, SP = see equations (1)–(3)
U = blade speed
V = nondimensional flow velocity
β = blade angle measured from radial; β_2 negative when facing forward
γ = flow pitch angle; see Fig. 5
Δ = nondimensional specific size $= (0.5\psi)^{0.25}/(\pi\phi/4)^{0.5}$ at BEP
η = total-to-total efficiency of fan = QP/shaft power
ν = kinematic viscosity
ρ = density
ϕ = nondimensional flow coefficient = $Q/0.25\pi D_2^2 U_2$
ψ = nondimensional total-pressure rise across fan = $P/0.5\rho U_2^2$
Ω = nondimensional specific speed $= (\pi\phi)^{0.5}/(0.5\psi)^{0.75}$ at BEP

Subscripts

1 = rotor-blade entry
2 = rotor-blade exit
1, 2, 3, 4, 5 = holes of five-hole probe (see Fig. 5)
a, r, t = axial, radial, and tangential velocity components

Reference quantities for nondimensional parameters

for velocities: U_2
for pressures: $0.5\rho U_2^2$
for volume flow rate: $0.25\pi D_2^2 U_2$
for power per unit rotor area: ρU_2^3

and flow coefficient attainable by this type of fan; his data show a maximum efficiency of 0.52. Eck emphasizes the remarkedly silent operation of which squirrel-cage fans are capable.

Raj and Swim (1981) have measured the flow leaving a squirrel-cage fan rotor having $4b/D_1 = 2.5$. They found that the inlet flow filled only about three quarters of the blade span or rotor width. This is, of course, consistent with the flow pattern sketched in Fig. 2. The axial width of the filled portion of the rotor was found to be a strong function of circumferential position and of flow rate. Thus the inlet flow was highly asymmetric. As suggested by Fig. 2, the flow entering the rotor gradually changed from axial at the front, to radial at the back plate. The flow emerging from the rotor had little axial velocity even near the front, indicating that considerable turning from axial to radial occurred within the blade passages. All of these observations are in agreement with the results of the present investigation. Raj and Swim concentrated their attention on the flow at the rotor exit. They found that the flow exhibited the jet-wake velocity profile commonly found at the exit of centrifugal compressor and pump impellers.

Roth (1981) performed an experimentally based optimization study of squirrel-cage fans. His experiments included performance measurements for a series of rotors, all having area ratio $4b/D_1 = 2.0$ and $D_1/D_2 = 0.8$. Flow rate, Reynolds number, blade angles and number of blades were systematically varied. These rotors were run in a single casing geometry. The optimum rotor identified by these tests was run in casings of different widths and spiral angles. Some flow-field measurements were made in the casings. Roth also measured the relative flow at the exit of a series of narrower rotors ($4b/D_1 = 0.7$), which exhausted into a vaneless radial diffuser, thus ensuring axisymmetric flow. Performance was independent of Reynolds number, $\mathrm{Re} = U_2 D_2/\nu$, for values above about 3×10^5. Efficiency and total pressure rise were maximum with 40 rotor blades. They dropped sharply when 20 blades were used. Strongly forward-facing blades were found to be best: The total pressure rise, the flow rate, and the total efficiency at the best efficiency point (BEP) all reached maxima for $\beta_2 = -80$ deg. Narrow casings were found to give maximum efficiency; efficiencies at the BEP began to decline for casing-to-rotor-width ratios, B/b, in excess of about 1.1 for all spiral angles. A spiral angle of 5 deg gave the highest efficiency, 0.74. However the BEP and maximum flow rates were then only 25 percent of those for a spiral angle of 11 deg. Best efficiency was 0.65 with the 11 deg spiral angle.

The fan configurations with $B/b = 1.54$ exhibited bi-stable operating characteristics at flow rates somewhat above the BEP value. That is, the pressure rise at any given flow rate could assume one of two values, with a distinctly lower efficiency at the lower pressure-rise condition. Roth associated both this and the decline in best efficiencies for $B/b > 1.1$ with strong crossflows in the wider casings. These crossflows entailed increased mixing losses and a greater tendency to reverse flow in the front portion of the rotor. It should be noted that Roth's rotors apparently had shrouds whose inside diameter was greater than D_1, leaving the front face of the rotor partially open to reverse flow from the casing.

Roth's finding regarding the optimum casing width is at variance with that of other workers, who found that $B/b \simeq 2.5$ gave maximum efficiencies (Moser, 1957; Broeker, 1960; Dielmann, 1982). However these other workers obtained their results with relatively narrow rotors ($4b/D_1 \simeq 1$). These would not have had the extensive separation that occurs at the front of squirrel-cage rotors as noted by Roth (1981), Raj and Swim (1981), and others.

For flow coefficients ϕ below about 0.3 Roth found rotating stall in the rotors that exhausted into a radial diffuser. Rotating stall did not, however, occur for similar rotors exhausting into spiral casings. At low ϕ values the static pressure in spiral casings is circumferentially nonuniform, with maximum and minimum static pressures occurring just upstream and downstream, respectively, of the cutoff. A steady reverse flow pattern then occurs with flow from the casing through the rotor blades upstream of the cutoff; this fluid passes out through the blading again, into the low-static-pressure region in the casing downstream of the cutoff.

Like Raj and Swim (1981), Roth (1981) found jet-wake velocity profiles at the rotor exit, especially for blade exit angles β_2 near zero, which imply deceleration of the relative flow.

Several authors, including Gessner (1967), Roth (1981), Dielmann (1982), Shibl (1983), and Wright (1984), have noted the importance of reducing or eliminating the separation of the flow entering the rotor (see Fig. 2). Where the front of the rotor meets the stationary inlet surfaces of the fan unit, design details such as surface radii, clearance gap, and lip configuration can be very important. Dielmann reviews work that indicates that flow turning without appreciable separation can be achieved for $4b/D_1$ values up to about one. Several of the aforementioned authors have tried boundary layer control, either by tangential blowing or by suction, to assist the flow in turning to the radial direction. Separation has been avoided for $4b/D_1$ values as high as 2.2 (Shibl, 1983). By suitable design of the lip configuration at the clearance gap, air leaking from the casing can be used to provide boundary layer control. On the other hand, with poor lip design the leakage flow can cause increased disruption of the inflow.

Crossflow fans (Eck, 1973; Porter and Markland, 1970; Mazur and Singh, 1987) use rotors that are essentially the same as those of squirrel-cage fans. In crossflow fans, however, the flow is essentially two dimensional, taking place in planes perpendicular to the axis of rotation. The fluid both enters and leaves the rotor through its perimeter, passing through the blading twice. The flow is thus quite different from that in a squirrel-cage fan, except where, and if, reverse flow occurs in the latter.

3 Description of Experiments

Figure 4 is a schematic diagram of the apparatus used for the present experiments. It consisted essentially of a modified commercial squirrel-cage fan driven by a variable-speed electric motor. The original casing of the fan was replaced by large front and back panels, which were grooved to accept a flexible transparent plastic sheet that formed the spiral wall of the casing. The cross section of the casing was thus rectangular. Its width B was always 192 mm, but the spiral angle could be readily changed by inserting the plastic sheet into different grooves in the panels. The original shaft-bearing supports and inlet opening configuration were retained. A 293-mm-dia duct with a bellmouth was fitted to the fan's inlet opening. The fan discharged into a $200 \times 250 \times 1220$ mm rectangular outlet duct. At its exit, this duct was fitted with adjustable throttling plates which formed a variable height opening through which the flow returned into the laboratory room in the form of a rectangular free jet. The fan operating point was varied by adjusting the throttle opening.

The measurements necessary to determine fan performance were made as follows. Static pressure taps (0.8 mm i.d.) were installed on the bellmouth duct, on the casing spiral, near the casing exit, and 250 mm upstream of the throttle plates in the outlet duct. All pressures were measured with a multitube water manometer set at a slope of 1:9. A wattmeter was used to measure the electrical power supplied to the motor control unit. The control unit/motor system was calibrated on a dynamometer stand. The shaft power required to drive the fan could thus be determined. Rotor speed was measured with a stroboscope. A speed of 1100 rpm was used throughout the experiments, giving a Reynolds number $U_2 D_2/\nu = 3 \times 10^5$. The

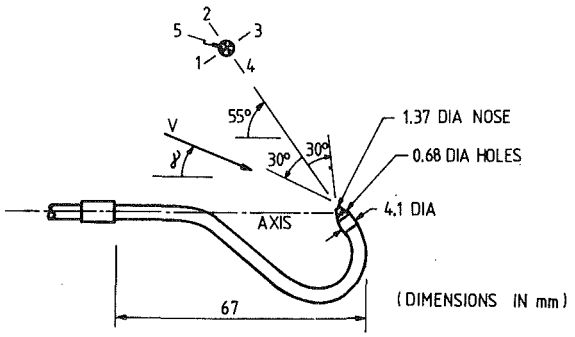

Fig. 5 Five-hole probe

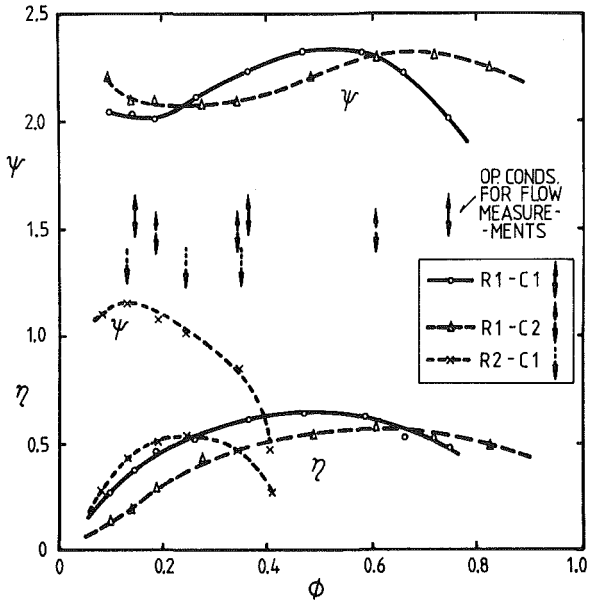

Fig. 6 Fan performance curves

volume flow rate through the fan was determined by traversing a Pitot-static tube near the vena contracta of the jet leaving the outlet duct. Detailed horizontal and vertical traverses were made for each throttle setting used during the experiments. The resulting velocity data for each setting were correlated with that for a single traverse across the jet at its centerline. Such single traverses were then used to determine the volume flow rate for the remainder of the experiments. This procedure was adopted after it was found that volume flow rates determined from bellmouth static pressure readings were inaccurate when the fan was highly throttled. The total-pressure rise across the fan was taken as the sum of the mean dynamic pressure and the measured static pressure (gage) in the outlet duct, plus a small correction (Massey, 1979) for the loss at the sudden enlargement where the casing joins the outlet duct.

The five-hole probe used for the flow-field measurements is shown in Fig. 5. It was calibrated in the potential core of a 50-mm-dia free jet. The calibrations showed some sensitivity to Reynolds number, based on probe tip diameter, for values below 2400. Only measurements with nondimensional velocity $V<0.25$ fell below this value. In use, the probe axis was always aligned with that of the fan rotor. The probe was rolled until its plane and that of the flow velocity vector coincided, as indicated by equality of the pressure sensed at holes 2 and 4. The pitch angle γ of the velocity vector (see Fig. 5), the dynamic pressure q, and the total pressure p_t were determined from calibration curves, which gave, respectively, $\gamma = f_1[p_1 - p_3)/(p_5 - \bar{p})]$, $q = (p_5 - p_{24})/f_2[\gamma]$ and $(p_t - p_5)/q = f_3[\gamma]$. The functions f_1, f_2, and f_3 were all single valued and continuous. f_2 and f_3 covered a useful range of $0 \lesssim \gamma \lesssim 110$ deg. Knowing the probe roll angle, as well as γ and q, the axial, radial, and tangential velocity components could be calculated at any measurement point. The static pressures were obtained by subtracting q from p_t.

The five-hole probe was mounted on long stiff tube whose axis was parallel to that of the fan rotor. The tube was mounted on a traverse gear situated upstream of the bellmouth. The traverse gear provided axial and roll motion and position measurement. For the measurements inside the rotor ($r/D_2 = 0.30$) and inside the casing ($r/D_2 = 0.64$) the probe assembly was introduced via the fan inlet opening and via holes in the front wall of the casing, respectively.

Table 2 gives uncertainty estimates. Some of these are relatively large. For the most part this is attributable to large fluctuations in the manometer readings, reflecting the highly turbulent and somewhat unsteady flow in the fan. Also, the five-hole probe calibration curves have steep slopes for flow angles γ in the ranges 0–10 and 100–110 deg, giving a high sensitivity to measurement errors in these ranges. The uncertainties are considered quite acceptable, however, because they do not compromise the objectives of the work, which were to gain an understanding of the flow and to identify the main origins of losses.

Table 2 Uncertainty estimates

Parameter	Estimated Uncertainty at 20:1 Odds
η	± 0.03
ϕ	± 0.02
ψ	± 0.1
p	± 0.05
p_t	± 0.03
V	$\pm 1.5\%$
Va	$\pm 8\%$
V_r, V_t	$\pm 10\%$
SP, FP	± 0.2
PL	± 0.3

The experimental program is outlined in the Introduction. The flow-field measurements were taken at 45-deg intervals around the circumference of the rotor. No measurements could be taken at the 0 and 45 deg positions outside the rotor ($r/D_2 = 0.64$) because there was insufficient clearance for the probe between the rotor and the casing spiral wall.

4 Results and Discussion

Performance curves for the three tested fan configurations (see Table 1) are shown in Fig. 6. Rotor 1, which is the rotor of the original commercial fan, gave peak efficiencies of 0.64 and 0.57 when run in Casings 1 and 2, respectively. The curves for Rotor 1 are typical of those for squirrel-cage fans. The casing of the original commercial fan had a throat area approximately midway between those of Casings 1 and 2. The 50 percent larger area of Casing 2 resulted in higher flow rate and lower peak efficiency, in agreement with the trends observed by Roth (1981).

The peak efficiencies achieved with Rotor 1 are quite consistent with those of other fluid machinery of comparable specific speed and diameter, see Fig. 3. As seen in Fig. 6, Rotor 2 produced much lower pressure rise and flow rates than Rotor 1. Its peak efficiency, at 0.53, is much lower than that suggested by Fig. 3. This indicates that Rotor 2 is a poor design, since other types of machine can achieve much higher efficiency for the same specific speed and diameter. Rotor 2 was built and tested only to provide comparative data; its poor performance was not unexpected. The radial exit angle of its blades implies a diffusing cascade and is, as Eck (1973) points out, a poor choice for this type of rotor.

As mentioned in the Introduction, detailed flow-field

measurements were made for each of the tested fan configurations at three flow rates, designated HIGH, MED (or BEP), and LOW. These operating points are indicated by arrows in Fig. 6. The flow exhibited generally similar behavior in all three fan configurations. Flow behavior was, however, distinctly dependent on the operating condition, HIGH, BEP, or LOW, of the fans. In this paper the overall results are illustrated in terms of those for the Rotor 1–Casing 1 (R1–C1) configuration. Figure 1 shows the coordinate system used in presenting the results. All flow parameters are nondimensional, as defined in the Nomenclature.

At the HIGH condition the flow is approximately axisymmetric both inside and outside the rotor. At the BEP condition some reverse flow exists in the vicinity of the cutoff, with fluid from the casing re-entering the rotor and flowing back out as outlined in Section 3. At the LOW condition, reverse flow and departure from axisymmetry are more pronounced.

Reverse flow, when it occurs, blocks part of the rotor-inlet region. Where there is no such blockage, the rotor-inlet region is occupied by incoming fluid. The axial velocity of this fluid is high, both in absolute terms and relative to the other two velocity components, at the front of the rotor; it decreases approximately linearly toward zero at the backplate. In reverse-flow regions the axial velocity is relatively small and may even be negative. Figure 7 illustrates these points. Outside the rotor, the axial velocity V_a is relatively small, especially at the BEP and LOW flow rates (usually below 0.3 at HIGH and below 0.1 at BEP and LOW flow rates). Since tangential velocities are high ($V_t \sim 1$) outside the rotor, the velocity vectors are approximately perpendicular to the fan axis. This does not, of course, preclude significant streamwise vorticity.

Results for radial and tangential velocity are presented in Fig. 8 in the form of vector components in r–θ planes. Data for three planes, $z/b = 0.17$, 0.54, and 0.79, are shown.

High values of tangential velocity inside the rotor are clearly indicative of reverse flow. Reverse flow is evident at both the BEP and the LOW flow rates. At the BEP condition reverse flow occurs only over the back two thirds or so of the rotor ($z/b > 0.3$); at LOW flow it extends over the entire width of the rotor and the flow is approximately two dimensional in the reversed zone. This portion of the rotor is functioning very much like a crossflow fan. Away from reverse flow regions, the tangential velocity inside the rotor is generally small; at low z/b the radial velocity is small in keeping with Fig. 2.

Outside the rotor, tangential velocities V_t are generally large, reflecting the work done by the rotor. For Rotor 1 V_t usually exceeds unity and tends to decrease with decreasing flow rate (see Fig. 8). This is as expected since Rotor 1 has forward facing blades. The blades of Rotor 2 are radial at exit and V_t values are somewhat less than 1.0 outside it, as expected. V_t also tends to decrease with decreasing flow rate for Rotor 2, presumably due to earlier flow separation from the baldes due to the increasing static-pressure rise across the rotor.

From Fig. 8 it can be seen that radial velocity V_r outside the rotor varies significantly with axial position z/b. In general, V_r is distinctly lower near the front of the casing, especially for $\theta > 180$ deg. This is, of course, consistent with Fig. 2. At the BEP and LOW flow rates, negative values of V_r appear. This indicates that the fluid engaged in reverse flow comes mainly from the front portion of the casing, between about $\theta = 180$ deg and $\theta = 360$ deg. The flow visualization work confirmed the measurements in this respect. Smoke introduced into the aforementioned portion of the casing showed the strongest tendency to appear inside the rotor.

Figure 9 presents sketches of the flow pattern in the fan. These sketches are based on the flow-field measurements, interpreted as outlined above, and on the flow visualization work.

Total, static, and dynamic pressure results are presented in Fig. 10. These results are consistent with, and support, the velocity results. Except in regions of reverse flow, total pressures inside the rotor are approximately uniform and slightly negative, reflecting entry losses. The dynamic pressure decreases toward the back of the rotor interior as the incoming fluid decelerates and turns toward the radial direction. Reverse flow regions inside the rotor can be identified as ones

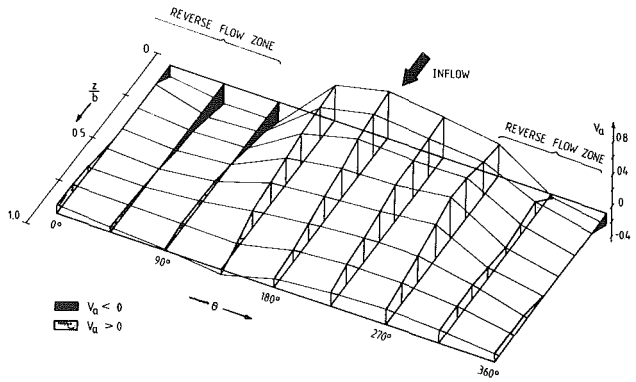

Fig. 7 Axial velocity distribution in the rotor inlet region ($r/D_2 = 0.3$) for the R1-C1 fan configuration at the LOW flow rate

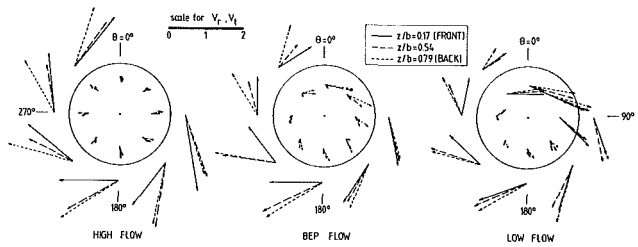

Fig. 8 Velocity vectors in r–θ planes at the HIGH, BEP, and LOW flow rates for the R1-C1 fan configuration

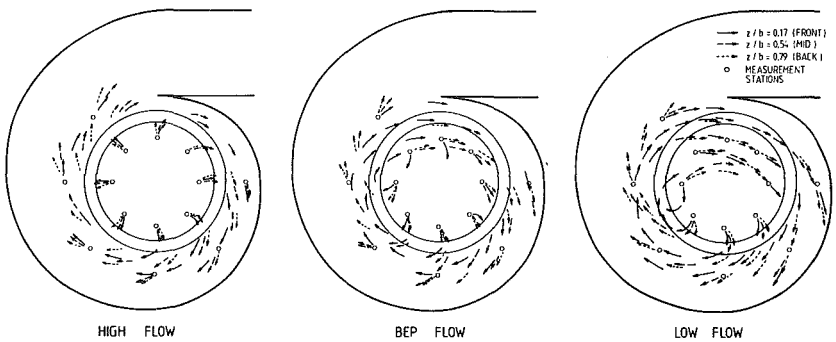

Fig. 9 Sketches of flow pattern at the HIGH, BEP, and LOW flow rates for the R1-C1 fan configuration

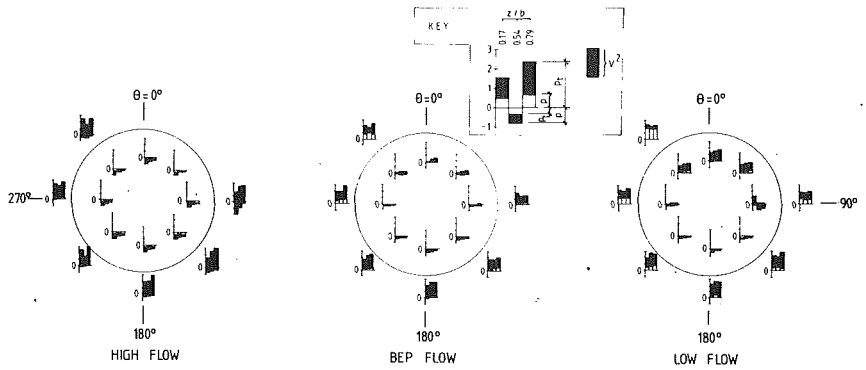

Fig. 10 Total, dynamic, and static pressure at the HIGH, BEP, and LOW flow rates for the R1-C1 fan configuration

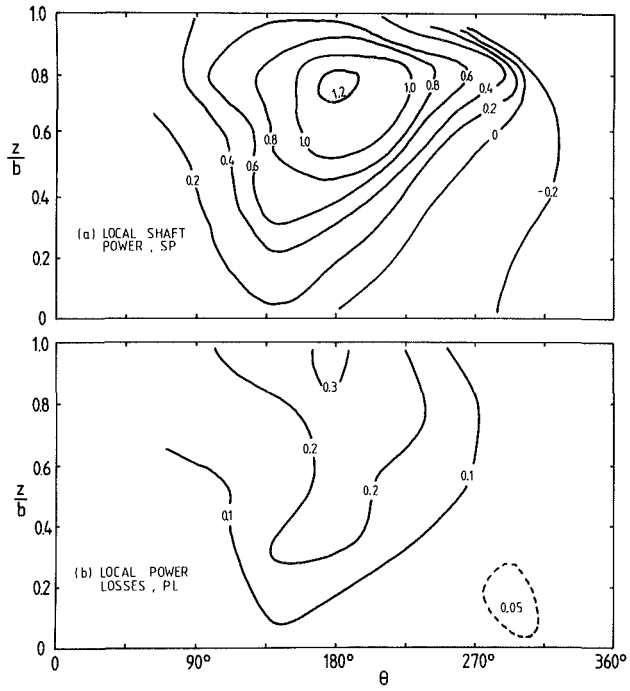

Fig. 11 Contours of local shaft power and power losses for the R1-C1 fan configuration at the BEP flow rate (see equations (1) to (3))

where the total pressure is positive, reflecting energy acquired by the fluid in its first pass through the rotor. Outside the rotor most of the flow's energy is kinetic, with the static pressure an important constituent only at the LOW flow rate, upstream of the cutoff. The static pressure outside the rotor of course increases as the fan is throttled to decrease the flow rate. Particularly at low flow rates there is a circumferential gradient of static pressure around the casing with a maximum being reached just upstream of the cutoff. This is typical of centrifugal pumps and fans operating at low flow rates.

Figure 11 shows contour plots of local nondimensional shaft power and power loss per unit rotor area, *SP* and *PL*, respectively, for the BEP operating point of the R1-C1 fan configuration. These parameters are defined as follows:

$$SP = 2\bar{V}_r(r_2V_{t2}/D_2 - r_1V_{t1}/D_2) \quad (1)$$

$$FP = 0.5\bar{V}_r(P_{t2} - P_{t1}) \quad (2)$$

$$PL = \pm(SP - FP) \quad (3)$$

(minus sign if *SP* is negative)

Recall that all the velocity components and pressures appearing in the right-hand sides of equation (1) and (2) are nondimensional, as defined in the Nomenclature. Equation (1) is just the Euler pump and turbine or angular momentum equation, applied locally. The right-hand side of equation (2) is the product of volume flow rate and total-pressure rise in a stream tube and *FP* is the nondimensional fluid power per unit rotor area. The subscripts 1 and 2 denote stations just inside and outside, respectively, of the rotor blades in a stream tube, which passes through the rotor. $\bar{V}_r$ denotes the mean radial velocity, $0.5\,(V_{r1} + V_{r2})$. Unfortunately the present flow-field data are not sufficiently dense to enable precise definition of streamtube end points 1 and 2; this could only be done to a rough approximation using flow pattern sketches such as those of Fig. 9, together with the axial velocity data. Furthermore, since measurements are available only at $r/D_1 = 0.37$ and $r/D_2 = 0.64$, a correction must be applied to the rV_t data values to account for angular mementum changes due to circumferential pressure variation along the streamtubes between the measurement radii and r_1 or r_2. Again, the low density of the data enables only a very approximate evaluation of the corrections. Thus, Figs. 11(*a*) and 11(*b*) are regarded as giving only a qualitative indication of the distributions of work input and rotor losses.

Both *SP* and *PL* are relatively small near the front of the rotor. This primarily reflects the low radial velocity and thus the low mass flow rate through this portion of the rotor. In the reverse flow zones ($270\text{ deg} \lesssim \theta \lesssim 360\text{ deg}$ in Fig. 11) the rotor extracts work from the fluid, as indicated by negative values of *SP*. Surprisingly, the data indicate that losses are small in the reverse flow zones. The ratios of local shaft power to fluid power often exceed one here; of course that is physically impossible and reflects the large uncertainty of these data. Nevertheless, present indications are that rotor losses are remarkably small in reverse flow zones.

The rotor efficiency was relatively insensitive to flow rate. It remained near 0.75 for both rotors, except at the LOW condition for the R1-C2 configuration. The variations of overall fan efficiency with flow rate appear to be due mainly to increased losses in the casing as the operating point moves away from the best efficiency point.

The present results show that the flow in squirrel-cage fans is complex but reasonably comprehensible. The main features of flow behavior were common to all three of the tested fan configurations. This suggests that it should be feasible to develop useful analysis methods by adopting a flow-simulation approach similar to that used by Elder and Gill (1985) and Lorett and Gopalakrishnan (1986) for centrifugal compressors and pumps, respectively. The results suggest that cascade correlations could be used to represent the effects of the rotor blading on the flow.

The preference for forward-facing blading has been confirmed. Radial blading produces relatively low tangential velocities, thus low total-pressure rise and low flow rates around the casing and out of the fan unit. Furthermore, radial blading is probably more susceptible to reverse flow because

of its higher reaction ratio; reverse flow is a possibility whenever the static pressure difference across the rotor blading exceeds 0.5 $\rho(U_2^2 - U_1^2)$.

The casing is very important. For any given rotor it substantially influences the maximum and the best-efficiency flow rate and the fan efficiency. Through its influence on the static-pressure distribution and crossflow pattern outside the rotor, it influences the occurrence of reverse flow. Moreover, with forward-facing blading, the bulk of any static-pressure rise across the fan must occur through conversion of dynamic pressure into static pressure in the casing.

5 Conclusions

Performance and flow-field measurements have been made on three squirrel-cage fan configurations.

The large values of rotor exit-to-inlet area ratio, $4b/D_1$, of these fans results in separation of the incoming flow. This is a major factor in causing particularly complex flow, with substantial axial and circumferential nonuniformity and reverse flow over much of the operating range. Although the flow patterns are complex, their main features are comprehensible and they are probably amenable to effective analysis.

Acknowledgments

The assistance of S. Booth with data-reduction computations is gratefully acknowledged, as is financial support from the Natural Sciences and Engineering Research Council of Canada under its Operating and Strategic grants programs.

References

Baljé, O. E., 1962, "A Study on Design Criteria and Matching of Turbomachines: Part B—Compressor and Pump Performance and Matching of Turbocomponents," ASME *Journal of Engineering for Power*, Vol. 84, pp. 103–114.

Broecker, E., 1960, "Druckgewinnung bei Turbulenter Drallströmung in Parallelwandigen Radialdiffusor," *Heizung, Lüftung, Haustechnik*, Vol. 11, pp. 173–178.

Csanady, G. T., 1964, *Theory of Turbomachines*, McGraw-Hill, New York, pp. 14–23.

Dielmann, K. P., 1982, "Heissgasventilatoren für den Industrieofenbau," Doctoral Dissertation, Fakultät für Bergbau und Hüttenwesen, Rhein-Westfälischen Technischen Hochschule Aachen, Aachen, Federal Republic of Germany.

Eck, B., 1973, *Fans*, 1st English ed., Pergamon Press, Oxford, pp. 139–153, 156–184.

Elder, R. L., and Gill, M. E., 1985, "A Discussion of the Factors Affecting Surge in Centrifugal Compressors," ASME *Journal of Engineering for Gas Turbines and Power*, Vol. 107, pp. 497–506.

Gessner, F. B., 1967, "An Experimental Study of Centrifugal Fan Inlet Flow and Its Influence on Fan Performance," ASME Paper No. 67-FE-21.

Lorett, J. A., and Gopalakrishnan, S., 1986, "Interaction Between Impeller and Volute of Pumps at Off-Design Conditions," ASME *Journal of Fluids Engineering*, Vol. 108, pp. 12–18.

Massey, B. S., 1979, *Mechanics of Fluids*, 4th ed., Van Nostrand Reinhold, New York, pp. 198–199.

Mazur, J., and Singh, T., 1987, "Momentum Exchanges and Energy Transfers in Cross Flow Fans," ASME Paper No. 87-GT-32.

Moser, K., 1957, "Untersuchungen von Spiralgehäusen an Radial ventilatoren," *Heizung, Lüftung, Haustechnik*, Vol. 8, pp. 319–321.

Porter, A. M., and Markland, E., 1970, "A Study of the Cross Flow Fan," *Journal of Mech. Eng. Science*, Vol. 12, pp. 421–431.

Raj, D., and Swim, W. B., 1981, "Measurements of the Mean Flow Velocity and Velocity Fluctuations at the Exit of an FC Centrifugal Fan Rotor," ASME *Journal of Engineering for Power*, Vol. 103, pp. 393–399.

Roth, H. W., 1981, "Optimierung von Trommelläufer—Ventilatoren," *Strömungsmechanik und Strömungsmaschinen*, Vol. 29, pp. 1–45.

Shibl, A., 1983, "The Effect of Boundary Layer Control on the Performance of Radial Fan Impellers," *Proc. 1983 Tokyo International Gas Turbine Congress*, Tokyo, Japan, pp. 471–478.

Wright, T., 1984, "Centrifugal Fan Performance With Inlet Clearance," ASME *Journal of Engineering for Gas Turbines and Power*, Vol. 106, pp. 906–912.

Flow Field Investigation in a Low-Solidity Inducer by Laser-Doppler Velocimetry

A. Boccazzi
C.N.P.M.—CNR,
Centro di Ricerca sulla Propulsione e l'Energetica,
Peschiera Borromeo, Italy

A. Perdichizzi
Dipartimento Meccanica,
Università di Brescia,
Brescia, Italy

U. Tabacco
C.N.P.M.—CNR,
Centro di Ricerca sulla Propulsione e l'Energetica,
Peschiera Borromeo, Italy

The results of an experimental investigation of the flow field within a low-solidity inducer at design and off-design flow rates are presented and discussed; particular attention is devoted to the analysis of the flow field, at the tip in front of the leading edge, for the flow rate close to the back-flow onset. The flow field was measured by means of a laser-Doppler velocimeter at four different axial positions upstream, within, and downstream of the inducer. Axial, tangential, and relative flow angle distributions, in the measuring planes, are presented for three different flow coefficients. At the lower flow rate, the plots show the presence of reverse flow in the region close to the hub downstream of the trailing edge. For the same flow rate, quite low axial velocities are detected at the tip. This is in agreement with pressure probe traverses carried out in a slightly downstream section; these measurements also show radial inward velocities of the same order of magnitude as the axial velocities. Circumferentially averaged losses were evaluated from specific work and total head rise given by pressure probes.

1 Introduction

In pump design, achieving the required performance may sometimes be compromised by the occurrence of cavitation at the rotor inlet. In high-specific-speed pumps, cavitation is generally present, and can lead to unacceptable pump duty, so it must be eliminated or at least reduced to minimum levels. The best method of increasing the suction characteristics of the pump is to provide the main pump with a cavitating inducer upstream of the centrifugal impeller. The function of this inducer is to operate with some cavitation and to provide sufficient head to the fluid to reabsorb vapor bubbles and prevent cavitation of the main impeller.

The inducer has found wide use in space applications, namely in rocket pumps, where conventional speed limits are strongly exceeded because of the design constraints (size and weight).

Despite their rather simple geometry, the flow field within the inducers is heavily affected by viscous and three-dimensional effects (tip leakage flows, blade and annulus wall boundary layers), as shown by Lakshminarayana (1974, 1977, 1982), who concluded that the flow is dominated by viscosity and turbulence effects. Moreover, at off-design conditions the flow field undergoes significant modifications leading to radially nonuniform distribution of flow conditions and to the occurrence of reverse flow in the tip region. Experimental works were carried out by several researchers (Tanaka, 1980; Carey, 1985; Howard, 1987) to study the flow field in high-specific-speed pumps at partial flow rates.

This paper shows the results of an experimental investigation of the internal flow field in a flat plate helical inducer, at three different flow coefficients. The data include velocity and flow angle plots in various planes at different axial positions, obtained by LDV and pressure probe measurements downstream of the rotor. The purpose is to understand the behavior of the flow through an inducer at partial flow rate, close to that corresponding to reverse flow occurrence. This kind of information can be used to match the inducer to the main pump rotor, in order to achieve good pump efficiency.

2 Experimental Apparatus

2.1 Test Rig and Inducer Characteristics. The schematic diagram of the test rig is shown in Fig. 1. It is a closed-loop pump test facility with heat exchanger, variable pressure suction reservoir, and degasifying tank. The hydrodynamic loop operation is controlled by a data acquisition system, based on a personal computer; readings of rpm, flow rate, head, and suction pressure were carried out in continuous sequence, during LDV measurements, to ensure rpm stability within 0.1 percent and mean value flow rate stability within 0.2 percent. The accuracy of the flow rate measurement, by venturi tube and differential pressure transducer, was 1 percent of the actual value. Tests were carried out at 1500 rpm.

The inlet pipe, which served as the inducer shroud, extends about 0.5 diameters upstream of the leading edge (LE) and 0.25 diameters downstream of the trailing edge of the rotor

Contributed by the International Gas Turbine Institute and presented at the 34th International Gas Turbine and Aeroengine Congress and Exhibition, Toronto, Ontario, Canada, June 4–8, 1989. Manuscript received at ASME Headquarters January 13, 1989. Paper No. 89-GT-54.

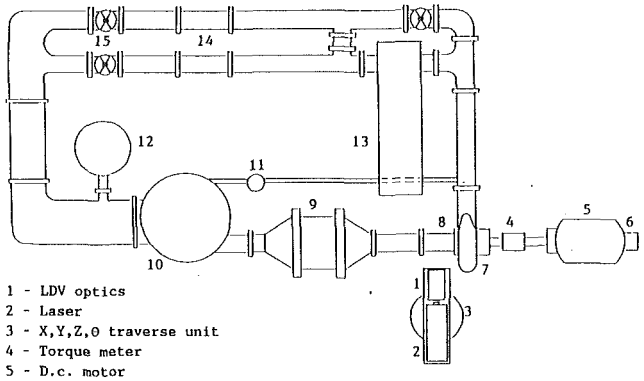

Fig. 1 Schematic diagram of the test facility

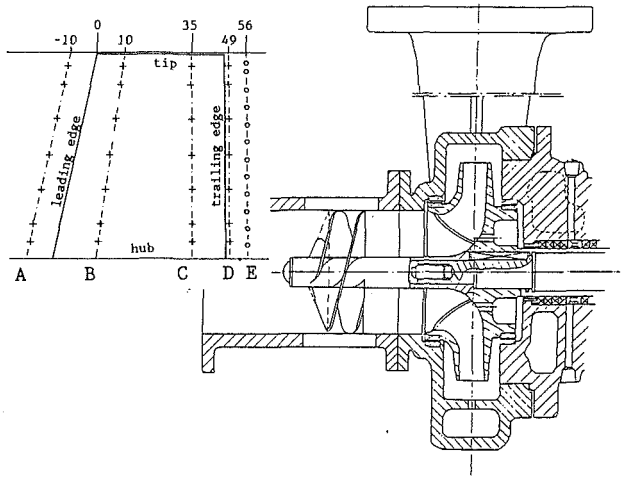

Fig. 2 Test pump and measuring planes

inducer; it was manufactured from perspex to allow flow visualization.

The rotor used for this investigation is the inducer of a commercial Worthington pump (Fig. 2). The blade shape is a helical surface with both hub and tip diameters maintained constant throughout the inducer.

Significant geometric features and design parameters are:

- blade solidity: 1.0 (tip), 1.6 (hub)
- number of blades: 3
- hub-tip ratio: 0.25
- blade angle from tangential direction: 11.4 deg (tip), 40.3 deg (hub)
- blade LE cone angle from radial direction: 13 deg
- diameter: 210 mm (tip), 50 mm (hub)
- blade thickness: 5 mm (tip), 10 mm (hub)
- BEP flow coefficient: $\phi = 0.1555$
- BEP flow rate: $Q = 300$ m^3/h
- BEP suction specific speed: SSS = 11,000

The inducer was spaced 100 mm from the impeller inlet section to allow LDV measurements and pressure probe traverses (United Sensor DA125).

2.2 LDV Measurement Procedure. The LDV system used for velocity measurements consists of a 3-W argon-ion laser with single-component dual beam fringe type optics operated in backscattering mode. A frequency shifter, using a single Bragg cell and electronic downmixing, was used to provide the frequency shifting necessary to detect reverse flow. Spatial filtering and beam expander modules were used to reduce unwanted scattered light detection, to increase backscattered signals, and to reduce probe volume. The entire optical unit was mounted on an X, Y, Z, θ traverse unit. Because of the high hub-to-tip ratio, a 600 mm focal length lens was used to reduce optical obstruction by the inducer blades; in this way it was possible to obtain measurements roughly up to 4 mm from the blade surface with a probe volume length of 1.3 mm.

Measurements were obtained using two different systems for the LDV signal analysis. A first complete set of measurements was carried out by a counter processor using a fixed fringe number (8) with a 5/8 validation criterion; optical access was through a curved glass window fitted in the inducer casing. In the upstream and downstream sections, measurements were repeated by a new LDV signal processor (Burst Spectrum Analizer) based on the Fourier transform of the Doppler signal for determination of frequency. In this case flat optical windows, sufficiently small to minimize the effect of window flatness, were used. By this second arrangement it was possible to obtain better quality results, reducing data scatter.

For both systems, the single validated burst was recorded together with the shaft angular position obtained from a 360 step encoder with one-degree resolution. About 30 velocity data points, for each shaft angle step of one degree, were collected for both axial and tangential velocity components. These data were then averaged on 5-deg windows to obtain shaft angle averaged values.

Seeding with polydispersed (10–20 μm) alumina particles was employed to improve data rate, allowing the photodetector to work with low anode current and minimize noise level. For these particles, the time constant, evaluated from the Basset equation as reported by Durst (1981), is τ = 18–70 μs. Assuming a mean flow velocity of 3 m/s, this implies that the particle recovery distance ($s = 3 \cdot \tau \cdot V$) downstream of a velocity step is 0.16–0.64 mm; therefore the particle slip is expected to be negligible.

Flow visualizations and five-hole pressure probe traverses were also carried out for various flow rates in order to get additional information about the flow field upstream and downstream of the rotor.

Nomenclature

b = blade axial chord at the tip
BEP = best efficiency point of the main pump
h = blade height
H = specific work
i = incidence angle
P_t = total pressure
P_s = static pressure
Q = flow rate
SSS = suction specific speed at BEP
U = inducer peripheral speed
V_a = axial absolute velocity component
V_t = tangential absolute velocity component
V_r = radial absolute velocity component
W = relative velocity
x = axial coordinate
y = spanwise coordinate
δ = deviation angle
ξ = loss coefficient = $1 - \Delta P_t/H$
ϕ = flow coefficient = V_a/U
ω = angular velocity

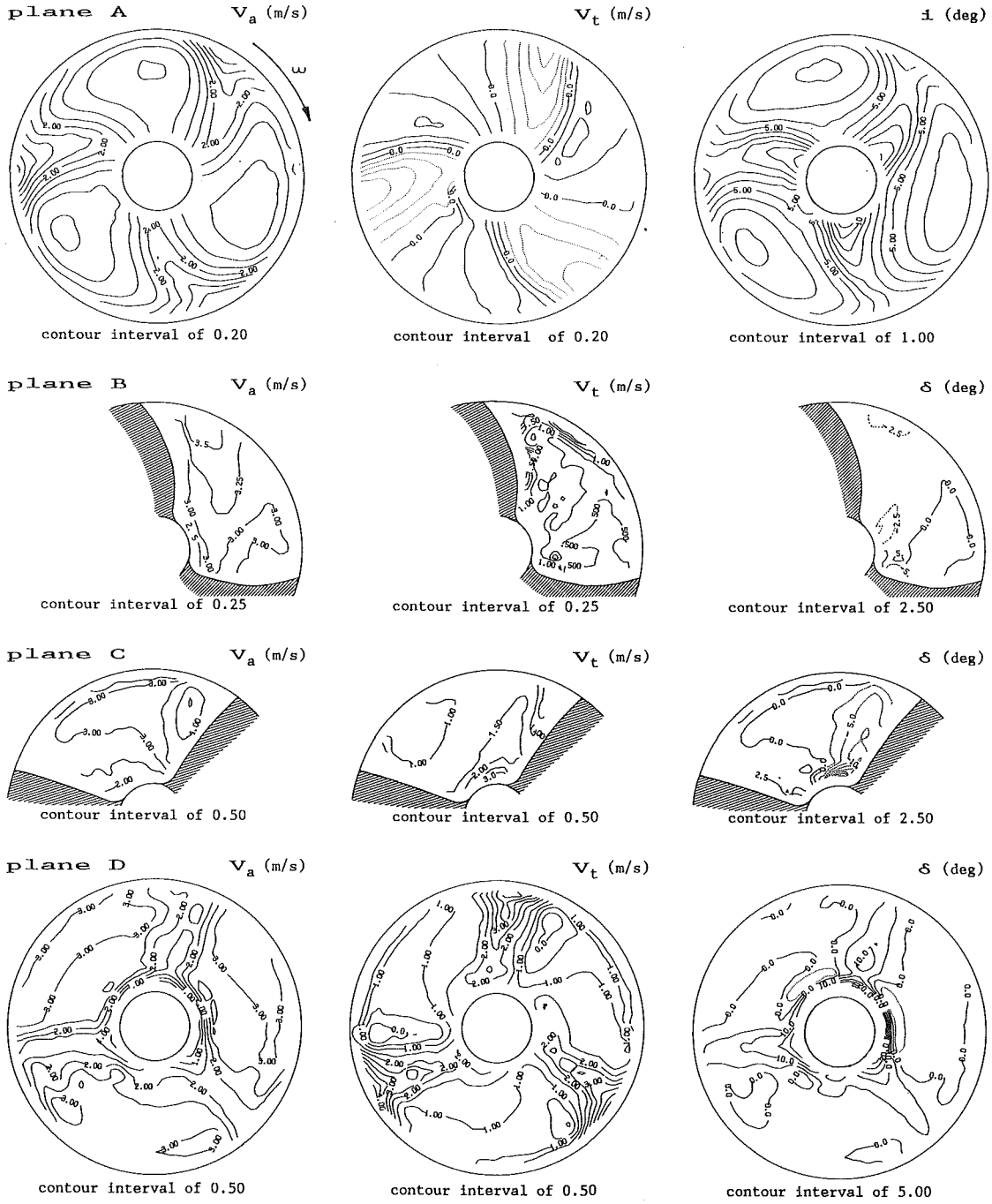

Fig. 3 Contour plots of axial velocity, tangential velocity, and flow deviation angle for $\phi = 0.129$

A complete set of LDV measurements was carried out for three different flow coefficients ($\Phi = 0.155, 0.129, 0.103$) in order to follow flow field evolution when reducing the flow rate, and to obtain information about the mechanism through which the reverse flow takes place. The four LDV measuring planes are shown in Fig. 2(A-D).

3 Results and Discussion

3.1 Design Flow Coefficient Measurements. As flow fields at $\Phi = 0.155$ and $\Phi = 0.129$ are substantially similar, measurements at the lower flow coefficient only are presented; contour plots of axial and tangential velocities as well as flow deviation from the blade angle are shown in Fig. 3. Dotted lines correspond to negative values of the velocity components.

The flow field upstream of the LE in the tip region (plane A) is nonuniform because of the presence of a developed boundary layer. The marked tangential nonuniformity is due to the blockage effect caused by blade thickness; the flow configuration looks like a wake flow but it is a pure potential flow effect related to the stagnation point at the leading edge of the blade. In the three large cores of uniform flow, related to the three blade passages, an incidence angle of about 3 deg is found; in the hub region the incidence increases considerably (up to 7-10 deg), as usual in a flat plate helical inducer.

In the first plane (B) inside the blade passage, the flow is almost uniform and the relative velocities are parallel to the blades.

In plane C higher axial velocities are found on the suction side of the blades, while minimum values are located on the pressure side at the hub. A quite large negative deviation angle region is noticed close to the suction side of the blades; much

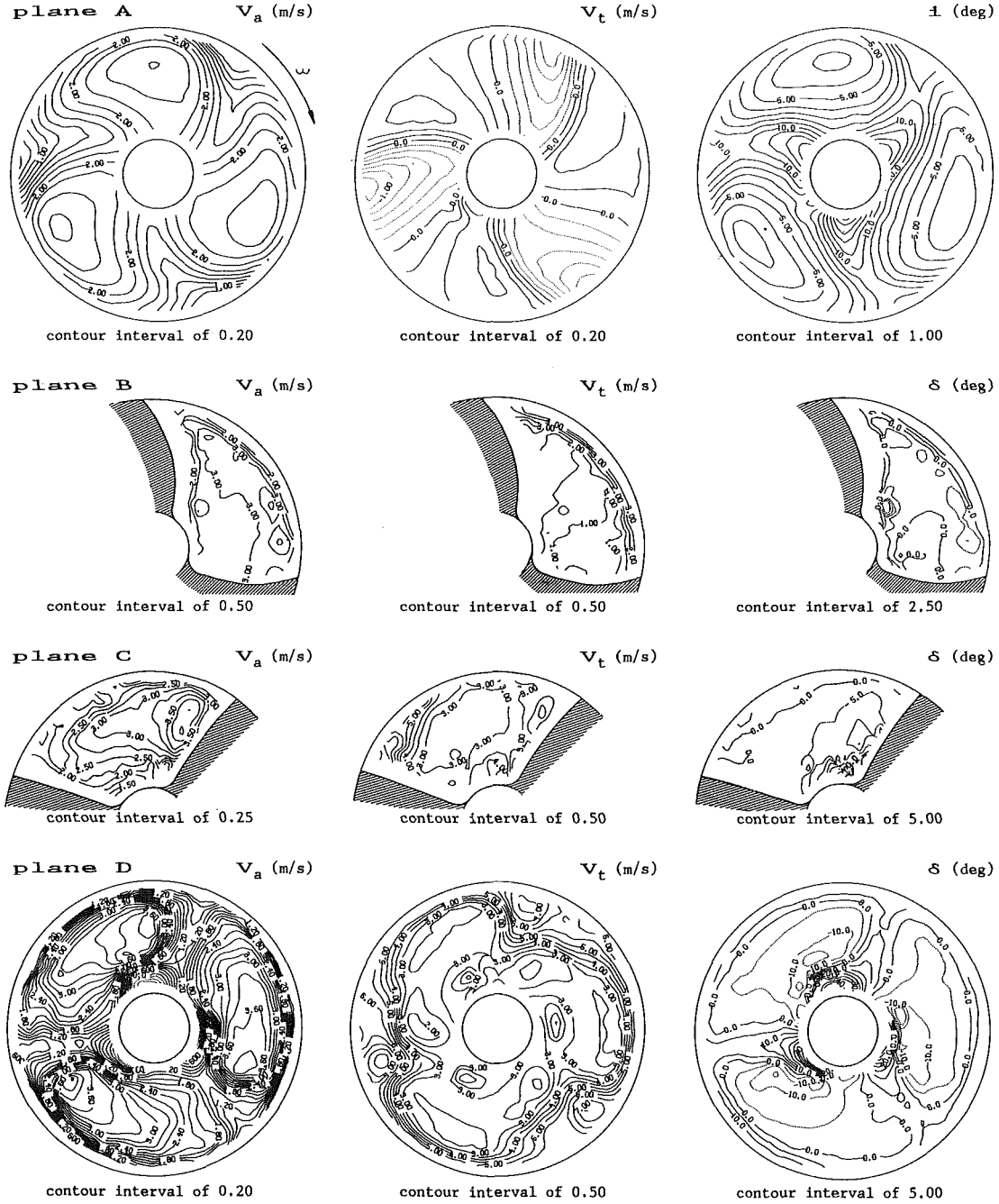

Fig. 4 Contour plots of axial velocity, tangential velocity, and flow deviation angle for $\phi = 0.103$

higher underturning angles (−40 deg), caused by the blunt TE, occur at the hub.

Downstream of the TE (plane D), there are three uniform flow cores, with about 3 m/s axial velocity and zero deviation angle, extending for a large portion of the blade height; between these cores, low axial and high tangential velocity regions clearly show the presence of the wakes related to the blades.

3.2 Reduced Flow Coefficient—Inlet Region. When the flow coefficient of the inducer is reduced to about 60 percent of the design one, it is known (Schiavello and Sen, 1980; Toyokura et al., 1969; Murakami and Heya, 1966) that in the tip region, at the LE, reverse flow occurs and, for a further reduction, reverse swirling flow extends considerably upstream of the leading edge. In order to show the details of the flow field in the leading edge region, LDV measurements were taken for a flow coefficient $\Phi = 0.103$ (66 percent of the design flow coefficient), which corresponds to the reverse flow onset in this inducer. Reverse flow was detected by flow visualizations with air injection at the casing wall. It should be pointed out that the back flow is just beginning and is confined in a thin layer close to the casing.

Contour plots for this flow coefficient are presented in Fig. 4. The results in plane A, compared with those obtained at $\Phi = 0.129$, show a significant decrease of axial velocities near the casing and an increase of negative tangential velocities, which lead to high incidence angles (up to 9 deg). In this situation a separation bubble is expected to form on the blade suction side; indeed in the measuring station nearest the casing wall the relative velocity vector distribution (Fig. 5) shows a zero axial velocity region in front of the suction side of the blades.

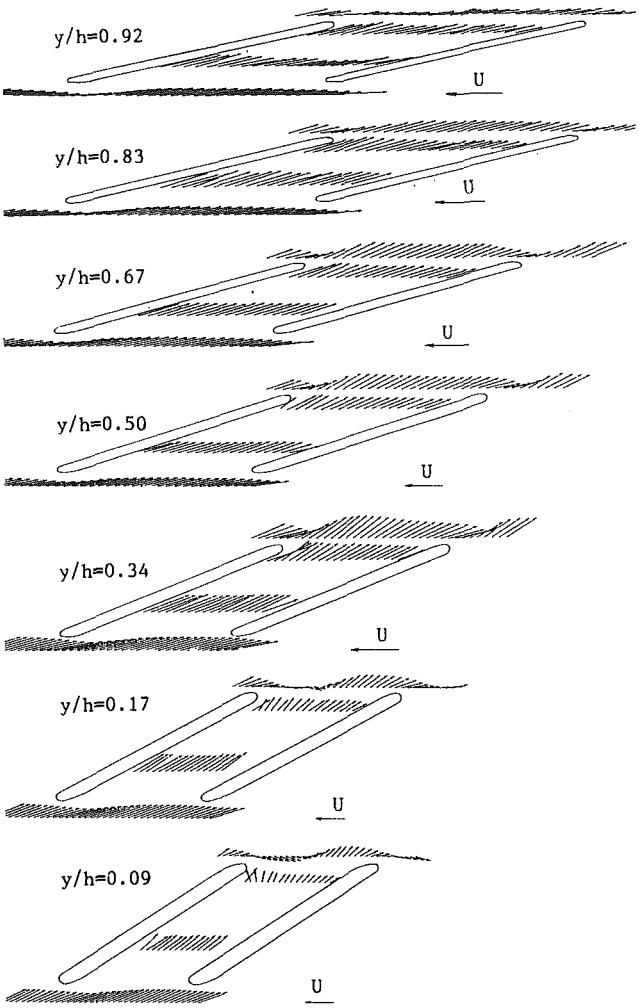

Fig. 5 Relative velocity vector distribution for $\phi = 0.103$

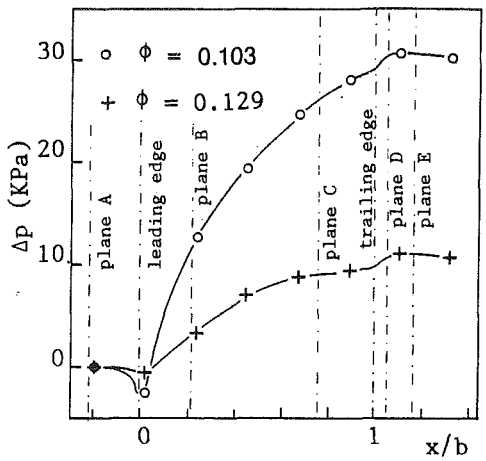

Fig. 6 Static pressures at the casing wall of the inducer

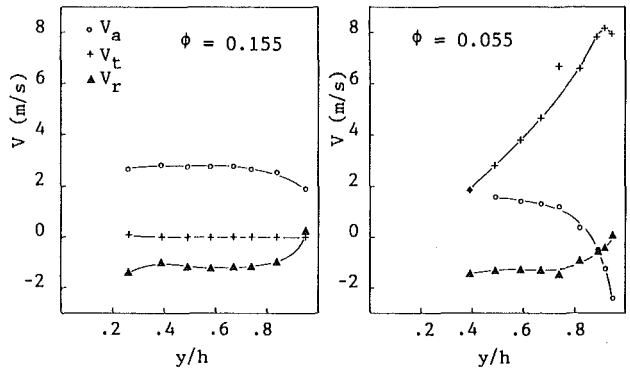

Fig. 7 Pressure probe measurements in plane A of axial, tangential, and radial velocity components for an inducer with higher solidity (De Ponti and Fagnani, 1975)

In plane B, low axial velocities and high positive tangential components are detected at the tip, revealing an appreciable decrease of the relative velocity; consistently an appreciable pressure rise was detected in this region by pressure tappings at the wall (Fig. 6). These features affect the flow field in the inlet region, reducing the upstream axial velocity component and producing a radial inward flow. Radial inward velocities (Fig. 7) were indeed detected by pressure probe measurements (De Ponti and Fagnani, 1975) in front of the LE of an inducer with the same geometry but higher axial chord. Actually in plane B at $y/h = 0.92$ (Fig. 5) the flow field seems to be affected by a radial inward flow, as the blade-to-blade stream-surface appears distorted in the circumferential direction.

From the relative velocity vector plot, at $y/h = 0.92$, it is expected that a further reduction of the flow rate would produce even smaller axial velocities, at the inlet all over the pitch, with a reverse flow in front of the blade suction side. This trend was confirmed by tip flow visualizations by air injection at the casing wall.

Abramian et al. (1988) and Carey et al. (1985) noticed an unexpected flow separation, in the tip region on the pressure side, in a well-developed reverse flow condition. From the above results it appears that further investigations are needed to clarify the mechanism through which the separation moves from suction to pressure side when decreasing the flow coefficient.

In the hub region, even if the blockage effect of the blade is larger and local high-incidence angles occur (up to 11 deg), no particular flow phenomena take place because of lower velocity.

3.3 Outlet Flow Field. In plane C (Fig. 4) the formation of a higher axial velocity core, on the suction side of the blade, is evident; toward the pressure side, the axial velocity component decreases almost uniformly all over the blade height, consistently with the blade loading. An overturning angle region is noticed on the suction side of the blade.

Between planes C and D a marked rearrangement of the flow rate distribution occurs. Contour plots, in section D, show in detail the complex flow configuration occurring immediately downstream of the TE; indeed three jet regions, with maximum velocity on the suction side of the wake near the midspan, are clearly detected. Approaching the casing wall, the axial velocity component decreases markedly while the tangential velocity component increases up to 6 m/s; this flow configuration is in agreement with the appreciable radial velocities measured by the pressure probe in plane E (Fig. 10) and seems to be caused by the significant pressure rise occurring at the tip. This could also be the result of interaction between inducer flow and the reverse flow occurring at the impeller inlet.

An important overturning angle is noticeable from both the deviation angle contour plot and the relative velocity vector distribution. This is a consequence of the above-mentioned convergence of the stream surfaces in the middle of the channel, which produces a significant axial velocity acceleration.

Near the hub (Fig. 5) reverse flow is present on almost half of the pitch; it is probably the effect of a secondary flow corner vortex developed from deviation of the hub boundary layer around the blunt TE; the diffusion at the TE may contribute to this phenomenon. From the relative velocity vectors at $y/$

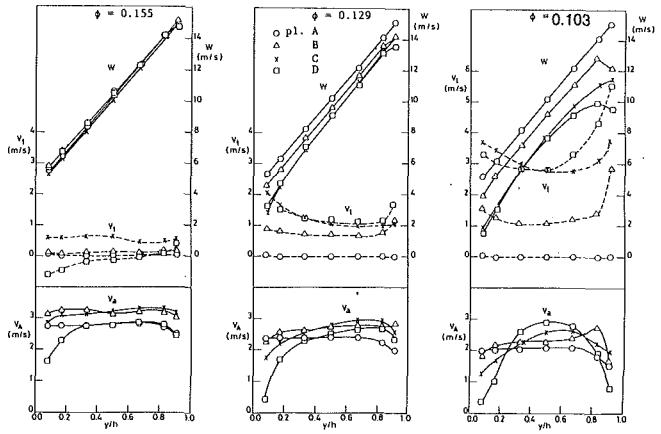

Fig. 8 LDV mass-averaged values of absolute velocity components and relative velocities

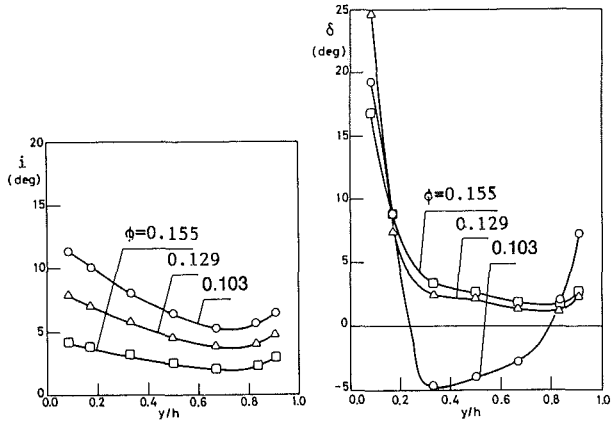

Fig. 9 Incidence and deviation angles evaluated from LDV measurements

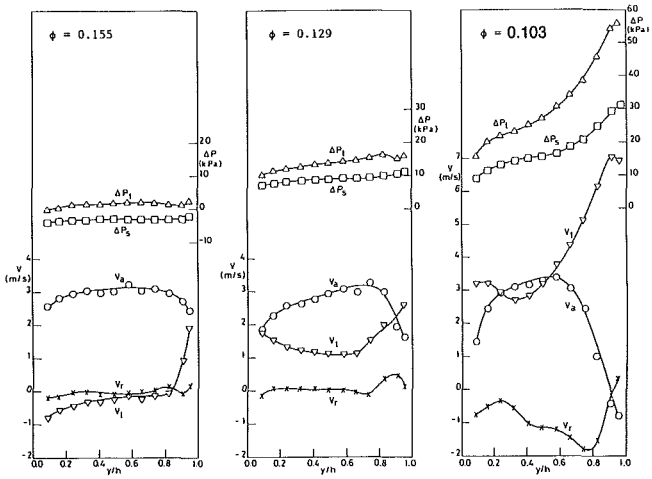

Fig. 10 Pressure probe traverses in plane E

h = 0.09 and 0.17, the presence of outward flows upstream of the TE can be deduced.

3.4 Circumferential Averaged Results. LDV data were mass averaged across the pitch to obtain, in each measuring plane, the spanwise distribution of the absolute velocity components and of the relative velocities; these results, for the flow coefficients investigated, are presented in Fig. 8. Incidence and deviation angles for the same flow rates are plotted in Fig. 9.

In order to obtain total and static pressure rise distribution along the channel height, as well as the radial velocity component, pressure probe measurements were carried out in section E (7 mm downstream of section D). These results are presented in Fig. 10, although one has to take into account that stationary pressure probe measurements, downstream of a rotor, are subject to a certain degree of inaccuracy because of the flow unsteadiness.

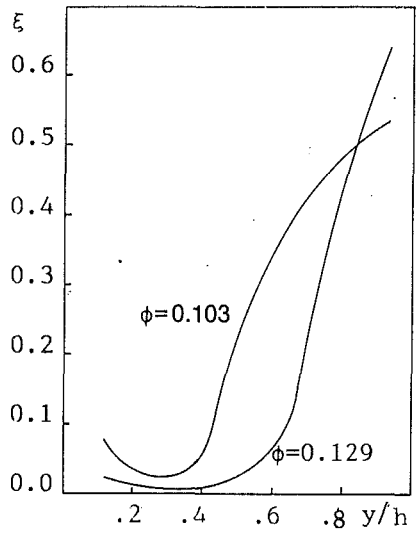

Fig. 11 Loss coefficient

For the case Φ = 0.155, it is evident that the inducer does not provide any head, and indeed no diffusion of relative velocity is noticeable; this is consistent with the deviation and the incidence angle distributions from which zero deflection throughout the rotor results. Between sections C and D the decrease in tangential component is related to the mixing losses at the TE.

By reducing the flow coefficient to 0.129, the incidence angle increases and the inducer provides an almost uniform pressure rise along the blade height; this is consistent with the relative velocity diffusion and the tangential velocity rise, which shows the increase of the specific work throughout the blade passage.

At Φ = 0.103, static and total pressure increase mainly in the tip region, where axial velocity component decreases. Between planes D and E, a further appreciable axial velocity decrease, down to negative values, is found at the tip, together with high tangential momentum. This is a typical behavior of an impeller recirculating flow. Substantial changes of the flow rate distribution can be noticed; in the middle of the blade height, flow undergoes a significant acceleration, whereas at hub and tip it decelerates. Radial inward velocities, up to 2 m/s (i.e., of the same order of magnitude as the axial ones), are shown by pressure probe measurements carried out in section E.

Figure 11 shows the losses evaluated from the specific work obtained by pressure probe measurements. The loss distribution appears almost similar for the two flow coefficients; a quite high loss level, i.e., up to 50 percent, is present near the tip just where high tangential velocity components and high total pressures are found. It should be noted that the extent of this region increases considerably toward the hub (up to y/h = 0.4) at the lowest flow coefficient.

For a broad evaluation of the impeller inducer interaction, LDV measurements of axial components, in section D, have been repeated without the inducer (Fig. 12). Large axial velocity components, up to 5 m/s, are found in the hub region, whereas at the tip recirculating flow is present. It is quite clear that the flow fields imposed by the impeller with and without inducer are quite different; moreover the recirculating flow, coming from the impeller, seems to produce a blockage effect, in the

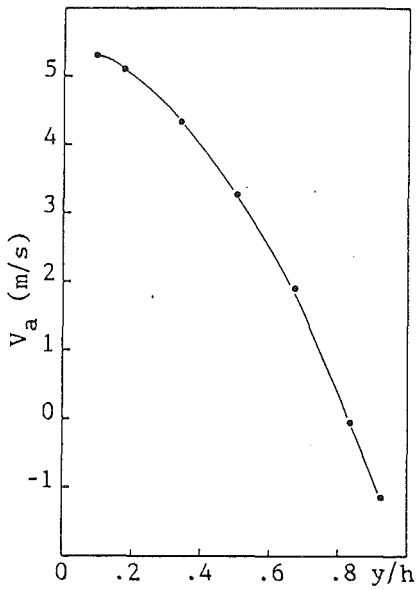

Fig. 12 Mass-averaged LDV measurements of axial velocity component in plane D, without the inducer, for ϕ = 0.103

meridional plane at the tip, and consequently a stream tube concentration at smaller radii.

4 Conclusions

The presented measurements allow a detailed view of the flow field in the inducer of a commercial centrifugal pump for three different flow coefficients, the smallest one corresponding to the back flow onset.

It was found that the back flow seems to be related to high relative velocities and high local incidence angles, occurring on the suction side at the tip, because of reduced axial velocities in front of the blade LE. This flow configuration is caused partly by the inlet boundary layer at the casing, but mostly by the static pressure rise, occurring just after the LE, which was detected by static pressure tappings at the casing wall.

At the lowest flow coefficient, the flow field at the outlet was found to be quite nonuniform; on the suction side of the wakes, near the midspan, there are three cores with high velocities that were found to be higher than that at Φ = 0.129. Approaching the hub, as well as the casing wall, the axial velocity component decreases considerably and, at the hub, a reverse flow region was detected on the suction side of the wake.

Important interaction phenomena, between inducer and centrifugal impeller, seem to take place; indeed quite different flow fields were found with and without the inducer.

Acknowledgments

This work was carried out on a pump kindly supplied by Worthington Pompe Italia.

The authors are grateful to Prof. B. Lakshminarayana and Prof. C. Osnaghi for the helpful discussions of the experimental results:

The authors wish also to thank Mr. P. Giuliani and Mr. C. Guarnieri for their continuous technical support.

References

Abramian, M., Howard, J. H. G., and Hermann, P., 1988, "An Investigation of Axial Pump Backflow and a Method for Its Control," ASME Paper No. 88-GT-31.

Boccazzi, A., Coghe, A., and Perdichizzi, A., 1986, "LDA Measurements on the Inducer of a Centrifugal Pump," presented at the Third International Symposium on Applications of Laser Anemometry to Fluid Mechanics, Lisbon, Portugal.

Carey, C., Fraser, S. M, Rachman, D., and Wilson, G., 1985, "Studies of the Flow of Air in a Model Mixed-Flow Pump by Laser Doppler Anemometry," Report No. 699, Parts 1 and 2, National Engineering Laboratory, East Kilbride, Glasgow, United Kingdom.

De Ponti, L., and Fagnani, G., 1975, "Indagine Teorico Sperimentale sul Funzionamento di una Pompa con Inducer con Particolare Riferimento alle Caratteristiche Locali della Vena Fluida all'Aspirazione ed alla Mandata dell'Inducer," Graduating thesis, Politecnico di Milano, Milan, Italy.

Durst, F., Melling, A., and Whitelaw, J. H., 1981, *Principle and Practice of Laser Doppler Anemometry*, Academic Press, London, United Kingdom.

Howard, J. H. G., Tropea, C., Almahroos, H. M., and Roeber, T. W., 1987, "LDV Measurements of the Axial Velocity Field Within and Ahead of an Axial Pump Inducer at Off-Design Flow Rate," *Proceedings of the ASME/JSME Thermal Engineering Conference*, Vol. 2, pp. 63-69.

Lakshminarayana, B., 1974, "Experimental and Analytical Investigation of Flow Through a Rocket Pump Inducer," *Fluid Mechanics and Design Turbomachinery*, NASA SP 304, Part 2, pp. 689-723.

Lakshminarayana, B., and Gorton, C. A., 1977, "Three-Dimensional Flow Field in Rocket Pump Inducers—Part 2: Three-Dimensional Viscid Flow Analysis, and Hot Wire Data on Three-Dimensional Mean Flow and Turbulence Inside the Rotor Passage," ASME *Journal of Fluids Engineering*, Vol. 99, pp. 176-186.

Lakshminarayana, B., 1982, "Fluid Dynamics of Inducers—A Review," ASME *Journal of Fluids Engineering*, Vol. 104, pp. 411-427.

Murakami, M., and Heya, N., 1966, "Swirling Flow in Suction Pipe of Centrifugal Pumps," *Bulletin of JSME*, Vol. 9, No. 34, pp. 344-352.

Schiavello, B., and Sen, M., 1980, "On the Prediction of Reverse Flow Onset at the Centrifugal Pump Inlet," *Performance Prediction of Centrifugal Pumps and Compressors*, ASME Symposium, New Orleans, LA.

Soltis, R. F., Anderson, D. A., and Sandercock, D. M., 1962, "Investigation of the Performance of a 78 Flat-Plate Helical Inducer," NASA TND-1170.

Tanaka, T., 1980, "An Experimental Study of Backflow Phenomena in a High Specific Speed Propeller Pump," ASME Paper No. 80-FE-6.

Toyokura, T., Kubota, N., and Akaike, S., 1969, "Studies on Back-Flow Mechanism of Turbomachines," *Bulletin of JSME*, Vol. 12, No. 50, pp. 215-223.

Experimental Investigation of Rotor–Stator Interaction in a Centrifugal Pump With Several Vaned Diffusers

N. Arndt[1]
Research Fellow.

A. J. Acosta
Professor.

C. E. Brennen
Professor.

T. K. Caughey
Professor.

California Institute of Technology,
Pasadena, CA 91125

This paper describes an experimental investigation of rotor–stator interaction in a centrifugal pump with several vaned diffusers. Steady and unsteady diffuser vane pressure measurements were made for a two-dimensional test impeller. Unsteady impeller blade pressure measurements were made for a second two-dimensional impeller with blade number and blade geometry identical to the two-dimensional impeller used for the diffuser vane pressure measurements. The experiments were conducted for different flow coefficients and different radial gaps between the impeller blade trailing edge and the diffuser vane leading edge (5 and 8 percent of the impeller discharge radius). The largest pressure fluctuations on the diffuser vanes and the impeller blades were found to be of the same order of magnitude as the total pressure rise across the pump. The largest pressure fluctuations on the diffuser vanes were observed to occur on the suction side of the vane near the vane leading edge, whereas on the impeller blades the largest fluctuations were observed to occur at the blade trailing edge. However, the dependence of the fluctuations on the flow coefficient was found to be different for the diffuser vanes and the impeller blades; on the vane suction side, the fluctuations were largest for the maximum flow coefficient and decreased with decreasing flow coefficient, whereas at the blade trailing edge, the fluctuations were smallest for the maximum flow coefficient and increased with decreasing flow coefficient. Increasing the number of the diffuser vanes resulted in a significant decrease of the impeller blade pressure fluctuations. The resulting lift on the diffuser vanes was computed from the vane pressure measurements; the magnitude of the fluctuating lift was found to be larger than the steady lift.

Introduction

Blade and vane design in diffuser pumps, and also in centrifugal compressors, is currently based upon the assumption that the flow in both the impeller and the diffuser is steady. This, however, implies that the radial gap between the impeller discharge and the diffuser inlet is large so that no flow unsteadiness of any kind due to rotor–stator interaction may occur. If, however, the radial gap between the impeller blades and the diffuser vanes is small, i.e., of the order of a small percentage of the impeller discharge radius, as it actually is for many diffuser pumps, there may be a strong interaction that may influence both the aerodynamic and the structural performance of the impeller blades and the diffuser vanes. Cavitation damage observed at the trailing edges of the impeller blades of high-speed centrifugal pumps, such as the High Pressure Oxygen Turbopump (HPOTP) of the Space Shuttle Main Engine (SSME) may also result from fluctuating blade pressures, which are due to rotor–stator interaction.

The rotor–stator interaction may be divided into two different mechanisms: potential flow interaction and wake interaction (Dring, 1982). The potential flow interaction between the two blade rows moving relative to each other arises because of the circulation about the blades and because of the potential fields, other than circulation, about the blades that are due to the finite thickness of the blades (Lefcort, 1965). The potential flow fields about a blade extend both upstream and downstream of a blade. The wake interaction refers to the unsteadiness induced at a blade row by the wakes shed by the blades of an upstream blade row and convected downstream. Both potential flow interaction and wake interaction may result in unsteady forces of significant size on both the impeller blades and the diffuser vanes. If the radial gap between the impeller blades and the diffuser vanes is small both interaction mechanisms will occur simultaneously, and will influence each other.

[1]Present address: MTU (Motoren-und Turbinen Union München GmbH), Postfach 500640, 8000 München 50, Federal Republic of Germany.

Contributed by the International Gas Turbine Institute and presented at the 34th International Gas Turbine and Aeroegine Congress and Exhibition, Toronto, Ontario, Canada, June 4–8, 1989. Manuscript received at ASME Headquarters January 13, 1989. Paper No. 89-GT-62.

Most of the work on blade row interaction with the aim of measuring unsteady blade pressures has been carried out on axial turbomachinery. Among others, Dring et al. (1982) investigated blade row interaction in an axial turbine and found both potential flow and wake interaction for closely spaced blade rows (15 percent based on chord). Significant pressure fluctuations of up to 72 percent of the exit dynamic pressure were measured near the leading edge of the rotor. Gallus (1979) and Gallus et al. (1980) reported measurements on axial compressors. The blade rows were spaced relatively far apart (60 percent based on chord), such that the potential flow interaction between the rotor and the stator was weak; i.e., the pressure fluctuations on the compressor stator were found to be considerably larger than those on the compressor rotor. In radial turbomachinery, impeller blade pressure measurements were reported by Iino and Kasai (1985). The radial gap between the impeller blades and the diffuser vanes was small, so that significant pressure fluctuations on the impeller blades were observed. Furthermore, it was found that blade and vane angle have an important influence on the blade pressure fluctuations. Flow field investigations in centrifugal compressors have been reported among others by Inoue and Cumptsy (1984) and Stein and Rautenberg (1988). Diffuser vane pressure measurements using the impeller of the High Pressure Turbopump of the Space Shuttle Main Engine were made by Arndt et al. (1989). Experiments were made for radial gaps of 1.5 and 4.5 percent (based on the impeller discharge radius) between the impeller blades and the diffuser vanes. The pressure fluctuations were found to be of the same order of magnitude as the total pressure rise across the pump.

To investigate the complete rotor-stator interaction mechanism, unsteady pressure measurements have to be made on both the impeller blades and the diffuser vanes. In this paper, the results of such measurements using a two-dimensional centrifugal test impeller and different vaned radial diffusers will be presented. To the authors' knowledge, this is the first publication reporting both unsteady impeller blade and unsteady diffuser vane pressure measurements in a diffuser pump. All measurements were obtained for non-cavitating flow.

Data will be presented on steady and unsteady diffuser vane pressure measurements along midvane height. Superimposing the steady and ensemble-averaged unsteady vane pressure, the ensemble-averaged vane pressure was obtained (it was assumed that the steady pressure value measured with mercury manometers was identical to the time mean pressure about which the piezoelectric pressure transducers, used for the unsteady measurements, measure the unsteady pressure). Steady and unsteady computations of the force on the vane were made from those pressure measurements. A second two-dimensional impeller, referred to as Impeller Z2, with the same blade number and the same blade geometry as Impeller Z1, was used for the impeller blade pressure measurements. For those measurements, different diffuser vane configurations were used to investigate the influence of the vane number and the vane leading edge mean line angle (also referred to as vane angle) on the impeller blade pressure fluctuations.

During the tests, the impellers could only be positioned at locations on an orbit concentric to the diffuser center (orbit radius = 1.27 mm), so that the radial gap between the impeller blade trailing edge and the leading edge of any instrumented diffuser vane could be varied between 5 and 8 percent of the impeller discharge radius. Similarly, for the impeller blade pressure measurements, the radial gap between the in-

Nomenclature

a_i, b_i = coefficient of the ith cos and the ith sin term in a Fourier series, normalized by $(1/2)\rho u_2^2$
A_2 = impeller discharge area
b_2 = impeller discharge width
b_3 = diffuser inlet width
c = vane chord
c_b = blade pressure coefficient $= p_b/(1/2)\rho u_2^2$
c_i = magnitude of ith Fourier coefficient $= \sqrt{a_i^2 + b_i^2}$
c_L = life coefficient $= L/(1/2)\rho u_2^2 c$
$\bar{c}_p$ = steady vane pressure coefficient $= (\bar{p}_v - \bar{p}_{up})/(1/2)\rho u_2^2$
$\tilde{c}_p$ = unsteady vane pressure coefficient $= \tilde{p}_v/(1/2)\rho u_2^2$
$\tilde{c}_{p,av}$ = ensemble-averaged unsteady vane pressure coefficient $= \tilde{p}_{v,av}/(1/2)\rho u_2^2$
$c_{p,\,av}$ = ensemble-averaged vane pressure coefficient = $\bar{c}_p + \tilde{c}_{p,av}$
d_2, d_3 = impeller discharge diameter, diffuser inlet diameter
$\mathbf{F}$ = force vector on diffuser vane
f = frequency
f_b = impeller blade passage frequency = z_b(rpm/60)
f_s = shaft frequency = (rpm/60)
f_v = diffuser vane passage frequency = z_v(rpm/60)
L = lift (component of the force vector on the vane normal to the chord joining the vane leading edge and the vane trailing edge)
p, p_t = pressure, total pressure
Q = flow rate
R = radius
R_2 = impeller discharge radius
R_3 = diffuser inlet radius
R_{mean} = mean line radius of the circular arc vanes
rpm = revolutions per minute
t_v = vane thickness
u_2 = impeller tip speed $= 2\pi R_2$(rpm/60)
x, y = diffuser vane coordinates
z_b, z_v = number of impeller blades, number of diffuser vanes
α^* = impeller blade trailing edge angle (= impeller blade angle)
β^* = diffuser vane leading edge mean line angle (= diffuser vane angle)
ξ = parametric diffuser vane coordinate
ρ = density
φ_i = phase of ith Fourier coefficient = $\tan^{-1}(a_i/b_i)$
ϕ = flow coefficient $= Q/u_2 A_2$
ψ = total head coefficient $= (p_{\text{down}} - p_{\text{up}})/\rho u_2^2$
ω = radian frequency $= 2\pi f$

Subscripts

av = ensemble averaged
b = impeller blade
down = downstream
max = maximum
s = shaft
up = upstream
v = diffuser vane

Superscripts

$\bar{}$ = steady
$\sim$ = unsteady

Abbreviations

FP = pressure side of impeller blade
FS = suction side of impeller blade
LE = diffuser vane leading edge
PCB = PCB Piezoelectronics, Inc., Depew, NY 14043
PS = diffuser vane pressure side
SS = diffuser vane suction side
TE = diffuser vane trailing edge

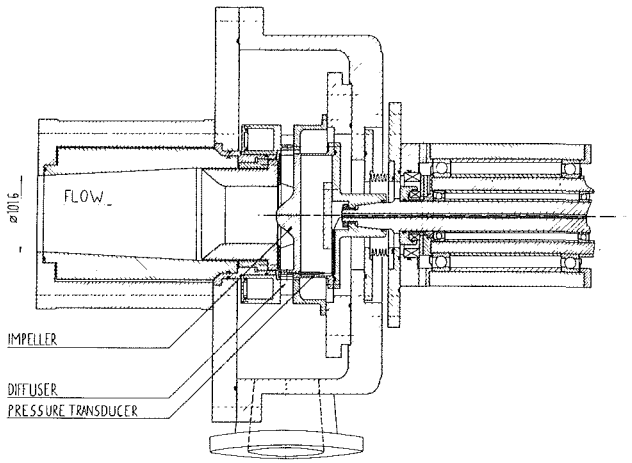

Fig. 1 Assembly drawing of the eccentric drive system and the test section with Impeller Z2 installed

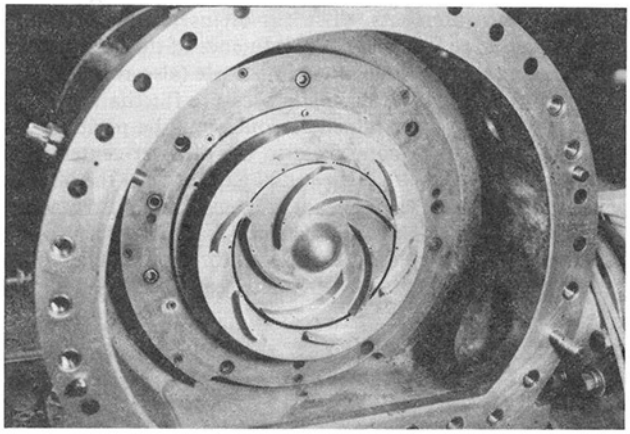

Fig. 2 Photograph of Impeller Z2 and Diffuser G installed in the test section (the front shroud of the impeller was removed to show the impeller blade shapes)

strumented impeller blade and the diffuser vanes varied between 5 and 8 percent of the impeller discharge radius during one impeller revolution. Are the blade and vane pressure fluctuations measured for the "local" radial gaps between the impeller blades and diffuser vanes representative for diffuser pumps in which the radial gap between the impeller blades and diffuser vanes is uniform? During one shaft revolution the impeller flow is subjected to disturbances at two different frequencies (low frequency disturbances such as rotating stall, etc., are excluded from this discussion since the present investigation did not focus on such phenomena); namely a disturbance due to the presence of the diffuser vanes occurring at vane passage frequency f_v, and a disturbance due to the varying radial gap between the impeller blades and diffuser vanes during one shaft revolution occurring at shaft frequency f_s. For the centrifugal pump stages investigated, the vane passage frequency was an order of magnitude larger than the shaft frequency ($6 \leq (f_v/f_s) \leq 12$). Hence, it is inferred that the flow about an impeller blade passing a diffuser vane at a certain radial gap can be considered "quasi-periodic." That is to say the pressure fluctuations experienced by a particular impeller blade and a particular diffuser vane are representative of the pressure fluctuations the impeller blades and the diffuser vanes experience in diffuser pumps with a uniform radial gap. The proximity of neighboring diffuser vanes (for the instrumented impeller blade) and neighboring impeller blades (for the instrumented diffuser vane) with a slightly different radial gap is considered to be a small perturbation with only a small effect on the blade and vane pressure fluctuations

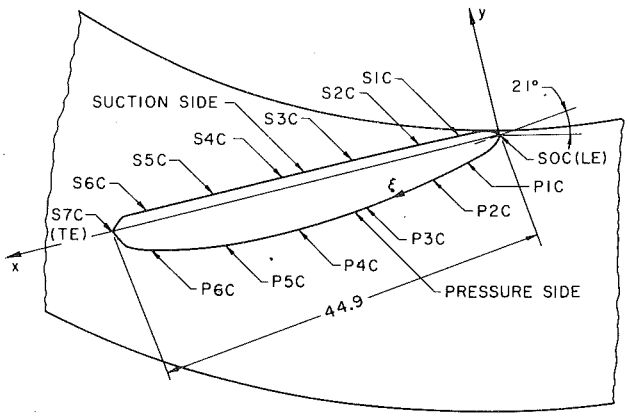

Fig. 3 Diffuser vane with pressure taps at midvane height

measured on the particular instrumented impeller blade and diffuser vane.

Test Facility and Instrumentation

The experiments were conducted in a recirculating water test loop. The facility has been described in detail by Arndt (1988). A simplified view of the test section with the two-dimensional test impeller for impeller blade pressure measurements, Impeller Z2, installed is shown in Fig. 1.

The two two-dimensional impellers have identical blade number and identical blade shape (five logarithmic spiraled blades with a blade angle of 25 deg). Impeller Z1 existed from previous work when the current investigation was started, and was used for most of the diffuser vane pressure measurements, but difficult to modify for impeller blade pressure measurements. Subsequently, Impeller Z2 was designed and built to permit impeller blade pressure measurements by mounting pressure transducers to the impeller. A photograph of Impeller Z2 installed in the test facility is shown in Fig. 2 (the front shroud of the impeller was removed to show the impeller blade shapes). Impeller blade pressure measurements were made at three pressure taps on the impeller blades, one on the blade pressure side ($R/R_2 = 0.987$), one at the impeller blade trailing edge ($R/R_2 = 1.0$), and one on the impeller blade suction side ($R/R_2 = 0.937$). The signals from the pressure transducers were transmitted by cables from the pressure transducers to a slip ring assembly and from there to the pressure transducer power supply.

Diffuser vane pressure measurements were made using a straight wall constant width diffuser with nine vanes, referred to as Diffuser S. No volute, however, is provided. Thus, the flow is discharged from the diffuser into a large housing. The shape of a vane, with the pressure taps at midvane height, is shown in Fig. 3. It is identical to the one used in an early version of the diffuser of the High Pressure Oxygen Turbopump (HPOTP) of the Space Shuttle Main Engine (SSME); however, the number of diffuser vanes was reduced from seventeen to nine. Unsteady vane pressure measurements using this diffuser and one half of the double-suction pump impeller of the HPOTP of the SSME have been reported by Arndt et al. (1989).

A second diffuser, of side wall geometry and diffuser channel width identical to Diffuser S, but permitting variable diffuser vane configurations was used to investigate the effects of the number of diffuser vanes and of the vane leading edge mean angle (also referred to as the vane angle), β^*, on the impeller blade pressure measurements. This diffuser employed circular arc vanes with the geometry listed in Table 2.

Four different diffusers were used for the unsteady impeller blade pressure measurements (diffuser vane pressure measurements could only be made with Diffuser S); the details

Table 1 Impellers

Impeller	z_b	α^*	d_2 (mm)	b_2 (mm)
Imp. Z1	5	25°	161.92	15.75
Imp. Z2	5	25°	161.92	15.75

Table 2 Geometry of the circular arc vanes

R_{mean}	88.91 mm
c	56.90 mm
t_v	4.19 mm

Table 3 Diffusers

Diffuser	Vane Type	z_v	β^*	d_3 (mm)	b_3 (mm)
Diff. F	cir. arc	12	20°	172.72	14.99
Diff. G	cir. arc	6	20°	172.72	14.99
Diff. H	cir. arc	6	10°	172.72	14.99
Diff. S	see fig.3	9	21°	172.72	14.99

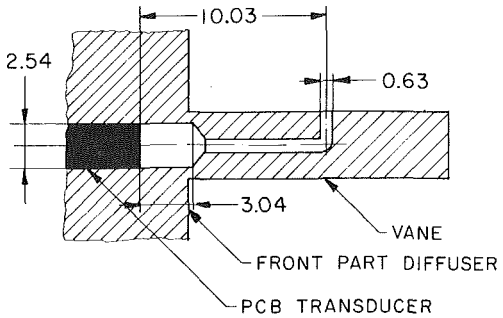

Fig. 4 Geometry of the diffuser vane and impeller blade pressure taps

are listed in Table 3. In Fig. 2, a photograph showing Impeller Z2, with the front shroud removed to show the impeller blade shapes, and Diffuser G is presented.

Steady pressure measurements were obtained by using conventional mercury manometers. The wall pressure about 350 mm upstream of the impeller inlet, $\bar{p}_{up}$, was used as reference pressure. The experimental error on the steady pressure measurements, i.e., on $(\bar{p}-\bar{p}_{up})$, was estimated to be ± 0.5 percent of $(\bar{p}-\bar{p}_{up})$.

Piezoelectric pressure transducers with built-in amplifiers from PCB Inc. were used for the unsteady measurements. This particular transducer (Model 105B02) was selected because of its small size (diaphragm diameter: 2.54 mm), high resonant frequency (250 kHz), and high resolution (~ 70 N/m^2). Because of the relatively short discharge time constant of the transducer of 1 s, static calibration means could not be used. Instead, the dynamic calibration provided by the manufacturer was used. The linearity of the calibration was within 2 percent. The resonant frequency of the impeller blade and the diffuser vane pressure taps, the geometry of which is shown in Fig. 4, was estimated to be approximately 8000 Hz. The spectrum of unsteady pressure measurements (Fig. 5) shows that the estimate of the resonant frequency was reasonable. It can be seen that the blade passage frequency and its higher harmonics are "far" removed from the resonant frequency of the pressure tap, so that amplification and phase shift were negligible.

The data were sampled and discretized in a 16-channel data acquisition system. An encoder on the main shaft was used to trigger the data acquisition system and to provide a clock for the data acquisition system. 1024 data points were taken during one shaft revolution. Since the signal contained some noise, the unsteady data were ensemble averaged over one impeller revolution. The experimental error was found to be less than ± 5 percent for the magnitude and less than ± 2 percent (360 deg corresponding to one impeller blade passage) for the phase of the ensemble-averaged unsteady pressure measurements.

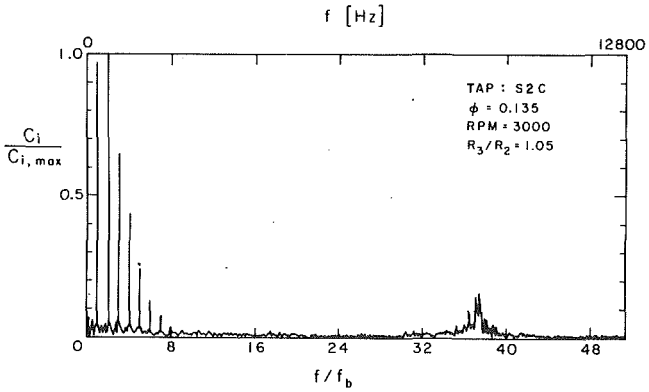

Fig. 5 Spectrum of unsteady diffuser vane pressure measurements for Impeller Z1 and Diffuser S at pressure tap S2C ($\phi = 0.135$, $R_3/R_2 = 1.05$, rpm = 3000)

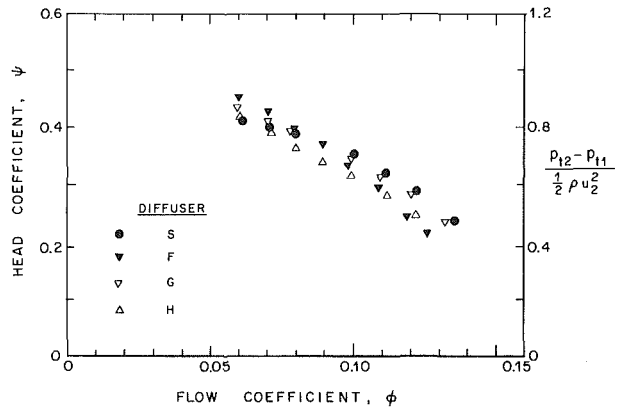

Fig. 6 Performance curves for Diffusers F, G, H, and S

Overall Performance

Performance curves for Impeller Z2 and the different vaned diffusers are shown in Fig. 6. The largest flow coefficients were obtained using Diffuser S (the modified SSME diffuser) and Diffuser G ($z_v = 6$, $\beta^* = 20$ deg). For those diffusers, the head rise for large flow coefficients, $\phi \geq 0.9$, was larger than for Diffuser F ($z_v = 12$, $\beta^* = 20$ deg) and for Diffuser H ($z_v = 6$, $\beta^* = 10$ deg). For low flow coefficients, $\phi \leq 0.07$, Diffuser F had the largest head rise. Diffuser H had the smallest head rise of all diffusers in the range of flow coefficients investigated.

Diffuser Vane Pressure Measurements for Diffuser S

Steady Vane Pressure Measurements and Steady Vane Lift Computations. The steady vane pressure measurements are presented as a steady pressure coefficient, normalized by the dynamic pressure based on impeller tip speed, $(1/2)\rho u_2^2$,

$$\bar{c}_p = \frac{\bar{p}_v - \bar{p}_{up}}{(1/2)\rho u_2^2}$$

Steady diffuser vane pressure measurements were made for three flow coefficients, $\phi = 0.135$, 0.10, and 0.06, two radial gaps between diffuser vanes and impeller blades (5 and 8 percent of the impeller discharge radius), and a rotational speed of 1200 rpm. The steady vane pressure distribution for the medium flow coefficient, $\phi = 0.10$, is shown in Fig. 7. The pressure distribution on the vane changes only slightly with increasing radial gap. Furthermore, the diffusion on the vane suction side can be clearly seen.

From the steady vane pressure measurements at midvane height, the steady force on the vane at midvane height was computed. The steady pressure distribution around the vane

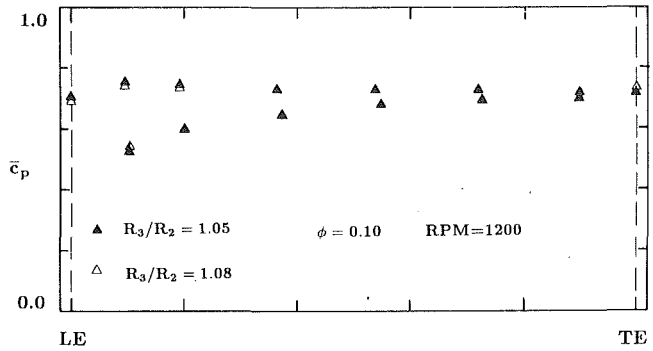

Fig. 7 Steady pressure measurements at midvane height for Impeller Z1 and Diffuser S ($\phi = 0.10$, $R_3/R_2 = 1.05$ and 1.08, rpm = 1200)

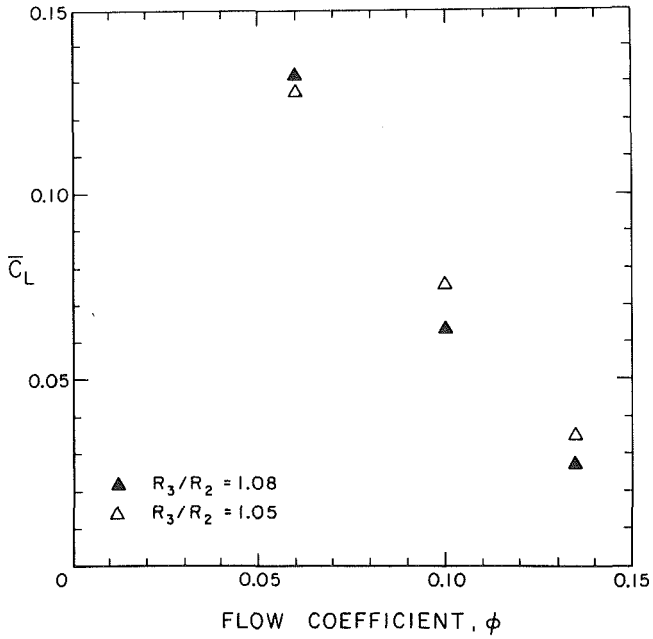

Fig. 8 Steady lift coefficient versus flow coefficient for Impeller Z1 and Diffuser S ($R_2/R_2 = 1.05$ and 1.08, rpm = 1200)

was obtained by fitting a third-order periodic spline through the measured data. A periodic spline fit was chosen to get continuity for the pressure and the first two pressure derivatives at the vane leading and the vane trailing edge. Hence, the steady force was computed from

$$\bar{\mathbf{F}} = -\oint (\tilde{p}_v - \tilde{p}_{up})(\xi)\mathbf{n}d\xi$$

The lift on the vane was defined as the component of the force on the vane normal to the chord joining the vane leading and trailing edges. The lift on the vane was defined as positive if the force component normal to the vane chord was in the positive y direction (Fig. 3). The lift is presented as a lift coefficient, normalized by the dynamic pressure based on impeller tip speed, $(1/2)\rho u_2^2$, and the vane chord c,

$$\bar{c}_L = \frac{L}{(1/2)\rho u_2^2 c}$$

The steady lift on the diffuser vane versus flow coefficient vanes is shown in Fig. 8. It can be seen that the steady lift increases significantly with decreasing flow coefficient. With the exception of the lowest flow coefficient, $\phi = 0.06$, the steady lift and moment decrease slightly with increasing radial gap.

Ensemble-Averaged Unsteady Vane Pressure Measurements and Spectra of Unsteady Vane Pressure Measurements. The

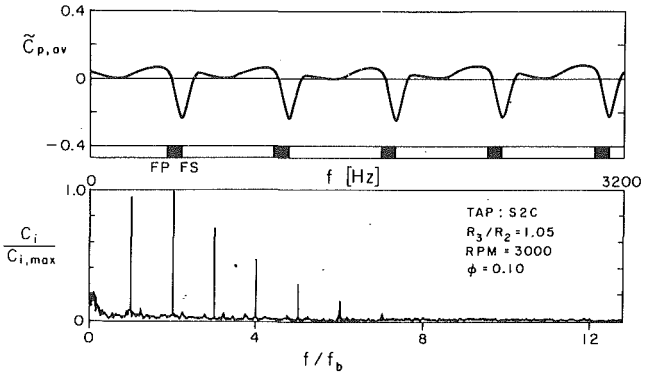

Fig. 9 Ensemble-averaged unsteady vane pressure measurements and spectrum of unsteady vane pressure at pressure tap S2C for Impeller Z1 and Diffuser S ($\phi = 0.10$, $R_3/R_2 = 1.05$, rpm = 3000)

unsteady vane pressure measurements were ensemble averaged, and will be presented as an ensemble-averaged vane pressure coefficient, normalized by the dynamic pressure based on impeller tip speed,

$$\tilde{c}_{p,av}(i) = \frac{1}{N}\sum_{j=1}^{N} \frac{\tilde{p}_v(i,j)}{(1/2)\rho u_2^2}$$

where N is the number of averaging periods, i the ith data point taken in any of the N averaging periods, and j the jth of the N averaging periods. During one averaging period, corresponding to one main shaft revolution (or five impeller blade passages), 1024 data points were taken. A total of 512 averaging periods was used for the ensemble averages. Furthermore, spectra of the unsteady data were obtained. In Fig. 9, a sample of the ensemble-averaged vane pressure fluctuations is presented. The measurements were made at pressure tap S2C, for the medium flow coefficient, $\phi = 0.10$, and $R_3/R_2 = 1.05$ (the pressure tap S2C was selected since the largest vane pressure fluctuations occurred at that measurement location). The ensemble-averaged vane pressure fluctuations are shown in the upper half of the figure. The position of the impeller blades is referenced to the diffuser vane leading edge. The magnitude of the Fourier coefficients relative to the magnitude of the largest Fourier coefficient ($c_i/c_{i,\max}$) is shown versus frequency (upper horizontal scale) and frequency normalized by impeller blade passage frequency (f/f_b) (lower horizontal scale) in the lower half of the figure.

It is evident that the pressure fluctuations are periodic with the impeller blade passage frequency, and of the same order of magnitude as the total pressure rise across the pump. The largest pressure at this particular measurement location (S2C) occurs right before the pressure side of the impeller blade trailing edge reaches the diffuser vane leading edge. As the blade trailing edge passes the vane leading edge, the pressure decreases sharply and attains its minimum as the suction side of the blade trailing edge reaches the vane leading edge. Then, the pressure rises sharply as the impeller blade moves away from the vane leading edge. Hence, most of the pressure fluctuations occur during a rather short time, corresponding to about one third of the impeller blade passage period. The spectrum of the unsteady pressure measurements at tap S2C is dominated by the impeller blade passage frequency and its higher harmonics. In fact, the second harmonic is slightly larger than the first.

Magnitude of Ensemble-Averaged Diffuser Vane Pressure Fluctuations. In the following figures, data on the magnitude of the ensemble-averaged unsteady vane pressure measurements at midvane height are presented. The magnitude of the pressure fluctuations is defined as the difference between the maximum and minimum pressure value in the averaging period, which corresponds to one impeller

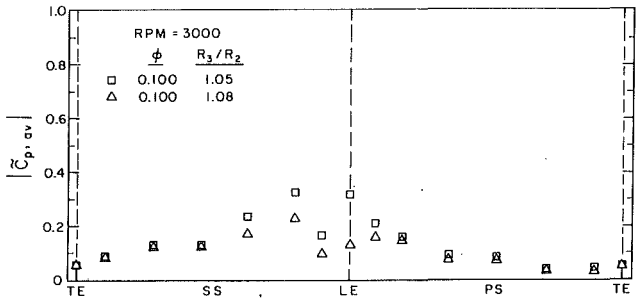

Fig. 10 Magnitude of ensemble-averaged vane pressure fluctuations at midvane height for Impeller Z1 and Diffuser S ($\phi = 0.10$, $R_3/R_2 = 1.05$ and 1.08, rpm = 3000)

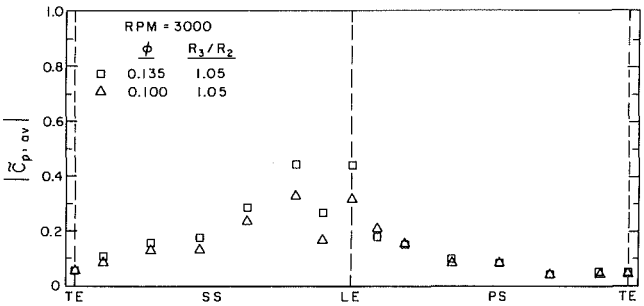

Fig. 11 Magnitude of ensemble-averaged vane pressure fluctuations at midvane height for Impeller Z1 and Diffuser S ($\phi = 0.135$ and 0.10, $R_3/R_2 = 1.05$, rpm = 3000)

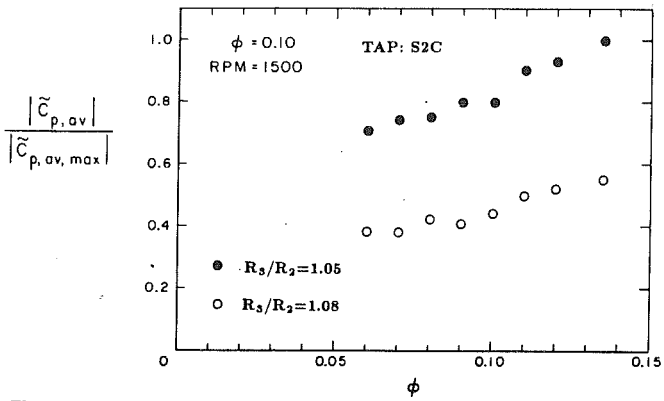

Fig. 12 Magnitude of ensemble-averaged vane pressure fluctuations at pressure tap S2C for Impeller Z1 and Diffuser S ($\phi = 0.06$-0.135, $R_3/R_2 = 1.05$ and 1.08, rpm = 1500)

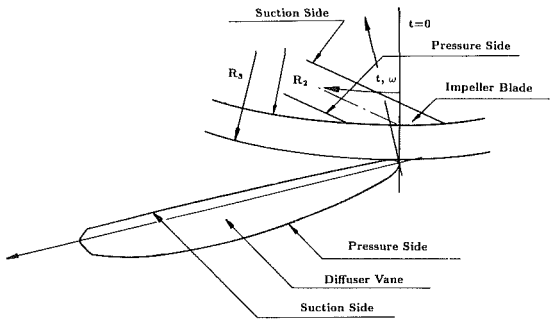

Fig. 13 Geometric reference configuration for phase computation

revolution. The largest fluctuations, independently of flow coefficient or radial gap, occur at the vane leading edge and on the front half of the vane suction side. Those fluctuations are of the same order of magnitude as the total pressure rise across the pump. The fluctuations are larger on the vane suction than on the vane pressure side. On the vane pressure side, they decrease monotonically from the leading edge to the trailing edge, whereas on the vane suction side they have a relative minimum at pressure tap S1C, and they decrease from pressure tap S2C monotonically to the vane trailing edge. For the two flow coefficients investigated, the largest fluctuations occur either at the vane leading edge or at pressure tap S2C.

Figure 10 shows the dependence of the fluctuations on the radial gap between impeller blades and diffuser vanes, $R_3/R_2 = 1.05$ and 1.08, for $\phi = 0.10$ and 3000 rpm. The large pressure fluctuations on the front half of the suction side, at the leading edge, and at the pressure tap on the pressure side closest to the leading edge decrease significantly with increasing radial gap. However, at the pressure taps on the rear half of the vane suction side and at the other pressure taps on the pressure side, the pressure fluctuations remain virtually unchanged.

Figure 11 compares the fluctuations for the two flow coefficients, $\phi = 0.135$ and 0.10, at 3000 rpm and $R_3/R_2 = 1.05$. At the leading edge and at all the pressure taps on the suction side, the fluctuations are larger for $\phi = 0.135$ than for $\phi = 0.10$. With the exception of pressure tap P1C, where the fluctuations are larger for $\phi = 0.10$ than for $\phi = 0.135$, the magnitude of the pressure fluctuations on the vane pressure side is nearly identical for the two flow coefficients.

For one pressure tap, S2C, unsteady vane pressure measurements were made over a range of flow coefficients, ranging from maximum flow coefficient, $\phi_{max} = 0.135$, to $\phi = 0.06$. The shaft speed during those tests was 1500 rpm (comparing the normalized pressure measurements for $\phi = 0.135$ and 0.10 made at 1500 and 3000 rpm, virtually no shaft speed dependence was found). In Fig. 12, the magnitude of the fluctuations as functions of flow coefficient and radial gap, relative to the magnitude of the fluctuation for maximum flow, $\phi = 0.135$, at a radial gap of 5 percent, are presented. It can be seen that the fluctuations are largest for the maximum flow coefficient and decrease with decreasing flow coefficient. Increasing the radial gap between impeller blades and diffuser vanes resulted in about a 50 percent decrease of the fluctuations. Comparing the normalized total pressure rise across the pump (Fig. 6) to the normalized impeller blade pressure fluctuations, it can be seen that the magnitude of the vane pressure fluctuations for the maximum flow coefficient, $\phi = 0.135$, is about 95 percent of the total pressure rise across the pump.

Steady and unsteady diffuser vane pressure measurements using one half of the double-suction pump of the High Pressure Oxygen Turbopump of the Space Shuttle Main Engine were reported by Arndt et al. (1989). The vane pressure fluctuations for comparable radial gaps between impeller blades and diffuser vanes were found to be of similar magnitude.

Magnitude and Phase of Fourier Coefficients of Ensemble-Averaged Vane Pressure Fluctuations. The magnitude and the phase of the Fourier coefficients corresponding to impeller blade passage frequency f_b, twice impeller blade passage frequency $2f_b$, and three times the impeller blade passage frequency $3f_b$, will be presented for the medium flow coefficient, $\phi = 0.10$, and a radial gap of 5 percent. A curve is drawn through the data points in Figs. 14 and 15 (magnitude and phase of the blade passage harmonics). The drawn curve has no significance other than to connect the data points as an aid in viewing the data.

The magnitudes of the Fourier coefficients are presented in Fig. 14. Note that the vertical scale, for the magnitude of the coefficients, is not a linear but a logarithmic one. The magnitude of the first harmonic, i.e., the impeller blade passage harmonic, is approximately equal at most pressure taps on the front half of the vane suction and the vane pressure side (taps P1C, P2C, S0C, S2C, and S3C). The

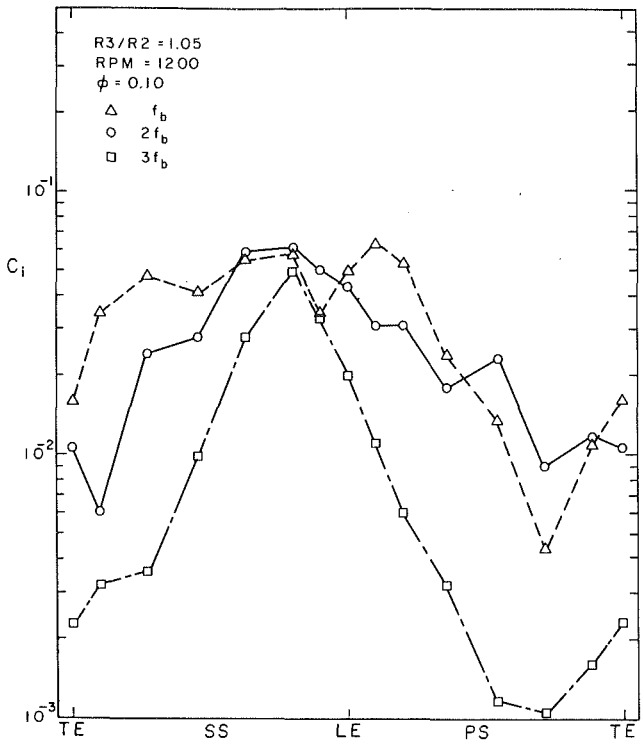

Fig. 14 Magnitude of the Fourier coefficients of impeller blade passage harmonics for Impeller Z1 and Diffuser S ($\phi = 0.10$, $R_3/R_2 = 1.05$, rpm = 1200)

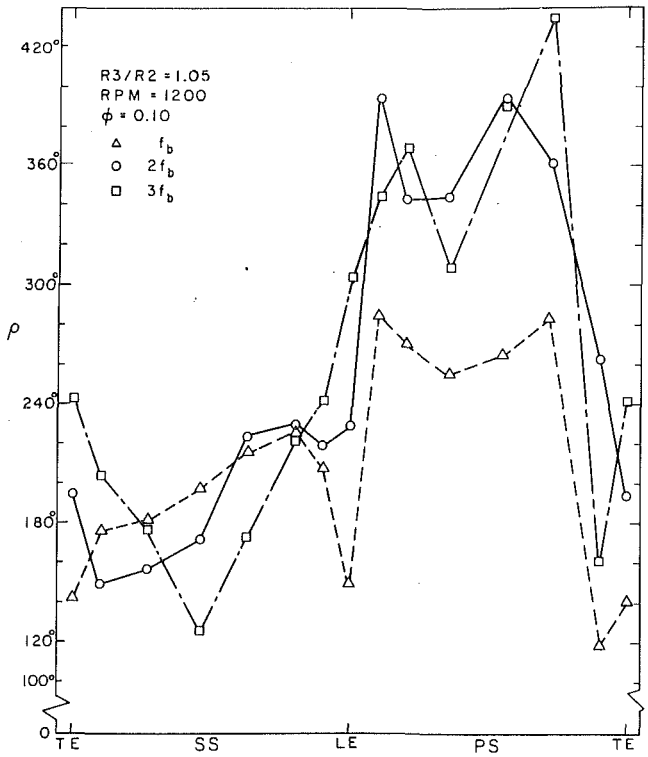

Fig. 15 Phase of the Fourier coefficients of impeller blade passage harmonics for Impeller Z1 and Diffuser S ($\phi = 0.10$, $R_3/R_2 = 1.05$, rpm = 1200)

magnitudes of the second and third blade passage harmonics, however, are significantly larger on the front half of the vane suction than on the vane pressure side. In fact, the magnitude of the second harmonic at the pressure taps on the front half of the vane suction side is as large or larger than the magnitude of the first harmonic. On the rear half of the vane suction side, the magnitude of the first harmonic is, however, significantly larger than the second harmonic. In contrast, on the rear half of the vane pressure side, the magnitude of the second harmonic is larger than the magnitude of the first harmonic.

Hence, the higher impeller blade passage harmonics do contribute significantly to the diffuser vane pressure fluctuations and cannot be neglected in an analysis.

The phase angle of the blade passage harmonics is shown in Fig. 15. The reference configuration, i.e., the geometric configuration at which the data-taking process was started, is shown schematically in Fig. 13. It can be seen that there is a significant difference in phase, of ≈ 70 deg, between the first impeller blade passage harmonic on the front half of the vane suction side and the front half of the vane pressure side.

Ensemble-Averaged Lift Computations. From the vane pressure measurements described earlier, the force on the vane at midvane height was computed. Since those measurements were obtained on different vanes, they had to be phase shifted to one reference vane for the force computations. Superimposing the steady and ensemble-averaged unsteady pressure measurements, the ensemble-averaged vane pressure distribution was obtained. From the ensemble-averaged pressure distribution, the ensemble-averaged force was computed. The ensemble-averaged pressure distribution on the vane was obtained by fitting a third order periodic spline through the measured pressure values. A periodic spline fit was chosen to get continuity for the pressure and the first two pressure derivatives at the leading and trailing edge. The ensemble-averaged force was computed from

$$\mathbf{F}_{av} = -\oint (\bar{p}_v + \tilde{p}_{v,av} - \bar{p}_{up})(\xi)\mathbf{n}d\xi$$

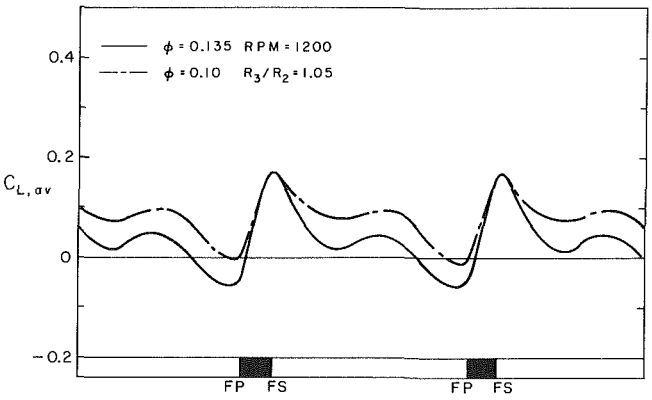

Fig. 16 Ensemble-averaged lift on the diffuser vane at midvane height for Impeller Z1 and Diffuser S ($\phi = 0.10$ and 0.135, $R_3/R_2 = 1.05$, rpm = 1200)

The lift on the vane was defined as the component of the force on the vane normal to the chord joining the vane leading and trailing edge. The lift on the vane was defined as positive if the force component normal to the vane chord was in the positive y direction (Fig. 3). The ensemble-averaged lift is presented as an ensemble-averaged lift coefficient, normalized by the dynamic pressure based on impeller tip speed, $(1/2)\rho u_2^2$, and the vane chord c,

$$c_{L,av} = \frac{L_{av}}{(1/2)\rho u_2^2}$$

In Figs. 16 and 17 data on the ensembled-averaged lift on the ratio of ensemble-averaged to steady lift are presented. The position of the impeller blade is referenced to the diffuser vane leading edge. The averaging period for ensemble averaging was one shaft revolution, corresponding to five impeller blade passages; the data for the first half of the shaft revolution are presented.

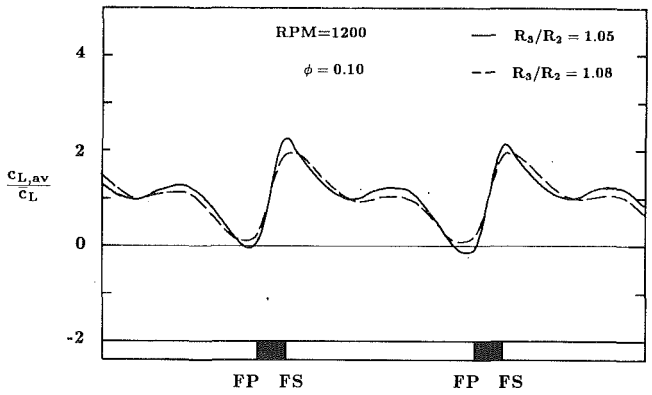

Fig. 17 Ratio of ensemble-averaged lift to steady lift on the diffuser vane at midvane height for Impeller Z1 and Diffuser S ($\phi = 0.10$, $R_3/R_2 = 1.05$ and 1.08, rpm = 1200)

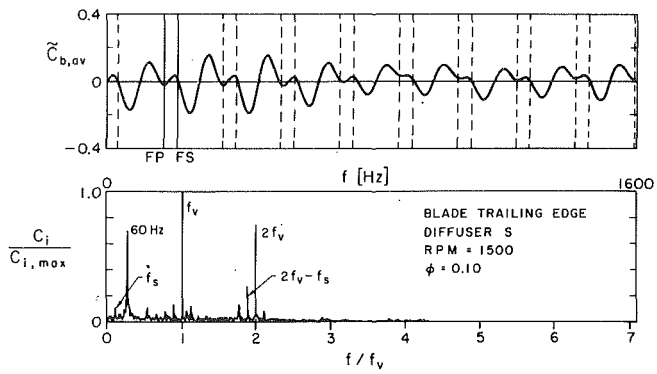

Fig. 18 Ensemble-averaged unsteady blade pressure measurements and spectrum of unsteady blade pressure measurements at the blade trailing edge pressure tap for Impeller Z2 and Diffuser S ($\phi = 0.10$, rpm = 1500)

In Fig. 16, the ensemble-averaged lift for the two flow coefficients investigated, $\phi = 0.135$ and $\phi = 0.10$, is shown for a radial gap of 5 percent. It can be seen that the lift fluctuations are larger for the maximum flow coefficient than for the medium flow coefficient. Minimum lift is attained as the pressure side of the impeller blade trailing edge reaches the vane leading edge. As the blade trailing edge passes the vane leading edge, the lift increases from its minimum to its maximum value, which is attained as the suction side of the impeller blade trailing edge reaches the vane leading edge. As the impeller blade moves away from the diffuser vane trailing edge, the lift does first decrease to approximately its mean value. Then the lift stays relatively constant for about a third of the blade passage period before dropping to its minimum value.

This behavior, i.e., the relatively constant lift on the diffuser vane for a significant part of the impeller blade passage period, is in contrast to the results on diffuser lift fluctuations using one half of the double-suction impeller of the High Pressure Oxygen Turbopump of the Space Shuttle Main Engine and Diffuser S (Arndt et al. 1989). For the impeller of the SSME, the lift on a diffuser vane of the same diffuser decreased strongly montonically from its maximum to its minimum value. The impeller of the SSME has more blades, eight in contrast to five for Impeller Z1. Hence, due to the smaller number of impeller blades, there is an interval of time in a blade passage period during which the influence of the impeller blade–diffuser vane interaction on the unsteady lift is small; i.e., the ensemble-averaged pressure distribution about the vane was observed to be nearly identical to the steady pressure distribution about the vane ($c_{p,av} \approx \bar{c}_p$). The magnitude of the lift fluctuations, however, was found to be approximately equal for the two impellers for comparable flow coefficients and radial gaps between impeller blades and diffuser vanes.

The ratio of the ensemble-averaged lift to the steady lift for the medium flow coefficient, $\phi = 0.10$, and radial gaps of 5 and 8 percent is shown in Fig. 17. For both radial gaps, the ratio is about 2, decreasing slightly with increasing radial gap.

Unsteady Impeller Blade Pressure Measurements Using Diffuser S

Unsteady impeller blade pressure measurements were made at three pressure taps on the impeller blades, one on the pressure side ($R/R_2 = 0.987$), one on the suction side ($R/R_2 = 0.937$), and one on the trailing edge ($R/R_2 = 1.00$). Herein, the measurements made for Diffuser S and the two-dimensional impeller are presented. Data were taken for eight flow coefficients, ranging from $\phi = 0.135$ to $\phi = 0.06$ at 1500 rpm. Since the impeller was positioned eccentrically to the diffuser center, the radial gap between impeller blade trailing edge and diffuser vane leading edge varied during one impeller revolution from 5 to 8 percent of the impeller discharge radius.

Ensemble-Averaged Unsteady Blade Pressure Measurements and Spectra of Unsteady Blade Pressure Measurements. Similarly to the unsteady vane pressure measurements, the unsteady blade pressure measurements were ensemble averaged, and will be presented as an ensemble-averaged blade pressure coefficient, normalized by the dynamic pressure based on impeller tip speed. Furthermore, spectra of the unsteady measurements were obtained.

In Fig. 18, the ensemble-averaged unsteady blade pressure measurements and the corresponding spectrum of the unsteady blade pressure measurements at the blade trailing edge pressure tap are presented for a medium flow coefficient, $\phi = 0.10$. In the upper part, the ensemble-averaged blade pressure fluctuations are shown. The pairs of broken lines indicate the passage of the pressure side and the suction side of the impeller blade trailing edge past the diffuser vane leading edge. The one pair of the solid lines indicates the passage of the pressure side and the suction side of the impeller blade trailing edge past the diffuser vane leading edge at the smallest radial distance between the instrumented impeller blade and the diffuser vanes. That smallest radial gap between the impeller blade trailing edge and the diffuser vane leading edge is 5 percent of the impeller discharge radius. In the lower part of the figure, the magnitude of the Fourier coefficients relative to the largest Fourier coefficient ($c_i/c_{i,\,max}$) is shown versus frequency (upper horizontal scale) and frequency normalized by impeller vane passage frequency (f/f_v) (lower horizontal scale).

It can be seen that the magnitude of the fluctuations varies significantly during one impeller revolution. This is due to the varying distance between the impeller blade trailing edge and the diffuser vane leading edges as the impeller completes one revolution. The trailing edge pressure fluctuations are largest during the vane passage following the smallest gap between the specific instrumented impeller blade and the diffuser vanes. The minimum pressure at the trailing edge pressure tap within each diffuser vane passage is attained after the impeller balde trailing edge has passed the diffuser vane leading edge. The trailing edge pressure then rises sharply to its maximum value, which is attained before the impeller blade trailing edge reaches the next vane leading edge.

In the corresponding spectrum of the unsteady blade pressure measurements, four different discrete frequency components can be found. First, vane passage frequency and its higher harmonics, $(f/f_v) = 1, 2, \ldots$, are the dominant fre-

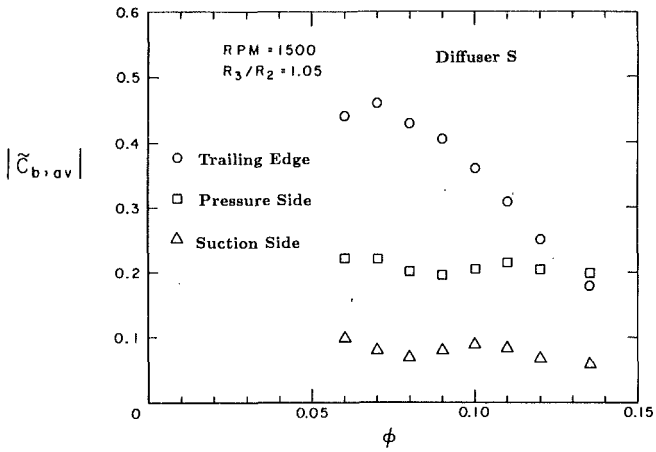

Fig. 19 Magnitude of ensemble-averaged pressure fluctuations at the three impeller blade pressure taps for Impeller Z2 and Diffuser S ($\phi = 0.06$–0.135, $R_3/R_2 = 1.05$, rpm = 1500)

quencies. This is similar to the diffuser vane pressure measurements presented previously. Secondly, a component at shaft frequency f_s can be seen. This component results from the varying radial gap between the impeller blades and the diffuser vanes as the impeller completes one shaft revolution. Thirdly, frequencies at $mf_v \pm nf_s$ (n, $m = 1, 2$) can have significant magnitude. These frequencies are the result of frequency modulation between the vane passage frequency f_v and the shaft frequency f_s

$$\sin(2\pi f_v t)\sin(2\pi f_s t) = 0.5(\cos((f_v - f_s)2\pi t) - \cos((f_v + f_s)2\pi t)$$

and hence result from the uneven radial gap between impeller blades and diffuser vanes. Fourthly, a strong 60 Hz signal and some very small higher harmonics can be seen. The 60 Hz signal is significantly larger than for the diffuser vane pressure measurements. The larger 60 Hz signal may be due to the 60 Hz motor speed control. That is, because of the 60 Hz output of the motor control, the drive shaft may induce both flow oscillations around the impeller blades and impeller vibrations at 60 Hz, which may be picked up by the transducer. Since the 60 Hz signal was very sharp and sufficiently far removed from the shaft frequency and vane passage frequency, it was not expected to influence the measurements. During the ensemble averaging process, the 60 Hz signal was processed out.

Magnitude of Ensemble-Averaged Blade Pressure Fluctuations. For the smallest radial gap, $R_3/R_2 = 1.05$, that is the closest position between the impeller blade and a diffuser vane as the impeller completes one revolution, the magnitudes of the ensemble-averaged blade pressure fluctuations are presented in Fig. 19. The measurements were made for a total of eight flow coefficients, ranging from maximum flow, $\phi = 0.135$, to $\phi = 0.06$.

It can be seen that the magnitudes of the pressure fluctuations range from the same order of magnitude as the total pressure rise across the pump at the trailing edge pressure tap to an order of magnitude smaller than the total pressure rise across the pump at the suction side pressure tap.

The largest fluctuations occur at the trailing edge. They increase significantly with decreasing flow coefficient, from $|\tilde{c}_{b,av}| = 0.17$ for $\phi = 0.135$ (maximum flow) to $|\tilde{c}_{b,av}| = 0.46$ for $\phi = 0.07$. Comparing the normalized total pressure rise across the pump as a function of flow coefficient (Fig. 6) to the normalized impeller blade pressure fluctuations as a function of flow coefficient, it can be observed that the magnitude of the pressure fluctuations can be as large as about 60 percent of the total pressure rise across the pump. Thus, the impeller blade pressure fluctuations can be of the same order of magnitude as the diffuser vane pressure fluctuations.

In contrast to the trailing edge pressure fluctuations, the pressure fluctuations at the pressure and suction side pressure taps are not significantly dependent upon flow coefficient. Maxima are attained for $\phi = 0.11$ at the pressure side pressure tap, for $\phi = 0.10$ at the suction side pressure tap, and for $\phi = 0.06$ at the suction and pressure side pressure tap. Minima are attained for maximum flow, $\phi = 0.135$, at both the pressure and suction side pressure tap, and for $\phi = 0.09$ at the pressure side pressure tap, and for $\phi = 0.08$ at the suction side pressure tap. The magnitude of the fluctuations at the pressure and suction side pressure tap, however, was found to be quite different. At the pressure side pressure tap, the fluctuations were about two to three times larger than at the suction side pressure tap. For maximum flow, the fluctuations at the pressure side pressure tap were even slightly larger than those at the trailing edge pressure tap. Not increasing significantly with decreasing flow coefficient, however, the fluctuations at the pressure side pressure tap for low flow coefficients were only about half as large as those at the trailing edge pressure tap.

Unsteady Impeller Blade Pressure Measurements Using Different Diffusers

Unsteady impeller blade pressure measurements were also made for a second diffuser, with sidewall geometry identical to that of Diffuser S, but permitting variable diffuser vane configurations. Three different vane configurations employing circular arc vanes were tested (see also Table 3). Diffuser F employed twelve vanes with a vane angle β^* of 20 deg, Diffuser G six vanes with a vane angle of 20 deg, and Diffuser H six vanes with a vane angle of 10 deg. Hence, the different diffuser vane configurations permitted an investigation of the influence of the diffuser vane number and of the diffuser vane angle on the impeller blade pressure fluctuations.

Magnitude of Ensemble-Averaged Blade Pressure Fluctuations. The influence of the different diffuser vane configurations on the unsteady impeller blade pressure measurements is presented in Fig. 20 for the trailing edge pressure tap, in Fig. 21 for the pressure side pressure tap, and in Fig. 22 for the suction side pressure tap. The largest pressure fluctuations occurred independently of the diffuser vane configuration at the impeller blade trailing edge. The number of diffuser vanes and the diffuser vane angle, however, were observed to have a significant influence on the pressure fluctuations at all three impeller blade pressure taps. The increase in vane number from six to twelve at a fixed vane angle of 20 deg resulted in a decrease of the blade pressure fluctuations at all blade pressure taps and for all flow coefficients. The reduction varied, depending upon flow coefficient and pressure tap, between 15 and 70 percent. At the trailing edge and at the pressure side pressure tap, the fluctuations decreased more strongly for the lower flow coefficients, whereas at the suction side pressure tap the fluctuations decreased more strongly for the large flow coefficients. Decreasing the vane angle from 20 deg to 10 deg for a constant number of diffuser vanes ($z_v = 6$) resulted for the pressure taps on the blade pressure and on the blade suction side in an increase of the pressure fluctuations for the large flow coefficients of up to 75 percent, whereas for low flow coefficients the fluctuations decreased by up to 30 percent. For the trailing edge pressure tap, the magnitude of the pressure fluctuations remained unchanged for large flow coefficients and decreased for low flow coefficients.

Discussion of the Impeller Blade Pressure Measurements. The impeller blade pressure fluctuations are assumed to be primarily the result of the potential interaction between the diffuser vanes and the impeller blades (Dring, 1982;

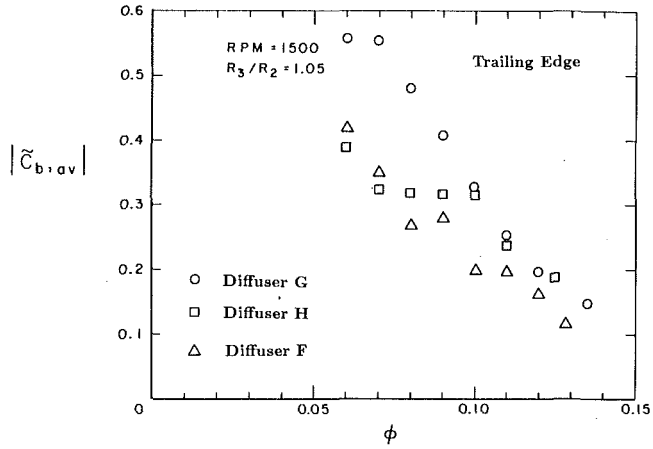

Fig. 20 Magnitude of ensemble-averaged pressure fluctuations at the pressure tap at the impeller blade trailing edge for Impeller Z2 and Diffuser F, G, and H ($\phi = 0.06$–0.135, $R_3/R_2 = 1.05$, rpm = 1500)

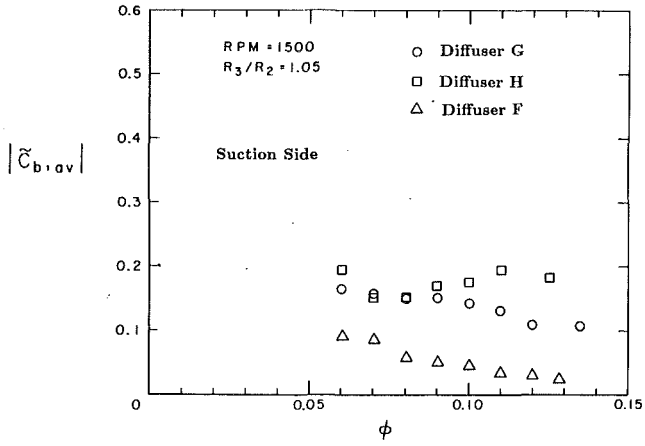

Fig. 22 Magnitude of ensemble-averaged pressure fluctuations at the pressure tap at the impeller blade suction side for Impeller Z2 and Diffusers F, G, and H ($\phi = 0.06$–0.135, $R_3/R_2 = 1.05$, rpm = 1500)

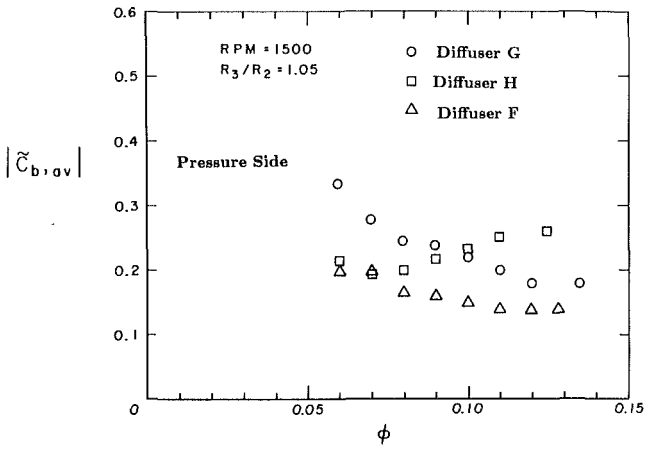

Fig. 21 Magnitude of ensemble-averaged pressure fluctuations at the pressure tap at the impeller blade pressure side for Impeller Z2 and Diffusers F, G, and H ($\phi = 0.06$–0.135, $R_3/R_2 = 1.5$, rpm = 1500)

Gallus, 1980). This was qualitatively confirmed by the unsteady impeller blade pressure measurements presented herein.

From the steady vane pressure measurements for Diffuser S, a significant increase in the lift on the diffuser vanes (and hence of the circulation about a diffuser vane) was observed when the flow coefficient was reduced (Fig. 8). Hence, the circulation about a single diffuser vane, sensed by the rotating impeller blades as a periodic fluctuation, was found to increase with decreasing flow coefficient. This may cause the increase of the pressure fluctuations at the blade trailing edge with decreasing flow coefficient observed for the unsteady impeller blade pressure measurements using Impeller Z2 and Diffuser S (Fig. 19).

Increasing the number of diffuser vanes in a vaned diffuser results in a decrease of the loading of a single diffuser vane. Therefore, the circulation about a single diffuser vane, sensed by the rotating impeller blades as a periodic fluctuation, also decreases. Comparing the results of the unsteady impeller blade pressure measurements for Impeller Z2 and Diffuser F($z_v = 12$, $\beta^* \approx 20$ deg) and Impeller Z2 and Diffuser G ($z_v = 6$, $\beta^* = 20$ deg), it can be seen that the impeller blade pressure fluctuations, at all three pressure taps and for the entire range of flow coefficients investigated, were smaller for the twelve-vaned than for the six-vaned diffuser (Figs. 20–22). This is very likely the result of the reduced circulation about a single diffuser vane, and may therefore confirm that the impeller blade pressure fluctuations are primarily the result of the potential flow interaction between impeller blades and diffuser vanes.

Summary and Conclusion

An experimental investigation of unsteady flow in a centrifugal pump with different vaned diffusers was carried out focusing on impeller blade-diffuser vane interaction. Steady and unsteady diffuser vane pressure measurements were made for a two-dimensional test impeller and a vaned diffuser for radial gaps of 5 and 8 percent of the impeller discharge radius.

It was found that:

- The pressure fluctuations were larger on the suction side than on the pressure side.
- The largest vane pressure fluctuations occurred on the vane suction side close to the leading edge. For a large flow coefficient, $\phi = 0.135$, and a radial gap of 5 percent, the magnitude of those fluctuations reached ≈ 95 percent of the total pressure rise across the pump for that particular flow coefficient.
- Increasing the radial gap between impeller blades and diffuser vanes from 5 to 8 percent resulted in a significant decrease of the large pressure fluctuations on the front half of the vane suction side.
- The fluctuating lift on the diffuser vane was about twice as large as the steady lift.

Unsteady impeller blade pressure measurements were made for a second two-dimensional test impeller with blade number and blade geometry identical to the two-dimensional impeller used for the diffuser vane pressure measurements, but permitting pressure transducers to be mounted to the impeller. Those measurements were made for the vaned diffuser used for the diffuser vane pressure measurements and a second diffuser of identical side wall geometry but permitting variable diffuser vane geometry to investigate the influence of the vane number and the influence of the vane angle on the impeller blade pressure fluctuations.

- The largest blade pressure fluctuations occurred at the impeller blade trailing edge, independently of the diffuser vane configuration.
- Those fluctuations increased significantly with decreasing flow coefficient, in contrast to the large pressure fluctuations at the diffuser vane suction side, which decreased with decreasing flow coefficient. For a low flow coefficient, $\phi = 0.06$, and a radial gap of 5 percent, the magnitude of

those fluctuations reached ≈ 60 percent of the total pressure rise across the pump for that particular flow coefficient.

- Increasing the vane number from six to twelve resulted in a significant decrease of the blade pressure fluctuations at all blade pressure taps (with the exception of low flow coefficients, the total pressure rise across the pump, however, was reduced as a result of the increased vane number).
- Decreasing the vane angle from 20 to 10 deg (for six diffuser vanes) resulted in a decrease of the large pressure fluctuations at the blade trailing edge, and in an increase of the pressure fluctuations at the suction side pressure tap (the total pressure rise across the pump, however, was reduced as a result of the decreased vane angle for all flow coefficients investigated).

In summary, it was found that pressure fluctuations, of the same order of magnitude as the total pressure rise across the pump, can occur on the impeller blades and the diffuser vanes if the radial gap between the impeller blades and the diffuser vanes is small, i.e., of the order of a small percentage of the impeller discharge radius. The large pressure fluctuations at the impeller blade trailing edge may be responsible for the cavitation damage occurring at the trailing edges of the impeller blades of high-speed centrifugal pumps. Furthermore, it was shown that the fluctuating lift on the diffuser vanes can be larger than the steady lift. For high-speed, high-performance pumps with closely spaced blade rows, this result should be considered in the structural design of the vane.

Acknowledgments

The authors are indebted to the NASA George Marshall Space Flight Center for the continued sponsorship of this research under contract No. NAS8-33108.

References

Arndt, N., 1988, "Experimental Investigation of Rotor-Stator Interaction in Diffuser Pumps," Ph.D. Thesis, Division of Engineering and Applied Science, California Institute of Technology.

Arndt, N., Acosta, A. J., Brennen, C. E., and Caughey, T. K., 1989, "Rotor-Stator Interaction in a Diffuser Pump," ASME JOURNAL OF TURBOMACHINERY, Vol. 111, pp. 213-221.

Dring, R. P., Joslyn, H. D., Hardin, L. W., and Wagner, J. H., 1982, "Turbine Rotor-Stator Interaction," ASME *Journal of Engineering for Power*, Vol. 104, pp. 729-742.

Gallus, H. E., 1979, "High Speed Blade-Wake Interactions," *von Kármán Institute for Fluid Mechanics Lecture Series 1979-3*, Vol. 2, Jan. 29-Feb. 2.

Gallus, H. E., Lambertz, J., and Wallmann, T., 1980. "Blade Row Interaction in an Axial Flow Subsonic Compressor Stage," ASME *Journal of Engineering for Power*, Vol. 102, pp. 169-177.

Iino, T., and Kasai, K., 1985, "An Analysis of Unsteady Flow Induced by Interaction Between a Centrifugal Impeller and a Vaned Diffuser" (in Japanese), *Transactions of the Japan Society of Mechanical Engineers*, Vol. 51, No. 471, pp. 154-159.

Inoue, M., and Cumptsy, N. A., 1984, "Experimental Study of Centrifugal Impeller Discharge Flow in Vaneless and Vaned Diffusers," ASME *Journal of Engineering for Gas Turbines and Power*, Vol. 106, pp. 455-467.

Lefcort, M. D., 1985, "An Investigation Into Unsteady Blade Forces in Turbomachines," ASME *Journal of Engineering for Power*, Vol. 87, pp. 345-354.

Stein, W., and Rautenberg, M., 1988, "Analysis of Measurements in Vaned Diffusers of Centrifugal Compressors," ASME JOURNAL OF TURBOMACHINERY, Vol. 110, No. 1, pp. 115-121.

A Comparison Between the Design Point and Near-Stall Performance of an Axial Compressor

N. M. McDougall[1]
Whittle Laboratory,
University of Cambridge,
Cambridge, United Kingdom

Detailed measurements have been made within an axial compressor operating both at design point and near stall. Rotor tip clearance was found to control the performance of the machine by influencing the flow within the rotor blade passages. This was not found to be the case in the stator blade row, where hub clearance was introduced beneath the blade tips. Although the passage flow was observed to be altered dramatically, no significant changes were apparent in the overall pressure rise or stall point. Small tip clearances in the rotor blade row resulted in the formation of corner separations at the hub, where the blade loading was highest. More representative clearances resulted in blockage at the tip due to the increased tip clearance flow. The effects that have been observed emphasize both the three-dimensional nature of the flow within compressor blade passages, and the importance of the flow in the endwall regions in determining the overall compressor performance.

Introduction

The work described in this paper forms part of a continuing program of research into axial compressor flow instabilities being carried out at the Whittle Laboratory in Cambridge. The most serious of these in terms of compressor performance is when the flow breaks down into rotating stall, where a zone or zones of low throughflow rotate around the annulus. Once rotating stall has occurred within a compressor, the pressure rise, mass flow, and efficiency are all reduced. It is crucial that stall be avoided, and new compressors are extensively tested to ensure that stall will not occur during normal operation. Nevertheless stall and surge do occur.

Stall inception can only be understood in the light of a basic understanding of the behavior of the flow in an unstalled compressor. With this in mind, the results presented here concentrate on aspects of the unstalled performance of a model compressor that was tested over a range of rotor tip and stator hub clearances. Measurements were made with the compressor operating both at design flow and at a flow rate just higher than when rotating stall was first observed. (The near-stall flow rate was a function of rotor tip clearance, as the stalling mass flow was altered by the changes in tip clearance.)

Apparatus

The tests were carried out on a high hub-tip ratio, single-stage model compressor. Brief details of the geometry and blading are given in Table 1, a complete description having been given by McDougall (1988). The blading used was of C4 section, designed to give almost constant work across the span. The blades were mounted within the compressor on a central stud on the blade profile stacking axis, which permitted the staggers of the aerofoils to be adjusted quite simply. (During the tests it was found that the small gap left between the blade and the curved surface on which it was mounted could alter the performance of the blade row as recorded by blade surface static tappings. For this reason the gap between the rotor blades and the hub was sealed using a silicone rubber compound.) As it was intended to study rotor stall, the stator stagger angles were increased to unload the

Table 1 Compressor geometry

Radius (mean)	0.6858m
Hub/Tip Ratio	0.8
Rotor (at R_{mean})	
No. of Blades	51
Stagger	47.9°
Camber	26.5°
Solidity	1.31
Chord	0.110m
Diffusion factor	0.51
Stator (at R_{mean})	
No. of Blades	36
Stagger	42.9°
Camber	24.5°
Solidity	0.95
Chord	0.114m
Diffusion factor	0.60 (Nominal Setting)
	0.43 (Closed Setting)

[1]Present address: YARD Ltd., Consulting Engineers, Charing Cross Tower, Glasgow.

Contributed by the International Gas Turbine Institute and presented at the 34th International Gas Turbine and Aeroengine Congress and Exhibition, Toronto, Ontario, Canada, June 4-8, 1989. Manuscript received at ASME Headquarters January 13, 1989. Paper No. 89-GT-70.

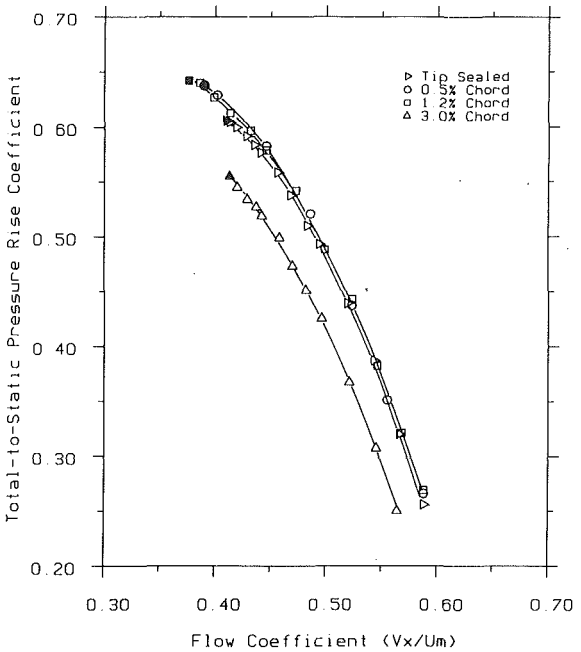

Fig. 1 Effect of variations in rotor tip clearance (solid symbols = stall points)

blades. All the tests presented below were carried out with the compressor thus biased toward stall in the rotor.

Traverses were carried out behind the rotor and stator blade rows using both pneumatic and hot-wire probes. The latter proved especially useful for performing measurements in the rotor-relative frame. Data was recorded automatically using a computer-driven analogue-to-digital converter, which was also used to monitor vibration levels and the rotor speed. Data were not recorded if the rotor speed was more than ±0.2 percent from the design speed of 8.33 rev/sec (500 rev/min).

Overall Compressor Performance

The initial study concentrated on the overall performance of the compressor as indicated by the head-flow characteristics. The variation in total-to-static pressure rise with flow coefficient was recorded, but unfortunately the corresponding efficiency measurements were not available.

Effect of Variation in Rotor Tip Clearance. Figure 1 shows the measured performance of the compressor tested at four tip-clearances. It should be noted that there is no special significance to the particular values of tip clearance used. They merely correspond to the available balsa-wood thicknesses used to rebuild the blade tips after the test at 3 percent clearance. The "tip-sealed" case was obtained using a closed-cell foam rubbing seal, which was fitted onto the rotor blade tips. The major effects of changing the tip clearance are apparent as alterations in the pressure rise across the machine operating range and in the flow coefficent at which the machine stalls (indicated by solid symbols on the diagram).

At tip clearance/chord ratios up to 1.2 percent the performance was largely independent of tip clearance, with the exception of the sealed case, which produced a slightly inferior pressure rise when compared to the two small clearance cases. The best performance in terms of stall point was obtained at a tip clearance/chord ratio of 1.2 percent. Once the clearance was increased to 3 percent of chord, the performance of the compressor dropped off dramatically, in terms of both pressure rise and flow coefficient at stall point.

Table 2 Effect of inlet velocity profile on stalling flow coefficient

Inlet Velocity Profile	Stalling Flow Coefficient (V_x/U_m)
"Standard"	0.42
"Thickened Hub"	0.40
"Thickened Casing"	0.43

Stator hub clearance was investigated in a similar way with regard to the overall performance. Two cases were investigated, a sealed case, simulating a shrouded stator, and a 2 percent of stator chord gap between the stator blade hub section and the stationary hub endwall. The results of these tests indicated that the effect of introducing stator hub clearance was much smaller than that observed due to rotor tip clearance. This is not surprising in view of the small design pressure rise for this blade row, particularly once the blades had been restaggered.

Effect of Inlet Boundary Layer Thickness. At the largest rotor tip clearance tested, 3 percent of rotor chord (most representative of rear stages in multistage compressors), an investigation was carried out on the effects of thickening the endwall boundary layers at entry to the stage. The various inlet conditions were produced using square teeth set normal to the endwall in question to thicken the boundary layers far upstream of the compressor rotor. The tests were carried out with a thin hub and casing boundary layer (the "standard" configuration) and one test each with a thickened hub boundary layer and then a thickened casing boundary layer. The "standard" configuration had integral thicknesses of order $\delta^* \approx 3$ mm and $\theta \approx 2$ mm on both endwalls. Once either boundary layer was thickened using the teeth, these thicknesses increased by a factor of three to $\delta^* \approx 10$ mm and $\theta \approx 6$ mm on the endwall in question.

Thickening either endwall boundary layer reduced the compressor total-to-static pressure rise over the entire range between maximum flow and the stall point. This was more marked with the thicker casing boundary layer due to the larger effective blockage at this radius. The alterations to the inlet profile also changed the flow coefficient at which the compressor stalled, as indicated in Table 2.

If the stall point with the standard velocity profile is used as a datum, the thicker casing profile caused a larger deterioration in stall margin than the thicker hub profile, with a loss in pressure rise accompanied by an increase in stalling flow coefficient. The thicker hub profile actually reduced the stalling flow coefficient, although this was accompanied by a reduction in pressure rise at stall.

Blade Passage Performance, Rotor

Area traverses were carried out downstream of the rotor blade row operating with the "standard" inlet velocity profile, to evaluate the blade passage performance at the various tip clearances. These tests were carried out with the stator hub sealed, simulating a shrouded stator.

Nomenclature

p_2 = downstream static pressure
p_{01} = upstream stagnation pressure
U_m = mean blade speed
V_x = axial velocity
ϕ = flow coefficient = V_x/U_m
ψ_{TS} = total-to-static pressure coefficent = $(p_2 - p_{01})/0.5\rho(U_m)^2$

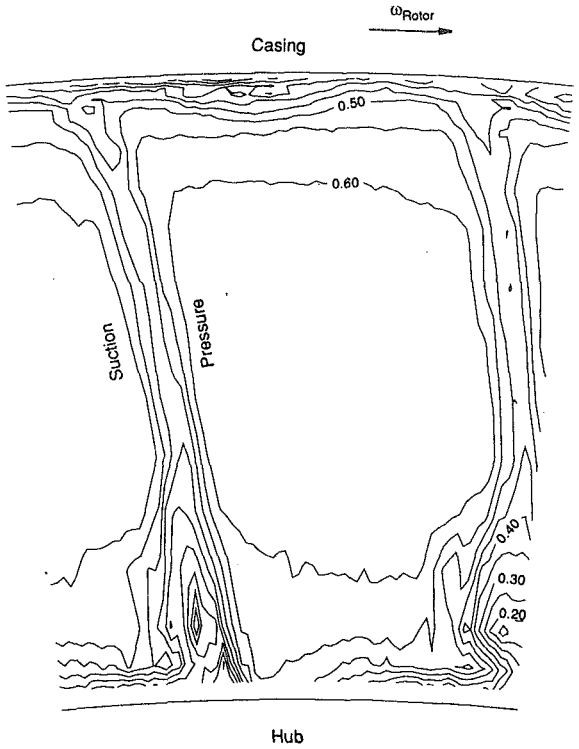

Fig. 2 Axial velocity ratio, rotor exit plane; design point ($\phi = 0.55$), tip clearance/chord ratio 0.5 percent

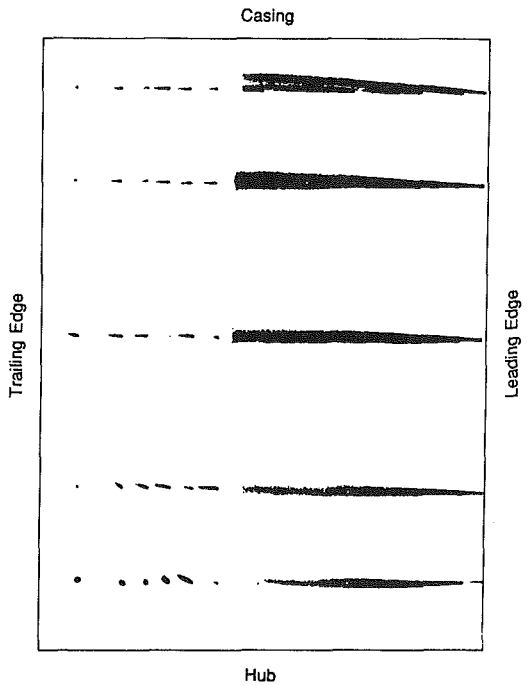

Fig. 3 Flow-visualization, rotor suction surface; design point ($\phi = 0.55$), tip clearance/chord ratio 0.5 percent

Design Point Operation. Figure 2 shows contours of axial velocity ratio (local axial velocity nondimensionalized by the mean blade speed) measured downstream of the rotor trailing edge plane, at a rotor tip clearance of 0.5 percent chord. The wakes shed from the blades are relatively thin, as are the hub and casing boundary layers. There is slight evidence of the blade wakes thickening as they approach the hub and casing endwalls on the suction surface side, but the effect is small and barely noticeable at the casing.

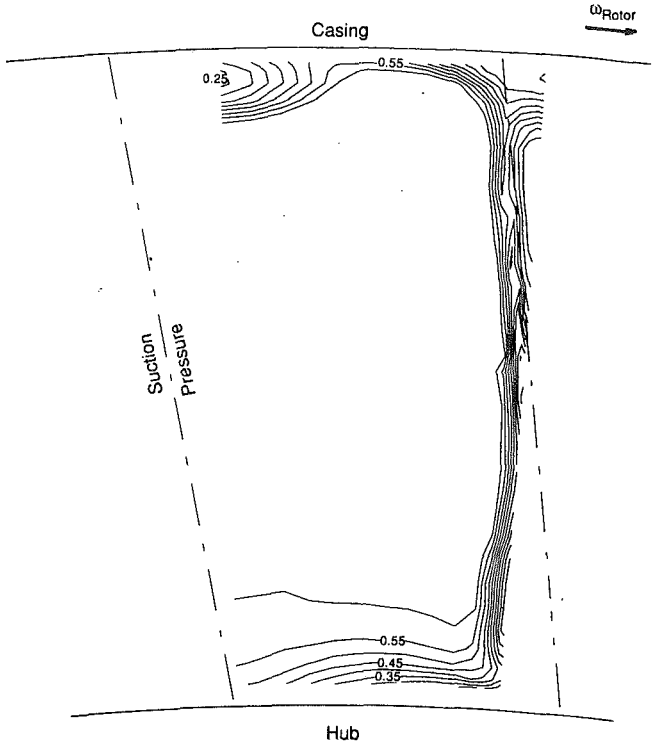

Fig. 4 Throughflow velocity ratio, rotor exit plane; design point ($\phi = 0.55$), tip clearance/chord ratio 3.0 percent

The casing endwall boundary layer is nonuniform across the pitch. At approximately 30 percent of pitch from the pressure surface there is a small accumulation of low axial velocity fluid, which is apparent as a local thickening of the boundary layer. The presence of this core of low-momentum fluid is downstream evidence of tip leakage flow.

Results obtained using the Ammonia-Ozalid flow visualization technique described by Dring and Joslyn (1979) on the rotor suction surface are shown in Fig. 3. The differing contrast of the ammonia traces along the blade chord was a result of the experimental technique rather than a change in the nature of the passage flow. The pattern of the gas traces indicates that the flow was attached over the majority of the aerofoil. There is little evidence of radial flow except for a small region close to the hub near the trailing edge of the blade. Here, the ammonia trace pattern does show some evidence of radial flow, indicating the presence of a small corner separation. On comparison with the results from the downstream traverse, it is clear that the pitchwise extent of this separation is limited.

Similar measurements were made downstream of the rotor with the tip clearance increased to 1.2 percent of chord. Both the traverse results and the surface flow visualization were qualitatively very similar to those obtained at the smaller clearance, and so they are not shown here.

A representative rotor tip clearance for a multistage compressor (the design intent) is 3 percent of chord. This is controlled by mechanical constraints rather than by aerodynamic design. Once the tip clearance was increased to this level the performance of the stage deteriorated noticeably. Figure 4 shows contours of throughflow velocity ratio (local streamwise velocity nondimensionalized by the mean blade speed) plotted at the design flow coefficient. The wake shed from the rotor suction surface is again thin, and the hub boundary layer thickness is similar to that recorded in the previous, tighter tip clearance cases. At the casing, the pitchwise nonuniformity in the boundary layer is much more pronounced. A core of low axial velocity fluid is clearly visible close to the pressure surface. Between the core and the suction surface of the

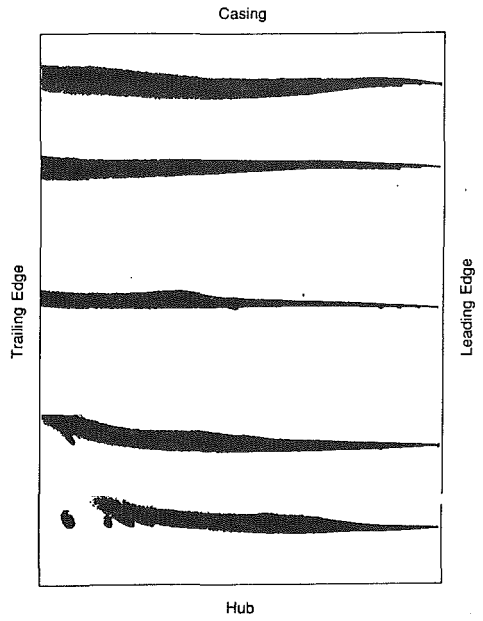

Fig. 5 Flow visualization, rotor suction surface; design point ($\phi = 0.55$), tip clearance/chord ratio 3.0 percent

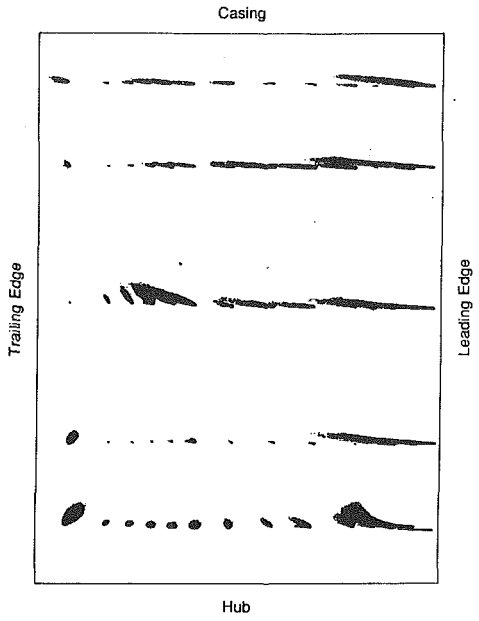

Fig. 7 Flow visualization, rotor suction surface; near stall ($\phi = 0.43$), tip clearance/chord ratio 0.5 percent

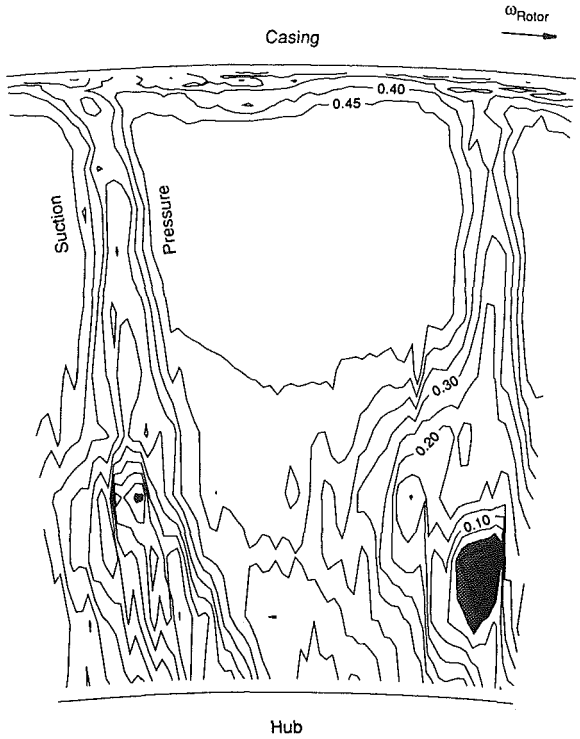

Fig. 6 Axial velocity ratio, rotor exit plane; near stall ($\phi = 0.43$), tip clearance/chord ratio 0.5 percent

boundary layer thins noticeably, and there is little broadening of the rotor blade wakes as they approach the casing.

Ammonia-Ozalid flow-visualization results for the rotor suction surface (Fig. 5) indicate the presence of a small corner separation close to the hub, but otherwise there is again little evidence of fluid with a strong radial component.

Near Stall Operation. As the mass flow through the compressor is reduced toward stall, the aerodynamic loading on both rotor and stator blade rows increases, and the flow in the endwall regions begin to deteriorate. The following results were obtained at a flow coefficient just higher than that at which the compressor stalled.

Once again, there was considerable similarity between the results obtained at 0.5 percent and 1.2 percent tip clearance. Downstream of the rotor at 0.5 percent rotor tip clearance (Fig. 6), the blade wakes have broadened to extend across most of the passage width at the hub, and it is no longer possible to distinguish between blade wake and hub endwall boundary layer in this region. At the casing, the endwall boundary layer is thicker than in the design flow case for this clearance, and the pitchwise nonuniformity is still apparent. On comparison with surface flow-visualization results at this clearance, shown in Fig. 7, the cause of the thickening is clearly a large corner separation at the junction between the hub and the blade suction surface. The separation extends across at least 75 percent of the span, with evidence of reversed flow close to the trailing edge near the hub. It should be emphasized that although the rotor blades appear to be "stalled" in a two-dimensional aerofoil sense, the compressor was *unstalled* during the tests.

When the tip clearance was increased to 1.2 percent of chord the performance of the compressor hardly changed. Both the downstream traverse results and the rotor suction surface flow visualization showed little dependence on tip clearance, and in view of the small change in stalling flow coefficient, few other measurements were made of the passage flow. However, the stall of this and the 3 percent tip clearance configuration was investigated in some detail and is discussed fully in the companion paper (McDougall et al., 1990).

Once the rotor tip clearance was increased to 3 percent of rotor chord, the performance of the stage deteriorated noticeably in terms of both the pressure rise produced and the stalling flow coefficient. This was reflected in the traverse results at rotor exit, shown as contours of throughflow velocity ratio in Fig. 8. The rotor wakes are broader than at design point for the same tip clearance, but the spread is much more uniform across the span. Also, there is no noticeable thickening toward the hub as seen when the tip clearance was 0.5 or 1.2 percent of chord at the near-stall flow coefficient. In addition, the low-velocity core structure seen previously near the pressure surface at the casing is no longer visible. It has been replaced by a more uniform endwall boundary layer that is much thicker than the depth of the previously visible core structure.

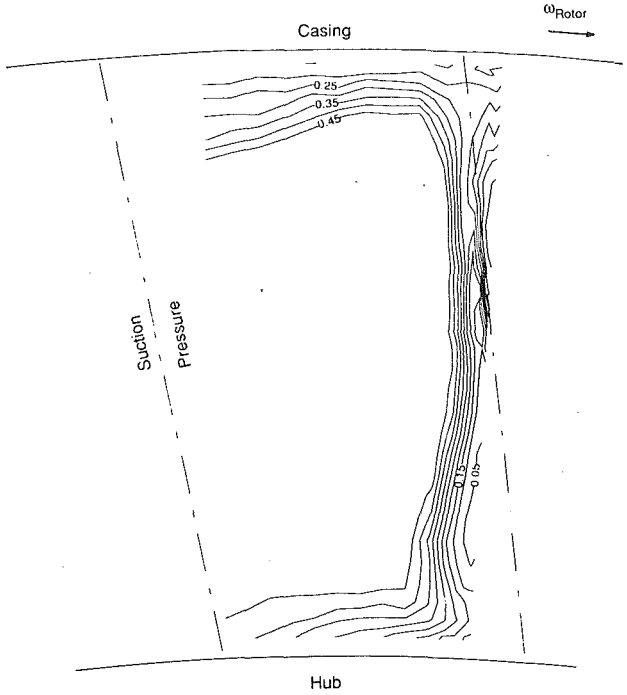

Fig. 8 Throughflow velocity ratio, rotor exit plane; near stall ($\phi = 0.43$), tip clearance/chord ratio 3.0 percent

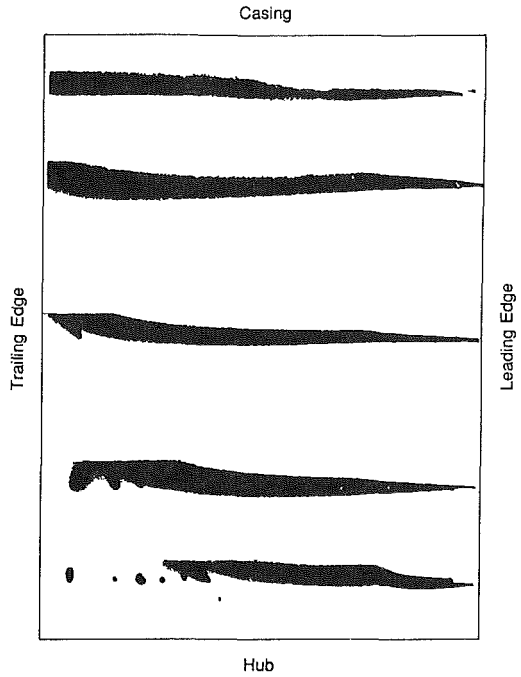

Fig. 9 Flow-visualization, rotor suction surface; near stall ($\phi = 0.43$), tip clearance/chord ratio 3.0 percent

Comparing these results with the surface flow-visualization results shown in Fig. 9, there is still evidence of a corner separation of reduced spanwise extent, but the circumferential extent of the separation is limited to a region 30 percent of the pitch from the suction surface at the hub, as seen in Fig. 8.

Blade Passage Performance, Stator

The following results were recorded with the rotor tip clearance set at 0.5 percent of rotor chord. Two cases were tested, one representing shrouded stators (no clearance between the hub and the stator blades) and one with a 2 percent

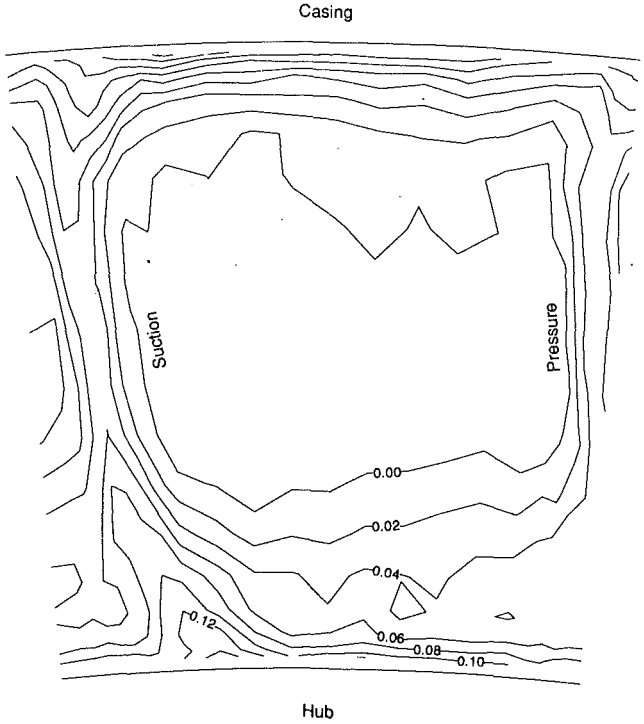

Fig. 10 Total pressure difference, stator exit plane; design point ($\phi = 0.55$), rotor tip clearance/chord ratio 0.5 percent, stator hub sealed

of chord clearance between the blade and (stationary) hub. At design point both configurations gave similar results, and consequently will be presented together. Near stall this was not the case and the results from the shrouded and unshrouded cases are presented separately.

Design Flow. Area traverses were carried out downstream of the stator blade row with a kiel probe. Figure 10 shows the results measured downstream of the sealed stator hub, presented as contours of total pressure difference. The reference inlet total pressure was based on a radial traverse downstream of the rotor, where the time-averaged total pressure was recorded. Thus the contours do not represent a true "total pressure loss," but are a total pressure difference, nondimensionalized by dynamic head based on mean blade speed. As such they are intended to give an impression of the passage performance. The contours show essentially the same features as recorded downstream of the rotor. The blade wakes and endwall boundary layers are all relatively thin, and there is little evidence of separated flow as the endwalls are approached. These features are hardly surprising when the loading of the stator blade row is considered.

Near Stall. Once stall is approached, the loading of the stator increases. The Leiblien Diffusion Factor (Leiblein, 1965) at this flow coefficient was predicted using a streamline curvature design program by Denton (1978) not to exceed 0.6 (the value normally assumed to mark a sudden increase in loss). However, the prediction made no allowance for the large corner separations within the rotor passages described above. The effect of these regions of separated flow is to increase the incidence onto the stator blade row near to the hub. Thus although the design intent was for a lightly loaded aerofoil, the stator hub loading was increased quite markedly as stall was approached due to the distorted inlet profile.

Shrouded Stator. Figure 11 shows the results from an area traverse at stator exit, again plotted as contours of total pressure difference. The contours show a dramatic thickening of the blade wakes away from the casing. The separations are

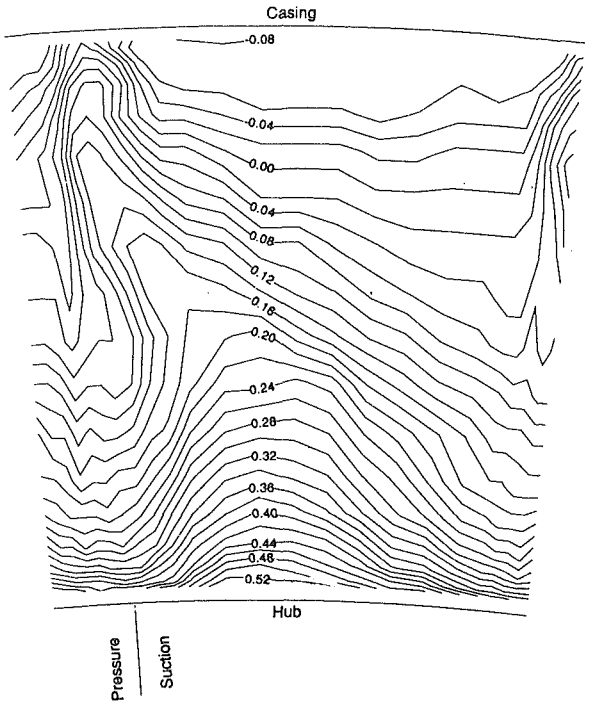

Fig. 11 Total pressure difference, stator exit plane; near stall ($\phi = 0.40$), rotor tip clearance/chord ratio 0.5 percent, stator hub sealed

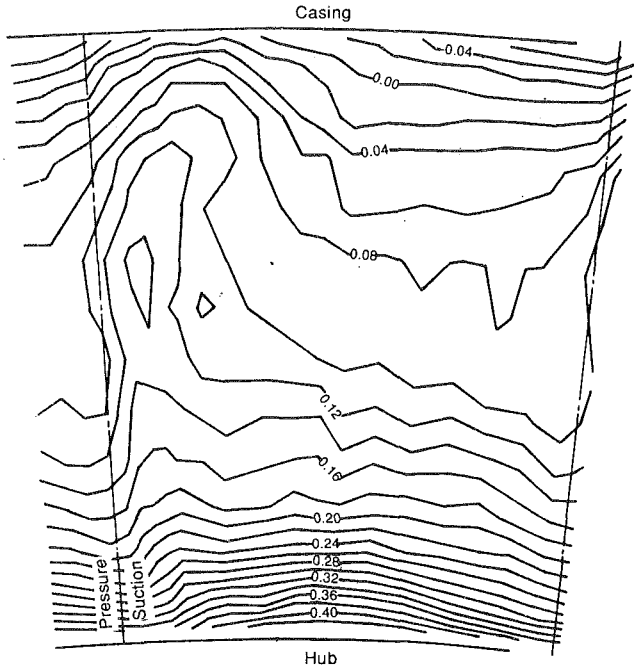

Fig. 13 Total pressure difference, stator exit plane; near stall ($\phi = 0.40$), rotor tip clearance/chord ratio 0.5 percent, stator hub clearance/chord ratio 2.0 percent

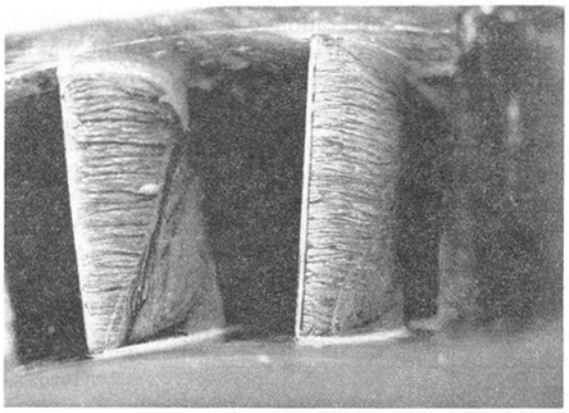

Fig. 12 Oil flow visualization, stator suction surface; near stall ($\phi = 0.40$), tip clearance/chord ratio 0.5 percent, stator hub sealed

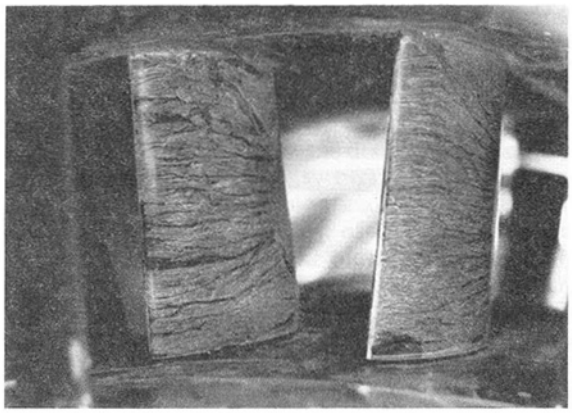

Fig. 14 Oil flow-visualization, stator suction surface; near stall ($\phi = 0.40$), rotor tip clearance/chord ratio 0.5 percent, stator hub clearance/chord ratio 2.0 percent

so large that it is impossible to identify a region of "clean" flow between the distorted wakes. Again it should be emphasized that although the blades are clearly "stalled" in a two-dimensional sense, the compressor was operating without rotating stall throughout all the tests.

The extent of this separated region within the blade passage is shown from the results of an oil and dye flow-visualization technique in Fig. 12. A suspension of fluorescent dye in oil was painted on a stator suction surface and the compressor was then run for a few minutes at the desired mass flow. The results show that the separation extends across 80 percent of the span from the hub at the trailing edge, and begins at approximately 15 percent of chord from the blade leading edge.

Unshrouded Stator. Once a clearance was introduced between the stator blade and the stationary hub the flow in the blade passage improved. Figure 13 shows the results from a traverse downstream of the blade row, which shows that the blade wakes have thinned and the extent of the corner separation has been reduced. The oil flow-visualization experiment was repeated for this configuration and the improvement in the passage flow is clearly visible in Fig. 14. The separated region is now limited to a small portion of the span near the trailing edge.

This change in passage performance has been predicted by a three-dimensional Navier–Stokes solver using a fairly course mesh (see McDougall and Dawes, 1987). The fact that the program was able to predict the two flows suggests that the improvement brought about by the inclusion of hub clearance is a gross flow effect, rather than the result of mixing or flow entrainment. The program, in its present state of development, is not capable of the modeling such "small scale" effects. However, its usefulness as a tool for comparing the flow in different configurations should not be understated, and indeed this will be returned to in the companion paper (McDougall et al., 1990).

Discussion

Two important points have emerged from this study of compressor performance on and off design. Firstly, there was

a clear relationship between compressor performance (both overall as measured by the head-flow characteristics, and in the blade passage flows) and rotor tip clearance. The same effect was not visible on the stator when a hub clearance was introduced, but this is to be expected as the design pressure rise for the stator blade row was kept deliberately small.

In terms of overall compressor performance, there was some evidence of an "optimum" tip clearance in terms of pressure rise and stall point. While no definitive statements can be made as only a limited number of tip clearances were tested and no efficiency measurements were made, there is clearly an optimum clearance between 1.2 and 3 percent of rotor chord in terms of pressure rise and stall point. Whether the same would be true if efficiency measurements were available for the same configurations is not clear. The approximate optimum clearance (≈ 1 percent of chord) is somewhat smaller than that which can readily be achieved in multistage compressors without some form of tip clearance control. Also of note is the fact that a sealed tip clearance gives inferior performance to a very small clearance. This again implies the existence of an optimum clearance somewhere between 1.2 and 3 percent of chord (0.7 to 2 percent of span for this build).

The influence of the tip clearance on the overall performance is due to alterations in the magnitude and effect of the tip leakage flow. This is reflected in the nature of the passage flow. At design point, there are no large regions of separated flow; the blade wakes and hub and casing boundary layers are thin. At tip clearances at or below 1.2 percent of rotor chord there is slight evidence in the downstream flow of a thickening of the casing endwall boundary layer toward the pressure surface, but the local increase in thickness is small. Once the tip clearance is increased to 3 percent, there is a clear "core" of low throughflow velocity fluid at this point in the casing boundary layer. The effect of this core of tip leakage fluid is to reduce the available flow area within the passage and hence reduce the passage diffusion. Consequently, near stall, the pitchwise extent of the hub corner separation is much smaller in the 3 percent tip clearance case than in the two smaller clearance cases. This effect may seem obvious, but it has important consequences when considering the breakdown of the flow within the compressor, and will be returned to later.

A further point emerges when the results from the area traverses downstream of the rotor and the suction surface flow-visualization results are compared. The flow-visualization results suggest that the effect of increasing the tip clearance is a marginal reduction in the spanwise extent of the corner separation, but they do not indicate the dramatic reduction in the pitchwise extent of the separated region. It is clear that surface flow visualization is an important tool in the analysis of blade passage flow, but is it to be remembered that the technique can only give really useful information when other results (such as downstream area traverses) are available to build up a more complete picture of the flow.

Conclusions

1 At design point, extensive regions of separated flow are not evident for a compressor designed within conventional loading limits.

2 With the stator stagger increased to reduce the incidence, separation of the flow within the stator was not a cause of stage stall. This was later confirmed with the stator at its nominal design stagger.

3 Tip clearance can have an overwhelming effect both for rotor and stator. Small clearance was found to be beneficial for both.

4 Large rotor tip clearances allowed large tip clearance flow, increased blockage, reduced pressure rise, and higher flow rate at stall. The optimum tip clearance was between 1.2 and 3 percent of rotor chord.

5 The change in the flow pattern brought about by the inclusion of hub clearance is caused by a major change in the nature of the passage flow. This has been demonstrated by predicting the change with a Navier–Stokes code using a coarse representation of the geometry.

6 Once again, it has been demonstrated that it is the flow in the endwall regions that dominates the flow pattern within the stage once the loadings are increased.

7 The results provide a firm basis for the study of stall inception.

Acknowledgments

The author would like to thank Rolls Royce plc and the S.E.R.C., who gave financial support to the project and the author under the CASE award scheme. Latterly the author was entirely supported by Rolls Royce, who granted a six month extension to the project, considerably benefitting the work.

The research was supervised by Dr. N. A. Cumpsty, whose criticism and ability to suggest alternative points of view was a continuous feature of my time in Cambridge. Dr. T. P. Hynes gave valuable help in the data analysis, and during several lengthy discussions on the results. The continued interest and encouragement from Mr. C. Freeman of Rolls Royce and Professor E. M. Greitzer of M.I.T. were also appreciated.

The author would also like to acknowledge the assistance given in preparing the test compressor and instrumentation by the Whittle Laboratories technical staff led by Mr. K. A. Bryant.

References

Denton, J. D., 1978, "Throughflow Calculations for Transonic Axial Flow Turbines," ASME *Journal of Engineering for Power*, Vol. 100.

Dring, R. P., and Joslyn, H. D., 1979, "Measurements of Turbine Rotor Blade Flows," in: *Measurement Methods in Rotating Components of Turbomachinery*, ASME, New York, pp. 51–58.

Leiblein, S., 1965, "Experimental Flow in 2-D Cascades," *Aerodynamic Design of Axial Compressors*, NASA SP36, Chap. 4.

McDougall, N. M., 1988, "Stall Inception in Axial Compressors," Ph.D. Dissertation, University of Cambridge, United Kingdom.

McDougall, N. M., Cumpsty, N. A., and Hynes, T. P., 1990, "Stall Inception in Axial Compressors," ASME JOURNAL OF TURBOMACHINERY, this issue.

McDougall, N. M., and Dawes, W. N., 1987, "A Numerical Simulation of the Strong Interaction Between a Compressor Blade Clearance Jet and Strongly Stalled Passage Flow," presented at the 7th GAMM Conference on Numerical Method in Fluid Mechanics.

N. M. McDougall[1]

N. A. Cumpsty

T. P. Hynes

Whittle Laboratory,
University of Cambridge,
Cambridge, United Kingdom

Stall Inception in Axial Compressors

Detailed measurements have been made of the transient stalling process in an axial compressor stage. The stage is of high hub-casing ratio and stall is initiated in the rotor. If the rotor tip clearance is small stall inception occurs at the hub, but at clearances typical for a multistage compressor the inception is at the tip. The crucial quantity in both cases is the blockage caused by the endwall boundary layer. Prior to stall, disturbances rotate around the inlet flow in sympathy with rotating variations in the endwall blockage; these can persist for some time prior to stall, rising and falling in amplitude before the final increase, which occurs as the compressor stalls.

Introduction

One of the limiting aspects of axial compressor behavior is the breakdown of the flow into either rotating stall or surge. In either case the unstalled compressor becomes unstable as the flow is reduced and as a result of stall the flow pattern is altered into one of these forms. (The word stall will be used here to describe the breakdown process following instability, while the stable operating process that can occur *after* the machine has stalled will be termed rotating stall.) Rotating stall and surge are alternative outcomes of instability of the same compressor, as was conclusively demonstrated by Greitzer (1976); it is not just the compressor but the parameters of the entire compression system that determine which will occur. More recently Moore and Greitzer (1986) and Greitzer and Moore (1986) have calculated the breakdown into both types of flow, but only when the variation of pressure rise with flow rate is prescribed for the compressor; in other words, it does not address the nature of the flow in the compressor itself. This paper is about the fluid mechanic processes that occur during stall.

One of the clearest descriptions of the conditions for a compressor to become unstable is given by Stenning (1980). The treatment is two dimensional so it is strictly only valid for compressors with high ratios of hub to casing diameter. It also assumes that the flow is axially symmetric and incompressible, the latter being reasonable for most subsonic stages, since it has been shown that the effects of Mach number are small for well-matched compressors. The analysis makes no assumption about the behavior of the compressor or the number of stages except that there can be no circumferential flow inside the machine—a reasonable assumption for most compressors that have small axial gaps between rotors and stators. The prediction of this simple analysis is that the compressor will be unstable when

$$\partial(p_2 - p_{01})/\partial V_x > 0$$

where p_2 is the static pressure at the outlet face of the compressor, p_{01} is the inlet stagnation pressure, and V_x is the axial velocity. Although the assumptions of the analysis are all reasonable, the common experience is that most compressors stall when $\partial(p_2 - p_{01})/\partial V_x$ is still significantly less than zero, i.e., on the "stable" part of the operating characteristic when $p_2 - p_{01}$ rises as flow rate is reduced. In practical terms this means that the compressor is stalling at flows larger than would seem necessary and that the operating range would appear to be unnecessarily reduced. The work described in this paper was an attempt to establish why this is so.

The analysis of compressor stability has usually avoided including any consideration of the compressor aerodynamics, choosing to treat the pressure rise-flow rate variation as an input parameter. However in describing the universal tendency of a stall cell to rotate, Emmons et al. (1955) did postulate a mechanism. They envisaged the cell causing separation of the flow from the suction surface of one blade; the blockage caused by this affects the upstream flow so that on one side of the cell the incidence is reduced and on the other it is increased. This succeeds in producing a disturbance that moves in the correct sense. In general rotation will occur when loss or pressure rise vary with incidence.

At the outset of this research there was an explanation for the stall occurring when $\partial(p_2 - p_{01})/\partial V_x < 0$, which was to be investigated. The idea for this was that each blade passage was similar to a diffuser, and diffusers are known to achieve peak pressure recovery when they have flow that is transiently separated. It was a conjecture that the compressors operate in this way near stall, and since the separations are stochastic the instability would occur when sufficient random blade separations occurred simultaneously. This explanation looked back to the Emmons et al. model for the stall cell, putting attention on blade separation. As will be seen in the present paper, it was an erroneous view, and gave insufficient weight to other evidence that already existed about the importance of endwall boundary layers and tip clearance. It has been widely recognized that increasing tip clearance can move the stall inception

[1]Present address: YARD Ltd., Consulting Engineers, Charing Cross Tower, Glasgow.

Contributed by the International Gas Turbine Institute and presented at the 34th International Gas Turbine and Aeroengine Congress and Exhibition, Toronto, Ontario, Canada, June 4–8, 1989. Manuscript received at ASME Headquarters January 13, 1989. Paper No. 89-GT-63.

Table 1 Compressor stage geometry

Rotor blade row

Radius (m)	camber (deg)	stagger (deg)	solidity
0.610	40.3	38.8	1.48
0.686	26.5	47.9	1.31
0.762	18.5	54.4	1.18

51 blades, chord=111 mm.

Stator blade row

Radius (m)	camber (deg)	design stagger (deg)	unloaded stagger (deg)	solidity
0.610	44.4	16.6	26.8	1.07
0.686	42.9	14.3	24.5	0.95
0.762	42.9	12.7	22.9	0.86

36 blades, chord=114 mm.
Rotor and stator both C4 profile on circular-arc camber line, thickness-chord ratio =0.10

point to significantly higher flow rates, for example, Smith (1969) and Freeman (1985).

Two different types of measurements are reported here. One set looks at the flow field outside the rotor passage, mainly upstream. The other was made in or at the exit from the blade passages. The interpretation of the in-passage measurements takes advantage of the detailed measurements of the time-mean flow in the same compressor reported by McDougall (1990). (The subject of that paper and the present one, together with the facilities and techniques, are described in greater detail by McDougall, 1988.) McDougall (1990) showed that changing the rotor tip clearance from 1.2 to 3 percent of the tip chord raised the flow coefficient at stall inception from about 0.37 up to 0.40, as well as reducing the pressure rise. The overall pressure rise and stall inception point were essentially identical for tip clearances of 0.5 and 1.2 percent. McDougall also showed that there could be significant regions of separated flow in either the rotor or stator passages without stall occurring. All the significant separated regions were three dimensional in character, originating near the hub or casing wall.

Because of changes in ideas as the work progressed, it is more straightforward to drop any pretense of chronological order in this work but instead to try to give a clear picture of the real processes at work.

Facilities and Techniques

The present experiments were performed on a single-stage, low-speed compressor with a hub–casing ratio of 0.8. A summary of the compressor geometry is given in Table 1 and details of the aerodynamic behavior are described by McDougall (1990). The stage was one for which the absolute velocity into the rotor is axial, and as a result the reaction was high, with about 80 percent of the pressure rise at design point being across the rotor. To remove any risk that stall was being initiated in the stator, the stator blades were staggered closed 10 deg from their design value so there was still less pressure rise across them. (Later tests showed identical stall behavior with the stators at their correct design stagger and this extra unloading was unnecessary.) The overall pressure rise–flow rate characteristic is shown in Fig. 1 for several ratios of tip clearance to blade chord.

A traverse gear was mounted on the rotor so that the flow could be surveyed with a hot-wire or Kiel probe. In addition, up to seven subminiature hot wires with probe stem diameter

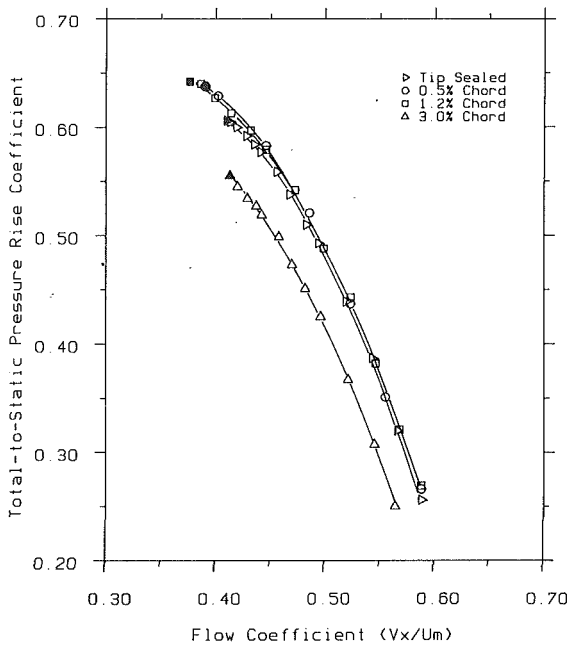

Fig. 1 Effect of variations in rotor tip clearance (solid symbols: stall point)

of 1 mm could be mounted on the rotor blades. Whenever hot-wires were used they were aligned to be normal to the expected local mean flow. All the unsteady data were logged by a computer. Stall is inherently stochastic and the instant when this would occur could not be predicted. A logging system was adopted whereby the data was logged continually with the computer memory being overwritten. When a stall was detected the contents of the memory were frozen so that events prior to the event could be recovered. In this way a high data sampling rate could be used with modest computer memory.

For these tests stall was initiated in one of two ways. In one case the throttle was closed to a point very near to stall and the compressor was left running until stall was initiated "naturally"; in fact stall was effected by inlet distortion from the room. In the other case, which was used for the ensemble averages, the compressor was brought to a point very close to stall and stall was initiated by placing a hand over the outlet from the throttle, this being just enough to bring more or less immediate stalling.

With the data logger it was possible to collect very large bodies of data but harder to present them in a compact and understandable way. One approach is illustrated in Fig. 2 where a cut-off threshold is specified and marks made on a bar chart when this was crossed. This simple technique has been extensively used because it allowed the most important effect to be displayed from several wires simultaneously.

Effect of Tip Clearance on Stall

The aerodynamic background to the differences illustrated by the overall pressure rise–flow rate characteristics, shown here as Fig. 1, is discussed by McDougall (1990). The performance was very similar for tip clearances equal to 0.5 and 1.2 percent of chord, but at 3 percent of chord the behavior was strikingly different. Not only was the pressure rise lower, but stall occurred at a higher flow coefficient with the larger

Nomenclature

p_2 = downstream static pressure
p_{01} = upstream stagnation pressure
U_m = mean blade speed
V_x = axial velocity
ϕ = flow coefficient = V_x/U_m
ψ_{TS} = total-to-static pressure coefficient
ω = rotational frequency

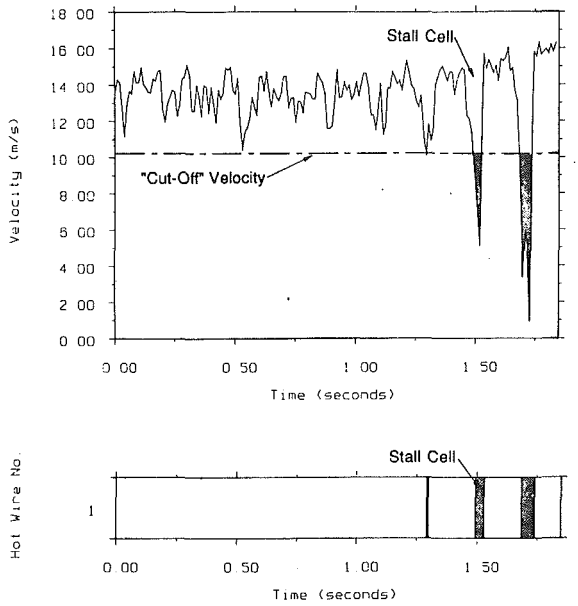

Fig. 2 Raw velocity-time trace and bar chart equivalent

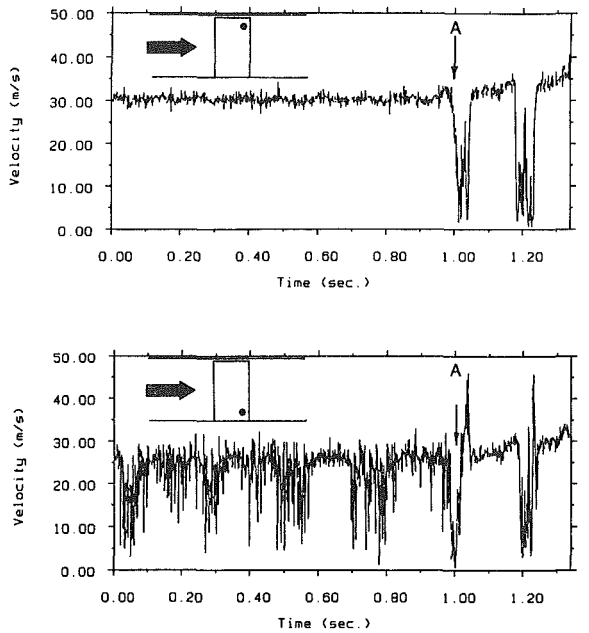

Fig. 3 Velocity-time traces recorded on the rotor during stall inception at the hub

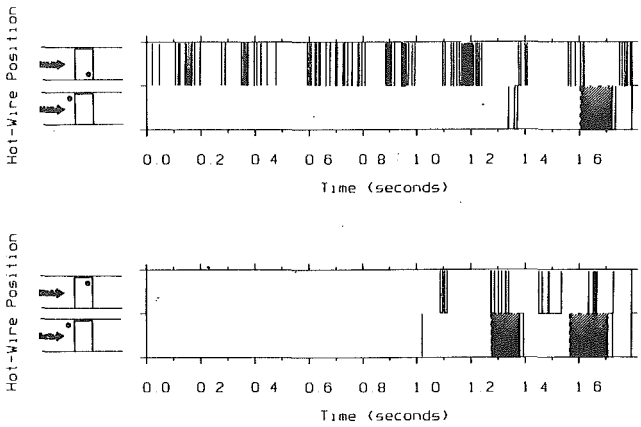

Fig. 4 Velocity measurements during hub stall shown in bar chart form (rotor tip clearance 1.2 percent chord)

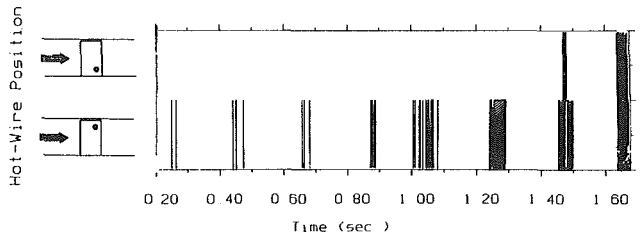

Fig. 5 Velocity measurements during tip stall shown in bar-chart form (rotor tip clearance 3.0 percent chord)

clearance. McDougall also showed contours of axial velocity at the rotor exit for flow coefficients near to stall. With the smaller clearances there was a buildup of low velocity flow from the hub over half the annulus, with a small pocket of reverse flow near the suction surface not far out from the hub. With the 3 percent clearance the boundary layer was thin near the hub but the casing boundary layer was thicker. The blockage produced by the clearance flow has reduced the blade pressure rise and as a result reduced the blockage at the hub.

For the build with 0.5 percent clearance, Fig. 3 shows velocity traces measured with hot wires mounted near the trailing edge on the suction surface of a rotor blade. At the time labeled A the compressor is stalled and from the point of view of inception the flow is no longer of interest. It is very clear from this that the periodic disturbance leading to stall can be seen much earlier near the hub. In bar-chart form Fig. 4 shows a similar test with 1.2 percent clearance. This time each case compares an on-blade hot wire with a hot wire upstream of the blade near the casing. The hot wire on the blade near the hub again shows up the effect long before it is visible near the tip on the blade. (It was found for all tip clearances that with the hot wire in the correct spanwise position near the exit from the rotor, the inception could be detected much earlier than when it was upstream or downstream.)

Figure 5 compares on-blade measurements with a clearance of 3 percent of chord. This time the behavior is quite different with the hot wire near the tip showing the incipient stall long before that at the hub. The fluid dynamic processes seem to be quite different with large and small tip clearance, although blockage is the critical quantity in each case. The precise value of clearance at which the change takes place must depend on many aspects of the design, not least the hub-casing radius ratio. Stall is normally initiated at the tips of rotors, see for example Freeman (1985), and 3 percent is believed to be a clearance likely to be encountered in multistage compressors. Most of the tests were therefore conducted with this geometry.

Flow Field Upstream of the Stage

Hot wires were installed at a number of positions upstream of the rotor aligned normal to the axial velocity. As will be shown below this was not the best place to spot the first signs of stall, although it was the only option open to Jackson (1987). The region ahead of the rotor does have advantages, compared with downstream, among which is its comparative freedom from turbulence and random unsteadiness. Spectral analysis had shown evidence of a spectral peak at about half rotor frequency, but this was not very clear. A better result came from a cross-correlation of signals from two wires 0.6 mean radii upstream of the rotor, set 90 deg of the circumference apart. The cross correlation, which used only the unsteady part of the signals, was performed in the standard manner. The cross correlation was not normalized so that an estimate for the disturbance magnitude can be obtained. The result is shown in Fig. 6. For a flow coefficient well away from stall there is

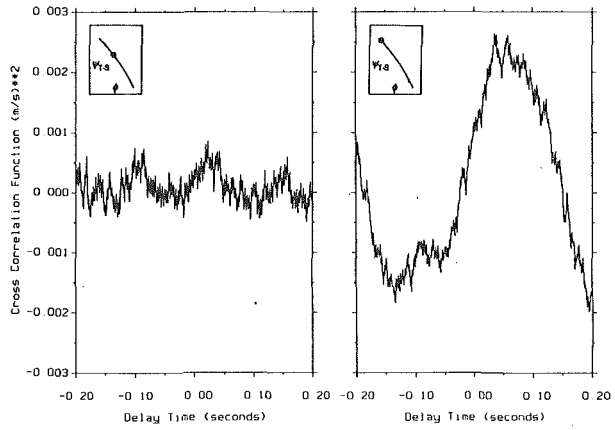

Fig. 6 Variation in cross correlation function measured upstream of the compressor as stall is approached

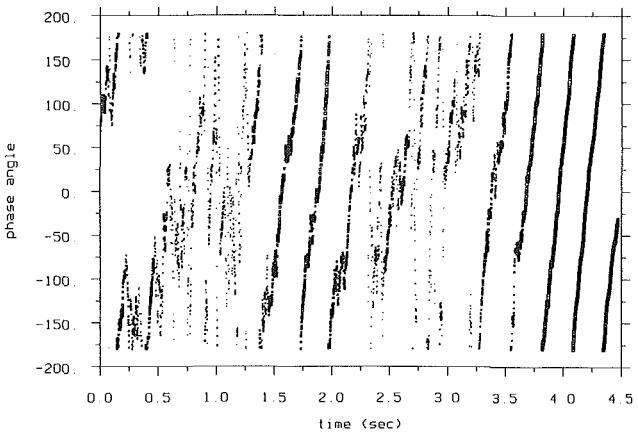

Fig. 7 Variation of phase of first circumferential harmonic with time during stall inception (arbitrary phase and time origins)

only a small cross correlation with a time delay appropriate to the speed of the rotor; this then denotes small nonuniformities of the rotor at the shaft frequency. Close to stall, however, there is a strong peak corresponding to a frequency of about 4 Hz, or about half the shaft frequency. The peak cross correlation shown in this figure corresponds to a velocity of about 0.3 percent of the free-stream axial velocity. What this figure does not show is that short time averages reveal a cross correlation that rises and falls with time. At some times there was essentially zero correlation and at other times it was as high as 0.006 m^2/s^2. Since the mean flow coefficient was about 0.4 and the mean blade speed was 36 m/s it is easy to show that a cross correlation of 0.006 m^2/s^2 corresponds to a perturbation of about 0.55 percent in the mean axial velocity. When the correlation was strongest the frequency could be more accurately determined as 4.1 Hz.

The correlation indicates that there is a pressure field rotating around the annulus at about 49 percent of rotor speed prior to the compressor stalling. It is only very close to stall that they can be detected. Nevertheless the amplitude rises and falls during this time so the existence of these disturbances is not the same as stall, nor does it indicate that stall is occurring or about to occur. The same pattern was observed whatever the tip clearance being used and there was likewise no significant difference in frequency. Since, as discussed above, the initiation of the stall was from the casing for large tip clearance and the hub for the smaller clearances, this indicates that the rotating disturbances ahead of the rotor were largely independent of the fluid mechanic process of stall. The amplitude of the disturbances was approximately constant across the

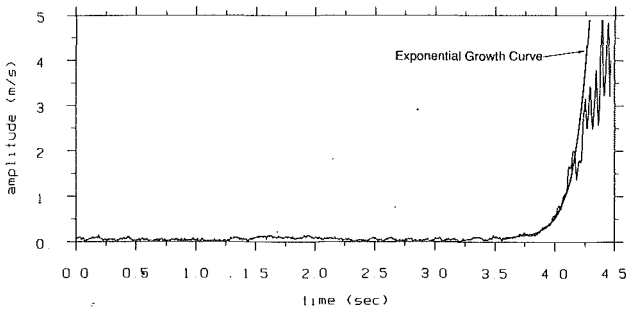

Fig. 8 Variation of amplitude of first circumferential harmonic with time during stall inception (arbitrary time origin)

annulus, indicating that it was essentially two dimensional in nature.

The cross correlation raised the signal-to-noise ratio by using two sensors. An alternative way of looking at the upstream disturbances was suggested in discussion with Messrs. Greitzer and Longley. The signals from six hot wires uniformly distributed around the circumference 0.6 mean radii ahead of the rotor were logged simultaneously as the compressor was allowed to stall. The signals were then Fourier analyzed at each instant to resolve the circumferential harmonics, of which the dominant one was the first order, i.e., one cycle around the circumference. The result is plotted in Fig. 7, where the size of the symbols used is a measure of the amplitude. Figure 7 shows the phase of the signal against time (with arbitrary origins for each) and the slope of the lines gives the phase velocity. When the signal is weakest the lines are steepest; this corresponds to the nonuniformity of the rotor at first order rotating at rotor speed. When the first-order mode is of larger amplitude, the phase speed is lower, about 0.5 times as large. The record shown in Fig. 7 is just leading up to stall, which occurs at about 4.25 s. It should be noted how the amplitude rises between about 1.5 and 2.0 s before falling, to rise again at about 3.25 s ultimately to stall. It is noteworthy that there appears to be no discontinuity in phase or frequency in changing from the small-amplitude disturbance to the large-amplitude stall cell. In both cases there is one cycle around the circumference, i.e., one cell, and the circumferential speed is about the same, just less than 50 percent of rotor speed. The same data, but this time displayed as the amplitude, are shown in Fig. 8. An exponential curve has been fitted to the data in the period after 3.5 s leading up to the breakdown into stall.

Measurements in Passage During Inception

Measurements of the flow inside the blade passage during stall inception were made with the largest tip clearance tested, 3 percent of chord. It was necessary to find where in the blade passage the stall could first be detected. The rotating-frame traverse gear was used to position a hot wire at different positions over the trailing edge plane while the compressor was stalled many times. A subminiature wire mounted on the suction surface of one blade was used as a reference. The position where the stall could be first detected is shown in Fig. 9, just outside the annulus and suction surface boundary layers.

Stall initiation is stochastic, since its time is not known, and it can occur anywhere around a perfectly uniform rotor. To make the measurements more repeatable and to allow the on-rotor instrumentation to be in the correct position requires the position of stall inception to be fixed in a particular part of the rotor circumference. The first approach for fixing the position around the rotor of stall inception was to restagger one of the blades so that it was at slightly greater incidence than the others. A variation tried was to hang an obstruction in a passage. It became clear, however, that this was not achieving the goal of fixing the stall inception, indeed it was having no

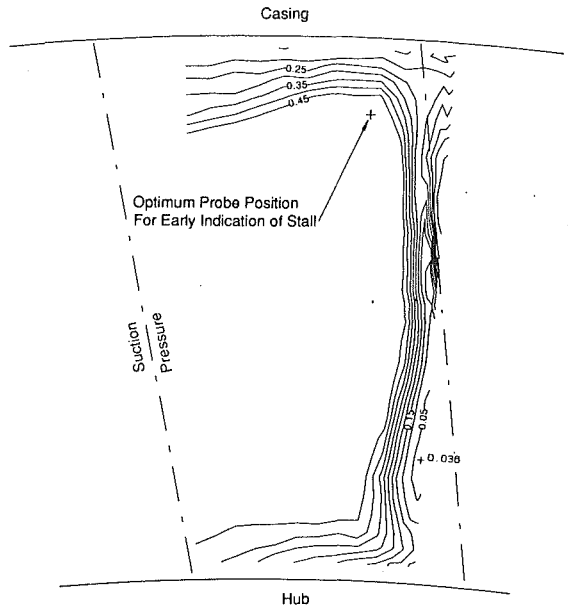

Fig. 9 Axial velocity ratio, rotor exit plane; ϕ = 0.429, tip clearance/chord ratio 3.0 percent

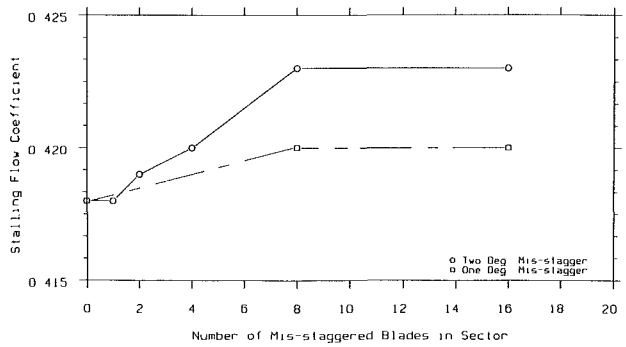

Fig. 10 Variation of stalling flow coefficient with size of mis-staggered sector

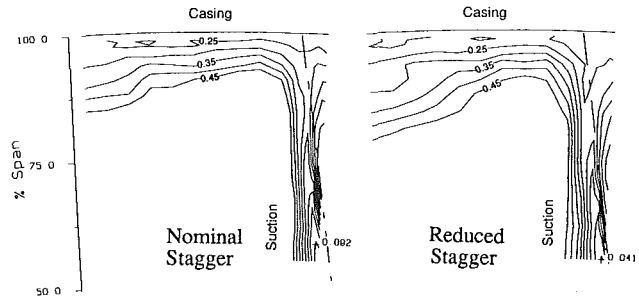

Fig. 11 Throughflow velocity ratio, rotor exit plane; near stall, rotor tip clearance/chord ratio 3.0 percent

measureable effect on the stall. No change in the flow coefficient at stall and no apparent fixing of the stall inception was produced when the perturbation was taken as far as completely removing a blade!

An alternative strategy was then tried, which was to restagger a group of blades by a small amount. Figure 10 shows clearly that there is an effect on the flow coefficient at stall for reductions in stagger of 1 deg or 2 deg; the effect increases progressively to reach its maximum value after about 8 blades. Even at its maximum the effect is still quite small, the flow coefficient at stall being increased by about 1 percent. The rotor had a total of 51 blades so eight restaggered blades gives an arc of about 60 deg. Figure 11 shows the measured through-

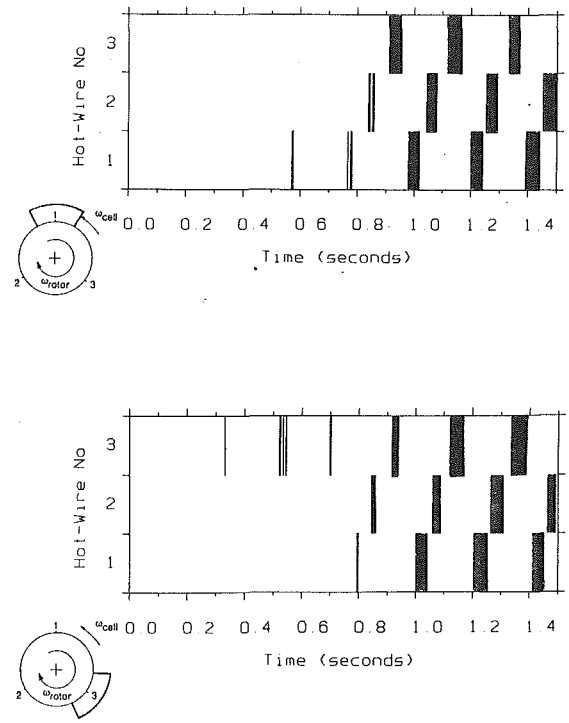

Fig. 12 Bar charts recorded during stall inception: top—Probe 1 at center of mis-staggered sector; bottom—Probe 3 at center of mis-staggered sector

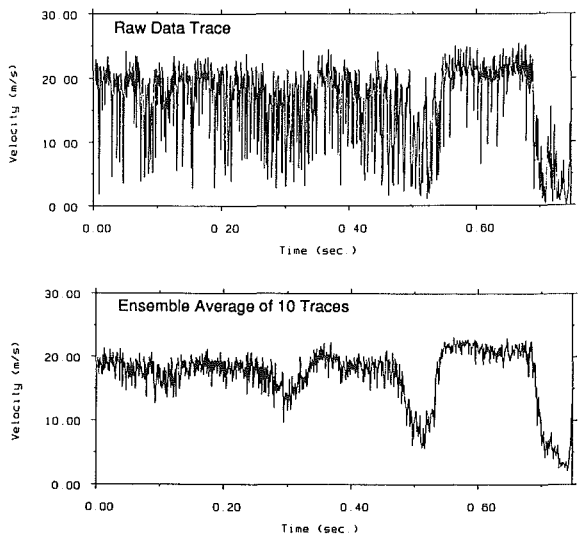

Fig. 13 Effect of number of samples on noise content in ensemble-averaged data

flow velocity contours at rotor exit with the rotor operating at virtually identical flow coefficients close to the stall point, in one case where the blade stagger is not reduced, in the other in the middle of the section of eight blades restaggered by 2 deg. The boundary layer close to the casing and the rotor wake there have been thickened but generally the flow is very similar, indicating that the flow has not been perturbed so seriously that it ceases to be similar to the unperturbed flow. Figure 12 shows bar charts obtained from hot wires mounted near the trailing edge on the suction surface. When the reduced stagger section was centered on hot wire 1 the velocity recorded by this sensor dropped much earlier than wires 2 and 3; when the reduced stagger sector covered hot wire 3 it was this sensor that showed the first signs of a fall in velocity.

With the phase of stall inception fixed with eight blades at

2 deg reduced stagger it was possible to obtain an impressive degree of repeatability, allowing the formation of ensemble averages of the velocity in the period up to stall inception. An example of the raw and ensemble-averaged data is shown in Fig. 13, taken at the trailing edge plane at midpitch and 80 percent of the span from the hub. (It was found that little improvement accrued from using more than 10 ensembles, though the running time increased linearly.) It was then possible to produce contours of throughflow velocity at different times during the stall inception ensemble averaged over 10 stall inceptions. Each of the contour plots is similar in appearance to Fig. 11 but the annulus boundary layer varies in thickness, particularly near the suction surface, in an approximately cyclic manner. The frequency is that of the rotating upstream disturbances, transposed into the rotating frame of reference. During some parts of the cycle the boundary layer is thinner than in the steady state prior to the initiation of the inception process. The amplitude increases with time until stall has occurred.

Discussion

There are two separate strands to the work described here. One is the behavior in and around the rotor blades, the other is the rotating perturbations detected upstream.

The rotating upstream perturbations had not been observed before, but since have been found in other compressors by Day (1988) and Garnier (1989). They are not in themselves surprising but represent the response of the upstream flowfield to the disturbance in the blades. They are then the modes of the system. If the blade disturbance were made to remain stationary, as with partial casing treatment in Cumpsty (1989), some of the upstream perturbation would be recognizable as a stationary pressure field. It is notable that the field appears to be essentially two-dimensional, not varying appreciably in the radial direction, and being similar for in-blade disturbances at the hub or at the casing. No explanation has been found for the dominance of the first-order mode with one cycle around the circumference, although the exponential decay will be larger for the higher modes. In tests on another machine Day (1988) has found that the second-order mode predominates. If the disturbance field is important it is not surprising that disturbances to one blade passage, even going as far as removing one blade, did not have much effect. This is because the coupling between the passage disturbance on a small circumferential scale and the first-order mode, which has the scale of the circumference some 51 times as large, is weak.

The amplitude of the upstream perturbations detected is quite small, around 0.5 percent of the mean axial velocity at its greatest prior to stall. This was detected 0.6 mean radii upstream of the rotor and, assuming exponential decay, would give about 0.9 percent at the rotor inlet. This, although small, is compared to the magnitude of the changes in flow coefficient at stall achieved by restaggering the blades by 2 deg (Fig. 10).

Many attempts have been made at predicting stall cell speed by considering small, two-dimensional disturbances. No method considers details of the flow in individual blade passages, but they rely instead on an actuator or semi-actuator disk to model each blade row. Their mixed success is not surprising in view of the measurements reported here. Nevertheless it seems clear that the rotational frequency is set not just by the flow processes taking place in the rotor itself but also by the dimensions of the upstream and downstream ducts and the boundary conditions to these ducts. In a multistage configuration the downstream blade rows will exert a large influence on this as well as on other aspects of the stall process.

The measurements made in and downstream of the passages have shown that stall inception occurs in different ways depending on the magnitude of the tip clearance. In each case it is the blockage caused by the endwall boundary layers, more properly the combination of the endwall and blade boundary layers. With large tip clearance the blockage near the casing appears sufficient to reduce the blockage near the hub and render the flow in this region relatively stable so that the inception occurs near the casing. At small tip clearances the flow rate at stall was lower, the blockage near the hub was large, and it was near the hub that the first unsteadiness leading to stall occurred. The speed of the disturbances detected upstream was very similar in each case, which may indicate that the wave speed is only weakly determined by the in-passage flow details.

At a tip clearance equal to 3 percent of chord the stall inception could be observed bringing about a fluctuation in the annulus boundary layer, particularly near the suction surface. The period of this disturbance corresponded, of course, to the period of the upstream disturbance after transposing to the moving frame of reference. The process leading to stall inception was highly repeatable, evidenced by the fact that ensemble averages could be achieved, and this makes it clear that the process, though not its position or start, are not random but highly deterministic.

A previous investigation related to the study of stall inception was reported by Jackson (1987) on a similar compressor. Jackson used hot wires upstream and downstream of the rotor but was unable to make measurements in the rotating frame of reference. He restaggered a single blade to fix the stall cell inception but it is now apparent that any fixing that occurred was originating in some other way. By examining the velocity traces measured upstream of the rotor Jackson estimated the stall cell speed from its first appearance until fully developed: The cell appeared to begin as a small cell traveling at near rotor speed and to decelerate rapidly in the absolute frame of reference as it grew in size. This supported the view that stall inception occurred when a particular blade, believed to be the restaggered one, experienced a conventional separation type stall along the lines proposed by Emmons et al. The current measurements made in the rotating frame show that this is not how stall begins. Stall can be detected much earlier in the rotating frame, yet from the first appearance of the disturbance it rotates at about 50 percent of the rotor speed. McDougall (1988) has shown that Jackson was in fact looking at cells that were fairly well developed when first detected and that the measurements upstream of the rotor gave an erroneous indication of speed change as a result of the simultaneous increase in cell size.

The measurements described link blockage in the endwall regions with a perturbation field upstream of the rotor, the amplitude increasing as the compressor undergoes stall. It does not provide an explanation for the stall occurring when the overall $\partial(p_2 - p_{01})/\partial V_x < 0$. Other evidence, some experimental, some computational, helps to explain this. A number of years ago measurements had been made in Cambridge on a rotor with a casing treatment over part of the circumference. These are now reported by Cumpsty (1989) and show that close to stall the boundary layer thickness upstream of the rotor varies around the circumference with this geometry; in the same direction as the rotor the thickness increases over the portion with no treatment and decreases sharply where there is treatment. The only explanation that could be found for this is that close to stall the untreated section is allowing flow to spill forward from one passage to the next. These measurements also showed a nonuniform pressure field upstream and downstream of the rotor, analogous to the upstream perturbations found in this present work. The pressure rise through the compressor was least where the inlet blockage was greatest, near the end of the untreated section. When the pressure rise and flow rate changes from these upstream and downstream perturbations were added to the mean values of $p_2 - p_{01}$ and V_x it is plausible to interpret the local value of $\partial(p_2 - p_{01})/\partial V_x$ as approximately equal to zero at the end of the no-casing-treatment section. In other words it is not necessary for the entire compressor annulus to satisfy the instability criterion

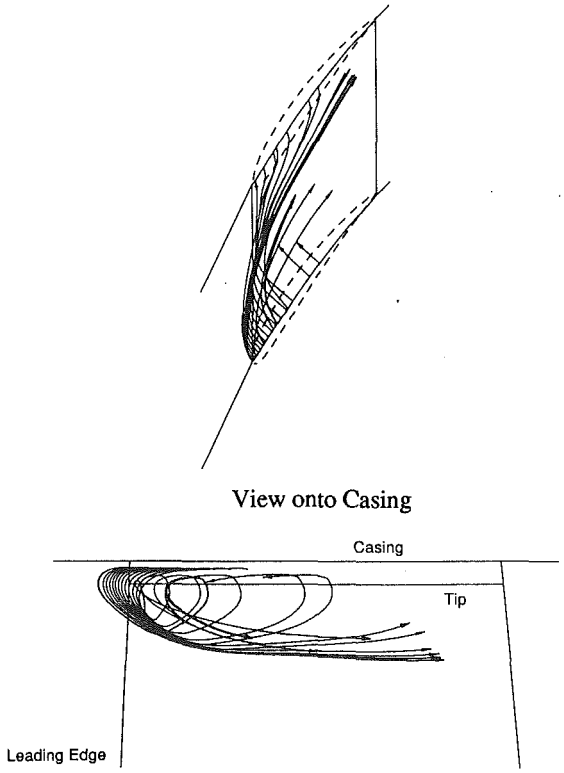

Fig. 14 Prediction of tip leakage flow—design point

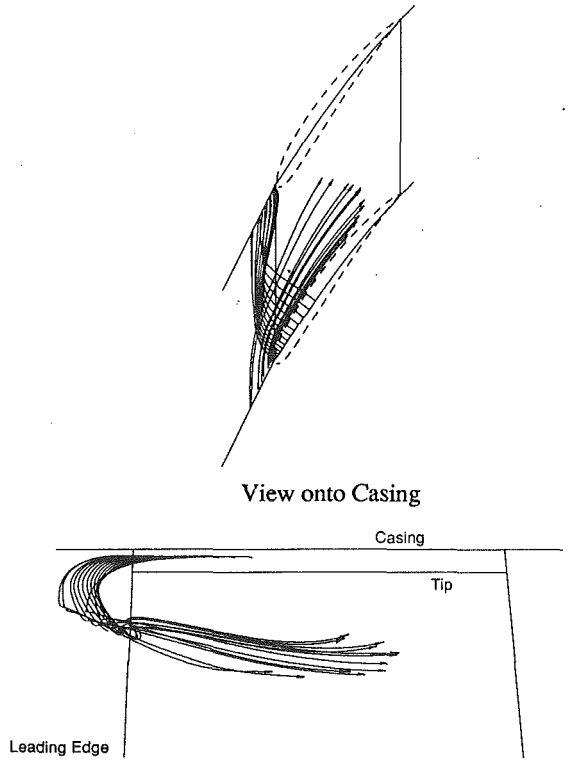

Fig. 15 Prediction of tip leakage flow—closer to stall

but only a section. When these measurements were made there was no other evidence, experimental or theoretical, to support the idea of flow spilling forward of the rotor.

Calculations of the flow around the tips of a rotor blade were performed using the Navier–Stokes solver written by Dawes (1987). (The success of this method in predicting a number of aspects of the flow was demonstrated by McDougall and Dawes, 1987, and also by McDougall, 1990.) Figure 14 shows predictions of the tip leakage flow at a condition close to the design flow coefficient, $\phi = 0.55$, with a tip clearance of 3 percent of the chord. In this case the tip clearance jet emerges with an upstream component of axial velocity, is turned by the main flow, and becomes what is usually referred to as the clearance vortex. At low flow coefficients the calculation would no longer converge. The lowest value at which full convergence could be obtained is $\phi = 0.48$, for which the clearance flow is shown in Fig. 15. This time the clearance jet does not pass down the blade passage but is spilled forward of the next blade into the next passage. On reflection it seems reasonable that the jet would go either downstream or upstream of the leading edge region of the next blade but not on the leading edge because this is a region of high static pressure. The spillage of flow from one passage to another helps explain why the downstream velocity contours are more nearly uniform on the casing at flow rates near to stall because the relatively well-defined jet is no longer present. It seems highly likely that with spilled flow small changes in pressure can bring quite large changes in flow entering the passages near the endwall. It also provides a mechanism by which the endwall boundary layer flow in one passage can affect others.

The prediction of spillage near to stall goes some way to explain the operation of the axial-skewed-slot type of casing treatment. Recent measurements with hub treatment under a stator have shown that sucking away the high loss fluid near the back of the blade or blowing near the front of the blade can delay stall (Lee and Greitzer, 1990). Suction near the back was expected but the benefit of blowing near the front was a surprise. It seems probable that the high momentum of the flow leaving the treatment slot is able to entrain the clearance jet and prevent it from spilling ahead of the next blade, thereby delaying the onset of instability.

The evidence that has come from this work and that reported by Cumpsty (1989) is that the collapse of the flow leading to instability and stall takes place over a relatively small part of the annulus. Other evidence points to this section being much larger than one blade pitch. The collapse of the flow leads to a change in the slope $\partial(p_2 - p_{01})/\partial V_x$ such that instability is possible. This is not in conflict with the theoretical studies of system instability, which take this gradient as an input variable. Hynes and Greitzer (1986), for example, show that it is the average of the gradient $\partial(p_2 - p_{01})/\partial V_x$ around the circumference that determines whether the compressor is unstable; the present work does not conflict with this. It has shown that the slope can change quite markedly in some regions of the circumference as a result of local changes to the flow and that an overall value of $\partial(p_2 - p_{01})/\partial V_x$ may not give a true indication of the nearness to stall.

A fashionable topic of research at the present time is active control of stall and surge: A control system will be linked to the compressor so that on recognizing the incipient stall an appropriate control action will be undertaken. One of the problems is the recognition of stall in the noisy environment of a compressor operating close to stall. The results shown in Figs. 7 and 8 are encouraging. They show that a low order mode is dominant and can be observed for some considerable time prior to stall. They also show that using a number of transducers and Fourier analyzing these to pick out any low-order modes that may be present is a way of eliminating much of the noise. It should be repeated, however, that the low-order modes are not the same as stall and that they were observed to rise and fall in amplitude for some time before stall inception occurred. What one can also say is that only very close to the conditions for stall were they ever of significant

amplitude, so their existence is evidence for the controller that remedial action to avoid stall is urgently required.

Conclusions

1 With high reaction stages the rotor is much more likely to be the cause of stall. For the same overall geometry a compressor can stall at the rotor hub for small tip clearance and at the rotor tip for larger clearance. At the level of clearance typical of multistage compressors tip stalling is more likely.

2 Attempts to fix where around the rotor circumference stall was initiated were unsuccessful when only one blade or blade passage was involved. Only when a significant part of the circumference was altered did it affect the stall point; the full effect was achieved when the alteration was to about 60 deg of the circumference.

3 The crucial property of the flow in the blade passages for determining the stall point is the endwall blockage. For the compressor stage used for this investigation the blockage becomes large on the hub at small tip clearances; at large tip clearances it becomes large at the casing. The dependence of casing blockage on tip clearance is believed to be general to most axial compressors. The variation in blockage revolves around the annulus; the speed was about 49 percent of the rotor speed for this compressor.

4 In the upstream flow field rotating variations in axial velocity were measured. These were in the first-order mode, with one cycle around the annulus and almost constant in the radial direction. The mode rotated around the annulus in sympathy with the variation in blockage at exit from the rotor. The speed of rotation was found to be about 50 percent of the rotor speed, similar to the fully developed stall cell speed. (This similarity is probably a coincidence for this stage and does not occur on all compressors.) At the rotor inlet plane the magnitude of the axial velocity associated with the upstream disturbance was about 1 percent of the mean axial velocity near the stall point.

5 Calculations have shown that the flow pattern associated with the tip clearance changes markedly as the flow rate is reduced. The tip-clearance jet no longer turns into the adjacent blade passage but spills into the next one along the row. This is believed to be an important reason for the sensitivity of the row to very small changes in inlet flow rate. The greater inlet blockage caused by the spilled flow leads to a reduced pressure rise across the row.

6 It would seem that stall can be incurred when the flow in only part of the annulus is unstable. This occurs first where the blockage is greatest.

7 The presence of stall could be detected much earlier with a sensor mounted on the rotor than with upstream or downstream measurements; maximum sensitivity was obtained with the hot wire just outside the boundary layer. With on-rotor hot wires the speeds of the prestall disturbances and of the stall cell itself were found to be similar and equal to about 50 percent of the rotor speed for this compressor stage. There is no evidence that the initially small stall cell is fixed to the rotor or rotates with an absolute velocity approximately that of the rotor.

Acknowledgments

This work was supported by a Rolls Royce-SERC Co-operative grant. The technical support of Rolls Royce is acknowledged, in particular the long-term guidance and comment from Mr. C. Freeman. Frequent and very useful discussions were held with Professor E. M. Greitzer of MIT, which was made possible by a NATO travel grant. Mr. John Longley has also contributed to our understanding of the project and to the analysis techniques. N. M. McDougall was supported for the first two years of this project on an SERC CASE award and after this entirely by Rolls Royce.

References

Cumpsty, N. A., 1989, "Casing Treatment on Part of the Circumference and the Effect on Compressor Stall," ASME Paper No. 89-GT-312.

Dawes, W. N., 1987, "A Numerical Analysis of the Three-Dimensional Viscous Flow in a Transonic Compressor Rotor and Comparison With Experiment," ASME JOURNAL OF TURBOMACHINERY, Vol. 109, pp. 83–90.

Day, I. J., 1988, Private Communication.

Emmons, H. W., Pearson, C. E., and Grant, H. P., 1955, "Compressor Surge and Stall Propagation," *Transactions of the ASME*, Vol. 79, pp. 455–469.

Freeman, C., 1985, "Effect of Tip Clearance Flow on Compressor Stability and Engine Performance," Von Karman Institute for Fluid Dynamics Lecture Series 1985-05.

Garnier, V., Paduano, J., Epstein, A. H., and Greitzer, E. M., 1989, "Rotating Stall Inception and Stall Precursors in Axial Flow Compressors," submitted to the 34th International Gas Turbine and Aeroengine Congress and Exhibition, Toronto.

Greitzer, E. M., 1976, "Surge and Rotating Stall in Axial Flow Compressors; Parts I and II," ASME *Journal of Engineering for Power*, Vol. 98, pp. 190–217.

Greitzer, E. M., and Moore, F. K., 1986, "A Theory of Post-stall Transients in Axial Compression Systems: Part II—Applications," ASME *Journal of Engineering for Gas Turbines and Power*, Vol. 108, pp. 231–239.

Hynes, T. P., and Greitzer, E. M., 1986, "A Method for Assessing Effects of Circumferential Flow Distortion on Compressor Stability," *Engine Response to Distorted Inflow Conditions*, AGARD-CP-400.

Jackson, A. D., 1987, "Stall Cell Development in an Axial Compressor," ASME JOURNAL OF TURBOMACHINERY, Vol. 109, pp. 492–498.

Lee, N., and Greitzer, E. M., 1990, "Effects of Endwall Suction and Blowing on Compressor Stability Enhancement," ASME JOURNAL OF TURBOMACHINERY, this issue.

McDougall, N. M., 1988, "Stall Inception in Axial Compressors," PhD Dissertation, University of Cambridge, Cambridge, United Kingdom.

McDougall, N. M., 1990, "A Comparison Between the Design Point and Near-Stall Performance of an Axial Compressor," ASME JOURNAL OF TURBOMACHINERY, this issue.

McDougall, N. M., and Dawes, W. N., 1987, "Numerical Simulation of the Strong Interaction Between a Compressor Blade Clearance Jet and Stalled Passage Flow," *7th GAMM Conference on Numerical Methods in Fluid Mechanics*, Belgium.

Moore, F. K., and Greitzer, E. M., 1986, "A Theory of Post-stall Transients in Axial Compression Systems: Part I—Development of Equations," ASME *Journal of Engineering for Gas Turbines and Power*, Vol. 108, pp. 68–76.

Smith, L. H., 1969, "Casing Boundary Layers in Multistage Compressors," *Proceedings of the Symposium on Flow Research on Blading*, A. B. Dzung, ed., Brown Boveri and Co. Ltd., Baden, Switzerland.

Stenning, A. H., 1980, "Rotating Stall and Surge," ASME *Journal of Fluids Engineering*, Vol. 102, pp. 14, 20.

amplitude, so their existence is evidence for the controller that remedial action to avoid stall is urgently required.

Conclusions

1 With high reaction stages the rotor is much more likely to be the cause of stall. For the same overall geometry a compressor can stall at the rotor hub for small tip clearance and at the rotor tip for larger clearance. At the level of clearance typical of multistage compressors tip stalling is more likely.

2 Attempts to fix where around the rotor circumference stall was initiated were unsuccessful when only one blade or blade passage was involved. Only when a significant part of the circumference was altered did it affect the stall point; the full effect was achieved when the alteration was to about 60 deg of the circumference.

3 The crucial property of the flow in the blade passages for determining the stall point is the endwall blockage. For the compressor stage used for this investigation the blockage becomes large on the hub at small tip clearances; at large tip clearances it becomes large at the casing. The dependence of casing blockage on tip clearance is believed to be general to most axial compressors. The variation in blockage revolves around the annulus; the speed was about 49 percent of the rotor speed for this compressor.

4 In the upstream flow field rotating variations in axial velocity were measured. These were in the first-order mode, with one cycle around the annulus and almost constant in the radial direction. The mode rotated around the annulus in sympathy with the variation in blockage at exit from the rotor. The speed of rotation was found to be about 50 percent of the rotor speed, similar to the fully developed stall cell speed. (This similarity is probably a coincidence for this stage and does not occur on all compressors.) At the rotor inlet plane the magnitude of the axial velocity associated with the upstream disturbance was about 1 percent of the mean axial velocity near the stall point.

5 Calculations have shown that the flow pattern associated with the tip clearance changes markedly as the flow rate is reduced. The tip-clearance jet no longer turns into the adjacent blade passage but spills into the next one along the row. This is believed to be an important reason for the sensitivity of the row to very small changes in inlet flow rate. The greater inlet blockage caused by the spilled flow leads to a reduced pressure rise across the row.

6 It would seem that stall can be incurred when the flow in only part of the annulus is unstable. This occurs first where the blockage is greatest.

7 The presence of stall could be detected much earlier with a sensor mounted on the rotor than with upstream or downstream measurements; maximum sensitivity was obtained with the hot wire just outside the boundary layer. With on-rotor hot wires the speeds of the prestall disturbances and of the stall cell itself were found to be similar and equal to about 50 percent of the rotor speed for this compressor stage. There is no evidence that the initially small stall cell is fixed to the rotor or rotates with an absolute velocity approximately that of the rotor.

Acknowledgments

This work was supported by a Rolls Royce-SERC Co-operative grant. The technical support of Rolls Royce is acknowledged, in particular the long-term guidance and comment from Mr. C. Freeman. Frequent and very useful discussions were held with Professor E. M. Greitzer of MIT, which was made possible by a NATO travel grant. Mr. John Longley has also contributed to our understanding of the project and to the analysis techniques. N. M. McDougall was supported for the first two years of this project on an SERC CASE award and after this entirely by Rolls Royce.

References

Cumpsty, N. A., 1989, "Casing Treatment on Part of the Circumference and the Effect on Compressor Stall," ASME Paper No. 89-GT-312.

Dawes, W. N., 1987, "A Numerical Analysis of the Three-Dimensional Viscous Flow in a Transonic Compressor Rotor and Comparison With Experiment," ASME JOURNAL OF TURBOMACHINERY, Vol. 109, pp. 83–90.

Day, I. J., 1988, Private Communication.

Emmons, H. W., Pearson, C. E., and Grant, H. P., 1955, "Compressor Surge and Stall Propagation," *Transactions of the ASME*, Vol. 79, pp. 455–469.

Freeman, C., 1985, "Effect of Tip Clearance Flow on Compressor Stability and Engine Performance," Von Karman Institute for Fluid Dynamics Lecture Series 1985-05.

Garnier, V., Paduano, J., Epstein, A. H., and Greitzer, E. M., 1989, "Rotating Stall Inception and Stall Precursors in Axial Flow Compressors," submitted to the 34th International Gas Turbine and Aeroengine Congress and Exhibition, Toronto.

Greitzer, E. M., 1976, "Surge and Rotating Stall in Axial Flow Compressors; Parts I and II," ASME *Journal of Engineering for Power*, Vol. 98, pp. 190–217.

Greitzer, E. M., and Moore, F. K., 1986, "A Theory of Post-stall Transients in Axial Compression Systems: Part II—Applications," ASME *Journal of Engineering for Gas Turbines and Power*, Vol. 108, pp. 231–239.

Hynes, T. P., and Greitzer, E. M., 1986, "A Method for Assessing Effects of Circumferential Flow Distortion on Compressor Stability," *Engine Response to Distorted Inflow Conditions*, AGARD-CP-400.

Jackson, A. D., 1987, "Stall Cell Development in an Axial Compressor," ASME JOURNAL OF TURBOMACHINERY, Vol. 109, pp. 492–498.

Lee, N., and Greitzer, E. M., 1990, "Effects of Endwall Suction and Blowing on Compressor Stability Enhancement," ASME JOURNAL OF TURBOMACHINERY, this issue.

McDougall, N. M., 1988, "Stall Inception in Axial Compressors," PhD Dissertation, University of Cambridge, Cambridge, United Kingdom.

McDougall, N. M., 1990, "A Comparison Between the Design Point and Near-Stall Performance of an Axial Compressor," ASME JOURNAL OF TURBOMACHINERY, this issue.

McDougall, N. M., and Dawes, W. N., 1987, "Numerical Simulation of the Strong Interaction Between a Compressor Blade Clearance Jet and Stalled Passage Flow," *7th GAMM Conference on Numerical Methods in Fluid Mechanics*, Belgium.

Moore, F. K., and Greitzer, E. M., 1986, "A Theory of Post-stall Transients in Axial Compression Systems: Part I—Development of Equations," ASME *Journal of Engineering for Gas Turbines and Power*, Vol. 108, pp. 68–76.

Smith, L. H., 1969, "Casing Boundary Layers in Multistage Compressors," *Proceedings of the Symposium on Flow Research on Blading*, A. B. Dzung, ed., Brown Boveri and Co. Ltd., Baden, Switzerland.

Stenning, A. H., 1980, "Rotating Stall and Surge," ASME *Journal of Fluids Engineering*, Vol. 102, pp. 14, 20.

DISCUSSION

I. J. Day[2]

With the advantage of additional measurements and the benefit of hindsight I would like to add a few points to this paper.

The authors introduce a number of terms to describe the flow field but do not make clear how, for example, the "rotating inlet pressure field" and the "periodic disturbances leading to stall" relate to each other or to the actual breakdown process. In simplistic terms the overall flow field prior to stall can be visualized as follows:

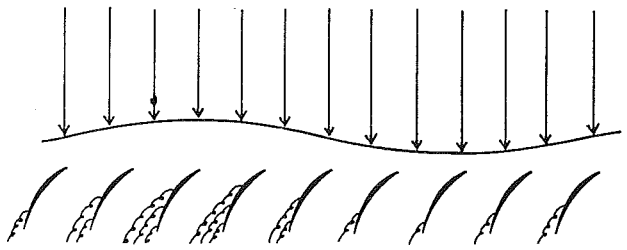

Here a rotating axial velocity perturbation in the incoming flow is directly linked to a periodic variation in the rotor blockage caused by the thickening and thinning of boundary layers or separated regions on the blades, endwalls and, in

[2]Whittle Laboratory, University Engineering Department, Cambridge University, Cambridge, CB3, United Kingdom.

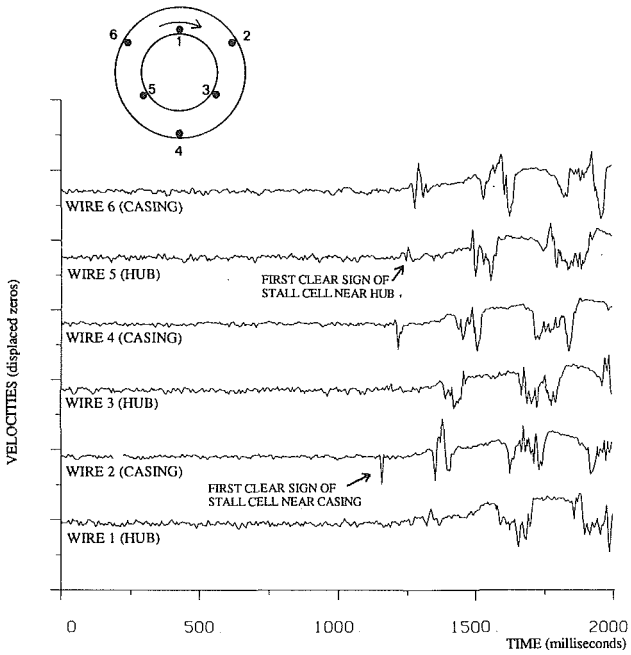

Fig. 16 Time traces from six hot-wires showing the first sign of stall appearing at the casing and not at the hub (tip clearance: 1.2 percent)

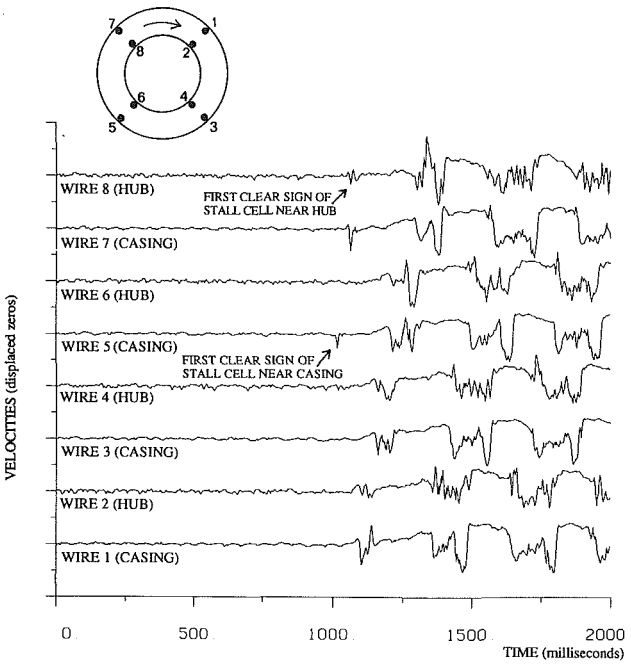

Fig. 17 Time traces from four pairs of hot-wires showing the first sign of stall appearing at the casing and not at the hub (tip clearance: 0.7 percent)

particular, the corners between the two. (My own measurements confirming this picture will be published shortly.)

A flow field such as that illustrated here might be termed "modal" in the sense that the circumferential harmonics of the machine are invoked. These modal oscillations usually become evident near the peak of the pressure rise characteristic. Their presence does not, however, indicate an irreversible or irretrievable downward slide into rotating stall, and at any point prior to the formation of a finite stall cell the flow can be returned to normal axisymmetric operation, without hysteresis, simply by increasing the mean throughflow.

The paper under discussion does make it clear that the presence of detectable circumferential waves does not imply stall, but this needs to be emphasized again because of a misinterpretation of the signals by McDougall et al. The authors placed their probes "just outside the annulus and suction surface boundary layers," the best possible position to detect the modally excited boundary layer fluctuations. These fluctuations are most marked where the boundary layer is thickest, i.e., near the casing for large tip clearances and near the hub for small tip clearances. What the authors failed to do, however, is to show that the stall cell originates from these regions where the boundary layer is thickest. The data reduction technique used in this work, i.e., signal cutoff levels, is unable to distinguish between boundary layer modulations and the formation of a finite stall cell.

Now the reason for emphasizing that early detection of boundary layer excitation is not the same as detecting the onset of stall is that recent measurements that I have made on the same compressor show that stall inception actually occurs at the casing not only for large tip clearances but for small clearances as well. This is a direct contradiction of what is claimed by McDougall et al. in the paper.

The measurements shown in the figures are typical examples obtained on the Deverson compressor in the stationary frame of reference, and consist of traces of velocity versus time as the throttle is inched closed until the compressor stalls. The results are examples of repeated measurements obtained with two fairly small tip clearances (1.2 percent and 0.7 percent of tip chord), both sufficiently small that McDougall et al. would have said that stalling would occur near the hub for this compressor. The hot wires were mounted 20 mm axially upstream of the rotor (tip chord length 108 mm). Six wires were used in one case, eight in the other, with half mounted close to the hub and half close to the casing.

In Fig. 16 the tip clearance was 1.2 percent of chord and it can be seen that steady axisymmetric flow is maintained until time $t = 1200$, at which point a very small stall cell appears near the *casing* on wire 2 and the machine begins its irretrievable slide into rotating stall. The first sign of a stall cell at the hub occurred later at wire 5. In Fig. 17 the tip clearance was 0.7 percent and stall inception was again first apparent near the casing at wire 5, being found only later near the hub at wire 8.

The conclusions to be drawn from this discussion are that, for the compressor used, the breakdown into stall occurs near the casing for all practical tip clearances and is not brought about by boundary layer thickening near the rotor hub. The variation in boundary layer thickness with time found near the hub by McDougall et al. is simply the response of the boundary layer (and possibly of separated flow) to modal unsteadiness in the flow field and is not necessarily the origin of the stall cell.

Authors' Closure

I would like to thank Dr. Day for his comments and note with interest that he has measured circumferential harmonic waves immediately prior to stall on a multistage compressor.

From Dr. Day's comments it is clear that there is some confusion over the difference between the appearance of the first stall cell and the appearance of a disturbance that indicates that the flow is about to break down. The measurements described in our paper were designed to provide information on the flow processes that lead to the breakdown of the normal flow pattern within the compressor into rotating stall. By definition, once a stall cell appears, stall inception has already occurred.

It would seem to me to be extremely unlikely that the rotor passage flow *always* breaks down at the tip, regardless of rotor tip clearance. Measurements made immediately prior to stall within the blade passages (see McDougall, 1990) have shown dramatic changes in the nature of the passage flow, and indeed the overall compressor performance, depending on the tip

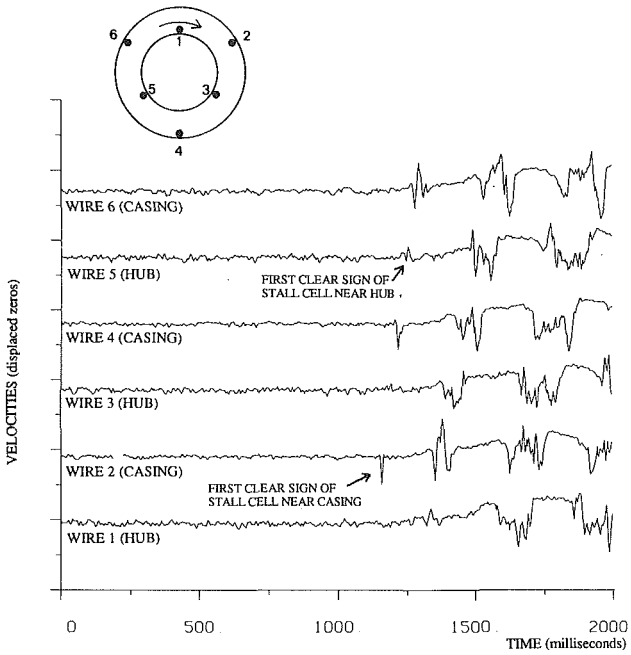

Fig. 16 Time traces from six hot-wires showing the first sign of stall appearing at the casing and not at the hub (tip clearance: 1.2 percent)

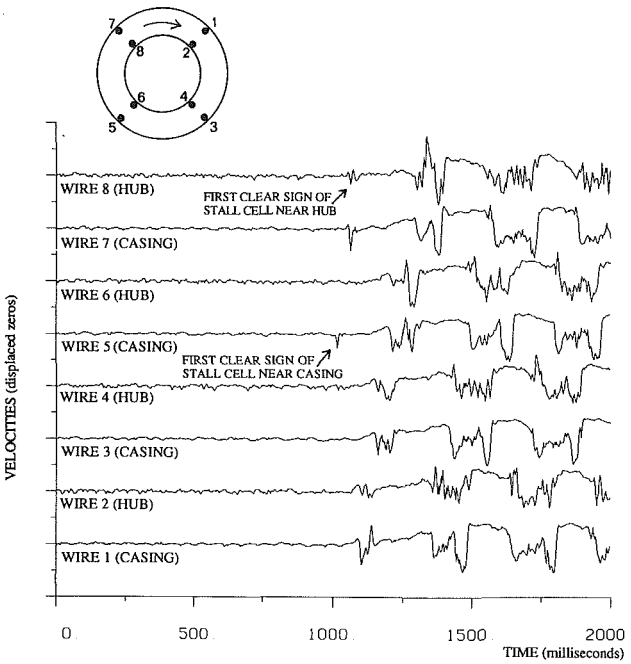

Fig. 17 Time traces from four pairs of hot-wires showing the first sign of stall appearing at the casing and not at the hub (tip clearance: 0.7 percent)

particular, the corners between the two. (My own measurements confirming this picture will be published shortly.)

A flow field such as that illustrated here might be termed "modal" in the sense that the circumferential harmonics of the machine are invoked. These modal oscillations usually become evident near the peak of the pressure rise characteristic. Their presence does not, however, indicate an irreversible or irretrievable downward slide into rotating stall, and at any point prior to the formation of a finite stall cell the flow can be returned to normal axisymmetric operation, without hysteresis, simply by increasing the mean throughflow.

The paper under discussion does make it clear that the presence of detectable circumferential waves does not imply stall, but this needs to be emphasized again because of a misinterpretation of the signals by McDougall et al. The authors placed their probes "just outside the annulus and suction surface boundary layers," the best possible position to detect the modally excited boundary layer fluctuations. These fluctuations are most marked where the boundary layer is thickest, i.e., near the casing for large tip clearances and near the hub for small tip clearances. What the authors failed to do, however, is to show that the stall cell originates from these regions where the boundary layer is thickest. The data reduction technique used in this work, i.e., signal cutoff levels, is unable to distinguish between boundary layer modulations and the formation of a finite stall cell.

Now the reason for emphasizing that early detection of boundary layer excitation is not the same as detecting the onset of stall is that recent measurements that I have made on the same compressor show that stall inception actually occurs at the casing not only for large tip clearances but for small clearances as well. This is a direct contradiction of what is claimed by McDougall et al. in the paper.

The measurements shown in the figures are typical examples obtained on the Deverson compressor in the stationary frame of reference, and consist of traces of velocity versus time as the throttle is inched closed until the compressor stalls. The results are examples of repeated measurements obtained with two fairly small tip clearances (1.2 percent and 0.7 percent of tip chord), both sufficiently small that McDougall et al. would have said that stalling would occur near the hub for this compressor. The hot wires were mounted 20 mm axially upstream of the rotor (tip chord length 108 mm). Six wires were used in one case, eight in the other, with half mounted close to the hub and half close to the casing.

In Fig. 16 the tip clearance was 1.2 percent of chord and it can be seen that steady axisymmetric flow is maintained until time $t = 1200$, at which point a very small stall cell appears near the *casing* on wire 2 and the machine begins its irretrievable slide into rotating stall. The first sign of a stall cell at the hub occurred later at wire 5. In Fig. 17 the tip clearance was 0.7 percent and stall inception was again first apparent near the casing at wire 5, being found only later near the hub at wire 8.

The conclusions to be drawn from this discussion are that, for the compressor used, the breakdown into stall occurs near the casing for all practical tip clearances and is not brought about by boundary layer thickening near the rotor hub. The variation in boundary layer thickness with time found near the hub by McDougall et al. is simply the response of the boundary layer (and possibly of separated flow) to modal unsteadiness in the flow field and is not necessarily the origin of the stall cell.

Authors' Closure

I would like to thank Dr. Day for his comments and note with interest that he has measured circumferential harmonic waves immediately prior to stall on a multistage compressor.

From Dr. Day's comments it is clear that there is some confusion over the difference between the appearance of the first stall cell and the appearance of a disturbance that indicates that the flow is about to break down. The measurements described in our paper were designed to provide information on the flow processes that lead to the breakdown of the normal flow pattern within the compressor into rotating stall. By definition, once a stall cell appears, stall inception has already occurred.

It would seem to me to be extremely unlikely that the rotor passage flow *always* breaks down at the tip, regardless of rotor tip clearance. Measurements made immediately prior to stall within the blade passages (see McDougall, 1990) have shown dramatic changes in the nature of the passage flow, and indeed the overall compressor performance, depending on the tip

clearance. I feel it is unwise to attempt to link the radius at which a stall cell is first observed some distance upstream of the compressor face with the radius of stall inception. It is possible that the flow might break down at the hub, and the low momentum fluid associated with the stalled flow subsequently migrate to the tip prior to emerging upstream of the compressor face.

Unfortunately measurements reported in our paper do not give any indication of the detailed fluid mechanical processes of flow breakdown within the rotor blade passages. What has been achieved is a recognition that it is not appropriate to consider the stalling process to be based on a series of random events occurring in individual blade passages. During stall inception, effects occurring with circumferential length scales much greater than one blade pitch are of prime importance. The ability to anticipate the onset of stall using the presence of the small amplitude disturbances may be useful, and there is obviously scope for major developments in this area.

Stability of Flow Through Multistage Axial Compressors

J. P. Longley

T. P. Hynes

Whittle Laboratory,
Cambridge University Engineering Dept.,
Cambridge, United Kingdom

This paper describes measurements of the performance of a research stage operating in isolation and as part of a multistage compressor. It is shown that the stall point and the stalled performance of the stage are properties of the system in which it operates rather than a property of the stage itself. The consequences of this for the estimation of the stall point for compressors and compression systems are discussed. The support that the measurements give to assumptions made by mathematical models which use the concept of an "underlying axisymmetric" characteristic, are highlighted.

Introduction

Recent advances in the modeling of flow through compression systems (Moore, 1984; Moore and Greitzer, 1986) have reopened the question of how much of the measured performance of a compressor is a true characteristic and how much is strongly influenced by the environment in which the compressor is tested. In particular, it is proposed that a compressor has an underlying "axisymmetric" characteristic extending, in all probability in a smooth manner, to flows lower than the isolated clean flow stall point. Further, it is proposed that the stall point and the stalled performance are a property of the system, rather than of the compressor alone.

The consequences of this environmental dependence are clearly far reaching. For example, Ham and Williams (1983) concluded that stability audits of engines conducted ignoring this fact often grossly under-predict surge margins in both clean and distorted flow.

Whether or not one component in a compression system will affect the stability of the flow through another depends upon how strongly their flowfields are coupled. Documented examples of the stall point of a compressor being somewhat affected by other components in the compression system are available, for example, Turner (1959) and Greitzer et al. (1977). However, in these cases changes in operating point at stall were not large. In addition one would have liked stronger evidence that the compressor contained no region of part or full span stall.

What is true for a compressor is also true for a stage or bladerow. When in a favorable environment (part of a multistage compressor), a stage or bladerow may operate in an axisymmetric manner at flows lower than its isolated clean flow stall point. The performance is then completely different at these low flow rates from that measured when the stage is tested in isolation or the bladerow tested in cascade. Part of the problem of predicting the stall point of a multistage axial compressor is thus how to assess the strength and nature of the flowfield coupling between stages.

The main aim of the work described in this paper was to demonstrate a definitive example of an underlying axisymmetric characteristic at flows below the isolated clean flow stall point. The experimental procedure for doing this was to measure the performance of a research stage in isolation and then again in what is, from a stalling point of view, a more favorable environment.

The environment was changed by the addition of two further downstream stages. These measurements are thus directly relevant to the problem of predicting the stall point of a multistage axial compressor. They provide a clear example of how strong the influence of flowfield coupling with other compression system components can be on the stall point of a stage and, by inference, on that of a compressor.

Experimental Facility

The compressor used was the recently refurbished C106 test facility at the Whittle Laboratory. (This was formerly at NGTE and was that used by Turner, 1959.) The C106 compressor is an axial flow, low-speed, high hub-to-tip ratio design where the number of stages and blade stagger angles may be varied. The general arrangement of the compressor is shown in Fig. 1 and its basic dimensions are listed in Table 1. (Further details are given by Longley, 1988.) The performance

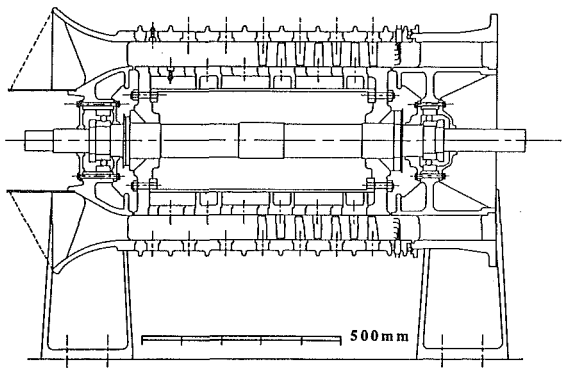

Fig. 1 General arrangement of C106 compressor (three-stage build)

Contributed by the International Gas Turbine Institute and presented at the 34th International Gas Turbine and Aeroengine Congress and Exhibition, Toronto, Ontario, Canada, June 4–8, 1989. Manuscript received at ASME Headquarters February 21, 1989. Paper No. 89-GT-311.

Table 1 Basic geometric details of the C106 test compressor

Hub to tip ratio	0.75	
Tip radius	254mm	(10")
Bladerow centreline axial separation	45.7mm	(1.8")
Number of blades rotor, stator	58, 60	
Mid-height chord	28.0mm	(1.1")
Nominal speed	2950rpm	
Mean blade speed	≈69.8m/s	
Reynolds number (at design)	1.7×10^5	

Table 2 Compressor blading details at design stagger settings

	Span	Hub 6%	Mid 50%	Tip 94%
IGV	Stagger	13.3°	13.5°	13.6°
	Camber	20.0°	17.0°	13.0°
	Thickness/Chord	10.4%	11.2%	12.4%
	Pitch/Chord	0.761	0.835	0.903
Rotor	Stagger	23.3°	38.5°	47.0°
	Camber	39.5°	25.0°	14.0°
	Thickness/Chord	12.4%	10.8%	8.6%
	Pitch/Chord	0.733	0.863	1.011
Stator	Stagger	30.7°	28.0°	25.2°
	Camber	36.0°	34.0°	31.0°
	Thickness/Chord	10.5%	11.2%	12.2%
	Pitch/Chord	0.761	0.841	0.910

of the research stage (with IGV's) was investigated in the following three builds:

Isolated build: Research stage with no downstream component.

Matched build: Research stage with two identical downstream stages.

Mismatched build: Research stage with two mismatched downstream stages (stagger increased by 10 deg).

The matched build is typical of low-speed multistage rig design, while the mismatched build is more typical of a high-speed compressor operating at part speed.

The research stage had a design flow coefficient of $\phi = 0.6$ and a design reaction of approximately 60 percent. All the blade profiles were C4 section and it was approximately a free vortex design. Table 2 lists the design blading configuration. To obtain more stable rear stages for the mismatched build the design stagger settings for these stages were increased by +10 deg. This effectively reduced their design flow coefficient to $\phi \approx 0.43$.

Measured Performance of the Research Stage

The inlet total to exit static pressure rise performance characteristics for the research stage for the three different test configurations are shown in Fig. 2. The data points shown (circles) are for unstalled axisymmetric operation. For reference, the first operating point in rotating stall is also shown (star) to indicate the abrupt transition at compression system instability. The important points are as follows. When the research stage is followed by two further similar stages (matched build), or when it is isolated, its pressure rise characteristic rises monotonically until stall; this is the normally encountered performance. When the research stage is followed by two stages that have a lower design flow coeffi-

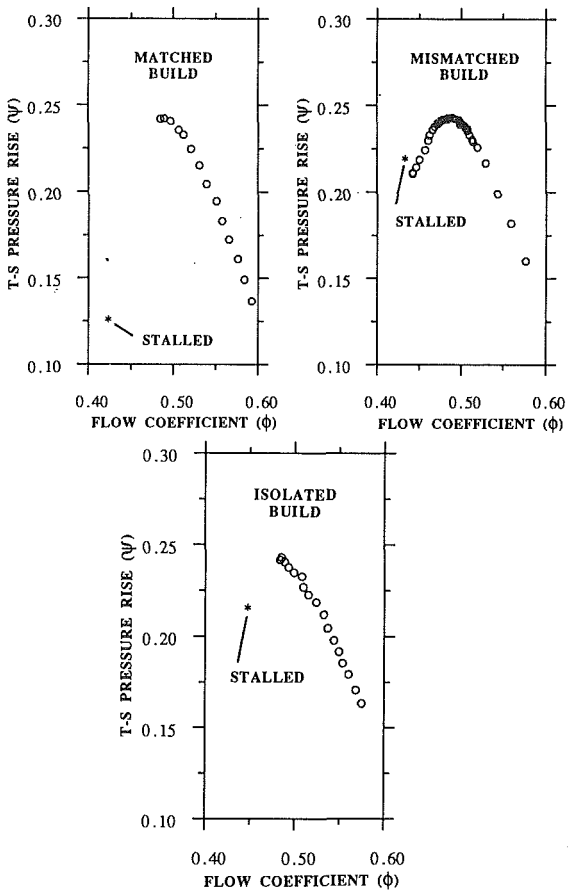

Fig. 2 Comparison of research stage performance for different operating environments (downstream components)

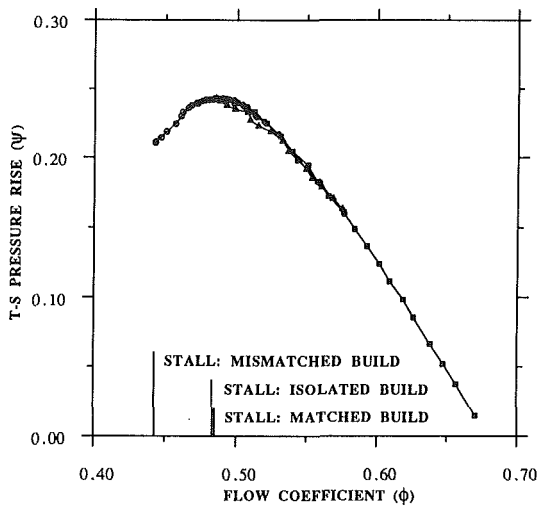

Fig. 3 Comparison of the unstalled axisymmetric performance of the research stage in the three different environments

Nomenclature

Relative incidence = blade inlet angle − relative inlet flow angle

Relative turning = relative exit flow angle − relative inlet flow angle

Relative loss = (loss in relative total pressure)/ρU^2

$\psi(\phi)$ = $(Ps_{exit} - Pt_{in})/\rho U^2$

ϕ = flow coefficient = axial velocity /U

U = mean blade speed

ρ = density

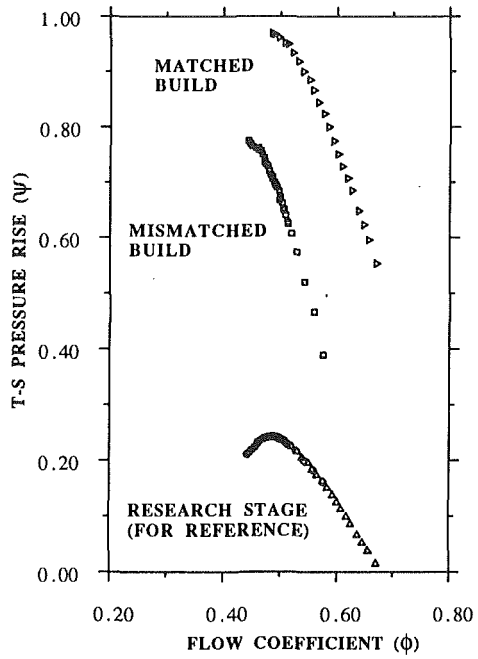

Fig. 4 Comparisons of the unstalled three-stage performance for the matched and mismatched build (research stage shown for reference)

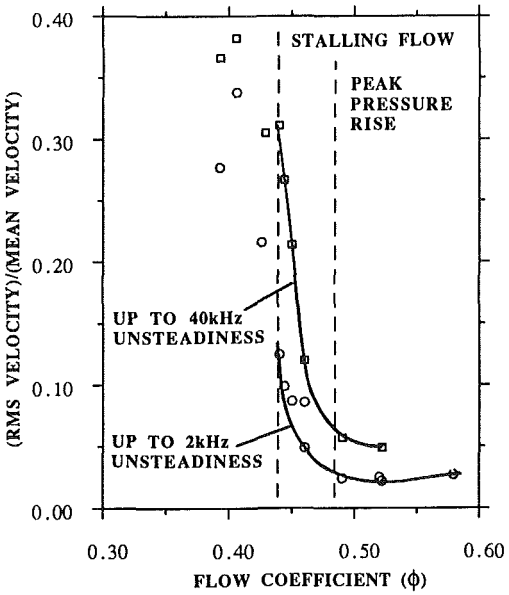

Fig. 5 Measured rms unsteadiness at 80 percent span behind the rotor bladerow in the research stage (mismatched build)

cient (mismatched build) the pressure rise performance again rises to a similar maximum value but then decreases. Instability does not occur until a *much* lower pressure rise and mass flow.

The best way to compare the precise shapes of the three performance characteristics is to overlay them on the same plot, as in Fig. 3. Because of the close similarity the different curves are difficult to distinguish. It is clear that the characteristics from the three builds all represent the same smooth curve. In passing, it is worth remarking that the performance (as measured by steady instrumentation) of the research stage in rotating stall *is* different for each of the three builds, as evidenced by the first point on the stalled portion of the characteristic. The pressure rise increases at stall for one of the builds.

The overall (three-stage) performance characteristics for the matched and mismatched builds are shown, in Fig. 4, for comparison. The fully matched build provided a much higher pressure rise than the mismatched one, and had almost zero slope at instability compared against a strong negative slope for the mismatched build.

It is important to note that in none of the test configurations were any adjustments made to the blading of the research stage. The change in the stable performance has resulted from the flowfield coupling between it and its environment. It is in no way related to the change that would result from, say, casing treatment, etc.

Steady Axisymmetric Performance

The significantly extended portion of the research stage characteristic, when it is part of the mistmatched build, has a strong positive slope and traditionally this would be expected to be unstable. We have described the performance on this portion as steady and axisymmetric. Clearly the flow in a compressor is never steady or truly axisymmetric. It is necessary at this point to clarify what is meant by this.

The key point is the length and time scale of any nonuniformity or unsteadiness present. Compressors have two length/time scales of interest. Firstly, small length scale ($\approx$ blade pitch) nonuniformities are associated with blade-to-blade variations and are inherent to all compressors. These correspond to unsteadiness at high frequencies comparable to that of blade passing ($\approx$2.8 kHz in this case). Secondly, large length scale ($\approx$ circumference) nonuniformities are associated with stall cells and inlet distortion. These correspond to unsteadiness at low frequencies up to a few times rotor rotational speed (up to perhaps 200 Hz in this case). We define flow to be steady and axisymmetric if there is no large length scale nonuniformity or unsteadiness present. (This is the sense in which it is used in mathematical modeling.)

Surveys of the flowfield using hot-wire anemometers indicated that the flow deteriorated most rapidly at the exit of rotor 1 at the tip and that full-span stall was the mode of instability. There was no region of part-span stall. All the following unsteady measurements presented are for this location (i.e., at exit to the rotor of the research stage near the tip). Unsteady measurements were taken at high frequency (40 kHz) and separately at low frequency (2 kHz) to facilitate the separation of the two time scales of interest.

The rms unsteadiness levels for the mismatched build are shown in Fig. 5 for a range of flow coefficients. At flow rates higher than the peak of the research stage's characteristic both the low-frequency and high-frequency unsteadiness levels are relatively small and approximately constant. As the mass flow is reduced into the region of positive characteristic slope, both unsteadiness levels rise, the higher frequency one slightly more rapidly. At the abrupt transition (rotating stall) the high-frequency rms unsteadiness levels change little and the low-frequency one approximately doubles.

Before stalling, the low frequency contributes 41 percent to the total unsteadiness; after stalling it contributes 72 percent. A possible interpretation is that the flowfield unsteadiness changes from a short time scale (blade passing frequency) to a much longer one (stall cell frequency). These rms levels alone, while persuasive, are not sufficient to justify this interpretation. A more extensive frequency analysis is required. At selected flow coefficients the "low" (2 kHz) and "high" (40 kHz) frequency velocity spectra were analyzed in more detail.

The low-frequency spectra are shown in Fig. 6 for the range 0–400 Hz (0 to $\approx$ 8 $\times$ rotor revolution frequency). At a point on the high flow side of the peak of the characteristic there is little unsteadiness and no predominant frequency. As the flow coefficient is reduced to just before the stalling flow (points 1

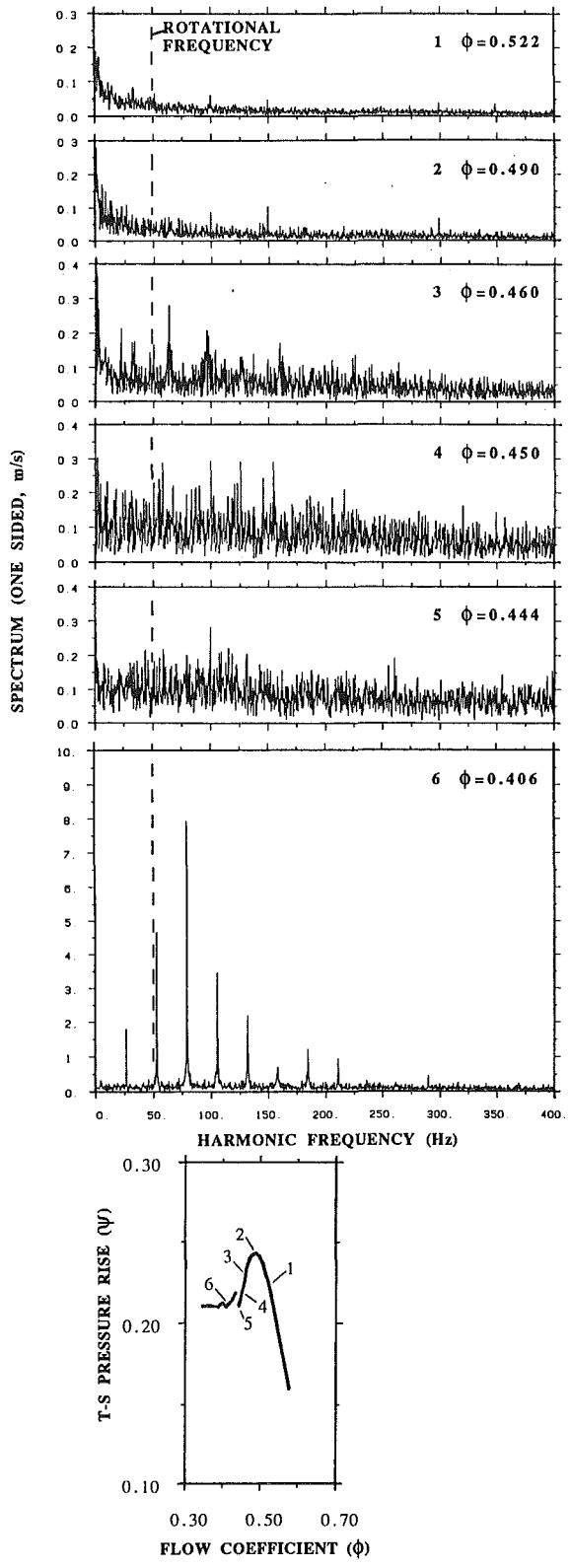

Fig. 6 Low-frequency spectral analysis of unsteadiness in research stage (mismatched build, 80 percent span behind the rotor)

to 5) the general level of unsteadiness increases but no predominant modes are detected. However, at instability, between points 5 and 6, there is a definite well-defined change in the spectrum of the velocity unsteadiness (note the change of a factor 10 in the scale of the vertical axis).

The high-frequency data spectra are shown in Figs. 7 for the range of 0–4 kHz (0 to 140 percent blade passing frequency).

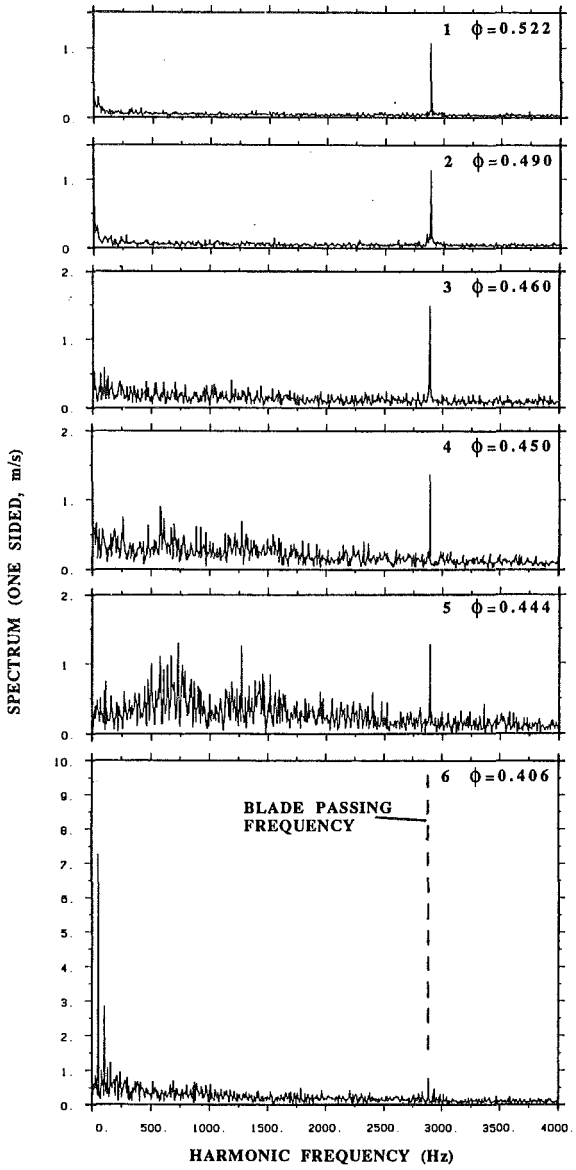

Fig. 7 High-frequency spectral analysis unsteadiness in research stage (mismatched build, 80 percent span behind the rotor)

On the high flow side of the peak all that is detected is the blade passing frequency ($\approx$ 2.8 kHz) and low-level broadband unsteadiness. As the flow coefficient is reduced the background level increases. Just prior to instability (ϕ = 0.444) there is a significant 500–1000 Hz bandwidth unsteadiness of amplitude similar to blade passing disturbances. As with the low-frequency data, at instability there is a definite well-defined change in the velocity spectrum.

It is just conceivable that the spectral analysis results were adversely influenced by a transient stall cell formation and decay. To ensure that this was not the case the above velocity traces were reprocessed as follows. Each trace was subdivided (10 intervals) and each subsample harmonically decomposed and an average of each frequency amplitude taken. The results showed no differences from the above.

To clarify further the distinct change in the nature of the velocity unsteadiness at stall, in Fig. 8 two sample traces are shown. The two points chosen were ϕ = 0.444 (just above stall) and ϕ = 0.426 (slightly below stall). The traces shown represent approximately eight rotor revolutions and clearly demonstrate the distinct difference in the nature of the compressor flowfield before and after instability.

Bladerow Performance for the Mismatched Build

The above results show that there is no abrupt change in the pressure rise performance of the research stage when part of the mismatched build as the mass flow is reduced. This extended, low flow, stage/bladerow performance cannot be measured in isolation nor in cascade. It is interesting to compare bladerow performance on both the high and low flow sides of the peak pressure rise. Inter-bladerow spanwise (radial) traverses throughout the research stage were done at two operating points, one on each side of the peak pressure rise. At IGV inlet the measurements are pitchwise representative while at IGV exit they are slightly affected by the IGV wakes. At rotor exit a stationary probe averaged over rotor wakes, while at stator exit a single radial traverse indicates only the midpitch flow.

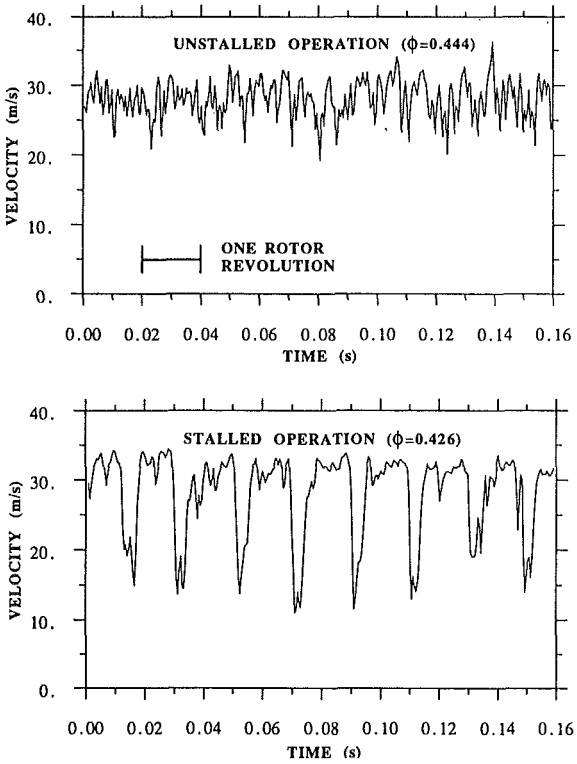

Fig. 8 Comparison of the velocity before and after flowfield instability (mismatched build, 80 percent span behind the rotor)

The axial velocity profiles measured as shown in Fig. 9. As the mass flow is reduced there is no significant change in the radial distribution of flow. The smaller change observed at stator exit, Fig. 9(*d*), indicates broader stator wakes. The relative conditions at rotor inlet and exit are shown in Fig. 10, together with the absolute flow angles in Fig. 11, for the same two operating points. These figures confirm that there is no abrupt change in the nature of the flowfield between the two operating points. Two points of interest are, firstly, that there is a large increase of the loss at the tip of the rotor bladerow (this is where the flowfield was observed to deteriorate dramatically). Secondly, the rotor relative turning is almost unchanged, indicating a significantly increased rotor deviation.

The pressure rise falls off at low flow due to increased blade loss and due to increased deviation. It is relevant to compare the relative importance of these two mechanisms, as it affects how bladerow performance data must be modeled or combined to obtain the overall compressor performance. There has, perhaps, been a tendency to emphasize correlations for loss rather than deviation in many bladerow stacking programs, possibly because only loss affects compressor efficiency, or because the main aims are design point calculations. Perhaps a different emphasis would be appropriate when attempting to predict compressor stall.

The spanwise mass average values for the flow properties

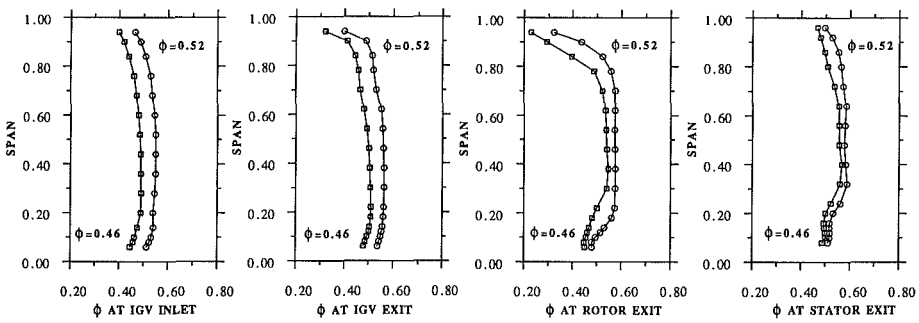

Fig. 9 Spanwise variation in flow coefficient throughout the research stage (mismatched build, operating points on both high and low flow sides of the peak pressure rise)

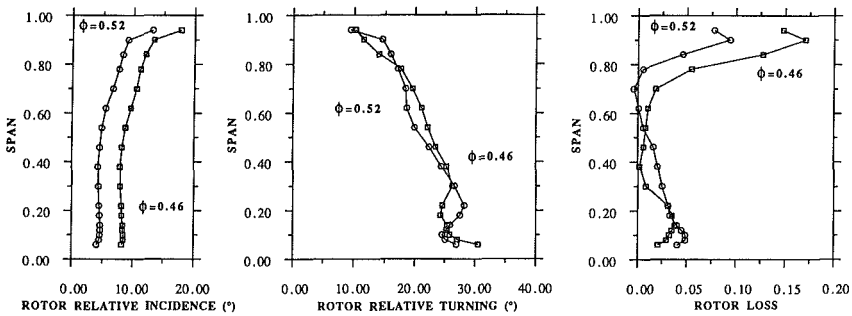

Fig. 10 Spanwise performance of the research stage rotor (mismatched build, operating points on both high and low flow sides of the peak pressure rise)

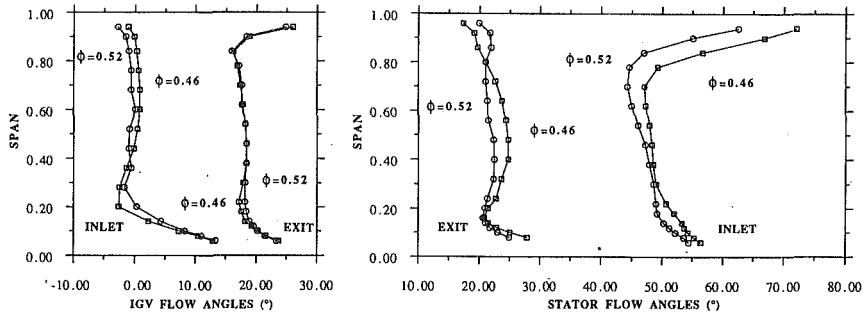

Fig. 11 Spanwise variation in absolute flow angles throughout the research stage (mismatched build, operating points on both high and low flow sides of the peak pressure rise)

Table 3 Spanwise mass average performance for the research stage for both the high and low flow operating points

	ϕ=0.52	ϕ=0.46	change
Swirl at IGV exit (abs.)	19.1°	19.1°	
Swirl at rotor inlet (rel.)	-57.7°	-61.4°	-3.7°
Swirl at rotor exit (rel.)	-36.8°	-39.9°	-3.1°
Swirl at stator inlet (abs.)	49.6°	52.9°	
Rotor turning (rel.)	20.9°	21.5°	0.6°
Rotor relative total pressure loss	0.025	0.037	0.012
Rotor 'deviation deficit'	—	0.041	0.041

are shown in Table 3. The reduction in rotor total pressure rise due directly to loss was measured to be 0.012, while that due to increases in rotor deviation (taking the higher flow coefficient as reference) was 0.041, more than three times as large. These quantities were estimated using independent pressure, flow angle, and velocity measurements, and the accuracy of the data can therefore be assessed. It is our estimate that the maximum error in either of these terms does not exceed 0.003. It seems clear, then, that for this research stage the pressure rise performance peaks due to the effect of the increased rotor deviation rather than the increased loss.

Interpretation

We interpret the measurements described in the previous sections as follows. When the research stage is isolated, or part of the matched build, stall takes place at an operating point where the flow in the rotor passages (the measurements indicate the tip region as being critical) first breaks down. A stall cell has a large circumferential length scale and any such disturbances must persist a considerable axial distance external to the research stage. The effect of the two mismatched stages is to oppose these disturbances: The rear stages are operating on a negatively sloped part of their characteristics and they will produce a low pressure whenever the mass flow is locally low. The flowfield through the compressor as a whole remains stable to much lower flow rates.

The action of the rear stages cannot, however, significantly affect the flow in individual blade passages within the research stage as these are of a much smaller length scale. In whatever manner the flow is breaking down there, be it separation of a boundary layer on a blade or endwall or be it spillage of the clearance vortex, it is destined to remain small scale, i.e., to be confined to one or at least a small number of blade passages. The passage flow is probably breaking down and recovering at various positions around the annulus more or less at random, as evidenced by the unsteady measurements. Operation of a compressor in this manner was first reported by Lambie (1988) and he called it "rough running."

From a practical point of view one can envisage different approaches to a compressor stall problem. Near design speed and flow it would probably not be acceptable to keep the flow in a stage (or a compressor) stable by relying on the stability of the flow through other stages (or compressors). Such "rough running" could easily cause long-term vibration problems and is unlikely to be compatible with highly efficient operation. A designer would probably seek to improve the flow in the particular stage (or compressor) giving trouble.

There is another class of problem, however, that makes only temporary demands upon stall margin. In particular, for those associated with inlet flow distortion, engine speed changes or short-duration power offtake demands, it would probably be preferable to accept a period of rough running provided compressor stall was avoided. This could be achieved if the coupling between the stage (or compressor) flowfield and that of other stable components in the system is sufficiently strong.

There has been considerable interest of late, in the possibility of active control systems to help with compressor stall problems. It is presumably as solutions to the short duration class of problems that they are envisaged being used. There seems no reason in principle why they should not be successful.

Comments on Coupling Prediction

In order to estimate whether or not the flow through a component can be held stable by flowfield coupling with a second, it is necessary to predict the mode of instability. There is, at present, no theoretical basis for doing this.

If the flowfield breaks down in a fundamentally two-dimensional manner, then such low-order circumferential disturbances decay axially in the gaps between components on a length scale of the order of a radius. In addition such disturbances decay much more slowly with axial distance through bladerows and through interspool gaps containing support vanes, as there is then resistance to crossflows. For axial distances between components typical of aeroengine applications, coupling for these two-dimensional disturbances is usually strong.

The stalling mode of a stage or compresssor can, however, be a fundamentally three-dimensional one (for example a high-order radial harmonic). Such disturbances decay axially on a much shorter length scale, and in addition blades and interspool vanes provide little resistance to their decay. Even the flowfields of bladerows within the same compressor are not necessarily coupled for this type of disturbance.

McDougall (1990) presents convincing results that a single-stage high hub-to-tip ratio compressor that he tested stalled in a two-dimensional, low-order circumferential harmonic manner. In addition, he demonstrated that this issue is not simply one of whether part or all of the span of individual blade passages is exhibiting flow breakdown. The results of Turner (1959) can only be explained if a two-dimensional stalling mode is assumed, as can those presented here.

Mathematical models invariably assume a two-dimensional mode and a traditional prediction is that an isolated compressor will stall at the peak of its pressure rise characteristic. For many compressors this is clearly not the case and this fact

is often cited as criticism. The models do in fact generally only reach this conclusion when component flowfields are perfectly coupled (i.e., gaps are neglected). It is our estimate that the gaps in this compressor are large enough to explain the slope at instability for the case of the overall characteristic for the mismatched build (Fig. 4).

There is, however, another aspect to this. The slope of the characteristic for the isolated build also appears negative at stall (Fig. 2). One of the assumptions of mathematical models is that the axisymmetric characteristics of a component are unaffected by the presence of others. The small degree to which this is not true can greatly influence the apparent slope at stall. Figure 3 demonstrates that the research stage performance is for all practical puproses unaffected by the presence of downstream stages, while Fig. 2 shows a marked apparent variation in slope. If one had used the zero slope criterion applied to the true axisymmetric characteristic as a prediction of the isolated stage stall, then the correct stall point would have been identified.

In one sense this point is pedantic, since characteristics are only accurate if measured (in which case the isolated stall point is also known). It does also tend to obscure the fact that the sensible use of these models is in predicting component flowfield coupling. Provided the stall mode is a two-dimensional one, this we believe they do successfully. An example of this was the design of this series of experiments. Performance characteristics were estimated using a bladerow stacking model and the degree of restagger of the rear stages was estimated assuming that the first harmonic would be responsible for instability. Despite the fact that the performance estimates were by no means perfect, we were able to predict the movement in the stall point to a satisfactory degree of accuracy.

Conclusions

From the research described and discussed in this paper the following conclusions may be made:

(*i*) It has been shown that the unstalled flow range of a stage when operating as part of a multistage compressor can be considerably greater than when that stage is operating in isolation.

(*ii*) The main reason for the turning over of the characteristic of the tested stage as the flow rate is reduced has been shown to be due to increased rotor deviation rather than increased blade loss.

(*iii*) Considerable experimental support has been found for the assumptions underlying recent mathematical models that a compressor has an underlying "axisymmetric" characteristic extending smoothly to flows below the clean flow stall point.

(*iv*) Experiments have confirmed that the stall point and the stalled performance of a stage, and by inference that of a compressor, are a property of the system in which it operates rather than of the stage or compressor alone.

Acknowledgments

The authors wish to acknowledge the assistance received from Dr. N. A. Cumpsty and Rolls Royce plc. for the loan of the C106 test facility. The many valuable contributions from Prof. E. M. Greitzer concerning the work were made possible by a NATO travel grant.

References

Greitzer, E. M., Mazzawy, R. S., and Fulkerson, D. A., 1977, "Flowfield Coupling Between Compression System Components in Asymmetric Flow," ASME Paper No. 77-GT-17.

Ham, C. J., and Williams, D. D., 1983, "Some Applications of Actuator and Semi-actuator Disk Theory to the Problem of Intake/Engine Compatibility," Tokyo International Gas Turbine Congress, 83-TOKYO-IGTC-50.

Lambie, D., 1988, Ph.D. Dissertation, Cambridge University Engineering Dept., United Kingdom.

Longley, J. P., 1988, "Inlet Distortion and Compressor Stability," Ph.D. Dissertation, Cambridge University Engineering Dept., United Kingdom.

McDougall, N. M., Cumpsty, N. A., and Hynes, T. P., 1990. "Stall Inception in Axial Compressors," ASME JOURNAL OF TURBOMACHINERY, this issue.

Moore, F. K., 1984, "A Theory of Rotating Stall of Multistage Axial Compressors: Parts I–III," ASME *Journal of Engineering for Gas Turbines and Power*, Vol. 106, pp. 313–336.

Moore, F. K., and Greitzer, E. M., 1986, "A Theory of Post-Stall Transients in Axial Compression Systems: Part I – Development of Equations," ASME *Journal of Engineering for Gas Turbines and Power*, Vol. 108, pp. 68–76.

Turner, R. C., 1959, "The Effect of Axial Spacing on the Surge Characteristics of Two Mismatched Axial Compressor Stages," Aeronautical Research Council, CP No. 431.

Effects of Endwall Suction and Blowing on Compressor Stability Enhancement

N. K. W. Lee

E. M. Greitzer

Gas Turbine Laboratory,
Department of Aeronautics and Astronautics,
Massachusetts Institute of Technology,
Cambridge, MA 02139

An experimental investigation was carried out to examine the effects on stall margin of flow injection into, and flow removal out of, the endwall region of an axial compressor blade row. A primary objective of the investigation was to clarify the mechanism by which casing treatment (which involves both removal and injection) suppresses stall in turbomachines. To simulate the relative motion between blade and treatment, the injection and removal took place through a slotted hub rotating beneath a cantilevered stator row. Overall performance data and detailed (time-averaged) flowfield measurements were obtained. Flow injection and removal both increased the stalling pressure rise, but neither was as effective as the wall treatment. Removal of high-blockage flow is thus not the sole reason for the observed stall margin improvement in casing or hub treatment; injection can also contribute significantly to stall suppression. The results indicate that the increase in stall pressure rise achieved with injection is linked to the streamwise momentum of the injected flow, and it is suggested that this should be the focus of further studies.

Introduction

Background. It is well known that the presence of grooves or slots (commonly known as "casing treatment") over the tips of compressor rotor blades can improve compressor stall margin. Not only is the stall point[1] moved to a lower mass flow rate, but the pressure rise at which stall appears is also increased. Improvement in stall margin, however, has generally been accompanied by a decrease in compressor efficiency (Fujita and Takata, 1984; Prince et al., 1975), the trend being that those treatments that are more useful in suppressing stall also have larger efficiency penalties. There has thus been considerable work to clarify the mechanism by which the stall margin improvement is achieved, with the goal of developing a rational method of casing treatment design that combines good stall performance and minimal loss in efficiency.

From the many different treatment configurations that have been tested (see, for example, Fujita and Takata, 1984; Prince et al., 1975; Tesch, 1971), one that has emerged as particularly effective in delaying stall is known as axial skewed grooves. Some of the features of the flow phenomena in this geometry were investigated by Smith and Cumpsty (1985). Using the same configuration on a *moving hub* underneath a set of *cantilevered stator blades*, Cheng et al. (1984) also found a marked improvement in (stator) stall margin. This "hub treatment" experiment, which was specifically designed so that the stator hub flow was similar to that in the tip region of a rotor, had the advantage of allowing the use of stationary instrumentation, making it easier to obtain blade-to-blade flow measurements.

Johnson and Greitzer (1987) (denoted henceforth as JG) subsequently examined the flow associated with the smooth (untreated) and treated hubs. With the smooth hub, blockage appeared in the middle of the stator flow passage near the trailing edge just before stall. In addition, the flow pattern and the trends seen in the speedlines as functions of wall and blade geometry were consistent with those observed by Smith and Cumpsty (1985) and Greitzer et al. (1979), which were investigations of rotor flows. These results imply that findings concerning hub treatment can be directly applied to the casing treatment situation, and this is the position from which the present work should be viewed.

With hub treatment, the blockage at the rear was removed due to flow into the grooves, with this flow emerging as a high-velocity jet near the leading edge. A sketch of this is shown in Fig. 1. The jet is strongest near the leading edge, but the extent of injection covers roughly the front half of the treatment, with flow removal occurring in the rear half.

Although the jet (also cited by Fujita and Takata, (1984, Smith and Cumpsty, 1985, and Takata and Tsukuda, 1977) had previously been believed to be the principal agent responsible for delaying stall, the data presented in JG had several features that did not lend obvious support to this. The jet traveled across the blade passage, impinged on the pressure surface, and then traveled toward the stator exit on the blade surface, i.e., it did not come close to the region of high blockage that existed in the smooth wall build. Flow removal, however, did occur in the area occupied by blockage. It was thus argued that removal of the retarded flow (blockage) near the hub trailing edge, rather than the jet near the leading edge,

[1] By this, we mean the onset of rotating stall.

Contributed by the International Gas Turbine Institute and presented at the 34th International Gas Turbine and Aeroengine Congress and Exhibition, Toronto, Ontario, Canada, June 4–8, 1989. Manuscript received at ASME Headquarters January 13, 1989. Paper No. 89-GT-64.

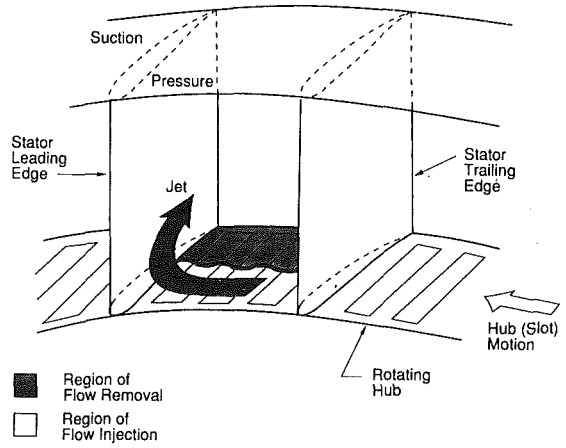

Fig. 1 Schematic of hub treatment slot inlet/exit flow conditions

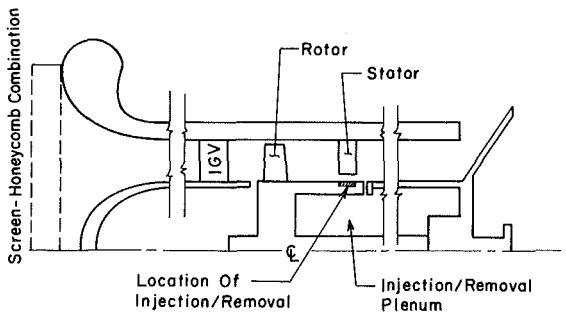

Fig. 2 Layout of compressor showing locations of injection/removal

was very important for delaying stall onset. Although such arguments are plausible, the data are by no means conclusive.

A key step in sorting out this question is to quantify the influence of the flow removal as well as of the jet. This can be done in a control experiment in which the two competing fluid mechanic effects are imposed separately. The present paper describes the results of such an experiment.

Objective and Overall Questions to be Answered. The overall objective was to provide diagnostic information concerning the mechanism of stall suppression by casing/hub treatment by separately simulating: (1) the jet at the front of the stator passage, and (2) the flow removal at the rear. To investigate the endwall flowfield in the case of injection, as well as to provide a check on the accuracy of simulation, the detailed blade-to-blade velocity field was obtained using hot-wire anemometry. Variation of compressor performance with the amount of endwall flow addition or removal was also documented.

If the hypothesis about suction playing the major role were correct, little or no stall margin improvement should result with an injection-only configuration. In contrast, there should be a large increase in stall margin with flow removal, similar to that obtained with the actual hub treatment. The present investigation is thus a (first-of-a-kind) experiment to quantify the roles played by the jet and the flow removal in delaying rotating stall.

Table 1 Flowpath geometry

	Rotor	Stator
Hub diameter (mm)	444	444
Casing diameter (mm)	597	597
Number of blades	44	45
Chord (mm)	38	38
Solidity at midspan	1.0	1.0
Aspect ratio	1.9	1.9
Camber (deg)	30	30
O.D. stagger angle (deg)	65	40
Midspan stagger angle (deg)	60	42.5
I.D. stagger angle (deg)	55	45
Blade clearance (mm)	0.8	1.9

Experimental Facility

Compressor Design and Critical Features. The design of the compressor is documented in detail by Cheng et al. (1984) and Prell (1981), but the following is repeated as background to the configuration used in the experiments:

1 Rotor and stator stagger angles are chosen such that the former is lightly loaded relative to the latter, i.e., the stator stalls at a considerably higher flow coefficient than the rotor.

2 The stator hub is designed with a high loading so that stall originates from this region.

3 Root clearance and stagger of the stator were selected according to the criteria presented by Koch (1981) to promote the required stall on the endwall.[2]

4 A large axial distance (roughly 1.1 span) was kept between rotor and stator, to decouple the rotor and stator flow fields.

5 The total pressure rise across the rotor hub was small compared to that across the tip, so that the stator operated with a hub radial distortion.

Table 1 lists the geometry of the rotor and stator blades and Fig. 2 shows a cross-sectional schematic of the compressor. The injection (removal) plenum was fed (emptied) via manifolds, which connected to the laboratory air supply (exhaust). Injection (removal) flow was metered via a calibrated orifice plate.

Design of Hub Treatment. It was desirable to examine the blowing and suction using a treatment configuration similar to that reported by Cheng et al. (1984) and by JG so that results could readily be compared. The previous experiments used 60-deg axial skewed slots with approximately 70 percent open area. These precise slot dimensions could not be maintained in the present set of experiments because of machining difficulties, and the open area was decreased to 50 percent. As will be seen, however, this had little effect on the performance.

A total of seven treatment configurations were tested. All were 60-deg axial skewed slots, but the axial length and the location on the hub varied. Figure 3 gives dimensions for the longest slot, which occupied 90 percent of the axial chord. The

[2] It has been found that wall treatment is only effective if the stall is associated with the growth of separation on the endwall. This has been termed "casing stall" by McDougall (1988) and "wall stall" by Greitzer et al. (1979) in earlier publications.

Nomenclature

A_{jet} = area of jet
$\bar{C}_x$ = average axial velocity through compressor
ΔP = static pressure rise across stator
U = mean blade speed of rotor
V_{jet} = absolute velocity of jet
V_{inlet} = reference stator inlet velocity
β_{inlet} = stator inlet angle
$\bar{\beta}_{inlet}$ = mean stator inlet angle
ρ = density of air

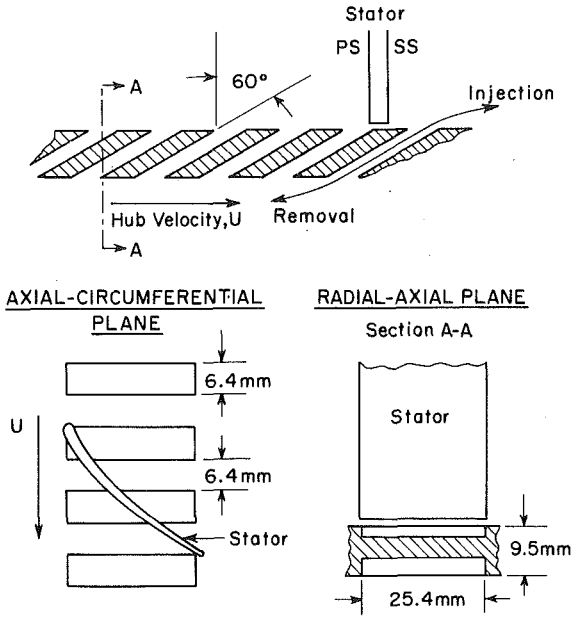

Fig. 3 Full 90 percent slot geometry showing stator location

slots extended all the way through the hubs, so that they were open to the injection/removal plenum. The designations used for the different configurations are:

Nomenclature	Nominal Extent of Slot (Referred to axial blade chord)
1. Full 90% slots	5–95%
2. 22.5% front	5–27.5%
3. 22.5% middle front	27.5–50%
4. 22.5% skewed middle front	27.5–50%
5. 22.5% rear	72.5–95%
6. 45% front	5–50%
7. 45% rear	50–95%

Figure 4 shows locations of the slots in the stator passage. With the "full 90% slots," the slot covers the middle 90 percent of the axial chord of the stator, similar to the original treatment. The "22.5% rear" has slots 22.5 percent of the axial chord in length, located at the rear part of the stator passage, etc. The "22.5% skewed middle front" were constructed so that the front and rear slot edges had a 45-deg angle relative to a plane perpendicular to the compressor axis. Relative flow at slot exit for these slots would be expected to be inclined roughly 45 deg to axial, measured in the plane of the slots (in addition to 60 deg from radial, measured in the r–θ plane).

Velocity and Pressure Instrumentation. A single hot-wire probe was used in obtaining three-dimensional time-averaged velcity data. The method used was based on a modification of that reported by Schmidt and Okiishi (1977). Hot-wire signals at three different wire orientations were combined to obtain the magnitude and direction of the local flow at each grid location in the stator passage.

Eight static pressure taps evenly spaced around the casing of the stator, at inlet and exit stations, were used to obtain the static pressure rise across the stator. Compressor mass flow measurements were deduced from static pressure measurements upstream of the inlet guide vanes and previously measured inlet displacement thicknesses.

Description of Experiments

The present series of experiments can be split into two parts: parametric study of the stator pressure rise characteristics (outer wall static pressure rise) with endwall flow injection or removal, and examination of the features of the stator velocity field in the presence of injection.

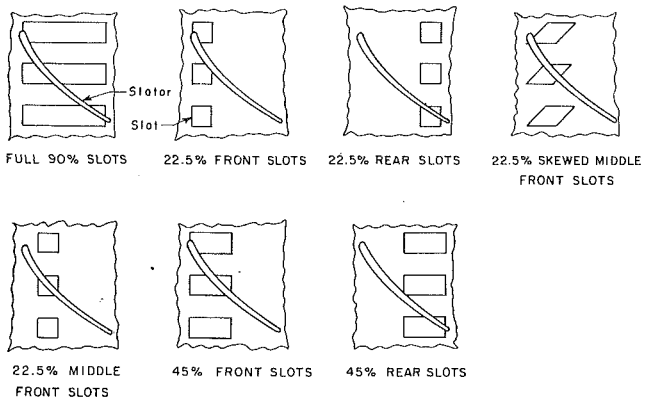

Fig. 4 Locations and nomenclature of slots tested

Pressure Rise Characteristics. The conditions of the parametric study were as follows. All characteristics were taken at a compressor speed of 2600 rpm, corresponding to a rotor tip Mach number of 0.24 and a Reynolds number, based on blade chord at the stator midspan, of 1.0×10^5. Previous tests with the baseline hub treatment and smooth wall showed that Reynolds number effects were small, at least down to 0.8×10^5 (2000 rpm) (Cheng et al., 1984).

The smooth hub and the full 90 percent slots were first tested without injection or removal. Because these slots were open to the plenum, a run was also made with the bottom of the slots sealed to eliminate interactions between the latter and the plenum.

Different hubs were tested with the injection or removal rate varied, up to 6 percent of the throughflow in some cases. For comparison, the measured mass flow (in and out) through the hub treatment previously tested was approximately 3.5 percent of the throughflow (there was, of course, no *net* inflow or outflow). The flow near the stator hub was monitored by a hot wire to identify the stall point.

Time-Averaged Stator Velocity Field Measurements. Three-dimensional, time-averaged stator flow field measurements were obtained for the 22.5 percent front slots at at blowing rate of 2.8 percent (expressed as percentage of the throughflow at $\bar{C}_x/U=0.342$). This configuration should simulate the jet in an actual hub treatment; comparison with hub treatment hot-wire results was carried out to verify this. Time-averaged flow field measurements were obtained, since the data reported in JG showed that substantial unsteadiness was present only in a small region close to the hub near the leading edge.

Experimental Results

Data Presentation Format. Pressure rise information was obtained with all of the hubs described earlier. Data showing the difference in performance obtained with smooth wall and with hub treatment are presented in Fig. 5. The stator static pressure rise ΔP is nondimensionalized in two alternative ways, using $1/2\,\rho U^2$ and $1/2\,\rho V_{\text{inlet}}^2$, where U is the mean blade speed, V_{inlet} is a reference stator inlet absolute velocity, and ρ is the density. Compressor mass flow is presented as flow coefficient, $\bar{C}_x/U$, where $\bar{C}_x$ is the average axial velocity measured upstream of the inlet guide vanes.

The stator inlet velocity V_{inlet} was obtained from $\bar{C}_x$ and the mean stator inlet angle $\bar{\beta}_{\text{inlet}}$ as

$$V_{\text{inlet}}=\frac{\bar{C}_x}{\cos\bar{\beta}_{\text{inlet}}} \tag{1}$$

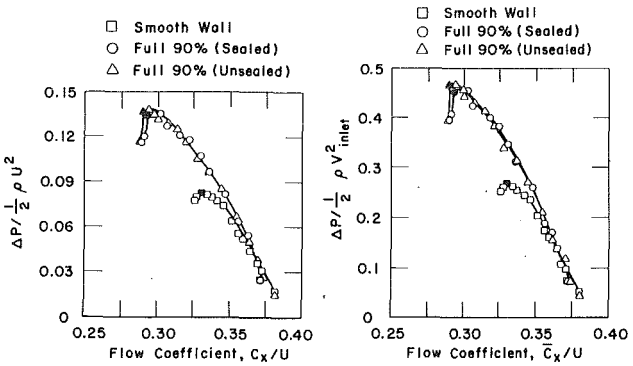

Fig. 5 Baseline stator static pressure rise: smooth wall and full 90 percent slots

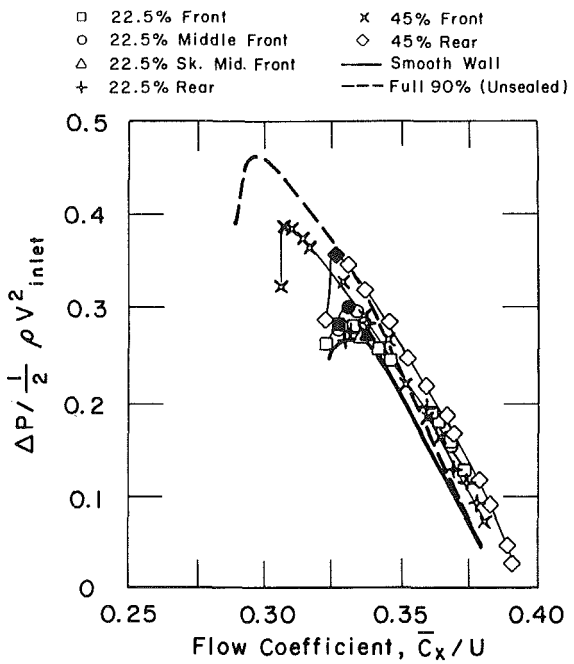

Fig. 6 Stator static pressure rise with no net injection or removal

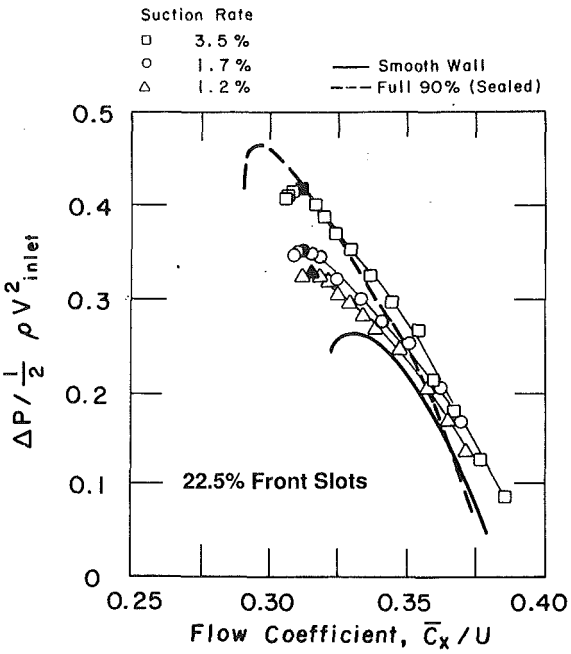

Fig. 7 Stator static pressure rise with removal: 22.5 percent front slots

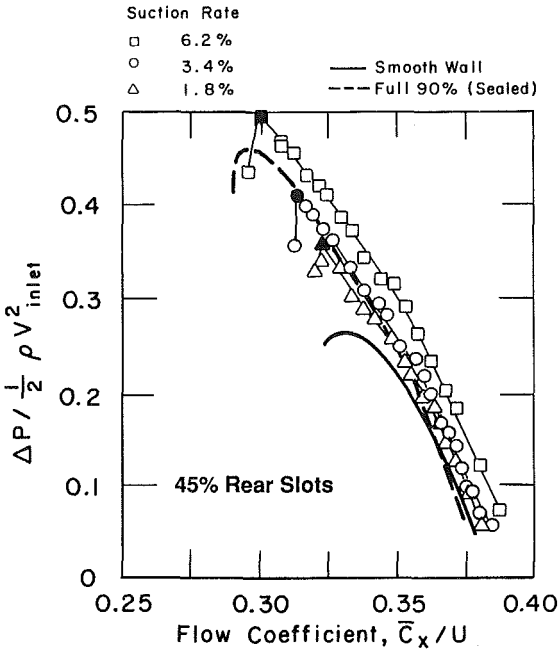

Fig. 8 Stator static pressure rise with removal: 45 percent rear slots

Radial traverse measurements of the inlet flow angle β_{inlet} (from which $\bar{\beta}_{inlet}$ is obtained) are given by Cheng et al. (1984) for values of $\bar{C}_x/U = 0.305$ and 0.345. Values of $\bar{\beta}_{inlet}$ between these mass flows were obtained by linear interpolation. The magnitudes of the stator absolute inlet velocity and flow angle vary from hub to tip, and there is no clear criterion for the "proper" normalizing dynamic pressure. The procedure followed here is to use V_{inlet} given by equation (1). For reference, the measured values of $\bar{\beta}_{inlet}$ were 52.5 deg (at $\bar{C}_x/U = 0.345$) to 55.5 deg (at $\bar{C}_x/U = 0.305$). It is to be emphasized, however, that we see no indication that the central conclusions of this study would be significantly altered by adoption of another definition of inlet dynamic pressure. Additional information about the stator inlet conditions and the overall stage performance can be found in Cheng (1982).

Figures 6 to 11 show the dependence of the stator static pressure rise on injection or removal rate. As stated, injection (removal) rate is given as percentage of the compressor main flow at $\bar{C}_x/U = 0.342$, the near-stall point for the smooth wall. Although there is no absolute criterion for selecting the normalizing compressor flow rate, 0.342 is used because it is the flow coefficient at which hot-wire measurements were taken.

The estimated measurement uncertainties of $\Delta P/1/2\rho U^2$ and $\Delta P/1/2\rho V^2_{inlet}$ were ±2 percent and ±3 percent of the stalling value of the smooth wall build, respectively. The uncertainty in flow coefficient was ±1 percent.

Compressor Pressure Rise Characteristics: Baseline Runs. The smooth wall build and the 90 percent hub treatment slot configuration, sealed at the slot bottom, are selected to be the baselines for assessing the effectiveness of various slots. This section presents results obtained with these geometries, with discussion given subsequently.

The characteristics for the smooth wall build as well as the 90 percent slot configuration are displayed in Figs. 5(*a*, *b*). Data for the slot configuration are shown both with and without the slot bottom sealed. The occurrence of rotating stall is marked by the solid point on each curve. In the experiment, stalling was identified with the appearance of large-

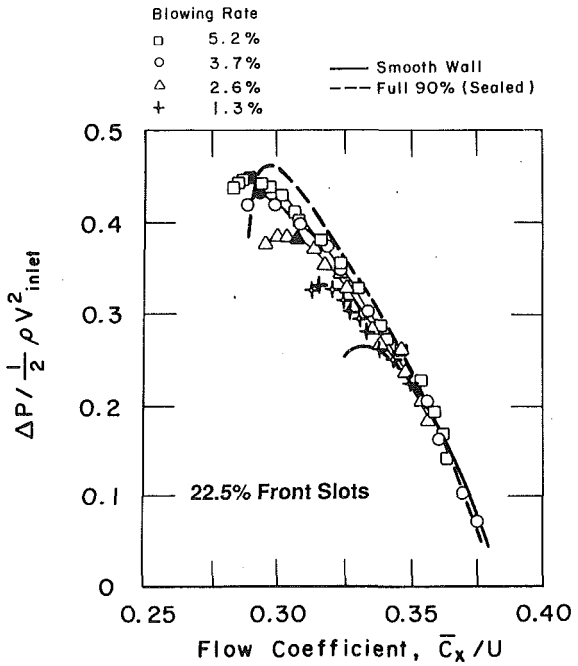

Fig. 9 Stator static pressure rise with injection: 22.5 percent front slots

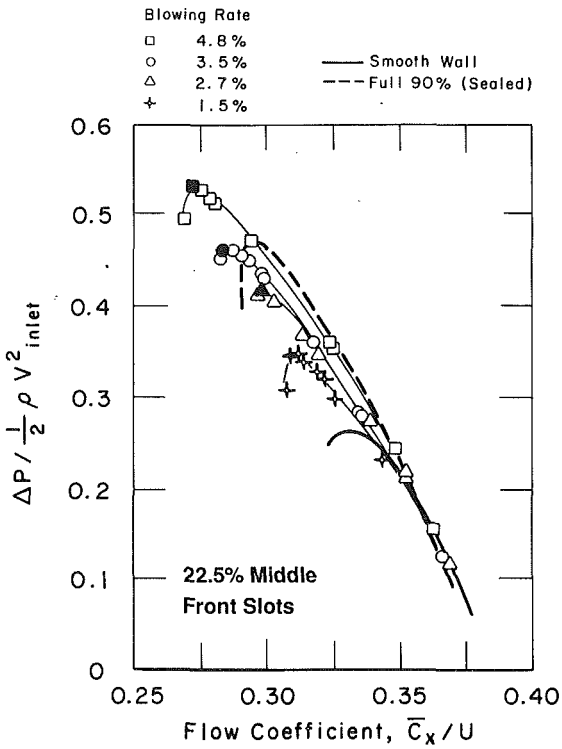

Fig. 10 Stator pressure rise with injection: 22.5 percent middle front slots

scale, high-amplitude unsteadiness in the flow field near the hub surface, and the onset point of this unsteadiness was quite distinct. The stall points are at, or very near, the peak of the pressure rise curve, and this will be seen for the other configurations described subsequently. With the smooth wall build, stall occurs at a pressure rise the same as reported in JG, $\Delta P/{}^1/_2\ \rho U^2 = 0.083$, although at a slightly lower (2 percent) value of $\bar{C}_x/U$. Possible explanations for the small shift may be the installation of an improved stator seal, or the improved rotor assembly and alignment procedure. In any event:

1 the speedlines for the present series of builds were repeatable,

2 the stalling pressure rise was the same as that documented previously, $\Delta P/{}^1/_2\rho U^2 = 0.083$ and $\Delta P/{}^1/_2\rho V^2_{\text{inlet}}) = 0.268$ in the two nondimensional forms, and

3 any changes between the present and the previous experiments in measured flow are much smaller than between smooth wall and hub treatment builds.

With the 90 percent slots sealed at the bottom, stall occurs at $\bar{C}_x/U = 0.297$, a 10 percent change from the smooth build. The stalling $\Delta P/{}^1/_2\rho U^2$ and $\Delta P/{}^1/_2\rho V^2_{\text{inlet}}$ are equal to 0.137 and 0.461, corresponding to 66 and 72 percent improvement over the smooth wall build, respectively. With the 90 percent slots unsealed, stall appears at a slightly lower $\bar{C}_x/U$ of 0.294, with the stalling $\Delta P/{}^1/_2\rho U^2 = 0.138$ and $\Delta P/{}^1/_2\rho V^2_{\text{inlet}} = 0.465$. Closing the bottom of the slots has little effect on peak pressure rise for this configuration.

Figures 5(*a*, *b*) also show that, whether the nondimensionalization is carried out using U^2 or V^2_{inlet}, the relative positions of the curves for smooth wall and for slotted endwall are quite similar. This was true over the full range of data obtained. As a consequence, we will present the subsequent data in the form $\Delta P/{}^1/_2\rho V^2_{\text{inlet}}$ as more closely representative of the stator performance viewed as a diffuser. An approximate conversion factor from units of $\Delta P/{}^1/_2\rho V^2_{\text{inlet}}$ to those of $\Delta P/{}^1/_2\rho U^2$ is 0.3, but for the actual data in terms of $\Delta P/{}^1/_2\rho U^2$, the report by Lee (1988) can be consulted.

For reference, the stall points reported in JG were at $\bar{C}_x/U = 0.295$, $\Delta P/{}^1/_2\rho U^2 = 0.145$, and $\Delta P/{}^1/_2\rho V^2_{\text{inlet}} = 0.488$ with the hub treatment. Those slots had 17 percent more open area, and this is viewed as the probable cause of the 5 percent larger stalling pressure rise, compared with the slots used in the present experiment.

Compressor Pressure Rise Characteristics: All Other Hub Geometries. Figure 6 presents speedlines obtained with no net injection or removal, for all the different hub geometries. Again, only $\Delta P/{}^1/_2\rho V^2_{\text{inlet}}$ is presented, but the plot of $\Delta P/{}^1/_2\rho U^2$ looks very similar, except for the scaling of the ordinate. The curves for the smooth wall and 90 percent unsealed are included for reference. Compared to the peak pressure rise of the smooth build, the 22.5 percent slots give improvements in $\Delta P/{}^1/_2\rho V^2_{\text{inlet}}$ of at most 10 percent, whereas the two 45 percent slots achieve roughly a 40 percent increase in peak pressure rise. Slots at the front of the stator generally perform better than slots at the rear. The 45 percent slots have a drop in performance at stall similar to that of the 90 percent slots.

A large number of compressor characteristics have been obtained with flow removal (suction) and injection. Rather than presenting them all, we will show representative curves with suction and then with injection, to indicate the main features obtained with each. A summary curve will then show the overall performance of the the geometries tested.

Figures 7 and 8 show representative pressure rise characteristics with *suction*. In both figures, and in all of Figs. 7 to 11, the pressure rise characteristics with smooth wall and with 90 percent sealed slots are shown for reference as solid and dashed lines, respectively. Data from the 22.5 percent front (in Fig. 7) and 45 percent rear (in Fig. 8) slots are shown for a range of suction rates. (The performance of the 45 percent rear slot was similar to the 22.5 percent rear slot, but the former is presented because a greater range of suction flows could be obtained.) Stall is suppressed at all suction rates compared with the smooth wall. It can also be seen that the characteristics with suction are displaced from those for the smooth wall as well as from the zero suction rate curves, even in the prestall regions, by amounts depending on the rate of removal; this will be discussed below.

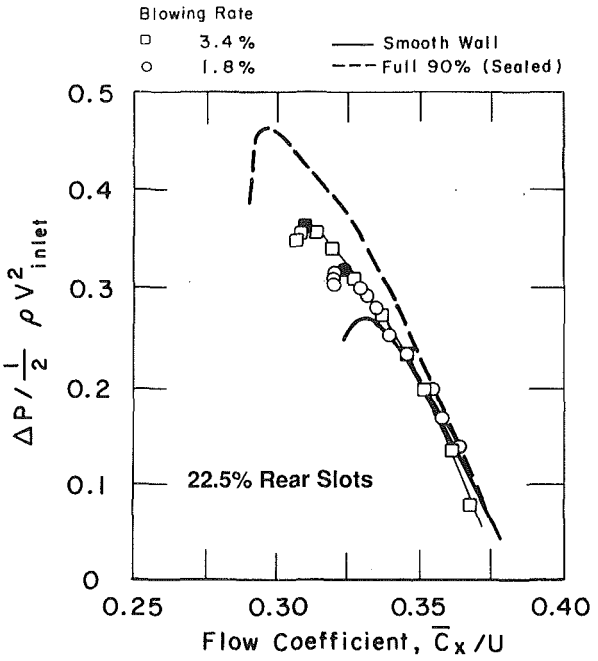

Fig. 11 Stator static pressure rise with injection: 22.5 percent rear slots

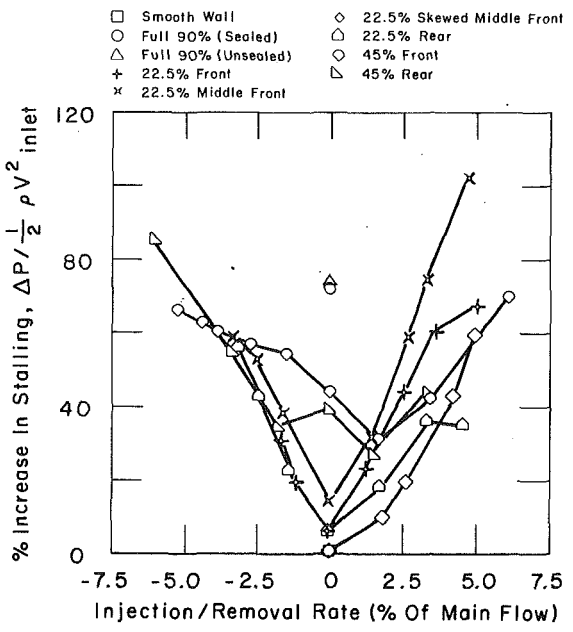

Fig. 12 Increase in stalling pressure rise over smooth wall for different slots

Representative characteristics obtained with different *injection* rates are shown in Figs. 9 (22.5 percent front), 10 (22.5 percent middle front), and 11 (22.5 percent rear). Injection increases the stalling pressure rise in all cases, but injection at the front of the passage is more effective than at the rear. The displacement in the prestall portion of the speedlines away from the smooth-wall baseline is smaller than that found with removal; this will also be elaborated on later.

Effects of Slot Flow Rate on Stalling Pressure Rise. Figure 12 shows the improvement in stalling pressure rise plotted as a function of the injection or removal rate for *all* of the hub geometries tested. Six different curves (actually straight line segments) are shown together with the stall points for solid wall and for the sealed and unsealed full 90 percent slots. The nondimensional pressure rise at stall is expressed as a percentage increase over the smooth wall value. Injection and removal rates are normalized by the compressor flow at a reference flow coefficient of 0.342, the flow at which the detailed measurements were made.

Several observations can be made from Fig. 12. First, for *flow removal* (suction):

1 Stalling pressure rise of the 22.5 percent slots and 45 percent front slots increases monotonically with suction rate over the range examined. This is not the case, however, with the 45 percent rear slots. With no suction, the increase in stalling pressure rise due to the latter is roughly 40 percent. As suction increases from zero, there is an initial drop in the stalling pressure rise, with a local minimum near 1.5 percent suction mass flow. Increases in suction from this point yield increases in stalling pressure rise, with the zero-suction value re-attained at a suction rate of 2.2 percent of the reference mass flow.

2 Effectiveness of the 45 percent front slots differs considerably from the 45 percent rear slots at low suction rates. The 45 percent front slots have good capability to delay stall at low suction rates (around 1.5 percent removal, say), giving a 55 percent increase in $\Delta P / {}^1/_2 \rho V^2_{inlet}$).

3 There is little difference between the 22.5 percent front and rear slots with suction. Effectiveness of the 22.5 percent middle front slots surpasses these two by approximately 10 percent, up to a level of roughly 3 percent suction.

4 All curves intersect at approximately 3.5 percent suction rate, which is the amount of slot flow in (and out of) the hub treatment used in JG. The stalling $\Delta P / {}^1/_2 \rho V^2_{inlet}$ of the 45 percent rear slots matches the full 90 percent slot performance with zero net flow at 5 percent suction.

For *flow injection* (blowing):

1 Slot effectiveness varies over the entire range investigated, in contrast to the behavior with suction.

2 With the 45 percent slots, a decrease in effectiveness occurs in both front and rear slots as injection rate increases from zero to 1.5 percent.

3 The stalling pressure rise of all the 22.5 percent slots increases monotonically with injection rate.

4 The 22.5 percent middle front outperforms all other 22.5 percent slots at all blowing rates, and outperforms the 45 percent slots at rates higher than 2 percent.

5 The 22.5 percent skewed middle front is considerably less effective than the 22.5 percent front or middle front.

6 The stalling pressure rise of the full 90 percent slot is equalled by the 22.5 percent middle front slots at 3.3. percent injection.

Discussions of the Parametric Results

Figure of Merit for Effectiveness Assessment. The primary figure of merit adopted to assess the effectiveness of various slots is the nondimensional stalling pressure rise attained, $\Delta P / {}^1/_2 \rho V^2_{inlet}$. Although one can debate the use of this criterion, its basis is that it is the endwall regions that give rise to stall and, more specifically, that stall is associated with a separation that arises on the endwall (McDougall, 1988). What is assessed, therefore, is the ability of the flow in this region to cope with a given nondimensional pressure rise. Use of the stall flow coefficient as a discriminant carries with it an ambiguity, because the upstream and downstream flow coefficients are different when there is mass addition or removal. As pointed out by Koch (1970), there is thus a shift in the pressure rise characteristic compared to the zero net flow situation, and the direction of the shift depends on whether the mass flow is measured upstream or downstream. (Note that, by averaging the upstream and downstream flow coefficients, it is possible to lessen the amount of the shift in the pressure rise characteristics. It does not appear to us, however, that any

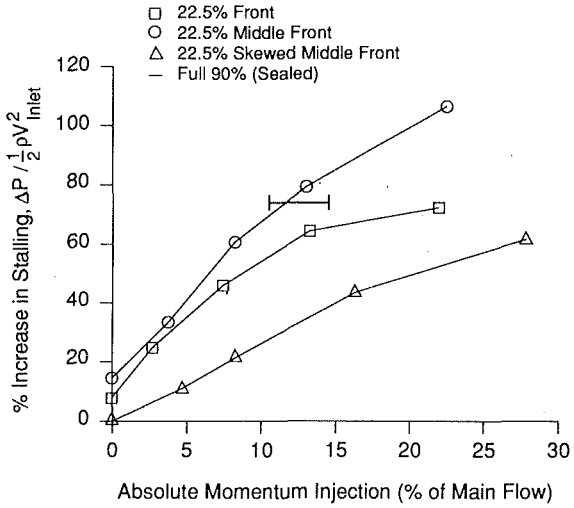

Fig. 13 Variation in stalling pressure rise increase with absolute momentum influx for 22.5 percent slots

clear advantage is gained by doing this or by basing the flow on a downstream measurement.)

$\Delta P/{}^1/_2\rho V^2_{\text{inlet}}$ is by no means the only figure of merit that can be used. If it is desired to assess performance of the stator in terms of the pressure rise only, $\Delta P/{}^1/_2\rho U^2$ is more relevant. However, the latter does not carry explicit information on inlet conditions, and our choice basically is an adoption of the common convention used for diffusers. In addition, as mentioned several times already, the trends are similar with either nondimensionalization, so that conclusions based on either $\Delta P/{}^1/_2\rho U^2$ or $\Delta P/{}^1/_2\rho V^2_{\text{inlet}}$ also correspond closely. The term "performance" will hereafter refer to the *stalling pressure rise normalized by the stator inlet dynamic head*, unless otherwise stated.

Performance With No Net Injection or Removal. The performance of the 90 percent slots is slightly (5 percent) lower than that of the hub treatment used in JG. In both those hub treatments, flow at the rear end of the stator passage is sucked into the slots, has work done on it by the hub, and emerges at the front as a high momentum jet. There are no hot-wire data for the 90 percent slots, so the exact amount of flow in and out of the slot in the present set of experiments is not known, but the similar performance of the present 90 percent slots and those used in JG suggests that slot flow in the former is close to the value of 3.5 percent measured in the latter.

With the 45 percent slots, performance at zero net flow drops to half of the value reached by the 90 percent slots. Even so, the increase in stall margin implies that there is *internal* injection and removal, similar to that in the 90 percent slots as described in the previous paragraph. For the 22.5 percent slots, the speedlines are similar to the smooth wall baseline, and one can conjecture that little internal injection or removal occurs in these slots.

Performance With Flow Removal. We first consider flow removal at the rear. The success of the 22.5 and 45 percent rear slots in suppressing stall (Figs. 8 and 12) supports the hypothesis that the removal of low-momentum fluid at the rear of hub or casing treatment slots can help delay stall. The trend one might expect, of increased stalling pressure rise with increased suction mass flow rate, is generally confirmed by the data for the 22.5 percent rear slots and for the 45 percent rear slots at high suction rates. The behavior of the 45 percent rear slots at low suction rates will be addressed subsequently.

Consider now local suction in the front half of the stator passage, through the 22.5 percent front and 22.5 percent middle front slots. The data in JG indicated that blockage does not appear at the front half of the passage, so it does not appear appropriate to talk about the direct action of removal on the blockage. Rather (as in the case of airfoil suction close to leading edges), removal in the front of the passage may alter the development of the endwall layer downstream of the location of suction. Both mechanisms, corresponding to suction at the rear and at the front, appear effective, as Fig. 12 shows little difference in the performance of the 22.5 percent front and rear slots over the entire suction regime.

The behavior of the 45 percent front and rear slots may be rationalized as follows. With no suction they operate like conventional hub treatments, drawing in low total pressure flow at the rear, doing work on it, and ejecting it as a jet at the front. As the suction gradually increases, however, there is a change from this recirculating flow (the zero suction rate situation) to a dominantly (or even totally) outward flow at high values of removal.

At 3.5 percent suction, the approximate amount of circulating slot flow in the 90 percent slots, the stalling $\Delta P/{}^1/_2\rho V^2_{\text{inlet}}$ of all slots is 55 percent higher than that of the smooth build, but is less than the 70 percent level attained by the 90 percent slots. This implies that suction is not the sole cause of the increase in stall margin and that the jet is also responsible for the increase.

The effects of flow removal cause the pressure rise with suction to be higher than the smooth wall value for a given flow coefficient at flows away from stall also. Appendix A describes a simple estimate of the increase in pressure rise in a diffusing cascade with suction, which agrees well with experimental data. It is emphasized, however, that the gain in *stalling* pressure rise is not due to inviscid effects, i.e., to increased diffusion, alone. Had suction been applied through slots located at the outer casing, instead of at the rotating hub, the hub flow would not be altered and the stalling pressure rise would not be expected to differ much from the value found in the smooth wall tests. In short, a necessary condition for the increase in stalling pressure rise is the increased ability of the hub endwall flow to tolerate this pressure rise.

Flow Injection. With endwall flow injection, there is much more variation in effectiveness among the slots. A simple control volume analysis (Appendix A) shows that the static pressure rise due to mixing of the jet with the stator main flow is small compared to the observed improvement in stalling pressure rise. The improvement is thus not a result of the bulk mixing of the jet with the main flow, but is due to local effects of the injection on the hub endwall flow.

Location and Orientation of Injection. With injection, the jet location as well as the jet mass flow govern the amount of improvement (Figs. 9 to 12). Injection through the 22.5 percent front and 22.5 percent middle front is much more effective than that through slots of the same size at the rear. (Comparison with the 22.5 percent skewed middle front is excluded for the present because of its different configuration.)

Although the results have been presented in terms of injection mass flow for simplicity, it might be expected that some measure of the injected flow momentum would be more closely related to the improvement in stalling pressure rise. Figure 13 thus gives performance of the 22.5 percent slots as a function of the *absolute injection momentum flux* (i.e., of the quantity $\rho V^2_{\text{jet}} A_{\text{jet}}$) irrespective of direction. The momentum flux is calculated based on measured injection mass flow, slot area, and slot angle, and is normalized by momentum flux of the main flow (based on $\bar{C}_x$) at the stall flow coefficient.

The solid bar in the figure shows the performance of the 90 percent slots. The momentum flux of the jet in this case is based on the measurements reported in JG; the bar length indicates the experimental uncertainty in the measurements.

In Fig. 13, the superior performance of the 22.5 percent middle front is again visible. This slot and the 22.5 percent

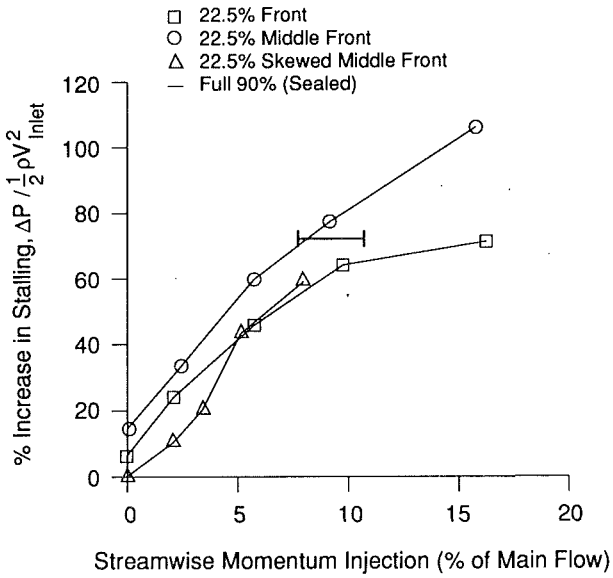

Fig. 14 Variation in stalling pressure rise increase with streamwise momentum influx for 22.5 percent slots

front, however, have similar performance over the range of momentum injection rates up to and including that found for the hub treatment used in the original experiments.

Re-orienting the jet at the middle front location so that it has less alignment with the main flow (i.e., injection through the 22.5 percent skewed middle front) results in considerably poorer performance. More specifically, the 22.5 percent skewed middle front, which was designed to have 40 percent less streamwise momentum flux than the 22.5 percent middle front[3] (at 12 percent absolute momentum influx), is 45 percent less effective than the 22.5 percent middle front at that amount of absolute momentum influx. This suggests, again as one might expect, that direction of influx is important and that there may be correlation between streamwise momentum influx and stall-delaying ability.

In Fig. 14, the effect of the streamwise component of jet momentum is brought out explicitly. The abscissa in the figure is the component of momentum flux in the streamwise direction, based on the assumption that the stator "free-stream" flow angle decreases linearly from inlet to exit.

Plotting the performance in terms of streamwise momentum can be seen (in Fig. 14) to bring the performance curves for the 22.5 percent skewed middle front much more in line with that of the other two slot configurations. From Figs. 13 and 14, therefore, it appears that the favorable effect on stall suppression is linked closely to the streamwise component of the jet momentum flux, although the phenomenological connection is still unresolved. One possible explanation is that the streamwise component of the jet helps delay stall by directly "energizing" the endwall leakage flow. Other mechanisms, however, can also be postulated, such as suppression of the clearance leakage flow (thereby suppressing stall). The former seems to us more plausible, but our view is that further investigation is needed to definitely assess the correct mechanism.

Detailed Flowfield Measurements. In addition to the overall measurements, the velocity field in the endwall region has also been examined for a configuration with injection. This is shown in Figs. 15 through 17, which contain different projections of velocities for: (*a*) the smooth wall, (*b*) the

[3]This was the largest difference available within the constraints of the experiment.

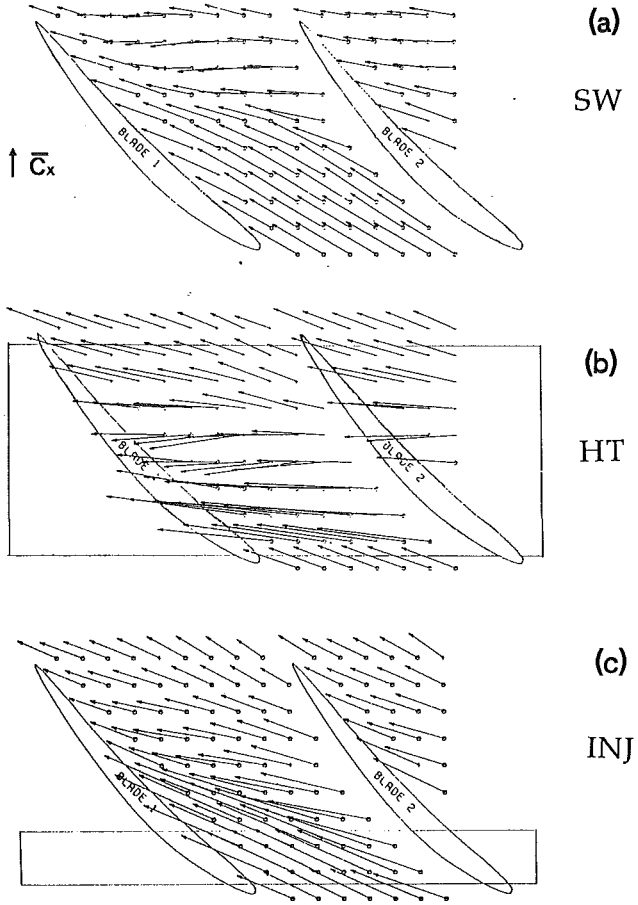

Fig. 15 Velocity vector projections on radial surface at 2 percent span from hub: (a) solid wall, (b) hub treatment slots, (c) injection from 22.5 percent front slots. Scale of $\bar{C}_x$ shown for reference. (Figures (a) and (b) taken from JG.)

treated hub used in JG, and (*c*) the 22.5 percent front with injection. Several aspects of the data will be discussed: accuracy of the simulation, comparison of rear passage endwall flow, and pitch-averaged streamwise velocity profile. In the velocity vector data shown, the convention adopted is that a circle and a cross at the root of a velocity vector represent flow coming out of and going into the plane of the paper, respectively.

Accuracy of Simulation. We first examine the relation between the flows with hub treatment and with injection. Figures 15(*a*, *b*, *c*) are views on a surface of constant radius at 2 percent span from the hub surface. In each of (*b*) and (*c*), a jet is seen to emerge from the endwall at the front of the stator passage. (The rectangular region marked in (*c*) represents the location of injection.) The jets in (*b*) and (*c*) behave similarly in that they both impinge on the pressure side of the left blade (blade 1 in the figure).

The trajectory of each jet after striking the blade is demonstrated in Figs. 16(*a*, *b*, *c*), which show projections on a plane parallel to the chord, 8 percent of pitch from the pressure surface. After impacting the blade, the jet can be seen to travel upward and toward the stator exit on the blade surface.

Note the correspondence between (*b*) and (*c*) from Figs. 15(*b*, *c*) and 16(*b*, *c*). The velocity magnitude of the jet in (*c*) is roughly three-quarters of the one in (*b*), but the trajectories of the jets in both cases are quite similar despite the velocity difference. As will be shown subsequently, pitch-averaged velocities are also closely similar. Hence, the injection does simulate the jet in a conventional hub treatment, with the

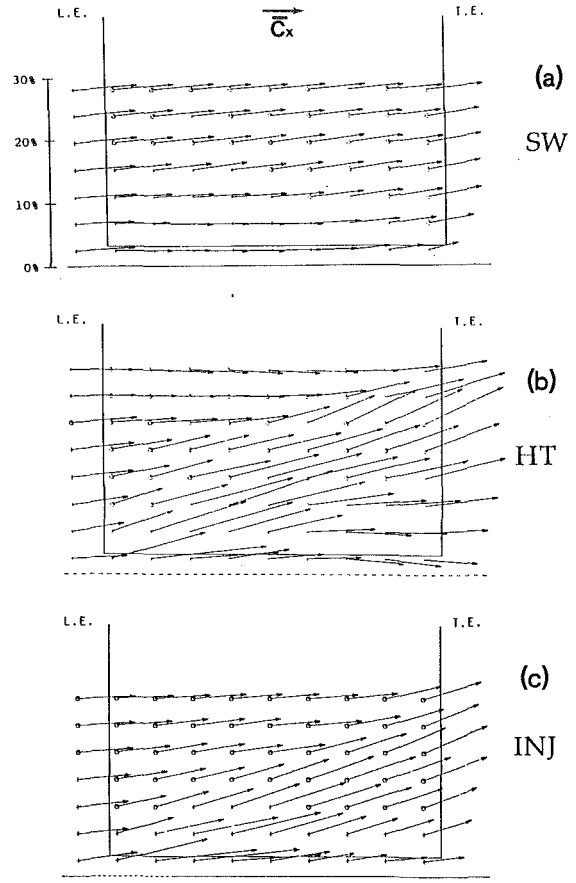

Fig. 16 Velocity vector projections on plane parallel to chordline, 8 percent pitch from pressure surface: (*a*) solid wall, (*b*) hub treatment slots, (*c*) injection from 22.5 percent front slots. Scale of $\bar{C}_x$ shown for reference. (Figures (a) and (b) taken from JG.)

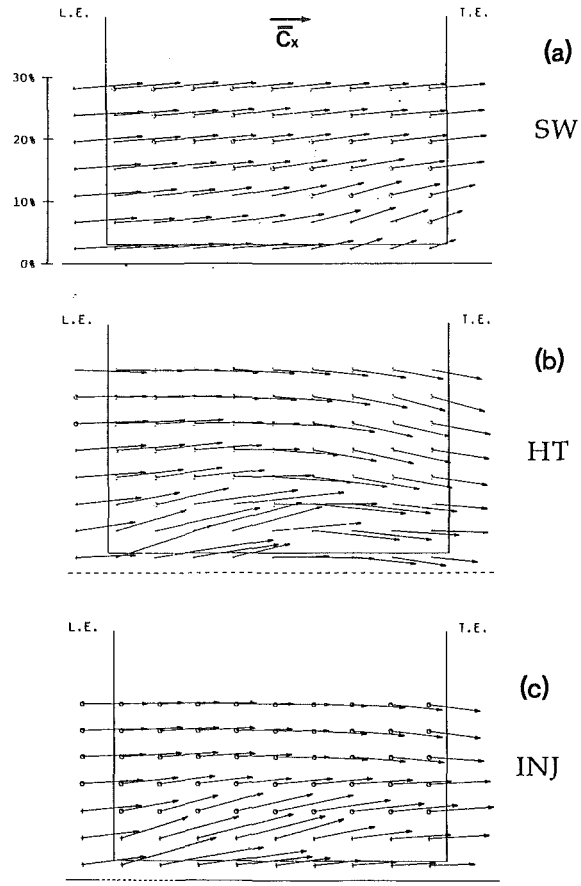

Fig. 17 Velocity vector projections on plane parallel to chordline, 28 percent pitch from pressure surface: (*a*) solid wall, (*b*) hub treatment slots, (*c*) injection from 22.5 percent front slots. Scale of $\bar{C}_x$ shown for reference. (Figures (a) and (b) taken from JG.)

overall jet trajectory represented diagrammatically as in Fig. 1.

Comparison of Rear Passage Endwall Flow. We now consider the flow in the rear of the passage. With the smooth hub, the flow near the trailing edge has only a small component of axial velocity (see Fig. 15*a*). In contrast, the same region of flow in Fig. 15(*c*) has much higher axial velocities, so that the blockage has decreased between 15(*a*) and 15(*c*). (Figure 15(*b*) represents a different situation, because flow is removed from the endwall.)

The same conclusion can be inferred from Figs. 17(*a*, *b*, *c*), which are planes parallel to the chord at 28 percent pitch from the pressure side, arranged in the same order as before. There are marked differences in the behavior of the rear-passage endwall flow for the three cases. Blockage corresponding to an area of small chordal velocities close to the hub is clearly visible near the trailing edge in (*a*). In contrast, in Fig. 17(*c*), no area with significantly decreased chordal velocities is seen. The flow at 2 percent span in the rear half of the passage is parallel to the hub surface. Furthermore, chordal velocities (which are, loosely, streamwise velocities) in that area are considerably higher than those in (*a*), and are comparable to those in the upper planes. In (*b*), again, the situation is very different from both (*a*) and (*c*), because the blockage is removed due to the flow entering the slots at the passage rear.

Pitch-Averaged Streamwise Velocity Profile. It is useful to examine the evolution of the pitch-averaged streamwise velocity through the stator passage. Figure 18 shows the pitch-averaged streamwise velocity normalized by the local annulus-averaged streamwise velocity. At the inlet to the stator (0 percent axial chord), all three profiles, corresponding to the smooth hub, the hub treatment, and the 22.5 percent front slots with 2.8 percent injection, have roughly the same shape. No significant reduction is seen in velocities near the hub surface, although some traces of the jet in (*c*) are visible.

At 8 percent axial chord, the effect of the jet is seen with the hub treatment and with the injection. There is a region of increased velocity covering approximately the lowest 10 percent of the span. At locations from 8 to 55 percent axial chord, an upward movement of the high-velocity region is seen, associated with the jet trajectory revealed in Fig. 16. The strong similarity between the injected flow and the hub treatment flow is also evident.

Up to 55 percent axial chord, the smooth wall profile shows no appreciable reduction in velocities close to the hub surface. Downstream of this axial location, however, there is considerable reduction in streamwise velocity near the wall. The streamwise velocity reduction also occurs with hub treatment and with injection, although it is much less severe. At the 100 percent axial chord location, flow at 2 percent span in the case of the smooth hub leaves the passage with a streamwise velocity that is 40 percent of the mean flow, compared to 60 percent in the other two cases. The general picture is that the streamwise velocity profile is substantially fuller with treatment or injection, compared to the situation with the smooth wall.

Examination of Secondary Circulation in the Stator Passage. We can also examine the secondary circulation in the passage. In Figs. 19 (*a*, *b*, *c*), the velocity at an axial location 90 percent chord from the leading edge is shown, with the

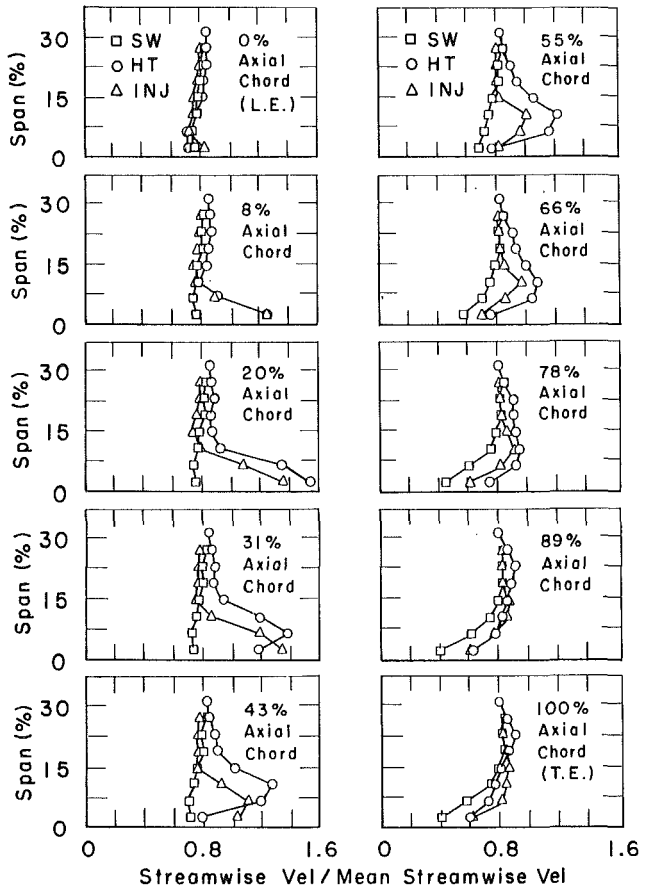

Fig. 18 Development of pitch-averaged streamwise velocity profiles through stator passage

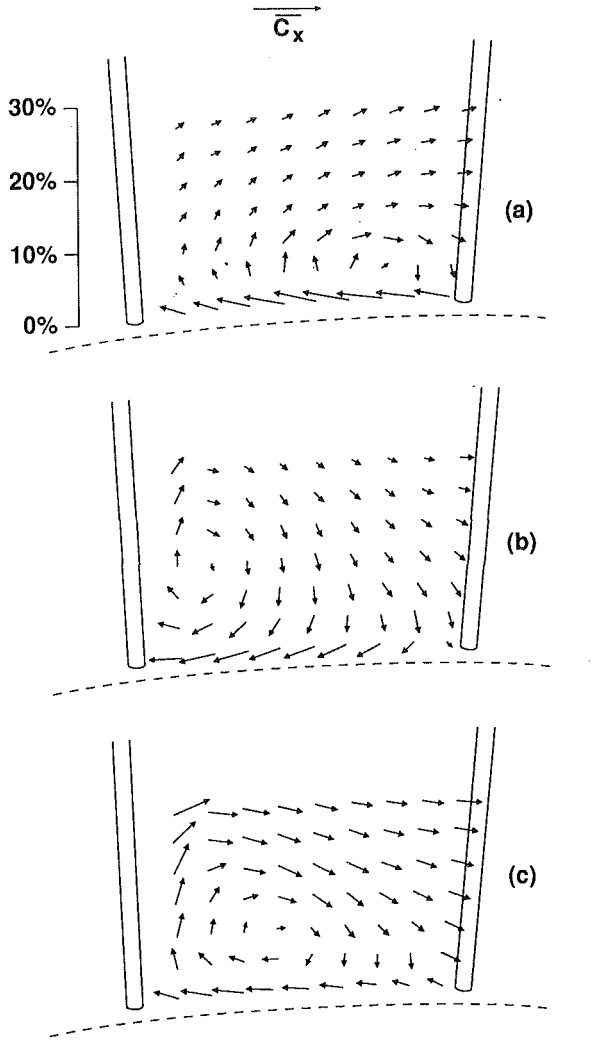

Fig. 19 Velocity vector projections on r-θ (axial) plane reviewed along direction of stagger: (a) solid wall, (b) hub treatment slots, (c) injection from 22.5 percent front slots. Scale of $\bar{C}_x$ shown for reference. (Figures (a) and (b) constructed from data of Johnson (1985).)

vectors viewed along the direction of stagger. This corresponds roughly to crossflow relative to a passage average streamwise direction, although the approximation cannot be pushed too far.

Figure 19(*a*) (smooth wall) indicates the flow structure associated with a tip leakage vortex. In both Figs. 19(*b*) (hub treatment) and 19(*c*) (injection), the vortex is nearer to the pressure surface and the secondary circulation has increased. The increased circulation is a result of the fluid injection (near the front of the passage); the injection jet has an associated impulse, which is directly connected with the generation of streamwise vorticity.

The downwash of the vortex seen with injection and with hub treatment transports high-velocity flow toward the hub. From the velocity measurements, the net streamwise momentum transported radially is 1.2 percent of the mean flow momentum (based on the velocity field at the 6 percent span station). This can be compared with 5.1 percent streamwise momentum flow due to the injection itself. Momentum transfer due to the increased circulation thus does not appear to be a dominant mechanism in casing treatment operations.

Even though not directly connected with hub or casing treatment, one observation concerning the flow with a smooth wall may also be of interest. The radial velocities associated with the clearance vortex are toward the endwall near the suction surface and away from the hub near the midpitch location. The result is that the suction corner is washed with high velocity fluid while there is an upwelling of fluid with very low axial velocity near the center of the passage. This is also seen in rotor data (e.g., Greitzer et al., 1979). A consequence is that, as is well known, the flow in the suction corner will be much healthier than in a situation with no clearance.

Suggestions for Future Work. Investigation of casing or hub treatment has so far been essentially all experimental, and it seems useful to examine the three-dimensional flow structure computationally. This would allow, for example, the trajectory of a "leakage element" to be tracked, so that the involvement of the leakage flow in the stall process can be studied. A further step is to simulate flow injection (or removal) by altering the boundary conditions. Again, by keeping track of the "leakage element," one should be able to tell if (and perhaps how) the jet alters the tip leakage flow. This might also clarify the role of streamwise momentum of the jet, which appears so important in the success of endwall injection.

Experiments using tracer gas would also seem useful for tracing out hub (or tip) leakage flow to assess the involvement in stall onset and the interaction with the jet. One way to do this is to release the gas in the endwall region close to the pressure surface in the adjacent blade passage, and measure its concentration in the passage of interest. The amount of leakage flow can then be known via the measured concentration of the gas. Such an experiment would be useful in that it directly examines the role of leakage flow, which is known to have a detrimental effect on the stall margin. The objective is not only to trace out the path of the leakage flow, but also to

see if the jet does cut down the amount of leakage, thereby delaying stall.

Summary

An experimental investigation was conducted of the effects on stall margin due to flow injection into, and removal from, the endwall of an axial compressor stator blade row. The experiment, which was carried out on a rotating hub beneath a cantilevered stator, was designed to simulate the injection and removal processes that occur with compressor wall treatment, and thus to clarify the mechanism of its operation.

Both injection at the front and removal at the rear of the blade passage increased the stall margin, but neither was as effective as the complete treatment. This implies that both removal of high-blockage flow from the rear of the slot and high-velocity injection at the front are responsible for stall margin improvement in casing or hub treatment.

The degree of stability enhancement achieved with suction did not depend strongly on the location; suction at the rear and front of the stator passage was equally effective. In general, the stall pressure rise increased monotonically with the amount of removal.

With endwall injection, both the amount of momentum injected and the location of the injection strongly affected the stall margin improvement. Injection through a location covering 27.5 to 50 percent of the passage worked as well as the full treatment; injection through a location covering 5 to 27.5 percent, which corresponds most closely to the simulation of the jet in the actual casing treatment, was less effective; and injection in the rear of the passage delayed stall by only a small amount.

The streamwise component of momentum was found to be an important factor to the success of endwall injection; the amount of stall suppression correlated with the streamwise momentum influx.

In the experiment, the stator stagger angle, inlet velocity triangles, and overall performance are representative of rotor tip behavior for geometries of current interest. This, coupled with the apparent insensitivity of stall inception in multistage compressors to the precise details of the blading (Koch, 1981) implies that the overall results should have considerable generality.

Acknowledgments

This work was supported by Allison Gas Turbine Division of General Motors and by the Air Force Office of Scientific Research. This support is gratefully acknowledged. We would also like to thank Mr. A. Crook, who suggested and implemented the view of the data presented in Fig. 19, as well as Professor F. E. Marble, Dr. C. S. Tan, and Dr. N. A. Cumpsty for helpful suggestions.

References

Cheng, P., 1982, "Effects of Compressor Hub Treatment on Stator Stall and Pressure Rise," MIT Gas Turbine Laboratory Report No. 167.

Cheng, P., Prell, M. E., Greitzer, E. M., and Tan, C. S., 1984, "Effects of Compressor Hub Treatment on Stator Stall Margin and Performance," *J. Aircraft*, Vol. 21, No. 7, pp. 469-475.

Fujita, H., and Takata, H., 1984, "A Study on Configurations of Casing Treatment for Axial Flow Compressors," *Bulletin of the JSME*, Vol. 27, No. 230, pp. 1675-1681.

Greitzer, E. M., Nikkanen, J. P., Haddad, D. E., Mazzawy, R. S., and Joslyn, H. D., 1979, "A Fundamental Criterion for the Application of Rotor Casing Treatment," ASME *Journal of Fluids Engineering*, Vol. 101, pp. 237-243.

Hunter, I. H., and Cumpsty, N. A., 1982, "Casing Wall Boundary-Layer Development Through an Isolated Compressor Rotor," ASME *Journal of Engineering for Power*, Vol. 104, pp. 805-817.

Johnson, M. C., 1985, "Effects of Hub Treatment on Compressor Endwall Flow Fields," M.S. Thesis, Department of Aeronautics and Astronautics, M.I.T., Cambridge, MA.

Johnson, M. C., and Greitzer, E. M., 1987, "Effects of Slotted Hub and Casing Treatments on Compressor Endwall Flowfields," ASME JOURNAL OF TURBOMACHINERY, Vol. 109, pp. 380-387.

Koch, C. C., 1970, "Experimental Evaluation of Outer Case Blowing or Bleeding of Single Stage Axial Flow Compressor, Part VI—Final Report," NASA CR-54592.

Koch, C. C., 1981, "Stalling Pressure Rise Capability of Axial Flow Compressor Stages," ASME *Journal of Engineering for Power*, Vol. 103, pp. 645-656.

Lee, N. K. W., 1988, "Effects of Compressor Endwall Suction and Blowing on Stability Enhancement," MIT Gas Turbine Laboratory Report No. 192.

McDougall, N. M., 1988, "Stall Inception in Axial Compressors," Ph.D. Thesis, Cambridge University, United Kingdom.

Prince, D. C., Jr., Wisler, D. C., and Hilvers, D. E., 1975, "Study of Casing Treatment Stall Margin Improvement Phenomena," ASME Paper No. 75-GT-60.

Schmidt, D. P., and Okiishi, T. H., 1977, "Multistage Axial-Flow Turbomachine Wake Production, Transport and Interaction," *AIAA Journal*, Vol. 15, No. 8.

Smith, G. D. J., 1980, "Casing Treatment in Axial Compressors," Ph.D. Thesis, Engineering Department, University of Cambridge, United Kingdom.

Smith, G. D. J., and Cumpsty, N. A., 1985, "Flow Phenomena in Compressor Casing Treatment," ASME *Journal of Engineering for Gas Turbines and Power*, Vol. 107, pp. 532-541.

Takata, H., and Tsukuda, Y., 1977, "Stall Margin Improvement by Casing Treatment—Its Mechanism and Effectiveness," ASME *Journal of Engineering for Power*, Vol. 99, 121-133.

Tesch, W. A., 1971, "Evaluation of Range and Distortion Tolerance for High Mach Number Transonic Fan Stages: Task IV Stage Data and Performance Report for Casing Treatment Investigations," NASA CR 72862.

APPENDIX

Change in Stator Pressure Rise Due to Suction or Injection: Operating Point Far From Stall

This appendix contains a brief discussion of the changes in pressure rise, due to suction and injection, that are observed at flows far from the stall point. A simple procedure for estimating these changes is described and the results are compared with the measurements. The analysis is sketched out only, but for full details one can refer to Lee (1988).

Suction. The basic premise is that for flows *well away from stall*, blockage is small so that, as a good approximation, we can neglect difference in deviation and blockage between smooth and slotted wall situations. The primary effect of the suction is thus an inviscid one. Application of Bernoulli's equation and continuity (in a one-dimensional form) yields an expression for the difference in pressure rise at any two suction rates, S_a and S_b,

$$\left(\frac{\Delta P}{\frac{1}{2}\rho V_{\text{inlet}}^2}\right)_b - \left(\frac{\Delta P}{\frac{1}{2}\rho V_{\text{inlet}}^2}\right)_a = \frac{\cos^2\beta_1}{\cos^2\beta_2}\left[1-\left(\frac{(1-S_b)}{(1-S_a)}\right)^2\right] \tag{A1}$$

where β_1 and β_2 are the stator inlet and exit flow angles.

If condition a is the smooth wall, $S_a = 0$ and expression (A1) reduces to

$$\left(\frac{\Delta P}{\frac{1}{2}\rho V_{\text{inlet}}^2}\right)_{\text{suction}} - \left(\frac{\Delta P}{\frac{1}{2}\rho V_{\text{inlet}}^2}\right)_{\text{no suction}} = \frac{\cos^2\beta_1}{\cos^2\beta_2}(1-(1-S)^2) \tag{A2}$$

where S is the suction rate.

Table A1 Estimated and measured differences in pressure rise due to suction alone

$\bar{C}_x/U$	$S(\%)$	Calculated $\frac{\Delta P_b - \Delta P_a}{1/2\rho V^2_{inlet}}$ $(\times 10^{-2})$	Measured $\frac{\Delta P_b - \Delta P_a}{1/2\rho V^2_{inlet}}$ $(\times 10^{-2})$
0.37	2.3	3.1	4.2
0.35	2.4	3.1	4.5
0.37	3.1	4.2	4.8
0.35	3.3	4.2	6.0
0.37	5.7	7.6	9.0
0.35	6.1	7.6	8.9

A more detailed analysis using an inlet velocity profile that varies linearly has also been carried out. The numerical results are within 5 percent of those obtained using the above model, however, and the latter approach suffices here.

A comparison of the calculated and measured differences in pressure rise due to suction is given in Table A1, and it can be seen that the analysis gives a reasonable estimate for the change in stator static pressure rise.

Injection. For the flow in the stator passage with injection, we model the process as occurring in two steps: jet injection and mixing, then diffusion. Again, the analysis is carried out in a one-dimensional manner (Lee, 1988) and we present only the final expression:

$$\left(\frac{\Delta P}{\frac{1}{2}\rho V^2_{inlet}}\right)_{inj} - \left(\frac{\Delta P}{\frac{1}{2}\rho V^2_{inlet}}\right)_{no\ inj}$$

$$= -b(2+b)\left(1+\left(\frac{A1}{A2}\right)^2\right) + 2b\cos\phi\cos\beta\frac{V_{jet}}{V_{inlet}} \quad (A3)$$

In this expression, $b = \dot{m}_j/\rho A_1 V_{inlet}$, $\dot{m}_j$ is the mass injection rate, V_{jet} is the jet absolute velocity, ϕ is the angle between the jet and a surface of constant radius, and β is the angle between the projection of the jet direction on a surface of constant radius and the cascade plane. The two quantities ϕ and β can be obtained from the hot-wire measurements. Mixing of jet and main flow occurs at area A_1. This is followed by diffusion from A_1 to A_2.

At a representative condition:

$$C_x/U = 0.345$$

$$b = 0.036$$

The calculated value of the increase in pressure rise is

$$\left(\frac{\Delta P}{\frac{1}{2}\rho V^2_{inlet}}\right)_{inj} - \left(\frac{\Delta P}{\frac{1}{2}\rho V^2_{inlet}}\right)_{no\ inj} = 0.01$$

and the measured value is 0.013. The calculated change in pressure rise is considerably less than that with suction, and this trend is also seen in the data in Figs. 7–11.

A. R. Azimian

R. L. Elder

A. B. McKenzie

Department of Turbomachinery
and Engineering Mechanics,
School of Mechanical Engineering,
Cranfield Institute of Technology,
Cranfield, Bedford,
MK43 OAL United Kingdom

Application of Recess Vaned Casing Treatment to Axial Flow Fans

The effect of applying a vaned recessed casing treatment to a single-stage axial flow fan has been investigated. The influences of the axial position of the recess relative to the rotor leading edge and other geometric modifications of the vane passage have been examined. Significant improvements in stall margin were observed without (in some builds) loss in peak efficiency. Slow and fast frequency response yawmeter probes have been used in the study to examine both the steady flow conditions and the unsteady flow caused by rotating stall.

Introduction

Extension of the fan stable flow range will provide a more flexible engine as its operating range is often limited by the surge (stall) line of the fan. Increasing the surge margin of the fan, therefore, is of high priority in any engine development program.

During recent years there have been many attempts to increase fan and compressor stall margin using various techniques such as variable inlet guide vanes (Mikolajczak and Pfeffer, 1974), bleed or blow off valves (Koch, 1900), and small-scale casing treatments (axial, skewed and circumferential slots, tapered or straight holes, honeycombs, etc.) (Smith and Cumpsty, 1984; Bailey and Voit, 1900; Osborn and Moore, 1900; Prince et al., 1975; Takata and Tsukuda, 1977; Fujita and Takata, 1984; Greitzer et al., 1979). Although these have useful applications, they also have disadvantages. The low-pressure axial fan industry, which suffers similar range problems, has developed an alternative large-scale or "recess vaned" casing treatment. Such a casing treatment is shown in Fig. 1 and involves the application of a large vaned recess in the outer casing of the fan, which extends partly over but mainly upstream of the rotor blades (Ivonov et al., 1900; Mahmoud et al., 1900; Bard, 1984; Miyake et al., 1985, 1986; Tanaka and Murata, 1985; Azimian et al., 1987). The operating principle appears to be that as the fan operation moves toward the stall line, some radially unbalanced flow (or in more severe cases some radially unbalanced reversed flow) is transported from the blade tips into the treatment, turned (by means of cambered vanes inside the recess), and reintroduced to the main flow upstream of the rotor. By proper arrangement of the outer recess, significant improvements in flow range can be obtained, often with minimal loss of unstalled efficiency. These results have all been achieved on industrial low-speed fans. The purpose of the present work was to investigate the ability of such devices to improve the stall margin of a low-speed axial flow fan rotor with aerospace-type loadings.

In the authors' previous paper (Azimian et al., 1987), the application of a large-scale casing treatment to an axial flow rotor–stator (stage) compressor was reported. In that paper the level of flow improvement was about 50 percent, which was achieved without loss of efficiency. Further studies indicated that stall was precipitated by stall at the hub of the stator blade. To avoid this limitation a fuller investigation of the isolated rotor has been made, the results of which are reviewed here.

Experimental Arrangement

The compressor facility used in this study was similar to that used in the previous investigation (i.e., a single low-speed axial flow fan rotor with tip speed of 39 m/s, tip diameter of 508

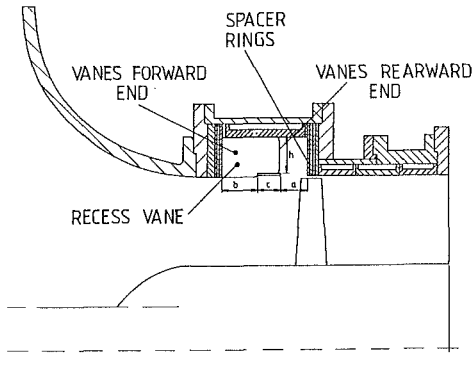

DESIGN VALUES OF TREATED CASING GEOMETRY

a = 33.780 mm
b = 56.380 mm
c = 30.000 mm
h = 50.000 mm

Fig. 1 General arrangement

Contributed by the International Gas Turbine Institute and presented at the 34th International Gas Turbine and Aeroengine Congress and Exhibition, Toronto, Ontario, Canada, June 4–8, 1989. Manuscript received at ASME Headquarters January 13, 1989. Paper No. 89-GT-68.

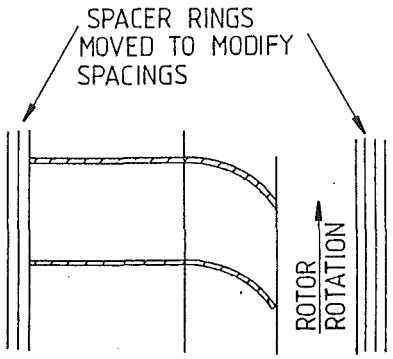

VANE NUMBER = 48 AND 24

SECTION OF RECESS VANE

Fig. 2 Vane arrangement

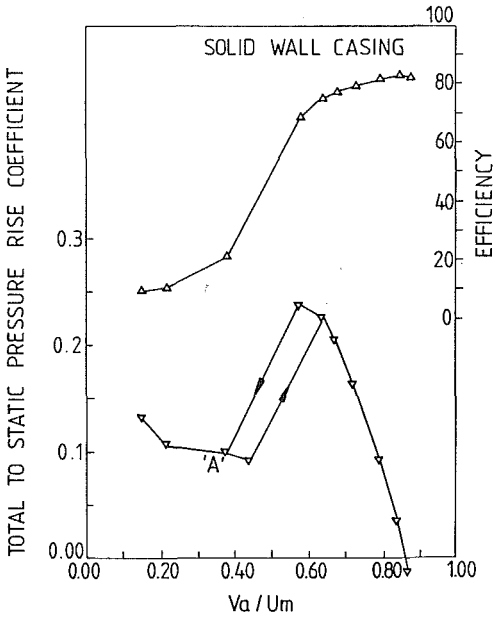

Fig. 3 Pressure rise characteristic of stage (rotor and stator)

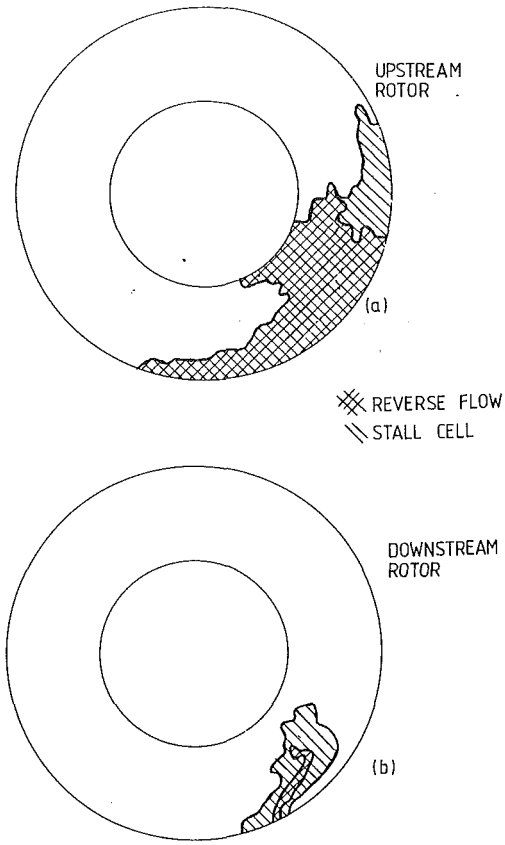

Fig. 4 Rotating stall pattern

mm (20 in.), 0.5 hub-to-tip ratio, and blade loading ($\Delta H/U^2_{HUB}$) of near unity at the hub. The fan is shown in Fig. 1 with the bladed recess located partly over and mainly upstream of the rotor blade. The vanes used inside the recess in this study are also shown in Fig. 2. Arrangements using both 24 and 48 vanes in the recess were examined.

Measurements of rotating stall were carried out by means of a fast response 4-mm-dia three-hole cylindrical yawmeter with three strain gage pressure transducers close coupled to the tappings (mounted in the cylindrical probe stem). This probe was able to measure a near-instantaneous value of total and static pressures and flow direction. Data acquisition was achieved through an analogue-to-digital interface to a microcomputer. The probe was calibrated for yaw angle, total and static pressure in a 400-mm-dia suction wind tunnel. The results of the calibration procedure were stored in a computer program that could be used to calculate yaw, static and total pressure from the transducer outputs following the method reported by Das and Jiang (1984).

During rotating stall measurements, the variation in flow angle can approach ±60 deg (i.e., upstream of the rotor the flow can vary from axial to 120 deg for stalled reverse flow). To achieve the dynamic range required the probe was positioned at more than one setting.

Experimental Results and Discussion

Solid Casing—Results. A characteristic for the stage is shown in Fig. 3. As mentioned in the previous work of the authors, a major criterion for the useful application of casing treatment was that the machine should be tip critical (i.e., the rotor tip should stall first). To investigate the stall process in the test rotor a comprehensive rotating stall study was carried out using the fast response yawmeter described above.

Nomenclature

Ca = axial chord of rotor tip
U = midspan blade speed
Va = axial component of velocity
X = distance between rotor leading edge and the rearward end of the treatment
ΔH = work input
$\Delta\phi_1$ = $1-\phi_{rs2}/\phi_{rs1}$
$\Delta\phi_2$ = $\phi_{rs1}/\phi_{rs2}{}^{*}\psi_{TS}{}^{1}/\psi_{TS2}-1$
η = efficiency
ρ = density of air
ϕ = flow coefficient = Va/U
ϕ_{rs1} = stall flow for the solid casing build
ϕ_{rs2} = stall flow for the treated build
ψ_{TS} = (P (exit static) $-P$ (inlet total))/ρU^2
ψ_{TS1} = stall pressure rise coefficient for the solid casing build
ψ_{TS2} = stall pressure rise coefficient for the treated build

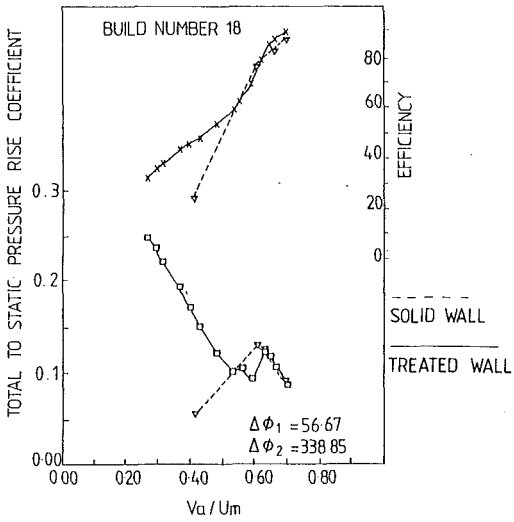

Fig. 5 Pressure rise characteristics with 19.6 percent of axial chord of rotor exposed

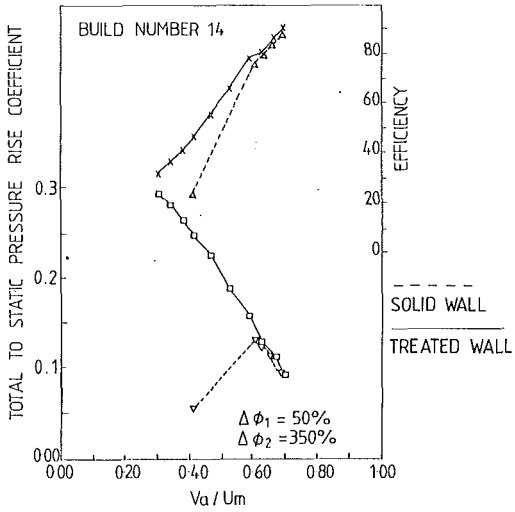

Fig. 7 Pressure rise characteristics with 67 percent of axial chord of rotor exposed to the treatment

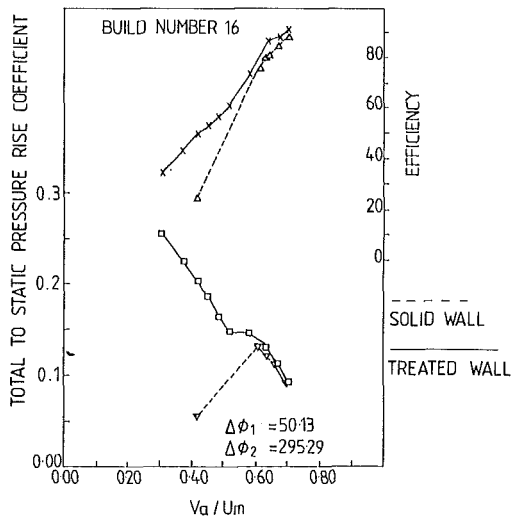

Fig. 6 Pressure rise characteristic with 43 percent of axial chord of rotor exposed to the treatment

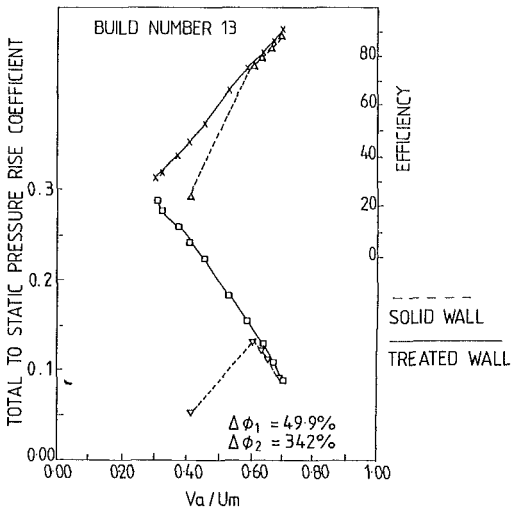

Fig. 8 Pressure rise characteristics with 79 percent of axial chord of rotor exposed to the treatment

A selected example of the results of these studies is shown in Fig. 4, which shows the circumferential extent of the stall cell just upstream and downstream of isolated rotor. The measurements were taken at point A on the performance map shown in Fig. 3 (this being the first stable operating point after the initiation of rotating stall).

Figure 4 indicates that the variation of yaw angle in front of the rotor involves a very dramatic change of angle from unstalled to stalled flow with some regions of reversed flow. The high flow angles inside the cell (spreading across the blade span) suggest the presence of a full-span stall cell. The figure also shows that the stall cell has a tapered shape from tip (widest) to hub. As no IGV's were used, the averaged flow angles in the unstalled condition in front of the rotor were almost zero.

The most important point to note from the fast response measurements of rotating stall was that, in this rig, the rotating stall was most severe at the rotor tip. The measurements also indicated that, when stalled, there was a region of reverse flow in front of the rotor that would strongly influence the flow in the tip region, and therefore the stall performance of the unit was likely to be modified by changes to the tip geometry or outer casing.

Casing Treatment Results. The stall margin improvement for both flow range and pressure rise are quantified using the following stall margin improvement parameters:

1 The first parameter attempts to quantify the performance change between the solid wall and the subsequent treated build. This parameter was used by Takata and Tsukada (1977) and is discussed by Smith and Cumpsty (1984).

$$\Delta\phi_1 = 1 - \phi_{rs2}/\phi_{rs1} \tag{1}$$

where $\Delta\phi_1$ is the stall margin improvement for flow and ϕ_{rs2} and ϕ_{rs1} are the mass flow coefficient at stall point for the treated build and solid wall, respectively.

2 A second performance parameter has been introduced by Smith and Cumpsty (1984), which attempts to accommodate both the changes in pressure and flow rate

$$\Delta\phi_2 = (\phi_{rs1}/\phi_{s2} * \Psi_{ts2}/\Psi_{ts1} - 1) \tag{2}$$

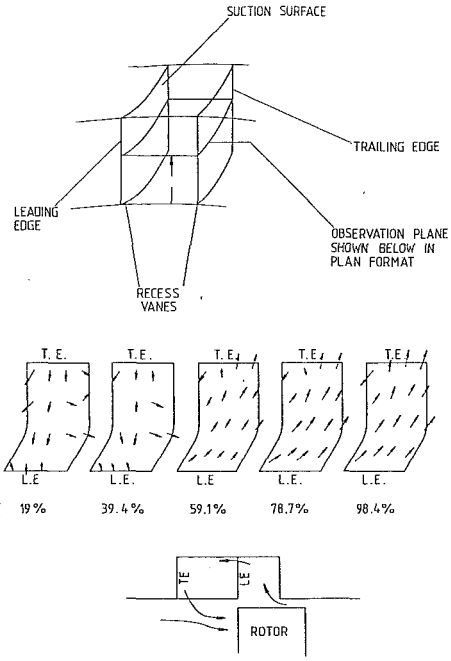

Fig. 9 Velocity distribution inside the recess vane passage (two-dimensional measurements) for a flow coefficient of 0.33

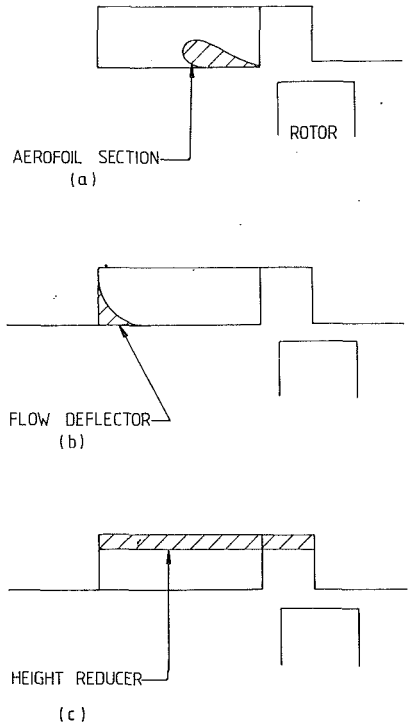

Fig. 10 Geometric modifications made to the recess

where $\Delta\phi_2$ is the stall margin improvement parameter, $\Psi^2_{ts(p2)}$ and $\Psi_{ts(p1)}$ are the peak pressure rise coefficients for the treated casing and solid wall, respectively (ϕ_{rsi} and ϕ_{rs2} are as defined above).

Of the various parameters that were effective in improving the operation of the treatment, the axial chord of the rotor exposed to the recess appeared to be very important and a number of tests covering a range of exposures were undertaken. The results (Figs. 5–8) show that significant improvements are possible with the treated builds. It appeared that for such builds, the reverse flow in the tip region was absorbed by the recess and turned back to the main flow with a reduced circumferential velocity component. It will be noted (Figs. 5 and 6) that for small percentages of the rotor chord exposed to the treatment, the rotor suffers a stall (inflection in the pressure rise characteristic) from which "recovery" is possible (no evidence of rotating stall was noted). After this recovery, operation of the unit continued to a smaller flow rate until the unit stalled abruptly. As the degree of exposure was increased the early stall gradually disappeared (Figs. 7 and 8). The stall margin parameter involving only flow ($\Delta\phi_1$) decreased modestly as the exposure increased, whereas the second parameter including the additional pressure available ($\Delta\phi_2$) increased modestly with exposure. In all cases, however, very significant improvements were noted. Of the various treated builds examined, that with 67 percent of its axial chord exposed to the recess (Fig. 7) was considered to be the optimum arrangement. Comparison of efficiency for this and the solid wall builds showed that for identical running points the efficiencies were almost the same (within experimental errors). This result agrees well with the similar findings reported by Miyake et al. (1987) for a lightly loaded industrial fan (i.e., low design value of $\Delta H/U^2$).

As already noted, the treated builds with an axial chord of less than 50 percent exposed suffered an early local stall, which led to lower effectiveness of the treatment (Figs. 5 and 6). This early stall appeared to be due to the smaller amounts of reverse flow being absorbed by the recess compared with builds with more than 50 percent exposure. Hence, it was considered that, for an optimum performance, considerable flow exchange between the recess and the main flow was desirable. It appeared, therefore, that the flow exchange between the main flow and the recess area was of great importance and further studies of the flow behavior inside the recess area would be helpful for a better understanding of the mechanism of the treatment.

To achieve this purpose an extensive flow investigation (by means of the fast response three-hole probe described earlier) inside the recess was carried out. To avoid any doubts about the flow direction, a small piece of wool tuft was glued to the end of the probe. At each radial position the central pressure tapping of the cylindrical probe was faced to the main flow direction, which was detected by the small piece of wool tuft (observation was possible through a perspex window). Measurements were carried out at 16 measuring positions inside the recess vane passage and at each position five radial traverses were made. The flow was observed to fluctuate providing significant measurement problems. This fluctuating flow was also noted by Miyake et al. (1987). Having incurred these measurement problems, the authors would like to propose that the results presented should be regarded as qualitative. The results are shown in Fig. 9, where the velocity vectors on five recess vane to recess vane planes are shown. The radial height of 19.7 percent is that closest to the rotor tip and that at 98.4 percent is closest to the outer casing of the recess. The leading edge (LE) in these pictures corresponds to the rearward end of the recess vane, i.e., closest to the rotor leading edge (Fig. 1). This examination of flow behavior inside the recess indicated that:

1 The flow entered the recess vane passage from the rearward end (closest to rotor LE) close to the outer casing of the recess and left the vane passage from the forward end where it mixed with the main flow. At lower flow rates, the recirculating flow behavior was stronger.

2 At lower flow rates, separation of the flow was observed on the suction side of the vanes indicating that the flow was suffering too much turning by the vanes.

Table 1 Stall margin improvements for various builds (isolated rotor)

Build Number	Description	Sketch	Percent of Axial Chord of Rotor Exposed X/Ca	Stall Margin Improvement for Flow Rate	Stall Margin Improvement With Effect of Pressure Rise
0	Solid Wall Casing (Standard Build)	Casing, Flow, Rotor	-	-	-
13	Recess With 48 Vanes	X, Rotor, Ca	79%	49.9%	342.7%
14	"	Rotor	67%	50%	350%
15	"	Rotor	55.3%	47.5%	315.9%
16	"	Rotor	43.3%	50.1% *	295.3%*
17	"	Rotor	31.3%	52.9% *	317% *
18	"	Rotor	19.6%	66.6% *	338% *
19	"	Rotor	7.6%	60.5% *	389% *
20	"	Rotor	-4.2%	66.7% *	333% *
21	"	Rotor	-16.3%	51.7% *	270% *
22	"	Rotor	-27.9%	45.3% *	238% *
25	Flow Deflector	Rotor	67%	55.5% *	265.6%*
27	Aerofoil Section at the Inner Side of the Recess	Rotor	67%	60.8%	468.8%
29	Aerofoil Section & Flow Deflector	Rotor	67%	58.9% *	269.8%*
31	Reduced Height	Rotor	67%	50.4%	360%
33	Reduced Height & Aerofoil Section	Rotor	67%	47.1%	332.2%

*An early stall exists (inflection in the pressure rise characteristic).

3 An examination of the flow inside the recess also showed that some of the flow reversed inside the recess area, creating recirculation in both the meridional and blade-to-blade planes.

4 There was considerable deflection of the fan inlet flow by the flow leaving the recess.

These results obtained from within the recess led to a further extensive investigation involving some modifications to the recess vane passages. To perform the modifications to the vane passage three elementary sections were developed, which could be attached to the existing vanes. These consisted of an "aerofoil section" (used to reduce the area from the rearward to forward of the vanes) (Fig. 10*a*); a "flow deflector" (used to modify the direction of the flow leaving the recess) (Fig. 10*b*); and finally a "height reducer" (used to reduce the height of the vane passage) (Fig. 10*c*). In addition several combinations of these sections, used with various spacers (at the forward end of the vanes), were tested. These and other results are summarized in Table 1.

Of the various modified configurations examined, it was observed that the "aerofoil section" (with its function of reducing the diffusion within the recess vane passage and forming a "core" for the recirculating flow) had the best results (Build 27, Table 1). It appeared that this modification to the area distribution reduced the flow separation from the suction side of the recess vanes.

Another parameter briefly studied was the effect of the number of recess vanes. This examination indicated that halving the vane number (i.e., from 48 to 24) slightly improved the performance of the "optimum" build. Further studies, however, are required with different numbers of vanes before drawing any specific conclusions on this point.

General Conclusions. A low-speed axial flow fan (with aerospace-type blade loadings) was used to investigate the influence of large-scale vaned recess casing treatments on the efficiency and flow range of an isolated rotor. Significant improvements in flow range were achieved, and by means of various types of slow and fast frequency response instruments, flow measurements were made, providing an insight into the operation of the devices. The general conclusions were as follows:

1 Test results with a solid casing indicated that as the machine stalled, regions of reverse flow occurred in the tip region. It appeared that modifications to the outer casing might modify these and the stall point of the rotor.

2 A vaned recess casing treatment provided considerable stall margin improvement. The increases in flow range were significantly larger than those reported for the more conventional casing treatments.

3 Of the various parameters tested, the axial chord of the rotor exposed to the recess area was found to be the most important.

4 Test results showed that treated builds with more than 50 percent of the axial chord exposed to the recess were favorable and it is proposed that a build with 67 percent is optimum for the machine studied.

5 For the optimum arrangement, no penalty in efficiency was noted, compared to a solid casing.

6 Flow behavior inside the recess was found to have high levels of unsteadiness. Inside the recess, large flow separations on the suction side of the recess vanes were observed.

7 By modifying the shape of the vane passage, the internal flow separation could be controlled and subsequent further modest improvements in performance achieved.

8 Reduction of the number of vanes to half of the original case (i.e., from 48 to 24) provided a further modest improvement.

It is therefore concluded that the vaned recess type of treatment can provide significant improvements to the flow range of an axial flow fan with aerospace-type loadings (high values of $\Delta H/U^2_{HUB}$ at the hub). Geometric constraints may inhibit the application of the method in certain circumstances; nevertheless, a reasonable range of applications appears possible. The studies reported here have concerned an isolated rotor, but significant improvements for a stage have also been noted, although the full-range improvements, indicated by the isolated rotor, were not obtained due to premature stator stall at the hub.

References

Azimian, A. R., McKenzie, A. B., and Elder, R. L., 1987, "A Tip Treatment for Axial Flow Fans and Compressors," *Trans. IMechE*, Apr.

Bailey, E. E., and Voit, C. H., 1900, "Some Observations of Effect of Porous Casing on Operating Range of a Single Axial-Flow Compressor Rotor," NASA TMX-2120.

Bard, H., 1984, "The Stabilisation of Axial Fan Performance," Flact Industri AB, Vaxjo, Sweden; IMechE Paper No. C120/84.

Das, D. K., and Jiang, H. K., 1984, "An Experimental Study of Rotating Stall in a Multistage Axial-Flow Compressor," ASME *Journal of Engineering for Gas Turbines and Power*, Vol. 106, pp. 542–551.

Fujita, H., and Takata, H., 1984, "A Study on Configurations of Casing Treatment for Axial Flow Compressors," *Bulletin of JSME*, Vol. XX, pp. XX.

Greitzer, E. M., Nikkanen, J. P., Haddad, D. E., Mazzawy, R. S., and Joslyn, J. D., 1979, "A Fundamental Criterion for the Application of Rotor Casing Treatment," ASME *Journal of Fluids Engineering*, Vol. 101, pp. 237–243.

Ivonov. S. K., Dudkin, V. E., Peredery, V. P., and Molchanov, V. N., 1900, UK Patent Application (19) GB (11) 2 124 303A.

Koch, C. C., 1900, "Experimental Evaluation of Outer Case Blowing or Bleeding of Single Stage Axial Flow Compressor," NASA CR-54592.

Mahmoud, A., Abdel-Fattah, X. X., and Russell, B. A., 1900, UK Patent Application (19) GV (11) 101685 A.

Mikolajczak, A. A., and Pfeffer, A. M., 1974, "Method to Increase Engine Stability and Tolerance to Distortion," AGARD LS 72 On Distortion Induced Engine Instability.

Miyake, Y., Noji, I., Nishikiyo, Y., and Murata, S., 1985, "The Performance Characteristic of an Air-Separator of an Axial Flow Fan," *Bulletin of JSME*, Vol. XX, pp. XX.

Miyake, Y., Inaba, T., Nishikawa, Y., Noji, I., and Kato, T., 1986, "A Study on the Flow Within the Flow Passage of an Axial Flow Fan Equipped With Air-Separator," *Bulletin of JSME*, Vol. XX, pp. XX.

Miyake, Y., Inaba, T., and Kato, T., 1987, "Improvement of Unstable Characteristic of an Axial Flow Fan by Air-Separator Equipment," ASME *Journal of Fluids Engineering*, Vol. 109, pp. 36-40.

Osborn, W. M., and Moore, R. D., 1900, "Effect of Casing Treatment on the Overall Performance of Axial Flow Transonic Fan Stage With Pressure Ratio of 1.75 and Tip Solidity of 1.5," NASA TMX-3477.

Prince, D. C., Jr., Wisler, D. C., and Hilvers, D. E., 1975, "A Study of Casing Treatment Stall Margin Improvement Phenomena," ASME Paper No. 75-GT-60.

Smith, G. D. J., and Cumpsty, N. A., 1984, "Flow Phenomena in Compressor Casing Treatment," ASME *Journal of Engineering for Gas Turbines and Power*, Vol. 106, pp. 532-541.

Takata, H., and Tsukada, Y., 1977, "Stall Margin Improvement by Casing Treatment—Its Mechanism and Effectiveness," ASME *Journal of Engineering for Power*, Vol. 99, pp. 121-133.

Tanaka, S., and Murata, S., 1985, "On the Partial Flow Rate Performance of Axial-Flow Compressor and Rotating Stall (3rd Report, on Devices for Improving the Unstable Performance and Stall Condition)," *Bulletin of JSME*, Vol. XX, pp. XX.

Blade Sweep for Low-Speed Axial Fans

T. Wright

W. E. Simmons

Department of Mechanical Engineering,
University of Alabama at Birmingham,
Birmingham, AL 35294

The available literature on aerodynamic and acoustic properties of axial fans with swept blades is presented and discussed with particular emphasis on noise mechanisms and the influence of high-intensity inlet turbulence on "excess" noise. The acoustic theory of Kerschen and Envia for swept cascades is applied to the problem of axial fan design. These results are compared to available data and a provisional model for specifying sweep angles is presented. The aerodynamic performance theory for swept-bladed rotors of Smith and Yeh is adapted for use in designing low-speed axial fans. Three prototype fans were designed using the resultant computer codes. One is a baseline fan with blade stocking lines radially oriented, and two are fans having swept blades of increasingly greater forward sweep. Aerodynamic testing shows that performance of the fans lies within a band width of about ± 2 percent of volume flow rate and pressure rise predictions in the region of design performance, effectively validating the design procedure for selection of the blading parameters. Noise testing of the fans was carried out and the results show an average noise reduction for the swept-bladed fans of about 7 dBA overall, and a reduction of pure tone noise at blade-pass frequency of about 10 dB compared to the zero-sweep baseline model, in close agreement with the theory of Kerschen and Envia.

Introduction

Fan noise in low-speed equipment has been identified as a primary source of overall noise in many heat-exchange applications. When used with engine or motor-driven equipment that has been designed for good noise control, attention must be directed to reduction of the fan-generated noise in order to reduce annoyance levels or to bring the equipment within maximum sound level specifications (Wright and Baladi, 1985). In order to approach the problem of fan noise reduction logically, it is necessary to identify the level of fan performance of interest, the speed and frequency range to be considered, and particularly the inflow environment in which the fan will operate.

For typical heat-exchange applications, a low-speed, low-pressure axial fan usually meets the design requirements most effectively in terms of performance capability and cost of equipment. Use of these fans in conjunction with a heat exchanger results in dominant components of generated noise associated with the ingestion by the fan of small-scale, high-intensity turbulence.

The focus of this work is to examine blade sweep as a means for alleviating the dominant source of noise, while providing a method of estimating the influence on fan performance.

As described by Wright (1976) and more recently by Chou (1987), the universal forms of noise spectra, typical of all rotors, are associated with random, periodic, or steady forces generated on the blade of the rotor. These various modes are defined by Wright as: steady thrust radiation; turbulent shedding noise and laminar shedding noise (rotor self-noise); discrete frequency noise; and "excess" rotor-noise. These modes are illustrated in Fig. 1, along with an ambient level of noise, as a spectrum of sound pressure level (SPL) plotted against the logarithm of frequency. On low-speed rotors, the self-noise generation is associated with either turbulent fluctuation in the blade boundary layers or the higher-frequency noise of laminar boundary layer shedding. For heat-exchange applications involving high levels of inflow turbulence and moderate blade Reynolds numbers, laminar shedding is an unlikely source of noise (Evans, 1971).

Standing out from these broad band noise levels, there will be discrete peaks of sound pressure associated with the blade pass frequency (bpf) of the fan and its harmonics, which will be generated by distortions in the inlet flow leading to unsteady surface pressure on the blades. The most significant remaining noise source for heat exchange applications falls into the "excess" category shown in Fig. 1. As pointed out by Aravamudan and Harris (1979), low-frequency, broad band turbulence noise generally becomes an important source of noise, in addition to excess discrete tones in low-pressure fans, when they are subjected to a "dirty" flow environment. This source of noise is associated with ingestion of turbulence and, in part, with self-generated turbulence on the blades. The ingested turbulence, primarily generated by a heat exchanger, fan supports, or other upstream obstructions, leads to random variations in angles of incidence at blade leading edges, causing fluctuating blade loads and surface pressures over a broad range of frequencies. Since these frequencies tend to center in the most sensitive ranges of the A-Scale, this noise source may well become a dominant consideration if the intensity of incoming disturbances is sufficiently large. This source of noise

Contributed by the International Gas Turbine Institute and presented at the 34th International Gas Turbine and Aeroengine Congress and Exhibition, Toronto, Ontario, Canada, June 4–8, 1989. Manuscript received at ASME Headquarters January 13, 1989. Paper No. 89-GT-53.

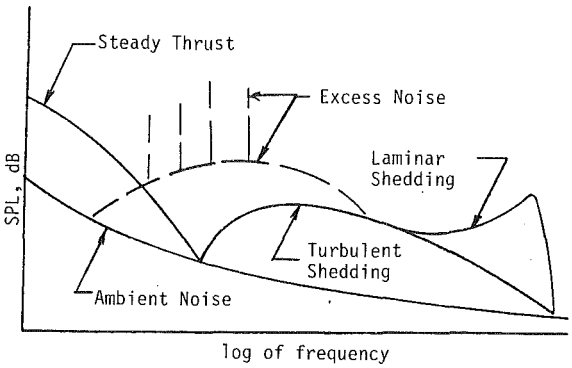

Fig. 1 Typical spectrum characteristics (S.E. Wright, 1976)

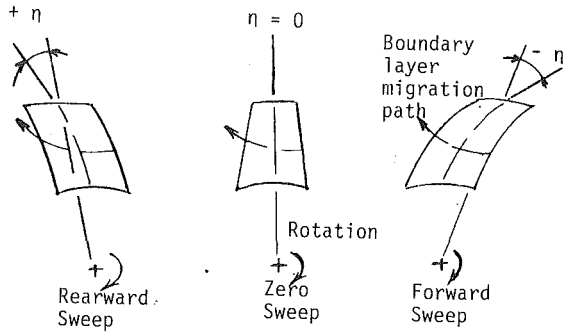

Fig. 2 Sweep definitions and comparative boundary layer centrifugation

is considered to be primarily in addition to the self-noise sources, which have been the subject of many investigations and for which there have been systematic noise reduction studies carried out (Wright, 1976; Hanson, 1980a, 1980b; Gallus et al., 1982).

Attemps to alleviate the influence of turbulence ingestion over the years have included the use of large axial separation from the turbulence source (to allow decay); skewing of obstructions to misalign the blade leading edge from the obstruction-induced wake; and more recently the use of sweep on blade planforms in order to achieve phase-shift canceling of noise generated at different blade radial stations (Metzger and Rohrback, 1986; Fukano et al., 1977, 1978a; Fukano and Takamatsu, 1986; Brown, 1975, Cummings et al., 1972).

The use of blade sweep for noise reduction appears to have been effective. Hanson (1984) studied the problem dealing primarily in terms of reduction of blade tonal noise through phase-shift cancellation of noise generated at different radial stations on a blade and by blade-to-blade interference. While his work shows that very large angles of blade sweep may be required, particularly for low-speed rotors, the works of Fukano (1978b), Brown (1975), Cummings (1972), and Fujita (1979), dealing more closely with dirty inflow environments, have shown experimentally that reasonable amounts of sweep may be very beneficial in reducing noise. In particular, the works of Kerschen (1983) and Envia and Kerschen (1984, 1986) seem to provide a theoretical basis for selecting a distribution of sweep angles along a blade, which will provide sharp reductions in the noise associated with turbulence ingestion.

The higher-frequency self-induced broad band noise identified with blade boundary layer turbulence (Wright, 1976) may also be influenced by sweeping the blades. Fukano (1977) has modeled vortex shedding from turbulent boundary layers over a wide range of frequencies to show the influence of excessive boundary layer displacement thickness near the blade trailing edge on this noise source. Amiet (1976, 1978) and Kim and George (1982) comment on this noise source as well. While these authors conclude that excessive thickness (of both boundary layer and blade physical thickness at the trailing edge) must be minimized, neither feels that the influence is expected to be very large. However, in the presence of blade sweep, trailing edge boundary layer thickness may be increased or decreased depending on the distribution of sweep angle and the planform shape of the blade. All blades, including radially straight ones, are subject to spanwise flow in the low-momentum regions of the blade surface boundary layers, primarily due to radial centrifugation of the fluid (Adkins and Smith, 1982). If conventional rearward sweep is used, then the natural curving path of the centrifuged boundary layer fluid will move farther outboard due to a longer available path before reaching the trailing edge. This will be particularly significant for very large sweep angles. Forward sweep by contrast severely limits the range of spanwise travel of low-momentum fluid by truncating the natural path at the trailing edge. In particular, at large sweep angles, the critical tip region of the blade should see boundary layers, which are thinner than on a straight, unswept blade when forward sweep is used; and boundary layers on rearward-swept blades should be thicker than those of an unswept blade in tip regions. This behavior is shown in Fig. 2, with conventions for

Nomenclature

c = blade chord, m
$\bar{C}_L$ = normalized lift coefficient $= C_L\ \alpha/C_L\ (\alpha=0)$
N_B = number of blades
M_R = blade relative Mach number
M_T = blade tip Mach number
m = wave mode
ΔP_s = static pressure rise across blade row, Pa, in. W.G.
P = shaft power, kW
Q = volume flow rate, m^3/s, ft^3/min
r = radial location of points on the stacking line, m
SPL = sound pressure level, dB @ 2×10^{-4} μbar
s = blade spacing, m
$\bar{v}$ = normalized perturbation velocity
α_{rel} = airfoil pitch angle relative to plane of rotation, deg
α_{cr} = critical value of cascade sweep angle, deg
α_{10} = cascade sweep angle for 10 dB noise suppression, deg
β_1 = blade relative inflow angle measured from axial direction, deg
η = geometric sweep angle measured positive relative to a radial line for the stacking line downstream of a radial line through the blade root, deg
η_s = static efficiency $= Q\ \Delta P_s/P$
θ = angle of misalignment of a convected gust, deg
λ = blade relative aerodynamic sweep angle, deg
μ = blade dihedral angle, measured positive relative to the plane of rotation for the stacking line downstream of the plane of rotation at the blade root, deg
ξ = peripheral angle describing stacking line, deg
σ = blade solidity $= c/s$

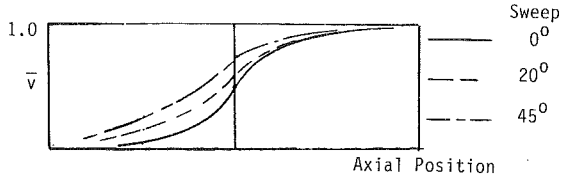

Fig. 3 Qualitative distribution of a normalized velocity perturbation: variation with sweep (after Lewis and Hill, 1971)

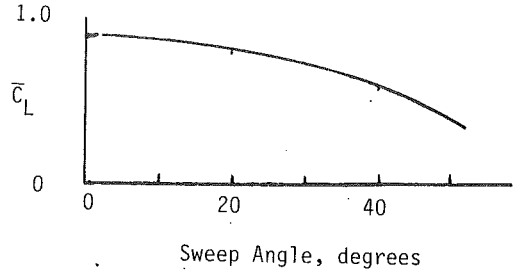

Fig. 4 Qualitative reduction in normalized lift coefficient with sweep (after Lewis and Hill, 1971)

sweep. Moreover, minimizing other sources of noise (Wright, 1976; Hanson, 1980a; Gallus et al., 1982; Fukano et al., 1986; Hanson, 1984; Longhouse, 1978) such as speed, loading, and tip-clearance effects may expose this effect to a more dominant role. The studies of Adkins and Smith (1982) may be used to quantify the fluid migration and the trailing edge boundary layer thickness change. It appears that in contrast to forward-swept blades, a rearward-swept blade will reduce noise associated with leading edge interaction with turbulence, but may increase noise associated with the higher-frequency broad band noise generated near the trailing edge. Forward sweep should reduce both forms. The work of Fukano (1978b) in which both forward and rearward sweep were experimentally investigated showed significantly enhanced noise reduction for forward-swept blades.

It appears then, based on the theoretical work, that sweep should yield noise reduction benefits – perhaps 10 to 20 dB in SPL in the noise component associated with ingestion of turbulence. The experimental work has shown reductions in the range of 5 to 10 dB SPL in the presence of all noise sources, with best results associated with forward sweep.

However, if a fan is to be equipped with swept blading, it is necessary to develop a clear picture of just how the aerodynamic performance of the fan will be influenced. Performance effects seem to fall into three main categories; the meridional flow through the fan annulus is modified; the channel flow distribution in a blade-to-blade plane is changed; and the boundary layer thickness distributions along the blade are modified due to changes in the spanwise flow. Lewis and Hill (1971) present an analytical procedure that shows the influence of sweep and dihedral on perturbations to the axial component of velocity experienced by cascade throughflow. The primary effect seems to be a lengthening of the axial region in which crossflow (radial velocity) adjustments are made, as illustrated qualitatively in Fig. 3 in terms of normalized perturbation velocities. This will affect both leading edge incidence and trailing edge deviation of the flow as well as the distribution of blade camber for optimal chordwise loading. In addition, for cascades of finite span, the endwalls interact strongly with perturbation to the axial flow component, leading to an exaggerated influence on blade-to-blade flows in regions very close to the endwalls. The earlier work of Smith and Yeh (1963) deals more extensively with the blade-to-blade flowfield. In that work it is shown that the primary effect of sweep in determining blade work is seen in an increase of the flow deviation from the cascade mean camber line. Figure 4 is a qualitative depiction of the decrease of lift coefficient in cascade as a function of sweep illustrating this behavior. If the blade sweep is laid out as a sheared "wing" configuration (sections parallel to the axis) but analyzed on a section that is perpendicular to the swept blade axis, comparison of the fluid turning through the swept section to that through the simple two-dimensional rule calculation provides a first-order measure of the increased deviation and loss of fluid work associated with sweep. The work also provides an analysis of endwall influence through a local downwash calculation at blade tip and root. Both forward and rearward sweep produce these end effects. Forward sweep leads to reduced deviation near the tip, within a length equal to about 20 percent of the blade tip chord, spanwise. Rearward sweep causes a corresponding region of increased deviation. For low blade solidity near the tip and fairly high blade number, this should be of secondary importance. Swept rotor test results and cascade experiments reported by Godwin serve to augment these analyses. Additional data on swept rotors are available (Mohammad et al., 1977; Mikkelson et al., 1984; Dittmar et al., 1981, 1982, 1983; Mitchell and Mikkelson, 1982; Block, 1984).

Spanwise boundary layer flow as affected by sweep will influence fluid turning in tip regions and modify total pressure losses. Here again, the work of Adkins and Smith should be useful in estimating changes in deviation and loss associated with viscous manifestations of sweep. It is expected, however, that these viscous influences will be secondary to the sweep-induced loss of flow turning and the induced downwash.

Modeling

The distribution and magnitude of blade sweep angles in this work are based on the work of Kerschen and Envia (1983, 1984, 1986). They analyzed the interaction between convected turbulent disturbances and the airfoil leading edge. Figure 5 illustrates the concepts that follow. By employing airfoil sweep, destructive interference occurs between acoustic pressures generated at adjacent spanwise locations (on the scale of the turbulent disturbance) on the same airfoil. Sufficient phase variation in the affected region produces exponentially decaying rather than propagating wave forms. For a mean flow Mach number less than about 0.5, moderate values of sweep (less than 30 deg) will result in a cutoff of the interaction noise propagation when an infinite airfoil is being considered. This infinite span cutoff occurs when a critical value of sweep angle α is selected by $\alpha_{cr} = \tan^{-1}(M_R)$ where M_R is the blade relative Mach number, if the gust or disturbance is aligned with the direction of mean motion. For airfoils of finite span, cutoff is incomplete, particularly at lower frequencies, due to end effects leading to localized incoherent radiation. The effectiveness of the sweep in achieving cutoff is also materially affected by the orientation of the convected disturbance to the direction of motion of the airfoil section. Here the critical angle is expressed as

$$\alpha_{cr} = \tan^{-1}\left[M_R\sqrt{1+\tan^2\theta} - \tan\theta\right]$$

where θ is the angle by which the disturbance is misaligned from the direction of mean motion. When the upwash/downwash components of the disturbance are aligned normal to the direction of motion or skewed ahead so as to increase effective sweep, best cancellation is achieved. With increasing misalignment such that effective sweep is reduced, considerably larger sweep angles are required to achieve substantial noise reductions. For example, with $M_R = 0.35$, values of 40 to 50 deg are required to obtain good noise reductions of lower frequencies and misaligned disturbances. Further extensions of the analysis (Envia and Kerschen, 1986) indicate that in a comparatively random field of disturbances,

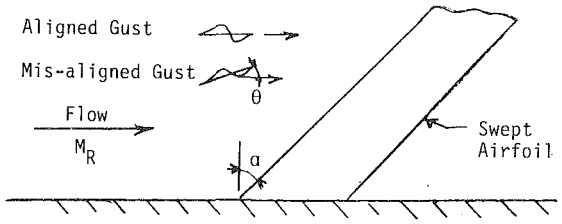

Fig. 5 Kerschen's model for a convected gust approaching a swept airfoil

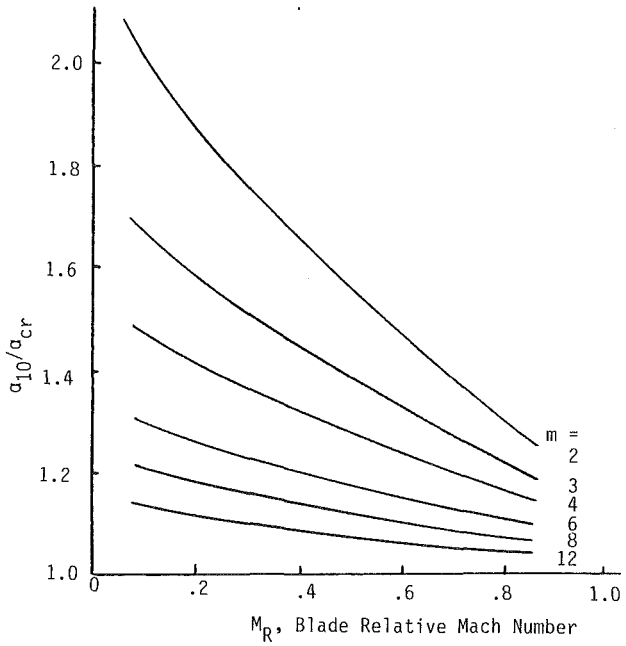

Fig. 6 Approximate envelope curves for 10 dB suppression of excess noise with finite span

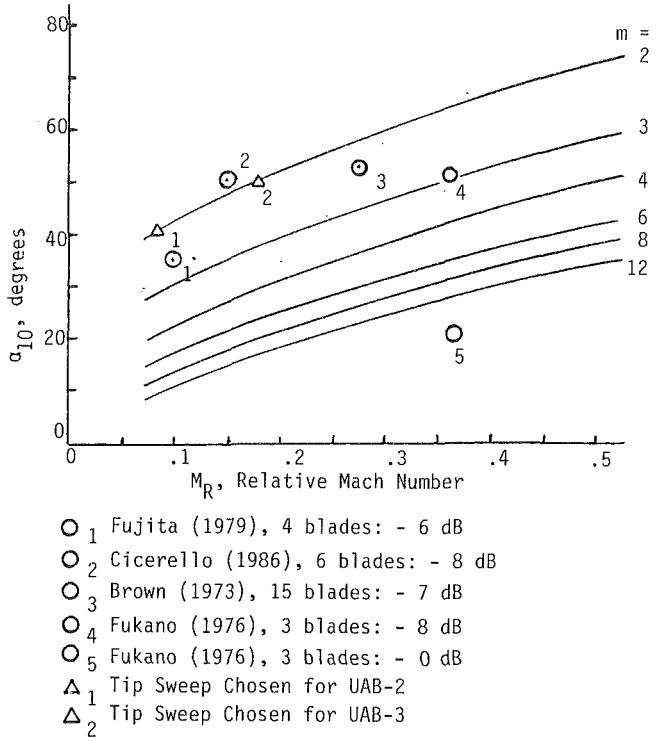

Fig. 7 Estimated envelope curves for sweep angles required for 10 dB reduction of a given mode (*m*); experimental results shown for perspective

sweep angles will have to exceed the ideal α_{cr} by a factor of 2 to 4 or more if reductions of noise from this source in the range of 10 dB are to be realized.

The influence of blade relative Mach number on these results follows the behavior suggested by Hanson (1984) in that the sweep angles required to achieve a significant reduction of noise at low M_R become proportionately much larger than the ideal α_{cr}. The examples of Kerschen et al. have been extended in this work to include the influence of M_R on suppression of the amplitude of the propagation strengths of the various wave number modes ($m = 1, 2. . .$) (Richards and Mead, 1968) using progressively larger sweep angles. The ratio of the maximum modal amplitude at values of α for fixed M_R and m were normalized by the zero sweep values. These values were investigated to determine the ratio (α_{10}/α_{cr}), which would provide a 10 dB reduction in the noise actually propagated in that mode. Figure 6 shows these results as envelope curves of (α_{10}/α_{cr}) versus M_R for $m = 2, 3, 4, 6, 8$, and 12. Proportionately higher angles of sweep are required at lower values of M_R, particularly for the lower mode numbers (lower frequency noise). These results may be modified to include the effect of adversely oriented disturbances up to 30 deg from a radial orientation as shown in Fig. 7. Actual required values of sweep angle decrease somewhat with decreasing M_R but are still comparatively large at $M_R = 0.1$ with $m = 2$: $\alpha_{10} = 42$ deg.

The swept-blade fans of Fukano (1986b), Fujita (1979), Brown (1975), and Cicerello (1986) are all experimentally successful fans in terms of significant levels of noise reduction. The published data on these fans are superposed on the estimated curves shown in Fig. 7. The points follow roughly along the curve between $m = 2$ and 3. The notable exception, Fukano's fan with a linearly skewed blade axis, lies well below the others but was totally unsuccessful in reducing noise.

For application to fan blades, it was proposed to sweep blade leading edges forward so that the radially local sweep angle should be equal to values of α_{10} based on local M_R and the curves in Fig. 7. In order to assure significant noise reduction in the preliminary testing, the values associated with $m = 2$ (and near the existing data) were conservatively chosen.

A general design procedure for the aerodynamic blading layout consists of calculation of an axisymmetric solution and a blade-to-blade solution. The three-dimensional flow produced by adding the results is called the primary flow and the inclusion of geometric sweep will produce a secondary flow. There is a general tendency for the flow not to remain on axisymmetric streamsurfaces even though no trailing vortex sheets occur because of these geometric differences. Following the arguments of Lewis and Hill (1971) and Smith and Yeh (1963), this streamsurface views the blade shapes that it crosses at a sweep angle λ. The flow direction makes an angle with the meridional direction, which has the axisymmetric stream surface cutting across the "apparent" blade chord of $c/\cos\lambda$. It is in this cross section that the correct fluid outlet angle can be calculated.

The difference between the "conventional method" of using the blade shapes viewed on a surface parallel to the axis to calculate the fluid deflection angle versus the correct method of using the actual blade shapes at the sweep angle (the "projection" method) shows that the conventional methods predict a smaller fluid outlet angle or greater fluid turning than the projection method. This is a general result for cascades without end constraints: Sweep tends to lessen the effect of a given cascade section in turning the flow.

For the blade-to-blade step one works with the flow on the axisymmetric streamsurface, but views this flow by looking parallel to the blade stacking line. The blade-to-blade calculations use cascade data (from the axisymmetric solution) in

conjuction with the blade geometry and flow angles of this spanwise projection (NASA, 1965).

By restricting attention to geometries with a cylindrical annulus, calculations of the fluid angles and the projected solidity can be simplified somewhat from the derivations of Smith and Yeh (1963).

Smith and Yeh (1963) also note that in an infinite-span swept cascade the fluid traversing the pressure side of a blade will move a greater distance in the spanwise direction than the fluid traversing the blade's suction side. If a hub (or casing) surface were present, these unequal movements could not occur and the flow pattern in the vicinity of the hub (or casing) would deviate from the infinite-span result. A downwash velocity perturbation, which is induced by a typical blade's vorticity and by the vorticities of all the other blades and image blades in the cascade required to represent endwall effects, can be calculated based on flow induced by kinked bound vortex lines. Smith and Yeh (1963) have developed a polynomial equation to approximate the downwash velocity perturbation to the main flow because of sweep; it is these results that are applied to low-speed axial fans in this work.

It is shown that the downwash velocity's influence on the blade camber line will increase the angle of attack because the downwash is always positive and will move the point of maximum camber forward because the camber line curvature is proportional to the chordwise rate of increase of the downwash velocity. When the sweep is negative (forward-swept), opposite conclusions about the angle of attack and maximum camber point apply. In almost all cases downwash decreases linearly to zero as distance from an endwall is increased.

At several points along the chord for each axisymmetric streamsurface the local angles β and η that apply for that streamsurface can be calculated to provide the stagger angles required. Equations for aerodynamic sweep (λ), projected chord (c), and projected blade spacing (s) provide the other important parameters as well as the correct solidity (σ) to use when designing the blade shape.

The methods of computation have been implemented into computer codes for axial fans (Wright, 1987). It was necessary to add two new arrays to the input files, which provide the required information on radial distributions of geometric sweep η, and the dihedral angle μ (illustrated in Fig. 8). For off-design analysis of a known geometry these arrays are simply added to the geometric input file. For purposes of design they must be stipulated beforehand based on the results of the acoustics study.

Those changes to blade pitch angle distributions associated with sweep-induced downwash have a tendency to cause near singularities in pitch-angle distributions at the hub and tip endwalls, and some judgments seems to be required in order to avoid bizarre geometry very near the blade ends. This effect in the present design work has been handled by "smoothing off" the pitch angle distributions generated by the computer to avoid sharp kinking of the blade surfaces and the codes have been modified to incorporate the smoothing. Figure 8 illustrates the method of blade layout and section configuration used in this work.

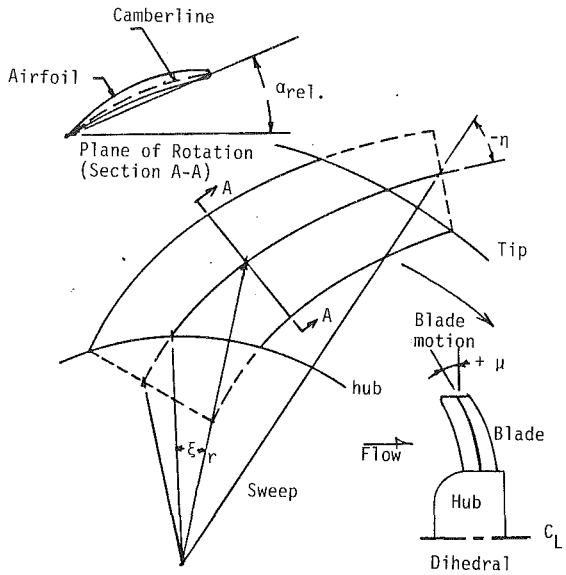

Fig. 8 Layout of blade stacking line with typical airfoil shown

Experiment

In order to evaluate the ability of the theory and the modified computer codes to provide blade design parameters and to predict performance correctly, a limited series of tests was planned. A "Baseline" fan was designed to provide a static pressure rise of 1.0 in. W.G. at 1500 ft^3/min flow rate with the fan running at 2500 rpm. The Baseline fan was designed with zero values of η and μ (no sweep, no dihedral) to be mounted and run in a heat-exchange system. Geometric details of this layout (UAB-1) are given in Table 1, and it may be noted that the fan design is a fairly conservative one, having eight blades of generous chord with a comparatively large hub-to-tip diameter ratio (55%).

Two other fans, of successively larger geometric sweep angles, were designed. These fans had zero dihedral ($\mu = 0$) and values of η corresponding to a 10 dB noise reduction at blade tip Mach number values of $M_T = 0.171$ (UAB-3) and 0.085 (UAB-2). These Mach numbers correspond to critical cutoff speeds of $N = 3000$ rpm and 1500 rpm, respectively, for $m = 2$ as shown in Fig. 3. The designs were constrained to yield the same computed performance values as the zero-sweep blade. Thus, the models were laid out to check on the theory for generating blade geometric parameters as functions of sweep, and to provide an evaluation of adequate sweep angles to suppress the excess noise associated with turbulence ingestion. Details of these two fans are given in Table 1 and are illustrated in the photographs of Fig. 9.

The test stand used in this work is shown schematically in Fig. 10. It consists of (1) a supply blower with a volume flow rate control damper, (2) a flow metering chamber employing ASME long-radius nozzles of 6-in. diameter, (3) a settling section for entry of the flow into the test fan, and (4) the test stand assembly itself. The chamber is equipped with piezometer rings for monitoring pressure drop across the nozzle plane and for determining the static pressure at the test fan inlet. The pressure-drop data across the nozzles are combined with wet and dry temperature measurements, barometric pressure measurements, and nozzle discharge coefficient calculations (as a function of nozzle throat Reynolds number) to calculate volume flow rate through the test fan. Pressure rise is calculated from the suppression of inlet static pressure and the downstream discharge to ambient conditions. Based on the accuracies of nozzle diameters, calculation of discharge coefficients, manometer resolution (0.001 in. WG) and density calculation, flow rate and pressure rise determinations are estimated to be accurate within $\pm 1/2$ percent at design point performance. The speed of the fan driver motor was measured with a magnetic proximity pickup coupled to an integrating digitizer circuit and monitored with a stroboscope tachometer. Errors in speed (and steadiness) were estimated at about $\pm$ 2 rpm (0.1 percent at test speeds). Power was provided to the 0.5 kW d-c motor through a variable a-c transformer connected to rectifier banks with amperage and voltage output meters. The drive motor and power supply were calibrated with a fan of

Table 1 Blade properties

r (in.)	α_{rel} (degrees)			ξ (degrees)			$-\eta$ (degrees)			σ	φ_c (degrees) camber			t/c %
All	-1	-2	-3	1	-2	-3	-1	-2	-3	All	-1	-2	-3	All
4.00	38.2	38.5	40.0	0	0	0	0	35.3	40.9	.940	26.9	27.1	27.1	10.0
4.64	30.8	33.8	35.8	0	6.8	8.3	0	36.3	42.8	.762	18.2	19.7	19.7	9.6
5.27	26.2	31.0	33.0	0	12.2	15.0	0	37.2	44.8	.627	13.5	15.5	15.5	9.2
5.91	23.1	29.0	31.8	0	17.5	21.5	0	38.1	46.6	.522	11.5	13.3	13.3	8.8
6.55	21.6	28.5	31.0	0	22.5	27.9	0	39.1	48.4	.436	11.6	13.0	13.0	8.4
7.18	20.7	28.5	31.0	0	27.1	33.8	0	40.0	50.0	.366	12.7	13.9	13.9	8.0

Thickness Distribution on Circular Arc Camberline: 65A-OXX

-1 refers to UAB-1, etc.

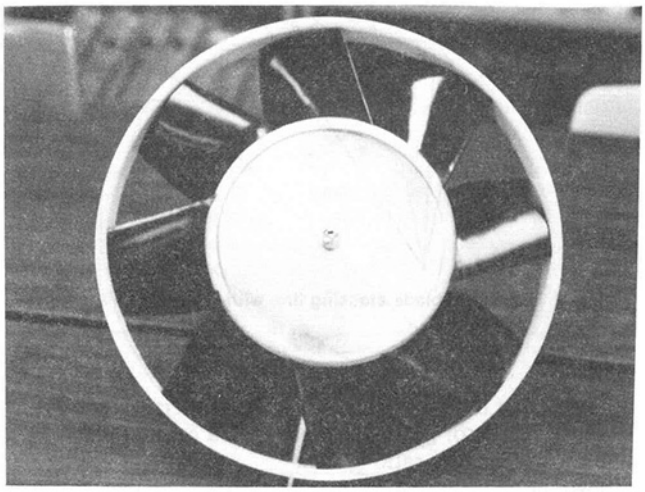

Fig. 9(a) The UAB-1 zero-sweep baseline fan

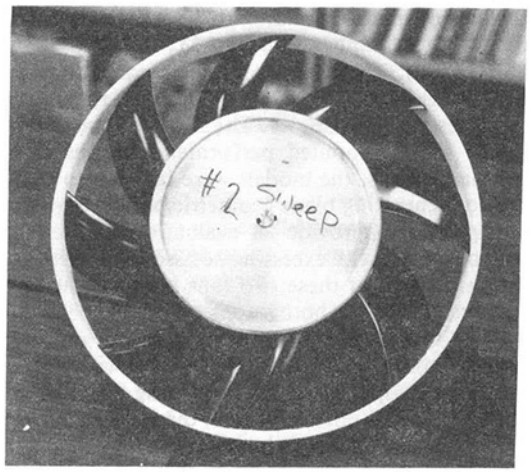

Fig. 9(b) The UAB-2 40-deg tip-sweep fan

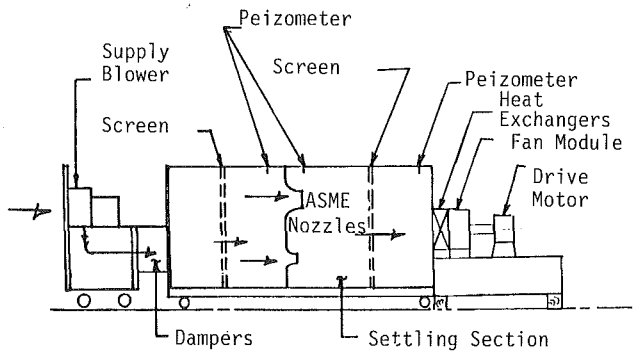

Fig. 10 Test stand for fan performance measurement

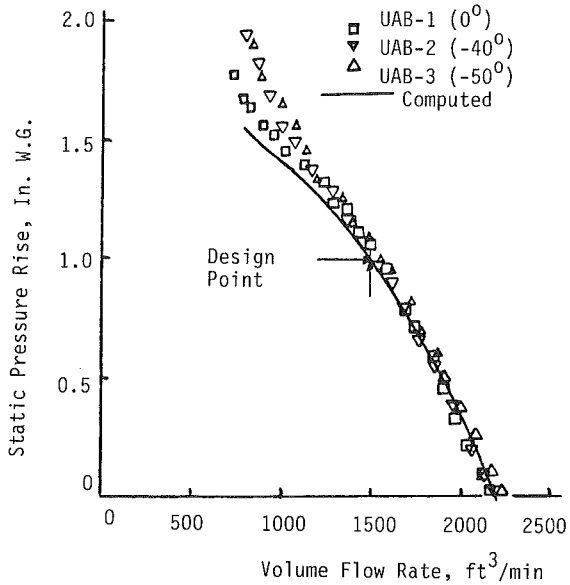

Fig. 11 Comparison of computed and tested performance for the model fans at 2500 rpm, standard density

accurately known performance and efficiency so that the meter readings could be used to estimate the fan shaft power absorption. Accuracy is considered to be only fair at ± 3 percent, leading to determination of efficiency within about ± 3 or 4 percent.

Figure 11 provides a summary of tested and computed performance for the fan models. Note that the heat exchanger was not in place for these tests so that overall fan performance could be evaluated. The design point values of $\Delta p_s = 1.0$ in. W.G. and 1500 ft^3/min are shown for comparison. Compared to the performance of the UAB-1 (unswept) at the design point, the UAB-3 performance is within about 2 percent in volume flow rate with the swept fan being the stronger of the two. The favorable effect of forward sweep on spanwise boundary layer flow probably accounts for the difference. It is noted that the forward swept fan retains a higher margin in performance as the flow rate of the fan is decreased and the sweep appears to delay any flow separation on the blading. This result is in agreement with the earlier work with forward-swept fan blading.

Figure 11 also shows the test results for the UAB-2 model with a geometric sweep angle of −40 deg at the blade tip. Performance at the design point again differs by about 2 percent in volume flow rate, with the −40 deg swept fan having slightly better performance than the zero degree model in this test.

The somewhat approximate efficiency results for these fans are summarized in terms of design point results: baseline − η_s = 0.42; − 50 deg sweep − η_s = 0.41; and the −40 deg sweep − η_s = 0.40. Given an error range of ± 3 percent, the results show no significant difference.

Noise testing was performed in an anechoic chamber owned by the project sponsor and sound measurements were taken with a single stationary microphone located on the fan centerline (upstream of the heat exchangers) at an axial distance of about two feet. SPL measurements are considered to be reasonably accurate (within ± 2 dB) but no attempt was made to determine overall sound power.

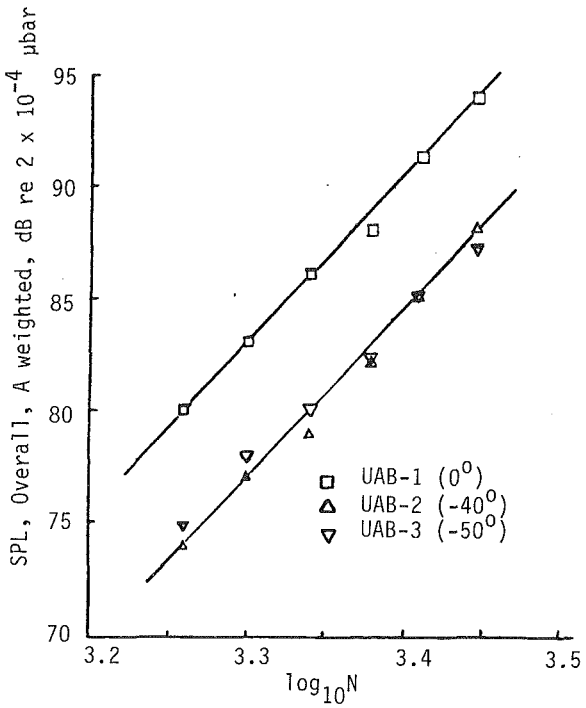

Fig. 12 Summary of overall noise data for the model fans

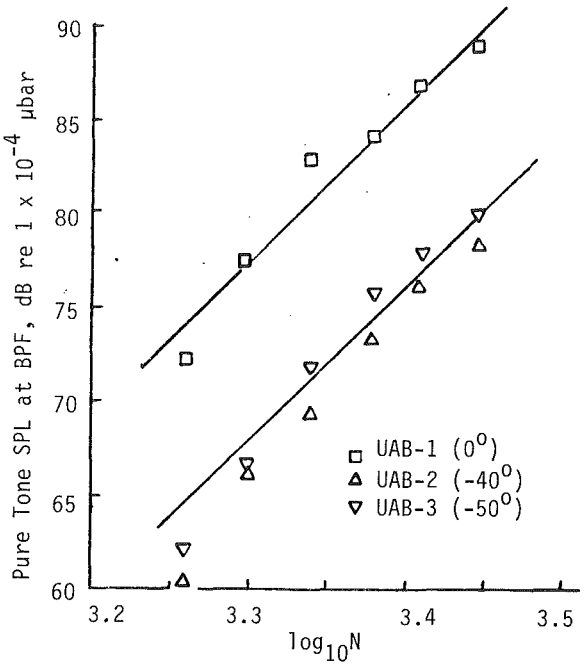

Fig. 13 Pure tone noise data at blade pass frequency for the model fans

Noise testing of the UAB model fans was carried out with each fan installed in the modular test stand and with a heat exchanger installed upstream of the fans to provide the requisite pressure drop and high-intensity, small-scale turbulence in the inflowing air.

Preliminary acoustic tests were run on the flow measurement test stand with the heat exchanger installed. With the fans running at 2500 rpm and pressure ahead of the heat exchanger balanced to barometric pressure (the design condition), the fans provided about 1450 ft^3/min volume flow rate. It was concluded that all of the fans were operating near their design flow conditions and that sound testing with the heat exchangers installed would provide a valid measure of acoustic performance.

The acoustic test results are summarized in Figs. 12 and 13. In Fig. 12, the overall sound pressure levels (SPL) weighted to A-scale values are presented for all three prototypes as a function of the logarithm of speed (in rpm). The baseline, zero-sweep fan shows a fairly low scatter array of data along a straight line with a slope of approximately 6.5. The swept-bladed fans are grouped roughly together along a line of similar slope with a reduction in magnitude of about 7 dBA or a little less. The overall reduction in noise attributable to sweep is thus close to the predicted levels. In Fig. 13, the results for the major pure-tone noise component at the blade passing frequency are shown. These data exhibit somewhat larger scatter but still group nicely, showing a reduction of blade-pass noise of about 10 dB as predicted by the theory. Basically, the noise test results follow the expectations growing from the work of Kerschen, Envia, and others.

Conclusions

The results of the aerodynamic testing indicate that the design procedure embodied in the computer programs correctly handles the influence of forward blade sweep in specifying the blade parameters. The method of Smith and Yeh (1963), currently being used in propeller design (Smith, 1987), is adequate for low-speed fan design in the present application. Acoustic criteria for blade sweep angles, based on the work of Kerschen and Envia (1983, 1986, 1984), are believed to be adequate for angle selection required to suppress excess noise due to turbulence ingestion. Acoustic measurements of the straight and swept-blade fans show significant noise savings, compared to the straight bladed baseline results, in the presence of highly turbulent inflow associated with an upstream heat exchanger.

It is planned that the existing models will be used for additional studies to provide increased understanding of several aspects of the aerodynamic performance of shrouded, swept-blade fans. In addition, it will be necessary to design, construct, and test several more model fans to explore the computation of minimum required blade-tip sweep angle.

References

Adkins, G. G., Jr., and Smith, L. H., Jr., 1982, "Spanwise Mixing in Axial-Flow Turbomachines," ASME *Journal of Engineering for Power*, Vol. 104, pp. 97-110.

Amiet, R. K., 1978, "Effect of the Incident Surface Pressure Field on Noise Due to Turbulent Flow Past a Trailing Edge," *Journal of Sound and Vibration*, Vol. 57, No. 2, pp. 305-312.

Amiet, R. K., 1976, "Noise Due to Turbulent Flow Past a Trailing Edge," *Journal of Sound and Vibration*, Vol. 47, No. 3, pp. 387-393.

Aravamudan, K. S., and Harris, W. L., 1979, "Low Frequency Broadband Noise Generated by a Model Rotor," *Journal of the Acoustic Society of America*, Vol. 66(2), pp. 522-533.

Block, P. J. W., 1984, "Installation Noise Measurements of Model SR and CR Propellers," NASA TM-85790.

Brown, N. A., 1973, *The Use of Skewed Blades for Ship Propellers and Truck Fans*, Bolt, Beranek and Newman.

Chou, Shau-Tak R., 1987, "A Study of Rotor Broadband Noise Mechanisms and Helicopter Tail Rotor Noise," Doctoral Thesis, Cornell University, Ithaca, NY.

Cicerello, A., and Gate, S.P.A., 1986, Private Communication.

Cummings, R. A., Morgan, W. B., and Boswell, R. J., 1972, "Highly Skewed Propellers," *Transactions of the SNAME*, Vol. 80, pp. 98-135.

Dittmar, J. H., Jeracki, R. J., "Additional Noise Data on the SR-3 Propeller," NASA TM-81736.

Dittmar, J. H., Stefko, G. L., and Jeracki, R. J., 1982, "Noise of the 10 Bladed, 40° Swept SR-6 Propeller in a Wind Tunnel," NASA TM-82950.

Dittmar, J. H., Stefko, G. L., and Jeracki, R. J., 1983, "Noise of the 10 Bladed, 60° Swept SR-5 Propeller in a Wind Tunnel," NASA TM-83054.

Envia, A., and Kerschen, E. J., 1986, "Noise Generated by Convected Gusts Interacting With Swept Airfoil Cascades," AIAA Paper No. 86-1872.

Envia, E., and Kerschen, E. J., 1984, "Noise Produced by the Interaction of a Rotor Wake With a Swept Stator Blade," AIAA Paper No. 84-2326.

Evans, B. J., 1971, "Effects of Free Stream Turbulence on Blade Per-

formance in a Compressor Cascade," Cambridge University Report No. CUED/A-Turbo/TR-26.

Fujita, H., 1979, "Noise Characteristics and Outlet Flow Field of Axial Flow Fans," *Noise-Con 79 Proceedings*, Purdue University, pp. 79–85.

Fukano, T., Senoo, Y., and Kodama, V., 1977, "Noise Generated by Low-Pressure Axial-Flow Fans – I: Modeling of the Turbulent Noise," *Journal of Sound and Vibration*, Vol. 50, pp. 53–74.

Fukano, T., Kodama, Y., and Takamatsu, Y., 1978a, "Noise Generated by Low-Pressure Axial Flow Fans – III: Effects of Rotational Frequency, Blade Thickness and Outer Blade Profile," *Journal of Sound and Vibration*, Vol. 56, No. 2, pp. 261–277.

Fukano, T., Kodama, Y., and Takamatsu, Y., 1978b, "Noise Generated by Low-Pressure Axial Fans – II: Effects of Number of Blades, Chord Length, and Chamber of Blades," *Journal of Sound and Vibration*, Vol. 50, 75–88.

Fukano, T., and Takamatsu, Y., 1986, "The Effects of Tip-Clearance on the Noise of Low Pressure Axial and Mixed Flow Fans," *Journal of Sound and Vibration*, Vol. 105, No. 2, pp. 291–308.

Gallus, H. E., Grollius, H., and Lambertz, J., 1982, "The Influence of Blade Number Ratio and Blade Row Spacing on Axial-Flow Compressor Stator Blade Dynamic Load and Stage Sound Pressure Level," ASME *Journal of Engineering for Power*, Vol. 104, pp. 633–641.

Godwin, W. R., 1999, "Effect of Sweep on Performance of Compressor Blade Sections as Indicated by Swept Blade Rotor, Unswept Blade Rotor and Cascade Tests," NACA TN-4062.

Hanson, D. B., 1980a, "Influence of Propeller Design Parameters on Far-Field Harmonic Noise in Forward Flight," *AIAA Journal*, Vol. 18, No. 11, pp. 1313–1319.

Hanson, D. B., 1980b, "Helicoidal Surface Theory for Harmonic Noise of Propellers in the Far Field," *AIAA Journal*, Vol. 18, No. 10, pp. 1213–1220.

Hanson, D. B., 1984, "Near-Field Frequency-Domain Theory for Propeller Noise," *AIAA Journal*, Vol. 23, No. 4, pp. 499–504.

Kerschen, E. J., 1983, "Noise Generation by a Finite Span Swept Airfoil," AIAA Paper No. 83-0768.

Kim, Y. N., and George, A. R., 1982, "Trailing Edge Noise from Hovering Rotors," *AIAA Journal*, Vol. 20, No. 9, pp. 1167–1174.

Lewis, R. I., and Hill, J. M., 1971, "The Influence of Sweep and Dihedral in Turbomachinery Blade Rows," *Journal of Mechanical Engineering Science*, Vol. 13, No. 4.

Longhouse, R. E., 1978, "Control of Tip-Vortex Noise of Axial Flow Fans by Rotating Shrouds," *Journal of Sound and Vibration*, Vol. 58, No. 2, pp. 201–214.

Metzger, F. B., and Rohrbach, C., 1986, "Benefits of Sweep for Advanced Turboprops," *AIAA Journal of Propulsion and Power*, Vol. 2, No. 6, pp. 534–540.

Mikkelson, D. C., Mitchell, G. A., and Bober, L. J., 1984, "Summary of Recent NASA Propeller Research," NASA TM-83733.

Mitchell, G. A., and Mikkelson, D. C., 1983, "Summary and Recent Results From the NASA Advanced High-Speed Propeller Research Program," NASA TM-82891.

Mohammad, K. P., and Raj, D. P., 1977, "Investigations on Axial Flow Fan Impellers With Forward Swept Blades," ASME Paper No. 77-FE-1.

NASA, 1965, "Aerodynamic Design of Axial-Flow Compressors," NASA SP-36.

Richards, E. J., and Mead, D. J., 1968, *Noise and Acoustics in Aeronautics*, J. Wiley, New York, pp. 228–230.

Smith, L. H., Jr., 1987, "Unducted Fan Aerodynamic Design," ASME JOURNAL OF TURBOMACHINERY, Vol. 109, pp. 313–324.

Smith, L. H., Jr., and Yeh, H., 1963 "Sweep and Dihedral Effect in Axial-Flow Turbomachinery," ASME *Journal of Basic Engineering*, Vol. 85, pp. 401–416.

Wright, S. E., 1976, "The Acoustic Spectrum of Axial Fans," *Journal of Sound and Vibration*, Vol. 45 (2), pp. 165–223.

Wright, T., and Ralston, S., 1987, "Computer Aided Design of Axial Fans Using Small Computers," *ASHRAE Transactions*, Vol. 93, Part 2.

Wright, T., Baladi, J. Y., and Hackworth, D. T., 1985, "Quiet Cooling System Design for a Traction Motor," ASME Paper No. 85-DET-137.